

AGARD-CP-454

AD-A221 594

AGARD

ADVISORY GROUP FOR AEROSPACE RESEARCH & DEVELOPMENT

7 RUE ANCELE 92200 NEUILLY SUR SEINE FRANCE

AGARD CONFERENCE PROCEEDINGS No.454

Atmospheric Propagation in the UV, Visible, IR and MM-Wave Region and Related Systems Aspects

DISTRIBUTION STATEMENT A

Approved for public release;
Distribution Unlimited

DTIC
ELECTE
MAY 17 1990
S a E D

NORTH ATLANTIC TREATY ORGANIZATION



This Document
Reproduced From
Best Available Copy

DISTRIBUTION AND AVAILABILITY
ON BACK COVER

90 05 16 188

NORTH ATLANTIC TREATY ORGANIZATION
 ADVISORY GROUP FOR AEROSPACE RESEARCH AND DEVELOPMENT
 (ORGANISATION DU TRAITE DE L'ATLANTIQUE NORD)



AGARD Conference Proceedings No.454
 ATMOSPHERIC PROPAGATION IN THE UV, VISIBLE, IR
 AND MM-WAVE REGION AND RELATED SYSTEMS ASPECTS

| | |
|--------------------|-------------------------------------|
| Accession For | |
| NTIS CRA&I | <input checked="" type="checkbox"/> |
| DTIC TAB | <input type="checkbox"/> |
| Unannounced | <input type="checkbox"/> |
| Justification | |
| By | |
| Distribution/ | |
| Availability Codes | |
| Dist | Avail and/or Special |
| A-1 | |

THE MISSION OF AGARD

According to its Charter, the mission of AGARD is to bring together the leading personalities of the NATO nations in the fields of science and technology relating to aerospace for the following purposes:

- Recommending effective ways for the member nations to use their research and development capabilities for the common benefit of the NATO community;
- Providing scientific and technical advice and assistance to the Military Committee in the field of aerospace research and development (with particular regard to its military application);
- Continuously stimulating advances in the aerospace sciences relevant to strengthening the common defence posture;
- Improving the co-operation among member nations in aerospace research and development;
- Exchange of scientific and technical information;
- Providing assistance to member nations for the purpose of increasing their scientific and technical potential;
- Rendering scientific and technical assistance, as requested, to other NATO bodies and to member nations in connection with research and development problems in the aerospace field.

The highest authority within AGARD is the National Delegates Board consisting of officially appointed senior representatives from each member nation. The mission of AGARD is carried out through the Panels which are composed of experts appointed by the National Delegates, the Consultant and Exchange Programme and the Aerospace Applications Studies Programme. The results of AGARD work are reported to the member nations and the NATO Authorities through the AGARD series of publications of which this is one.

Participation in AGARD activities is by invitation only and is normally limited to citizens of the NATO nations.

The content of this publication has been reproduced directly from material supplied by AGARD or the authors.

Published March 1990

Copyright © AGARD 1990
All Rights Reserved

ISBN 92-835-0548-4



*Printed by Specialised Printing Services Limited
40 Chigwell Lane, Loughton, Essex IG10 3TZ*

THEME

Atmospheric propagation of electromagnetic waves at frequencies above 30 GHz, i.e. millimeter (MM) waves and infra-red (IR), visible and to some extent also ultra-violet (UV) radiation, is of importance to many current and future military applications. Propagation phenomena affect and often limit navigation, communications, surveillance, search, target acquisition, fire control, autonomous weapons guidance, kill assessment, countermeasures and medium to high power laser applications.

Recent advances in components and technology have prompted extensive studies and novel applications in the above wavelength region. Specifically, second generation infra-red detector technology, smart image processing, as well as active coherent detection systems, i.e. millimeter wave and laser radars, have required dedicated propagation studies, including much longer ranges over land and sea, multiple scattering effects and especially turbulence induced systems limitations.

An exchange of information between scientists and engineers involved in research and development in this wavelength region will benefit further development of systems and explore new areas of research as well as military and civilian applications. The following topics were discussed:

- 1 — Propagation measurements;
- 2 — Propagation models;
- 3 — Sensing of the propagation environment;
- 4 — System aspects and performance modelling;
- 5 — Countermeasures.

The term propagation included atmospheric absorption, scattering, path radiance effects, turbulence effects and blooming, as created by the ambient atmosphere and by the battle-field effects. The term sensing covered in-situ as well as remote techniques. Systems performance modelling and countermeasures concentrated on topics which are directly related to those propagation effects.

* * *

La propagation des ondes électromagnétiques à des fréquences supérieures à 30 GHz, c'est à dire les ondes millimétriques (MM) et l'infrarouge (IR), les rayonnements visibles et dans une certaine mesure ultra-violet, a de l'importance pour bon nombre d'applications militaires actuelles et futures. Les phénomènes de propagation ont une influence qui est souvent limitative sur la navigation, les télécommunications, la surveillance, la détection, l'acquisition de la cible, la conduite de tir, le guidage des missiles autonomes, les prévisions de destruction, les contremesures et les applications des lasers de moyenne à haute puissance.

Les progrès réalisés dernièrement dans le domaine de la technologie des composants ont amené des études importantes, lesquelles ont débouché sur des applications novatrices dans la gamme de fréquence citée ci-dessus. En particulier, la technologie de la deuxième génération des capteurs infra-rouges, le traitement intelligent des images ainsi que les systèmes actifs de détection cohérente, c'est à dire les radars à laser et les radars à ondes millimétriques, ont exigé la réalisation d'études spécifiques à la propagation, qui tiennent compte de portée beaucoup plus grandes au-dessus de la terre et de la mer, des effets multiples de diffusion et les limitations imposées aux systèmes par la turbulence atmosphérique.

Un échange d'informations entre les scientifiques et ingénieurs travaillant dans ce domaine favorise le développement ultérieur des systèmes en question tout en permettant d'examiner de nouvelles possibilités de recherche et des applications civiles et militaires. Les sujets suivants furent abordés:

- 1 — La mesure de la propagation;
- 2 — La modélisation de la propagation;
- 3 — La détection du milieu de propagation;
- 4 — Les aspects des systèmes et la modélisation des performances;
- 5 — Les contremesures.

Le terme "propagation" comprend les notions suivantes, l'absorption atmosphérique, la diffusion, les effets de la luminance énergétique selon le parcours, les effets de la turbulence et l'efflorescence, créés par l'atmosphère ambiante et par les effets du champ de bataille.

Le terme "détection" comprend ici les techniques de détection in situ aussi bien que la télé-détection. La modélisation des performances de systèmes et les contremesures concernent principalement des sujets ayant un rapport direct avec les effets de la propagation cités plus haut.

ELECTROMAGNETIC WAVE PROPAGATION PANEL OFFICERS

Chairman: Prof. C.Goutelard
Directeur LETTI
Université Paris-Sud
9, Avenue de la Division Leclerc
94230 Cachan
France

Deputy Chairman: Ir H.Vissinga
van Kempenstraat 30
2252 VH Voorschoten
Netherlands

TECHNICAL PROGRAMME COMMITTEE

CHAIRMEN

Dr D.Höhn
Direktor, Forschungsinstitut für Optik
Schloß Kreßbach
D-7400 Tübingen
Federal Republic of Germany

Dr J.H.Richter
Head, Ocean and Atmospheric Sciences Division
Naval Ocean Systems Center
Code 54
San Diego, 92152-5000
United States

MEMBERS

Prof. Dr J.B.Andersen
Institut for Elektroniske Systemer
Aalborg Universitet
DK-9000 Aalborg
Denmark

Dr J.E.A.Selby
Grumman Corporate Research Center
MS — AO8 — 35
S. Oyster Bay Road
Bethpage, NY 11714
United States

Dr J.Fritz
ONERA
BP 72
92322 Chatillon Cedex
France

Dr F.E.Niles
Atmospheric Sciences Laboratory
White Sands Missile Range
NM 88002-5501
United States

Dr H.M.Lamberton
Royal Signal and Radar Establishment
EM1
Malvern Works WR14 3PS
United Kingdom

Dr P.L.Roney
Defence Research Establishment
Valcartier
PO Box 8800
Courcellette, Quebec GOA 1R0
Canada

Dr C.W.Lamberts
Physics and Electronics Laboratory
TNO, (Physics Group)
Oude Waalsdorperweg 63
2597 AK Den Haag
Netherlands

ELECTROMAGNETIC WAVE PROPAGATION PANEL EXECUTIVE

From Europe
L. Col. P.A.Brunelli
AGARD — EPP Executive
7, rue Ancelle
92200 Neuilly sur Seine
France

From USA and Canada
AGARD — NATO
ATTN: EPP Executive
APO New York 09777

CONTENTS

| | Page |
|-------------------------------|-----------|
| THEME | iii |
| TECHNICAL PROGRAMME COMMITTEE | iv |
| PREFACE | viii |
| | Reference |

SESSION I — PROPAGATION MEASUREMENTS (A)

Session Chairman: Dr Roney

| | |
|--|----|
| A SURVEY OF THE MARITIME-AEROSOL DATA COLLECTED AT SOUTH UIST AND THE IMPLICATIONS FOR THE LOWTRAN MARITIME AEROSOL MODEL by N.P.Tolliday, M.H.Smith, P.M.Park and I.E.Consterdine | 1 |
| L'ATMOSPHERE MARINE MEDITERRANEE ET SES EFFETS SUR LES AEROSOLS ET LA TRANSMISSION INFRAROUGE (The Mediterranean Marine Environment and its Effects on Aerosols and Infrared Transmission) par M.Tanguy | 2 |
| Paper 3 (withdrawn) | |
| NEW SPECTRAL FEATURES OF STRATOSPHERIC TRACE GASES by A.Goldman, F.J.Murcray, R.D.Blatherwick, F.H.Murcray, J.J.Kosters, D.G.Murcray and C.P.Rinsland | 4 |
| MINIMIZING THE EFFECTS OF THE ATMOSPHERE IN THE OBSERVATION OF ULTRAVIOLET RADIATION by A.V.Dentamaro, C.G.Stergis and V.C.Baisley | 5 |
| ULTRAVIOLET PROPAGATION IN THE PRESENCE OF FLUORESCING AEROSOLS by J.B.Gillespie, Y.Yee, D.Rosen and D.R.Brown | 6* |

SESSION I — PROPAGATION MEASUREMENTS (B)

Session Chairman: Prof. Andersen

| | |
|--|----|
| SCINTILLATION OF MILLIMETER-WAVE INTENSITY AND PHASE CAUSED BY TURBULENCE AND PRECIPITATION by R.J.Hill, S.F.Clifford, R.J.Lataitis and A.D.Sarna | 7 |
| MILLIMETRIC, INFRARED AND OPTICAL PROPAGATION STUDIES OVER A 500M PATH by C.J.Gibbins | 8 |
| EVAPORATION DUCT EFFECTS AT MILLIMETER WAVELENGTHS by K.D.Anderson | 9 |
| REPORT ON STC/TECHNISCHE UNIVERSITEIT (TU) DELFT EXTREMELY HIGH FREQUENCY (EHF) RADIO RELAY STUDY by N.P.Mansfield, L.P.Ligthart, R.J.Niemeljer and J.S.van Sinttruyen | 10 |
| Paper 11 (withdrawn) | |
| MM-WAVE REGION PROPAGATION EXPERIMENTS BY SATELLITE by P.Ricci and A.Florio | 12 |

SESSION II — PROPAGATION MODELS (A)

Session Chairman: Dr Selby

| | |
|---|----|
| LOWTRAN 7: STATUS, REVIEW AND IMPACT FOR SHORT-TO-LONG-WAVELENGTH INFRARED APPLICATIONS by F.A.Kueizys, G.P.Anderson, E.P.Shettle, L.W.Abreu, J.H.Chetwynd Jr, J.E.A.Selby, W.O.Gallery and S.A.Clough | 13 |
|---|----|

| | Reference |
|--|-----------|
| PROPAGATION ENVIRONMENTS, EFFECTS, AND DECISION AIDS by F.E.Niles, M.G.Heaps, R.C.Shirkey, L.D.Duncan and M.A.Seagraves | 14 |
| MODELS OF AEROSOLS, CLOUDS AND PRECIPITATION FOR ATMOSPHERIC PROPAGATION STUDIES by E.P.Shettle | 15 |
| INTERPRETING METEOROLOGICAL DATA REPORTS FOR LOWTRAN 6 NAVY AEROSOL MODEL EXTINCTION CALCULATIONS by A.J.Beaulieu | 16 |
| THE NAVAL OCEANIC VERTICAL AEROSOL MODEL: PROGRESS REPORT by S.G.Gathman, G.de Leeuw, K.L.Davidson and D.R.Jensen | 17 |
| MODELLING MILLIMETER-WAVE PROPAGATION EFFECTS IN THE ATMOSPHERE by H.J.Liebe and G.A.Hufford | 18 |
| MODELLING OF OPTICALLY AND IR EFFECTIVE ATMOSPHERIC TURBULENCE by V.Thiermann and A.Kohnle | 19 |
| <u>SESSION II – PROPAGATION MODELS (B)</u> Session Chairman: Mr Christophe | |
| HIGH INTENSITY LASER BEAM INTERACTIONS WITH SINGLE DROPLETS by R.K.Chang and A.S.Kwok | 20 |
| INCLUSION OF CLOUDS AND RAIN IN ATMOSPHERIC SLANT PATH CALCULATIONS by C.W.Lui, M.W.P.Cann and R.W.Nicholls | 21 |
| INFRARED PROPAGATION IN THE AIR-SEA BOUNDARY LAYER by R.Larsen, K.A.Preedy and G.Drake | 22 |
| A TEMPERATURE-DEPENDENT REGULAR INFRARED BAND MODEL FOR ABSORPTION AND DISPERSION by P.L.Roney | 23 |
| Paper 24 (withdrawn) | |
| UV SPECTRAL SIMULATIONS USING LOWTRAN 7 by G.P.Anderson, F.X.Kneizys, E.P.Shettle, L.W.Abreu, J.H.Chetwynd, R.E.Huffman and L.A.Hall | 25 |
| MILLIMETER-WAVE PROPAGATION IN THE EVAPORATION DUCT by M.F.Levy and K.H.Craig | 26 |
| <u>SESSION III – SENSING OF THE PROPAGATION ENVIRONMENT</u> Session Chairman: Dr Lamberts | |
| LIDAR MEASUREMENTS OF THE OPTICAL PROPAGATION ENVIRONMENT by T.D.Wilkerson, U.N.Singh, A.Notari and W.C.Braun | 27 |
| LIDAR MEASUREMENT OF CONCENTRATION AND TURBULENCE IN BATTLEFIELD OBSCURANTS by B.T.N.Evans and G.Roy | 28 |
| CIRRUS CLOUD OPTICAL PROPERTIES MEASURED WITH THE UNIVERSITY OF WISCONSIN HIGH SPECTRAL RESOLUTION AND VOLUME IMAGING LIDARS by E.W.Eloranta and C.J.Grund | 29 |
| VERIFICATION OF KLETT'S METHOD BY COMPARISON OF LIDAR AND TRANSMISSOMETER MEASUREMENTS by W.Carnuth | 30 |
| TECHNIQUE FOR SELECTING AN AEROSOL MODEL USEFUL FOR INFRARED ATMOSPHERIC TRANSMITTANCE CALCULATIONS by H.G.Hughes | 31 |

| | Reference |
|---|-----------|
| HIGH-ALTITUDE ATMOSPHERIC CLOUD EFFECTS ON EO/IR SENSOR PERFORMANCE by E.E.Uthe and J.M.Livingston | 32* |
| RADAR SCATTEROMETRY AND POLARIMETRY AT 220 GHz by R.E.McIntosh and J.B.Mead | 33 |
| MILLIMETER-WAVE BISTATIC SCATTERING BY TERRAIN by F.T.Ulaby | 34 |
| MODELLING UV-VISIBLE RADIATION OBSERVED FROM SPACE by D.E.Anderson, Jr. and D.J.Strickland | 35 |

SESSION IV – SYSTEM ASPECTS AND PERFORMANCE MODELLING (A)

Session Chairman: Dr Lamberton

| | |
|--|-----|
| ATMOSPHERIC EFFECTS ON POTENTIAL TACTICAL HIGH ENERGY LASER SYSTEMS by H.J.Auermann | 36* |
| ATMOSPHERIC PERFORMANCE STATISTICS FOR IR BROAD-BAND AND LASER SYSTEMS BASED UPON OPAQUE DATA (N.U.) by D.Clement, D.H.Höhn, W.Jessen and A.Kohnle | 37* |
| CALCULATION OF IR PROPAGATION STATISTICS IN THE EASTERN ATLANTIC FOR SURVEILLANCE SYSTEM PERFORMANCE ASSESSMENT by J.M.Ridout | 38 |
| Paper 39 (withdrawn) | |
| ABSORPTION OF THE INFRARED RADIATION OF HOT EXHAUST PLUMES BY ATMOSPHERIC GASES by H.M.A.Schleijpen | 40* |
| PERFORMANCE OF AN IMAGING UV SENSOR SYSTEM FOR MISSILE WARNING AND GUIDANCE VERSUS COMPARABLE IR SYSTEMS by R.Dirscherl | 41* |
| Paper 42 (withdrawn) | |

SESSION IV – SYSTEM ASPECTS AND PERFORMANCE MODELLING (B)

Session Chairman: Dr Niles

| | |
|---|-----|
| COMPUTATION OF BROAD SPECTRAL BAND ELECTRO-OPTICAL SYSTEM TRANSMITTANCE RESPONSE CHARACTERISTICS TO MILITARY SMOKES AND OBSCURANTS USING FIELD TEST DATA FROM TRANSMISSOMETER SYSTEM MEASUREMENTS by W.M.Farmer, R.Davis, R.Laughman and W.Watkins | 43 |
| DYNAMIC CHANGES IN IMAGES AND SCENES DUE TO ENVIRONMENTAL FACTORS by W.Watkins, F.Krantowitz and S.Crow | 44* |
| EFFECT OF ATMOSPHERIC TURBULENCE ON ELECTRO-OPTICAL SYSTEMS by W.B.Miller, J.C.Ricklin and D.H.Marlin | 45 |
| ATMOSPHERIC MODELLING STUDIES: A MODELLING COMPARISON BETWEEN IR AND MILLIMETRIC ATMOSPHERIC PROPAGATION by A.R.Tooth | 46 |
| FORMULES DE CALCUL RAPIDE DE LA TRANSMISSION INFRAROUGE EXEMPLES DE CALCUL (Fast Method for Computing Infrared Transmission, Computation Examples) par A.M.Bouchardy and A.P.Jurchat | 47 |

* Printed in classified publication CP454 (Supplement).

PREFACE

With the symposium "Atmospheric Propagation in the UV, Visible, IR and MM-wave Region and Related Systems Aspects", the AGARD Electromagnetic Wave Propagation Panel (EPP) adhered to its practice of periodically reviewing the recent advances in this technical area. This field is still expanding and is of great importance to the development of modern systems and their most effective application. Atmospheric propagation is crucial to the performance of all systems operating from the UV to the MM-wave region because it limits their operational ranges, which depend on the prevailing environmental conditions and their history. In other cases, propagation effects permit specific applications, e.g., warning devices based on scattered radiation. The importance of such a symposium was already evident shortly after the call for papers by the large number of very appropriate contributions. The result was a stimulating meeting at Copenhagen, Denmark, 9-13 October 1989. The Conference proceedings contain all papers and following discussions. Volume one deals with the unclassified portion and volume two with the classified session of the meeting.

The contributions have shown, that within the last decade many atmospheric propagation problems relevant to electro-optical and laser systems, including battlefield effects, have been investigated experimentally and theoretically with such a quality, that quite sophisticated propagation codes and systems performance models are available for both armament oriented systems analyses and development of tactical decision aids. The symposium has also pointed out that still-developing, electro-optical and MM-wave technologies require additional, complex, propagation research efforts and studies for operationally-relevant systems performance analyses.

The following areas were identified as requiring future research:

- Transfer of information/images through the atmosphere in addition to studies related to the basic effects, such as emission, absorption, scattering, refraction and turbulence.
- Effects of complex backgrounds, e.g., atmospheric emission, specific cloud patterns, properties of the sea-air-environment.
- Propagation effects related to UV-applications.
- Propagation effects related to high power laser beams.
- Propagation and background effects related to space-to-ground observation tasks, in addition to the ground-to-ground and air-to-ground/ground-to-air scenarios over land and sea.
- Effects within optically dense media, e.g., multiple-scattering effects in clouds and smogs.

The above areas were either specifically addressed by contributions, or they were identified during the course of the presentations and discussions.

In summary, the symposium provided the intended review on the state-of-the-art in this field of systems-oriented atmospheric research, discussed experimental, modelling and theoretical aspects, and indicated clearly the most essential areas of current and future defence-oriented atmospheric research related to UV, visual, IR and MM-wave-systems.

Gratefully acknowledged are the cooperation and assistance received by the members of the Programme Committee and the session chairmen: Prof. Dr J.B.Andersen, Dr J.Fritz, Mr F.Christophe, Dr H.M.Lamberton, Dr. C.W.Lamberts, Dr F.E.Niles, Dr P.L.Roney and Dr J.E.A.Selby.

Appreciation is furthermore expressed to all who helped in the organization of the symposium and in the compilation of the Proceedings, to authors and contributors to discussions, to the host coordinators, to the AGARD staff, especially the EPP executive, Lt Col. P.A.Brunelli.

D.H.Höhn and J.H.Richter
Co-chairmen and editors

A SURVEY OF THE MARITIME-AEROSOL DATA COLLECTED AT SOUTH UIST AND THE IMPLICATIONS FOR THE LOWTRAN MARITIME AEROSOL MODEL

N P Tolliday, ARE Portsmouth
M H Smith, PM Park and
I E Consterdine
University of Manchester
Institute of Science and Technology
Manchester, England UK

SUMMARY

Over the period 1979 until 1980, Umist (University of Manchester Institute of Science and Technology) have been funded by ARE (MOD) Portsmouth to carry out a Maritime Aerosol Study. This paper is a survey of the results obtained and some comments on how well the data conforms to the LOWTRAN maritime aerosol model.

Aerosol loadings and spectral distributions have been measured, over numerous 2-4 week periods since 1979, at a coastal site on the island of South Uist, situated off north-west Scotland. Aerosol size distributions, covering the radius range 0.08 to 23.5 microns, were measured by Particle Measuring Systems optical particle counters, together with basic meteorological observations. Generally, these instruments were mounted on a 10 m tower situated at the head of a gently sloping, west-facing beach; the observations were shown to be representative of open ocean conditions for maritime air masses.

Two further field projects were conducted at this site during the Spring and Summer of 1986. The Spring project was characterised by an intense cyclone which gave rise to local wind speeds exceeding 40 m/s whilst, during the Summer, much calmer conditions prevailed with an extended period of very low wind speeds. Thus, data were obtained encompassing wind speeds from essentially zero to values in excess of 30 m/s.

These observations demonstrated that volumetric loadings of marine aerosol continue increasing for all measured wind speeds, contrary to earlier speculation suggesting a limit beyond 12-15 m/s.

The low wind speed period permitted the relaxation response of the atmosphere to be investigated, and the decay of the aerosol loadings, for various size categories, over this period was found to be consistent with a simple turbulent deposition model.

Variations in aerosol spectral shape with wind speed will be presented, and demonstrate that particulate volume and surface area are dominated by the larger particles for moderate and high wind speeds. The consequences of these findings for the LOWTRAN Maritime Aerosol Model and for atmospheric propagation at visible and infra red wavelengths are discussed.

1. INTRODUCTION

Sea-salt particles are injected into the marine boundary layer when bubbles, produced principally by whitecapping, burst at the sea surface. This aerosol production rate is primarily dependent upon the local wind speed, but is also influenced by other factors - eg wind speed history, fetch, water temperature, air-sea temperature difference^{1,2}, salinity³ and water contaminants⁴. This locally-produced aerosol (with particle radii generally exceeding 1 μ m) will be mixed with that already present in the atmosphere, consisting primarily of small particles ($r < 0.5\mu$ m) having residence times of several days which may have travelled hundreds of kilometres from continental or anthropogenic sources^{5,6,7}. Under strong wind conditions, this aerosol will be further supplemented by spindrift, comprising sea spray droplets torn directly from wave crests by the action of the wind and whose radii may extend to several tens of micrometres.

The aerosol observed at the site is the resultant of these production mechanisms and other dynamical processes. Changes in relative humidity cause shifts in aerosol spectral shape⁸, though these effects are generally not well pronounced under maritime conditions, where the size spectra show relatively little variation with particle radius. Also, observed aerosol concentrations are dependent upon atmospheric stability which influences their mixing and dispersal throughout the atmospheric boundary layer.

In addition to their role in the exchange of heat, moisture and momentum between ocean and atmosphere⁹, particles produced at the sea surface are of intrinsic interest for numerous reasons. Firstly, sea-salt particles form a major constituent of cloud condensation nuclei and the quantity and quality of such particles deposited on land may also be important in determining the physical and chemical characteristics of coastal soils and plants. Thus, measurements of aerosol loadings under a variety of meteorological conditions are directly relevant to global salt budgets¹⁰.

Secondly, atmospheric attenuation of radiation at visible and infra-red wavelengths may be substantially affected by these particles¹¹. Increasing wind speeds over the ocean surface lead not only to greater numbers of particles but, also are capable of producing and dispersing particles of larger sizes. Thus, at moderate and high wind

speeds, the combined surface area and volume loading of the suspended material will be dominated by particles with radii beyond $1/\mu\text{m}$ or so, in contrast with continental conditions where, generally, these parameters are governed by much smaller particles.

Finally, relationships between aerosol particles in the marine boundary layer and satellite-detected radiances have been explored¹² and suggest that, under specific conditions, satellite images may be used to monitor characteristics of the boundary layer such as optical depth and relative humidity variations. The more general problem of the influence of surface-generated sea-salt aerosol upon remote sensing of the sea surface characteristics and the atmospheric boundary layer properties would benefit from more detailed information regarding the production and dispersal of these particles.

2. AEROSOL OBSERVATIONS

Over the past decade, an extensive series of field investigations of atmospheric particulates, with radii from 0.08 to $23.5/\mu\text{m}$, have been conducted at the coastal site of Ardivachar Point on the island of South Uist, off the north-west coast of Scotland. The site, whose position and topography is illustrated in Figure 1, faces the North Atlantic ocean across a gently-sloping beach. A detailed description of the equipment and field site may be found in an earlier paper¹, together with the comprehensive analysis of 118 days' data from this site, gathered during 2 to 4 week periods between 1980 and 1983.

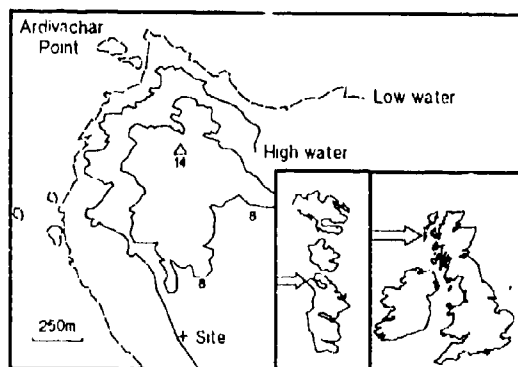


Figure 1. The topography of the site on South Uist.

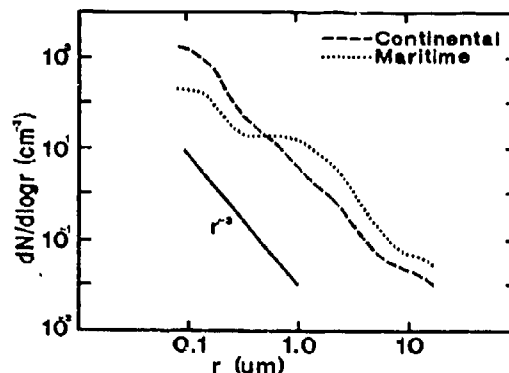


Figure 2. Comparison of continental and maritime spectra averaged for all 1980 and 1981 data.

In this work, and in subsequent studies, sampled air masses were split into continental and maritime groups on the basis of air trajectory analysis: confirmation of the validity of this synoptic method of air mass characterisation was provided by a supplementary technique involving the measurement of radon daughter product concentrations^{13,14}. Spectral number distributions from the earlier work, averaged separately over the entire maritime and continental air mass sampling periods, are presented in Figure 2. The mean meteorological conditions were broadly similar for the two air mass categories, as were the overall aerosol loadings, but the spectral shapes are clearly distinct. The data for the continental air approximates closely to the Junge r^{-3} power law, as illustrated in the figure. In the maritime case, the concentration of the smaller particles is greatly reduced whilst substantially greater numbers are present at larger sizes. Thus, the maritime aerosol may be regarded as a distribution in which the continental component has been uniformly depleted by loss mechanism, but to which a component of sea surface origin has been added.

Very little marine aerosol data has been collected at high wind speeds, to the extent that the quantity of sea salt in the atmosphere at wind speeds greater than 15 ms^{-1} is not known with any certainty. However, Meteorological Office data for the period 1960 to 1980 show that wind speeds greater than this value are far from uncommon over both the North and South Atlantic Oceans, and that hurricane-force winds may occur during any month. The earlier South Uist investigations suggested that the rate of increase of aerosol with wind speed decreased markedly above 14 ms^{-1} , and remained approximately level up to the upper limit of the data set at 19 ms^{-1} . Unfortunately, the comparative scarcity of data at these higher wind speeds left room for speculation and other workers have suggested wind speeds ranging from 12 to 15 ms^{-1} beyond which aerosol concentrations might be regarded as levelling off^{15,16}.

During 1986, two further field studies were conducted at Ardivachar Point utilising a similar, though not identical, experimental arrangement. Once again, aerosol size distributions, over the radius range from 0.08 to $23.5/\mu\text{m}$, were measured by means of Particle Measuring Systems (PMS) instruments, consisting of an ASASP-300 and an FSSP-100, together with basic meteorological parameters. These aerosol probes, kept pointing into wind by an automatic wind vane and servo system, were mounted on a 10 m tower, placed at the top of the west-facing beach, and were approximately 14 m above mean sea level. The earlier investigations had demonstrated that such measurements were representative of open ocean conditions for maritime air masses, with generally insignificant influence upon the aerosol measurements at this height from the usually weakly-developed surf zone¹⁷.

The first of these investigations¹⁸, conducted during March, was characterised by a depression which formed in the North Atlantic, deepened rapidly and passed directly over the site, giving rise to local wind speeds gusting beyond 40 ms^{-1} . Site wind speeds had increased steadily as the cyclone approached, reaching a maximum of about 30 ms^{-1} from the south before reducing to around 9 ms^{-1} as the 'eye' of the cyclone passed over. As this 'eye' moved on, the wind direction switched abruptly to the north-west and its speed rose rapidly over the next few minutes, until it was gusting to about 44 ms^{-1} . Although the violence of this storm caused power failures throughout the islands and, indeed, came close to destroying the measuring equipment, valid data was gathered for some portions of the high wind speed episode, thereby substantially extending the data set to wind speeds greater than 30 ms^{-1} .

During the second investigation, in August 1986, there was a period at the beginning of the study when the wind speed remained below 7 ms^{-1} for several days. The Beaufort sea state throughout this period was 1 or 2, with little or no whitecapping beyond the surf zone. This period was characterised by very low particle counts for all size categories and by extremely good visibilities, with islands situated up to 80 km away being clearly observed. Under such anticyclonic conditions, with slack air and low wind speeds, air mass trajectory analysis becomes very uncertain and site wind direction is generally a better indicator of the maritime or continental nature of the air mass. The validity of partitioning the data set on this basis was again verified by the radon counting technique (see Table 1). Toward the end of this study, wind speeds rose steadily under the influence of an approaching depression, overlapping the observations recorded during the previous study.

Table 1. Radon Data for Autumn 1986

| Date | Time | Radon Count | Wind Direction |
|------|------|-------------------|----------------|
| | GMT | pCm ⁻³ | °T |
| 16.8 | 1010 | 5.53 | --- |
| 16.8 | 1510 | 13.60 | --- |
| 17.8 | 1110 | 5.39 | --- |
| 17.8 | 1525 | 3.24 | 334 |
| 18.8 | 0915 | 5.40 | 298 |
| 18.8 | 1610 | 1.58 | 279 |
| 19.8 | 0915 | 12.27 | 20 |
| 19.8 | 1500 | 10.31 | 68 |
| 20.8 | 0850 | 1.70 | 44 |
| 20.8 | 1600 | 0.55 | 328 |
| 21.8 | 0926 | 1.41 | 58 |
| 21.8 | 1430 | 1.84 | 50 |
| 22.8 | 0945 | 7.45 | 46 |
| 22.8 | 1520 | 7.37 | 38 |
| 23.8 | 0915 | 7.45 | 16 |
| 23.8 | 1545 | 7.79 | 351 |
| 24.8 | 0925 | 3.75 | 54 |
| 24.8 | 1410 | 2.72 | 8 |
| 26.8 | 2015 | 8.65 | 359 |
| 27.8 | 0900 | 6.69 | 1 |
| 27.8 | 1530 | 3.14 | 352 |
| 27.8 | 2025 | 3.03 | 352 |
| 28.8 | 0825 | 1.31 | 8 |
| 28.8 | 1440 | 4.19 | 351 |
| 28.8 | 2000 | 2.00 | 339 |
| 30.8 | 0825 | 3.79 | 349 |
| 31.8 | 0920 | 1.40 | 211 |
| 31.8 | 1430 | 0.58 | 198 |
| 31.8 | 2000 | 3.22 | 273 |
| 1.9 | 0815 | 1.96 | 258 |

3. DATA ANALYSIS

3.1 Aerosol sampling instruments. There are several difficulties with data from PMS probes which must be considered if the introduction of errors into the data analysis is to be avoided. The problem of non-isotropic sampling was dealt with during data collection by keeping the probes oriented into wind. The problem of non-isokinetic sampling has been examined¹⁹ and the results show that the volume sampling rate approximately doubles when the wind speed equals the static ventilation rate of each instrument. The volume sampling rate of each instrument was corrected for wind speed effects, accordingly, in the data analysis presented herein.

The third difficulty with these devices is their multi-valued response for water droplets around $1 \mu\text{m}$ in size²⁰. One solution is to add the data into size bands which contain sufficient numbers of the original data channels to effectively smooth the discontinuities. A similar technique was applied in the analysis of the variation of aerosol loading with wind speed, presented in this paper, where the data are grouped into size bands as shown in Table 2.

Table 2. Grouping of Aerosol Data into Size Bands

| Size Band | Radius Range (μm) | Probe | Ranges | Channels |
|-----------|-----------------------------------|-------|--------|----------|
| 1 | 0.09 - 0.125 | ASASP | 3 | 4 - 10 |
| 2 | 0.125 - 0.25 | ASASP | 2 | 2 - 11 |
| | | | 3 | 11 - 15 |
| 3 | 0.25 - 0.5 | ASASP | 1 | 5 - 15 |
| 4 | 0.5 - 1 | FSSP | 3 | 2 - 3 |
| 5 | 1 - 2 | FSSP | 2 | 2 - 3 |
| | | | 3 | 4 - 7 |
| 6 | 2 - 4 | FSSP | 1 | 2 - 3 |
| | | | 2 | 4 - 7 |
| | | | 3 | 8 - 15 |
| 7 | 4 - 8 | FSSP | 0 | 3 - 5 |
| | | | 1 | 4 - 7 |
| | | | 2 | 8 - 15 |
| 8 | 8 - 16 | FSSP | 0 | 6 - 10 |
| | | | 1 | 8 - 15 |
| 9 | 16 - 23.5 | FSSP | 0 | 11 - 15 |

3.2 Variation of aerosol loadings with wind speed. In order to demonstrate the influence of wind speed on different sizes of particulates, the data were grouped into wind speed bins 1 ms^{-1} wide, and the averaged value of the concentration for each bin plotted. Only maritime data were included in this analysis, selected on the basis of the wind direction being between 190° and 300° . Graphs of particle concentration against wind speed are shown in Figure 3 for selected size bands. A typical range bar - one standard deviation long - is drawn for each size band: their extent is indicative not so much of errors in the experimental observations, but rather of the larger number of influences other than wind speed which affect the marine aerosol concentrations. It is interesting to note that, for particle above $4 \mu\text{m}$ radius, the increase in concentration does not level off at wind speeds of about 12 or 15 ms^{-1} . Indeed, for the largest size category, as the wind speed increases from 15 to 34 ms^{-1} , the concentration increases by a factor of about 4.

Table 3 presents relationships, derived by means of a simple weighted least-squares fitting procedure, showing the variation of both number concentration and particular volumetric loading with wind speed, for each of the size categories listed in Table 1. The smallest particles exhibit the least significant relationship with wind speed, which is reasonable given that the major source of them is often other than sea surface bubble bursting. Of the other size ranges, concentration of particles from 1 to $4 \mu\text{m}$ radius show less significant relationships with wind speed. This response is unlikely to be a result of the multivalued response mentioned above, as the data bins are large enough to integrate across this region. It is possibly due to these size bands falling between the two types of marine aerosol droplet - film drops and jet drops. The exact position of the divide is undetermined and possibly varies; results from a laboratory model breaking wave suggest film drops, although decreasing rapidly in number from the peak at sub-micrometre sizes, remain in the majority until about $7 \mu\text{m}$ radius, with jet drops providing an increasing proportion of the aerosol at larger sizes²¹. Analysis of field data²² puts the transition at about $1 \mu\text{m}$ radius, whilst other workers suggest that at 80 per cent relative humidity, $2 \mu\text{m}$ radius is more likely²³.

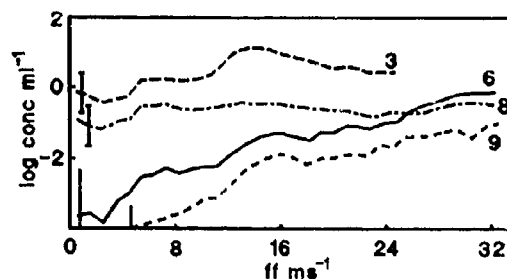


Figure 3. The increase in particle concentration with wind-speed ff for size bands as listed in Table 1.

Table 3. Linear Regression Coefficients of Aerosol Concentration and Volumetric Loadings on Wind Speed

| Size Band (Name) | Coefficients (Concentration) | | | Coefficients (Volume) | | |
|---------------------|---------------------------------|---------|------|--------------------------|---------|------|
| | a | b | r | c | d | |
| 1 | 0.0285 | 1.7524 | 0.40 | 0.0759 | -1.5429 | 0.51 |
| 2 | 0.0404 | 1.1918 | 0.79 | 0.0946 | -1.3134 | 0.80 |
| 3 | 0.0995 | -0.3433 | 0.87 | 0.2265 | -4.0905 | 0.89 |
| 4 | 0.0442 | -0.2660 | 0.77 | 0.0978 | 0.3225 | 0.76 |
| 5 | 0.0112 | -0.3697 | 0.58 | 0.0431 | 1.6160 | 0.65 |
| 6 | 0.0264 | -0.6125 | 0.63 | 0.0604 | 3.1247 | 0.62 |
| 7 | 0.0456 | -1.6829 | 0.81 | 0.1288 | 2.3273 | 0.86 |
| 8 | 0.1293 | -3.3681 | 0.95 | 0.3339 | 0.4689 | 0.95 |
| 9 | 0.1688 | -4.8236 | 0.94 | 0.3836 | -0.7404 | 0.94 |

$\text{Log}_{10} \text{ concentration} = a * \text{wind speed} + b$, with correlation coefficient r ;
 $\text{Log}_e \text{ volume} = c * \text{wind speed} + d$, with correlation coefficient r .

In order to compare these data with the earlier studies at this site, the data were converted into the same format, that is, into averaged volumetric aerosol loadings versus wind speed. The results are shown in Figure 4 for particles size ranges labelled 'large' and 'ultra-large' in the earlier paper. It may be noted from a comparison of Figure 4 with Figure 3 that the volumetric increase with wind speed is greater than the concentration increase; this is due to the proportionate increase in the concentration of the larger particles.

The two data sets show good general agreement in the region of overlap, with the 1986 data set considerably extending the previous published data. The major discrepancy is for the 'ultra-large' particles at very low wind speeds. Most of these data belong to the anticyclonic period in the summer of 1986, described earlier, when the sea state remained at or below 2 for several days. In such conditions, no relationship between wind speed and particle concentration of this size is to be expected, since there will have been virtually no sea-surface production. The residual concentration will thus depend upon the particles' fall-out times and the time elapsed since significant amounts of whitecapping occurred. The 'large' particles show less of a discrepancy here, but in anticyclonic conditions are probably suffering some land influence.

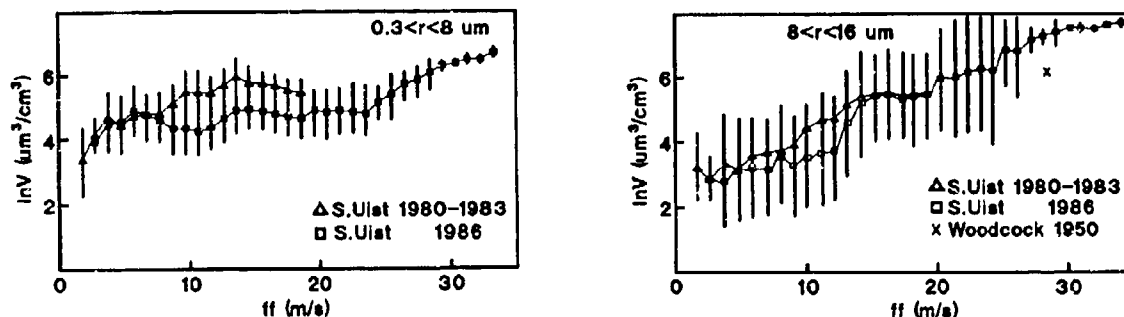


Figure 4. Volumetric aerosol loadings V as a function of wind speed ff . The open triangles are data from Exton et al¹, the closed squares are data from South Uist, 1986. Particle sizes (a) $0.3 \leq r \leq 8/\mu\text{m}$ (b) $8 \leq r \leq 16/\mu\text{m}$.

There is some suggestion of a levelling off towards the extreme high wind speed end of the data set, but this is likely to be an artefact of the data; the highest wind speeds are only measured for a short period of time, and so equilibrium conditions for that wind speed are less likely to become established. Also, lower wind speeds can occur when the sea state is determined by previous, higher wind speeds, which will increase the averaged concentration at those values.

3.3 Changes in aerosol spectral distribution with wind speed. In order to demonstrate the influence of wind speed upon aerosol spectral shape, the aerosol particle counts were grouped into 1 ms^{-1} wind speed bands, in a similar manner to the analysis in the previous section but, in this case, the counts were summed for each PMS instrument range and channel. Selected wind speeds from the data for South Uist are presented in Figure 5.

Generally, no consistent changes are apparent for particles smaller than about $1/\mu\text{m}$ radius, as might be expected since these particles are not predominantly of sea surface origin. However, for the larger particles, substantial increases in concentration with wind speed may be noted, with a 'hump' appearing in the spectrum at around $10/\mu\text{m}$ radius at the higher wind velocities. Observations made from a ship in the North Sea during the HEXOS project indicate that, whilst the ship was in shallow water (about 18 m depth), this 'hump' was even more pronounced than in the South Uist measurements, but was significantly less evident when observations were made in deeper water (about 40 m depth).

3.4 Aerosol concentration response at low wind speeds. The low wind speed period encountered during August, and shown in Figure 6, was examined thoroughly in the hope it might yield information on particle loss rates, and to provide some estimate of the true very low wind speed background particle count at the South Uist site. However, before the decay in the particle concentrations over the period could be investigated, perturbations within the data set had to be removed. Brief episodes of continental influence resulting from changes in wind direction showed up very clearly as pronounced increases in concentrations over the smaller particle size bands. Also, a short period of heavy precipitation provided a sharp peak in the temporal trace of large particle concentration plots indicate a consistent decrease in concentration with time during the low wind period, as shown for the $2-4/\mu\text{m}$ radius band in Figure 7.

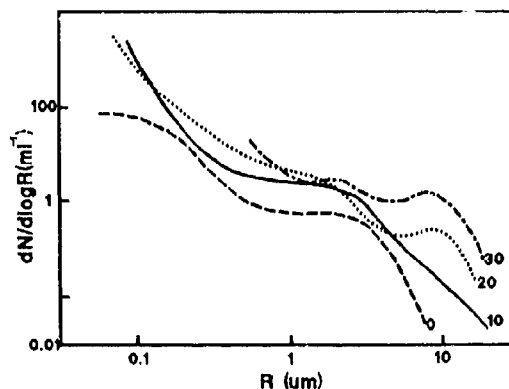


Figure 5. Aerosol spectral distributions for selected wind speeds (ms^{-1})

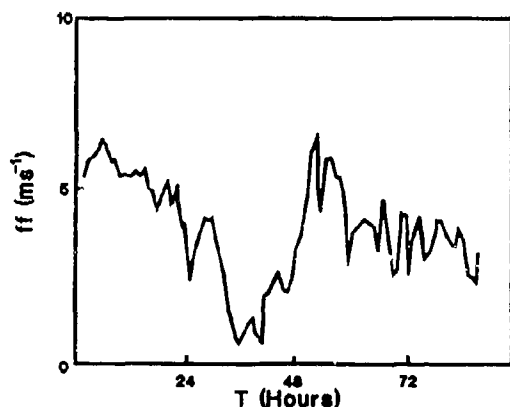


Figure 6. Wind speed against time elapsed T for low wind episode.

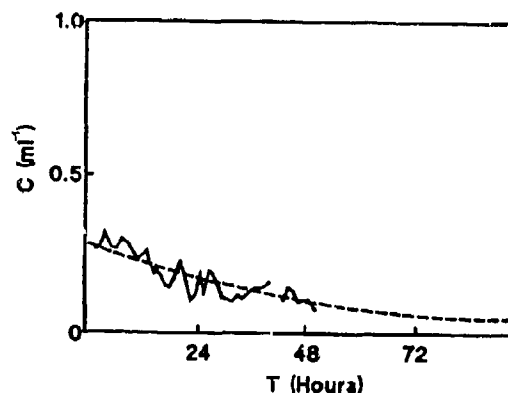


Figure 7. Decay of particle concentration C (2-4/ μ m band) with elapsed time T.

Exponential decay expressions of the form

$$C = C_{t=0} \exp(-t/T) \quad (1)$$

where t and T are the elapsed time and the time constant, respectively, and C is the hourly-averaged aerosol concentration were fitted to both the first maritime period only (over approximately the first 36 hours) and to all the maritime data within the low wind speed episode. The results of this analysis are presented in Table 4 and demonstrate that the smallest particle concentrations show no significant trend, as might be expected since they are likely to be still being generated from sources other than the sea surface. The 1-2/ μ m particle concentrations also show no significant trend and the poor fits for these particles may be instrumental. Particles of radius greater than 2/ μ m have better fits when the short data sets are used, whilst, for the 0.25 to 1/ μ m particles, better fits are obtained with the extended data set. These findings seem reasonable as the smaller particles have longer residence times.

Table 4. Exponential Fit Parameters

| Size Band / μ m radius | FIRST MARITIME DATA | | | ALL MARITIME DATA | | |
|-------------------------------|---------------------|-------------------|-------|-------------------|-------------------|-------|
| | T hours | conc ($t=0$) | cc | T hours | conc ($t=0$) | cc |
| 0.09 - 0.125 | -137.5 | 9.400 | 0.22 | 235.8 | 11.70 | -0.22 |
| 0.25 - 0.5 | 391.5 | 1.018 | -0.10 | 47.03 | 1.515 | -0.67 |
| 0.5 - 1 | 50.29 | 1.115 | -0.71 | 36.63 | 1.325 | -0.84 |
| 1 - 2 | 1063.29 | 0.360 | -0.18 | 4811.4 | 0.357 | -0.04 |
| 2 - 4 | 39.4 | 0.236 | -0.84 | 40.00 | 0.241 | -0.82 |
| 4 - 8 | 31.13 | 0.027 | -0.85 | 35.12 | 0.026 | -0.80 |
| 8 - 16 | 17.42 | 1.32E-3 | -0.70 | 35.43 | 8.61E-4 | -0.60 |

4. ATMOSPHERIC EXTINCTION

The extinction of electromagnetic radiation by aerosol particulates may be readily calculated by means of the expression

$$E = n \sum_{all} r Q(r, \lambda) n(r) r^2 \quad (2)$$

where E is the atmospheric extinction, $n(r)$ is the concentration of particles of radius r and $Q(r, \lambda)$ is the extinction efficiency (or cross-section) for a particle of radius r at wavelength λ . Similarly, the scattering or absorption due to the presence of aerosol particles may be determined by substituting appropriate Mie efficiency factors in Eq(2).

Calculation of atmospheric extinctions in this manner is inhibited by the substantial computational effort required to obtain the relevant Mie efficiencies for each particle size and wavelength of light. In order to facilitate such calculations, tables of computed efficiency factors were produced by means of available algorithms²⁵ for the particle radii measured by the PMS probes, at a wide range of wavelengths and refractive indices. The efficiency factors were calculated for the centre values of each of the PMS channels, on the assumption that such values are representative of the full probe channel. Limited tests suggest that this approach was adequate for the purposes of this investigation.

The composition of aerosol particles in the maritime environment might be expected to result in a refractive index, at a given wavelength, somewhere between that of sea salt and water, with its exact value dependent upon the relative proportions of these two constituents and, hence, upon the relative humidity²⁶. For the South Uist data, a relative humidity of 80 per cent was assumed and Mie efficiency factors were calculated accordingly.

Values of atmospheric extinction at various wavelengths from 0.2 to 40 μm were derived using Equation (2) for the particle size distributions in each of the 1 ms^{-1} wide wind speed bands. There is considerable overlap between the various probe ranges and, as mentioned previously, the probes exhibit a multi-valued response characteristic for particles of radius of about 1 μm . In general, range 0 of the ASASP is better avoided completely, whilst the lowest channels in each range should be omitted as they are susceptible to electrical noise. Experience indicates that the ranges and channels listed in Table 5 provide a wide range of particle sizes with no overlap and little distortion.

Table 5. PMS Probe Data used in Calculations of Extinction Coefficients

| Probe | Range | Channels | Particle Radii (μm) |
|-------|-------|----------|----------------------------------|
| ASASP | 3 | 4 - 15 | 0.09 - 0.15 |
| | 2 | 4 - 10 | 0.15 - 0.24 |
| | 1 | 3 - 15 | 0.24 - 0.5 |
| FSSP | 3 | 2 - 15 | 0.5 - 4 |
| | 1 | 4 - 15 | 4 - 16 |
| | 0 | 11 - 15 | 16 - 23.5 |

The results of these calculations of the atmospheric extinction due to maritime aerosol particles within the 0.09 to 23.5 μm radius band are presented in Figure 8, and it is immediately apparent that there is generally little variation in extinction with wavelength at all but the lowest wind speeds. These findings are in marked contrast to the continental aerosol case, when atmospheric extinction is generally dominated by the smaller aerosol particles with radii around 0.1 μm . In these circumstances, atmospheric visibility will be strongly dependent upon wavelength and may vary by more than an order of magnitude over the range of wavelengths considered, with substantially lower extinction coefficients being observed at the longer wavelengths.

Atmospheric extinction of electromagnetic radiation is dependent upon the total cross-sectional area of the particles, these will come to dominate the total cross-sectional area. The extinction efficiency of particles tends to a constant value of two as the particle size increases and, thus, in the maritime environment under moderate or strong wind conditions, atmospheric extinction will be dominated by particles with radii of 1 μm or greater; and extinction coefficients will be similar for all visible and infra-red wavelengths.

In this situation, especially for the highest wind conditions, particles larger than those measured by the FSSP-100 (that is, larger than 23.5 μm radius) may contribute a major, or even dominant, fraction of the total aerosol extinction, even though present in relatively small numbers. Thus, in order to calculate extinction coefficients to a greater degree of accuracy, some estimate should be made of the concentrations of these larger aerosol particles for the highest wind speeds (beyond about 15 or 20 ms^{-1}).

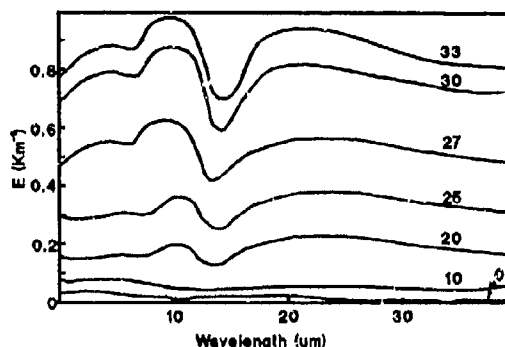


Figure 8. Atmospheric extinction E due to aerosol particles against wavelength λ for selected wind speeds (ms^{-1}).

5. COMPARISON OF LOWTRAN CALCULATED EXTINCTION WITH MEASURED AEROSOL EXTINCTION

The aerosol extinction was calculated using LOWTRAN6 Maritime Aerosol Model. The following inputs to LOWTRAN were used:

Pressure - 1000 millibars
 Relative Humidity - 80%
 Temperature - 10 °C
 Wind Speed - 0, 10, 20, 25, 27, 30, 33 ms^{-1}
 Average Wind Speed was taken as the instantaneous wind speed

| Visibilities | Wsp(ms ⁻¹) | Vis (km) |
|--------------|------------------------|----------|
| | 0 | >20 |
| | 10 | >20 |
| | 20 | 20 |
| | 25 | 13.3 |
| | 27 | 8.9 |
| | 30 | 6.0 |
| | 33 | 5.0 |

Precipitation - None
Air Mass No - 1

LOWTRAN5 appears to assume that above a wind speed of 20 ms⁻¹ there is no further increase in wind driven aerosol with increase in wind speed. The data from South Uist suggests that there are considerable increases in aerosol loadings with wind speed above 20 ms⁻¹. In order to carry out a comparison of measured aerosol extinction versus LOWTRAN calculated extinction at the higher wind speeds the restriction on wind speeds above 20 ms⁻¹ was removed from the LOWTRAN program.

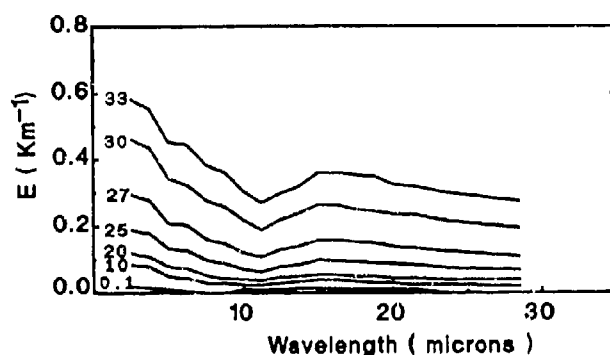


Figure 9. Lowtran calculated extinction for various wind speeds in ms⁻¹, Air Mass No - 1

The LOWTRAN calculated extinction versus wavelength for various wind speeds up to 33 ms⁻¹ can be seen in Figure 9. A direct comparison of the measured versus calculated extinction for wind speeds up to 20 ms⁻¹ is shown in Figure 10.

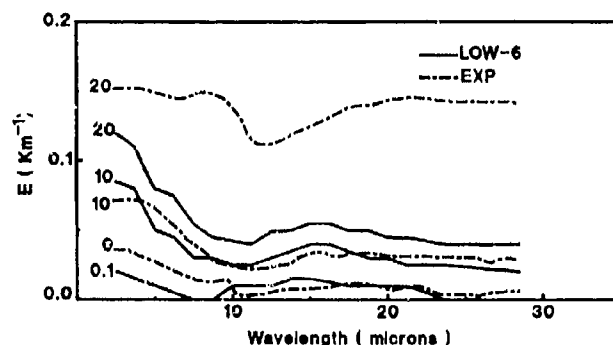


Figure 10. Comparison of the measured versus calculated extinction for wind speeds up to 20 ms⁻¹

The measured aerosol extinction at 10 microns wavelength is approximately a factor of 4 greater than the LOWTRAN calculated value, whereas at a wavelength of 5 microns the measured value of extinction is greater by a factor 2 than the calculated extinction. These differences in the values of extinction are not too surprising since the absolute calibration of this type of aerosol counting instrument is very difficult to achieve. What is more difficult to explain is the difference in the variation of extinction with wavelength. In the LOWTRAN calculations there is a considerable drop in extinction from very small wavelengths up to a wavelength of 10 microns, whereas there is little variation in measured extinction in this region.

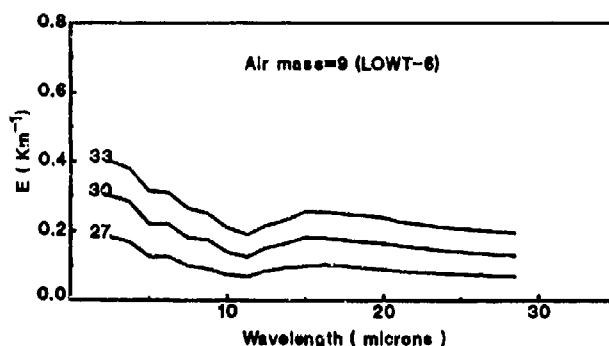


Figure 11. LOWTRAN calculated extinction for Air Mass No = 9

In order to test the sensitivity of the calculation to the Air Mass No used, calculations were performed using an Air Mass No of 9. The results are shown in Figure 11. The absolute value of extinction is reduced but the variation of extinction with wavelength remains similar to the results where an Air Mass No of 1 was used.

6. FUTURE MEASUREMENTS

Radon Concentrations Over the NE Atlantic Ocean. The UMIST Atmospheric Physics Research Group will carry out a NERC/MOD supported project on a ship named the 'Charles Darwin' between Iceland and the Faroe Islands during October and November of 1989. The investigation is concerned with measurements of the exchange of heat, momentum and moisture between ocean and atmosphere under various environmental conditions. Also the measurement of aerosol particulate loadings and size spectra will be undertaken and sea-air particle fluxes will be derived. These data will be of substantially greater utility to the Ministry of Defence if simultaneous measurements of other parameters are made. In particular the predictions of the LOWTRAN model will be much more readily tested against observations if the air mass characteristics is assessed, especially close to Iceland where air mass characteristics are uncertain. Consequently ARE are funding UMIST to extend this study to include measurement of radon concentration to establish air mass type.

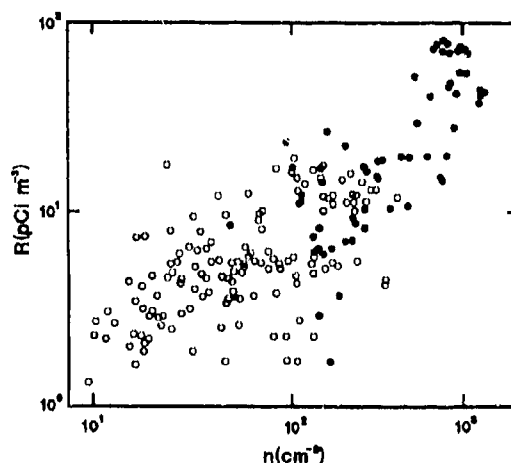


Figure 12. Correlation of Radon Concentration with Small Particulate Concentration

Previous studies in the Outer Hebrides have shown that radon concentrations correlate very closely with both small particulate concentrations (radii less than about 0.2 microns) see Figure 12, and continental influence as indicated by air trajectory analysis. Radionuclide activities of less than 6 pCi/m³ were associated with maritime air masses with higher activities indicating proportionately greater contributions from continental sources.

Similar observations to those conducted in South Uist will be made compared with small aerosol concentrations and air trajectories in order to determine whether significant periods of continental influence exist and, if found there relationship to the general meteorological situation established. Air mass characteristics appropriate for input to the LOWTRAN model will be derived.

7. CONCLUSIONS

For the first time data have been collected at surface wind speeds in excess of 30 ms^{-1} , which is of interest as these wind speeds are not uncommon over open oceans. When plotted with other lower wind speed data sets, for non-cyclonic conditions at the same site, all data are consistent. Concentrations of the larger particles do not level off at wind speeds above 15 ms^{-1} , as previously suggested, but the largest increase by a factor of 4 as wind speeds exceed 30 ms^{-1} , corresponding to a volumetric increase of more than an order of magnitude. It should be emphasised that the measurement range in these South Uist experiments extends only as far as $23.5 \mu\text{m}$ radius. The spectra show increasingly more of the largest particles measured with increasing wind speed indicating that the quantities of aerosol present for sizes beyond this upper limit are also increasing. Thus, the increase in volumetric loading in the size band $16\text{--}23.5 \mu\text{m}$ radius is likely to be a serious underestimate of the increase in total sea-salt loading.

Estimates of atmospheric extinction for these maritime conditions at high wind speeds show little variation for wavelengths from the visible to the infra-red and emphasise the importance of information on the particulate size spectrum in such environments.

Comparisons with LOWTRAN calculated extinction indicated that the LOWTRAN6 maritime aerosol model apparently assumes that above a wind speed of 20 ms^{-1} there is no further increase in wind driven aerosol with increase in wind speed. The South Uist measurements indicate that this is not the case in practice.

The comparisons show that at a wavelength of 10 microns the measured aerosol extinction is approximately a factor of 4 greater than the LOWTRAN calculated value, whereas at a wavelength of 5 microns the extinction is a factor of 2 greater. The LOWTRAN calculations predict a considerable drop in extinction from very short wavelengths up to 10 microns, whereas there is little variation in extinction in this region calculated from the aerosol measurements.

8. REFERENCES

1. H J Exton, J Latham, P M Park, S J Perry, M H Smith and R R Allan, "The production and dispersal of marine aerosol", *Quart J R Met Soc* 111, 517-537 (1985).
2. E C Monahan, I O'Muircheartaigh, "Optimal power-law description of oceanic whitecap coverage dependence on windspeed", *J Phys Oceanog* 10, 2094-2099 (1980).
3. J Wu, "Oceanic whitecaps and sea state", *J Phys Oceanog* 9, 1964-1968 (1979).
4. D C Blanchard and E J Hoffman, "Control of jet drop dynamics by organic material in sea water", *J Geophys Res* 83(C12), 6187-6191 (1963).
5. C E Junge, "Our knowledge of the physico-chemistry of aerosols in the undisturbed marine environment", *J Geophys Res* 77(27), 5183-5200 (1972).
6. R E Larson, R A Lamontagne, P E Wilkness, W I Whitman "Radon-222, CO_2 , CH_4 and continental dust over the Greenland and Norwegian seas", *Nature* 240, 345-7 (1972).
7. G Gravenhorst, "Maritime sulphate over the North Atlantic", *Atmos Env* 12(1-3), 707-13 (1978).
8. J W Fitzgerald, "Approximation formulas for the equilibrium size of an aerosol particle as a function of its dry size and composition and the ambient relative humidity", *J Appl Meteor* 14, 1044 (1975).
9. S C Ling and T W Kao, "Parameterisation of the moisture and heat transfer process over the ocean under whitecap sea states", *J Phys Ocean* 6, 306-315 (1976).
10. D C Blanchard, A H Woodcock and R J Cipriano, "The vertical distribution of the concentration of sea salt in the marine atmosphere near Hawaii", *Tellus* 36, 118-125 (1984).
11. H G Pughes and J H Richter, "Extinction coefficients calculated from aerosol size distributions measured in a marine environment", *Opt Eng* 19, 616-620 (1980).
12. P A Durkee, D R Jensen, E E Hindman, T H Vonder Haar, "The relationship between marine aerosol particles and satellite-detached radiance", *J Geophys Res* 91, 4063-4072 (1986).
13. R E Larson, "Correlation between radon and CCN concentration", *J Geophys Res* 79, 3476-7 (1974).
14. R E Larson, D J Bressan, K W Marlow, T A Wojciechowski and J L Heffner, "A comparison of concentrations of fission products, Radon-222 and cloud condensation nuclei over the North Atlantic", *Pure and Appl Geophys* 1175(5), 874-84 (1979).
15. G de Leeuw, "Private communication" (1985).

16. D J Erickson, J T Merrill and R A Duce, "Seasonal estimates of global atmospheric sea-salt distributions", J Geo Res 91(D1), 1067-72 (1986).
17. G L Trusty and T H Cosden, "Aerosol measurements at an optical propagation site on the Outer Hebrides", NRL Rept 8800, Naval Research Laboratories, Washington DC (1984).
18. M H Smith, I E Consterdine and P M Park, "Atmospheric loadings of marine aerosol during a Hebridean cyclone", Quart J Roy Met Soc 116 (1989).
19. T W Choularton, I E Consterdine, B A Gardiner, M J Gay, M K Hill, J Latham and I M Stromberg, "Field studies of the optical and microphysical characteristics of clouds enveloping Great Dun Fell", Quart J R Met Soc 112, 131-48 (1986).
20. R G Pinnick and J Auverman, "Response characteristics of Knollenberg light-scattering counters", J Aerosol Sci 10(1), 55-74 (1979).
21. R J Cipriano and D C Blanchard, "Bubble and aerosol spectra produced by a laboratory 'breaking wave'", J Geophys Res 86(C9), 8085-92 (1981).
22. A H Woodcock, "Smaller salt particles in oceanic air and bubble behaviour in the sea", J Geophys Res 77, 5316-21 (1972).
23. D K Woolf, P A Bowyer and E C Monahan, "Discriminating between film drops and jet drops produced by a simulated whitecap", J Geophys Res 92(C5), 5142-50 (1987).
24. A H Woodcock, "Sea salt in a tropical storm", J Appl Met 7, 397-401 (1950).
25. J V Dave, "Subroutines for computing the parameters of the electromagnetic radiation scattered by a sphere", Report No 320-3237, IBM Scientific Centre Palo Alto, Calif USA (1968).
26. E P Shettle and R W Fenn "Models for the aerosols of the lower atmosphere and the effects of humidity variations on the optical properties", AFGL-TR-79-0214 Environmental Research Papers No 676 (1979).

Copyright (C) Controller HMSO London 1989

DISCUSSION

J. SELBY

You mentioned that aerosols were measured at South Uist over the size range 0.08 - 23.5 μm . Since your measurements were conducted under high wind speed conditions, I would expect one to find very large droplets present (50 - 100 μm). Why did you not use the PMS OAP-200 instrument? This would have allowed you to measure droplet sizes from 20 to 500 μm . Also, do you plan to continue measurements of this kind?

AUTHOR'S REPLY

I agree; it would have been useful to measure larger droplet sizes. There are no plans to continue this work at present.

J. SELBY (COMMENT)

I would expect the true extinction coefficients to be higher than what you measured.

E. SHETTLE

In doing the comparisons with the LOWTRAN aerosol models, did you directly extract the aerosol values from the code or did you carry out the transmission calculations for observed conditions and subtract the expected molecular contribution which would introduce more uncertainty in the aerosol component?

AUTHOR'S REPLY

A full LOWTRAN 6 calculation was performed and the values of aerosol extinction abstracted from the output.

**L'ATMOSPHERE MARINE MEDITERRANEEENNE
ET SES EFFETS SUR LES AEROSOLS ET LA TRANSMISSION INFRAROUGE**

Melle TANGUY Mireille.-Thèse CNRS/DCN
CESDA - Les Oursinières 83220 Le Pradet - FRANCE

Résumé : L'expérimentation que nous menons actuellement repose sur la validation du code LOWTRAN6 dans le cadre du calcul de la transmission atmosphérique d'un rayonnement infrarouge dans la couche limite marine en milieu méditerranéen. Le dispositif optoélectronique implanté en bord de mer se compose d'un transmissiomètre permettant d'évaluer la transmission sur les bandes $3\mu\text{m}$ - $5\mu\text{m}$ et $8\mu\text{m}$ - $12\mu\text{m}$ le long d'un trajet horizontal de 8 km à une altitude de 40 mètres au dessus de la mer. Afin de mettre en évidence des corrélations possibles entre les différents phénomènes, une station météorologique automatique et une sonde optique CSASP-100-HV fonctionnent en parallèle. En complément, une étude du comportement de la densité en aérosols en fonction de la localisation de la mesure et des conditions météorologiques a été entreprise à bord de bâtiments de la Marine nationale française.

I - INTRODUCTION.

L'évolution de la Transmission atmosphérique dépend d'un grand nombre de facteurs tels que sa composition moléculaire et particulaire, les conditions climatiques et la nature de l'onde elle-même.

Depuis de nombreuses années, des équipes de chercheurs élaborent et améliorent des modélisations du calcul de transmission atmosphérique. C'est le cas du code LOWTRAN, amorcé en 1971 par le groupe AFGL, dont la 6ème version⁽¹⁾ propose un modèle d'aérosols, le NAVY MARITIME, lequel est susceptible d'évoluer suivant les paramètres météorologiques comme la vitesse du vent, l'hygrométrie, le coefficient de masse d'air.

Ce modèle a été mis au point à partir de mesures effectuées en régions tropicales, équatoriales et subarctiques. La finalité de l'étude que nous poursuivons au Centre CESDA de la DCN à Toulon (France) entre dans le cadre des travaux sur la prédiction de portée des systèmes de détection infrarouge et consiste à valider le Code Lowtran6 dans le cas d'une atmosphère marine de type *méditerranéen*.

L'intérêt du choix du domaine spectrale infrarouge, en particulier les bandes $3\mu\text{m}$ - $5\mu\text{m}$ et $8\mu\text{m}$ - $12\mu\text{m}$, reste stratégique et provient du caractère passif et réalisable de jour comme de nuit de la détection dans cette gamme de longueurs d'onde.

II - DISPOSITIF EXPERIMENTAL.

A - LE TRANSMISSIONOMETRE.

Un système optoélectronique appartenant au CELAR, appelé Transmissiomètre, mis au point en laboratoire par l'ONERA, a été implanté en site réel sur la côte méditerranéenne en Rade de TOULON.

La transmission atmosphérique large bande étudiée est obtenue par mesure différentielle grâce à deux corps noirs chauffés à 1000 K, dont l'un, de mesure, est placé au CERTEL et le second, de référence, à une distance de 8 Km.

Un ensemble d'optiques collimate le rayonnement à une altitude constante de 40 mètres au dessus du niveau de la mer jusqu'à une pupille de réception. Là, un télescope focalise le faisceau vers un détecteur qui fut dans un premier temps pyroélectrique et sera remplacé par un détecteur quantique. Une détection synchrone est utilisée afin de s'affranchir des flux parasites ambiants.

Un plateau tournant comportant six filtres permet de sélectionner successivement les six bandes spectrales suivantes:

- 3 μ m-4,1 μ m 3 μ m-5 μ m 3,4 μ m-5 μ m
- 8 μ m-10 μ m 8 μ m-11 μ m 8 μ m-12 μ m

Pour chaque filtre, un miroir escamotable permet alternativement de mesurer le rayonnement source et le rayonnement de référence.

Un programme élaboré sur le microordinateur HP 9310 opère automatiquement la gestion de commande des différents appareils requis pour une mesure ainsi que l'acquisition, le traitement et l'archivage des données.

Le choix initial d'un détecteur pyroélectrique provient du programme OPAQUE de mesure de la transmission atmosphérique sur courte distance (500 mètres) dans le cadre du groupe OTAN panel IV RSG8. Cet appareil s'est avéré inadapté à la configuration en site réel pour une distance de 8 Km, en particulier pour les mesures de transmission sur la bande 8 μ m-12 μ m, le rapport signal sur bruit se trouvant être proche de l'unité lors de conditions météorologiques défavorables.

L'implantation d'un détecteur quantique de meilleure détectivité a donc été décidé, mais rencontre quelques difficultés de mise en place. C'est pourquoi un nombre limité de mesures de transmission a pu être effectué jusqu'à présent.

B - LA STATION METEOROLOGIQUE.

Les paramètres météorologiques tels que :

- la vitesse du vent instantané
- la direction du vent
- la température de l'air sec
- la température de l'air humide
- la pression atmosphérique

sont mesurés à l'aide de capteurs extérieurs

Les signaux correspondants sont numérisés grâce à une station météorologique automatique PULSONIC 800 et transmis par interface RS232 au microordinateur HP 9310.

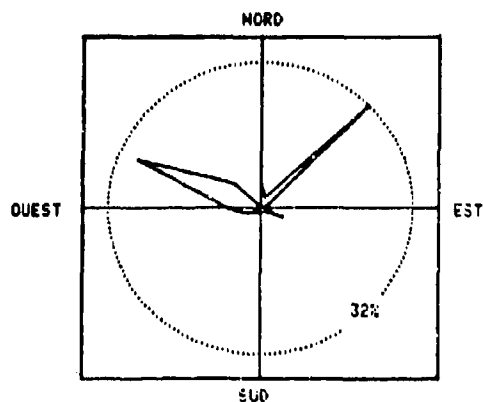


Figure n°1 : Rose des vents
Période Sept.Oct.Nov..
Rade de Toulon.

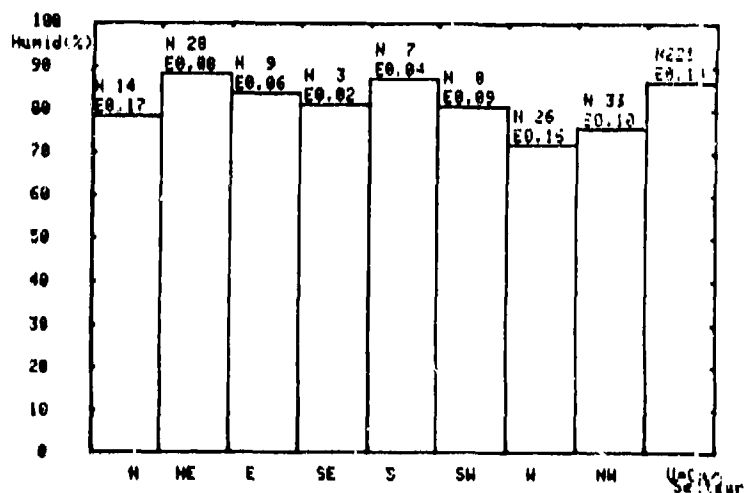


Figure n°2 : Histogramme
des moyennes d'humidité
en fonction des secteurs
de vents.

N : nombre de mesures.
E : écart-type normalisé
à la moyenne.

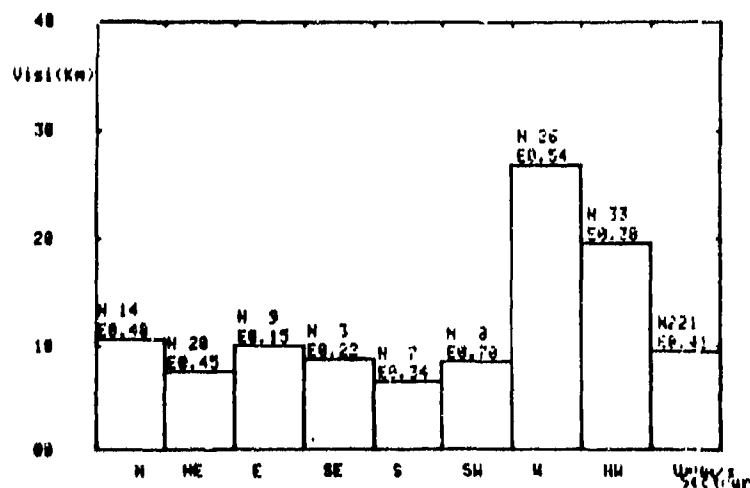


Figure n°3 : Histogramme
des moyennes de visibilité
en fonction des secteurs
de vents.

C - LA SONDE GRANULOMETRIQUE.

D'autre part, des mesures de granulométrie en aérosols marins sont réalisées au moyen d'un compteur de particules CSASP 100 HV de type Knollenberg de P.M.S. Cette sonde fonctionne selon le principe de diffusion par une particule d'un faisceau laser HeNe. La gamme de mesure s'étend à des diamètres compris entre 0,5 et 47 μm .

La sonde est reliée à une centrale d'acquisition PDS 300 qui analyse et classe les données de la sonde grâce à son calculateur. L'option choisie parmi sept disponibles est la représentation de la densité en aérosols par unité de volume et par largeur de classe en fonction du diamètre des particules présentes sur le site. Le résultat des calculs du PDS 300 est ensuite transmis au HP 9310 pour y être stocké.

III - EXPLOITATION DES PREMIERS RESULTATS.

La rose des vents (figure n°1) met en évidence deux directions privilégiées : un vent de WNW appelé plus communément MISTRAL et un vent d'Est qui généralement apporte la pluie sur les régions méditerranéennes.

Les histogrammes des figures n°2 et 3 mettent en avant les propriétés des vents propres au milieu méditerranéen.

En effet, les vents d'Est et NE se forment lors d'une dépression dans le Golfe de Gênes, sont porteurs en général d'une atmosphère chargée en humidité, de même pour les vents de Sud d'origine pleinement marine. Par contre, le Mistral, descendant de la vallée du Rhône et résultant de l'anticyclone des Açores, est plus sec et tend à chasser brumes et brouillards, comme on peut l'observer par la moyenne de visibilité rencontrée pour ces secteurs de vent (figure n°3).

Il est donc fort possible que le taux de transmission atmosphérique soit affecté par l'origine des différents vents comme semble le montrer la figure n°4, où les valeurs les plus fortes de transmission dans la bande 3 μm -5 μm sont atteintes dans le cas du Mistral.

Les figures n°5 et 6 nous proposent des corrélations plus ou moins fortes entre différents paramètres.

Tout en limitant la validité des valeurs de visibilité, lesquelles sont obtenues à partir de l'évaluation de l'œil humain, on remarque que le comportement des transmissions sur la bande 3 μm -5 μm n'est pas linéairement dépendant des mesures de visibilité (figure n°6).

IV - LE CODE LOWTRAN

Les codes LOWTRAN développés depuis 1971 calculent la luminance et les transmissions atmosphériques moyennées sur des intervalles de 20 cm^{-1} de 350 à 40 000 cm^{-1} (soit un domaine de longueurs d'onde allant de 0,25 à 28,5 μm). Ce code utilisant pour l'absorption un modèle de bandes à un seul paramètre, inclut les effets de l'absorption du continuum, la diffusion moléculaire et l'extinction par les aérosols.

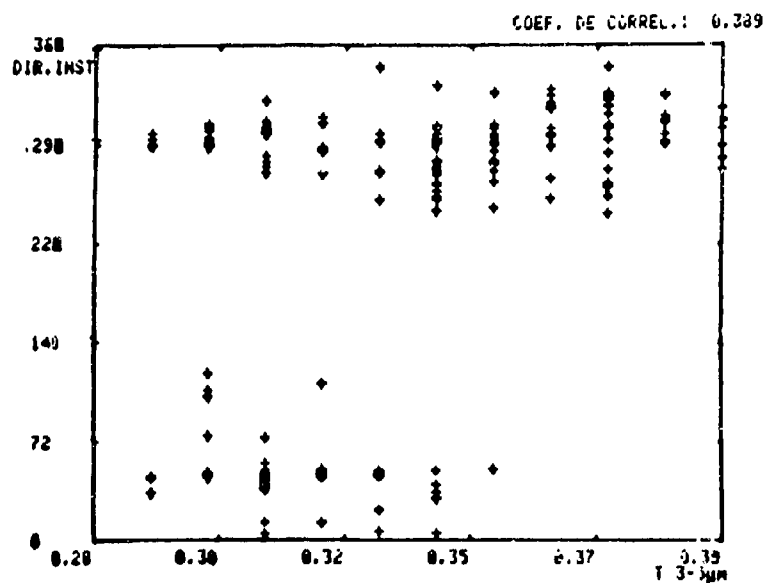


Figure n°4 : Evolution de la transmission sur la bande 3µm-5µm en fonction des directions du vent.

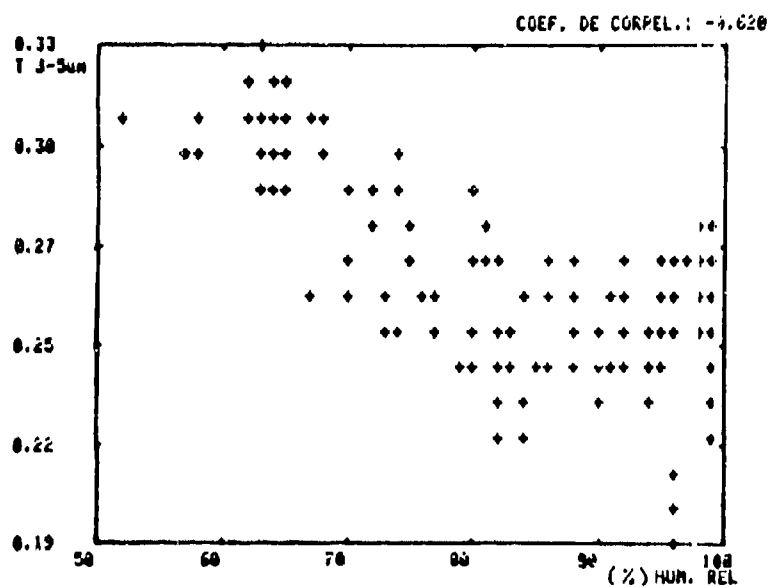


Figure n°5 : Evolution de la transmission sur la bande 3µm-5µm en fonction de l'humidité relative.

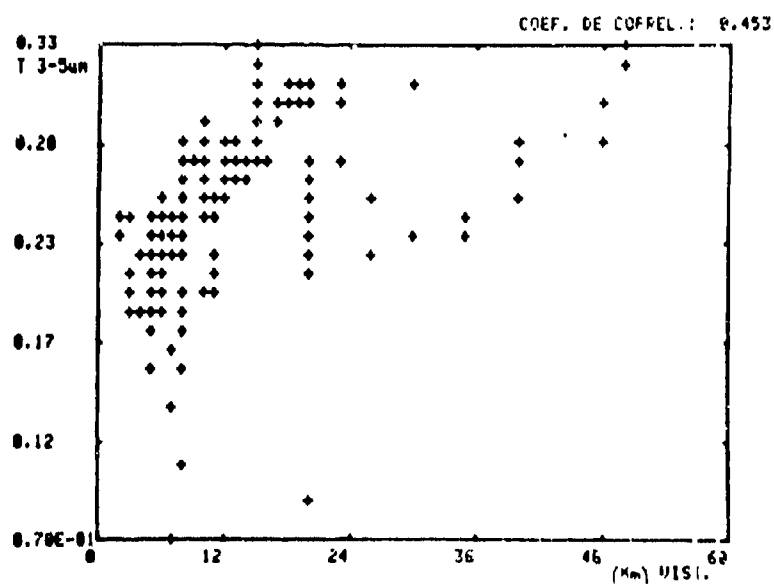


Figure n°6 : Evolution de la transmission sur la bande 3µm-5µm en fonction de la visibilité.

L'amélioration apportée au code LOWTRAN qui apparaît dans la version LOWTRAN 6 est l'introduction d'un modèle d'aérosols appelé NAVY MARITIME⁽²⁾. Celui-ci résulte d'une série de mesures de profils granulométriques pris lors de conditions météorologiques différentes.

L'influence du vent, des courants de masse d'air ainsi que de l'hygro-métrie sur la taille et la concentration en aérosols y est mise en évidence. Dans ce modèle, les aérosols sont générés par l'évaporation des embruns et des gouttes de films et de jets à la surface de la mer. Les particules ainsi formées sont ensuite réparties dans l'atmosphère. Ces phénomènes de générations dépendent du vent et sont liés au déferlement des vagues. Une fois en suspension, ces gouttelettes subissent des mécanismes de tri par gravité et de mélange par turbulence. En dehors des processus de lessivage de l'atmosphère, les petites particules ont une durée de résidence longue dans la couche limite tandis que les particules de grandes dimensions contribuent peu à la population à long terme des aérosols.

Le modèle NAVY-MARITIME distingue trois types de populations d'aérosols, chacun décrit par une distribution lognormale.

$$DN(R)/DR = A1 \times 1/f \times \exp(-\ln(R / f \times R_i)^2)$$

$$\begin{aligned} \text{avec} \quad A1 &= 2000 \times (AM)^2 \\ A2 &= \max(0,5 ; 5,866 \times (V_{\text{moy}} - 2,2)) \\ A3 &= \max(0,000014 ; 0,01527 \times (V_{\text{inst}} - 2,2)) \\ f &= (2 - RH/100) / (6 \times (1 - RH/100)) \end{aligned}$$

où AM : coefficient de masse d'air
 V_{inst} : vitesse instantané du vent.
 V_{moy} : vitesse du vent moyennée sur les précédentes 24 heures
 RH : humidité relative
 R_i : rayons modaux correspondants au maximum de chaque mode
 $R1 = 0,03 \mu\text{m}$; $R2 = 0,24 \mu\text{m}$; $R3 = 2 \mu\text{m}$

Les coefficients qui apparaissent dans la forme analytique de la distribution des aérosols sont déterminés empiriquement à partir d'observations météorologiques récentes.

La composante la plus fine de l'aérosol ($A1$) correspond à une composante continentale liée à l'aérosol de fond supposé indépendant du vent. Relatif au temps de déplacement de la masse d'air, le paramètre AM prend des valeurs entières comprises entre 1 et 10 (1 représente un aérosol purement marin, 10 un apport continental important).

La deuxième composante, la composante permanente de l'aérosol marin, est fonction de l'histoire du vent, qui suivant sa force tend à provoquer la formation de la houle, cette composante sera donc fonction de la vitesse moyenne du vent dans les dernières 24 heures.

La troisième composante correspond à l'arrachement des gouttelettes par le vent en cours sur les vagues déjà présentes et sera exprimée en fonction de la vitesse instantanée du vent.

L'extinction et l'absorption par les aérosols à différentes longueurs d'onde ont été calculées par la Théorie de MIE pour des indices de réfraction liés aux différentes composantes de l'aérosol. Les données concernant les aérosols sont alors intégrées au programme LOWTRAN6 sous la forme de tableaux de coefficients d'extinction et d'absorption pour une série de valeurs discrètes de longueurs d'onde (40 valeurs) et d'hygrométrie (50% - 85% - 90% - 99%). Les valeurs particulières sont obtenues par interpolation.

V - MESURES GRANULOMETRIQUES

Notant la localisation de la mesure de Transmission parallèlement aux prises de profils en aérosols et l'éventualité d'une influence côtière trop fréquente, il s'est avéré intéressant et nécessaire d'étendre le site d'étude à une atmosphère pleinement marine.

Ainsi, plusieurs expérimentations ont pu être effectuées à bord de bâtiments de la Marine Nationale française, en particulier lors d'une mission de représentation en Tunisie du bâtiment d'expérimentation L'Ile d'Oléron.

Une étude du comportement des profils de concentrations d'aérosols a été amorcée afin de mettre en évidence l'influence des conditions météorologiques ou encore du site géographique.

A - INSTRUMENTATION

Le matériel utilisé pour ces expérimentations se compose :

- de la sonde optique granulométrique CSASP 100 HV
- d'un système d'acquisition P.D.S 300 de la société P.M.S
- d'un microordinateur et d'une imprimante APPLE II

A - METEOROLOGIE

Les données météorologiques sont notées une fois par mesure granulométrique à partir des appareils intégrés au navire :

- vitesse du vent
- direction du vent
- hygrométrie
- pression
- visibilité estimée par un observateur

C - CONFIGURATION

Afin d'éviter au maximum les perturbations causées par la configuration du bâtiment et pour des problèmes de connexions électriques, l'ensemble des appareils d'acquisition est installé à l'intérieur et sur le toit de la cabine abritant l'ascenseur au dessus du hangar avant.

Pour restreindre l'influence de la convection naturelle due au chauffage du sol par les rayonnements solaires, la sonde a été isolée de la paroi d'acier par un support en bois lissé.

L'entrée de la sonde est dirigée face au sens de la marche ayant pris soin auparavant de vérifier que le débit de la sonde à l'intérieur du champ de mesure reste inchangé quelque soit la vitesse du bâtiment. La mesure s'effectue ainsi à une hauteur de 10 mètres au dessus de la mer.

D - EXTRAIT DU JOURNAL DES MESURES

Les vents cités ci-après correspondent à les sources de courant aérien qui peuvent être locales, telles des brises de terre ou de mer liées aux températures et heures de la journée, mais ne font pas forcément référence aux secteurs de vent définis dans le paragraphe III. Précisons que la zone touchée par le vent d'EST (ch.III) s'étend jusqu'au Nord de la Corse, et que le Mistral peut descendre jusqu'au Nord de la Sardaigne.

Journée du 16 juin (figure n°7):

Phénomènes évolutifs :

Départ de Toulon faisant route sur Cap Corse.

Eloignement des terres jusqu'à 16 heures, c.a.d., jusqu'à mi-parcours entre Toulon-Corse : 45 nautiques de la côte.

Vent changeant SE à E force 2 le matin et jusqu'à 16 heures, puis vent de S à SW force 3 à 5 jusqu'à 19 heures.

Observations :

Diminution des concentrations dans la gamme de diamètre inférieur à 1,75 μ m, qui serait due à l'absence de houle et à un éloignement progressif des côtes, donc à une diminution de l'influence continentale porteuse de particules de petits diamètres (profil — — — à profil — + —) , d'autant plus que le vent faible et de secteur Est ne rencontre donc pas de terre à proximité du point de mesure.

Puis augmentation de la concentration des particules de diamètre supérieur à 1,75 μ m coïncidant à une élévation de la force du vent (profil ---). Simultanément, accroissement de la densité de particules de D inférieur à 1,75 μ m mais plus faible que le matin. L'explication vient peut-être du fait que , quoiqu'on se rapproche des côtes corsees, le vent de secteur SW , malgré un renforcement , reste pleinement marin et affaiblit l'influence continentale. En outre, l'apport d'aérosols de fond semble annihilé par la présence d'un vent tournant au SW, contrecarrant l'établissement d'un régime de houle.

Nuit du 17 au 18 juin.(figure n°8)

Phénomènes évolutifs :

Navigation le long de la côte EST de Sardaigne.

Distance à la côte : 10 à 20 nautiques.

Vent de secteur NE force 3, faiblissant vers 2 h 30', puis forcissant

PROFIL DE DENSITE EN AEROSOLS.

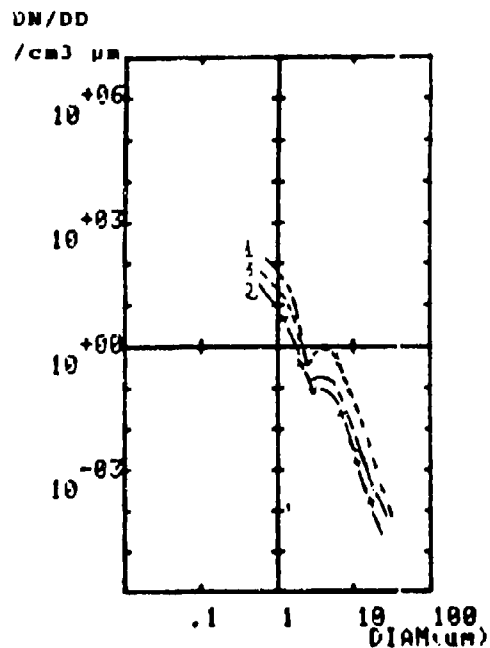


Figure n°7 : Journée du 16 Juin.
 1 — — — : 3 Nques des côtes
 2 — + — : 40 Nques des côtes
 3 - - - : Vent de SW (19h)
 forçant 3 à 5

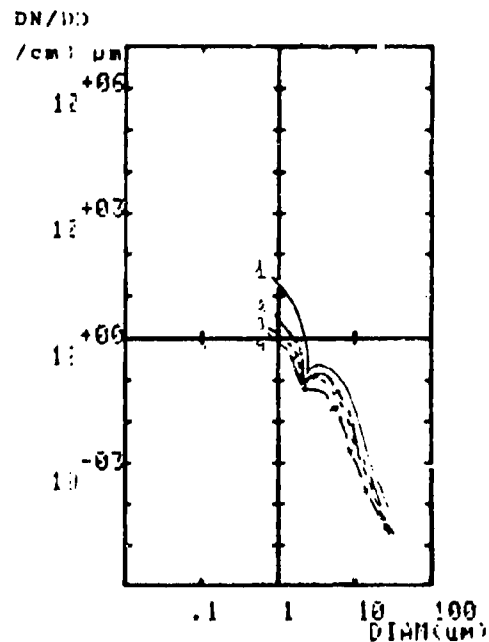


Figure n°8 : Nuit du 17-18 Juin.
 1 — — — : 17 juin; 2 Nques; vent NE4
 2 - - - : Vent de NE 3
 3 - - - : Vent de NE 2
 4 — + — : Vent force 0 } 15 Nques

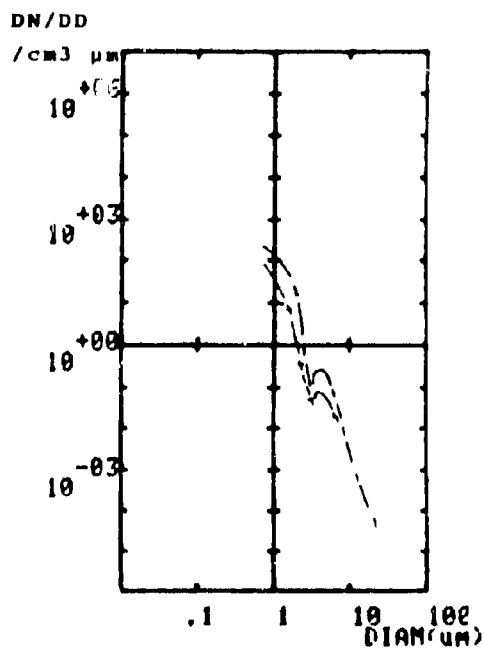


Figure n°9 : Nuit du 26-27 Juin.
 — — — : NNW5 60 Nques
 — + — : NNW5 80 Nques

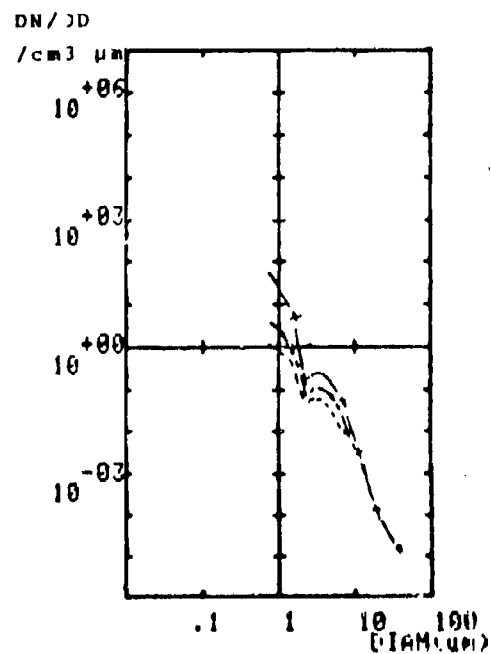


Figure n°10 : Sardaigne.
 — + — : NNW4 à 5 ; 20 Nques
 - - - : force 0
 — - — : NE 3

jusqu'au matin.

Observations :

Evolution relativement logique des profils avec la vitesse du vent. Tous les diamètres jusqu'à 10 μ m sont touchés par les variations de force du vent.

Remarques :

Les profils enregistrés durant la nuit sont nettement plus bas que ceux pris lors de la précédente journée. Il faut préciser que la côte n'était qu'à 1 à 2 nautiques alors que pendant la nuit, nous naviguions à 15 nautiques environ des côtes.

De plus, longeant l'île par l'Ouest, ceci combiné à un vent de NE force 2 à 3 provoque une influence côtière assez importante le 17 juin, si on tient compte du passage récent de la masse d'air au dessus des terres. Par contre, durant la nuit, le fait de longer la Sardaigne par l'Est avec un vent de NE, nous oblige à considérer l'influence continentale comme nulle, l'Italie se trouvant à 100 nautiques à l'Est.

Nuit du 26 au 27 juin. (figure n°9)

Phénomènes évolutifs :

Vent fort de secteur NNW.

Navigation en pleine mer, traversée Cap Corse-Toulon.

Observations :

Forte concentration de particules inférieures à 8 μ m due vraisemblablement au vent de NNW soufflant depuis la veille provoquant un régime de houle et un apport continental croissant, d'autant plus qu'on se rapproche de la côte française.

figure n°10 :

Trajet 1 : le long de la côte Est Sardaigne

Trajet 2 : même trajet en sens inverse

Vent de NNW force 4 pour trajet 1

Vent de NE force 2 à 0 à 3 pour trajet 2.

Profil coïncidant pour des diamètres supérieurs à 10 μ m.

Concentrations dix à quinze fois plus élevées pour trajet 1 sur la gamme de diamètres inférieure à 10 μ m.

Non seulement le vent est plus fort, mais il passe au dessus des terres de Sardaigne, donc apport d'aérosols continentaux et d'embruns. La mesure se fait à 15 à 20 nautiques des côtes donc on peut dire que la mer peut relativement se former, mais la présence de l'île casse vraisemblablement la houle qui se forme sous l'action du vent de NW.

Si on compare un profil d'aérosols pris à 3 mètres au dessus du niveau de la mer par vent faible à un profil pris à 6 mètres par temps de

fort Mistral et mer agitée, on observe une coïncidence des points de mesure jusqu'à des diamètres de 26 μm et une apparition de diamètres supérieurs dans le cas du vent fort. La mesure ayant été effectuée à l'intérieur de la rade de Toulon, le phénomène de houle n'a pas pu s'amorcer. En outre, l'origine continentale du vent et la proximité des côtes ont davantage pour conséquence un lessivage de l'atmosphère qu'un apport d'aérosols marins.

VI - INTRODUCTION A LA VALIDATION DU CODE LOWTRAN 6

La forme analytique du modèle NAVY MARITIME paraît être une bonne approche des profils mesurés en Mer Méditerranée, quoique sous-estimant les concentrations dans la gamme de 1 μm à 10 μm .

En outre, une modification nécessaire a été de prendre pour R3, rayon modal relatif au vent en cours, une valeur de 1 μm , le point d'inflexion correspondant au troisième mode du NAVY MARITIME étant apparemment légèrement décalé par rapport aux mesures (figure n°11).

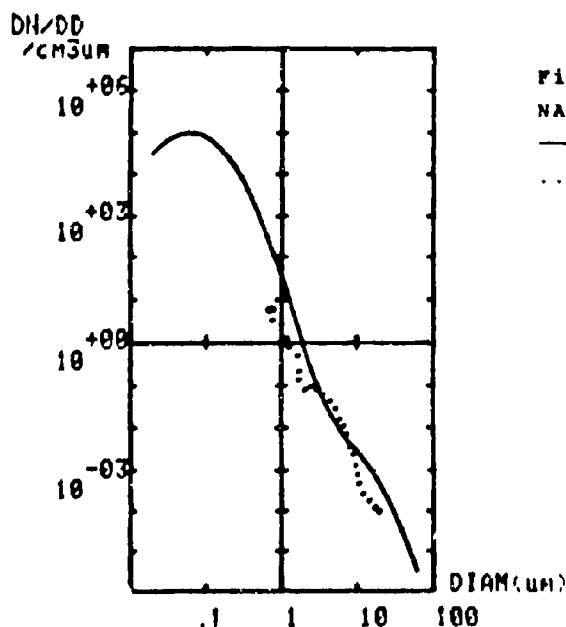


Figure n°11 : Comparaison du modèle NAVY MARITIME et d'un profil mesuré.
 — : Navy Maritime ; R3 = 2 μm
 : Profil mesuré à 3 m. d'altitude

Un programme s'appuyant sur la Théorie de MIE⁽²⁾ permet de calculer les coefficients d'extinction et d'absorption par les aérosols à partir d'un modèle de profil Navy Maritime réajusté. La démarche consiste ensuite à intégrer ces résultats dans la carte du code LOWTRAN correspondant à l'option "User Defined" et de lancer le calcul avec la visibilité mesurée.

Le processus de calcul du Code Lowtran dans sa partie contribution aérosols est le suivant :

$$T_{aer} = \text{EXP} (- K_{extaer} () \times \text{HAZE} \times \text{RANGE})$$

RANGE : longueur du trajet
 Kext() : coefficient d'extinction calculé pour chaque longueur d'onde et normalisé au coefficient à 0,55 μm .
 HAZE : coefficient d'extinction à 0,55 μm calculé à partir de la visibilité introduite par l'utilisateur.

: 3,92 / vis. observée

Si on utilise comme coefficient de normalisation le coefficient d'extinction calculé par le programme de MIE à $0,55\mu\text{m}$ et que la visibilité mesurée est introduite, le Code Lowtran nous donne une transmission de 8% sur la bande $3\mu\text{m}$ - $5\mu\text{m}$. Par contre, si les coefficients insérés dans la carte "User Defined" sont de la forme :

coeff() calculés par programme de MIE / HAZE

avec HAZE = 3,92 / Visibilité observée

la transmission obtenue par le code Lowtran devient 22 %, et se rapproche nettement de celle mesurée simultanément avec le profil en aérosols et évaluée à 28 % sur la bande $3\mu\text{m}$ - $5\mu\text{m}$.

La différence vient du fait que le profil utilisé dans le calcul des coefficients de MIE a été enregistré à 3 mètres de hauteur, alors que la mesure de transmission s'effectue à 40 mètres d'altitude. En considérant que les concentrations sont susceptibles de diminuer lorsqu'on monte en altitude, la transmission calculée à cette même hauteur ne pourra être que meilleure.

Cependant, dans le cas où l'option "Navy Maritime" a été choisie avec les paramètres météorologiques mesurés sur le site, le code Lowtran nous évalue la transmission à 17 %, ce qui nous éloigne de la valeur mesurée.

VII - CONCLUSION

La spécificité et l'intérêt de la connaissance du milieu méditerranéen nous encouragent à approfondir le comportement des différents paramètres mis en jeu (transmission, conditions météorologiques, localisation...). Des mesures systématiques de transmission atmosphérique sont prévues pour les mois à venir après l'implantation du détecteur quantique, lequel permettra une précision plus importante de la mesure et une extension à la bande $8\mu\text{m}$ - $12\mu\text{m}$. De même, la campagne de mesures granulométriques en mer se poursuit dans le cadre de la validation du modèle Navy Maritime.

Remerciements :

Que le responsable, Mr Hervé BONHOMMET, ainsi que les membres du groupe Optronique soient chaleureusement remerciés pour leur aide apportée à l'amélioration du Transmissiomètre.

Bibliographie :

- 1 - F.X.KNEIZYS, EP.SHUTTLE, "Atmospheric transmittance/radiance : Computer Code Lowtran6", ERP n°846, AFGL, TR-83-0187, 1983.
- 2 - Stuart G.GATHMAN, "Optical properties of the marine aerosol as predicted by the Navy aerosol model", Opt. Eng., vol.22 n°1, (1983), 057-062.
- 3 - M.TIMMERMAN, Von Karman Institute, "Computation of light scattering phenomena in L.D.V", Mai 1981, note technique n°139.

DISCUSSION

D. HÖHN

What experimental method did you use to measure aerosol size distributions up to about 40 m above the sea surface?

AUTHOR'S REPLY

In a marine environment, measurements were made between 3-15 m depending on the kind of Navy ship available. For higher altitudes, we used an elevator between 3-45 m located at a cliff. Effects of the cliff may have affected the aerosol size distributions.

E. SHUTTLE

Your results showed the measured transmission was higher than predicted by the LOWTRAN 6 Navy Maritime Aerosol Model which means the aerosol extinction for LOWTRAN was higher than your measurements which is the reverse of what the previous speaker showed.

AUTHOR'S REPLY

There may be a difference between the S. Uist and the Mediterranean environments.

E. SHUTTLE

The change in the Navy Maritime Aerosol Model between LOWTRAN 6 and LOWTRAN 7, as pointed out by J. Ridout, does in fact tend to reduce the numbers of the larger aerosols which could explain some of the differences. This change was provided to AFGL by S. Gathman of NRL based on measurements of H. Hughes at NOSC. Also, the uncertainties in the molecular contribution due to errors in measuring the temperature and relative humidity could account for some of the differences.

AUTHOR'S REPLY

I sincerely regret that my data on the Navy Maritime Aerosol Model are already obsolete. I should get the latest version of the model, particularly since it addresses the third mode of the aerosol distribution covering particle sizes larger than 2 micron in radius. This size range considerably affects transmission in the 3-5 micron and 8-12 micron bands.

J. RIDOUT

I agree that the values presented in the first paper do contradict somewhat those of the second but we were discussing only aerosol extinction. Also this paper used a different equation for the quantity A_3 than the first.

AUTHOR'S REPLY

The new Navy Maritime Aerosol Model, at first sight, seems to lower the wind effect on aerosol concentration and, therefore, restore the transmission rates in the IR; this brings the results of our experiments into closer agreement.

NEW SPECTRAL FEATURES OF STRATOSPHERIC TRACE GASES

A. Goldman, F. J. Murcray, R. D. Blatherwick, J. J. Kusters,
F. H. Murcray, and D. G. Murcray
Department of Physics
University of Denver
Denver, Colorado 80208 USA

C. P. Rinsland
Atmospheric Sciences Division
NASA Langley Research Center
Hampton, Virginia 23665 USA

A new Michelson-type interferometer system operating in the infrared at very high resolution (0.002-0.003 wavenumber FWHM) has been used to record numerous balloon-borne solar absorption spectra of the stratosphere, ground-based solar absorption spectra, and laboratory spectra of molecules of atmospheric interest. In the present work, we report results obtained for several important stratospheric trace gases, HNO_3 , ClONO_2 , HO_2NO_2 , NO_2 , and COF_2 , in the 8- to 12- μm spectral region. Many new features of these gases have been identified in the stratospheric spectra. Comparison of the new spectra with line-by-line simulations shows previous spectral line parameters are often inadequate. New analysis of high resolution laboratory and atmospheric spectra and improved theoretical calculations will be required for many bands. Preliminary versions of several sets of improved line parameters under development are presented.

1. Introduction

(NU) A new Michelson-type interferometer system capable of recording broadband infrared absorption spectra at an unapodized FWHM resolution of 0.002 wavenumber has recently become operational for field and laboratory use. This instrument, which is operated by the University of Denver Atmospheric Spectroscopy Group, is a modified version of a commercial instrument (Bomem model DA3.002) and has been used to record numerous balloon-borne solar absorption spectra of the stratosphere, ground-based solar absorption spectra, and laboratory spectra of molecules of atmospheric interest. A description of the spectrometer system has been reported [Murcray et al., 1989].¹ In this paper, we present the analysis of these spectra to obtain new information on the absorption by five important stratospheric trace gases, HNO_3 , ClONO_2 , HO_2NO_2 , NO_2 , and COF_2 , in the 8- to 12- μm region. Numerous new absorption features of these gases have been observed in the balloon-borne and laboratory spectra. Sample flight and laboratory spectra in regions useful for quantifying the concentrations of these gases in the stratosphere are presented. Analysis of the new features shows much of the available line parameters are inadequate, and new spectroscopic studies are required. Preliminary versions of several sets of improved line parameters under development are presented.

(NU) The balloon-borne solar spectra were obtained during two recent flights from 32°N latitude. The first flight occurred on the afternoon of November 18, 1987, from Fort Sumner, New Mexico. Data were obtained on the ground, during ascent, and from the float altitude of 37 km for solar zenith angles less than 85°. These spectra cover 700 to 1350 wavenumber at 0.002 wavenumber resolution. The second flight was conducted from Palestine, Texas, on the afternoon and early evening of June 6, 1988. During this flight, 0.003 wavenumber resolution spectra were recorded from high sun angles through a solar astronomical zenith angle of 94.81° (tangent height of 15.4 km). Lower sun data were then recorded at reduced resolution (0.02 wavenumber) for zenith angles down to 95.41°. The data from the second flight cover 650 to 1300 wavenumber. Selected regions of the spectra from both flights have been published in an atlas format with line positions and identifications of the measured atmospheric and solar features [Goldman et al., 1988a].² For well resolved lines, the positions have an estimated accuracy of ± 0.0002 wavenumber with respect to standard calibration lines of CO_2 and N_2O . Results of an analysis of the ^{18}O -isotopic composition of stratospheric ozone above 37 km altitude obtained from analysis of these spectra with significantly improved normal and isotopic ozone line parameters has also been reported [Goldman et al., 1988b].³

2. Results

2.1 Nitric Acid (HNO_3)

(NU) Recently, a number of important infrared and far infrared bands of nitric acid have been analyzed at high resolution for the first time: the ν_6 , ν_7 , and ν_8 bands by Maki and Olson [1988],⁴ the ν_9 band by Goldman et al., [1988c],⁵ and the $\nu_8 + \nu_9$ band by A. Maki (private communication, 1988). Based on these studies, line-by-line spectroscopic parameters have been generated for use in atmospheric studies (A. Maki, private communication, 1988). The ν_9 fundamental (band center 763.154 wavenumber) and the $\nu_8 + \nu_9$ combination band (band center 1205.707 wavenumber) fall within the region covered by the new balloon flight and laboratory spectra.

(NU) The ν_8 fundamental band is relatively weak, but it contributes significant absorption over long atmospheric paths. The Q branch at 763.1 wavenumber is the most prominent feature and was identified several years ago in 0.02 wavenumber resolution stratospheric solar absorption spectra [Goldman et al., 1982;⁶ 1987].⁷ Figure 1 shows the 762.0-764.0 wavenumber region containing the Q branch in a 0.002 wavenumber resolution HNO_3 laboratory spectrum and a sequence of stratospheric spectra obtained at 0.003 wavenumber resolution during the June 1988 balloon flight. All of the spectra are on the same scale, but have been offset vertically for clarity. The uppermost solar spectrum is the sum of 24 stratospheric scans, recorded while the solar zenith angle increased from 63° to 73° , so the value listed in the figure (68°) represents an average. The other spectra are low sun scans with tangent heights of 26.1, 21.0 and 15.6 km. The strongest part of the Q branch appears in the solar spectra as an unresolved feature overlapped by a number of lines of ozone. The HNO_3 feature is first detectable at a tangent height of 30.3 km (not shown in the figure) and is then observed to strengthen rapidly with decreasing tangent height. Figure 2 compares a balloon flight spectrum over a narrower interval along with simulations generated for the same atmospheric ray path using the new HNO_3 line parameters, O_3 line parameters from the work of Pickett et al., [1988],⁸ the 1986 HITRAN compilation [Rothman et al., 1987],⁹ and the reference volume mixing ratio profiles of Smith [1982].¹⁰ The HNO_3 Q branch absorption in the measured and calculated spectra are in good agreement. The O_3 line parameters provide a significant improvement over those on the 1986 HITRAN compilation [Rothman et al., 1987].

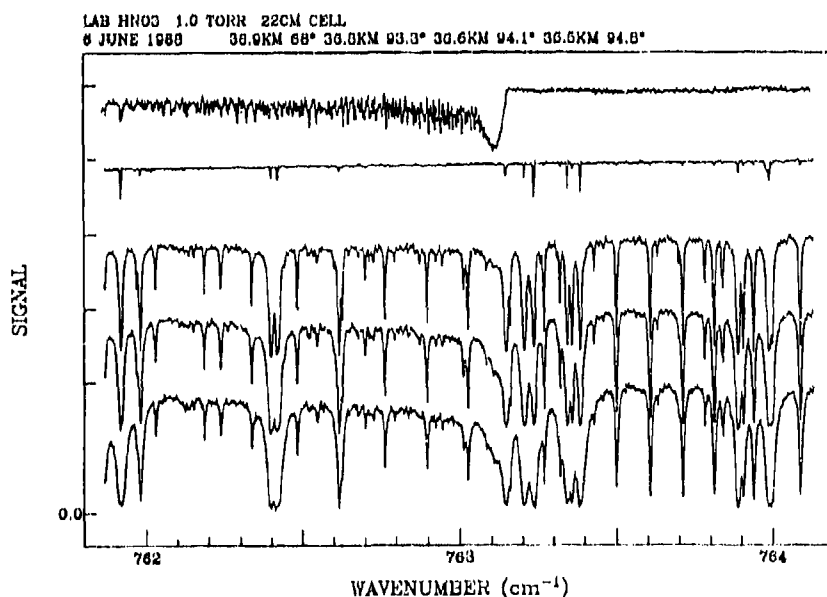


Fig. 1. Laboratory spectrum of HNO_3 at 0.002 cm^{-1} resolution (top) and a sequence of 0.003 cm^{-1} resolution stratospheric solar absorption spectra in the 762 to 764 cm^{-1} region covering the 763.1 cm^{-1} HNO_3 ν_8 band Q branch.

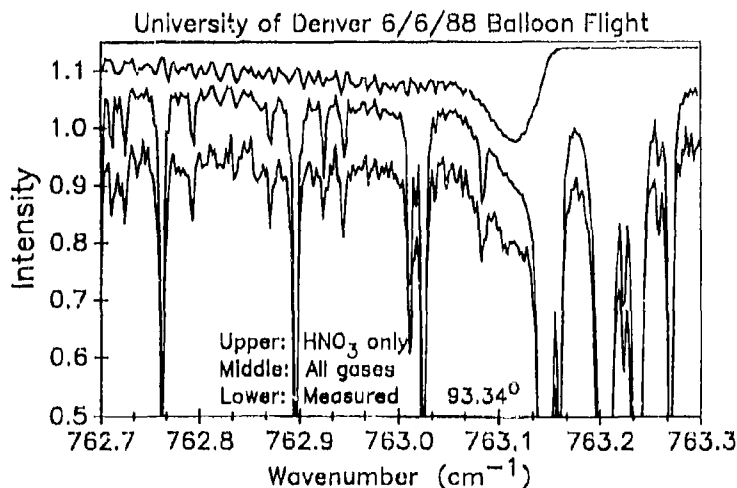


Fig. 2. Comparison of a 0.003 cm^{-1} resolution balloon flight spectrum with line-by-line simulations in the region of the ν_8 band Q branch of HNO_3 at 763 cm^{-1} .

(NU) Laboratory spectra [Goldman et al., 1971;¹¹ Maki and Olson, 1988]⁴ show the HNO_3 ν_8 band P and R branches are strongest near about 745 and 780 wavenumber. The R branch is significantly more intense than the P branch due to vibration-rotation interactions. It has been possible to identify numerous weak HNO_3 features near the R branch peak in the new balloon-borne solar spectra. Of particular interest are the features that can be identified in the region of the 780.2-wavenumber ν_4 ClONO_2 Q branch. These features are discussed in the next section.

(NU) Figure 3 shows a sequence of the high resolution flight data along with a laboratory spectrum of HNO_3 in the 1204 to 1206 wavenumber region, which covers the $\nu_8 + \nu_9$ HNO_3 Q branch at 1205.6 wavenumber. As in the case of the ν_8 band, the Q branch is the most prominent feature of this band. Weaker features of the HNO_3 $\nu_8 + \nu_9$ band have also been identified in the stratospheric spectra from about 1180 to 1220 wavenumber. In Figure 4 a narrower section of the Q branch region from one of the flight spectrum is plotted on an expanded vertical scale along with a simulation of the data including the HNO_3 line parameters generated recently by A. Maki (private communication, 1988). The agreement between the positions and relative intensities of the measured and calculated features is very good. Additional comparisons of the new theoretical parameters with high resolution laboratory data are required for the validation of both the ν_8 and $\nu_8 + \nu_9$ line intensities before atmospheric HNO_3 profiles derived from these features can be presented.

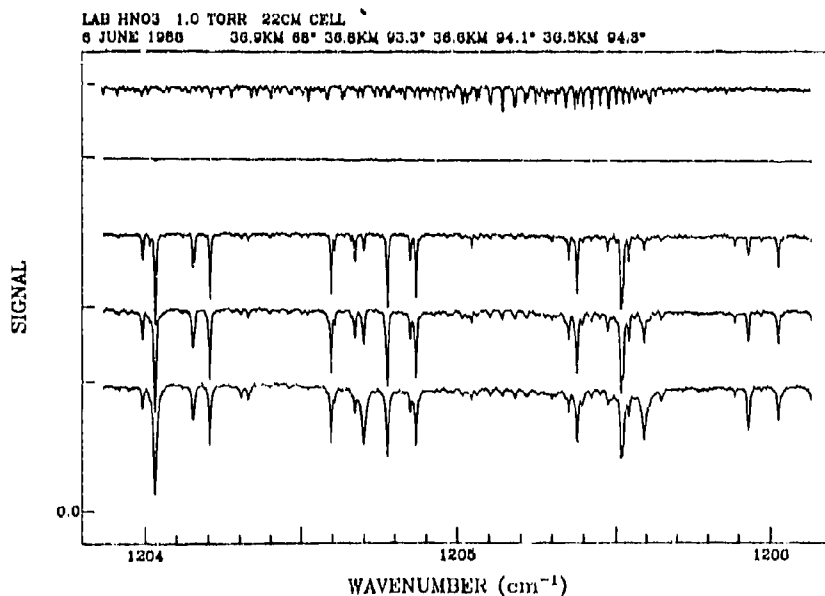


Fig. 3. Laboratory spectrum of HNO_3 at 0.002 cm^{-1} resolution (top) and a sequence of 0.003 cm^{-1} resolution stratospheric solar absorption spectra covering the 1205.6 cm^{-1} HNO_3 ν_8 band Q branch. The laboratory spectrum was recorded with 1.0 Torr of HNO_3 in a 22 cm path length absorption cell at 23°C .

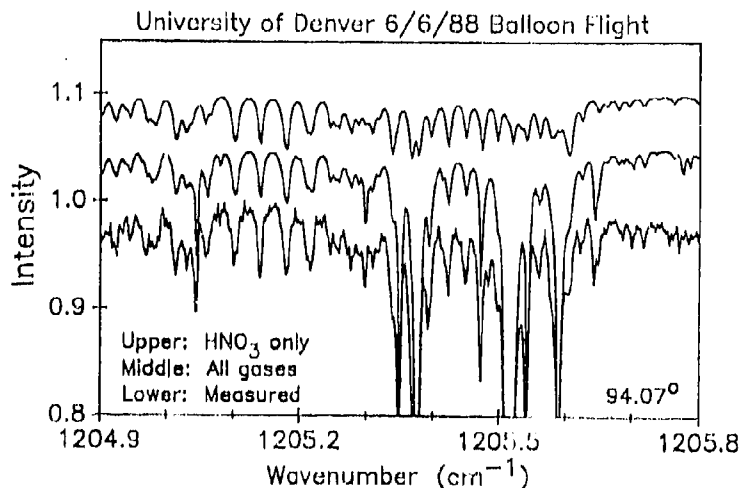


Fig. 4. Comparison of a 0.003 cm^{-1} resolution balloon flight spectrum with line-by-line simulations in the region of the $\nu_8 + \nu_9$ band Q branch of HNO_3 at 1205.6 cm^{-1} .

(NU) The high resolution of the new balloon-borne and laboratory spectra has also revealed the need for improvement in the parameters for the ν_5 and $2\nu_9$ HNO_3 bands. These discrepancies are not apparent at lower resolution in the regions most favorable for quantitative analysis of HNO_3 [cf. Goldman et al., 1984;¹² Murcray et al., 1987;¹³ Rinsland et al., 1988].¹⁴ Figure 5 presents a sequence of June 1988 balloon flight spectra in the 868 to 870 wavenumber region, which is dominated by the regularly-spaced series of P-branch manifolds from the HNO_3 ν_5 band. These features are first observed at a tangent height of 33.7 km, and then strengthen rapidly as the zenith angle increases. In the lower stratosphere, it can be seen that some of the fine structure within the manifolds is lost due to pressure-broadening of the lines. Figure 6 shows a comparison between a lower stratospheric balloon-borne spectrum at 0.003 wavenumber resolution and simulations of the absorption calculated using the reference HNO_3 volume mixing ratio profile of Smith [1992].¹⁰ The absorption in this region is almost entirely due to HNO_3 with the strongest features resulting from ν_5 band P25 manifold at 868.1 wavenumber. The upper panel shows a predicted spectrum computed with the parameters on the 1986 HITRAN compilation [Rothman et al., 1987];⁹ the lower panel presents a calculation with a set of revised line positions for HNO_3 . As can be seen from the figure, there is close agreement between the predicted and measured intensities of the P-branch manifold features in both calculations. However, in the upper figure the calculated positions for some of the individual lines within the manifold are significantly different than the measured values. At this resolution, these discrepancies, which are produced by level crossing resonances between the Fermi interacting ν_5 and $2\nu_9$ vibrational states, are quite apparent. The revised calculation, from work in progress by A. Maki (private communication, 1988), correctly accounts for the resonance perturbations, as shown in the lower figure. Similar agreement is obtained for the other manifolds in the region of atmospheric interest (860-875 wavenumber). Additional work is needed, however, since discrepancies between measurement and calculation remain for the weaker features outside the manifolds (e.g. Fig. 6).

2.2 Chlorine Nitrate (ClONO_2)

(NU) In Figure 7, we show a sequence of four 0.003 wavenumber resolution stratospheric solar spectra from the June 1988 flight in the 780 to 782 wavenumber region covering the ClONO_2 ν_4 band Q branch at 780.2 wavenumber. The ClONO_2 ν_4 band Q branch is clearly visible in spectra at solar zenith angles below 92° . In contrast to earlier lower resolution measurements [Rinsland et al., 1985;¹⁵ Zander et al., 1986;¹⁶ Zander et al., 1987],¹⁷ the O_3 line at 780.2143 wavenumber and the CO_2 line at 780.2314 wavenumber are resolved and are clearly much narrower than the ClONO_2 Q branch absorption. The O_3 line occurs close to the ClONO_2 Q branch absorption peak at 780.213 wavenumber, whereas the CO_2 transition, the stronger of the two lines, is centered about 0.018 wavenumber above the peak, in agreement with simulations with the linelist.

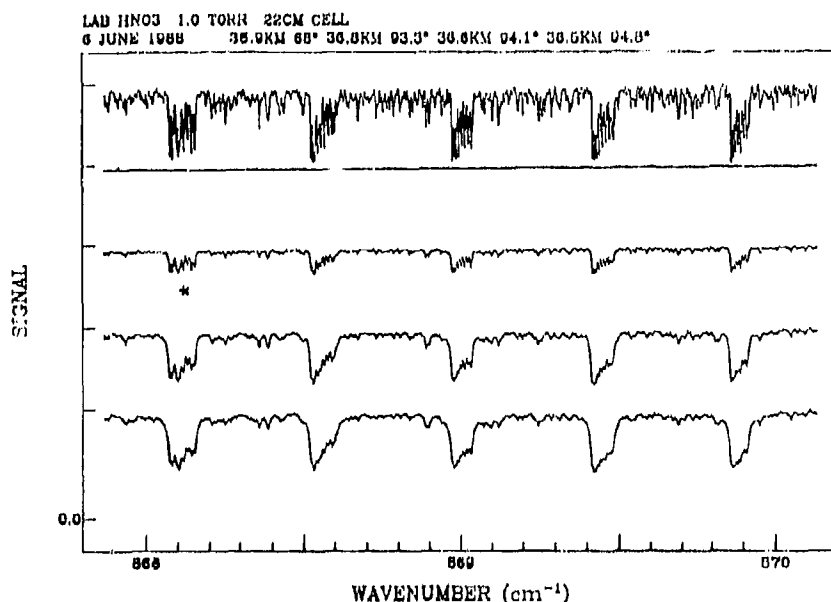


Fig. 5. Laboratory spectrum of HNO_3 at 0.002 cm^{-1} resolution (top) and a sequence of 0.003 cm^{-1} resolution stratospheric solar absorption spectra in the 868 to 870 cm^{-1} region showing several P branch manifolds of the HNO_3 ν_5 band. An asterisk marks the manifold shown on an expanded scale in Fig. 5.

(NU) Figure 8 shows two laboratory spectra of ClONO_2 and two laboratory spectra of HNO_3 in the 780 to 782 wavenumber region at 0.002 cm^{-1} resolution. As can be seen from the figure, significant HNO_3 absorption is observed throughout the region with a number of lines overlapping the ClONO_2 Q branch. Earlier laboratory spectra [Murcray et al., 1984]¹⁸ show the ClONO_2 Q branch as an unresolved feature at 0.02 cm^{-1} resolution. The new higher resolution laboratory spectra show significant fine

structure within the Q branch. The structure is consistent with the features observed recently in tunable diode laser spectra (D. Smart, NPL, private communication, 1988) and suggests the effect of resolution may be important in evaluating cross sections for the ClONO_2 Q branch. Indeed, comparisons of peak absorption cross sections reported for the ClONO_2 Q branch at room temperature (e.g. Davidson et al. [1987];¹⁹ Ballard et al. [1988])²⁰ and resolution-degraded versions of the new laboratory spectra show the peak cross section increases substantially from ~ 0.06 to 0.002 wavenumber resolution, but more than 30% differences exist between the results of the various laboratories (S.T. Massie and A. Goldman unpublished results, 1988). Hence, much further work is needed before stratospheric ClONO_2 can be quantified accurately from infrared measurements.

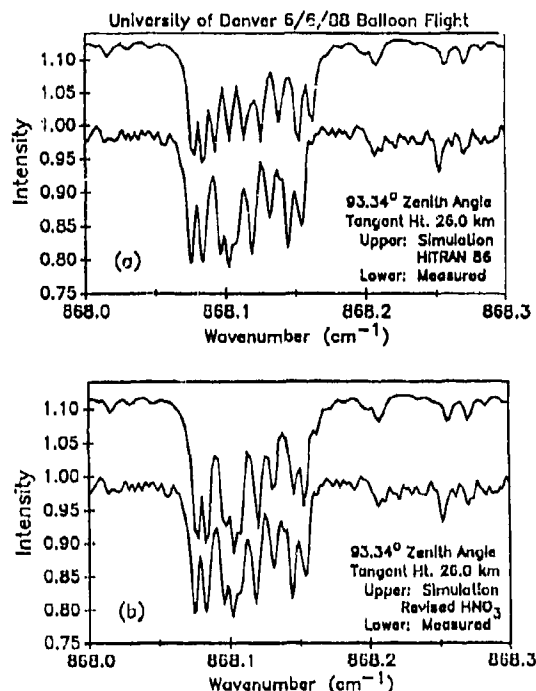


Fig. 6. Comparison of a 0.003 cm^{-1} resolution balloon flight spectrum with line-by-line simulations in the region of the HNO_3 P25 manifold at 868.1 cm^{-1} . The balloon flight spectrum was recorded at a float of altitude 36.75 km. In the upper panel (a), the synthetic spectrum was generated with the HNO_3 line parameters on the 1986 HITRAN compilation [Rothman et al., 1987]. In the lower panel (b), the simulation was generated with the P-branch manifolds positions shifted to account for resonances between rotational levels of the ν_5 and $2\nu_9$ interacting vibrational states.

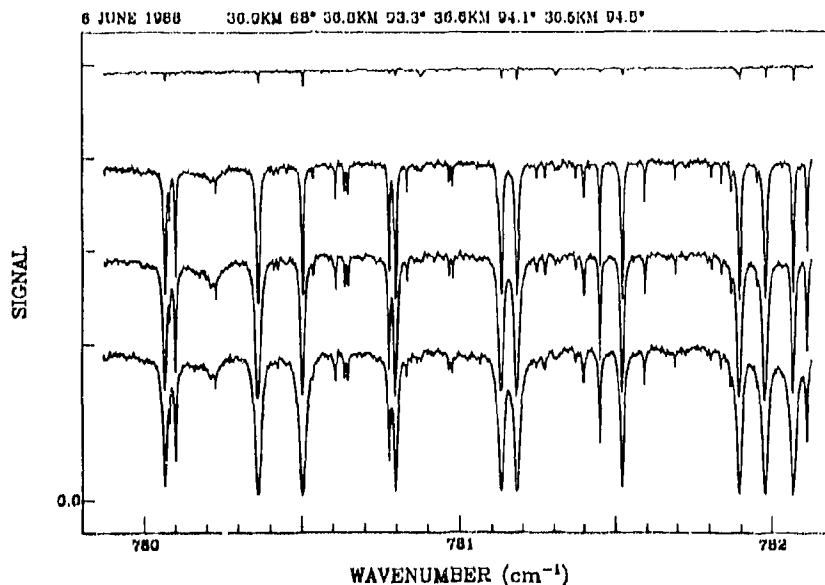


Fig. 7. Sequence of 0.003 cm^{-1} resolution stratospheric solar absorption spectra in the 780 to 782 cm^{-1} region covering the ClONO_2 ν_4 band Q branch at 780.2 cm^{-1} .

LAB HNO₃ 1.0 TORR 2.5 TORR 22 CM CELL
LAB ClONO₂ 0.6 TORR 1.24 TORR 10 CM CELL

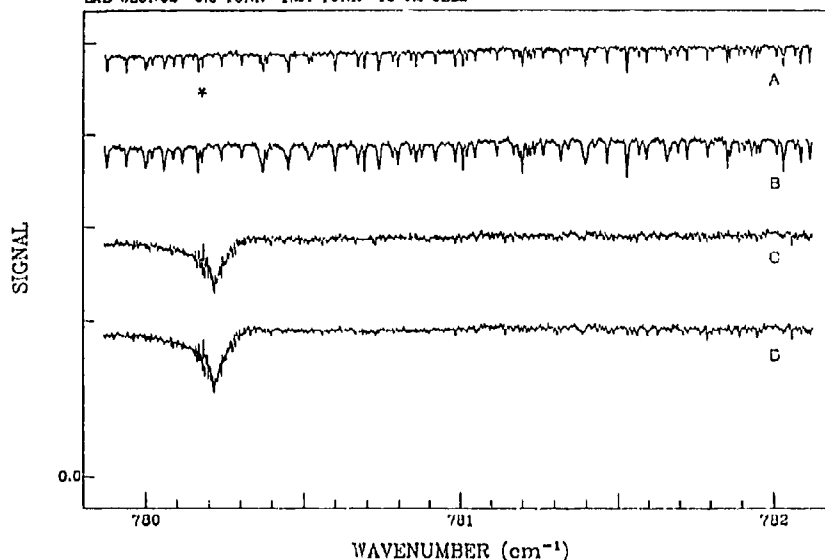


Fig. 8. The 780-782 cm⁻¹ region of two HNO₃ and two ClONO₂ laboratory spectra recorded at 0.002 cm⁻¹ resolution with the University of Denver interferometer system. The upper two spectra were obtained with HNO₃ in a 22 cm path at 23.0°C. The lower two spectra were recorded with ClONO₂ in a 10 cm path length cell at the same temperature. Asterisk marks the two HNO₃ features identified in the balloon flight spectra in Fig. 9.

(NU) The 780.2 wavenumber region at 0.003 wavenumber resolution is shown on an expanded scale in Figure 9, where a balloon-borne solar spectrum of the lower stratosphere and a simulation of the data are presented. The solar spectrum was obtained by coadding June 6, 1988 flight spectra recorded at astronomical zenith angles of 94.07° and 94.81° (tangent heights of 21.0 and 15.4 km, respectively). The simulations include the new line parameters for the HNO₃ ν_8 band and ClONO₂ empirical line parameters from the study of Rinsland et al. [1985]; 158 line parameters for other gases and the volume mixing ratio profiles are the same as those used in simulating the HNO₃ ν_8 branch region. It can be seen that significant HNO₃ absorption is predicted in this interval. The asterisks indicate two features in the balloon flight spectra with measured positions of 780.165 and 780.179 wavenumber. These features are superimposed on broad absorption by the low wave number wing of the unresolved ClONO₂ Q branch. The positions and strengths of these two features correspond closely with peaks in the calculated HNO₃ absorption spectrum at 780.1664 and 780.1737 wavenumber, each of which is an unresolved doublet in the line list. These predicted features are also marked with asterisks in the 0.002 wavenumber resolution laboratory spectra presented in Fig. 8. The two HNO₃ features were observed previously as a single unresolved peak near 780.180 wavenumber in 0.01-0.02 wavenumber resolution solar spectra (Rinsland et al. [1985],¹⁵ Zander et al. [1986],¹⁶ and Zander and Demoulin [1988]).²¹

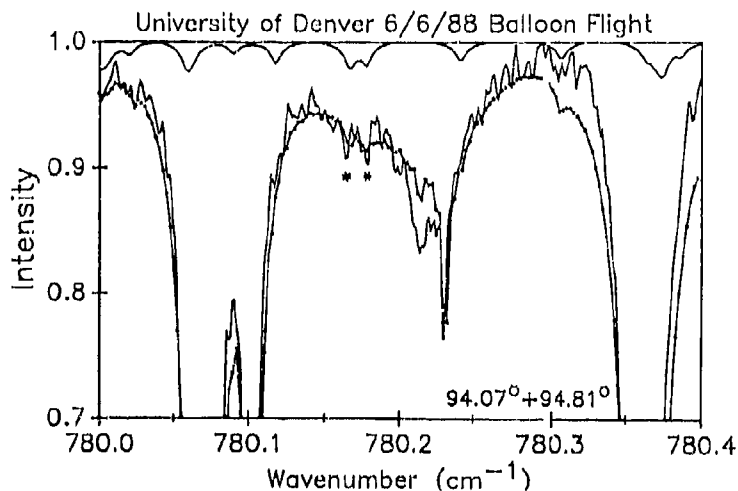


Fig. 9. Comparison of a 0.003 cm⁻¹ resolution balloon flight spectrum with line-by-line simulations in the region of the ν_8 band ClONO₂ Q branch at 780.2 cm⁻¹. The spectrum at top is a calculation of the HNO₃ absorption. The lower simulation was generated with all gases, including HNO₃. Asterisks indicate two features assigned to HNO₃ that overlap the ClONO₂ Q branch. Nearby lines of CO₂ and O₃ are also identified (see text for details).

(NU) The weaker ν_3 band Q branch at 809.4 wavenumber falls directly on top of a strong CO_2 line at 809.3717 wavenumber, so the ClONO_2 fine structure cannot be seen. Away from the CO_2 line, the weaker fine structure is not visible, but the broad depression from this band between 809.0 and 809.7 wavenumber can be detected on the 94.07° and 94.81° scans (tangent heights of 21.0 and 15.4 km, respectively) by overlaying the low sun data on the coadded high sun spectrum. In addition, in the lowest zenith angle scans recorded during the flight (95.2°, 95.3°, and 95.4°), the ν_7 Q branch of CHClF_2 (CFC-22) at 809.1 wavenumber appears on the low wavenumber side of the ClONO_2 broad feature, in agreement with the analysis by Zander et al. [1987].

(NU) The flight spectra also show absorption by the 1292 wavenumber ClONO_2 ν_2 band Q branch, the strongest feature of ClONO_2 in the infrared. Because of the improved spectral resolution, significant fine structure within the Q branch has been observed for the first time in both the laboratory and flight spectra. However, stratospheric quantification from this spectral region is difficult because of absorption by numerous interfering lines from several molecules [Goldman et al., 1987]. At present, the primary problems are the poor agreement between the reported low temperature ClONO_2 ν_2 band cross sections [Davidson et al., 1987; Ballard et al., 1988] and the absence of line-by-line parameters for the HNO_3 lines which absorb significantly in this region. Absorption is produced by the ν_3 (1307 wavenumber) and the stronger ν_4 (1326 wavenumber) bands. Recent high resolution laboratory studies of the HNO_3 band [Webster et al., 1985; Webster, 1988] are being extended to cover the 1290 to 1295 wavenumber region (R. D. May, private communication, 1988).

2.3 Peroxynitric acid (HO_2NO_2)

(NU) In Figure 10, we show a HO_2NO_2 laboratory spectrum at 0.004 wavenumber resolution (top) and the sequence of four 0.003 wavenumber resolution stratospheric solar spectra from the June 1988 balloon flight. This region contains the HO_2NO_2 ν_6 Q branch at 802.7 wavenumber, which is relatively free of strong atmospheric interference and is the most suitable infrared HO_2NO_2 feature for atmospheric measurement. Line positions and identifications of stratospheric and solar features derived for this region from the flight spectra have been included in the new stratospheric atlas [Goldman et al., 1988a]. The laboratory spectrum shows two prominent peaks near 802.57 and 802.79 wavenumber within the Q branch (marked by asterisks). In addition, fine structure not apparent at 0.04 wavenumber resolution [Murray et al., 1984] can be seen. Similar fine structure is observed in the very high resolution laboratory spectra presented by Webster [1988] and May et al. [1988]. When plotted on an expanded scale, the laboratory spectrum in Fig. 10 shows each of the two peaks is split at the higher resolution into two nearly equal intensity components. The feature at 802.57 wavenumber resolves into components at 802.5697 and 802.5754 wavenumber. In the lower stratosphere, these components would undoubtedly be pressure-broadened into a single feature at 802.5726 wavenumber with a FWHM of about 0.006 wavenumber. Similarly, the 802.79 wavenumber feature resolves into two components at 802.7859 wavenumber and 802.7903 wavenumber, which blend into a feature centered at 802.7881 wavenumber with a FWHM of about 0.006 wavenumber.

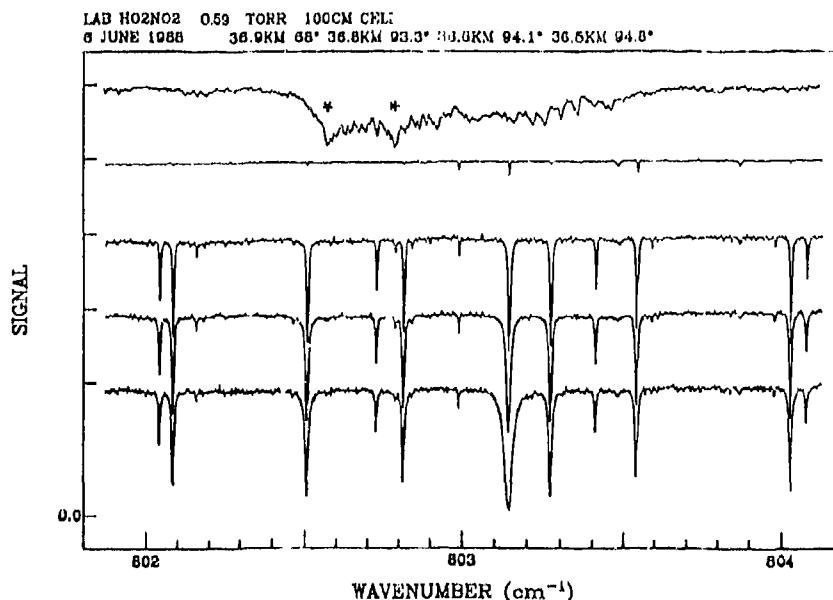


Fig. 10. Laboratory spectrum of HO_2NO_2 recorded at 0.004 cm^{-1} resolution (top) and a sequence of 0.003 cm^{-1} resolution stratospheric solar absorption spectra from the June 1988 balloon flight. The spectral region contains the relatively strong HO_2NO_2 ν_6 band Q branch at 802.7 cm^{-1} . Asterisks beneath the laboratory spectrum show two peaks in the Q branch observed previously in 0.04 cm^{-1} resolution laboratory spectra [Murray et al., 1984].

(NU) Figure 11 shows the HO_2NO_2 Q branch region in a lower stratospheric solar absorption spectrum at 0.003 wavenumber resolution obtained by coadding 4 of the scans from the June 6, 1988 balloon flight. A weak feature at 802.5728 wavenumber (marked by an asterisk) coincides very well with the lower frequency HO_2NO_2 peak observed in the laboratory data. This feature has also been observed in 0.01 wavenumber stratospheric solar spectra recorded by the ATMOS instrument during the Spacelab 3 mission [Rinsland et al., 1986a],²⁵ but the ATMOS data yield a slightly higher measured position of 802.5767 ± 0.0004 wavenumber. Both measurements are lower than the position of a nearby CO_2 line (R16 of the 11101-10002 band of $^{16}\text{O}^{12}\text{C}^{18}\text{O}$), which is listed at 802.5844 wavenumber on the 1986 HITRAN compilation [Rothman et al., 1987].⁹ Although this CO_2 line has not been measured in the laboratory, both the upper and lower vibrational levels have molecular constants that are well determined from high resolution measurements [Rothman, 1986],²⁶ so the position of this line should be accurately computed. The coadded solar spectrum in Fig. 6 shows no evidence for this CO_2 line at its predicted position, which is too far away to be blended with the HO_2NO_2 peak at the high resolution of the data. Also, it can be noted that the 802.5728 wavenumber feature is significantly broader than nearby single lines, indicating that it cannot be attributed solely to a single, absorption line. The HO_2NO_2 feature at 802.7881 wavenumber is less than a resolution element from a much stronger O_3 line at 802.7900 wavenumber and is therefore masked. In contrast to the ATMOS observations [Rinsland et al., 1986a],²⁵ the balloon-borne spectra do not show evidence for broad absorption by the HO_2NO_2 Q branch envelope.

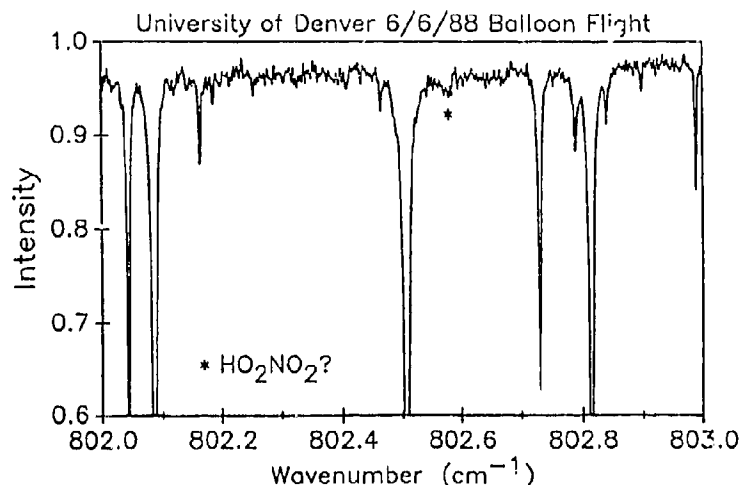


Fig. 11. Balloon-borne lower stratospheric solar absorption spectrum (0.003 cm^{-1} resolution) in the region of the HO_2NO_2 Q branch at 802.7 cm^{-1} . The spectral data are plotted on an expanded vertical scale to show an absorption feature at 802.5728 cm^{-1} (marked by an asterisk) tentatively assigned to HO_2NO_2 .

2.4 Nitrogen dioxide (NO_2)

(NU) In previous studies, spectral lines from both the ν_3 (1617 wavenumber) and the $\nu_1 + \nu_3$ (2906 wavenumber) bands have been used extensively for the identification and consistent quantification of atmospheric NO_2 from balloons, aircraft, and ground-based measurements [WMO, 1986;²⁷ Flaud et al., 1988;²⁸ Goldman and Chen, 1988].²⁹ The high resolution of the present flight data shows the fine structure of several Q branches of the much weaker ν_2 band, especially in the 800-830 wavenumber region, where interference by other species is small. These Q branches have been observed as unresolved features in the ATMOS stratospheric spectra [Zander et al., 1986;¹⁶ Rinsland et al., 1987].³⁰

(NU) Figure 12 shows two balloon-borne solar spectra in the region of the Q_4 subbranch of NO_2 at 825.6 wavenumber and simultaneous least-squares best fits to both spectra. The NO_2 line parameters used in the calculation were taken from the HITRAN 1986 compilation [Rothman et al., 1987];⁹ the calculated absorption features are in good agreement with those in the flight data. The quantitative results are in general agreement with results obtained from other stratospheric data covering the ν_3 and the $\nu_1 + \nu_3$ bands. The more recent study of the NO_2 ν_2 band by Perrin et al. [1988]³¹ should provide further improvement in the line parameters in the near future. The O_3 line parameters used here are from Pickett et al. [1988].⁸ As noted for the other intervals, these new O_3 parameters produce significantly better results than those on the 1986 HITRAN compilation [Rothman et al., 1987].⁹

2.5 Carbonyl fluoride (COF_2)

(NU) COF_2 was first observed in the stratosphere from analysis of the ATMOS/Spacelab 3 spectra where features in the 1925-1960 wavenumber (unresolved ν_1 band manifolds), 1249-1255 wavenumber (ν_4 band features) and 774 wavenumber (unresolved ν_6 band Q branch) regions were identified [Rinsland et al., 1986b].³² At the time, no spectral line parameters were available, and empirical absorption parameters in the ν_1 and the ν_6 regions were used to determine preliminary COF_2 vertical profiles.

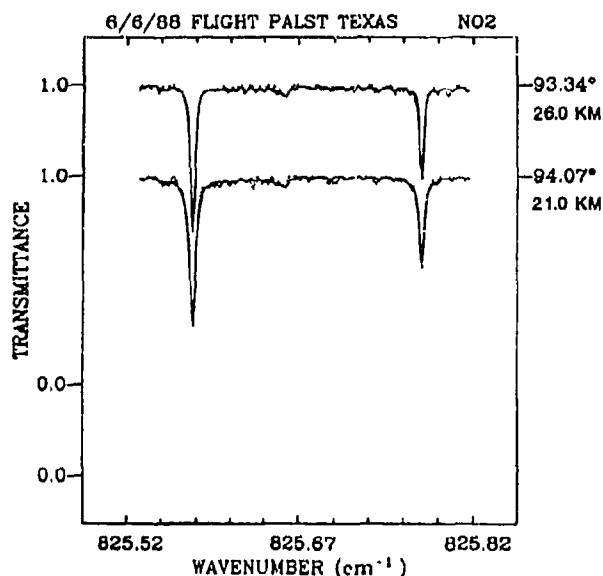


Fig. 12. Examples of simultaneous least-squares fits of two stratospheric spectra in the region of the R_{Q4} subbranch of NO_2 v_2 band at 825.6 cm^{-1} . The measured spectra was recorded at 0.003 cm^{-1} resolution during the June 1988 balloon flight. The least-squares best-fit spectra (smooth curves) are in good agreement with the measurements.

(NU) The flight data presented here reveal numerous resolved COF_2 lines (actually K-doublets) of the v_4 band, such as those shown in Fig. 13 for the 1250-1252 wavenumber region, as well as absorption by the v_4 band Q branch at 774 wavenumber as shown in Fig. 14. Since the ATMOS analysis, line parameters for the v_6 band have become available [Thakur et al. 1987]³⁵ and were used in the present studies. Recent laboratory spectra recorded at 0.002 wavenumber with the Denver Interferometer system (such as shown in Fig. 13) were used in the present study for generating individual line parameters for the 1230-1260 wavenumber region. This was feasible because of the preliminary v_4 band analysis by Lewis-Bevan et al. [1986],³³ from which it was possible to derive assignments, spectroscopic constants, positions, lower state energies, and relative line intensities. After scaling the intensities, synthetic spectra fit the laboratory spectra very well over limited spectral regions, including the most favorable regions for analyzing the v_4 band features in the stratospheric spectra (near 1250 and 1235 wavenumber). The new line parameters are available from the authors on request. However, the effects of perturbations can be seen in the spectra, since the locations of several lines are displaced from their predicted positions. Hence, additional work is needed to explain these perturbations before a reliable list of parameters can be calculated for the entire band.

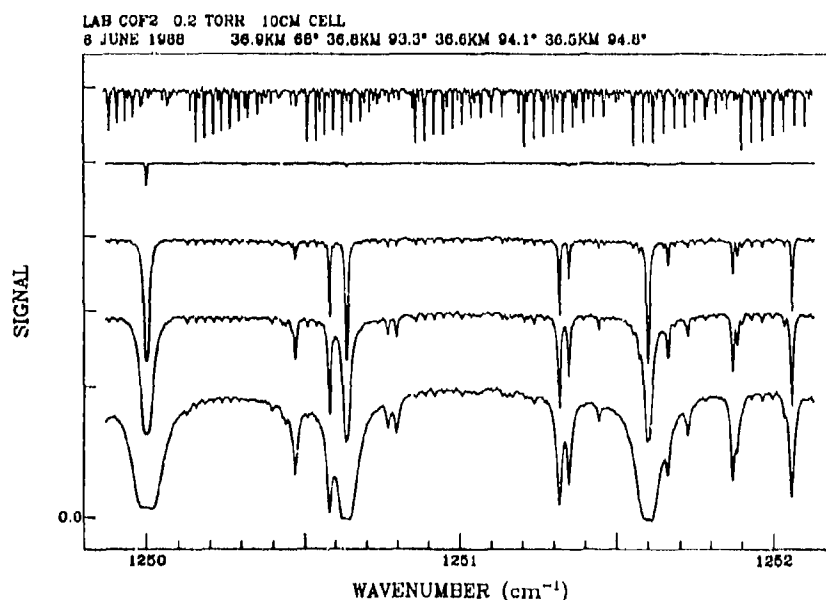


Fig. 13. Laboratory spectrum of COF_2 recorded at 0.002 cm^{-1} resolution (top) and a sequence of 0.003 cm^{-1} resolution stratospheric solar absorption spectra from the June 1988 balloon flight. The spectral region contains several manifolds of the COF_2 v_4 band.

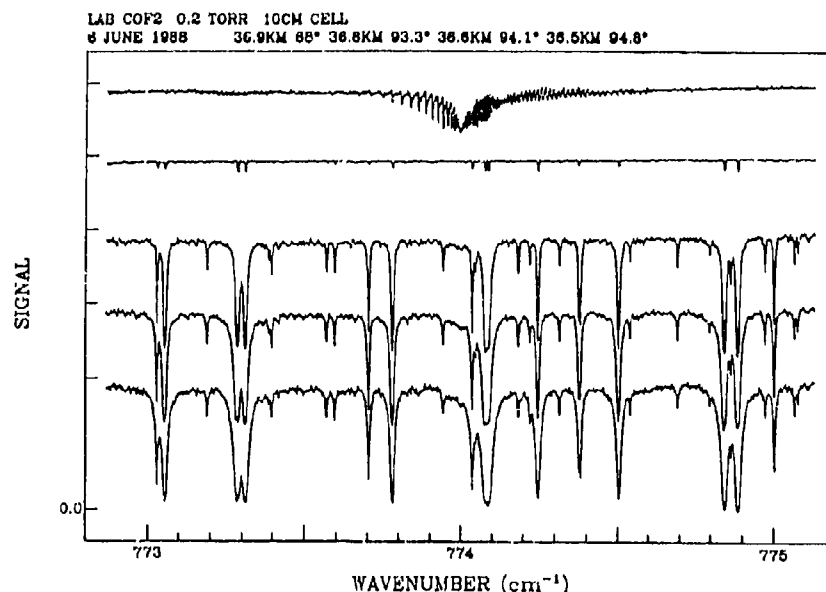


Fig. 14. Laboratory spectrum of COF₂ recorded at 0.002 cm⁻¹ resolution (top) and a sequence of 0.003 cm⁻¹ resolution stratospheric solar absorption spectra from the June 1988 balloon flight. The spectral region contains the Q branch of the COF₂ ν₆ band.

(NU) The 0.02 wavenumber resolution laboratory spectrum of COF₂ in the atlas of Murcray et al. [1984]¹⁸ shows absorption by the ν₄ band extending from about 1210 to 1270 wavenumber. The new 0.002 wavenumber resolution laboratory spectra (such as in Fig. 13) show numerous resolved lines over this interval, many of which are clearly seen in the flight spectra between 1230 and 1260 wavenumber. This interval is also the most favorable infrared region for detecting HOCl and H₂O₂. Hence, an accurate set of spectroscopic parameters for the COF₂ ν₄ band is needed to calculate the effects of COF₂ spectral interference near the predicted H₂O₂ and HOCl line positions. While no H₂O₂ and HOCl lines have been identified yet in the new balloon spectra, it has been noted that the H₂O₂ line parameters on the 1986 HITRAN compilation [Rothman et al., 1987]⁹ do not reproduce our recent 0.002 wavenumber resolution H₂O₂ laboratory spectra, particularly in the wings of the band. A new analysis based on the new laboratory spectra is in progress. The recently improved O₃ line parameters (see Goldman et al. [1988b]³ for a description) provide good simulations to the stratospheric O₃ lines in this region.

(NU) Both the ν₄ and the ν₆ COF₂ regions have been used for preliminary simulations of the flight spectra, as shown in Fig. 15 and 16. The initial results suggest the possibility of an increase in the concentrations of stratospheric COF₂ as compared to those measured by ATMOS [Rinsland et al. 1986b].³² Further analysis of the laboratory spectra to obtain improved energy levels and line intensities is in progress and will be used for more detailed quantification of stratospheric COF₂.

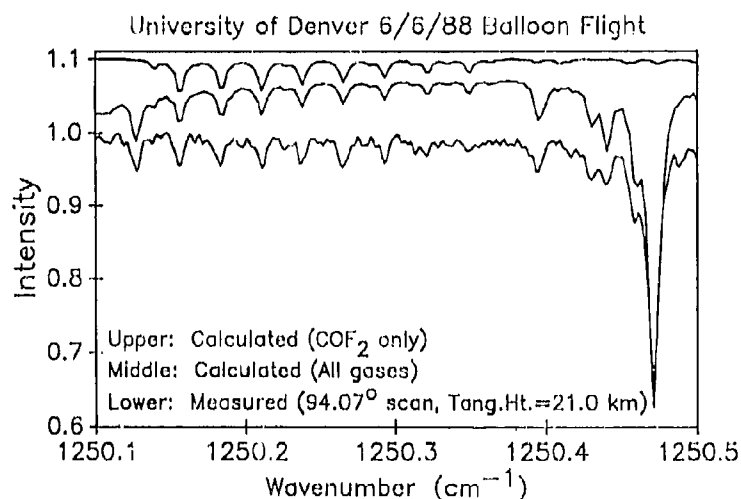


Fig. 15. Comparison of a 0.003 cm⁻¹ resolution balloon flight spectrum with line-by-line simulations in a region containing a number of features of the ν₄ band of COF₂. The solar spectrum was recorded from a float altitude of 36.63 km.

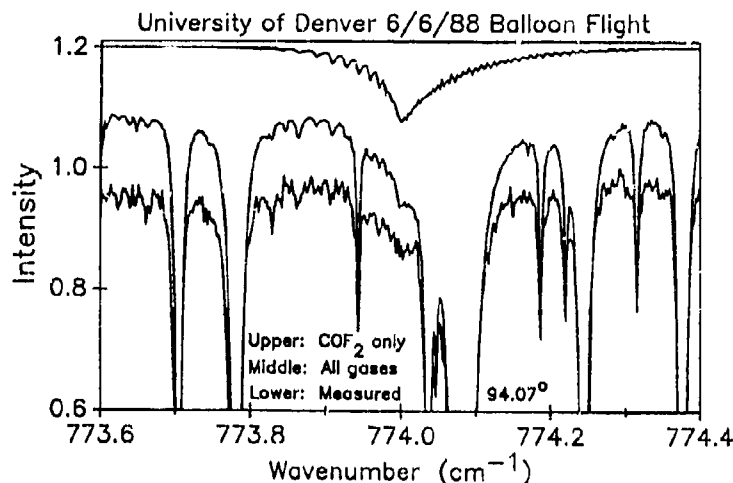


Fig. 16. Comparison of a 0.003 cm^{-1} resolution balloon flight spectrum with line-by-line simulations in the region of the ν_6 band Q branch of COF_2 . The solar spectrum was recorded from a float altitude of 36.63 km with the tangent height computed to be 21.0 km.

(NU) Based on the analysis of the ν_2 band of COF_2 at 963 wavenumber reported by Lewis-Bevan et al. [1985],³⁴ a listing of predicted line positions, relative intensities, and lower state energies has been generated. After scaling the intensities, simulations with these parameters show good agreement with the new high resolution laboratory spectra. Although the predicted features of this band are quite weak, a few weak features of this band near 955 wavenumber have been tentatively identified in the balloon flight spectra.

3. Summary and Conclusions

(NU) We have reported the analysis of new infrared spectroscopic observations of several important stratospheric trace gases obtained with a 0.002 wavenumber resolution interferometer system. The molecules studied are HNO_3 , ClONO_2 , HO_2NO_2 , NO_2 , and COF_2 . The stratospheric solar spectra, ground-based solar spectra, and laboratory spectra reveal new details of the absorption by these molecules in the 8- to 12- μm window region, which is important in determining the radiative heat balance of the atmosphere. It has been possible to assign numerous previously unidentified features to these gases in the stratospheric spectra and incorporate new spectroscopic parameters for their simulation. Many of these features are not accounted for in the available line parameters compilations. The excellent agreement between the highly precise laboratory and stratospheric positions and the broadened width of the 802.5728 wavenumber feature in the flight data provide significant new evidence for absorption by the HO_2NO_2 802.7-wavenumber Q branch in the lower stratosphere. The improved resolution of the flight measurements has also revealed additional details of the interference in the ClONO_2 780.2 wavenumber Q branch region, including the identification of two overlapping HNO_3 features. New features of other trace gases (e.g. CF_4 in the 1283 wavenumber region) have been identified in the stratospheric spectra and are currently under study.

(NU) The present work has shown previous spectral line parameters are often inadequate at the high resolution of the new balloon-borne spectra, and new analysis of high resolution laboratory and atmospheric spectra and improved theoretical calculations are required for many molecular bands of atmospheric interest. Such preliminary studies have been presented here. Additional studies will be needed for accurate quantification of the vertical profiles of these and other gases in the stratosphere from high resolution spectra.

References

1. Murcray, F.J., J.J. Kusters, R.D. Blatherwick, J. Olson, and D.G. Murcray, High resolution solar spectrometer system for measuring atmospheric constituents, submitted to Appl. Opt., 1989.
2. Goldman, A., R.D. Blatherwick, J.J. Kusters, F.J. Murcray, J.W. Van Allen, F.H. Murcray, and D.G. Murcray, Atlas of very high resolution stratospheric IR absorption spectra, Preliminary Edition, November, 1988, Department of Physics, University of Denver, Denver, Colorado., 1988a.
3. Goldman, A., F.J. Murcray, D.G. Murcray, J.J. Kusters, C.P. Rinsland, C. Camy-Peyret, J.-M. Flaud, and A. Barbe, Isotopic abundance of stratospheric ozone from balloon-borne high resolution infrared solar spectra, submitted to J. Geophys. Res., 1988b.
4. Maki, A.G., and W.B. Olson, Infrared spectrum of the ν_6 , ν_7 , and ν_8 bands of HNO_3 , J. Mol. Spectrosc., in press, 1988.
5. Goldman, A., J.B. Burkholder, C.J. Howard, R. Escribano, and A.G. Maki, Spectroscopic constants for the ν_9 infrared band of HNO_3 , J. Mol. Spectrosc., **131**, 1988c, 195-200.

6. Goldman, A., R.D. Blatherwick, F.J. Murcray, J.W. Van Allen, F.H. Murcray, and D.G. Murcray, Atlas of stratospheric IR absorption spectra, Appl. Opt., 21, 1982, 1163-1164.
7. Goldman, A., R.D. Blatherwick, F.J. Murcray, J.W. Van Allen, F.H. Murcray, and D.G. Murcray, New atlas of stratospheric IR absorption spectra, Vol. 1, Line positions and identifications; Vol. 2, The spectra, Department of Physics, University of Denver, Denver, Colo., 1987.
8. Pickett, H.M., E.A. Cohen, L.R. Brown, C.P. Rinsland, M.A.H. Smith, V. Malathy Devi, A. Goldman, A. Barbe, B. Carli, M. Carlotti, The vibrational and rotational spectra of ozone for the (0,1,0) and (0,2,0) states, J. Mol. Spectrosc., 128, (1988), 151-171.
9. Rothman, L.S., R.R. Gamache, A. Goldman, L.R. Brown, R.A. Toth, H.M. Pickett, R.L. Poynter, J.-M. Flaud, C. Camy-Peyret, A. Barbe, N. Husson, C.P. Rinsland, and M.A.H. Smith, The HITRAN database: 1986 edition, Appl. Opt., 26, 1987, 4058-4097.
10. Smith, M.A.H., Compilation of atmospheric gas concentration profiles from 0 to 50, NASA Tech. Memo. 83289, NASA Langley Research Center, Hampton, VA., 1982.
11. Goldman, A., T.G. Kyle, and F.S. Bonomo, Statistical band model parameters and integrated intensities for the 5.9- μ , 7.5- μ , and 11.3- μ bands of HNO_3 vapor, Appl. Opt., 10, 1971, 65-73.
12. Goldman, A., J.R. Gillis, C.P. Rinsland, F.J. Murcray, and D.G. Murcray, Stratospheric HNO_3 quantification from line-by-line, nonlinear least-squares analysis of high-resolution balloon-borne solar absorption spectra in the 870- cm^{-1} region, Appl. Opt., 23, 1984, 3252-3255.
13. Murcray, F.J., F.H. Murcray, A. Goldman, D.G. Murcray, and C.P. Rinsland, Infrared measurements of several nitrogen species above the South Pole in December 1980 and November-December 1986, J. Geophys. Res., 92, 1987, 13373-13376.
14. Rinsland, C.P., A. Goldman, F.J. Murcray, F.H. Murcray, R.D. Blatherwick, and D.G. Murcray, Infrared measurements of atmospheric gases above Mauna Loa, Hawaii, in February 1987, J. Geophys. Res., 93, 1988, 12607-12626.
15. Rinsland, C.P., A. Goldman, D.G. Murcray, F.J. Murcray, F.S. Bonomo, R.D. Blatherwick, V. Malathy Devi, M.A.H. Smith, and P.L. Rinsland, Tentative identification of the 780-wavenumber ν_4 Q branch of chlorine nitrate in high-resolution solar absorption spectra of the stratosphere, J. Geophys. Res., 90, 1985, 7931-7943.
16. Zander, R., C.P. Rinsland, C.B. Farmer, L.R. Brown, and R.H. Norton, Observation of several chlorine nitrate (ClONO_2) bands in stratospheric infrared spectra, Geophys. Res. Lett., 13, 1986, 757-760.
17. Zander, R., C.P. Rinsland, C.B. Farmer, and R.H. Norton, Infrared spectroscopic measurements of halogenated source gases in the stratosphere with the ATMOS instrument, J. Geophys. Res., 92, 1987, 9836-9850.
18. Murcray, D.G., F.J. Murcray, A. Goldman, F.S. Bonomo, and R.D. Blatherwick, High resolution IR laboratory spectra, Appl. Opt., 23, 1984, 3502.
19. Davidson, J.A., C.A. Cantrell, R.E. Shetter, A.H. McDaniel, and J.G. Calvert, Absolute infrared absorption cross sections for ClONO_2 at 296 and 233 K, J. Geophys. Res., 92, 1987, 10921-10925.
20. Ballard, J., W.B. Johnston, M.R. Gunson, and P.T. Wassell, Absolute absorption coefficients of ClONO_2 at stratospheric temperatures, J. Geophys. Res., 93, 1988, 1659-1665.
21. Zander, R., and Ph. Demoulin, Spectroscopic evidence for the presence of the ν_4 -Q branch of Chlorine Nitrate (ClONO_2) in ground-based infrared solar spectra, J. Atmos. Chem., 6, 1988, 191-200.
22. Webster, C.R., R.D. May, and M.R. Gunson, Tunable diode laser stark modulation spectroscopy for rotational assignment of the HNO_3 7.5 μm band, Chem. Phys. Lett., 121, 1985, 429-436.
23. Webster, C.R., Stratospheric composition measurements of Earth and Titan using high-resolution tunable diode laser spectroscopy, J. Quant. Spectrosc. Radiat. Transfer, in press, 1988.
24. May, R.D., L.T. Molina, and C.R. Webster, Tunable diode laser measurements of HO_2NO_2 absorption coefficients near 12.5 μm , J. Phys. Chem., 92, 1988, 4667-4669.
25. Rinsland, C.P., R. Zander, C.B. Farmer, R.H. Norton, L.R. Brown, J.M. Russell III, and J.H. Park, Evidence for the presence of the 802.7-wavenumber band Q branch of HO_2NO_2 in high resolution solar absorption spectra of the stratosphere, Geophys. Res. Lett., 13, 1986a, 761-764.
26. Rothman, L.S., Infrared energy levels and intensities of carbon dioxide. Part 3, Appl. Opt., 25, 1986, 1795-1816.
27. World Meteorological Organization, Atmospheric ozone 1985: Assessment of our understanding of the processes controlling its present distribution and change, WMO Rep. 16, Geneva, Switzerland, 1986.
28. Flaud, J.-M., C. Camy-Peyret, J.W. Brault, C.P. Rinsland, and D. Cariolle, Nighttime and daytime variation of atmospheric NO_2 from ground-based infrared measurements, Geophys. Res. Lett., 15, 1988, 261-264.
29. Goldman, A., and D. Chen, Bibliography of high-resolution microwave to infrared field measurements of atmospheric gases 1985-1988, Department of Physics, University of Denver, December 15, 1988.
30. Rinsland, C.P., R. Zander, C.B. Farmer, R.H. Norton, and J.M. Russell III, Concentration of ethane (C_2H_6) in the lower stratosphere and upper troposphere and acetylene (C_2H_2) in the upper troposphere deduced from atmospheric trace molecule spectroscopy/spacelab 3 spectra, J. Geophys. Res., 92, 1987, 11951-11964.

31. Perrin, A., C. Camy-Peyret, Flaud, J.-M., and J. Kauppinen, The ν_2 band of $^{14}\text{N}^{16}\text{O}_2$ - spin - rotation perturbations in the (010) state, *J. Mol. Spectrosc.*, 130, 1988, 168-182.
32. Rinsland, C.P., R. Zander, L.R. Brown, C.B. Farmer, J.H. Park, R.H. Norton, J.M. Russell III, and O.F. Raper, Detection of carbonyl fluoride in the stratosphere, *Geophys. Res. Lett.*, 13, 1986b, 769-772.
33. Lewis-Bevan, W., A.J. Merer, M.C.L. Gerry, A.J. Morton-Jones, and P.B. Davies, Analysis of the high-resolution DTR spectrum of the ν_4 band of carbonyl fluoride, *Molecular Spectroscopy Symposium*, Riccone, Italy, 1986.
34. Lewis-Bevan, W., A.J. Merer, M.C.L. Gerry, P.B. Davies, and A.J. Morton-Jones, The high-resolution infrared spectrum of the 2_0^1 band of carbonyl fluoride: Determination of the far infrared laser frequencies, *J. Mol. Spectrosc.*, 113, 1985, 458-471.
35. Thakur, K.B., K. Narahari Rao, R.R. Friedl, C.P. Rinsland, and V. Malathy Devi, Analysis of high resolution fourier transform spectra of the ν_6 band of carbonyl fluoride, *J. Mol. Spectrosc.*, 123, (1987), 255-266.

Acknowledgements. This research was supported in part by NSF and in part by NASA. We thank A. Maki for sending us his calculations of the new HNO_3 line parameters and D. Rolens and P. Manning for part of the computer processing of the data. Acknowledgement is made to the National Science Foundation, for computer time used in this project.

DISCUSSION

J. SELBY

You mentioned that it is very important to characterize the atmospheric path along your line of sight to the sun. I agree this is very important. However, for low sun angles, when the sun is near the horizon, the transmission along the line-of-sight to the top and bottom of the solar disc can vary significantly and it is necessary to account for this when simulating your measurement conditions. Do you account for this?

AUTHOR'S REPLY

Yes.

MINIMIZING THE EFFECTS OF THE ATMOSPHERE IN THE OBSERVATION OF ULTRAVIOLET RADIATION

by

A.V.Dentamaro

Science Applications International Corporation
6 Fortune Drive
Billerica, MA 01821

C.G.Stergis and V.C.Baisley
Geophysics Laboratory (AFSC)

GL/LIU
Hanscom AFB, MA 01731
United States

Ground measurements have been performed which provide us with an accurate method of measuring ultraviolet radiation sources propagating through the atmosphere. This method of measurement effectively minimizes the influence of the atmosphere in the detection of UV sources at equal or greater altitude at the specific time the measurements are being made, allowing us to evaluate propagation losses. Radiation of wavelength 3000-3700 Å was collected and recorded by a UV imager mounted onto an 18-inch Cassegrain telescope situated on Santa Ynez Mountain, California at an altitude of 1.26 km above sea level. Various meteorological and topographical conditions determine the transmittance of the incident starlight through the atmosphere. Our measurements were taken under optimum conditions (little or no cloud cover, visibility greater than 20 km). The atmospheric transmittance code LOWTRAN 6 was used to generate transmittance as a function of observation angle and meteorological range (quantitative measurement of visibility). Comparing the measured intensity of one star to its known absolute intensity above the atmosphere determines the transmittance for any point in the sky. In addition, extinction coefficients were measured at our observation point and at ground level using a photometer and a standard UV source. Both the stellar and photometer data indicate that the meteorological range during our ten day period of observation varied from 20 to 30 km. Therefore, our method was useful in accounting for changes in the atmosphere. Under these optimum viewing conditions, ground-based measurements of various high altitude sources of radiation such as rocket plumes or vehicle glow with a maximum error due to transmission losses of 10% should be possible.

2. INTRODUCTION

Atmospheric effects in the observation and identification of distant radiation-emitting sources depends strongly on observation point and existing meteorologic conditions. Aerosol absorption and molecular scattering are main contributors to this problem. Since the presence of the atmosphere will inevitably result in some loss of transmission, it would be useful to develop a method of observation which will minimize the effects of the atmosphere in intensity measurements of distant sources. This requires knowing the state of the atmosphere accurately at the time these measurements are being made and being able to account for any fluctuations in the data.

The computer code LOWTRAN 6 which was developed at the Geophysics Laboratory¹ has been seen to accurately calculate radiances and transmittances for a wide range of atmospheric and seasonal conditions for radiation of wavelength $\lambda = 2000 \text{ Å} - 40 \mu\text{m}$. An example of LOWTRAN's usefulness in making transmittance calculations is shown in Figure 1. Here transmittance as a function of near-UV wavelength is seen for observation out to space from sea level along a slant path of 45° elevation. The curves are generated assuming a 1962 Standard atmosphere with rural-type aerosol extinction of moderate concentration. However, these calculated values can only reflect the true atmospheric conditions which are averaged over some finite time scale. If the location of one's observation point is subject to rapidly varying weather conditions, the error inherent in one's measurements may be unacceptable.

Experimental error can be reduced if a direct calculation of atmospheric transmittance can be made just prior to or immediately following the set of principal measurements. Such transmittance measurements are possible by way of several methods. One such method is calculation of ground level extinction which has the advantage of being fairly accurate although somewhat inconvenient. A second option, and one that allows itself more readily to swift execution is the measurement of known stellar sources. These are performed using the same instrumentation which is involved in the principal measurements. This procedure has the further advantage of the apparent stellar intensities being measurable over a variety of slant path geometries, thereby allowing for azimuthal as well as altitude-dependent determination of atmospheric transmissions.

3. FIELD EXPERIMENTS

In the initial experiment, measurements of stellar radiation in the wavelength range $\lambda = 3000 - 3700 \text{ Å}$ were made during the period 18-25 January 1989 from an observation point atop Santa Ynez Mountain, California at an altitude of 1.26 km above sea level. At this position, we were above 70% of the approximately two kilometer maritime boundary layer. The instrumentation is basically the same as described in a previous paper². An f/7.3, 131 in. focal length Cassegrain telescope mounted on a CINE sextant is used for purpose of light collection.

Stellar sources were manually brought into focus with the help of a small tracking scope mounted beside the 18-in. Cassegrain. Several inches behind the telescope was placed a UV imager which consisted of a filter wheel followed by the image tube assembly, after which the 25 mm diameter phosphor image was relayed onto an interline transfer CCD-type solid state television camera. A magnetic tape cassette

recorder was used to store the data (see Figure 2). In order to account for the wide range of intensities which were to be encountered and to prevent possible saturation of the photocathode, the exposure time for the images could be varied from one to 15 msec. Stars of extremely strong intensity could be handled with the addition of neutral density filters to the basic band pass filter (see Figure 3). One slot in the filter wheel was reserved for a quartz lens to aid in the location of very dim stars.

About one minute of useable data was taken for each star in which the object of the measurement was to keep the stellar image in the middle of the video screen to decrease the effects of optical aberration and non-uniformities in the image display. In addition, a centrally located image made data retrieval and subsequent analysis more manageable. Again, possible saturation of signal was monitored during observation with a portable voltmeter. Back in the laboratory, the data was analyzed on a Zenith 248 using a frame-grabbing routine to freeze the tape frame and then digitize the recorded image.

The sums of the analogue digital units (ADU) were recorded for each star and calibration of our imaging system yielded an equivalent photon flux. Variations in the readings, and therefore in the atmosphere were observed by "snapping" the image of the star for every few seconds of real-time data and comparing the resulting sums of ADUs. This point will be expanded upon in later sections.

In the second part of our experiment, ground measurements of the extinction coefficients were performed using a Hanovia mercury lamp as a portable source of near-UV radiation. The lamp was powered by a portable generator and was moved to various distances away from our detection system. The source itself was encased in a plastic box with a collimated opening. The output of the lamp approximated a point source for the distances involved. Sighting scopes were placed on source and detector alike in order to facilitate alignment. After being allowed to warm up for about 20 minutes, the lamp emitted at a fairly constant intensity, with any such small change being noted and accounted for in the final analysis. In this part of the experiment, detection was provided by a solar blind UV photometer consisting of an EMR photomultiplier with Rb_2Te photocathode. Photon counting techniques were employed in measurements of intensity as a function of distance.

Ground measurements were performed at two sites; one at the observation point at the top of Santa Ynez Mountain along a slant path of $\sim 60^\circ$ with respect to the horizontal (Site M) and at a second point located at 400 feet above sea level (Site L). These latter measurements were made each morning of our stay at Vandenberg AFB and were taken in order to give us an idea of the general meteorological range (or visibility, v) of the area. The measurements performed atop the mountain were made just previous to stellar observation. LOWTRAN was used to calculate the effective meteorological range which corresponds to the measured extinction coefficient, k (see Table 1).

Table 1. Measured values of the extinction coefficient along a horizontal path at 400 feet above sea level (Site L) and atop Santa Ynez Mountain at an altitude of 1.26 km (Site M). The equivalent meteorological range (v) as calculated by LOWTRAN is also listed. A 1962 Standard atmosphere with rural extinction is used.

| Date | Local time | Site | Extinction coefficient k (km^{-1}) | Met. Range v (km) |
|--------|------------|------|---|---------------------|
| 18 Jan | 1400 | L | 0.32 | 37 |
| 20 Jan | 1030 | L | 0.21 | 100 |
| 21 Jan | 0900 | L | 0.31 | 40 |
| 22 Jan | 1100 | L | 0.63 | 12 |
| 24 Jan | 0900 | L | 0.62 | 14 |
| 20 Jan | 1700 | M | 0.32 | 26 |
| 21 Jan | 1600 | M | 0.73 | 6 |
| 25 Jan | 0700 | M | 0.27 | 30 |

It should be noted how LOWTRAN is able to discriminate between the two paths used in Table 1. As an example, even though the extinction was measured to be 0.32 km^{-1} on 18 Jan at Site L and on 20 Jan at Site M, the effective values of v reflect the change in altitude and slant path.

4. MODELS

Table 2 lists some of the stars which were visible during our observation period. the photon flux for each star was obtained from data of the Orbiting Astronomical Observatory (OAO-II)³ and represents the integrated total photons/ $\text{cm}^2\text{-sec}$ within the 3000-3700 Å bandwidth striking the top of the atmosphere (see Figure 4). Comparing our measured photon fluxes to those in Table 2 gives the transmittance of the atmosphere for a particular observation elevation angle θ_1 at a certain point in time. LOWTRAN can then be used to yield a value of meteorological range which is equivalent to a determination of aerosol concentration. The basic input parameters for this calculation is altitude of observation point, h_1 ; elevation angle of sighting path and an appropriate model atmosphere and aerosol type.

Santa Ynez's proximity to the Pacific Ocean and various rural surroundings allow for several possible models. Rural extinction assumes the existence of the products of reactions between various gases (water soluble substances, organic compounds) in the atmosphere and the presence of dust particles from the surface. Maritime aerosols are mostly sea-salt particles with a continental component similar to rural models, but with the larger particles eliminated.

We have generated curves of transmittance T versus Q_1 for combinations of two different atmospheres and aerosol extinction models at varying aerosol concentrations (see Table 3) with $v=2-100$ km, $h_1=1.26$ km and $\lambda=3000-3700$ Å. It is seen that at larger values of elevation angle, there is little variation in transmittance over a wide range of visibility values. Figure 5 shows that for zenith viewing angle, there is no more than a 25% change in the value of transmittance for a tenfold change in meteorological range. Therefore, short term variations in the atmosphere are not expected to be immediately observable for intensity measurements made for Q_1 greater than 60° . However, at $Q_1 = 20^\circ$, transmittance can vary by a factor of two with the same tenfold change in v .

Table 2. Integrated stellar photon fluxes ($\lambda = 3000-3700$ Å).

| Star | Photon flux ϕ (photons/cm ² -sec) |
|--------------------------|---|
| Sirius (α CMa) | 1.6×10^6 |
| Rigel (μ Ori) | 8.0×10^5 |
| ζ Ori | 3.7×10^5 |
| Procyon (α CMi) | 1.9×10^5 |
| Capella (α Aur) | 1.6×10^5 |
| η UMa | 9.3×10^4 |
| Arcturus (α Boo) | 2.6×10^4 |
| Polaris (α UMi) | 2.1×10^4 |

The transmittance curves of Figure 5 are correspondingly more sensitive to a change in atmospheric model and aerosol type for shorter meteorological range. Maritime extinction aerosol models generally increase the values of T for different elevation angles by three to four percent over those for rural extinction. Midlatitude winter profiles generally predict transmittance values that run about two percent smaller than those for the 1962 standard model. This means that the maximum error involved in our transmittance values due to model dependence is about six percent.

Transmittance versus visibility and elevation angle is described by the simple equation

$$T(v, \theta) = b(v) \exp[-L(\theta) A(v)] \quad (1)$$

where b and A are visibility-dependent variables; the former is dimensionless while A has the units of an extinction coefficient (km⁻¹). $L(\theta)$ is the length of the sight path through the atmosphere as seen in Figure 6, and is given by the equation

$$L(\theta) = \sqrt{R^2 \sin^2 \theta + r^2} + 2rR - R \sin \theta \quad (2)$$

where θ is recognized as the elevation angle Q_1 , R is the radius of the Earth (6370 km), and r is the thickness of the atmosphere (taken to be 100 km).

Table 3. Model atmosphere generated by LOWTRAN 6 and used in this work.

| Model | Atmosphere | Aerosol(Extinction) |
|-------|--------------------|---------------------|
| A | 1962 Standard | Rural |
| B | 1962 Standard | Maritime |
| C | Midlatitude Winter | Rural |
| D | Midlatitude Winter | Maritime |

5. RESULTS

Our observations are limited to the nights of 20, 21 and 25 January 1989. Attempts to collimate the 18 in. telescope in order to afford daytime viewing have been unsuccessful, and so all measurements will be restricted until after twilight. Weather conditions at our observation sight at 1.26 km altitude were for the most part favorable.

Our analysis of the Vandenberg data will be confined to relative measurements of stellar intensities as a function of elevation angle. This will eliminate any error involved in the calibration of our instrument. Error inherent to the OAO-II data or in the calculations of total integrated photon fluxes might be avoided by comparing the signal from a single star at various elevation angles. However, since a time lapse of one to two hours is needed in order for a star to rise or set an appreciable distance, this method assumes that the atmosphere is remaining fairly constant over this time period. This effectively removes study of short term variations in the atmosphere. As will be seen in the error analysis section, measurements taken at higher elevation angles tend to be more reliable in that there is consistently a smaller spread in the data in these cases. Whenever possible, we will work with data taken at elevation angles of at least 60°. Unless otherwise stated, Model A (Table 3) will be used for all calculations.

Three basic calculations will be made:

- 1) Determination of average meteorological range values for the nights of observation,
- 2) Determination of short-term (one to two hours) variations in the atmosphere,
- 3) Determination of long-term (over several days) variations.

On the nights of 21 and 25 January, several stars were observed in the early evening sky and again about one hour later after they had risen at least 10° in elevation angle.

Table 4. Photometric measurements of sums of analogue digital units (ADU) for the night of 25 January 1989 (normalized to 1 ms exposure time).

| Local Time | Star | Elevation Angle | Avg. sum of ADU |
|------------|------------|-----------------|-----------------|
| 0250 | η UMa | 57° | 2293 \pm 15% |
| | Arcturus | 47° | 502 \pm 20% |
| 0420 | η UMa | 71° | 2666 \pm 18% |
| | Arcturus | 65° | 580 \pm 18% |

If we first assume that the atmosphere atop Santa Ynez peak is slowly varying, we may compare the relative apparent intensity of a single star, η UMa, when it is at $\theta_1 = 57^\circ$ and again when it has risen to 71° (see Table 4). The ratio of the apparent intensities I of Arcturus when at these two positions is calculated from our data to be

$$\frac{I(\theta_1 = 71^\circ)}{I(\theta_1 = 57^\circ)} = \frac{T(71^\circ)}{T(57^\circ)} = 1.163 \pm 31\% \quad (3)$$

Equation (3) shows that the ratio of the apparent intensities (or, equivalently, photon fluxes) for one star at two different elevation angles is equal to the ratio of the transmittances at these two angles for some choice of atmospheric model. Using the transmittance curves in Figure 5 puts the meteorological range for 25 January at about 30-50 km. Using Table 4 and performing the same calculation with the data for Arcturus over the same time period, we get

$$\frac{T(65^\circ)}{T(47^\circ)} = 1.14 \pm 29\% \quad (4)$$

This ratio allows an exceptionally high value of visibility ($v > 100$ km) to be within the limits of error, which seems unlikely by all the other data available. This may be due to a value for the apparent intensity of Arcturus which is inconsistent with the other values measured at 0420 hrs. If this value is eliminated, the ratio in Equation (4) becomes $1.30 \pm 20\%$, which yields $v \sim 30$ km, which falls into line with the η UMa data.

Table 5. Photometric measurements of sums of analogue digital units (ADU) for the night of 21 January 1989 (normalized to 1 ms exposure time).

| Local Time | Star | Elevation Angle | Avg. sum of ADU |
|------------|-------------|-----------------|-----------------|
| 1745 | Capella | 50° | 1925 \pm 5% |
| | ζ Ori | 28° | 2307 \pm 14% |
| 1900 | Capella | 64° | 2027 \pm 10% |
| | ζ Ori | 38° | 3793 \pm 11% |

Table 5 lists similar data for the night of 21 January 1989. Generally, it is seen that the data for the stars Capella and ζ Ori have a smaller spread in the measured apparent intensities. Analysis is the same as for the 25 January data. The ratio of the intensities of Capella after it has risen 14° is

$$\frac{T(64^\circ)}{T(50^\circ)} = 1.05 \pm 13\% \quad (5)$$

Using the transmittance curves in Figure 5, this places a lower limit of the meteorological range at $v = 25$ km. The ζ Ori data over the same time period yields

$$\frac{T(38^\circ)}{T(28^\circ)} = 1.65 \pm 18\% \quad (6)$$

which again pushes our value of v closer to 30 km.

Variations in the atmosphere over this 75 minute period on 21 January may be examined by calculating independent values of v at 1745 hrs and at 1900 hrs:

$$\frac{T(\theta_1; \text{Capella})}{T(\theta_1; \zeta \text{ Ori})} = \frac{I_{\text{Cap}} \phi_{\zeta \text{ Ori}}}{I_{\zeta \text{ Ori}} \phi_{\text{Cap}}} \quad (7)$$

where I is again the measured apparent intensity of the star and ϕ is the absolute photon flux taken from Table 2. For the 1900 hrs data, we get

$$\frac{T(64^\circ)}{T(38^\circ)} = 1.84 \pm 16\% \quad (8)$$

This now places an upper limit on v for 21 January at 35 km. A similar calculation for the early evening data (1745 hrs) yields $v < 20$ km. Because the absolute stellar photon flux for Arcturus varies very rapidly with wavelength in the region 3000-3700 Å, inconsistent results are obtained when Equation 7 is applied to the data in Table 4. Much of the other data for 25 January involves large error in the values of I due to observation at small elevation angles.

Values of extinction from ground measurements at Site M in Table 1 indicate that the nights of 20 and 25 January should be noticeably clearer than 21 January, but the results are just not conclusive. Calculations for 20 January again indicate $v = 20$ -30 km. However, further indications of long-term variations can most easily be investigated by seeing how the apparent intensity of a single star at the same elevation angle varies from night to night. Polaris traces out a counter-clockwise path in the sky at an elevation angle equal to the northern latitude of one's observation point (34.5° N for Santa Ynez Mountain) with $\Delta\theta_1 \sim 1^\circ$. Measurements of the apparent intensity of Polaris for the three nights were equal within experimental error. Similarly, due to large error in some instances, it was not possible to positively confirm short-term variations in the data. There is some indication that the weather was improving during the course of the night on 21 January and similarly deteriorating on 25 January, but again nothing definite may be concluded at this time.

Table 6 shows the magnitude of error involved if a visibility of 50 km is mistakenly calculated to be 25 km. As was noted earlier, the situation gets progressively more serious with sight paths approaching the level of the horizon.

Table 6. Error in transmittance value as a function of elevation angle between 25 km and 50 km meteorological range (Model A).

| Elevation angle | $T(v = 25 \text{ km})$ | $T(v = 50 \text{ km})$ | % Error |
|-----------------|------------------------|------------------------|---------|
| 15° | 0.030 | 0.043 | 43.3 |
| 30° | 0.134 | 0.163 | 21.6 |
| 60° | 0.284 | 0.317 | 11.6 |
| 90° | 0.330 | 0.362 | 9.7 |

6. ERROR ANALYSIS

As has been noted, the apparent intensity of a star is seen to fluctuate, or "twinkle" over very short time scales. This effect increases at the lower elevation angles as is seen in the data of 25 January in Table 7. The observed intensity of η UMa at an elevation angle of 71° was seen to vary by about 11% over a 24 second period. By contrast, the apparent intensity of the low-lying Vega ($\theta_1 = 8^\circ$) was seen to vary by up to 74% over a 36 second period. This was expected since at the lower elevation angle of 8° , the path of observation corresponds to a column through the atmosphere which is five times longer than for $\theta_1 = 71^\circ$. This increases the probability that light winds may sweep aerosols into and out of the line-of-sight. Correspondingly, the error in the Sirius ($\theta_1 = 19^\circ$) data lies between these two

angular extremes. In looking for a further explanation for the error in these measurements, turbulence effects may also be a consideration, but their contribution is not easy to measure. Our position on top of a mountain where winds are a large factor in atmospheric conditions tends to mask the role which turbulence effects may play. Also, the fact that we are not "locked" onto a star during these measurements, but must instead depend upon our telescope operator to manually hold the image for us must be taken into consideration. The resulting fluctuations from this movement in the image in the telescope may well be larger than competing effects.

Table 7. Fluctuations in ADU measurements over time for 25 January 1989.

| Star (Q_{51}) | Total sum of ADU |
|-----------------------------|-------------------------------|
| Vega (8°) | 1527 \pm 47% ^{74%} |
| Sirius (19°) | 2846 \pm 34% |
| η UMa (71°) | 1493 \pm 11% |

Calculational error is small compared to these very short term effects. The data of OAO-II has been seen to be accurate for $\lambda > 2500 \text{ \AA}$ and has been used in the calibration of the long successful International Ultraviolet Explorer (IUE) Project for this wavelength range⁴. Whenever possible, our measurements were made using stars that exhibit photon flux curves that are flat with respect to wavelength as shown in Figure 4. A maximum error of about 4.5% is present in our integrated values of photon flux (Table 2) since an average value of transmittance over the 3000-3700 \AA band has been used. This error can be reduced by performing these calculations using the formula

$$\Phi_{\text{total}}(\lambda=3000-3700 \text{ \AA}) = \Phi^{\lambda}(\lambda) T_{\text{filt}}(\lambda) T_{\text{atm}}(\lambda) \Delta\lambda \quad (7)$$

where $\Phi^{\lambda} = \Phi / \lambda$, T_{filt} is the filter transmission as given in Figure 3, T_{atm} is the wavelength-dependent transmittance of the atmosphere, and $\Delta\lambda$ may correspond to the resolution of either the OAO-II data (20 \AA) or of LOWTRAN (20 cm^{-1}).

The reading error in Q_{51} is about $\pm 3\%$ which corresponds in Figure 5 to a maximum error in transmittance of $\pm 2\%$ (for $30^{\circ} < Q_{51} < 75^{\circ}$, smaller outside of this range). This error can be reduced, and has been in some cases presented here, by using a computer code that employs a rotation of reference frames to convert the right ascension (RA) and declination (DEC) of any star into its apparent position in the sky. Table 8 shows the position of Capella (RA=5.22 hrs, DEC=45.95 $^{\circ}$)⁵ as a function of time for the night of 21 January at Santa Ynez Mountain (34.5 $^{\circ}$ N lat).

Finally, calculating relative transmittances using Equation (1) to fit the curves of Figure 5 introduces about 2% error in the value of T . Therefore, taking all present error into account, we find that for look angles greater than 60° , our values for transmittance should be accurate to within 15% at any time, agreeing with the entries in Table 6.

Table 8. Position in sky of Capella for the night of 21 January (34.5 $^{\circ}$ N. latitude)

| Time (hrs) | Azimuthal Position | Elevation Angle |
|------------|-------------------------|------------------|
| 1600 | 37.11 $^{\circ}$ N of E | 31.20 $^{\circ}$ |
| 1700 | 33.86 $^{\circ}$ N of E | 41.28 $^{\circ}$ |
| 1800 | 32.47 $^{\circ}$ N of E | 51.65 $^{\circ}$ |
| 1900 | 34.41 $^{\circ}$ N of E | 62.01 $^{\circ}$ |
| 2000 | 44.37 $^{\circ}$ N of E | 71.70 $^{\circ}$ |
| 2100 | 76.87 $^{\circ}$ N of E | 78.19 $^{\circ}$ |
| 2200 | 33.17 $^{\circ}$ W of N | 75.75 $^{\circ}$ |
| 2300 | 52.08 $^{\circ}$ W of N | 67.13 $^{\circ}$ |

7. CONCLUSIONS

Whenever feasible, we see that measurements of meteorological range are most accurate for $\theta > 60^{\circ}$. However, if measurements must be made at lower angles, the above-described method of stellar observation provides the advantage of allowing the observer some idea of the error involved in his measurements for any spatial point. This is illustrated by the values in Table 7. Using ground measurements of extinction, it was seen that the visibility on 20 January was about four times greater than that of the following night. In fact, the relatively high value of $k = 0.73 \text{ km}^{-1}$ which was measured on 21 January was due to a diffuse fog lying just around the top of the mountain. However, by the time stellar measurements were made one hour later, this mist had dissipated, leaving a fairly clear sky. Conversely, although ground visibility was good at Site M on 20 January ($k = 0.32 \text{ km}^{-1}$), high cirrus clouds made stellar observation impossible.

The relative results presented here give some insight into what problems may be expected in our measurements of UV radiation through the atmosphere. Ideally, one would like to be able to observe a single star at some point in the sky and be able to calculate a value for T at any other spatial location. However, since terrain plays an important part in these calculations, trying to relate the value of T at two widely separated points in this way may lead to inconsistent results.

The results presented here represent only a small part of the data analysis. Further study of the error due to short term variations in the atmosphere as shown in Table 7 is needed. We have yet to reduce this data.

The period of 18-25 January was one of relatively clear weather and high visibility. These conditions were needed for the initial set of calculations. As our methods improve, we plan to repeat these experiments at different altitudes and during different seasons. This will allow us to perform measurements under a wide range of conditions. Stellar measurements were made under less favorable conditions during a two-week period in September 1988 at Tranquillon Peak, California (0.75 km above sea level). We were able to determine that the average meteorological range for this location and time frame was on the order of 10 km. In addition, weather conditions tended to be quite volatile, changing from clear sky to total cloud cover and rain within an hour in some cases.

Our detection system, while being adequate for the purposes described above, becomes very important when the observation of very distant sources becomes necessary. The spatial resolution of a single pixel is 10 rad which is equivalent to five meter resolution at 500 km distance. This ability coupled to our method of stellar transmission measurements makes the system a powerful tool in the quantitative study of remote sources of UV radiation.

As a final note, it should be emphasized that these measurements are only the first iteration and that absolute photometric measurements will bring an improvement in our methods as long as the choice of atmospheric model is appropriate. Relative measurements, while useful in relaxing the model-dependence of the calculations, can hide inconsistencies in the data that will be exposed by absolute results.

8. REFERENCES

1. F.X. Kneizys, E.P. Shettle, W.O. Gallery, J.H. Chetwynd Jr., L.W. Abreu, J.E.A. Selby, S.A. Clough and R.W. Fenn, "Atmospheric Transmittance/ Radiance Computer Code LOWTRAN 6", 1983, AEGI-TR-83-0187.
2. A.V. Dentamaro, C.G. Stergis and V.C. Ralsley, "Spatial Dependence of the Transmission of UV Radiation Through the Atmosphere", Proceedings of the SPIE 1988 Technical Symposium Southeast on Optics, Electro-Optics and Sensors, Orlando, FL, 1988, 258.
3. A.D. Code and M.R. Meade, "Ultraviolet Photometry from the Orbiting Astronomical Observatory. XXXII. An atlas of Ultraviolet Stellar Spectra", *Astro. J.* 39, 1979, 195.
4. A. Hoggess, "The International Ultraviolet Explorer", Proceedings of the SPIE International Society of Optical Engineers 279, 1979, 168.
5. Burnham's Celestial Handbook, Vol 1-3, New York, Dover Publications, Inc., 1978.

9. ACKNOWLEDGEMENTS

The authors would like to thank Vahan Yterian and Keith Evans for their assistance in making these field measurements and to Dr. Donald Collins for developing the software used to analyze the photometric data.

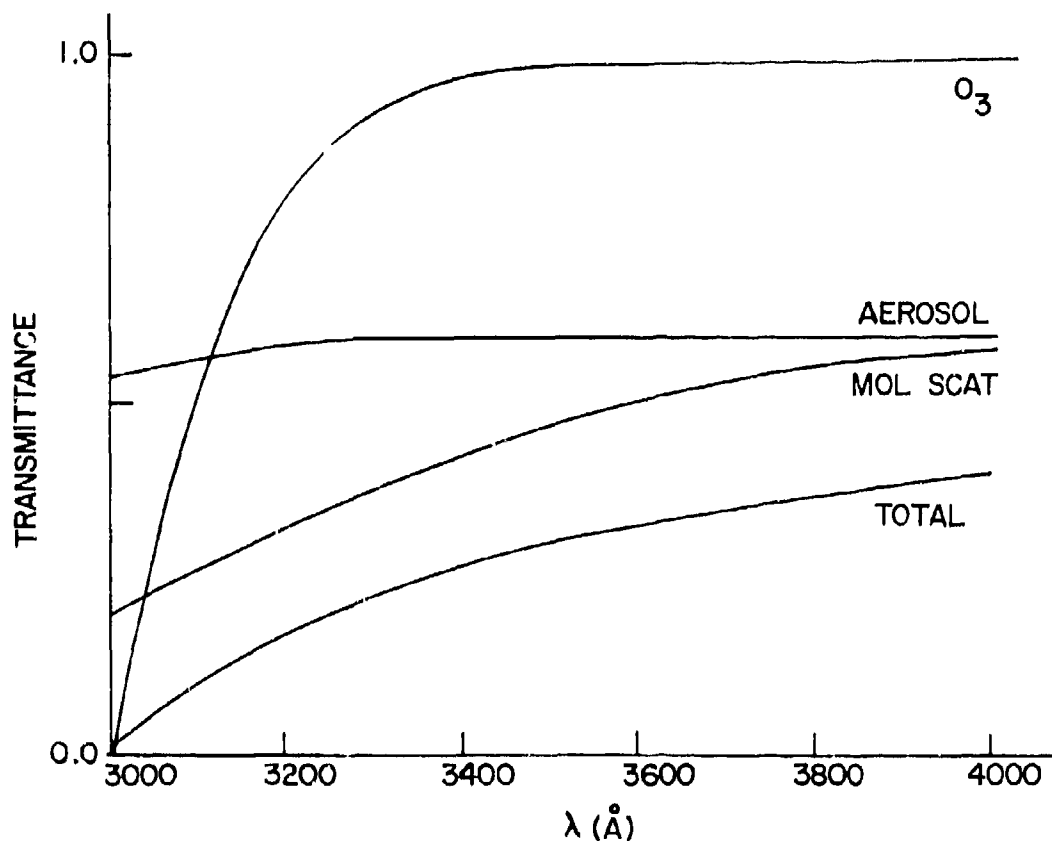


Figure 1. Total and partial transmittances due to ozone absorption, molecular scattering and aerosol absorption in the Earth's atmosphere. A 1962 Standard Atmosphere with rural extinction is used. Meteorological range is 23 km, elevation angle is 45° and $\lambda=3000-4000 \text{ \AA}$.

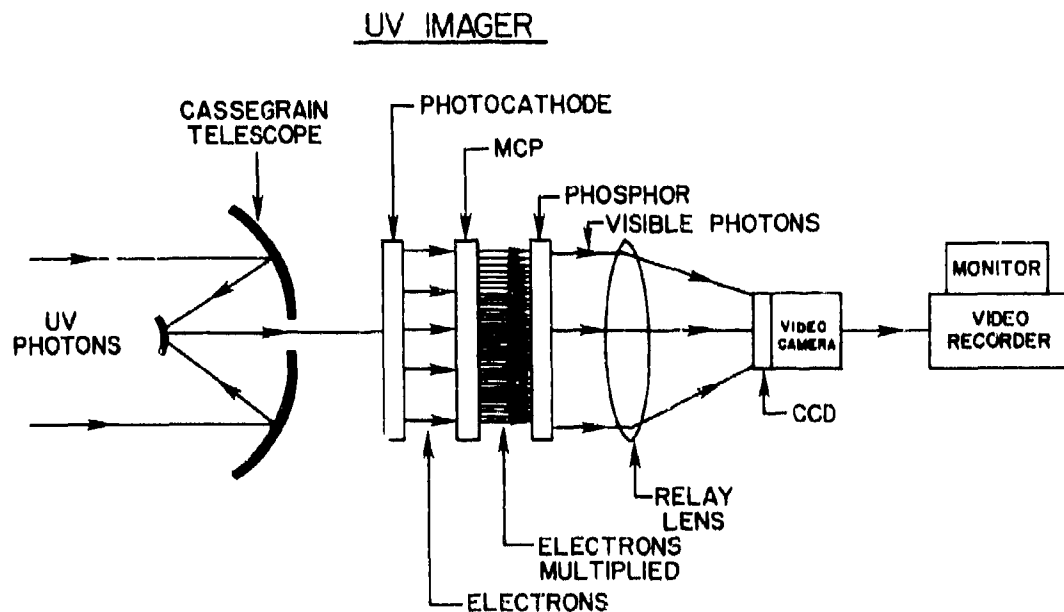


Figure 2. Experimental set-up of telescope-UV imager-video monitor.

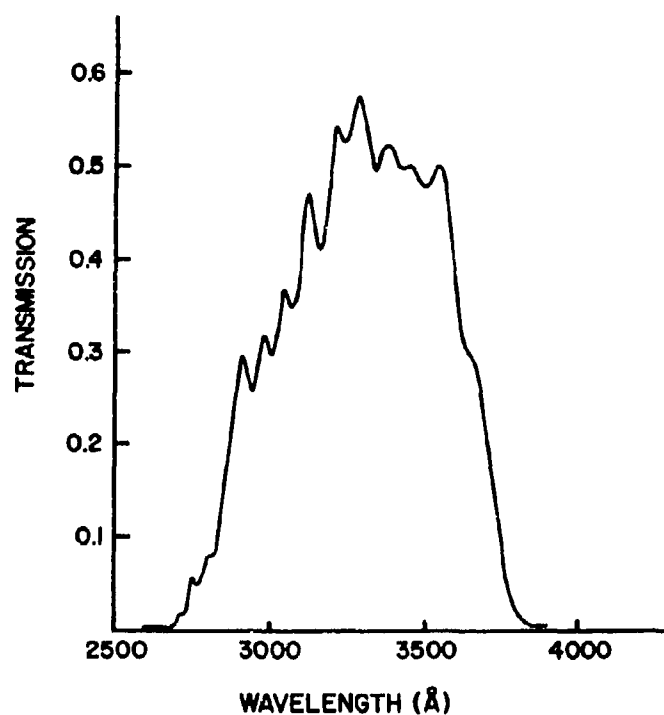


Figure 3. Transmission curve for primary filter used in the experiment. Atmospheric ozone cuts off at 3000 Å.

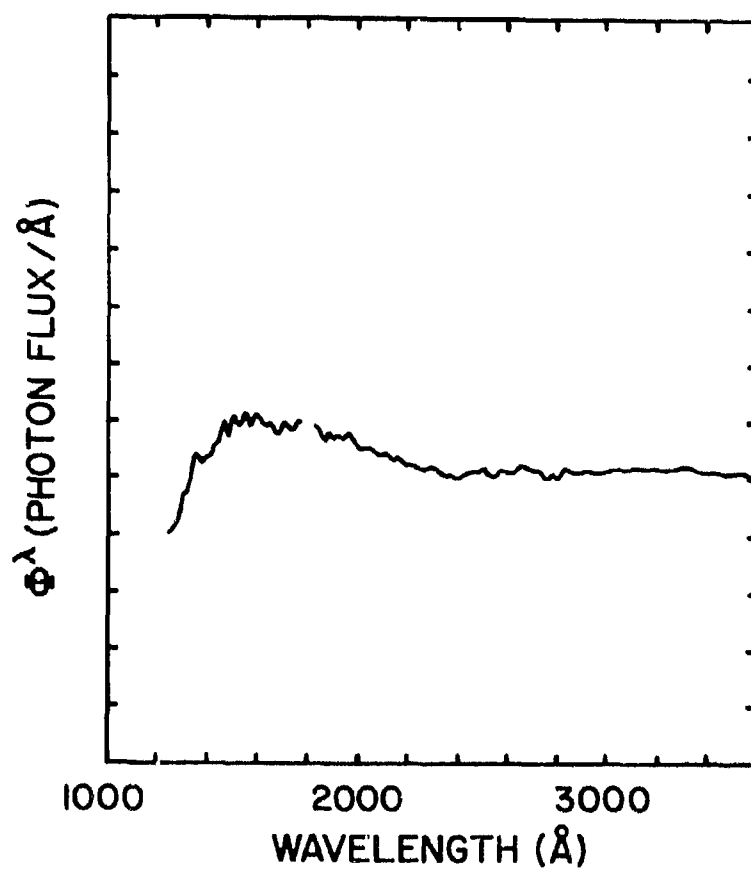


Figure 4. Sample photon flux curve for Procyon (α CMi). For $\lambda > 3000$ Å, $\phi^\lambda \sim 1.3 \times 10^{-8}$ ergs/cm²-sec-Å. (Reproduced from Code and Meade, Reference 3.)

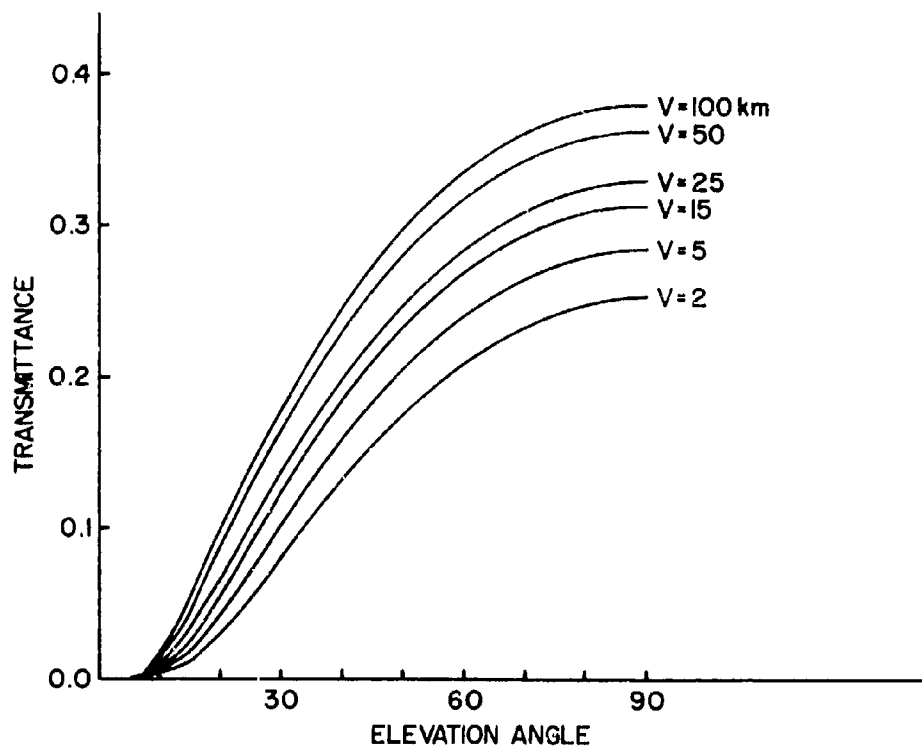


Figure 5. Transmittance as a function of elevation angle for $v = 2, 5, 15, 25, 50$ and 100 km. Curves use atmospheric model A with $h_1 = 1.26$ km, $\lambda = 3000-3700$ Å.

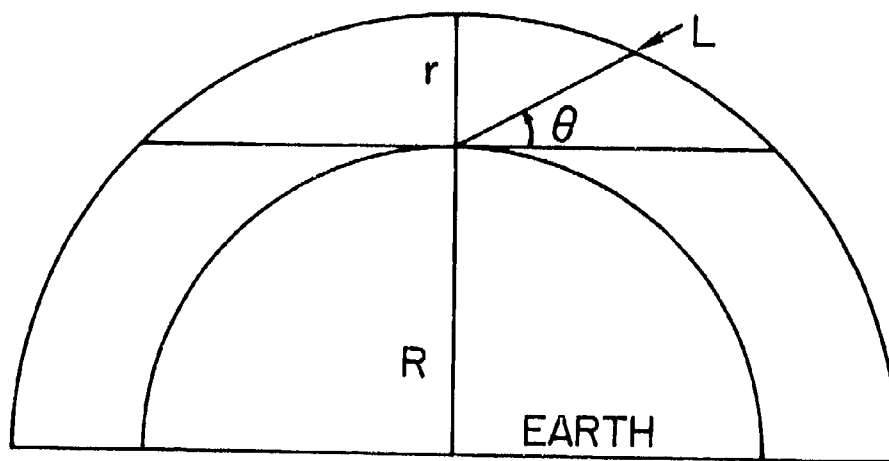


Figure 6. Geometry of the slant path, L , through the Earth's atmosphere. The Earth's radius, $R = 6370$ km, and the thickness of the atmosphere is taken to be $r = 100$ km.

DISCUSSION**R. DIRSCHERL**

Have you looked at atmospheric transmission in the "solar-blind" wavelength region with your instrumentation?

AUTHOR'S REPLY

The ozone absorption in the atmosphere cuts off all transmission of radiation from space for wavelengths shorter than 0.3 microns. We have not looked for transmission below this cut-off.

SCINTILLATION OF MILLIMETER-WAVE INTENSITY AND PHASE CAUSED BY TURBULENCE AND PRECIPITATION

by

R.J. Hill, S.F. Clifford, R.J. Latalis, and A.D. Sarma
Wave Propagation Laboratory
Environmental Research Laboratories
National Oceanic and Atmospheric Administration
325 Broadway, Boulder, CO 80303
U.S.A.

SUMMARY

A propagation experiment over exceptionally flat farm land was performed near Flatville, Illinois [1] and [2]. Extensive micrometeorological (hereafter abbreviated as micromet) measurements were made simultaneously. Because of the excellent horizontal homogeneity of the site, these micromet data determine the turbulence statistics along the entire propagation path. Instrumentation for measurements of rain as well as fog and snow were deployed [2]. There were five experiment sessions, each about a month long. Several millimeter-wave frequencies between 116 and 230 GHz were used. Results for data during inclement weather were reported in [2].

Below we review some results of these studies and present new results for temporal spectra of intensity and phase difference obtained during precipitation.

THE EXPERIMENT

Figure 1 shows the experiment layout. The millimeter-wave beam propagated a distance of 1374 m at a uniform height of $3.68 \text{ m} \pm 0.1 \text{ m}$ from the transmitter van to the receiver antennas. There were four receiving antennas, hence six antenna pairs. The separations of the receiving antennas ranged from 1.4 to 10 m. The millimeter-wave intensity was measured at each of the four antennas, and the phase difference between antennas was obtained for each antenna pair. The two overlapping optical propagation paths in Fig. 1 were 670 m each at a height of 3.78 m. These gave the path-averaged optical refractive-index structure parameter (C_n^2) as well as the cross-path component of the wind.

Locations of instrumented towers denoted as meteorological stations (met. sta.) 1 and 2 are shown in Fig. 1. At these stations the mean temperature and humidity were recorded from psychrometers, a propeller-vane anemometer gave wind speed and direction, a three-axis sonic anemometer gave the fluctuating components of the wind vector, platinum resistance-wire thermometers gave the fluctuating temperature, and Lyman- α hygrometers recorded the humidity fluctuations. During precipitation only the data from the psychrometers and propeller-vane anemometers are reliable.

Weighing-bucket rain gauges and optical rain gauges were deployed as shown in Fig. 1. Several rain rate and particle-sizing instruments were deployed near the millimeter-wave receiver as described in [2].

RESULTS

In [1] we presented data for the effects of clear-air turbulence when refraction fluctuations dominated the propagation statistics. The intensity variances and phase difference variances were shown to be in agreement with scattering theory. The probability density functions (PDFs) of intensity was closely lognormal, and the PDF of phase difference was normal. However, the intensity variances are not adequately described by current theory when absorption fluctuations have a significant effect on intensity fluctuations; the intensity PDFs are no longer lognormal, but are peculiar to the data run.

Effects of absorption fluctuations are evident in temporal frequency spectra. Figure 2 shows a measured intensity spectrum as a function of temporal frequency in hertz. The high-frequency part of the spectrum is the solid curve in Fig. 2; it is caused by clear-air refraction fluctuations. It is accurately described by the spherical-wave theory developed in Refs. [3] and [6]; this theory, including the effect of aperture averaging [3], gives the dashed curve in Fig. 2. If aperture averaging is neglected, then the theoretical curve would lie on top of the $f^{-3/2}$ asymptote, shown as the solid line in Fig. 2, thereby predicting too great spectral values at the highest frequencies. The theoretical curve is positioned horizontally as required by the value of the cross-path wind component. During the data run giving Fig. 2, there was a sudden increase in the humidity along the entire propagation path. The high-frequency measured spectrum in Fig. 2 was obtained from the first half of the time series prior to the increase in humidity. The spectrum over the whole time series gives the dashed curve and continues to higher frequencies in a manner nearly

identical to the high-frequency solid curve. The dashed low-frequency part of the spectrum arises from the sudden increase in humidity, and accounts for nearly all the intensity variance over the whole time series. The effect of absorption fluctuations is typically described by theory that is applicable to absorption fluctuations of size much smaller than the propagation path; therefore, the event which produced Fig. 2 is not described by existing theory. Such an event produces an intensity PDF that is not lognormal.

Figure 3 shows three simultaneously measured phase-difference temporal spectra. These spectra are obtained from the same data run that gave Fig. 2. The phase differences in Fig. 3 were obtained from antennas separated horizontally by 1.4, 4.3, and 10.0 m. These spectra correspond to clear-air turbulence conditions in the absence of precipitation. It is seen that the low-frequency content of the spectra grows as the antenna separation increases; the phase-difference variance increases correspondingly. This is, of course, because the difference between spaced antennas gives a high-pass spatial filter which, according to the frozen-flow hypothesis, is equivalent to a high-pass temporal filter. The corresponding theoretical spectra [3] are over-plotted in Fig. 3; their horizontal position is as required by the measured mean cross-path wind component and the frozen-flow hypothesis. The set of three theoretical spectra is shifted vertically to match the data; the positions of these three spectra relative to each other are fixed as required by theory. A Von Karman refractive-index spectrum with a 2.8-m outer scale is used for the theoretical calculation; a larger outer scale would produce greater values at low frequencies in the theoretical phase-difference spectra of Fig. 3. Absorption fluctuations have negligible effect on phase-difference spectra [3].

Figure 4 shows a temporal spectrum of intensity illustrating three effects. At the highest frequencies an enhancement caused by scattering by raindrops is evident. This was first identified in these data by A.D. Sarma [4]. The average rain rate was about 5 mm h⁻¹. A theory for the temporal spectrum caused by rain scattering is given in [5]; however, the theory [5] applies for drops that are much larger than the wavelength, which is not our case. This theory predicts that $W_i(f)$ is independent of f at low temporal frequencies; this is represented by the f^{-1} asymptote in Fig. 4. The theory [5] predicts a rapid decrease of $W_i(f)$ for $f \geq 1$ kHz; the rapid decrease in Fig. 4 at much lower temporal frequencies than 1 kHz is probably the effect of aperture averaging.

The second effect evident in Fig. 4 is in the frequency range from about 5×10^3 Hz to 2 Hz; this effect is caused by turbulent fluctuations in the real part of the refractive index of the air; it would exist even in the absence of rain. This effect is described in numerous experimental and theoretical papers [3]. Our wave is diverged so the spherical-wave spectrum [6] is a good approximation; this is shown in Fig. 4. The failure of this theory to match the data is caused by the parallel alignment of the wind to the propagation path; the average cross-path wind component was 0.4 m s⁻¹ but the mean wind speed was 5 m s⁻¹. The fluctuations of the cross-path wind component were comparable with its mean value of 0.4 m s⁻¹; also, instances occurred when the local wind blew across path in the opposite direction from the average direction. On the other hand, theories such as those in [6] and [3] require steady cross-path wind, although it may have a different value at different positions along the path, because such theories obtain the temporal spectrum from a translation of the spatial spectrum. Tatarskii [7] gave a partial theory for the case of fluctuating cross-path wind and plane wave propagation. Figure 2 shows that the theory in [6] is an excellent approximation for the high-frequency refraction-fluctuation-induced spectrum in the case of steady cross-path wind. Clearly, Fig. 4 shows that the effect of cross-path wind fluctuations causes a spreading of the clear-air-turbulence-induced spectrum. It is fortunate that the wind was nearly parallel to the propagation path; if the 5 m s⁻¹ wind had been perpendicular to the path, then the turbulence-induced portion of the temporal spectrum would be displaced toward higher frequencies in Fig. 4 by more than a factor of 10, thereby obscuring the raindrop scattering effects.

The third effect shown in Fig. 4 occurs at temporal frequencies less than about 5×10^3 Hz. Temporal variations in rain rate cause variations of path-integrated absorption, which in turn cause this low-frequency enhancement of the spectrum in Fig. 4. Variation of clear-air absorption (say by water vapor) is a well-known cause of similar low-frequency enhancements of intensity temporal spectra for millimeter waves (as in Fig. 2); receiver drift is another possible cause. For the data in Fig. 4, we know that variation of rain rate is the cause rather than clear-air absorption because measured rain rate and millimeter-wave intensity follow each other in a negatively correlated manner. In fact, oscillations in rain rate were observed [8] that can account for the spectral peak near 10^3 Hz in Fig. 4.

Figure 5 shows a phase-difference temporal spectrum corresponding to the data shown in Fig. 4. The phase difference was obtained from antennas spaced 1.4-m apart, horizontally. A theoretical phase-difference spectrum calculated using a 2.8-m outer scale is also shown in Fig. 5. The phase-difference spectrum induced by fluctuations in the real part of the refractive index is wider than the corresponding intensity spectrum. The effects of cross-path wind variability are therefore much less evident in the phase-difference spectrum of Fig. 5 than in the intensity spectrum of Fig. 4. A high-frequency enhancement caused by raindrop scattering is also seen in Fig. 5. This enhancement has a ragged appearance because of spectral spikes caused by

mechanical vibrations of the steel beam on which the antennas were mounted. If phase is measured with a single antenna, variation of path-integrated refraction can produce low-frequency enhancement in single-antenna phase temporal spectra analogous to that caused in intensity spectra by variation of path-integrated absorption. Taking the difference of phases between spaced antennas eliminates this low-frequency enhancement; none is seen in Fig. 5.

Figure 4 shows that all three effects give appreciable contributions to the intensity variance. On the other hand, Fig. 5 shows that the phase-difference variance is dominated by the air-turbulence effect and that rain scattering has a negligible effect. For greater separations of antennas the contribution of turbulence to the phase-difference variance is observed to increase, but the contribution by raindrop scattering is observed to decrease.

Figure 6 shows a measured temporal spectrum of intensity obtained during a mixture of drizzle, wet snow, and patchy fog. The average precipitation rate is about 1 mm h^{-1} . The clear-air turbulence-induced theoretical spectrum is given by the dashed curve; as in Figs. 2 and 4, this curve is positioned on the horizontal axis as required by the cross-path wind speed and moved vertically to match the measured spectrum. The wind was steady in direction and nearly straight from the east (and thus perpendicular to the propagation path). The speed from the propeller-vane anemometers varied from 0.7 to 1.5 m s^{-1} for the data in Fig. 6. Perhaps part of the measured spectrum in this figure can be attributed to clear-air turbulence; however, clear-air refraction fluctuations might contribute much less than is indicated by the dashed curve. There is an enhancement of the spectrum at frequencies greater than 3 Hz which could be attributed to scattering by rain drops; a line corresponding to an f^{-1} asymptote is given for comparison in Fig. 6. This interpretation is the same as for Fig. 4. However, the data in Fig. 6 contain so much noise that the spectrum may be entirely noise at frequencies exceeding 3 Hz . The spectrum is not plotted in Fig. 6 for frequencies from 20 to 50 Hz because of large noise spikes [2]. The features of the millimeter-wave intensity time series over the data run are very similar to the inverted time series from the two optical rain gauges. This suggests that the large low-frequency bump in Fig. 6 is due to path-integrated rain-induced attenuation [2]. The intensity variance is obviously dominated by this low-frequency effect. The psychrometers showed very little variation of humidity and temperature during the run, so we conclude that the low-frequency effect is not due to clear-air absorption fluctuations.

One phase-difference temporal spectrum from data obtained simultaneously with that producing the intensity spectrum in Fig. 6 is presented in [2]; reference [2] suggests that the phase-difference spectrum was caused by clear-air turbulence (excluding raindrop scattering). However, when the phase-difference data are considered as in Fig. 3, the measured spectra do not compare with each other in a manner consistent with clear-air turbulence, nor do they compare reasonably with the theoretical spectra. Moreover, the phase-difference time series were peculiar, suggesting instrumental difficulties. Also, these spectra have extraordinarily large noise spikes due to mechanical vibrations at 3 - 50 Hz (Nyquist); the antialiasing filtering was, by error, inadequate to prevent aliasing of any such vibration noise (or other noise sources) that might have existed from 50 to 100 Hz . Thus we conclude that the phase difference spectra were contaminated by noise, possibly from several noise sources. This deduction, as well as the discussion of Fig. 6, is a reinterpretation of the data presented in [2].

Figure 7 shows the intensity temporal spectrum obtained from conditions of blowing snow. The corresponding clear-air turbulence theoretical spectrum is plotted as the dashed curve; this curve is aligned horizontally as required by the mean value of the cross-path wind component, and it is displaced vertically to match the data. The mean wind was blowing from 24° west of north at a speed of 14.4 m s^{-1} ; its mean cross-path component was therefore about 6 m s^{-1} . Because of the small mean angle of 24° between the propagation path and the mean wind direction, the cross-path component varied during the run. Thus we expect some spreading of the part of the measured temporal spectrum which is caused by clear-air refraction fluctuations (the air excluding the snow). However, this variability of wind and the spreading effect are much less than is shown in Fig. 4.

In Fig. 7 there is an enhancement relative to the dashed theoretical curve at frequencies exceeding 10 Hz . It is likely that this enhancement is caused by scattering from snow particles, although there is some noise at frequencies greater than 20 Hz . Figure 7 shows that most of the intensity variance derives from the large feature at frequencies less than 0.5 Hz . There are four likely reasons for this feature. First, receiver or transmitter drift may cause it. The intensities measured from separate antennas have very similar long-term behavior for this data run, so receiver drift seems unlikely; transmitter drift cannot be assessed. Second, this feature could be due to absorption fluctuations caused by temperature and humidity fluctuations in the air (excluding snow particles). However, the psychrometers measured exceptionally stable values of temperature and humidity so this is not a likely cause (barring malfunctions of the psychrometer, such as dry bulbs collecting ice deposits or iced bulbs becoming ice free). Third, wet snow had fallen earlier in the day when the temperature was -3°C ; the conditions during the data run corresponding to Fig. 7 were blowing and

drifting snow and an air temperature of -4°C ; it may be that an underlying icy surface had formed that was sufficient to cause reflections of the millimeter-wave beam. Interference between direct and reflected beams can produce intensity fluctuations; such fluctuations might be enhanced by drifting snow alternately covering and exposing patches of the icy surface. Fourth, this feature in Fig. 7 may be due to path-averaged attenuation fluctuations caused by the snow particles. It is probable that either multipath interference or snow-induced attenuation caused this low-frequency behavior.

Three phase-difference temporal spectra are shown in Fig. 8 for horizontal antenna separations of 1.4, 4.3, and 10.0 m. These spectra are from data obtained simultaneously with the intensity data that yielded Fig. 7. The corresponding theoretical spectra arising from fluctuations in the real part of the refractive index of air (excluding snow particles) are shown as dashed curves. As in Fig. 3, the theoretical curves are aligned horizontally as required by the mean value of the cross-path wind component, and are displaced vertically to match the data; however, the three theoretical curves are fixed in position relative to each other as required by the theory. The outer scale was assumed to be 2.8 m for the theoretical curves. When measured clear-air turbulence spectra caused by refraction fluctuations are graphed as in Figs. 2 and 3, the ratio of the maximum of the phase-difference spectrum for the 1.4-m antenna separation to the maximum of the intensity spectrum is about 2.4; this value depends weakly on the outer scale, but not on the refractive-index structure parameter. The ratio of corresponding maxima in Figs. 7 and 8 is in good agreement with this value of 2.4. This supports the hypothesis that the high-frequency bump in the intensity spectrum of Fig. 7 and at least part of the phase-difference spectra in Fig. 8 are due to fluctuations in the real part of the refractive index of the air (excluding snow particles). However, the phase difference spectra in Fig. 8 have far more low-frequency content than predicted by clear-air turbulence theory. This might be due to receiver drift (independent of whether the intensity temporal spectrum suffers from such drift) or it could be due to multipath interference (which can support the idea that the intensity spectrum is affected by multipath interference).

At frequencies exceeding 5 Hz the spikes caused by mechanical vibrations are evident in Fig. 8. (These have been described in connection with Fig. 5.) Perhaps the spectral level in the gaps between the spikes in Fig. 8 is caused by scattering by snow particles, particularly because this spectral level is greater for the two smaller antenna separations than for the 10.0 m separation. However, this is very speculative because of the strong noise spikes. The discussion of Figs. 7 and 8 is a reinterpretation of the data presented in [2].

REFERENCES

1. R. J. Hill, R. A. Bohlander, S. F. Clifford, R. W. McMillan, J. T. Priestley, and W. P. Schoenfeld, "Turbulence-induced millimeter-wave scintillation compared with micrometeorological measurements," *IEEE Trans. Geosci. Remote Sens.* 26, 330-342 (1988).
2. R. A. Bohlander, R. W. McMillan, E. M. Patterson, S. F. Clifford, R. J. Hill, J. T. Priestley, and W. P. Schoenfeld, "Fluctuations in millimeter-wave signals propagated through inclement weather," *IEEE Trans. Geosci. Remote Sens.* 26, 343-354 (1988).
3. R. J. Latatis, R. J. Hill, S. F. Clifford, R. A. Bohlander, R. W. McMillan, and W. P. Schoenfeld, "Millimeter wave temporal frequency spectra for spherical wave propagation through a turbulent absorbing atmosphere," (preprint) (1989).
4. A. D. Sarma, R. J. Hill, and R. J. Latatis, "Effect of rain on millimeter wave amplitude scintillation spectra," *International Conf. on Millimeter Wave & Microwave*, Dehradun, India, March 14-16, Defense Electronics Applications Laboratory, Raipur Road, Dehradun-248001, India (1990).
5. T. Wang and S. F. Clifford, "Use of rainfall-induced optical scintillations to measure path averaged rain parameters," *J. Opt. Soc. Am.* 65, 927-937 (1975).
6. S. F. Clifford, "Temporal frequency spectra for a spherical wave propagating through atmospheric turbulence," *J. Opt. Soc. Am.* 61, 1285-1292 (1971).
7. V. I. Tatanskii, The effect of the turbulent atmosphere on wave propagation, Springfield, PA: National Technical Information Service, U.S. Department of Commerce, 1971.
8. R. B. Fritz, R. J. Hill, J. T. Priestley, and W. P. Schoenfeld, "Evidence for an oscillatory rain rate in a midwestern winter rain," *J. Appl. Meteorol.* 27, 195-197 (1988).

ACKNOWLEDGMENTS

Many people contributed to the experiment, as evidenced by acknowledgments elsewhere [1, 2, 3]. We particularly thank R. W. McMillan, R. A. Bohlander, and J. T. Priestley. Dr. A. D. Sarma is supported by a National Research Council Research Associateship, and his work is supported by the U.S. Army Research Office under MIPR. 125-88.

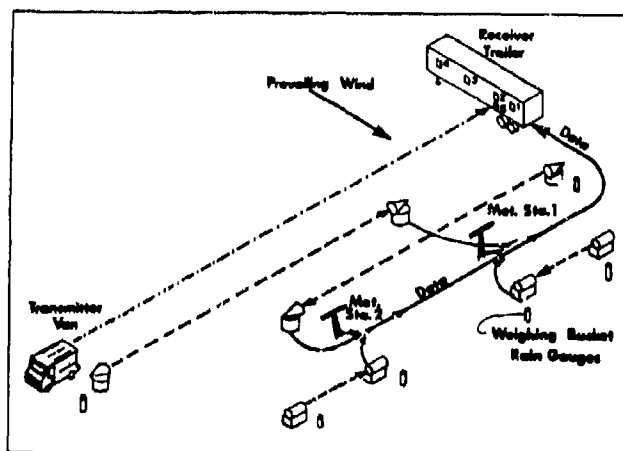


Fig. 1. The instrument positions at the experiment site. The dashed and dotted line denotes the millimeter-wave propagation path (1.374 km); the long-dashed lines, the optical propagation paths (670 m each); and the short-dashed lines, the optical rain gauge paths (50 m each). Solid lines show the flow of micro-meteorological data to the data acquisition system in the receiver trailer. Antennas are numbered 1 to 5 in the receiver trailer.

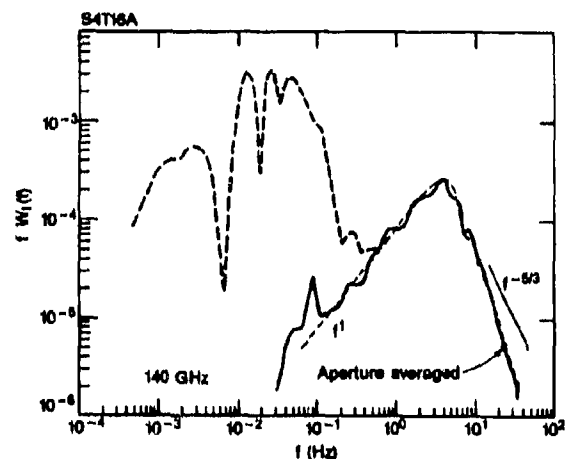


Fig. 2. Intensity spectrum from clear-air-turbulence conditions illustrating the effect of a change in absorption during the data run.

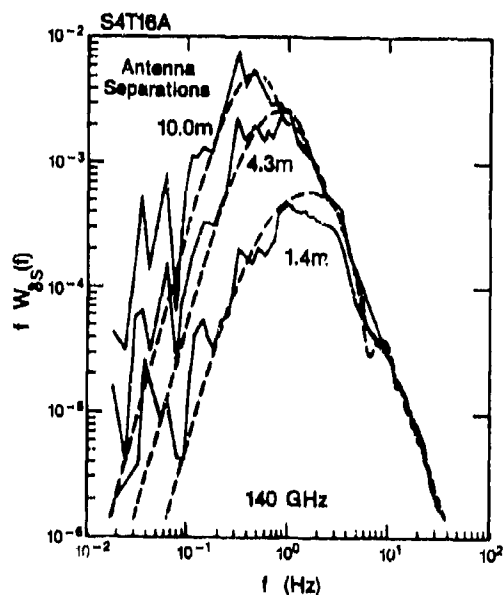


Fig. 3. Three phase-difference spectra corresponding to the data in Fig. 2, including their theoretical spectra.

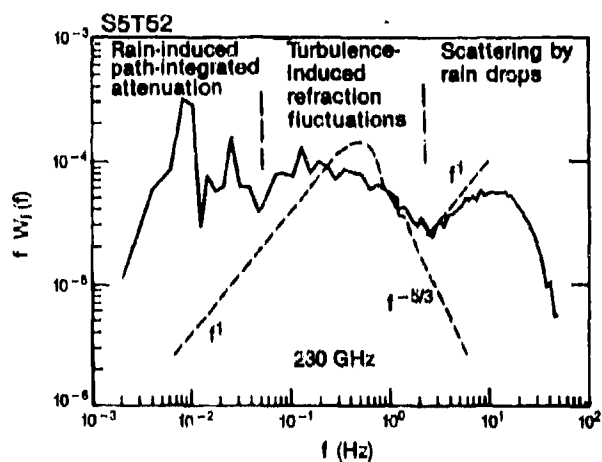


Fig. 4. Intensity spectrum obtained during rain.

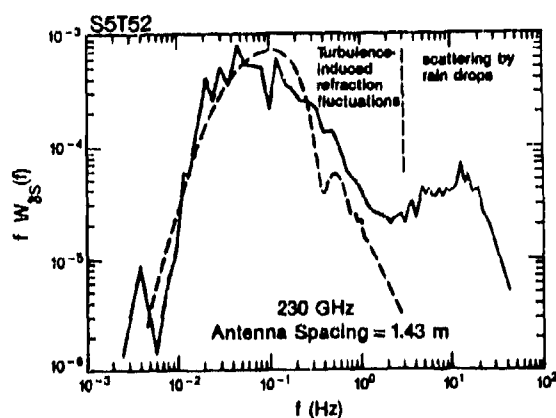


Fig. 5. Phase-difference spectrum obtained during the same rain data as in Fig. 4.

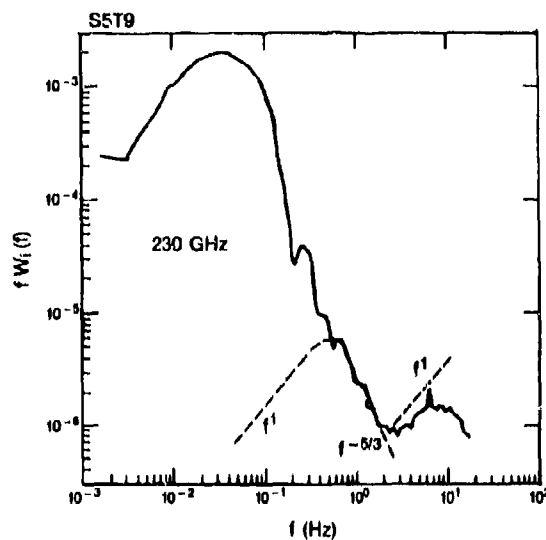


Fig. 6. Intensity spectrum obtained during a mixture of very light rain, wet snow, and patchy fog.

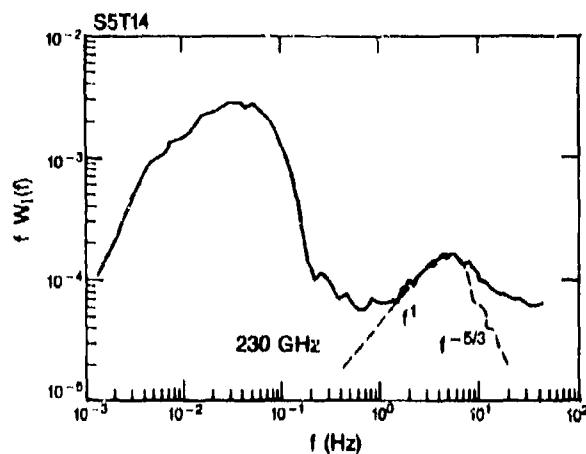


Fig. 7. Intensity spectrum obtained during blowing and drifting snow.

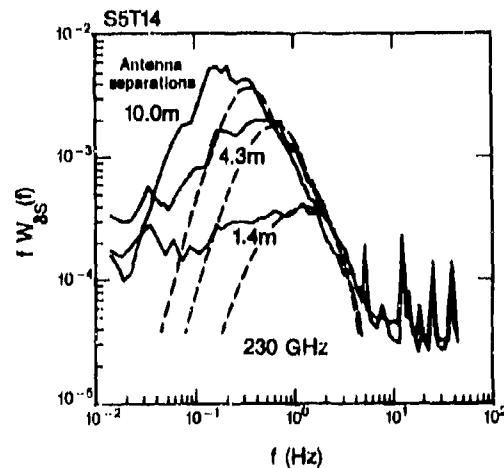


Fig. 8. Three phase difference spectra from the same data run that gave Fig. 7.

DISCUSSION

A. WAGENNAAR

Did you manage to keep your antennas dry during the snow measurements?

AUTHOR'S REPLY

The antennas were placed in a dry room behind a polyethylene screen.

MILLIMETRIC, INFRARED AND OPTICAL PROPAGATION STUDIES OVER A 500 m PATH

C J Gibbins
Rutherford Appleton Laboratory
Chilton
Didcot
Oxfordshire, OX11 0QX
UK

SUMMARY

A 500 m propagation range has been developed with transmission links operating at frequencies of 37, 57, 97, 137 and 210 GHz and at wavelengths of 10.6 and 0.63 μm . A comprehensive set of meteorological observations includes rainfall and snowfall rates, raindrop size distributions, temperature and humidity, microwave refractive index, surface pressure and wind velocity. Measurements from the range are being used to compile an extensive propagation and meteorological database with which a variety of studies are being carried out; these include detailed investigations into individual events, aimed towards obtaining a deeper understanding of the interaction between electromagnetic radiation and the prevailing meteorological phenomena such as rain, snow, fog and atmospheric turbulence. Statistical analysis of the database, on the other hand, is directed towards obtaining information on the reliability of future communications systems, so that average and extreme values of systems performance can be assessed. Such studies facilitate the development of prediction procedures based on existing meteorological data for future systems planning, and an assessment of the relative merits of different wavebands, important to the increasing development and deployment of multi-spectral sensors.

1. INTRODUCTION

The continuing and ever-increasing requirement for new communications systems, with higher data-rates and thus wider bandwidths, imposes severe demands on the electromagnetic spectrum. Although a re-useable resource, the spectrum as at present utilized is becoming over-populated and congested, leading to additional problems and constraints such as interference between adjacent channels and restricted bandwidths (and thus channel capacity). In order to accommodate new systems development and an expansion in communications channel capacities it becomes necessary to consider exploitation and utilization of higher and higher frequencies, extending well into the millimetre-wavelength regions of the electromagnetic spectrum. These regions are now becoming more accessible for communications systems through recent advances and developments in component and systems technology, which is improving the availability of cost-effective, reliable and compact hardware and thus creating new opportunities and possibilities hitherto either not achievable or not practicable at lower frequencies.

At the higher frequencies, however, a number of additional factors, not generally considered at the longer wavelengths currently in commercial use, can impact rather dramatically on the capability and reliability of future communications systems, which need to be included in the assessment and/or design of such systems. The most important of these are the influences of atmospheric gases and the prevailing meteorology. At frequencies above about 10 GHz, electromagnetic radiation begins to interact with the neutral atmosphere (primarily in the troposphere) and with the various meteorological phenomena, in particular hydrometeors in the form of precipitation, giving rise to additional sources of signal attenuation which must be considered in the design of high-frequency communications systems. Gaseous attenuation, due to absorption by molecular oxygen and water vapour, is omnipresent and slowly-varying, and can now be evaluated with a high degree of confidence using well-understood models (e.g. Liebe ¹). Signal attenuation by precipitation, however, is highly variable, in both space and time; its evaluation and prediction is thus much less certain. Since precipitation is a stochastic process, the resultant attenuation is customarily determined or assessed statistically, generally in the form of levels of attenuation (fade margins) which may be exceeded for specified percentages of time determined by the level of reliability required for a particular communications system or service, under the range of meteorological conditions appropriate to the location for which the service is planned. Such averages of systems performance are further supplemented by an assessment of extremes.

In general, two separate and distinct methods to assess fade margins may be available to systems designers - direct measurements of propagation conditions over extended periods of time in the appropriate climatological region or a prediction from a knowledge of the prevailing meteorology. Implicit in the latter is a detailed understanding of the physical mechanisms of the various atmospheric and meteorological phenomena and their interactions with incident electromagnetic radiation over a wide range of wavelengths. For frequencies up to about 30 GHz (i.e. up to and including the microwave region of the electromagnetic spectrum), extensive databanks exist of direct long-term measurements of propagation under different climatological conditions, while prediction procedures developed from such data are found generally to provide accep-

table estimates of, for example, fade margins, for use in link budgets (CCIR²). At frequencies above 30 GHz (i.e. the millimetric spectrum), however, the reliability of the various prediction procedures becomes less certain, since there are as yet insufficient propagation data available either for direct application or for the development of new, or improvement and testing of existing, prediction techniques.

In order to contribute to the availability of propagation data at frequencies above 30 GHz, the Rutherford Appleton Laboratory has designed and operated the 500 m Millimetre-Wave Experimental Range at Chilbolton (MWERAC) in Hampshire, UK (latitude 51°8'N, longitude 1°26'W, elevation 84 m). The range is a well-instrumented open-air laboratory in which simultaneous transmissions are monitored continuously over a path for which atmospheric conditions are essentially constant, in the millimetric, infrared and optical wavebands, in conjunction with a comprehensive set of meteorological observations. The data obtained are used for a variety of studies into the influence of precipitation, including rain, snow and hail, the effects of other hydrometeors such as fog and of atmospheric turbulence, which causes scintillations in received signal amplitudes, and the variability of atmospheric attenuation due to changes in humidity, temperature and pressure. From such studies will emerge a more detailed knowledge of the interaction between electromagnetic radiation and the various meteorological phenomena which prevail, in particular the ranges and magnitudes of those meteorological parameters which become of significant importance at millimetric wavelengths, in order to facilitate the development of improved propagation models to describe adequately the above-noted effects. Furthermore, statistical analysis of the data is yielding valuable information both for direct application to the design and planning of future communications systems and the development and testing of prediction models, to estimate attenuation from, for example, basic meteorological data of the type routinely collected by weather bureaux throughout the world. Such statistical analyses are also of importance to an assessment of the relative merits of different wavebands, i.e. millimetric, infrared or optical, relevant to the increasing consideration and deployment of multi-spectral sensors and systems.

The present paper describes briefly the 500 m range and its facilities, and gives some examples of detailed analyses of rainfall attenuation which are currently being carried out, together with examples of the effects of other hydrometeors such as snow and fog, and of propagation through turbulence. Some preliminary results are also included on the statistics of propagation conditions.

2. THE 500 m PROPAGATION RANGE

The 500 m range comprises a set of single-pass, continuous-wave (CW) transmission links, situated 4 m above flat grassland, operating at frequencies of 37, 57, 97, 137 and 210 GHz, all with vertical polarization, and at wavelengths of 10.6 μm in the infrared and 0.63 μm in the optical wavebands, with random polarization. An extensive set of meteorological instruments complements the propagation measurements, and include rapid-response (10 second) rain gauges at three locations along the range, a rapid-response snow/hail gauge, measurements of temperature and humidity at a variety of locations and heights above the ground, a distrometer for measuring the distribution of raindrop sizes, a microwave refractometer to determine variations in atmospheric refractive index, surface pressure and wind speed and direction.

A block diagram of the range, which has been described in detail elsewhere³, is shown in Figure 1. The transmitters and receivers, which are operated in elevated temperature-controlled cabins, are supported independently from the ground, to isolate the systems from any vibrations within the cabins. The signals are transmitted and received through windows fabricated from material selected to be transparent in the particular wavelength regions for each system, while the windows themselves are protected by hoods of sufficient size to prevent interaction with the beams and to eliminate the deposition of raindrops, etc., on the windows.

All links, their system monitors and meteorological sensors are connected to a data-collection computer via a universal interface bus. In the normal continuous mode of operation, the outputs from all channels (i.e. signal strengths, meteorological instruments, system monitors, etc.) are recorded on magnetic tape every 10 seconds. Additionally, when attenuation is detected on the range, for example by precipitation, or when scintillation occurs, the 57, 97 and 137 GHz and 0.63 μm links (together with the refractometer, when required) are recorded separately at a higher data-rate of 100 samples per second. Analogue chart recorders are used to provide a continuous monitor of all links and meteorological instruments, as a quick-look facility, as a diagnostic tool, when necessary, and to determine the occurrence, identification and classification of events. The links are calibrated automatically at 6 hourly intervals (except when an event is in progress) by inserting known values of additional attenuation into the transmitters.

The raw data are subsequently calibrated and validated to compile an extensive data-base in the form of time series of calibrated attenuations and meteorological parameters for the events, which is then used for analytical and statistical studies of propagation and related meteorology. The analytical studies concentrate on investigations into individual events according to their origin, i.e. into the attenuation caused by rain, snow and fog, and the effects of turbulence (i.e. scintillation); statistical studies are designed to yield probability distributions of attenuations (i.e. fading), of durations of fades of specified depth and the return periods between

such fades, together with related investigations of precipitation.

3. ATTENUATION BY RAIN

Rainfall attenuation depends primarily on the size, shape, orientation and complex dielectric constant of raindrops and on the wavelength and polarization of the incident electromagnetic radiation. The theoretical description of scattering and absorption by rain was first developed by Mie⁴ for spherical drops, while the extension to consider non-spherical drops was carried out by Oguchi and Hosoya⁵. The calculation of rainfall attenuation, however, remains non-trivial, since rain is a highly amorphous medium, with an intrinsic variability in composition, in spatial distribution and in time. Of these, perhaps the least certain is the composition of rain, in particular the distribution of the sizes of raindrops, which determines magnitude and wavelength-dependence of the scattering of incident electromagnetic radiation, the dominant source of rainfall attenuation. A number of empirical drop-size distributions have been measured or proposed in the literature, for example by Laws and Parsons⁶, Marshall and Palmer⁷ and by Joss et al.⁸. Of these, perhaps the most widely used is that of Laws and Parsons.

The numerical evaluation of rainfall attenuation, even for idealized drop-size distributions, involves lengthy and complex scattering calculations, and it has become customary to abbreviate such calculations by means of a simple power law relationship

$$\text{Attenuation, } \gamma = aR^b, \text{ dB km}^{-1} \quad (1)$$

where R is the rainfall rate in mm h^{-1} and the coefficients a and b depend on frequency, the temperature of the rain and on the plane of polarization if non-spherical drops are considered. Values for these coefficients have been tabulated for spherical drops⁹ and for non-spherical drops¹⁰, for the Laws and Parsons drop-size distribution. However, there is increasing evidence¹¹ that this distribution underestimates the number of very small raindrops, and since rainfall attenuation at frequencies above 30 GHz depends increasingly on the smaller raindrops, the above tabulations may thus underestimate the magnitude of rainfall attenuation at the shorter millimetric wavelengths. Hence, other drop-size distributions, in particular negative-exponential distributions (of which the Marshall-Palmer distribution is an example), have been considered more appropriate to the millimetric region¹¹. The propagation measurements made through rain on the 500 m range have accordingly been used to investigate the applicability of such distributions and their variants.

As an example, Figure 2 shows a time series of attenuations measured during rain at 37, 57 and 97 GHz and at $10.6 \mu\text{m}$ in the infrared, together with the path-mean rainfall rate, determined by averaging the three raingauges located along the range. As can be seen, the correlation between attenuation and rainfall rate is, in general, very good, with the attenuation increasing, as expected, with frequency in the millimetre-wave part of the spectrum; furthermore, it is evident that such multifrequency measurements contain much information on the composition of rain, which, since conditions along the 500 m path are essentially constant (i.e. there is little or no spatial variation), is determined principally by the distribution of raindrop sizes.

At frequencies above about 100 GHz, rainfall attenuation approaches the so-called "optical limit" and the extinction coefficient is simply twice the geometrical cross-section, i.e. $\frac{1}{2}\pi D^2$, where D is the diameter of the (spherical) raindrops.

The attenuation coefficient is given, in dB km^{-1} , by

$$\gamma = 4.343 \int_0^\infty Q_e(D) N(D) dD \quad (2)$$

where $Q_e(D)$ is the scattering cross-section of a raindrop of diameter D , and $N(D)$ is the drop-size distribution. As a generalization, it is convenient to consider a gamma-distribution of raindrop sizes, thus:

$$N(D) = N_0 D^n \exp(-\Lambda D) \quad (3)$$

where the special case of $n = 0$ represents the negative exponential distribution. In this expression, both N_0 and Λ are functions of rainfall rate. For the case $n = 0$, then, the attenuation in the optical limit can be written (in dB km^{-1}) as

$$\gamma = 4.343 \int_0^\infty \frac{\pi D^2}{2} N_0 \exp(-\Lambda D^2) dD \quad (4)$$

$$= 4.343 \frac{\pi}{2} N_0 \frac{\Gamma(3)}{\Lambda^3} \approx 4.343 \pi \frac{N_0}{\Lambda^3} + \dots$$

There is experimental evidence that attenuations, in the infrared and optical regions are adequately described by such an expression.

Now, the rainfall rate is given in terms of N_0 and Λ as

$$R = \frac{\pi}{6} \int_0^{\infty} v(D) N(D) D^3 dD \quad (5)$$

where $v(D)$ is the terminal velocity of the raindrops. Using the model for terminal velocities developed by Atlas et al.¹⁶, Equation (5) can be solved to yield the analytical expression

$$R = \frac{\pi N_0}{\Lambda^3} \left[c - \frac{d}{(1 + \frac{6}{\Lambda})^4} \right] \quad (6)$$

where c and d are numerical constants. Similar expressions can be developed for the more complex distributions in which $n = 1$ or 2 , for example.

Thus, given rainfall rate and the corresponding attenuation in the optical limit, Equations (4) and (6) can be used to investigate details of the distribution of raindrop sizes. For example, the 10.6 μm attenuations and rainfall rates shown in Figure 2 have been used to derive values for N_0 and Λ for a number of Γ -type distributions, with $n = 0, 1$ and 2 . Figure 3 shows the resultant values as a function of rainfall rate for the case where $n = 2$. Two distinct regions can be observed; at low rainfall rates, below about 7 mm h^{-1} , both N_0 and Λ decrease rapidly with increasing rainfall rate, while for higher rainfall rates N_0 and Λ become nearly independent of rainfall rate.

In order to evaluate the applicability of such Γ -distributions of raindrop sizes, the attenuation at 37, 57 and 97 GHz have accordingly been calculated using Equation (2), with the appropriate scattering cross-sections (for spherical drops) and the values of N_0 and Λ shown in Figure 3. These calculated values have then been compared with the experimental measurements shown in Figure 2. The comparison at 97 GHz, between measured and thus-calculated attenuations, is shown in Figure 4, again for the case where $n = 2$. The continuous line represents equal values of attenuation, i.e. when the ratio of calculated to measured attenuations is unity. In general, good agreement is found between measured millimetre-wave attenuations and those calculated from the drop-size distributions derived from rainfall rate and infrared attenuation, for such Γ -type distributions.

Further investigations into such distributions, in particular including the case of non-spherical raindrops, should provide more insight into those distributions of raindrop sizes most appropriate to attenuation calculations at millimetric wavelengths, which could then be employed to develop simple and reliable propagation models and prediction procedures, for example of the type given by Equation (1).

As noted above, rainfall attenuation increases with increasing frequency, up to about 100 GHz, above which it becomes substantially independent of frequency as the optical limit is approached. With the development of multi-spectral sensors, operating simultaneously in different wavebands, it becomes important to provide confirmation of this theoretical prediction for a wide range of meteorological conditions. Since rain dominates the statistics of propagation, rainfall attenuation in the different wavebands on the 500 m range have been compared over the period of one year. As an example, Figure 5 compares the maximum (peak) attenuation measured at 97 GHz during each rain event over the period with the corresponding peak attenuation at 10.6 μm . The broken line indicates equal attenuations in each waveband, and the measurements scatter approximately equally either side. Rainfall attenuation may thus be considered comparable in both the millimetric and infrared wavebands, while similar comparisons between the infrared and optical wavebands have suggested that infrared attenuation in rain is perhaps 10-20% greater than optical attenuation.

4. ATTENUATION BY SNOW

While there are rather few data available on propagation through rain at millimetric wavelengths, there is a marked paucity of information, both experimental and theoretical, on attenuation by frozen precipitation. Bohlander et al.¹⁶ have reported intense rapid fluctuations in signal levels at 116 GHz received through snow, but do not comment on attenuation.

Snow is generally more difficult to quantify than rain, since it is a very complex form of precipitation, being a mixture of water, ice and air in varying proportions, depending on the type of snow and the ambient temperature. Snow has a refractive index which is smaller than that for water, and might thus be expected to attenuate less than rain with an equivalent liquid water content. However, the large size and non-sphericity of snowflakes (especially in sleet) can produce greater attenuations than spheres of comparable volume, especially in wet or melting snow.

The study of snow attenuation is further complicated by difficulties in determining effective and accurate snowfall rates, since entrainment of snowflakes by wind can produce large horizontal components in the direction of snowfall (and even vertical eddies in the vicinity of obstacles) which can significantly reduce deposit or capture rates at or near snow gauges. It has been found, however, that a significant improvement in capture efficiency can be obtained by surrounding the snow gauge with a

wind shield to reduce wind speed in the vicinity of the gauge. The wind shield used on the 500 m range, for example, in the form of a half-open picket fence, 1 m high and 5 m in diameter, was found to reduce wind speeds by up to 50% around and over the snow gauge. The snow gauge itself is based on the rapid-response rain gauge, with a larger collecting funnel to increase sensitivity and with thermostatically-controlled heaters to ensure rapid melting of the frozen precipitation.

An example of attenuations measured in snow is given in Figure 6, which shows a time series of attenuation at 37, 57 and 97 GHz and at 0.63 μm , together with the snow (equivalent rain) rate. The correlation between attenuation and snow rate is, in general, very good, especially when the attenuation is delayed slightly in time, to allow for the time taken for the snow to melt and pass through the snow gauge. For the event shown in Figure 6, a delay of 30 seconds yielded the highest degree of correlation, while other snow events required delays of up to two minutes. The unheated rain gauges located along the range, however, indicated a peak snowfall rate some five minutes after the main peak shown in Figure 6, and continued to register precipitation for some 30 minutes after the snow event had ended, due to slow melting of snow which had accumulated in the collecting funnel. The air temperature at the onset of this snow event was about 3°C, dropping to 0.5°C during the course of the event.

Since there is no general theoretical description of attenuation by snow at millimetric wavelengths, it is of interest to try to establish empirical relationships, for use in prediction procedures, and to compare such attenuations with those expected for rainfall at the equivalent rain rates. Figure 7, for example, shows the attenuations measured at 97 GHz as a function of snow rate. The continuous line is a least-squares regression to a relation in the form of Equation (1), while the broken line is the CCIR predicted rain attenuation (for vertical polarization). It can be observed that, for the same amount of liquid water deposited on the ground, the attenuation through snow is approximately twice that expected for rain, for the event shown in Figure 6. For the other snow events which have been studied to date, which have comprised mainly wet snow, it has also been found that, in general, snow attenuation is greater than rain attenuation, for the same equivalent rain rate. On the other hand, dry snow, which tends to be less frequent even than wet snow in this region, is expected to produce rather less attenuation than rain of the same equivalent liquid water deposit rate.

5. ATTENUATION BY FOG

In comparison with the hydrometeors discussed above, fog attenuation is comparatively small at millimetric wavelengths, although it can, of course, be severe in the infrared and optical wavebands. Fog is composed of suspended droplets of water which are rarely more than 0.1 mm in diameter and generally are very much smaller, being comparable to infrared and optical wavelengths. In these spectral regions, then, scattering, and hence attenuation, can be considerable. At millimetric wavelengths, however, the Rayleigh approximation becomes valid and scattering losses are practically negligible. The bulk of attenuation in fog is then caused mainly by absorption and depends thus on the density of water within the fog, the extent of the fog and its index of refraction. Since the density of fog is generally small, little attenuation is expected at millimetric wavelengths, especially in comparison with rainfall attenuation.

As an example, and to confirm the arguments presented above, Figure 8 shows the attenuations measured at 0.63 μm and at 57 GHz as a function of the attenuation measured simultaneously at 10.6 μm , during a typical fog event. Most fog events are found to attenuate more than the dynamic ranges of the optical and infrared links, which are ~ 80 dB km⁻¹ and ~ 35 dB km⁻¹, respectively. At millimetric wavelengths, however, attenuations rarely exceed 1 dB km⁻¹, as demonstrated at 57 GHz in Figure 8.

Figure 8 also shows that the ratio of attenuations at 0.63 μm and 10.6 μm changes during the development and dispersal of the fog. The "hysteresis" has been observed in a number of fog events and can be either clockwise or counterclockwise, as a function of time. An explanation for this effect has been sought in terms of changes in the distribution of the sizes of suspended water droplets during the evolution of fogs. When, for a given optical attenuation (or visibility), the infrared attenuation is greater during the development of the fog than during its dispersal, the mean drop size may perhaps have decreased, possibly through evaporation. On the other hand, in fogs where the infrared attenuation is larger during dispersal than it was in the onset of the fog, at a given visibility, the mean drop size may have increased, perhaps by accretion or change of air volume, by winds for example. With only two measurement frequencies sensitive to drop size, however, it will not generally be possible to derive any detailed information on drop-size distributions in fog, as has been done for rainfall (see Manabe et al. and Section 3). It is nevertheless clear that there are some interesting phenomena occurring in fog events which warrant further investigation, and the development of propagation models to describe fog will enable qualitative, and even perhaps semi-quantitative, conclusions to be made on the evolution of fogs from data such as that in Figure 8.

6. TURBULENT EFFECTS - SIGNAL SCINTILLATION

Rapid fluctuations in atmospheric refractive index, together with physical move-

ments of inhomogeneous air, caused by the natural turbulence of the atmosphere, give rise to scintillation of signals. The theory of propagation through a turbulent medium was developed originally by Tatarski²⁰ for optical wavelengths and was later shown to be valid for the microwave regions of the electromagnetic spectrum²¹. In this treatment, scintillations due to small-scale irregularities in the spatial distributions of temperature, humidity and pressure can be characterized in terms of the statistical variance of the fluctuations in received signal power. For the case where the size of such irregularities (scales) is greater than the diameter of the first Fresnel zone, the variance in power level (i.e. in the logarithm of signal amplitude) is given by²⁰

$$\sigma^2 = 23.4 C_n^2 \left\{ \frac{2\pi}{\lambda} \right\}^{7/6} L^{11/6} \quad \text{dB}^2 \quad (7)$$

where C_n^2 is the refractive index structure parameter, λ is the signal wavelength in metres and L is the pathlength in metres. Conventionally, most studies of scintillation effects make use of this equation.

Now, as part of its programme of investigating a variety of propagation phenomena, the Rutherford Appleton Laboratory has studied the effects of flames on radiowave transmissions²². A flame, approximately 3 m wide, 3 m high and 0.5 m thick, was generated with a bank of five high-velocity burners, fed with forced combustion air and using gasoil as the fuel. The hydrocarbon flame was positioned in turn to fill completely the beams of the transmission links, approximately 50 m from the transmitters. (The first Fresnel zones are typically 1-1.5 m in diameter at their maxima).

The flame produced little attenuation at millimetric wavelengths, less than 0.2 dB; at 10.6 μm about 3 dB attenuation occurred, increasing to 15-20 dB at 0.63 μm . The dominant effect at millimetric wavelengths was scintillation, and the results have thus been analyzed in terms Eq. (7).

Figure 9 shows the variance σ^2 in signal power (dB) received through clear air (before and after the flame tests) and that received through the flame, as a function of signal frequency, determined from the 10 s sampled data. The continuous lines are best-fit curves with a $\nu^{7/6}$ dependence (vide Eq. (7)). The agreement with this frequency dependence is, in general, very good in both the clear-air transmissions and during transmissions through the flame, indicating that the turbid conditions within the flame can be adequately described by the "Kolmogorov two-thirds law" which is the basis of Eq. (7). The dominant effect of the presence of flame within the transmitted beams is an increase in the level of scintillation, i.e. the variance in received signal, by about one order of magnitude.

The data shown in Figure 9, together with Eq. (7), can be used to obtain values for the refractive-index structure parameter C_n^2 . For the clear-air case, the results yield a value of $C_n^2 = 4.8 \times 10^{-13} \text{ m}^{-2/3}$, which falls within the range to be expected²³, i.e. 10^{-15} to $10^{-10} \text{ m}^{-2/3}$. For the case of transmission through flame, if L is equated with the thickness of the flame, a value of $1.8 \times 10^{-6} \text{ m}^{2/3}$ is obtained, indicating the extremely high degree of turbidity within the flame.

Signal scintillations before, during and after the flame tests were also recorded at the higher data-collection rate of 100 Hz. These data have been used to examine the spectrum of fluctuations, by Fourier transformation of the time-series of signal levels. Figure 10 shows the resultant power spectral densities for both clear-air transmission and for propagation through flame, observed at 57 GHz. Since all the oscillators in the system are free-running, the transmission links essentially provide two-dimensional measurements of scintillation, for which Tatarski²⁰ showed that the spectrum of fluctuations should decay by $\omega^{-5/3}$, where ω is the fluctuation frequency. For clear-air transmission, this is indeed found to be the case, as shown in Figure 10. However, the presence of flame in the propagation path introduces a component in the fluctuations which decays by $\omega^{-11/3}$, suggesting the existence of a third dimension in the measurement. A possible explanation for this may be that the flame behaves as a highly variable lens; since gasoil has a large refractive index ($n \approx 1.45$) it is not unreasonable to assume that the burning vapour would have a refractivity greater than the surrounding air. The flame may thus introduce a variable focusing and defocusing effect, giving rise to a corresponding interference between direct and indirect rays within the first Fresnel zone. Such a focussing effect has been observed at optical wavelengths²⁴, together with the appearance of interference fringes at or near the focal plane, while the degree of ray-bending required to produce destructive interference at the receiving antenna (~ 9 minutes of arc) has also been observed in flame at microwave frequencies²⁵.

7. STATISTICAL STUDIES OF PROPAGATION

The event-based investigations considered above are primarily directed towards obtaining a deeper insight into the mechanisms of interaction between electromagnetic radiation and the various atmospheric and meteorological phenomena which prevail. Such studies are important to the development of propagation models to facilitate the use of basic meteorological data in the prediction of propagation conditions. As an adjunct to such investigations, and to provide the means to develop and test such prediction procedures, an extensive statistical analysis of propagation along the 500 m range is being carried out; products from this analysis include probability distributions of, for example, (a) the levels of attenuation and rainfall rates which were exceeded

during the measurement period; (b) durations of fades of different depths and the return periods between such fades; (c) instantaneous ratios of attenuation at different frequencies, to facilitate scaling of data from one frequency to another; (d) rates of change in attenuation, of particular importance to digital systems. These statistical products are provided on annual, quarterly and monthly time-scales and can be classified according to type of event, i.e. rain, snow, fog, etc.

For such statistical information to have significance, it is clearly essential that the propagation measurements should extend over considerable periods of time, in order to average over the natural year-to-year variability in climate, and to assess the extrema from long-term averages. While this long-term investigation is necessarily still in progress, some preliminary results will be included here, with the caveat that they represent only one year's data.

One of the more fundamental parameters in planning communications systems is an estimate of a fade margin, appropriate to a specified level of reliability for the particular service, for inclusion in link budgets. It thus becomes important to determine the percentages of time that various levels of attenuation may be exceeded over a given duration - typically one year, and preferably averaged over several years. While such longer-term averages are still being compiled, as noted above, a preliminary cumulative distribution of the attenuations measured on the 500 m range during its first year of operation is presented in Figure 11, for all events and for attenuations up to 20 dB km⁻¹. At any given time percentage, the attenuations increase, in general, with frequency, as expected for rainfall attenuation, which dominates the statistics of propagation at millimetric wavelengths.

The dramatic increase in attenuation at infrared and optical wavelengths, however, is due not to rain, but to fog, the incidence of which is typically 2-3% of the year in the southern part of the United Kingdom, and which, as noted in Section 5, has only a very minor effect at millimetric wavelengths. Comparisons of the different wavebands, such as in Figure 11 for all events, or Figure 5 for rain events only, for example, are of relevance to the design, application and operation of multispectral sensors; since the various spectral regions exhibit different propagation properties, while the particular technologies employed in each spectral region also possess different merits, data such as in Figures 5 and 11 can provide an insight into the possible development of multispectral systems to overcome some of the disadvantages of single-frequency systems, to provide more reliable and effective services in the future.

Cumulative distributions similar to Figure 11 have also been obtained for attenuations in rain only and for rainfall rates. By obtaining from these distributions equiprobable values for attenuation and rainfall rates for insertion into Eq. (1), it becomes possible to test statistically the models used to derive the tabulated values for the coefficients a and b; such comparisons will have more significance than analyses of individual events. The results of such testing to date tends to confirm that, in general, the published values underestimate rainfall attenuation at the shorter millimetric wavelengths, as noted in Section 3 and in reference 11.

While distributions such as in Figure 11 indicate the likelihood that a fade of a given depth might occur, they provide no information on how long such a fade might last, nor indeed on the time until the next. Such information is of particular importance to the operation of communications systems, in order to be able to relate outages, i.e. fading, to system availability, or, if a particularly high degree of reliability is required, in planning systems to include space-diversity facilities, for example. Accordingly, the data have further been analyzed to investigate the distribution of fade durations and the return periods between such fades. The minimum fade duration considered was 30 s, i.e. three consecutive measurements of attenuation in excess of a given threshold. Figure 12 shows the probability distributions for fades of different durations, from 30 s to over 3 hours, measured at 97 GHz, while Figure 13 shows the analogous distributions of the return periods between the fading levels in Figure 12. While these distributions should not be regarded as definitive, particularly as they are based on only one year's data, it is relevant to note that they bear a striking resemblance to a log-normal distribution, This has also been observed at other frequencies and for other propagation paths, and suggests that, given a more complete database covering periods of several years, it may be possible to develop empirical models to predict attenuation, fade duration and return periods, which will be of great value in the planning, design and operation of future communications systems.

8. SUMMARY

This paper has described the 500 m Millimetre Wave Experimental Range at Chilton, operated by the Rutherford Appleton Laboratory, to investigate the effects of the atmosphere and its prevailing meteorology on the propagation of electromagnetic radiation in the millimetric, infrared and optical wavebands. Examples have been given of investigations with rainfall attenuation, the effects of other hydrometeors such as snow and fog and propagation through turbulent media, together with some preliminary results on the statistics of propagation conditions, of relevance to systems planning.

9. REFERENCES

1. Liebe, H.J. "An updated model for millimeter-wave propagation in moist air". *Radio Science*, 20, 1985, 1069-1089.
2. CCIR. "Propagation in Non-Ionized Media". Vol. 5. Recommendations and Reports of the CCIR, 1986. ITU, Geneva.
3. Gibbins, C.J., Carter, D.G., Eggett, P.A., Lidiard, K.A., Pike, M.G., Tracey, M.A., White, E.H., Woodroffe, J.M. and Yilmaz, U.M. "A 500 m experimental range for propagation studies at millimetre, infrared and optical wavelengths", *J.IERE*, 57, 1987, 227-234.
4. Mie, G. "Contribution to the optics of suspended media, specifically colloidal metal suspensions". (In German). *Ann. Physik*, 25, 1908, 377-445.
5. Oguchi, T. and Hosoya, Y. "Scattering properties of oblate raindrops and cross-polarization of radiowaves due to rain. Part II: Calculations at microwave and millimetre wave regions". *J. Radio Res. Labs (Japan)*. 21, 1974, 151-259.
6. Laws, J.O. and Parsons, D.A. "The relation of raindrop size to intensity". *Trans. Amer. Geophys. Union*, 24, 1943, 452-460.
7. Marshall, J.S. and Palmer, W. McK. "The distribution of raindrops with size". *J. Meteorol.* 5, 1948, 165-166.
8. Joss, J., Thames, J.C. and Waldvogel, A. "The variations of raindrop size distributions at Locarno". *Proc. Intl. Conf. on Cloud Physics*, Toronto, Canada, 1968.
9. Olsen, R.L., Rodgers, D.V. and Hodge, D.B. "The ar^b relation in the calculation of rain attenuation". *IEEE. Trans. Ant. Prop.* AP26, 1978, 318-329.
10. CCIR Report 721-2. "Attenuation by hydrometeors, in particular precipitation, and other atmospheric particles". Recommendations and Reports of the CCIR, 1986, Vol 5., ITU, Geneva.
11. Manabe, T., Ihara, T., Awaka, J. and Furuhashi, Y. "The relationship of raindrop size distribution to attenuations at 50, 80, 140 and 240 GHz". *IEEE. Trans. Ant. Prop.*, AP35, 1987, 1326-1330.
12. Deirmendjian, D. "Electromagnetic Scattering on Spherical Polydispersions". Elsevier, New York, 1969.
13. Sokolov, A.V. "Attenuation of visible and infrared radiation in rain and snow". *Rad. Eng. Electron. Phys.*, 15, 1970, 2175-2178.
14. Buijs, J.H. and Janssen, L.H. "Comparison of simultaneous measurements at visible light, infrared (3-5 μ m) and mm waves (94 GHz)". Report No PHL 1981-04, National Defence Research Organization, TNO, Netherlands, 1981.
15. Atlas, D., Srivastava, R.C. and Sekhon, R.S. "Doppler radar characterization of precipitation at vertical incidence". *Rev. Geophys. Space. Phys.*, 11, 1973, 1-35.
16. Bohlander, R.A., McMillan, R.W., Guillory, D.M., Hill, R.J., Priestley, J.T., Clifford, S.F. and Olsen, R. "Fluctuations in millimeter signals". *Proc. 10th Intl. Conf. on Infrared and Mm Waves*. Lake Buena Vista, Florida, USA, December 1985.
17. Saduki, M.N.O. "Refractive index of snow at microwave frequencies". *Appl. Opt.*, 24, 1985, 572-575.
18. Atlas, D., Kerker, M. and Hitchfield, W. "Scattering and attenuation by non-spherical particles". *J. Atmos. Terr. Phys.*, 3, 1953, 108-119.
19. Yilmaz, U.M. and Eggett, P.A. "Report on snowfall-rate gauge". DURPP Research Note 58, Rutherford Appleton Laboratory, UK, 1985.
20. Tatarski, V.I. "Wave Propagation in a Turbulent Medium". McGraw-Hill, New York, 1961.
21. Clifford, S.F. and Strohbehn, J.W. "The theory of microwave line-of-sight propagation through a turbulent medium". *IEEE Trans. Ant. Prop.*, AP18, 1970, 264-274.
22. Gibbins, C.J. and Chadha, R. "Millimetre-wave propagation through hydrocarbon flame". *IEE Proc. Pt H.*, 134, 1987, 169-173.
23. CCIR Report 563-2. "Radiometeorological data". Recommendations and Reports of the CCIR, 1986, Vol. 5, ITU, Geneva.

24. Michaelis, M.M. "Laser beam guidance by flames". Am. J. Phys., 48, 1980, 990-991.
25. Palmer, T.Y. "Visible, infrared (IR) and microwave propagation in and near large flames". Proc. SPIE Int. Soc. Opt. Eng. 305, 1981, 28-30.
26. COST. "Influence of the atmosphere on radio propagation on satellite earth paths at frequencies above 10 GHz". COST Project 205, Alta Frequenza, LIV, 1985, 157-181.

10. ACKNOWLEDGEMENTS

The author is grateful to A Maitra for his invaluable assistance in the dropsize distribution analysis of rainfall attenuations.

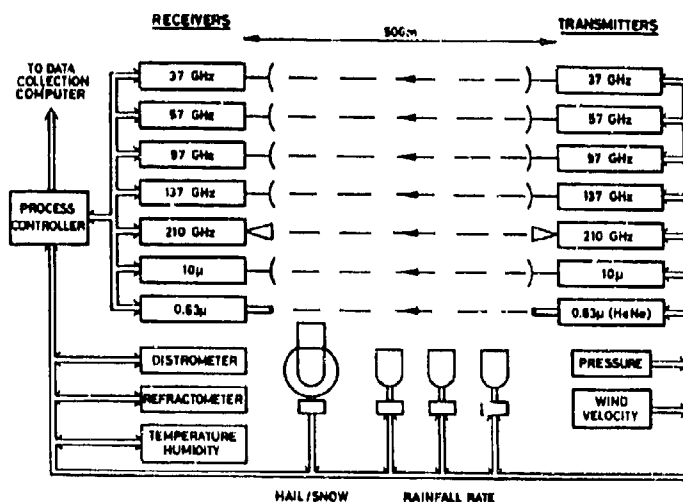


Figure 1. Block diagram of the 500 m range. (Courtesy IEE).

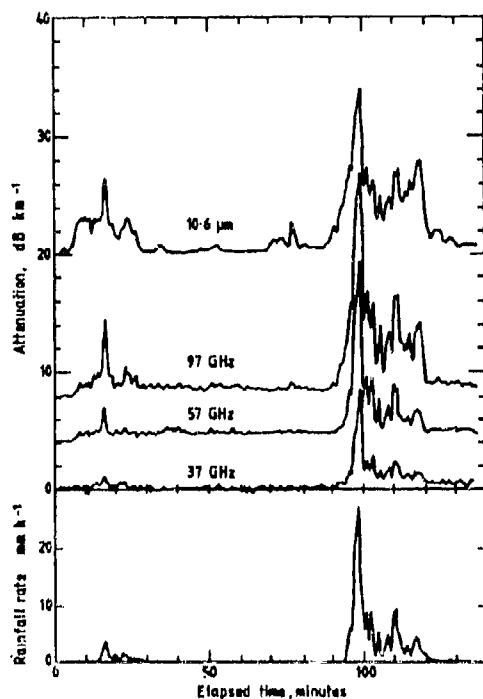


Figure 2. Time series of rain attenuations at 37, 57 and 97 GHz and at 10.6 μm , together with path-mean rainfall rate.

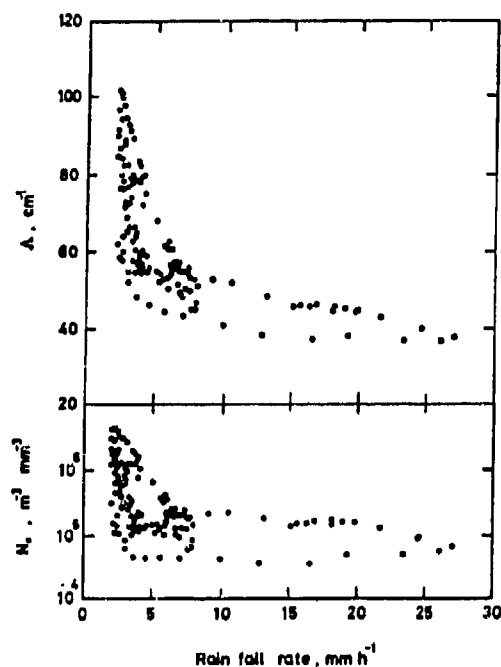


Figure 3. Values for N_0 and A for a Γ -distribution of raindrop sizes, deduced from the rainfall rate and 10.6 μm attenuation in Fig. 2.

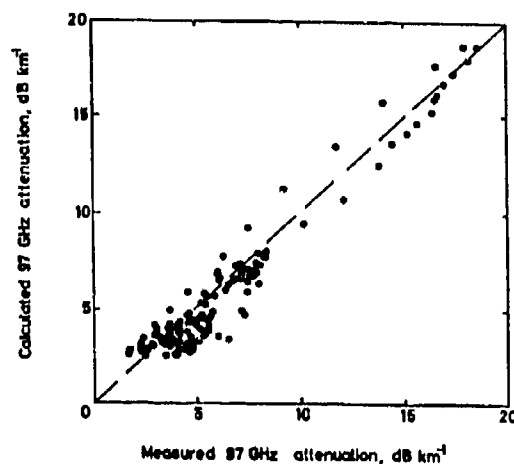


Figure 4. Comparison of 97 GHz attenuation calculated from the dropsize distribution in Fig. 3 with measured 97 GHz attenuation.

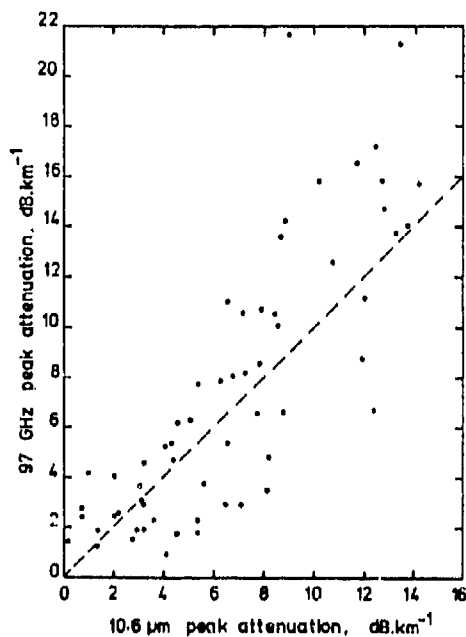


Figure 5. Comparison of peak attenuations measured in rain at 97 GHz and 10.6 μm .

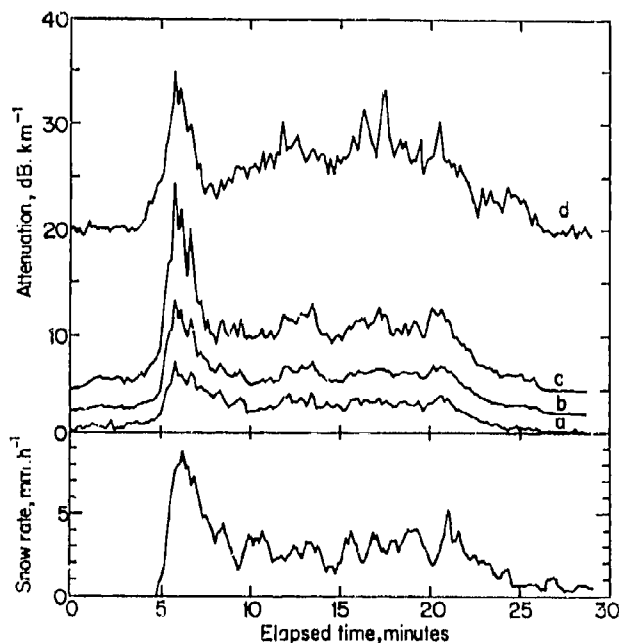


Figure 6. Time series of snow attenuations at (a) 37 GHz, (b) 57 GHz, (c) 97 GHz and (d) 0.63 μm , together with snow (equivalent rain) rate.

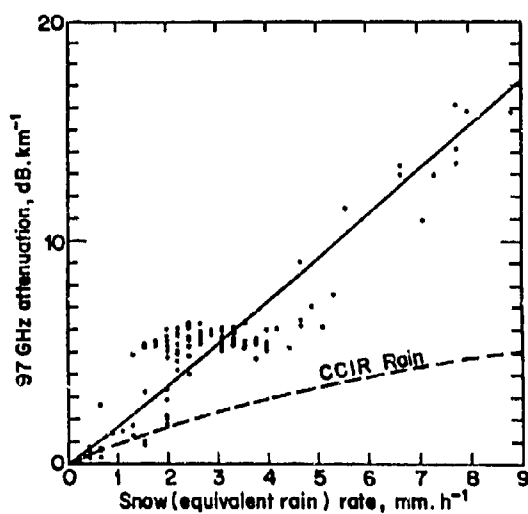


Figure 7. Comparison of 97 GHz snow attenuations in Fig. 6 with snow rate.

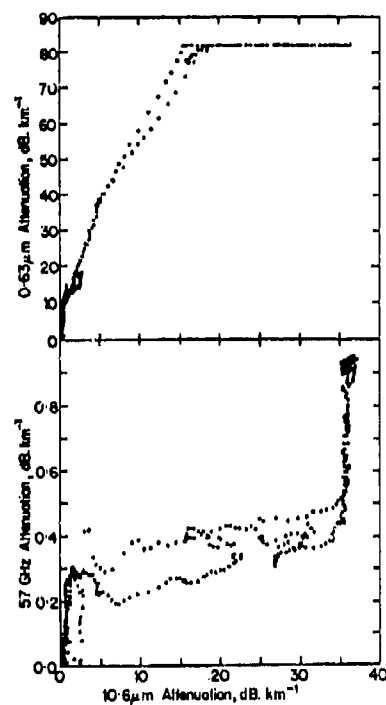


Figure 8. Comparison of fog attenuations at 0.63 μm and 57 GHz with 10.6 μm attenuation.

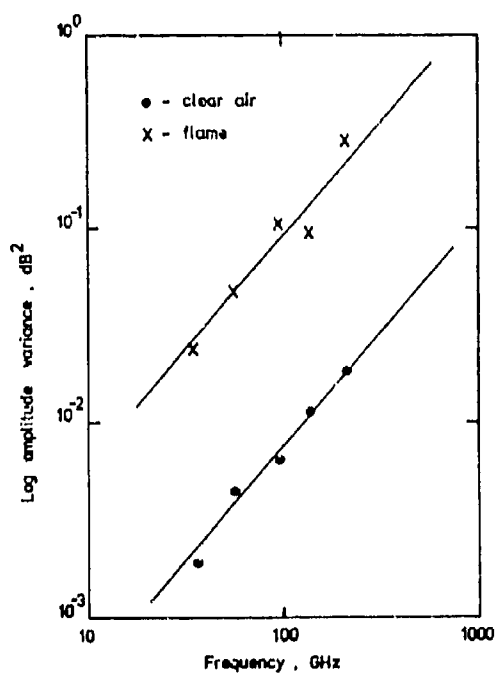


Figure 9. Log-amplitude variance of scintillations measured in propagation through clear air and through flame. (Courtesy IEE).

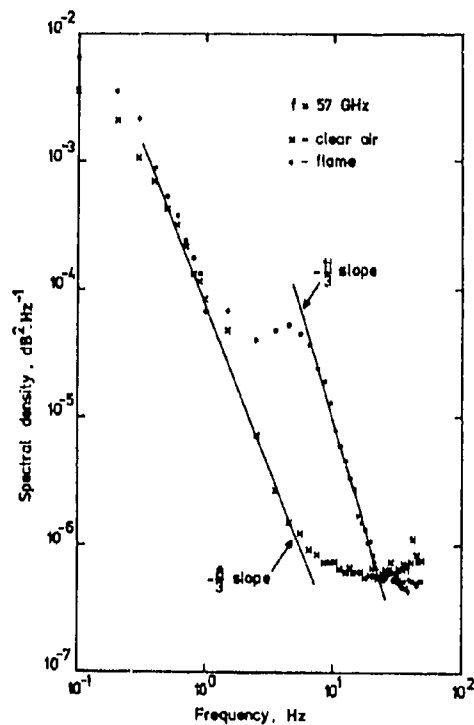


Figure 10. Power spectral density of fluctuations measured at 57 GHz in propagation through flames. (Courtesy IEE).

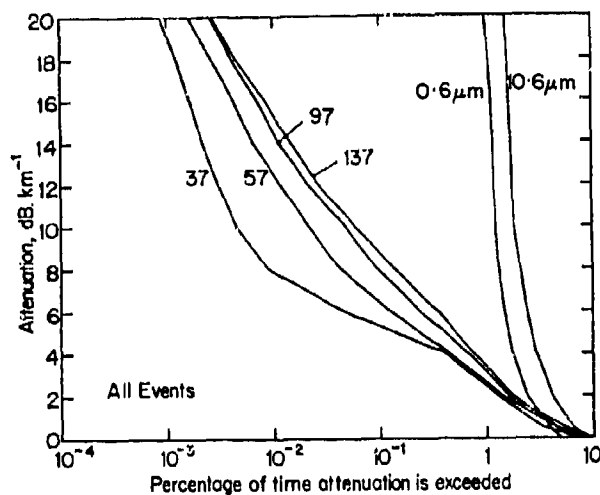


Figure 11. Percentage of time various levels of attenuation were exceeded on the 500 m range during one year. (Courtesy IEE).

Figure 12. Probability distributions of the durations of fades between 2 and 8 dB km⁻¹.

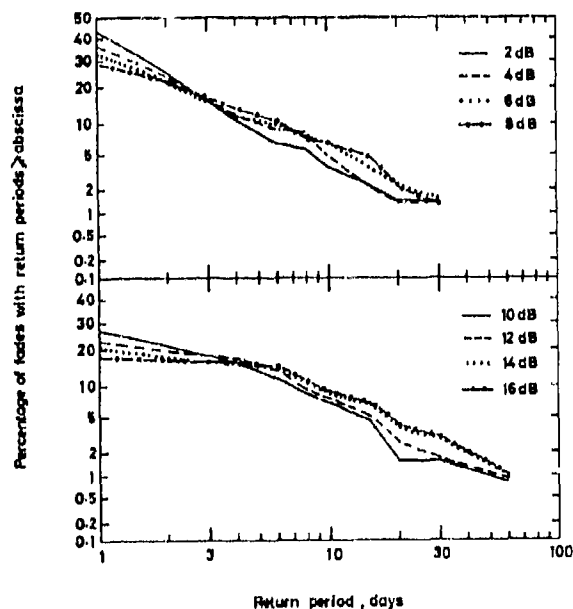
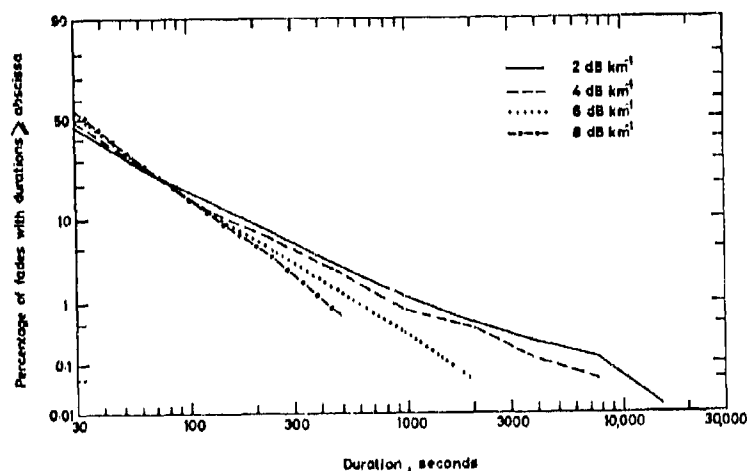


Figure 13. Probability distributions of the return periods between fades of 2 to 16 dB km⁻¹.

DISCUSSION

E. LAMBERTON

Your results show that, in most adverse conditions, the IR attenuation is less than the visible. The statistics of availability (Fig 11) indicated the converse. Could you please comment.

AUTHOR'S REPLY

This is to some extent an artifact in this particular set of data. During the period analyzed in Fig 11, the visible link was not operational for some of the time, and several long fog events were thus not included. Further analysis of subsequent data, which is still in progress, shows the more expected situation in which visible attenuation, particularly in fog, is greater than at infrared wavelengths.

E. SMITTLE

In comparing the 97 GHz and 10.6 μ m attenuation during rain, did you look at possible forward scatter effects on the measured attenuation? Since for the rain drops which are large compared with IR wavelengths, the forward scattered diffraction peak will have an angular spread which is comparable to the field of view of many transmissometers. The result will be for the smaller wavelengths more of the forward scattered light will be detected by the transmissometer leading to higher measured transmissions and lower attenuation coefficients. This is consistent with your results particularly for larger attenuations where the larger drops are more prevalent.

AUTHOR'S REPLY

Forward scattering effects were not considered in this analysis - the attenuations were simply those measured on the range.

EVAPORATION DUCT EFFECTS AT MILLIMETER WAVELENGTHS

by

K.D. Anderson

Ocean and Atmospheric Sciences Division
Naval Ocean Systems Center
San Diego, CA 92152-5000
United States

Summary

The evaporation duct strongly influences low-altitude over-the horizon propagation at millimeter wavelengths. Results from more than 2000 hours of propagation and meteorological measurements made at 94 GHz on a 40.6 km over-horizon, over-water path along the southern California coast show that the average received power was 63 dB greater than expected for propagation in a nonducting, or normal, atmosphere; 90 percent of the measurements were at least 55 dB greater than the normal atmosphere.

A numerical model of transmission loss based on observed surface meteorology is discussed and results are compared to measured transmission loss. On average, modeling results underestimate the transmission loss by 10 dB. In addition, results from modeling based on an independent climatology of evaporation duct heights for the area are shown to be adequate for most propagation assessment purposes. The reliability and reasonable accuracy of the model provide a strong justification for utilizing the technique to assess millimeter wave communication and radar systems operating in many, if not all, ocean regions.

LIST OF SYMBOLS

- δ Evaporation duct height (m).
- $\Delta\phi$ Potential refractivity difference between air and sea.
- R Bulk Richardson's number.
- Γ Empirical profile coefficient.

INTRODUCTION

The evaporation duct is a nearly permanent propagation mechanism created by a rapid decrease of moisture immediately above the ocean surface. Air adjacent to the surface is saturated with water vapor and rapidly dries out with increasing height until an ambient value of water vapor content is reached, which is dependent on general meteorological conditions. The nearly logarithmic decrease in vapor pressure causes the refractivity gradient to decrease faster than -157 N/km, which is a trapping condition. The height at which dN/dz equals -157 N/km is defined as the evaporation duct height and is a measure of the strength of the duct. Typical duct heights are between a few meters and approximately 30 meters with a world-average value of 13.6 meters [1]. Because these ducts are vertically thin, strong trapping is infrequently observed for frequencies below 2 GHz.

For low-altitude, over-water applications, the evaporation duct has been shown to be a reliable propagation phenomena that can dramatically increase beyond-the-horizon signal levels for frequencies greater than 2 GHz [2]-[4]. Although the highest frequency reported in previous work is 35 GHz, the results show that the magnitude of signal enhancement (referenced to diffraction) increases with increasing frequency. An analysis of the Aegean Sea measurements [4] shows that median received signal power on a 35-km path is 2, 15, 27, and 30 dB above diffraction for frequencies of 1, 3, 9.6, and 18 GHz respectively. Received signal power at 35 GHz on this path is consistently 30 to 45 dB above diffraction [4].

Effects of evaporation ducting on over-the-horizon signal propagation at 94 GHz are presented. Results from more than 2000 hours of RF measurements made on a 40.6 km path along the southern California coast are analyzed in terms of path loss (equivalent to transmission loss) which is defined as the ratio of transmitted to received power assuming loss-free isotropic antennas. Numerical propagation modeling results based on measured and climatological surface meteorology are compared to measured path loss. These comparisons are good and the results strongly support using the propagation model to predict the performance of millimeter wave systems operating near the surface in all ocean regions.

A brief review of the evaporation duct model and the propagation model used in this analysis precedes a discussion of the experiment and the results.

Models

In practice, boundary-layer theory relates bulk surface meteorological measurements of air temperature, sea temperature, wind speed, and humidity to the vertical profile of refractivity and thus the evaporation duct height. In a thermally neutral atmosphere where the air-sea temperature difference is 0, the modified refractivity profile is given by

$$M(z) = M(0) + 0.125(z - \delta \ln((z + z_0)/z_0)) \quad (1)$$

where z is height above the ocean, δ is evaporation duct height, and z_0 is a length characterizing boundary roughness. For a thermally non-neutral atmosphere, stability terms are incorporated into Eq. (1) (See Jaske, [3]). However, for common departures from neutrality, propagation

calculations indicate that a neutral profile is a reasonable approximation, provided that duct height for the neutral profile is calculated from observed meteorology. In this analysis, evaporation duct height is computed from surface observations using the Jeske model [3],[5] as implemented by Hitney [6] with thermal stability modifications suggested by Paulus [7].

Numerical propagation modeling techniques have shown good agreement to RF measurement results when single-station surface meteorological observations are available to determine the refractivity-versus-altitude profile of the evaporation duct [8]. In a maritime environment, the assumption of lateral homogeneity (vertical profile of refractivity invariant along the path of propagation) is generally good [8],[9] and justifies a waveguide formalism [10]-[12] approach to the analysis of propagation through the troposphere. Numerical results are derived from a computer program called "MLAYER" which is an enhanced version of the "XWVG" program [13]. MLAYER assumes that the vertical profile of refractivity over the sea can be approximated by an arbitrary number of linear segments and uses an ingenious technique [14] to find all complex modes that propagate with attenuation rates below a specified value. Surface roughness is developed from Kirchhoff-Huygens theory in terms of rms bump height, σ , which is related to wind speed as $\sigma = 0.0031u^2$, where u is wind speed (m/s) [15],[16].

The determination of the vertical refractivity profile is crucial to the MLAYER calculations. For neutral and stable conditions, the duct height is

$$\delta = \frac{-\Delta\phi}{1.32 + 0.0867 \cdot R/\Gamma \cdot (0.75 - \Delta\phi)} \quad (2)$$

where ϕ is the potential refractivity difference between the air and sea surface, R is the bulk Richardson's number, and Γ is an empirical profile coefficient. Eq. (2) assumes that bulk parameters are measured at a height of 6 m and that z_0 is 0.00015 m. Under neutral conditions, R is zero, hence the potential refractivity difference is $\phi = -1.32 \cdot \delta$. The potential refractivity gradient (under neutral and stable conditions) is

$$\frac{\Delta\phi}{\Delta z} = \frac{\Delta\phi \cdot [1/z + 0.0867 \cdot R/\Gamma]}{10.60 + 0.52 \cdot R/\Gamma} \quad (3)$$

where z is the height above the surface. Again, under strictly neutral conditions, Eq. (3) reduces to $\Delta\phi/\Delta z = \Delta\phi/(10.60 \cdot z)$. The potential refractivity gradient is related to the refractivity gradient as

$\Delta\phi/\Delta z = \Delta N/\Delta z + 0.032$ and to the modified refractivity gradient as $\Delta\phi/\Delta z = \Delta M/\Delta z - 0.125$. Using Eqs. (2) and (3), the modified refractivity profile was determined for evaporation duct heights from 0 to 20 m in 2 m intervals. These profiles are shown in Fig. 1 where the surface modified refractivity is referenced to 0 M-units. Path loss calculations were made for five rms bump heights; 0.0 (smooth surface), 0.025, 0.100, 0.250, and 0.500 m corresponding to wind speeds of 0.0, 4.3, 8.6, 13.6, and 19.2 knots.

For a one-way transmission system, signal power at the receiver is

$$P_r = P_t + G_t - L + G_r + G_a \quad (4)$$

where P_t is power transmitted, G_t and G_r are transmitter and receiver antenna gains, and G_a is additional gain measured from the receiver antenna to the point in the receiver where power is measured. Assuming transmission-line losses and other hardware-related losses are accounted for in P_t or G_r , the loss L can be written as $L = L_m + L_e$, where L_m is loss due to molecular absorption and L_e is loss accounting for all other environmental and geometrical losses. The advantage of treating L as the sum of two independent terms is that L_m then depends on observable air temperature and humidity, whereas L_e depends on the same two observables in addition to sea temperature and wind speed. Of course, both loss terms depend on geometry of the transmission path; L_m is the product of attenuation rate and path length, and L_e involves a complicated dependency on the refractivity profile, path length, and antenna heights.

Range dependency of absorption-free path loss (L_e) at a frequency of 94 GHz is shown in Fig. 2 for a normal atmosphere, denoted by 0 duct height, and for evaporation duct profiles (neutral stability) corresponding to duct heights of 2, 4, 6, and 8 m. In this case, transmitter and receiver are 5 and 9.7 m above a smooth sea surface, and coherent signal propagation (modal phasing included) is assumed. At a range separation of 40 km, L_e for transmission through a normal atmosphere is about 250 dB (assuming a typical 0.7 dB/km molecular absorption attenuation rate, total path loss is about 280 dB). For propagation in an atmosphere represented by a refractivity profile corresponding to an evaporation duct height of two meters (a relatively shallow duct), L_e is approximately 184 dB -- a "gain" of 66 dB compared to the diffraction reference. With an 8-m evaporation duct, path loss increases with range at a fairly consistent rate of about 0.2 dB/km beyond 30 km.

Path loss variation with receiver height is shown in Fig. 3 for a path separation of 40.6 km. The transmitter is located 5 m above a smooth surface. In a normal atmosphere, path loss for a receiver located 20 m above the surface is about 230 dB. For this same receiver in an environment of a 2-m evaporation duct, path loss is about 178 dB; a gain of 52 dB even though both transmitter and receiver are outside of the duct.

Surface roughness effects are shown in Fig. 4 for a transmitter at 5 m, receiver at 9.7 m, and a fixed path separation of 40.6 km. Incoherent signal propagation (modal phase is ignored) is used to represent absorption-free loss, L_e . Higher wind speeds generally increase loss with respect to a smooth surface, except for a normal atmosphere where the waveguide modes are

evanescent. For duct heights above 10 m, path loss at the two highest wind speeds are nearly equal. Above 16 m, path loss for wind speeds greater than about 8 knots are nearly equal. In these highly trapped cases, many weakly attenuated modes are found and the aggregate effect is for convergence of the mode sums to a limiting value. At 94 GHz, the limiting value of surface roughness appears to be a bump height of 0.5 m.

EQUIPMENT DESCRIPTION

A 40.6-km transmission path along the Southern California coast was chosen and instrumented for the measurement program. The path is shown in Fig. 5. The transmitter antenna was located 3 m above mean low water (mlw) at the Del Mar Boat Basin facility of the U.S. Marine Corps Base at Camp Pendleton, CA. This antenna, a horizontally polarized 12-inch-diameter lens with a 0.7° beamwidth, was centered along the path at an elevation angle of zero degrees. The horizon is 9.2 km and is shown as a dashed arc in Fig. 5.

The receiver site was at the western end of Scripps Pier, located at the University of California at San Diego, CA. This pier extended 335 m from the shore, which, in all but the worst storms, placed the receiver beyond the surf zone (this pier has since been torn down and replaced by a new structure). The receiver antenna was located 9.7 m above mlw (horizon of 12.9 km) and was pointed towards the transmitter with an elevation angle of zero degrees.

The RF transmitter was similar to the receiver which is shown in Fig. 6. An X-Band oscillator, phase-locked to a stable 103-MHz crystal source, phase-locked a 94-GHz Gunn diode. Approximately 23 dBm of transmitter power was generated by an injection-locked IMPATT diode. At the receiver, the 103-MHz crystal source was offset from the transmitter crystal reference to generate an IF of 59.8 MHz which was monitored by a spectrum analyzer. Although the controller could adjust analyzer functions to optimize signal detection, the analyzer was typically set for a frequency span of 181.7 KHz, no integration, and with video and resolution bandwidths of 3 KHz. Signal power and frequency were recorded with an effective sample time of 340 milliseconds.

System "constants" (power transmitted, antenna gains, and RF-to-IF gain of the receiver) are listed in Table 1. Total path loss is related to observed received signal power as $L = 157 - P_r$, which is the sum of the system constants minus the power received (see Eq. 4). Minimum detectable signal power at the analyzer was -83 dBm, which corresponds to a maximum detectable path loss of ~ 240 dB ($L = 157 - (-83)$). Diffraction is about 250 dB for the geometry of the path (See Fig. 2). Therefore, without evaporation ducting, the signal should be 10 dB below the receiver noise level and should not be detectable. However, the expected gain of about 60 dB through evaporation ducting, less the expected molecular absorption loss of about 30 dB, places the signal at about 220 dB which is detectable by the receiver.

The dynamic range of the analyzer was sufficient to lock onto and track the signal in all conditions, except when there was precipitation along the path, which was rare. A moderate rain shower, uniform along the path, could increase path loss by 100 dB, making any practical reception impossible. As a reference, the basic free-space transmission loss, $(4\pi d/\lambda)^2$, is 164 dB, where d is the range separation and λ is the wavelength.

Air temperature, sea temperature, relative humidity, wind speed, and wind direction were recorded at Scripps Pier in conjunction with the RF measurements. Table 2 describes the surface meteorological sensors, which were monitored by a data acquisition system that sampled and stored the data every 10 seconds.

In operation, measurements were recorded 24 hours per day. To reduce the volume of data, statistics of rms and standard deviation were locally computed for 10-minute intervals. Approximately 60 samples of surface meteorology and approximately 1000 samples of power monitored at the analyzer were used to compute these statistics. The local data (statistics) were automatically transferred for further analysis via modem lines to computers at Naval Ocean Systems Center, about 10 miles south of the receiver site.

Evaporation duct height and molecular absorption were computed from observed rms values of surface meteorology. Absorption-free path loss was determined by a look-up procedure into a precomputed two dimensional table. One dimension of this table was evaporation duct height from 0 to 20 m in 2-m intervals; the other dimension was rms bump height specified at 0 (smooth surface), 0.25, and 0.50 m.

RESULTS

MEASUREMENTS

Measurements began in late July 1986 and continued through early July 1987. Eight periods, totaling 102 days of operations, were completed during this time. Table 3 lists the time periods in which measurements were made.

One-way transmission path data were analyzed by comparing observed rms path loss (transmission loss) to path loss computed for both evaporation duct height and rms bump height, which were calculated from surface meteorological quantities measured at the receiver site. Absorption-free path loss calculated by MLAYER was modified by adding molecular absorption loss calculated from surface meteorology (reference [17]) in order to compare it to observed total path loss. Molecular absorption loss during the entire measurement program averaged approximately 30 dB.

Figure 7 shows the time-series of surface meteorology, measured path loss, and predicted path loss for a representative measurement period. Figure 7(a) is a time-series plot of measured air temperature (C), relative humidity (e), and wind speed (knots). Also included in this figure is

the computed molecular absorption (dB), labeled as α . The time shown on the abscissa is plotted in local time; hour 00 is associated with the tic mark above the first character in the day label. Gaps in the data (around August 8) were due to software and hardware failures that were manually corrected.

In this period, relative humidity was nearly always greater than 90 % and accompanied with light winds. Sea temperature was fairly constant at about 20 degrees Celsius. Figure 7(b) shows the air-sea temperature difference and the calculated evaporation duct height. Diurnal changes of about 3 degrees Celsius in air temperature are observed early in this period and become less pronounced later. Wind direction, Fig. 7(c), shows some land-sea breeze effects up until about August 4th when the breeze became fairly constant from the northwest. Fig. 7(d) shows the observed and predicted path loss. Predicted path loss is derived from adding the calculated absorption to the path loss calculated for the evaporation duct height on a point-by-point basis. Considering that the propagation model assumes spatial and temporal homogeneity along the entire 40.6 km path, the time-series agreement between the observed and predicted path loss is remarkable.

With no evaporation ducting, the estimated path loss is the sum of the diffraction path loss and the molecular absorption. The diffraction loss for the path geometry is 250 dB; the average molecular absorption loss is seen to be about 35 dB (Fig. 7(a)); therefore the estimated path loss with no evaporation ducting is about 285 dB. From Fig. 7(d), the average observed path loss is about 225 dB, which is 60 dB less than what is expected using normal or 4/3 earth propagation prediction models. However, the observed path loss is about 60 dB greater than the free-space level (164 dB) which means that radar applications are unlikely unless the target has a large radar cross-section.

ALL MEASUREMENT PERIODS COMBINED

The crucial parameter that relates path loss to surface meteorological conditions is evaporation duct height. A scatter plot of difference between observed and predicted path loss in relation to calculated duct height is shown in Fig. 8. All 102 days of observations, more than 12,000 data points, are included. Predicted path loss, on average, underestimates observed path loss by approximately 10 dB and, in the extremes, underestimates by nearly 40 dB and overestimates by 22 dB. A trend line, computed from a histogram of scatter, indicates median error. The trend is for error to increase with duct height up to heights of about 5 m; median error is relatively flat for higher duct heights.

Wind speed strongly affects both evaporation duct height and surface roughness. Higher winds generally increase duct height and increase attenuation due to roughness. A scatter plot of error in path loss with relation to wind speed is shown in Fig. 9. A trend line indicates that median error is about 2.5 dB for winds less than 1 knot and increases to ~ 14 dB at about 5 knots. For winds greater than about 5 knots, error remains nearly constant at about 14 dB. It is tempting to reduce the error bias by modifying rms bump height because the surface roughness formulation in MLAYER is one of the largest uncertainties at millimeter wavelengths. However, the measurement program was designed to test for gross environmental effects; a modification to rms bump height or surface roughness formulation cannot be justified from this data.

CLIMATOLOGY

A comparison of observed absorption-free path loss to predictions derived from a separate climatology of evaporation duct heights [1] illustrates an application of the propagation model to the assessment of a millimeter wave system. The evaporation duct climatology is based on 15 years of surface meteorological observations (normally taken by ships at sea) from which the distribution of evaporation duct heights were computed. All ocean areas were analyzed in $10^\circ \times 10^\circ$ grids (Marsden Squares). For the San Diego off-shore area, the evaporation duct height frequency distribution, Fig. 18, shows a peak for duct heights between 6 and 10 m. Duct heights greater than 20 m are infrequent. Combining this distribution with the results shown in Fig. 4 (0.25 m bump height), gives an accumulated frequency distribution which is shown as a solid line in Fig. 11. Observed absorption-free path loss is plotted on the same figure as a dotted line. Free space and diffraction fields are referenced. Although the predicted path loss distribution consistently underestimates the observed, it is clearly a better predictor compared to assuming a normal atmosphere representation of the environment. In the worst case, it is only some 10 dB less than observed, whereas the difference is about 4 dB at the 50 percent level. The observed path loss reduction from diffraction exceeds 63 dB half of the time; 90 percent of the time the reduction exceeds 55 dB. Both predicted and observed distributions show that path loss is 45 dB less than the diffraction reference 100 percent of the time (the occurrence of rain was negligible during the measurements).

CONCLUSIONS

Low altitude propagation of millimeter waves at ranges beyond the radio horizon is strongly influenced by the evaporation duct; for the propagation path used, received power levels are on the order of 50 to 100 dB greater than the power levels expected for propagation through a nonducting or normal atmosphere.

A single-station measurement of surface meteorology is adequate to analyze millimeter wave propagation over the ocean. On a point-by-point comparison, modeling typically underestimates observations by about 10 dB; the error is probably due to incomplete considerations of both horizontal heterogeneity and surface roughness effects. Direct sensing of the environment on the scale of kilometers in the horizontal and meters in the vertical is impractical, however, planetary boundary layer models and remote sensing techniques may, in the future, offer

considerable improvement to the propagation analysis. The formulation of surface roughness in the propagation model is one area that is actively being examined for a more complete understanding.

In summary, the increase in received signal strength due to the presence of the evaporation duct has been realistically modeled and provides an accurate estimate of actual millimeter wave system performance. The significant system "gain" due to evaporation ducting is clearly an important consideration in the design stages of moderate range, over-water millimeter wave systems.

REFERENCES

- [1] W.L. Patterson, "Climatology of marine atmospheric refractive effects," Naval Ocean Syst. Cen. Tech. Doc. 573, 523 pp., December 1986.
- [2] M. Katzin, R.W. Bauchman, and W. Binnian, "3- and 9-centimeter propagation in low ocean ducts," Proc. IRE, vol. 35, pp. 891-905, September 1947.
- [3] H. Jeske, "Die Ausbreitung elektromagnetischer Wellen im cm- bis m-Band über dem Meer unter besonderer Berücksichtigung der meteorologischen Bedingungen in der maritimen Grenzschicht," Hamburger Geophys. Einzelschriften, Hamburg, DeGruyter and Co., 1965.
- [4] J.H. Richter and H.V. Hitney, "Antenna heights for the optimum utilization of the oceanic evaporation duct," Naval Ocean Syst. Cen. Tech. Doc. 1209, 513 pp., January 1988.
- [5] H. Jeske, "State and limits of prediction methods of radar wave propagation conditions over sea," paper presented at the NATO Advanced Study Institute, Sorrento, Italy, 5-14 June 1973.
- [6] H.V. Hitney, "Propagation modeling in the evaporation duct," Naval Electronics Lab. Cen. Tech. Rep. 1947, 38 pp., April 1975.
- [7] R.A. Paulus, "Practical application of an evaporation duct model," Radio Sci., vol. 20, pp. 887-896, 1985.
- [8] H.V. Hitney, J.H. Richter, R.A. Pappert, K.D. Anderson, and G.B. Baumgartner, Jr., "Tropospheric radio propagation assessment," Proc. IEEE, vol. 73, pp. 265-283, 1985.
- [9] H. Jeske, "The state of radar-range prediction over sea," Tropospheric Radio Wave Propagation Part II, AGARD, pp. 50-1,50-6, February 1971.
- [10] H.G. Booker and W. Walkinshaw, "The mode theory of tropospheric refraction and its relation to waveguides and diffraction," in Meteorological Factors in Radio Wave Propagation. London, England: The Physical Society, 1946, pp. 80-127.
- [11] K.G. Budden, The Waveguide Mode Theory of Wave Propagation. London, England: Logos Press, 1961.
- [12] L.M. Brekhovskikh, Waves in Layered Media, 2nd ed. New York: Pergamon, 1970.
- [13] G.B. Baumgartner, Jr., "XWVG: A waveguide program for trilinear tropospheric ducts," Naval Ocean Syst. Cen. Tech. Doc 610, 206 pp., June 1983.
- [14] D.G. Morfitt and C.H. Shellman, "'MODESRCH', an improved computer program for obtaining ELF/VLF/LF mode constants in an earth atmosphere waveguide," Interim Rep. 77T, prepared for the Defense Nuclear Agency by the Naval Electronics Lab. Cen. (now Naval Ocean Syst. Cen.), 227 pp., October 1976.
- [15] W.D. Ament, "Toward a theory of reflection by a rough surface," Proc. IRE, vol. 41, pp. 142-146, 1953.
- [16] O.M. Phillips, Dynamics of the Upper Ocean. London: Cambridge Univ. Press, 1966.
- [17] H.J. Liebe, K.C. Allen, G.R. Hand, R.H. Espeland, and E.J. Violette, "Millimeter-wave propagation in moist air: model versus path data," NTIA Report 85-171, 54 pp., March 1985.

Table 1 RF System Constants

| Component | Value |
|--------------------------|--------|
| Transmitter power | 23 dBm |
| Transmitter antenna gain | 47 dBi |
| Receiver antenna gain | 47 dBi |
| Receiver RF-to-IF gain | 40 dB |

Table 2 Surface Meteorological Sensors

| Sensor | Type | Accuracy | Response |
|-------------------|-------------------|-----------|----------|
| Air temperature | Platinum RTD | 0.1 deg C | 10 sec |
| Sea temperature | Platinum RTD | 0.1 deg C | 30 sec |
| Relative humidity | Crystallite fiber | 6 % | 60 sec |
| Wind speed | Cup | 1 % | 1.5 m |
| Wind direction | Vane | 1 deg | 1.1 m |

Table 3 Dates of Measurements

| Start | End |
|-------------------|--------------|
| July 29, 1986 | August 10 |
| September 2, 1986 | September 11 |
| October 7, 1986 | October 20 |
| November 18, 1986 | November 23 |
| December 1, 1986 | December 23 |
| January 13, 1987 | January 30 |
| May 4, 1987 | May 14 |
| June 30, 1987 | July 5 |

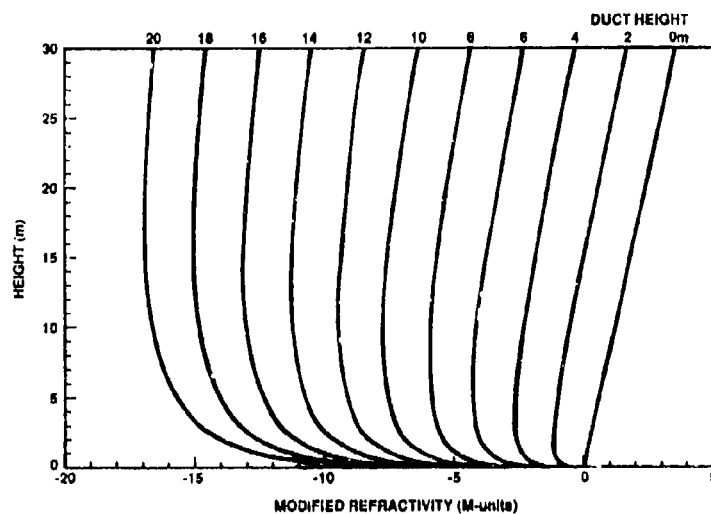


Fig. 1. Evaporation duct profiles for duct heights from 0 (normal) to 20 m in 2 m increments. Surface modified refractivity is referenced to 0 M-units.

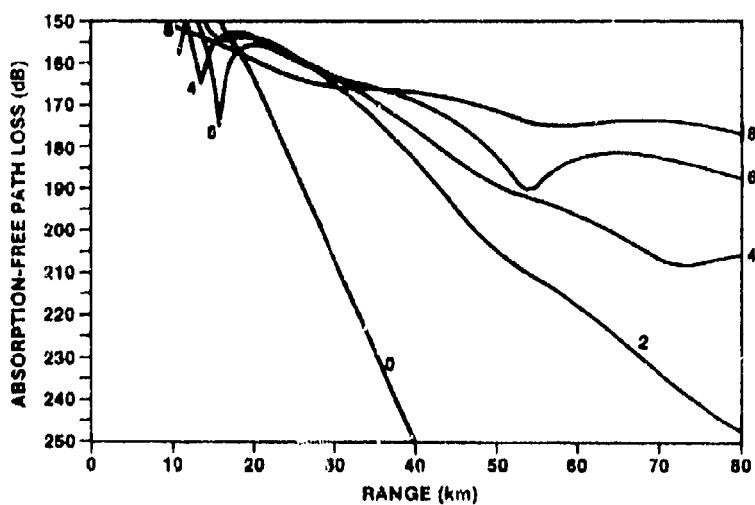


Fig. 2. Absorption-free path loss vs range for evaporation duct heights of 0 (normal), 2, 4, 6, and 8 m. Coherent mode summation and smooth surface.

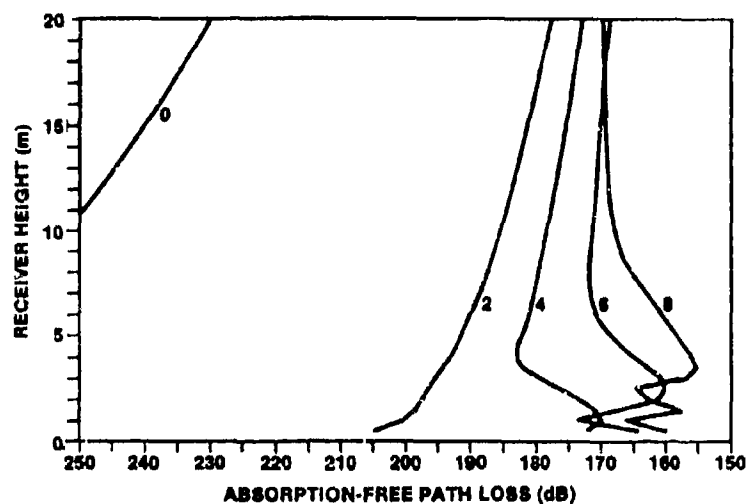


Fig. 3. Absorption-free path loss (incoherent) for a transmitter at 5 m, range separation of 40.6 km, and a smooth surface. The curves are labeled with the duct height.

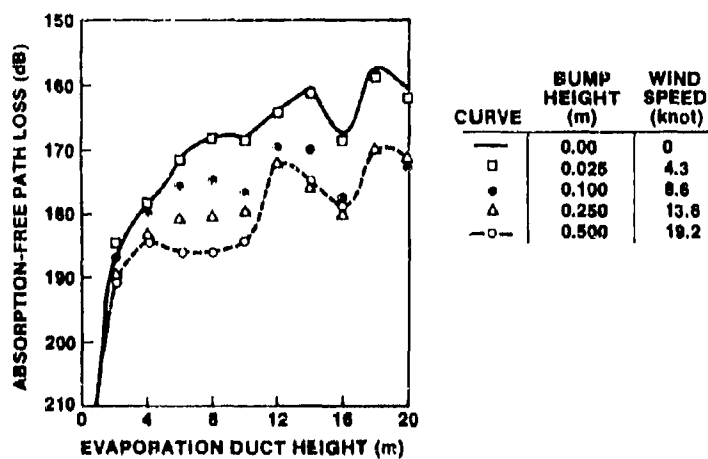


Fig. 4. Effects of surface roughness at 94 GHz. Transmitter at 5 m, receiver at 9.7 m, and range separation of 40.6 km. The rms bump height, expressing the surface roughness, is derived from Kirchhoff-Huygens Theory (see Asent, 1953; Phillips, 1966).

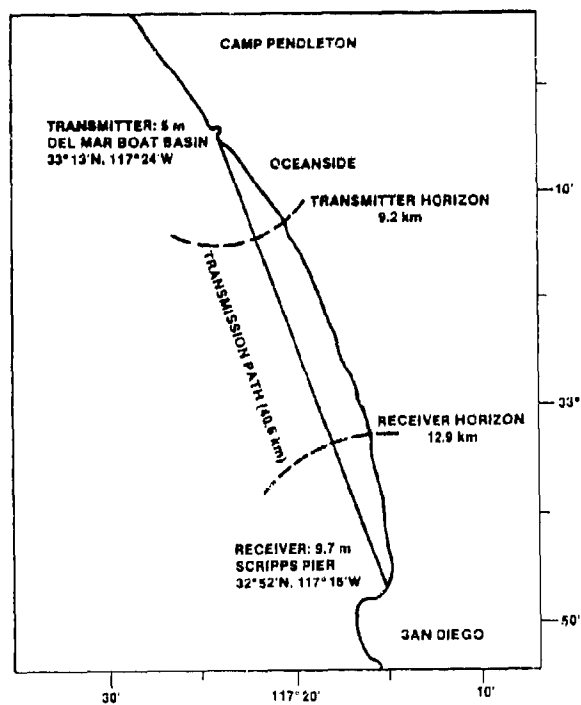


Fig. 5. Transmission path from Camp Pendleton to Scripps Pier, CA. Normal radio horizon is indicated by the dashed arcs centered on the transmitter and receiver sites.

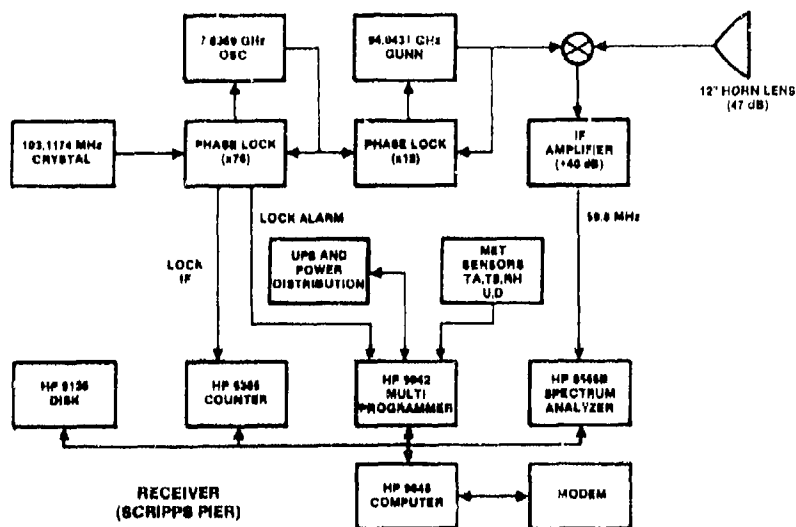


Fig. 6. Receiver system installed at Scripps Pier, CA.

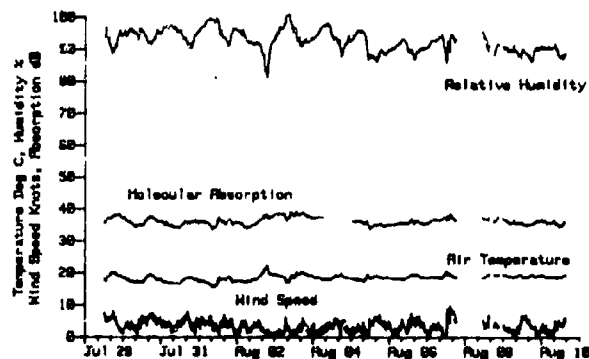


Fig. 7a. Air temperature, relative humidity, and wind speed measured at Scripps Pier. Molecular absorption at 94 GHz calculated from surface meteorological measurements.

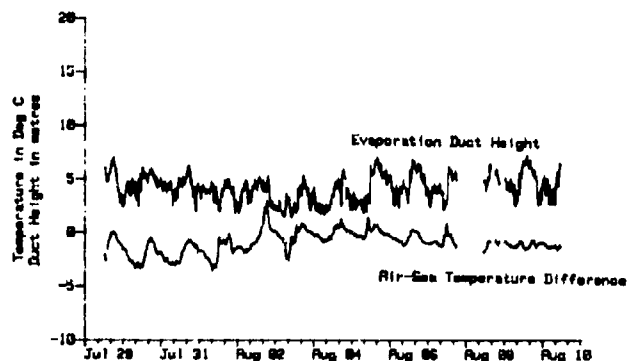


Fig. 7b. Air-sea temperature difference at Scripps Pier and calculated evaporation duct height.

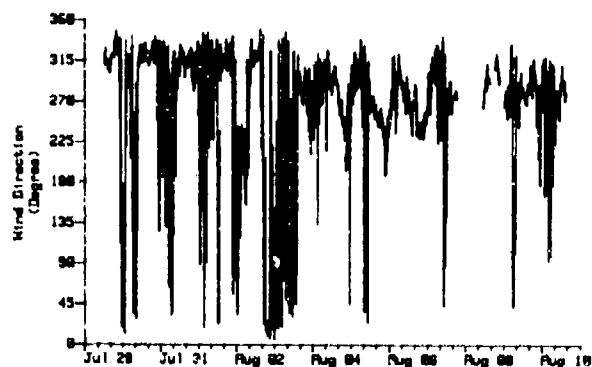


Fig. 7c. Wind direction at Scripps Pier.

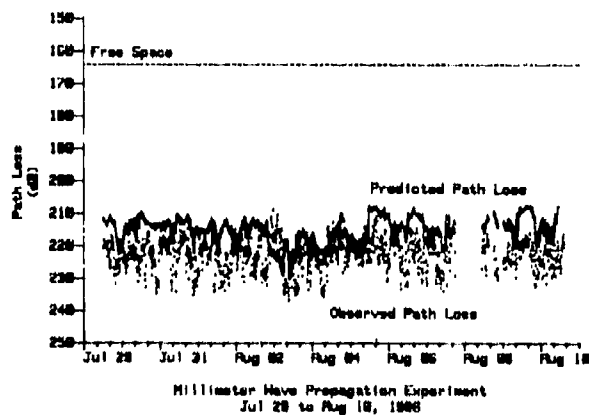


Fig. 7d. Measured path loss (dotted) and predicted path loss (solid).

Fig. 7. Meteorological and radio data recorded in the measurement period from July 29 to August 10, 1986. Predicted path loss, shown as the solid curve in Fig. 7d, tends to underestimate the measured path loss (dotted curve) by 10 dB.

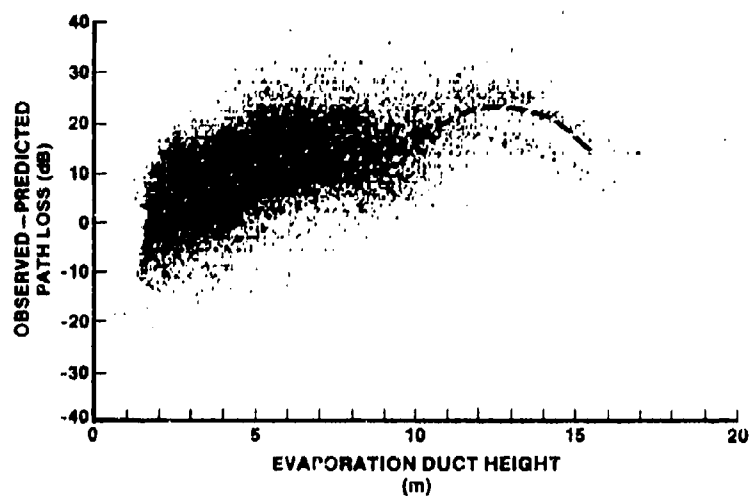


Fig. 8. Error (dB) between predicted and observed path loss in relation to observed evaporation duct height. All data measured, without qualification, are presented. A positive error indicates prediction underestimates observation.

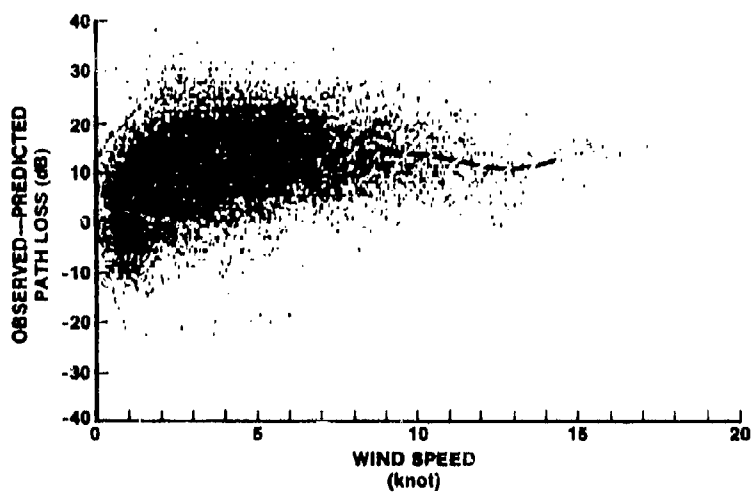


Fig. 9. Path loss error (dB) in terms of observed wind speed (knt) for all measurements.

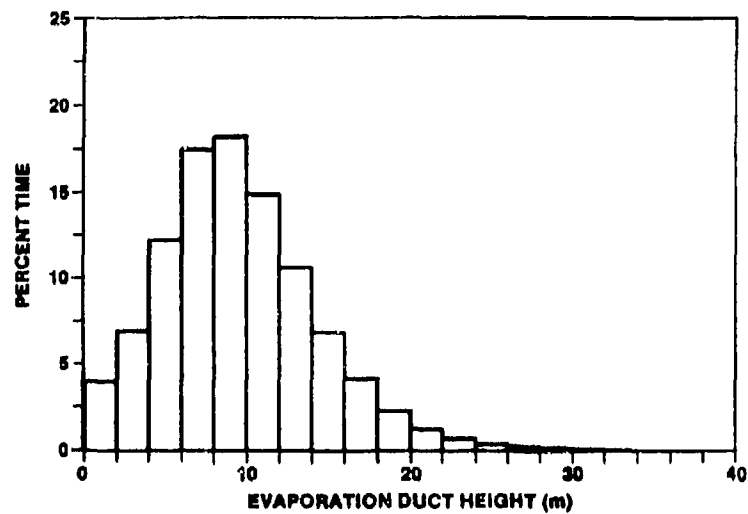


Fig. 10. Climatological evaporation duct height distribution for the San Diego off-shore area.

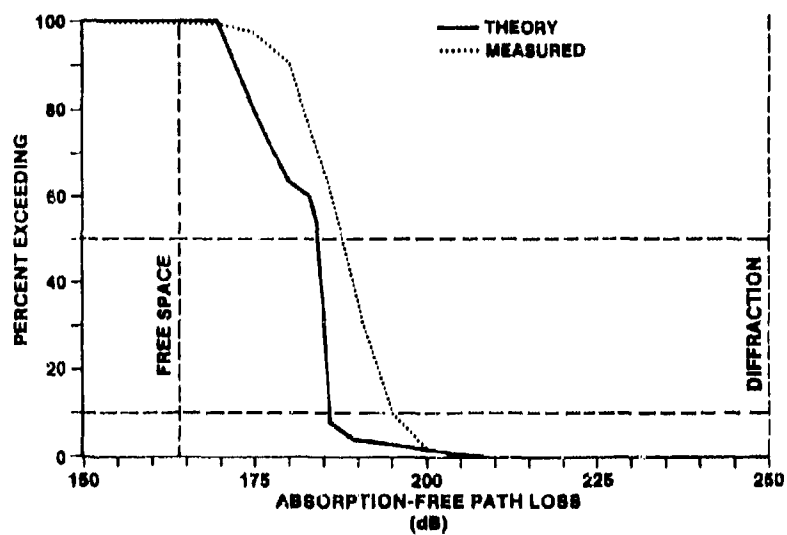


Fig. 11. Absorption-free path loss distribution predicted from the distribution in Fig. 10 compared to the measured (dotted curve). Total path loss can be approximated by reading the desired percentage and adding 30 dB (average absorption loss) to the corresponding abscissa coordinate.

DISCUSSION

M. LEVY

Does diffuse reflection from the rough sea surface contribute to transmission loss? Is it modeled? It might explain the discrepancy between measurements and prediction.

AUTHOR'S REPLY

We presently model sea surface roughness effects by simple modification of the reflection coefficient. A rigorous approach is being incorporated into our treatment using the parabolic equation approximation.

J. BACH ANDERSEN

Do you assume horizontal homogeneity of the duct, and could deviations explain the observed path loss?

AUTHOR'S REPLY

Yes, horizontal homogeneity is assumed and this is clearly not always correct. Spatial and temporal variations over the path maybe a major factor in explaining the differences between the observed and predicted path loss. However, our present modeling explains the 60dB signal enhancement above what one would expect under standard atmospheric conditions and seems to be a satisfactory first order approximation.

J. RICHTER (COMMENT)

In response to Professor Bach Andersen's question, horizontal inhomogeneity of ducting conditions along the path may certainly be one of the reasons for discrepancies between calculated and measured field strength values. Ducting parameters were measured only at one end of the propagation path and horizontal homogeneity was assumed along the path.

D. HÖHN

Are similar effects possible over land, under specific conditions, like melting snow, after rain, etc?

AUTHOR'S REPLY

In my opinion, it is unlikely to see similar effects over land. The surface would have to be relatively smooth over ranges of tens of kilometers and provide an unlimited moisture source.

REPORT ON STC/TECHNISCHE UNIVERSITEIT (TU) DELFT EXTREMELY HIGH FREQUENCY (EHF) RADIO RELAY STUDY

by

N.P. Mansfield
SHAPE Technical Centre
P.O. Box 174
2501 GA The Hague
The Netherlands

L.P. Ligthart, R.J. Niemeijer, J.S. van Sinttruyen
Delft University of Technology
Faculty of Electrical Engineering
Delft
The Netherlands

SUMMARY

Preliminary results of a joint Extremely High Frequency (EHF) radio relay trial between SHAPE Technical Centre (STC) and the Delft University of Technology (DUT) are presented. The trial was established to study the effects of meteorological disturbances, of which rain is the principle cause, on a digital radio relay path 12.7 km long operating at 37.5 GHz. Practical use for these radio relay links is found in local grade connections in an Integrated Services Digital Network (ISDN).

1. INTRODUCTION

A joint study between SHAPE Technical Centre, The Hague, and the Delft University of Technology was started in 1987, with the goal to investigate when and how often the micro-structures within rain cells disturb the CCITT performance objectives. Therefore a 12.7 km experimental radio relay link was established between DUT and FEL-TNO The Hague, operating at 37.5 GHz. The disturbances of the radio link were quantified by measuring the signal loss due to precipitation, in terms of bit error rate and signal attenuation, and the rate of precipitation at three points on the path. Measurements were carried out continuously until April 1988. From the data collected, some events were selected for further analysis. The remaining data consisted of 23,000 records.

The user service performance objectives for digital radio-relay systems to support ISDN are contained in a series of complementary CCITT and CCIR Recommendations. The CCITT has chosen to specify performance in Recommendation G.821 in terms of errored intervals (EI). However, since ISDN circuits mostly will be multiplexed on the transmission link, direct measurement of EI on the link is not likely to be representative for the channel performance. In digital radio systems the figure-of-merit traditionally is the bit error ratio (BER).

In this study the digital link is characterized on the basis of the CCITT Recommendation G.821. The error performance objectives for transmission links to establish local grade international ISDN connections are shown in Table 1. These objectives have been set under the condition that a BER of 10^{-6} just satisfies the quality specifications for reception, and a BER of 10^{-3} , measured per second intervals and lasting for at least 10 seconds, makes the connection unavailable. Dependent on error correction coding techniques, reliable reception can be maintained for a BER as high as 10^{-3} .

2. THEORETICAL CONSIDERATIONS

Above 300 MHz up to 10 GHz the main propagation aspects to be studied are the characterization of multipath propagation coming from:

- reflection at the earth's surface;
- refraction in a clear air layered troposphere;
- diffraction at obstructions like hills, buildings, etc.

Above 10 GHz the radio wave propagation studies in the troposphere are extended with investigations of:

- attenuation due to gas absorption effects;
- attenuation, scattering and depolarization by hydrometeors in the radio beam like snow, hail and melting particles.

By selection of the radio frequencies between the absorption lines, the corresponding attenuation can be minimized.

So far the hydrometeor scattering on a digital radio system is considered as a pure attenuator in the transfer function to characterize the path. No dispersion - due to scattering from distinct rain cells and their micro-structure, located within the Fresnel zone of the path - is assumed. For verification it is then sufficient to measure the attenuation statistics on the link together with a separate measurement of the received power level, in particular the BER, as function of the Carrier-to-Noise Ratio.

3. CONFIGURATION OF THE TRIAL

An assessment of NATO's current requirements showed that the primary interest was in short terrestrial transmission links 10-15 km long. The two sites selected for the trial were located at FEL-TNO The Hague (next to STC) and Delft UT, which are in line of sight and have a radio path of 12.7 km. The outline of the radio relay equipment characteristics are shown in Table 2.

The BER test blocks were transmitted outwardly from Delft UT to the FEL-TNO The Hague and then relayed inwardly back to Delft UT, where any errors detected were encountered. With a transmission rate of 5 Mbps and a block-length of 100 Mb, BER measurements were done in a 20 seconds interval using a Data Error Analyzer. Recording of DER only occurred if it exceeded 10^{-8} . The received power level then also was recorded by measuring the receiver AGC voltage, which had a linear relationship with the received power level. Rain rate measuring sites were selected such that there was one at each end close to the radio relay equipment and a third approximately midpath. The rain rate integration time was set to 20 seconds to be compatible with the BER measurements. A threshold collection value was set to 2 mm/hr, in order to avoid collecting an excessive amount of data and to avoid data on isolated bursts of only 2-3 normalized drops in a 20 second sample.

The gain margin of the equipment equals 157 dB and determines the maximum tolerable propagation path losses before the received power level reaches -68 dBm. This level refers to the r.f. power at the mixer input of the radio relay equipment for a BER of 10^{-8} and a transmission rate of 20 Mbps.

The clear air propagation losses along the path consist of free space loss and oxygen absorption. With a path length of 12.7 km and frequency of 37.5 GHz, the free space loss equals 146 dB. The oxygen absorption at 37.5 GHz lies between 0.06 and 0.07 dB/km [3], that is an additional loss of between 0.76 and 0.89 dB for the 12.7 km path. The total clear air loss then equals 146.9 dB.

The theoretical system margin is defined as the gain margin minus the total clear air propagation losses and hence equals 10.1 dB. This means that an additional loss of 10.1 dB along the path can be tolerated without introducing BER's greater than 10^{-8} . The excess attenuation due to rain is dependent on the structure of rainfall (size distribution, shape, canting angle, temperature and fall velocity of raindrops). In homogeneous rain the relationship between the attenuation coefficient and the rain intensity is given by:

$$\gamma = K R^\alpha$$

where γ = excess attenuation [dB/km]
 R = rain rate [mm/hr]
 K and α are frequency and polarization dependent.

Relevant values for K and α are shown in Table 3 as given in [3].

An assessment of the maximum tolerable homogeneous rain rate over a 12.7 km path is made by using averaged figures in Table 3 (frequency 37.5 GHz, polarization 45°) and the subsequent theoretical system margin:

$$\text{Maximum loss} = 10.1 \text{ dB} / 12.7 \text{ km} = 0.80 \text{ dB/km}$$

By inserting these values into $\gamma = K R^\alpha$ the maximum rain rate is approximately determined as:

$$R = 3 - 4 \text{ mm/hr}$$

Widespread or stratiform rain only occurs at very low rain rates, below about 2 mm/hr. Cumulative rainfall data available indicated that these conditions would exist for less than 0.1% of the year [3]. The theoretical calculations show that the link was likely to be unaffected by low rain rates unless the transmitter power was reduced to a minimum. The inward radio link from FEL-TNO The Hague to Delft UT was established in clear air conditions. The transmitter power at FEL-TNO The Hague was reduced such that the received power level at Delft UT was about -69 dBm. Hence, no errors occurred in clear air conditions, but the inward link would be sensitive to propagation path disturbances. The outward link from Delft UT to FEL-TNO The Hague was set to maximum power such that the inward link would collapse before bit errors were introduced on the outward link. Thus BER measurements could be considered to have taken place over the inward path only.

4. ANALYSIS OF TRIAL RESULTS

Initial analysis consisted of an assessment on how the medium attenuated the signal power. With the prior knowledge that significant attenuation of received signal power would take place during periods of intense rainfall between May to September a set of BER data measurements was selected for analysis. This sample contained over 23,000 records and was considered a statistical meaningful sample size. The mean and maximum deviation in BER versus received signal level are plotted in Fig.1 and are compared with the result of reducing the FEL-TNO The Hague relay transmitter power manually. The data collected contained power measurements in increments of 0.1 dB.

The received signal power attenuation for a BER of 10^{-8} versus the number of records was analyzed. The corresponding results for a BER of 10^{-9} were also made by extrapolating the results from Fig.1, that is a parallel line 5 dB lower. The results of this analysis are shown in Fig.2.

The cumulative distribution of error time was analyzed for a BER of 10^{-3} . This shows that, in this set-up with no power control, the maximum length of error was 30 blocks corresponding to 10 minutes. For 17% of the total errored time, errors were confined to single blocks corresponding to 20 seconds.

Initial analysis of the rain rate data collected, consisted of a quality assessment. Data collected at STC, Ypenburg and Delft for the period March 9 to September 4 was assessed individually and collectively. The cumulative distribution of point rain rate for each individual gauge is shown in Fig.3. The combined averages for all three gauges are shown in Fig.4. The results are consistent with only a small variation at the STC site due to its close proximity to the coast. The total rain observation time the rain rate exceeded 2 mm/hr was nearly 100 hours over a period of 148 days. This means that each point on the path was disturbed for about 2.8% of the total time.

5. CONCLUSIONS

The aim of the first phase of the trial was to derive general conclusions from a communications system engineering standpoint and to determine the method for the subsequent study. The general conclusions from a system engineering standpoint are as follows:

The relationship between BER and received power can be regarded as linear over the range of BER 10^{-8} to 10^{-5} . This makes it possible to simply couple the receiver power level to the BER in order to provide adaptive power control.

Overall link availability, for a BER of 10^{-8} and less than 5 dB attenuation, was found to be 99.5%. This means that with a link margin of 5 dB only the degraded minutes and errored seconds performance objectives for local grade international ISDN connections included in CCITT Recommendation G.821 (Table 1/G.821) would be fulfilled. This was considered to be significant during one of the worst summers on record (certainly worst month).

Long periods of rainfall at low rain rates had no effect on link availability, thus the effects of low rain rates on line of sight radio relay paths operating in the 37.5 GHz band may be disregarded from a communications standpoint.

A link margin of 5 dB would be unlikely to meet the severely errored seconds objectives for local grade international ISDN connections included in CCITT Recommendation G.821 (Table 1/G.821). Whether the objectives can be met by increasing the link margin or by coding requires further investigation.

Even at very low rain rates a rain cell structure can exist. It was concluded from this measurement campaign that low level rain rates were of no further interest.

At higher precipitation rates the rain forms cells. The nature of this phenomenon is such that it is unlikely that two cells will cross a communication path at the same time. This means that the excess attenuation is, to some extent, independent of link length. Thus the use of relays are unlikely to improve link availability.

6. ACKNOWLEDGMENT

The advice, support and technical assistance given by

At SHAPE Technical Centre

Mr. F.A.O. Eenhooorn
Mr. P.J. op den Brouw
Mr. W.K. Sakrova
Mr. W.J. Servaas

At Technische Universiteit Delft

Mr. C. van Dissel

are all gratefully acknowledged.

7. REFERENCES

1. L.P. Ligthart, J.S. van Sinttruyen, "FMCW Radar Remote Sensing of Hydrometeors", AGARD Conference Proceedings No. 419, 21-1, 21-15. Scattering and Propagation in Random Media, Rome, May 1987.
2. W. Klaassen, "Radar Observations and Simulation of the melting layer of precipitation", J. Atmos. Sci., Vol.45, No.24, December 1988.
3. F.Fedi, "Attenuation due to rain on a terrestrial path", Ann. des Telecomm., Vol.48, No.4, April 1979.

| Performance classification | Objective |
|----------------------------|--|
| Degraded minutes | Fewer than 0.4% of one minute intervals in any month to have a BER worse than 1.10^{-6} |
| Severely errored seconds | For local grade connections, fewer than 0.054% of one second intervals in any month to have a BER worse than 1.10^{-3} |
| Errored seconds | Fewer than 0.32% of one second intervals in any month to have any errors (equivalent to 92% error-free seconds) |

Table 1: Performance Objectives for local grade international ISDN connections.

| | |
|----------------------|--|
| Transmit frequencies | Station at DUT 37.66 GHz Station at FEL-TNO 37.43 GHz |
| Modulation | Analogue FM |
| Transmit Power | 100 mW (nominal) |
| Transmit losses | -1.4 dB |
| Polarization | Linear, 45 degrees orientation between vertical and horizontal |
| Antenna gain | 35 dB, 10.3 inch diameter lens assembly |
| Antenna beamwidth | 2.5 degrees |

Table 2: Outline of radio relay equipment characteristics.

| Frequency GHz | K | | α | |
|---------------|--------|--------|----------|--------|
| | H | V | H | V |
| 35 | 0.2629 | 0.2334 | 0.9789 | 0.9633 |
| 40 | 0.3495 | 0.3098 | 0.9391 | 0.9287 |

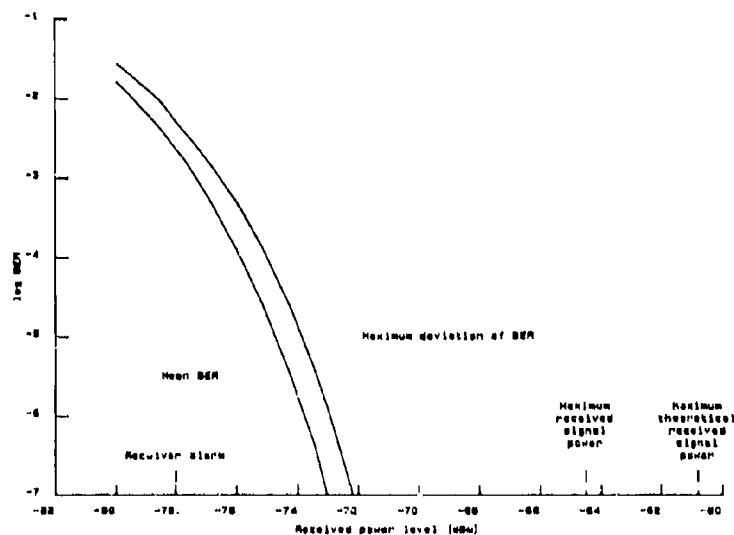
Table 3: Values for K and α for horizontal (H) and vertical (V) polarization.

Figure 1. Mean and maximum deviation in BER vs received signal level.

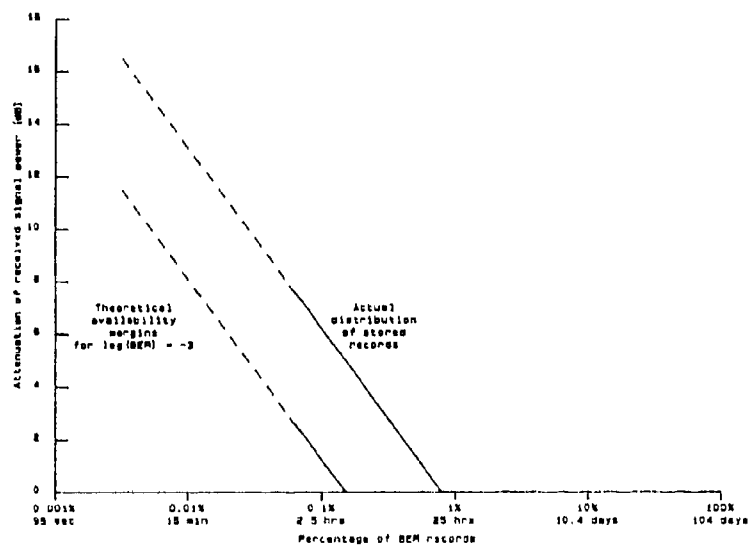


Figure 2. Distribution of BER records vs attenuation of received signal power.

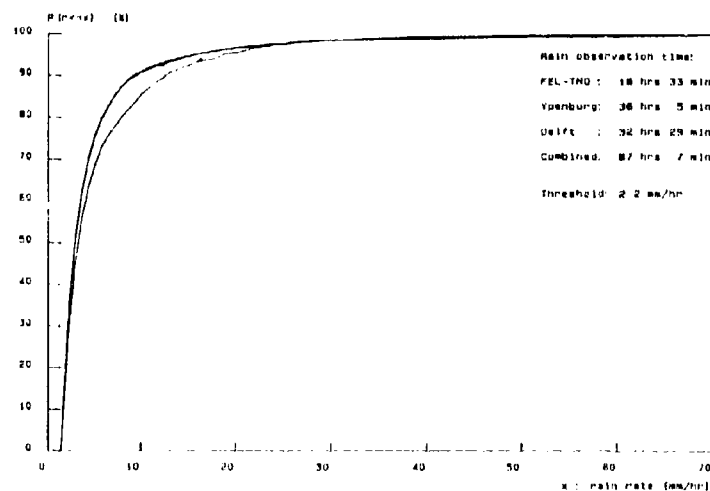


Figure 3. Cumulative distribution of point rain rate.

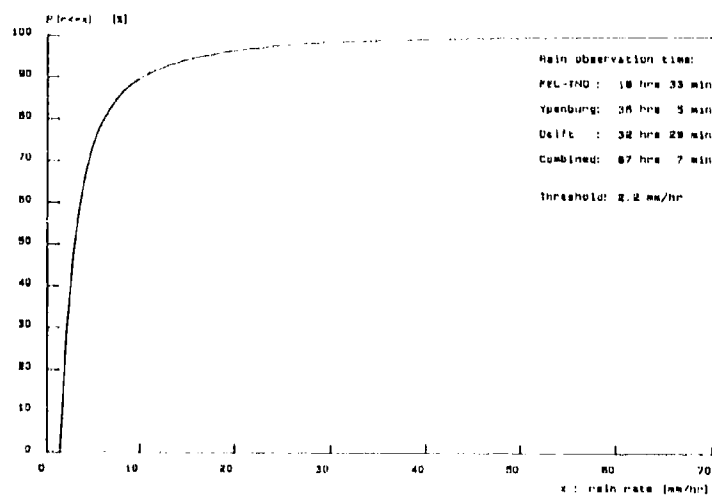


Figure 4. Combined cumulative distribution of rain rate.

DISCUSSION

C. GIBBINS

What kind of rain gauge did you use?

AUTHOR'S REPLY

Each gauge is comprised of a rain collector/drop counter, and a pulse shaping/integration unit. The rain was collected by means of a funnel and formed into drops of uniform size. These falling drops intersected an infrared light beam and were counted.

C. GOUTELARD

You envision the use of coding techniques to improve relay link performance. Considering the observed outage time, I think that you have to use very powerful codes like the FIRE codes, or even better, the KASAMI codes. Their decoding is complex and may be very expensive because of the speed you are using. Do you have any solutions in mind?

AUTHOR'S REPLY

Up to now we did not pay much attention to coding in very great detail. Depending on the costs involved for either increasing the transmitter power, coding or a combination of these, we hope to be able to reach a recommendation about the most cost-effective solution at the end of the second phase of the trial.

MM-WAVE REGION PROPAGATION EXPERIMENTS BY SATELLITE

PAOLO RICCI - ANTONIO FLORIO
Selenia Spazio - Italy
via Saccomuro, 24 - 00131 Roma

1 SUMMARY

This paper is aiming to the topics of the RF propagation experiments, related to the earth space communications by means of geostationary satellites, at frequencies exceeding the 30 GHz value, as lower limit of the mm-wave region.

The Selenia Spazio activity is outlined, as study, development and implementation, with reference to the on board payload and earth stations able to carry out the atmospheric propagation experiments associated with different satellites, for instance Olympus and Italsat.

Olympus system, at the time being in course of in-orbit tests after the launch, will have experiments at 20/30 GHz, just below the mm-wave band, and includes a 12.5 GHz beacon which will be used as reference to crosscorrelate the behaviors at different frequencies, to extend the measurement dynamics of the coherent receivers and as possible reference for antenna autotracking.

The next step will be with Italsat, the Italian satellite scheduled for the launch at the end of 90, allowing the first mm-wave propagation experiment for space communications at 40/50 GHz, across the outmost of the European zone; also in this case a third beacon at lower frequency (20 GHz) is foreseen as multipurpose reference.

Selenia Spazio, prime contractor of Italsat satellite, is involved in the design and development of the earth stations, which will be used to carry out the experiments over the Italian territory. Due to the performance margins and operating flexibility of these stations, their installation site can be situated over the European coverage zone as well.

The functional configuration of the earth stations is presented and the related propagation experiments are described in terms of performances and from an operational point of view. Copolar/crosspolar characteristics and scintillation phenomena are included.

The triple frequency configuration (20/40/50 GHz) and the use of radiometric and meteorological sensors, associated with the earth station, will give the opportunity to crosscorrelate the experiments results and to extend their dynamics capabilities.

Suitable calibration procedures and error corrections about the acquired data, to be recorded and processed, improve the measurements accuracy.

The propagation experiments results at 40/50 GHz will have interest both in the civilian and military fields, for instance for secure communications and countermeasures.

The use of higher frequency values, until and beyond 100 GHz, is envisaged in other study activities for atmospheric propagation experiments, referred to other satellites, for instance SAT2, and other stations, which could be derived from the Italsat ones, with similar architecture: in this case the triple frequency configuration at 45/90/135 GHz is considered.

The mm-wave propagation experiments results can provide suitable guidelines for link design optimization and to identify the opportunity of using frequency/polarization/site diversity configurations in the different communication scenarios.

2 THE 30 GHz LIMIT: THE STEP FROM OLYMPUS TO ITALSAT

In the near future advanced satellites, such as Olympus, Italsat and Acts, will be operating on an experimental/preoperational basis.

The high frequencies involved, together with the sophisticated technics employed by these satellite communication systems, require reliable information data on signal loss, depolarization and any other signal impairment introduced by the radiowaves propagation through the earth's atmosphere.

The Olympus propagation experiment allows accurate measurements of the following characteristics:

- absolute attenuation of vertically polarized signals at 12.5 and 30 GHz, and of vertically and horizontally polarized signals at 20 GHz;
- differential attenuation and phase between vertical and horizontal polarizations at 20 GHz;
- amplitude and phase cross-polarization discrimination at 12.5, 20 and 30 GHz.

Also the instantaneous or fast variations of the signals to be measured (scintillation and fade rates) will be of interest for many reasons, for instance automatic level control definition, reacquisition characteristics and performance evaluation of various types of tracking systems employed in the ground stations antennas.

These basic data gathered at different sites for long time periods, together with radiometer clear sky temperature and meteorologic measurements, will be a unique source of information for a better understanding of the behavior of electromagnetic waves at 12.5, 20 and 30 GHz travelling across the earth's atmosphere.

Propagation data gathered from previous experiments have shown that, in order to obtain statistically meaningful results, at least five years of measurements and data analysis are required. It is also expected that several 20/30 GHz communication systems will be operative before the end of this century, even considering that the realization and launching of a new satellite needs six years of time or something like this.

On the basis of these considerations, one can think that, while on the one hand the Olympus propagation experiment might have little time margins compared to the scheduling of the above mentioned next generation 20/30 GHz systems, on the other hand it is time to start experimenting with frequencies higher than those generated by the Olympus propagation payload.

For the reasons the Italian National Space Plan comprised, since the early eighties, a European coverage propagation payload at 40/50 GHz with a third reference beacon at 20 GHz, to be embarked on board the Italsat satellite, scheduled to be launched within the next year.

The measurements which can be performed at 20, 40 and 50 GHz, using the Italsat propagation payload, are similar to those outlined above for Olympus at 12.5, 20 and 30 GHz; in the case of Italsat the beacon switched in polarization between vertical and horizontal is that at 50 GHz (for Olympus is that at 20 GHz).

Moreover the beacon at 40 GHz is circularly polarized and there is the possibility to measure amplitude and phase distortions suffered by this signal over a frequency band of 1 GHz.

3 PROPAGATION ACTIVITIES IN SELENIA SPAZIO

In the frame of propagation activities for satellite communications, Selenia Spazio is involved in the design and implementation of on board payload equipment and related ground stations, for different frequency bands above 20 GHz, corresponding to various programs.

The main activities are referred to the Olympus and Italsat geostationary satellites, positioned in longitude at 19°W and 13°E respectively, each one transmitting three beacon signals B0, B1, B2 (see table 3.1) coherent in frequency, being originated by a common master oscillator.

TABLE 3.1

BEACON FREQUENCIES OF OLYMPUS, ITALSAT AND SAT2 SYSTEMS

| | BEACON B0 | BEACON B1 | BEACON B2 |
|---------|------------|-----------------|-----------------|
| OLYMPUS | 12.502 GHz | 19.770 GHz * | 29.656 GHz |
| ITALSAT | 18.685 GHz | 39.592 GHz | 49.490 GHz * |
| SAT 2 | 44.58 GHz | 89.16 GHz * | 133.74 GHz |

* INDICATES THE BEACON SWITCHED IN POLARIZATION

Selenia Spazio is carrying out the development/implementation of Olympus and Italsat propagation earth stations, which will be used by the national group of Italian Experimenters (CSELT, CSTS, FUB, ISPT, SIP, TELESPIAZIO).

Three types of propagation station are involved: first one is the main station for Olympus, able to receive all the three relative beacons and detect copolar and x-polar signals, as in phase and quadrature components (the antenna aperture diameter is 3.5 m); second type is the main station for Italsat, similar to that of Olympus from a functional point of view, but of course at different frequencies; third type is a small station for Olympus, with antenna aperture diameter of 1.5 m, able to receive and detect only the B1 beacon at about 20 GHz, as copolar amplitude for a single polarization plane.

Moreover the small station is capable also to be pointed (as antenna boresight) toward Italsat satellite and to be tuned on its first beacon B0 at about 19 GHz, as possible operative reconfiguration.

A first contract, already awarded to Selenia Spazio since the middle of '88, is funded by the National Council of Researches and the new Italian Space Agency, and has as object the development and realization of two main stations, one for Olympus and the other for Italsat, to be installed near Milan.

A second contract, since the middle of '89, is funded by the National Agency for Telephone services (ASST), and has as object the provision of four main stations, two for Olympus and two for Italsat, to be installed in Rome and Turin (as pair Olympus + Italsat). This second contract includes also the realization of 25 small stations, two radiometers at 13 GHz, three radiometers in dual band 20/30 GHz (one of which transportable) and meteorological sensors.

The 25 small stations will be located all over the Italian territory, to investigate the propagation behavior in each region and the possible space diversity characteristics.

As extension, a 20/30 GHz communication experiment in space diversity will be performed, through Olympus satellite, by means of one station in Lario and two stations in Rome, being these stations derived from those dedicated to communication service or test (fixed or transportable type).

By using the main propagation stations, auxiliary or small stations, radiometers and meteorological sensors, there will be the possibility to collect propagation data at different frequencies, different polarizations, different site locations and to properly correlate the propagation data with the associated radiometric and meteo data, in order to get a complete experiment data base for the subsequent statistical analysis and processing.

Another preparatory involvement of Selenia Spazio is the design configuration study for higher frequency propagation, up to 100 GHz and beyond, for instance with reference to the SATZ satellite, using three beacons at about 45, 90 and 135 GHz (see table 3.1).

4 CHARACTERIZATION OF THE ITALSAT PROPAGATION PAYLOAD (20/40/50 GHz)

The propagation payload configuration, of Italsat satellite, is shown in Fig. 4.1; it is constituted by three transmitters, each with its own antenna, operating at 20 GHz, 40 GHz and 50 GHz respectively (redundancy details are not shown).

The 20 GHz beacon antenna is shared with the global coverage 20/30 GHz payload.

The three beacon frequencies are coherent each other, being derived by multiplication from a common master crystal oscillator.

The Italsat propagation payload shown in Fig. 4.1 has a configuration derived from the SIRIO experiments results.

As far SIRIO (12/18 GHz) is concerned, in fact beacon signals are generated on the ground station so that some control of the modulation and transmission parameters could be useful for measurement algorithm tuning during the experiment phase.

The subsequent experiments foreseen with Olympus (12/20/30 GHz) and Italsat (20/40/50 GHz) are designed for satellite generated beacons derived from a single common oscillator.

In particular the Italsat propagation payload includes both the polarization switch at 50 GHz and the modulation of the 40 GHz circularly polarized beacon, to carry out amplitude, phase, and polarization measurements.

The characteristics of Italsat beacons are provided in table 4.1.

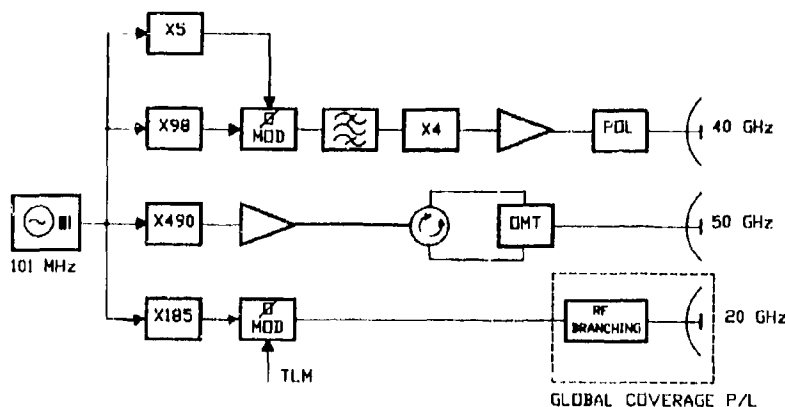


FIG. 4.1 - BLOCK DIAGRAM OF THE ITALSAT PROPAGATION PAYLOAD

TABLE 4.1
CHARACTERISTICS OF ITALSAT BEACONS

| BEACON | FREQ. (GHz) | POLARIZATION | EIRP (dBW) | MODULATION | FREQUENCY STABILITY |
|--------|-------------|---------------------------|------------|---|---|
| B0 | 18.685 | V | 20 | Phase modulation M=1RAD TLM subcarrier at 65.536 KHz | ± 0.3 PPM on 24 hrs ± 4 ppm on 5 years |
| B1 | 39.592 | Circular (RHCP) | 27.8 | Phase modulation, M=1RAD fm = 505 MHz | |
| B2 | 49.490 | V/H switched at 933 Hz | 25 | — | |

The V (vertical) polarization plane is received on ground tilted by 20° eastward with respect to the meridian plane passing through Rome.

The H (horizontal) polarization plane is orthogonal to the V plane.

B2 beacon at 50 GHz has a polarization plane switching continuously between V and H, at a rate of 933 Hz.

The Bo beacon (20 GHz) on ground coverage is corresponding to the Italian territory global coverage.

The 40/50 GHz propagation experiment has an european coverage as depicted in Fig. 4.2, with half-power beamwidth of 3 degrees and boresight intersection in the point 47° N of latitude/10°E of longitude, being the satellite positioned at 13°E of longitude along the geostationary orbit.

Phase jitter for each beacon is limited within 0.15 radians RMS, when measured by a PLL receiver with 50 Hz bandwidth. The polarization isolation is better than 30 dB through the service coverage.

The Bo beacon at 20 GHz will be operated continuously. B1 and B2 beacons, at 40 and 50 GHz, will be operated continuously, excluding the eclipse periods.

Bo beacon provides the tracking reference for TT&C and communication earth stations, besides to be used for propagation measurements.

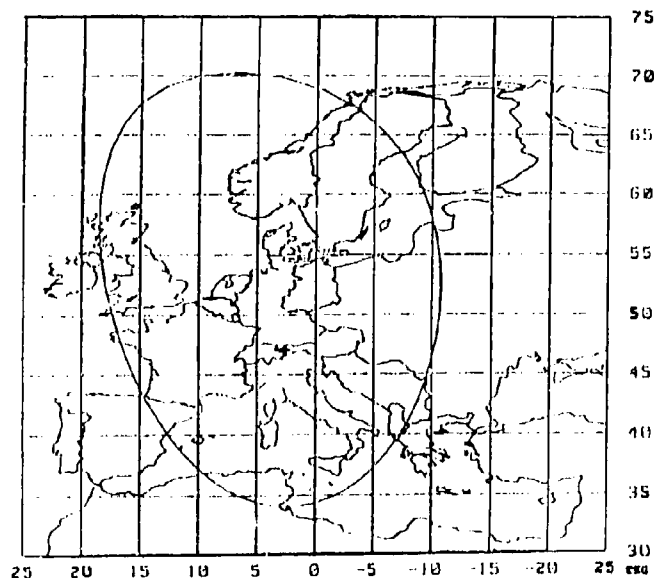


FIG. 4.2 EUROPEAN COVERAGE FOR 40/50 GHz EXPERIMENT

5 ITALSAT PROPAGATION EARTH STATIONS

5.1 Technical Description

The Italsat propagation experiment earth station have a very similar architecture of the Olympus propagation station.

The main station for the Italsat is composed of six different subsystems:

- Antenna and tracking
- RF Front End
- Conversion Chains
- Measurement and control
- Data Acquisition
- Station Auxiliary Equipment

In the first subsystem, the antenna feed is divided in the dual band feed at 40/50 GHz and the 20 GHz feed with monopulse.

The earth station simplified layout of Fig. 5.1 evidences the housing of the different equipment, distributed in three sections, namely the antenna base, the shelter and the equipment room.

First location (outdoor) houses the antenna with its structure and angular pointing mechanical devices, all RF parts with associated analog circuits, including also the A/D conversion and digital detection circuits. The equipment room houses the Data Acquisition S/S with its computer and associated peripherals. The antenna control unit and motors power unit are located into the shelter.

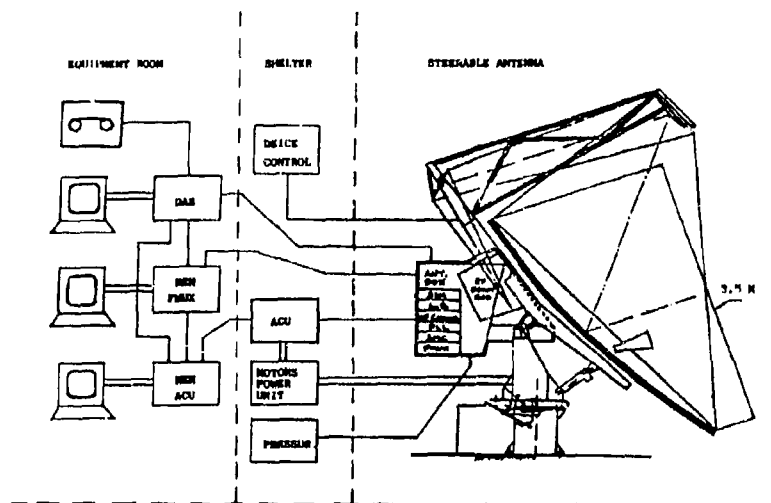


FIG. 5.1 MAIN PROPAGATION STATION SUMMARY LAYOUT

As shown in the general block diagram of Fig. 5.2, the antenna feed provides copolar and crosspolar signals, for the three beacons, to the three corresponding receiving channels; another dual output is that of Delta-AZ and delta-EL, at the same frequency of the 80 beacon.

Each dual chain receiving channel is equipped with RF and IF switching network, multiplexing on each of the two chains both copolar and x-polar signals, while avoiding any loss on the C/N₀ ratio; in this way we can minimize the effect of the possible chains mismatching on the XPD measurement accuracy. The intrinsic redundancy of the dual chains can be exploited for possible reconfigurations.

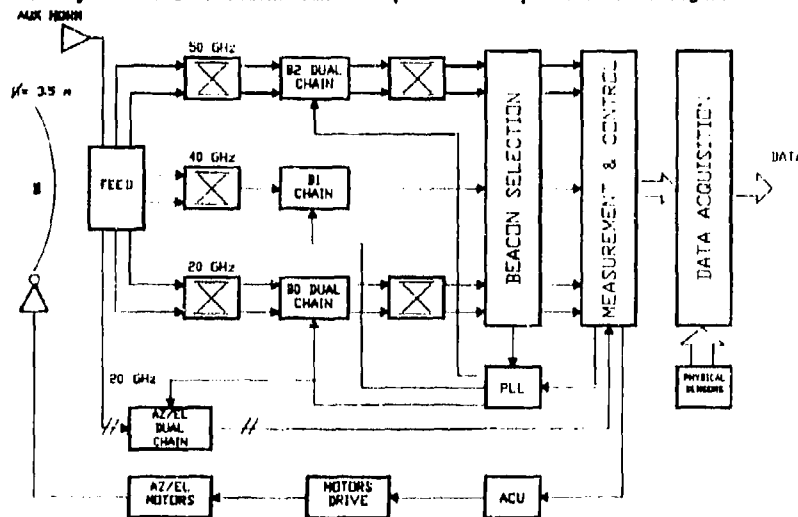


FIG. 5.2 - FUNCTIONAL BLOCK DIAGRAM OF ITALSAT PROPAGATION STATION

The 40 GHz chain, for B1 beacon in circular polarization and with ± 505 MHz sidetones modulation, is a single chain, for sake of simplicity and cost reduction: copolar and xpolar signals are time multiplexed into the same RX chain, without any mismatching but accepting the corresponding multiplexing loss.

The beacon receivers can be locked to any one of the three beacons, by means of a suitable switch on the copolar signals, due to the coherent configuration of the local oscillators and conversion chains. Antenna is of the offset cassegrain type, with aperture diameter of 3.5 m and multiband feed, including the monopulse sensor at 20 GHz for autotracking (see Fig. 5.3). The multiband feed is composed of a central horn at 40/50 GHz and an array of peripheral horns at 20 GHz, which are used for the B0 beacon receive and for the 20 GHz monopulse sensor.

The feed network provides copolar and x-polar outputs for each beacon and includes rotating polarizers, to meet the needs of polarization alignment, depending on the site location. A calibration horn at 50 GHz, with high polarization purity, is provided, in order to measure in clear sky and compensate the x-polarization residual, induced by the satellite antenna or other effects. After the LNA amplification, each beacon signal is down converted, in a multiple conversion chain, to 25 KHz.

The conversion chain architecture, represented in Fig. 5.4 for the beacons at 20 and 40 GHz, and in Fig. 5.5 for the beacon at 50 GHz, permits to minimize the inherent receiver phase jitter so allowing very accurate phase and amplitude measurements.

The choice of a so small value (25 KHz) for the last IF frequency is determined by two main reasons:

- simplicity of implementation of a small predetection bandwidth, proportioned with the PLL noise bandwidth 2 BL of about 100 Hz;
- to limit the sampling frequency, of the last IF signals, at 100 KHz, in the A/D converters of the Measurement and control S/S (SMC).

Last IF signal at 25 KHz is sent to the SMC S/S, which provides the A/D conversion, the digital coherent detection (in phase and in quadrature components) and post-detection digital filtering of the propagation data.

An antisideband capability is foreseen against possible false locks on the sidetones at 933 Hz far from the carrier for the 50 GHz beacon (B2) switched in polarization, and at 65.6 KHz far from the carrier for the 20 GHz beacon (B0) modulated by the TLM subcarrier.

The data processed by SMC S/S, together with radiometric and meteo-sensors outputs, are provided to the Data Acquisition S/S, which performs the data recording, errors correction and preparation for the successive statistical analysis.

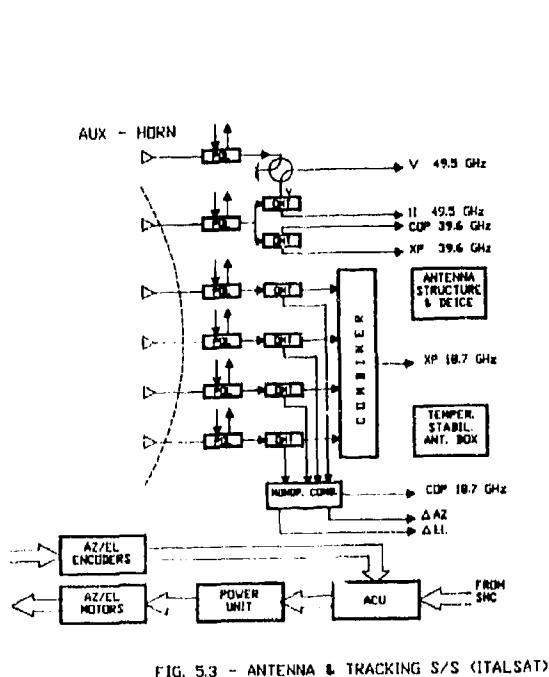
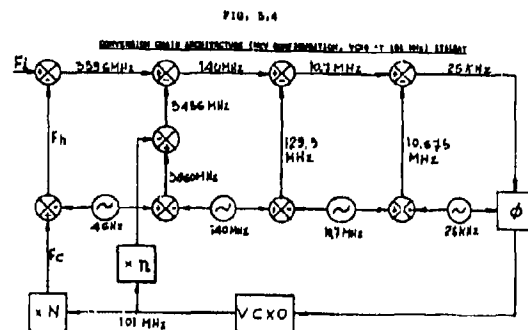
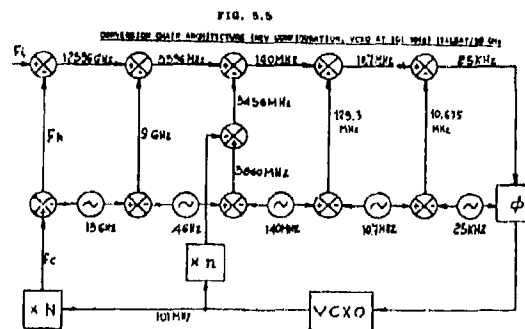


FIG. 5.3 - ANTENNA & TRACKING S/S (ITALSAT)



$$F_h = \begin{pmatrix} 10.000 \text{ GHz} \\ 20.500 \end{pmatrix} \quad F_c = \begin{pmatrix} 10.000 \text{ GHz} \\ 20.500 \end{pmatrix} \quad F_{101} = \begin{pmatrix} 100 \text{ (21) } \times 0.1 \\ 100 \text{ (11) } \times 0.1 \end{pmatrix} \quad F_{25} = \begin{pmatrix} 10.000 \text{ GHz} \\ 20.500 \end{pmatrix}$$



$$F_h = 17.500 \text{ GHz} \quad F_c = 10.000 \text{ GHz} \quad F_{101} = 100 \times 10^{-3} \times 24 \quad F_{25} = 25 \times 10^{-3} \text{ GHz}$$

5.2 PERFORMANCES CHARACTERISTICS

Table 5.1 reports a summary of performances characteristics relevant to the Italsat propagation station, which are depending on the beacon frequency.

The antenna parameters, in terms of gain and HPBW, are relevant to a circular aperture diameter of 3.5 m. The overall RX noise figure includes the insertion loss of the RF switching network preceding the LNA. The system G/T and C/N₀ values are referred to an antenna noise temperature of 290°K, as in bad weather, so that the corresponding fade margin values are completely available, as fading attenuation dynamic range, measurable on the same beacon used for lock reference (see link budget in Table 5.2).

In the coherent receiver, a PLL noise bandwidth, double sided, of 100 Hz is used.

Other station characteristics, common to the three beacons, are resumed in table 5.3; in particular the antenna available steering ranges, for the polarization alignment, Az and El pointing, allow a station site location not only anywhere in Italy, but also in the outmost of Europe.

Moreover the antenna is equipped with a heating device, able to avoid the deposit of water or the cumulation of ice or snow on the reflecting surfaces, up to a max snow falling rate of 50 mm/h. The overall station power consumption is 10.9 KW without deice and 20.9 KW with operating deice.

TABLE 5.1
ITALSAT PROPAGATION STATION CHARACTERISTICS SUMMARY

| | | | |
|---|------|------|--------------|
| BEACON FREQUENCY (GHz) | 18.7 | 39.6 | 49.5 |
| POLARIZATION | V | RHCP | V/H SWITCHED |
| ANTENNA GAIN (dB) | 54.7 | 60.9 | 61.9 |
| OVERALL RX NOISE FIGURE (dB) | 5.1 | 5.8 | 8.5 |
| ANTENNA HPBW (DEG.) | 0.30 | 0.14 | 0.11 |
| ANTENNA TRACK. ERROR AT 1 σ (% OF HPBW) | 4.3 | 9.3 | 11.8 |
| SYSTEM G/T (dB °K) | 25 | 30.4 | 28.6 |
| NOMINAL AVAIL. C/NO (dB Hz) | 60.2 | 60.6 | 58.1 |
| SYSTEM FADE MARGIN FOR PLL BW = 100 Hz (dB) | 32.9 | 33.0 | 30.1 |

TABLE 5.2
ITALSAT PROPAGATION LINK BUDGET IN TRACKING

| BEACON | B0 | B1 | B2 (+) | B2 (++) | UNIT |
|----------------------------------|--------|--------|--------|---------|---------|
| 1. FREQUENCY | 18.68 | 39.6 | 49.49 | 49.49 | GHz |
| 2. EIRP (SAT.) | 20.0 | 27.8 | 25.0 | 25.0 | dBW |
| 3. SPACE LOSS | 209.5 | 216.0 | 217.9 | 217.9 | dB |
| 4. ATTENUATION OF ATMOSPHERE | 0.9 | 1.2 | 3.2 | 3.2 | dB |
| 5. POINTING LOSS | 0.0 | 0.1 | 0.2 | 0.2 | dB |
| 6. G/T (STATION) | 25.0 | 30.4 | 28.6 | 28.6 | dB/ K |
| 7. BOLTZMANN CONSTANT | -228.6 | -228.6 | -228.6 | -228.6 | dB/Hz K |
| 8. SWITCHING AND MODUL. LOSS | 3.0 | 9.0 | 3.0 | NA | dB |
| 9. C/NO AVAIL. | 60.2 | 60.6 | 58.1 | 61.1 | dBHz |
| 10. PLL NOISE BANDWIDTH | 20.0 | 20.0 | 20.0 | 20.0 | dBHz |
| 11. PLL THRESHOLD | 7.0 | 7.0 | 7.0 | 7.0 | dB |
| 12. DEGRADAT. DUE TO PHASE NOISE | 0.3 | 0.6 | 1.0 | 1.0 | dB |
| 13. MARGIN (FADE) | 32.9 | 33.0 | 30.1 | 33.1 | dB |

NOTES:

(+) BEACON SWITCHED IN POLARIZATION AT 933 Hz

(++) BEACON WITHOUT POLARIZATION SWITCHING

TABLE 5.3
OTHER MAIN STATION CHARACTERISTICS (ITALSAT)

| | |
|---|------------------|
| - BEACON SELECTION FOR PLL REFERENCE | |
| - ANTISIDEBAND CAPABILITY | |
| - HIGH AMPLITUDE AND PHASE ACCURACY/STABILITY, THROUGH TIGHT THERMAL CONDITIONING, AND COMPENSATION/CALIBRATION DEVICES | |
| - RX CHAINS AMPLITUDE NONLINEARITY OVER A DYNAMICS OF +10/-50dB | ≤ 0.1 dB |
| - ANTENNA XPD | ≥ 30 dB |
| - POLARIZATION ALIGNMENT RANGE | $\pm 20^\circ$ |
| - ANTENNA AUTOTRACKING | |
| - ANTENNA STEERING IN AZ | $\pm 90^\circ$ |
| - ANTENNA STEERING IN EL | $1 \pm 60^\circ$ |
| - LOCK-IN THRESHOLD, AS C/N IN PLL BW = 100 Hz | ≤ 7 dB |
| - THRESHOLD DEGRADATION DUE TO PHASE NOISE | ≤ 1 dB |
| - MINIMIZATION OF ACQUISITION/REACQUIS. TIME | |
| - TAPE UNIT MEMORY CAPACITY | 40 MBYTES |
| - TOTAL TAPE DUTY CYCLE | 6 DAYS |
| - OVERALL STATION MASS | 4.9 TONS |
| - OVERALL STATION POWER CONS. | 10.9/20.9 KW |

5.3 OPERATING MODES

Italsat propagation station has five operating modes, as indicated in the flow diagram of Fig. 5.6. In stand-by, alarm and calibration modes, the acquisition of data can be operating, but the acquired data are not considered valid, as far the propagation experiment is concerned. In stand-by mode, the station is on, accepting manual commands for the determination of its configuration, to be used in data acquisition modes or in calibration mode.

For the data acquisition modes it is possible to set the selection of the lock on beacon B0, or beacon B1, or beacon B2, the RF and IF switch matrices operating conditions, the redundancy configuration, the antenna pointing in stand-by and so on. Data acquisition modes are divided in normal mode, with all channels/chains normally operating, and back up mode (following a failure of the satellite or station), which in turn can be subdivided in partial data acquisition or degraded data acquisition operation, with different station configurations, depending on the type of failure and consequent recovery action.

Alarm mode arises whenever there is a satellite beacon(s) failure, or very deep fade, or station failure; it includes also the transient phases related to the beacon frequency and antenna tracking acquisition.

Depending on the type of alarm, the station can return to the data acquisition modes either in automatic way (at the end of alarm condition, or by possible reconfigurations), or manually through the stand-by mode.

Calibration mode is constituted by two off-line operations: antenna calibration and RX chains calibration, performed in general by means of manual commands.

Antenna calibration is performed in condition of clear sky, about every month (following the experimenter choice), with the duration of one day; during the antenna calibration, it is possible to use a reference auxiliary horn, for what concerns the X-polarization error. RX chains calibration can be performed in any weather condition, with a duration of about 1.5 hours, by disconnecting the antenna and injecting the signal of a built-in calibrated satellite simulator into the RF Front End; the repetition time of RX chains calibration is about three days.

All parameters measured and recorded during the calibration mode are properly processed, in order to prepare and provide the correction data, to be used during the acquisition modes for the on-line errors correction.

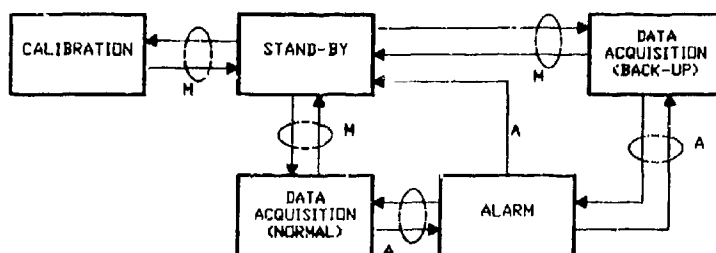


FIG. 5.6 - FLOW DIAGRAM OF PROPAGATION STATION OPERATIVE MODES

6 A FURTHER STEP UP TO 100 GHz AND ABOVE

Pushing the frequency to higher values than those of Italsat, a new step is envisaged in the SAT2 project, in the field of atmospheric propagation experiments (see Table 3.1 for the related beacon frequencies).

The main characteristics of the on board payload are the following:

- three coherent beacon frequencies at about 44.5, 89 and 133.5 GHz (Bo, B1 and B2);
- linear polarization for Bo and B2 beacons; polarization switched between the two orthogonal linear components for beacon B1;
- european coverage with half power beamwidth of 2.8° and boresight intersection in the point 47°N of latitude/75°E of longitude, being the satellite positioned at 7.5°E of longitude along the geostationary arc.

For what concerns the receiving station, it can be derived from the Italsat one.

The modifications on the Italsat station to adapt its characteristics for propagation at 44.5/89/133.5 GHz consist mainly in a new development of the antenna, with an aperture diameter probably in the range 1 to 1.5 meters, the use of suitable low noise devices for the RF Front End and suitable frequency generation circuits for local oscillators.

In particular at 44.5 GHz a LNA with noise figure of 5 dB about could be envisaged, using HEMT devices, whereas at 89 and 133.5 GHz it is probably preferable a solution with direct input mixer, followed by LNA at lower frequency.

Minor modifications could be addressed to the analog receiving section at frequency lower than 4 GHz and to the digital section; for instance, a PLL double sided noise bandwidth of 150 Hz should be defined instead of the 100 Hz of Italsat, to cope with the expected phase noise spectrum.

7 CONCLUSION

The propagation experiments using the Olympus and Italsat payloads are the continuation of previous programs, intended for preparing the implementation of future communication systems in new Extremely High Frequency Bands.

These experiments appear to be properly phased with the planning for Satellite Communication Systems both for Military and Civilian Applications which are expected to come in operations in the next decade and after.

The measurements will require some few years for reliable data gathering and will provide to the System Designers valuable data for link performance predictions.

DISCUSSION

G. HAGM

It would be potentially useful to correlate meteorological satellite data on clouds with the measured channel distortion in the 1 GHz bandwidth for the satellite-to-ground path. If high correlations are observed, then meteorological satellite data can be used to predict distortion on satellite paths which are not so well instrumented as the ones you have described. Do you plan to compare meteorological satellite cloud data with your measured distortion data?

AUTHOR'S REPLY

At the moment this is not considered (only local meteorological sensors are foreseen). The suggestion appears, however, very interesting and should be considered for implementation. This would be, however, contingent upon cooperation among the various participants in the experiments. As an example, the data gathered by the various stations should be available and compatible for subsequent common processing with meteorological satellite maps.

G. HAGM

Can you comment on how you selected 5 years as the duration of the experiment over which you will gather the propagation statistics.

AUTHOR'S REPLY

The stringent continuity of service requirements for operational systems require reliable propagation statistics; therefore, multiple year experimental data are needed. The 5 year duration for these experiments is derived from other investigations where significant differences of propagation statistics have been observed each year.

LOWTRAN 7: Status, Review, and Impact for Short-to-Long-Wavelength Infrared Applications

F. X. Kneizys, G. P. Anderson, E. P. Shettle,
L. W. Abreu, J. H. Chetwynd, Jr.
Air Force Geophysics Laboratory/OPE
Hanscom AFB, MA 01731, USA

J. E. A. Selby
Grumman Corporate Research Center, Bethpage, NY 11714-3580, USA

W. O. Gallery
Optimetrix, Inc., Bedford, MA 01730, USA

S. A. Clough
AER Associates, Cambridge, MA 02139, USA

SUMMARY

A summary of the recent improvements, modifications, and updates to the LOWTRAN 7 atmospheric transmittance and radiance computer program will be given.

There have been some significant changes to the LOWTRAN model in the latest version, LOWTRAN 7,^{1,2} that affect the manner in which the basic atmospheric transmittance and radiance calculations are performed as well as providing the user with greater flexibility and more capabilities. The LOWTRAN 7 code now calculates atmospheric transmittance, atmospheric background radiance, single-scattered and earth-reflected solar and lunar radiance, direct solar irradiance, and multiple-scattered solar and thermal radiance. The spectral range of the code has been extended from 0 to 50,000 cm^{-1} (i.e., 0.2 μm to infinity) at a spectral resolution of 20 cm^{-1} . The program can cope with any observer/target geometry and can include the effects of molecular, aerosol, fog, rain, and cloud absorption and scattering. Some of the basic changes to LOWTRAN 7--in particular the introduction of new molecular absorption transmission functions and separating the transmittances due to CO_2 , N_2O , CO, CH_4 and O_2 (previously assumed to have a combined effect)--will give rise to differences in the transmittance and radiance calculations (compared to those obtained with LOWTRAN 6) depending on the observer/target viewing geometry and spectral region.

The dual purpose of this paper is to indicate how the new changes to LOWTRAN 7 affect atmospheric transmittance and background radiance calculations for specific applications. We will concentrate on both high-altitude, long-range and low-altitude, moderate-range scenarios and will show the impact that the recent changes to LOWTRAN 7 have made on the short, medium, and long wavelength infrared atmospheric attenuation and background radiance, compared to calculations with LOWTRAN 6.

1. INTRODUCTION

Since its conception, the LOWTRAN computer program has been used widely by workers in many fields of atmosphere-related science, first as a tool for predicting atmospheric transmissions (LOWTRAN 2³, LOWTRAN 3⁴, and LOWTRAN 3B⁵) and later for atmospheric background radiance and transmittance calculations (LOWTRAN 4⁶, LOWTRAN 5⁷, and LOWTRAN 6⁸) for any given geometry from 0.25 μm to 28.5 μm (i.e., from 350 to 40,000 cm^{-1}). The latest version of the computer code, LOWTRAN 7, version 3.6, was released in February of this year. With LOWTRAN 7, the wavelength range has now been expanded to cover from 0.2 μm in the ultraviolet to the millimeter wave region (0-50,000 cm^{-1}). The computer program was designed as a simple and flexible band model that will allow fast, reasonably accurate, low-resolution atmospheric transmittance and radiance calculations to be made over broad regions of the spectrum for any required atmospheric path geometry. LOWTRAN 7 includes all of the important physical mechanisms (with the exception of turbulence) that affect atmospheric propagation and radiance. LOWTRAN has proved valuable for the development and evaluation of many optical systems working in ultraviolet, visible, and infrared parts of the spectrum, and the latest version of the program, LOWTRAN 7, now provides even more capabilities to the user.

We will briefly review the status and capabilities of LOWTRAN 7 and go on to show the effects these changes have on atmospheric transmission and radiance calculations (compared to those of LOWTRAN 6) for different scenarios in the ultraviolet, visible, 3-5 μm , and 8-14 μm regions.

2. FUNDAMENTALS OF LOWTRAN 7

The LOWTRAN 7 computer program allows the user to calculate the atmospheric transmittance, atmospheric background thermal radiance, single-scattered and earth-reflected solar and lunar radiance, direct solar irradiance, and multiple-scattered solar and thermal radiance at a spectral resolution of 20 cm^{-1} in steps of 5 cm^{-1} from 0 to 50,000 cm^{-1} ; i.e., for wavelengths in excess of 0.2 μm . The total atmospheric transmittance is treated as the product of the individual transmittances due to:

1. molecular absorption
2. molecular scattering
3. aerosol, fog, rain, and cloud extinction (scattering and absorption).

The transmittance due to molecular absorption is further subdivided into more components and is now calculated as the product of the separate transmittances due to:

1. H_2O , O_3 , CO_2 , N_2O , CO , CH_4 , O_2 , NO , NO_2 , NH_3 , SO_2 , HNO_3
2. H_2O continuum (over the entire spectrum)
3. N_2 continuum (in the 2000-2700 cm^{-1} region).

A selection of atmospheric aerosol models is given in LOWTRAN 7; these are divided into altitude regions corresponding to the boundary layer (0-2 km), troposphere (2-10 km), stratosphere and upper atmosphere (10-120 km). The boundary layer models include Rural, Urban, Maritime, tropospheric, a Navy Maritime, and a desert aerosol. Representative aerosol models also are included for the troposphere and upper atmospheric regions. Two fog models are included together with a selection of rain and cloud models. The user also has the option to substitute other aerosol models or measured values.

The six reference atmospheric geographical and seasonal models for tropical, midlatitude summer and winter, subarctic summer and winter, and the U.S. Standard Atmosphere, which provided temperature, pressure, and H_2O , and O_3 concentrations as a function of altitude from 0 to 100 km in LOWTRAN 6, have now been extended in LOWTRAN 7 to include density and N_2O , CO , and CH_4 mixing ratio variability with altitude.^{9,10,32} The remaining six molecular species are each described by a single vertical profile. When adding meteorological data to LOWTRAN 7, the user is given much greater flexibility in the choice of units that will be accepted by the program. Spherical earth geometry is assumed, and refraction and earth curvature effects are included in the atmospheric slant path calculations.

3. NEW FEATURES IN LOWTRAN 7

Some examples of the important additions and modifications to LOWTRAN will be discussed here. All of the previous capabilities and user options contained in LOWTRAN 6 have been retained.

A broader spectral coverage (0-50,000 cm^{-1}) is now possible with LOWTRAN 7 after the extension of the various molecular, aerosol, and hydrometeor spectral absorption and scattering models to shorter wavelengths in the UV and higher wavelengths in the IR and millimeter wave regions. Two examples of this are given in Figs. 1 and 2. Figure 1 shows the transmittance from 10 km altitude to space (zenith viewing) plotted on a logarithmic wavelength scale from 0.2 μm to 1000 μm . It can be seen from Fig. 1 that relatively high atmospheric transmittances are possible at the far infrared wavelengths for atmospheric path geometries that lie above most of the water vapor contained in the earth's troposphere. At sea level the picture is quite different and, as can be seen in Fig. 2, far infrared radiation is propagated only over very short distances.

The 20 cm^{-1} spectral resolution, chosen for LOWTRAN from its conception, was thought to be practical for most broad band applications in the visible and IR. However, if we look at the corresponding resolution in micrometers, $\Delta\lambda$, (see Table 1) we will see that it corresponds to a progressively coarser resolution as one proceeds further into the infrared and millimeter wave region. Conversely, at the shorter wavelengths the corresponding resolution, $\Delta\lambda$, increases rapidly, and is probably adequate for most sensors at the UV end of the spectrum. For example, at a wavelength of 0.2 μm (or 2000 \AA) the corresponding resolution of LOWTRAN 7 is equivalent to 0.8 \AA .

Table 1. Spectral Resolution of LOWTRAN 7 In Terms of Wavelength (μm) Corresponding to 20 cm^{-1}

| $\lambda(\mu\text{m})$ | .2 | .5 | 1 | 2 | 5 | 10 | 20 | 50 | 100 | 1000 | 10,000 |
|------------------------------|--------------------|--------------------|--------|-------|------|------|-----|-----|-----|------|-----------------|
| $\Delta\lambda(\mu\text{m})$ | 8×10^{-5} | 5×10^{-4} | 0.002 | 0.008 | 0.05 | 0.2 | 0.8 | 5.0 | 20 | 2000 | 2×10^5 |
| $\nu(\text{cm}^{-1})$ | 50,000 | 20,000 | 10,000 | 5000 | 2000 | 1000 | 500 | 200 | 100 | 10 | 1 |
| $\Delta\nu(\text{cm}^{-1})$ | 20 | 20 | 20 | 20 | 20 | 20 | 20 | 20 | 20 | 20 | 20 |

3.1 H_2O CONTINUUM

The H_2O continuum in the 7-14 μm region has been updated from that used in LOWTRAN 6. The H_2O self-broadened absorption coefficients in this region have been reduced by approximately 20%, based on laboratory measurements of Burch et al.^{11,12} and the atmospheric field measurements of Devir et al.¹³ With this correction both LOWTRAN 7 and the line-by-line computer code FASCOD2 are consistent with each other.

An example of the improvement that the correction above has made can be seen from Fig. 3, which shows the calculated transmittance for a 8.6 km path at sea level with LOWTRAN 6 and LOWTRAN 7 compared to a low-resolution CVF transmissometer measurement by Devir et al.¹³ in the 10 μm region.

There are still some outstanding issues to be resolved with the H_2O continuum. In particular, the validity of the temperature extrapolation to low temperatures needs to be verified.

3.2 UV AND VISIBLE

In extending the wavelength range of LOWTRAN 7 to 0.2 μm in the ultraviolet, O_2 absorption due to the Herzberg continuum and part of the Schumann-Runge band has been included,¹⁴⁻¹⁸ together with an extension of the

O₃ Hartley band from 0.25 μm to 0.2 μm . The absorption coefficients for the Hartley and Huggins O₃ bands also have been updated using more recent, higher-resolution data¹⁹⁻²² including quadratic temperature-dependent terms. A detailed discussion of the origin of the near UV measurements used in LOWTRAN 7 and their uncertainties is given in a companion paper by Anderson et al.²³ in these proceedings and will not be repeated here.

3.3 TRANSMISSION FUNCTIONS

One of the major differences between LOWTRAN 7 and LOWTRAN 6 lies in the transmission functions. Both computer codes assume a single parameter band model to describe the molecular absorption component of the atmospheric transmittance, but the models are quite different.

For LOWTRAN 6⁸ and all previous versions of the program³⁻⁷ the atmospheric molecular constituents were separated into 6 groups: (a) H₂O, (b) O₃, (c) the uniformly mixed constituents CO₂, N₂O, CO, CH₄ and O₂, (d) H₂O continuum, (e) the nitrogen continuum, and (f) UV and visible O₃.

For the first three groups, it was assumed that the average transmittance over a 20 cm⁻¹ interval was given by an expression of the form,

$$\bar{\tau}(\nu) = \int [C(\nu)UP^n] \quad (1)$$

where $\bar{\tau}$ the transmission function, $C(\nu)$, the spectrally varying absorption coefficient, and the parameter, n , were determined from laboratory transmittance measurements for each absorption band of the gases above over the infrared portion of the spectrum (0.8 - 28.5 μm). The parameters U and P represent the quantity of absorber and effective atmospheric pressure for a unit path length. The quantity UP^n is the "effective absorber amount" for the atmospheric path. The transmission functions for each of the components (a), (b), and (c) above were thus determined empirically and based on averages of transmittance measurements taken over many absorption bands.

In LOWTRAN 7 a different approach was taken, which was developed by Pierluissi and Maragoudakis.²⁴ For this approach, a double exponential transmission function was assumed where the average transmittance over a 20 cm⁻¹ spectral interval was given by:

$$\bar{\tau}(\nu) = \exp[-C(\nu)U(P/P_0)^n(T_0/T)^m] \quad (2)$$

where the parameters C , a , m , and n were determined from line-by-line calculations using FASCOD2²⁵ with the HITRAN86²⁶ molecular line parameter data base where the results were degraded in resolution to 20 cm⁻¹ (full width at half maximum). Average values of a , m , and n were determined for discrete spectral regions for each of the following molecular species: H₂O, CO₂, O₃, N₂O, CO, CH₄, and O₂ as well as the trace gases NO, NO₂, NH₃ and SO₂. The spectral intervals for which the new band model constants were determined for each of the molecules above are given in Table 2.

Table 2. Summary of Spectral Regions Over Which New Molecular Absorption Band Model Parameters Are Defined

| ABSORBER | SPECTRAL RANGE (cm ⁻¹) |
|-------------------------------------|---|
| WATER VAPOR (H ₂ O) | 0-17860 |
| OZONE (O ₃) | 0-200, 515-1275, 1330-2295, 2670-3260, 13000-24200, 27500-50000 |
| <u>UNIFORMLY MIXED GASES</u> | |
| CARBON DIOXIDE (CO ₂) | 425-1440, 1805-2855, 3070-4085, 4530-5380, 5905-7025, 7395-7785, 8030-8335, 9340-9670 |
| NITROUS OXIDE (N ₂ O) | 0-120, 490-775, 865-995, 1065-1385, 1545-2040, 2090-2655, 2705-2865, 3245-3925, 4260-4470, 4540-4785, 4910-5165 |
| CARBON MONOXIDE (CO) | 0-175, 1940-2285, 4040-4370 |
| METHANE (CH ₄) | 1065-1775, 2345-3230, 4110-4690, 5865-8135 |
| OXYGEN (O ₂) | 0-265, 7850-8080, 9235-9490, 12850-13220, 14300-14600, 15685-15955 |
| <u>TRACE GASES</u> | |
| NITRIC OXIDE (NO) | 1700-2005 |
| NITROGEN DIOXIDE (NO ₂) | 580-925, 1515-1695, 2800-2970 |
| AMMONIA (NH ₃) | 0-2150 |
| SULPHUR DIOXIDE (SO ₂) | 0-185, 400-850, 950-1480, 2415-2580 |

Separate transmission functions are used for each of the molecular species in LOWTRAN 7, allowing the user the option of varying the relative mixing ratios of the gases, which was not possible with LOWTRAN 6 and its predecessors. Treating the transmittances of each molecule separately should also improve the accuracy of LOWTRAN in overlap regions between strong absorption bands of different molecules: e.g., CO₂ and N₂O in the 4.5 μm region.

3.4 AEROSOL MODELS

The aerosol, fog, rain, and cloud model absorption and scattering coefficients in LOWTRAN 6 were extended to the millimeter wavelength region. In addition, the Navy Maritime aerosol model was modified to improve its wind

speed dependence for the large particle component. The background stratospheric model also has been updated to utilize more recent refractive index and size distribution measurements.²⁷

A new desert aerosol model has been added, which includes a wind speed dependence.^{28,29} LOWTRAN 7 will now modify the aerosol altitude profiles to account for elevated ground level cases.³⁰

The five cloud models contained in FASCOD2²⁵ have been added to LOWTRAN 7; these correspond to cumulus, stratus, alto-stratus, stratocumulus, and nimbostratus. The altitude and droplet density profiles for these models are given in Fig. 4. Two new cirrus models with more realistic wavelength dependences and separate scattering, absorption, and asymmetry parameters also have been incorporated into LOWTRAN 7 (see companion paper by Shettle³¹).

3.5 ALTITUDE PROFILES OF MOLECULAR SPECIES

LOWTRAN 7 now incorporates a set of model atmosphere temperature, pressure, and constituent profiles compatible with FASCOD2.^{25,32} While the maximum altitude of these profiles has been increased from 100 to 120 km, the default specifications for the standard six cases is still 100 km. An example of the U.S. Standard Profiles is shown in Fig. 5.

In previous versions of LOWTRAN³⁻⁸ we assumed the mixing ratios of the gases CO₂, N₂O, CO, CH₄ and O₂ were assumed to be invariant with altitude (and to be fixed at 330, 0.23, 0.01, 1.6, and 2.01 x 10⁵ ppm, respectively). In general, the new profiles can be significantly different; as can be seen from Fig. 5.

The mixing ratios of the gases N₂O, CO, and CH₄ at sea level used with the 1976 U.S. Standard Atmosphere model are now assumed to be 0.32, 0.15, and 1.7, respectively. With LOWTRAN 7, the user has the capability of either using the standard mixing ratio altitude profiles^{9,10,32} or substituting different ones.

3.6 MULTIPLE SCATTERING

The treatment of multiple scattering in LOWTRAN 7 has been a major addition to the computer code. An adaptation of the two-stream approximation method has been used for each layer together with an adding method for combining subsequent layers. A detailed description of this is given by Isaacs et al.^{33,34}

In this approach the adding method is used at each layer boundary to determine the combined transmittance, absorbance, reflectance and fluxes that include contributions from the entire atmosphere as well as reflected components of the thermal and scattered solar or lunar radiance from the earth's surface and/or a cloud boundary. This procedure is then repeated for each model atmosphere layer boundary from sea level to space (even though the path line-of-sight required for a given calculation may be limited to a few layers). Thus, if the multiple scattering option is selected, it involves a large number of calculations for every layer in the atmosphere, and, consequently, it will take much longer for LOWTRAN 7 to run.

For the current version of LOWTRAN 7, the assumption of a plane parallel atmosphere was adopted for the multiple-scattered contributions. This assumption does create some problems for radiance calculations where the solar zenith angle exceeds 75° or 80°. However, for solar zenith angles less than 75°, we have shown that the plane parallel atmosphere assumption used in LOWTRAN 7 agrees with more exact multiple-scattering codes to within 20%.

Some examples of multiple- and single-scattering calculations are given in Fig. 6 for a zenith-viewing observer at sea level with the sun at 10°, 60°, and 80° from the zenith. Figure 6 shows the dependence of background radiance on solar zenith angle in the 1 to 5 μm region for an upward-looking observer at sea level. Also shown in the figure is the thermal radiance component (which is bounded by the 218K blackbody function, the temperature of which corresponds to that of the first layer of the Midlatitude Summer Atmosphere in which the observer is located). The solid curves to the left of the figure show the single-scattered solar radiance and the dashed curves above them indicate the multiply scattered component for each of the solar elevation angles. It can be seen that the multiple-scattering component starts becoming important only at the larger solar zenith angles for this geometry. The influence of changing the (visual) meteorological range for a single solar zenith angle of 60° is shown in Fig. 7. Thus, the effect of reducing the visual (meteorological) range has an effect similar to an increase in the solar zenith angle (see Fig. 6). Figures 6 and 7 not only show the relative importance of single versus multiple scattering, but also the importance of scattered solar radiation compared to thermal radiance in the short-wavelength infrared region, where the two processes are in competition (i.e., 3-4 μm). Using the single-scattering option in LOWTRAN 7 in the LWIR (long wavelength infrared) region tends to overestimate the thermal radiance by only a few percent compared to the multiple-scattering calculation for this scenario. Therefore, for many applications, the use of the single-scattering option may be sufficient.

Some problems encountered with the application of multiple scattering are discussed in Section 6 below.

3.7 SOLAR IRRADIANCE FUNCTION

The extraterrestrial solar irradiance function has been updated in LOWTRAN 7 and is based on more recent compilations of measurements by Van Hoosier et al.^{35,36}, Neckel and Labs³⁷, and Wehrli³⁸ as well as those of Thekaikara.³⁹ The new solar irradiance function covers the spectral region from 0 to 57,470 cm^{-1} at a spectral resolution of 20-100 cm^{-1} , more nearly compatible with the molecular absorption parameters. Examples of the differences between LOWTRAN 7 and LOWTRAN 6 calculations of the solar irradiance are shown in Figs. 8(a) and (b), respectively. These figures show the solar irradiance at the top of the earth's atmosphere (upper curve) and the attenuated solar irradiance at sea level (lower curve) with the sun directly overhead. The LOWTRAN 7 results (Fig. 8a)

reveal considerably more spectral structure than the earlier LOWTRAN 6 calculations below $0.6 \mu\text{m}$ (see Fig. 8b). In addition, the LOWTRAN 7 results are a little higher and exhibit a more rounded peak irradiance between 0.5 and $0.7 \mu\text{m}$ than those obtained with LOWTRAN 6.

4. LOWTRAN 6 AND LOWTRAN 7 COMPARISONS

Some examples are given, which show the influence that many of the basic changes incorporated into LOWTRAN 7 will have on atmospheric transmittance and radiance calculations for specific scenarios, compared to calculations with LOWTRAN 6 and FASCOD2 (for some cases) where the FASCOD2 line-by-line calculations are degraded in resolution to 20 cm^{-1} (full width at half maximum).

Figure 9 shows the atmospheric transmittance for a vertical path to space from sea level in the $3\text{--}5 \mu\text{m}$ and $7\text{--}14 \mu\text{m}$ regions calculated with LOWTRAN 6, LOWTRAN 7, and FASCOD2 (assuming a Midlatitude Summer Atmosphere with no aerosol attenuation).

For this case, the three models are in generally good agreement with LOWTRAN 6 giving slightly higher transmittance values in the $3\text{--}5 \mu\text{m}$ region and somewhat lower values in the $8\text{--}12 \mu\text{m}$ region compared to LOWTRAN 7. A closer examination of the figures shows that there are some spectral regions (e.g., $3.4\text{--}3.8 \mu\text{m}$) where the LOWTRAN 6 calculations are in better agreement with FASCOD2 than with LOWTRAN 7.

Similar results are seen in Fig. 10, which gives the atmospheric transmittance for a 10 km horizontal path at sea level in the $3\text{--}5 \mu\text{m}$ and $7\text{--}14 \mu\text{m}$ regions, again assuming the Midlatitude Summer Atmospheric model with no aerosol present. One might also note that the LOWTRAN 7 and FASCOD2 calculations on the long wavelength edge of the $4\text{--}3 \mu\text{m}$ CO_2 band indicate a wider absorption region than LOWTRAN 6, whereas on the short wavelength edge of the band the FASCOD2 transmittance does not fall off as rapidly as the LOWTRAN 6 or 7 results (see Figs. 9 and 10).

Next, the results of the three transmission models are compared for a high-altitude, long-range scenario. Figure 11 shows the transmittance for a 500 km slant path from 10.97 km altitude to 4.57 km assuming the U.S. Standard Atmosphere. For this scenario the atmospheric path reaches a tangent height (lowest altitude) of approximately 2.9 km . It should be noted that the scales on Figs. 11 (a) and (b) are different and that the peak transmittance value in the $4.7 \mu\text{m}$ region is an order of magnitude less than the corresponding peak in the $8\text{--}12 \mu\text{m}$ region. In the $4.7 \mu\text{m}$ region, the LOWTRAN 7 results lie between those of FASCOD2 and LOWTRAN 6, with LOWTRAN 6 overestimating the width of the transmittance spike. On the short wavelength edge of the band, LOWTRAN 6 overestimates the transmittance compared to LOWTRAN 7 and FASCOD2, which is the reverse of what was seen for the examples given in Figs. 9 and 10. In the $8\text{--}12 \mu\text{m}$ region, the results given in Fig. 11 are similar to those of Figs. 9 and 10, namely, that in the $10\text{--}12 \mu\text{m}$ region the LOWTRAN 7 transmittances are lower than those calculated by FASCOD2 whereas between 8 and $8.5 \mu\text{m}$ they are higher.

Figure 12 provides some insight as to the dominant attenuation mechanisms in the two wavelength regions, for the 500 km path scenario discussed in Fig. 11. In the $7\text{--}14 \mu\text{m}$ region, Figs. 12 (c) and (d), it is apparent that the H_2O continuum and O_3 absorption dominate the transmittance level. The influence of H_2O , CO_2 , N_2O , and CH_4 line absorption, which also controls the edges of this window region, also is shown in Fig. 12 together with the aerosol extinction contribution.

In the $4\text{--}5 \mu\text{m}$ region, the interaction of the competing mechanisms, which gives rise to the transmittance spikes shown in Fig. 11(a), is more complex, as can be seen from Figs. 12(a) and (b). The width of the absorption region around $4.2 \mu\text{m}$ is controlled mainly by the nitrogen continuum on the short wavelength edge and a combination of CO_2 , N_2O , and the nitrogen continuum on the long wavelength edge. The role of the H_2O continuum, H_2O , CO_2 , and N_2O in shaping the outer edge of the 4.7 and $4 \mu\text{m}$ spikes also can be seen from Figs. 12(a) and (b).

5. PROBLEM AREAS

LOWTRAN 7, as released in February 1989, is undergoing a continuing validation, particularly by its expanded user base. There is a commitment to verify and correct problems, with full notification to all known users. Because of the newness of the code, the first set of errata have not been finalized. Some potential problem areas include:

1. An opacity test which defines zero transmittance as $\exp(-20)$, i.e., optical depths greater than 20, was used in LOWTRAN 7 which is not recognized as valid. This has a negligible effect in most spectral ranges but can lead to discernible contamination for very large opacities in the UV spectral range. This exponential test can be reset to any larger value compatible with the user's computer. Caution should, therefore, be taken when using the original version of LOWTRAN 7 in the ultraviolet solar blind region for background radiance calculations in the lower atmosphere. An example of this is shown in Fig. 13 for the downwelling radiance in the $0.20\text{--}0.3 \mu\text{m}$ region, calculated for an observer at sea level looking upward with the sun overhead. For this scenario the background radiance level should be orders of magnitude less than given in Fig. 13.
2. Over a portion of the extraterrestrial solar irradiance data compendium used in LOWTRAN 7 the number of significant figures tabulated by Wehrli³⁸ reduces to two at the longer wavelengths (extending to the mid-infrared region). Consequently, the solar irradiance function can exhibit a 3% step discontinuity in the mid-IR region.
3. The multiple-scattering algorithm within a single layer may encounter boundary definition incompatibilities; in addition, the solar multiple scattering calculations are not correct for zenith angles larger than 80° .

Corrections for the above problems are currently available or under development. Users are encouraged to communicate directly with L.W. Abreu, AFGL/OPE, Hanscom AFB, Ma 01731 concerning any questions related to LOWTRAN 7.

6. FUTURE PLANS

A higher-resolution band model option for LOWTRAN 7 is currently being tested and evaluated. This model, which is called MOUTRAN, will enable the user to make calculations at selected resolutions, within certain constraints, up to a maximum resolution of 2 cm^{-1} .

7. CONCLUSIONS

Examples of the differences among LOWTRAN 6, LOWTRAN 7, and FASCOD2 calculations were given for some typical low-altitude and high-altitude scenarios. In general, LOWTRAN 7 atmospheric transmittance calculations will be more optimistic in the $8\text{-}14 \mu\text{m}$ region and a little more pessimistic in the $4\text{-}5 \mu\text{m}$ region than those of LOWTRAN 6. The corresponding LOWTRAN 7 atmospheric background radiance values will be lower than those calculated with LOWTRAN 6 in the $10 \mu\text{m}$ region (due to the reduced H_2O continuum in that region.)

There were some instances in which the LOWTRAN 6 calculations agreed more closely with those of FASCOD2 than LOWTRAN 7. The reason for this is probably due to the smoothing of the FASCOD2 calculations in fitting results to the double exponential transmission functions used in LOWTRAN 7, but we assume the FASCOD2 results to be correct.

The interaction of the different mechanisms that shape the $3\text{-}5 \mu\text{m}$ and $8\text{-}12 \mu\text{m}$ transmittance windows are quite complex and depend very much on the observer/target viewing geometry. For many long range scenarios at high altitude where the path geometry does extend to lower altitudes in the troposphere, the effects of the H_2O continuum in the $8\text{-}14 \mu\text{m}$ and both the H_2O and the N_2 continua in the $3\text{-}5 \mu\text{m}$ region can still play a dominant role in shaping these window regions.

It is difficult to make general statements concerning single versus multiple scattering. For upward viewing geometries, we find that, at the longer wavelengths where the thermal emission dominates, the single-scattering algorithm gives slightly higher radiance values than the multiple-scattering algorithm, but for many applications the differences are small. At wavelengths below $4 \mu\text{m}$ where solar scattering is greater than the thermal emission, the multiple-scattering component (due to scattered solar radiation) is always higher than that calculated by the single-scattering option. The magnitude of the difference depends on the relative solar/observer viewing geometry. For downward-viewing scenarios, the radiance due to ground reflections of solar radiation can be dominant in $2\text{-}4 \mu\text{m}$ region.

Both the extension of LOWTRAN 7 to $0.2 \mu\text{m}$ and the inclusion of multiple scattering will greatly enhance its use in the UV region of the spectrum for many applications. The extension of LOWTRAN 7 into the millimeter region of the spectrum will enhance its application for earth/atmospheric heat budget calculations and other LWIR calculations. However, because of the 20 cm^{-1} resolution, which has been preserved, LOWTRAN 7 will not provide a useful tool for millimeter wave atmospheric transmittance calculations; FASCOD2 can be used over these spectral ranges. A higher-resolution version of LOWTRAN 7 (to 2 cm^{-1}) is currently being evaluated and will permit users greater flexibility.

Many more options are currently available in LOWTRAN 7, which allow the user to vary independently the concentrations of the individual molecular gases and their altitude dependence, as well as constructing specific model atmospheres, with selected combinations of meteorological conditions, aerosols, clouds, and solar orientations for a given target/observer geometry.

Work will continue to validate LOWTRAN 7 against field measurements made under known atmospheric environmental conditions.

Comments, concerns, and questions on LOWTRAN 7 can be addressed directly to:

L.W. Abreu
AFGL/OPE
Hanscom AFB, MA 01731, U.S.A.

8. REFERENCES

1. Kneizys, F. X., Shettle, E. P., Abreu, L. W., Chetwynd, Jr., J. H., Anderson, G. P., Gallery, W. O., Selby, J. E. A., and Clough, S. A., Users Guide to LOWTRAN 7, AFGL-TR-88-0177, AD A206773, 1988.
2. Kneizys, F. X., Shettle, E. P., Abreu, L. W., Anderson, G. P., Chetwynd, Jr., J. H., Gallery, W. O., Selby, J. E. A., and Clough, S. A., Atmospheric Transmittance/Radiance: The LOWTRAN 7 Model, in preparation.
3. Selby, J. E. A., and McClatchey, R. A., Atmospheric Transmittance from 0.25 to $28.5 \mu\text{m}$: Computer Code LOWTRAN 2, AFCRL-TR-72-0745, AD A763721, 1972.

4. Selby, J. E. A., and McClatchey, R. A., Atmospheric Transmittance from 0.25 to 28.5 μm : Computer Code LOWTRAN 3, AFCL-TR-75-0255, AD A017734, 1975.
5. Selby, J. E. A., Shettle, E. P., and McClatchey, R. A., Atmospheric Transmittance from 0.25 to 28.5 μm : Supplement LOWTRAN 3B, AFGL-TR-76-0258, AD A040701, 1976.
6. Selby, J. E. A., Kneizys, F. X., Chetwynd, Jr., J. H., and McClatchey, R. A., Atmospheric Transmittance/Radiance: Computer Code LOWTRAN 4, AFGL-TR-78-0053, AD A058643, 1978.
7. Kneizys, F. X., Shettle, E. P., Gallery, W. O., Chetwynd, Jr., J. H., Abreu, L. W., Selby, J. E. A., Fenn, R. W., and McClatchey, R. A., Atmospheric Transmittance/Radiance: Computer Code LOWTRAN 5, AFGL-TR-80-0067, AD A058643, 1980.
8. Kneizys, F. X., Shettle, E. P., Gallery, W. O., Chetwynd, Jr., J. H., Abreu, L. W., Selby, J. E. A., and Fenn, R. W., Atmospheric Transmittance/Radiance: Computer Code LOWTRAN 6, AFGL-TR-83-0187, AD A137796, 1983.
9. NASA U.S. Standard Atmosphere Supplements (1966), U. S. Government Printing Office, Washington, DC, 1966.
10. NASA U.S. Standard Atmosphere Supplements (1976), U. S. Government Printing Office, Washington, DC, 1976.
11. Burch, D. E., and Alt, R. L., Continuum Absorption by H_2O in the 700-1200 cm^{-1} and 2400-2800 cm^{-1} Windows, AFGL-TR-84-0128, AD A147391, 1984.
12. Burch, D. E., Absorption by H_2O in Narrow Windows between 3000 and 4200 cm^{-1} , AFGL-TR-85-0036, AD A166648, 1985.
13. Devir, A. D., Ben-Shalom, A., Lipson, S. G., Oppenheim, U. P., and Ribak, E., Atmospheric Transmittance Measurements: Comparison with LOWTRAN 6, Report RAA/99-85, Technion-Israel Institute of Technology, Haifa 32000, Israel, 1985.
14. Yoshino, K., Cheung, A.S.-C., Esmond, J. R., Parkinson, W. H., Freeman, D. E., Guberman, S. L., Jenourier, A., Coquart, B., and Merienne, M. F., "Improved Absorption Cross Sections of Oxygen in the Wavelength Region 205-240 nm of the Herzberg Continuum," Planet Space Sci. 36:1469-1475 (1988).
15. Johnston, H. S., Paige, M., and Yao, F., "Oxygen Absorption Cross Sections in the Herzberg Continuum and between 206 and 327K," J. Geophys. Res. 89:11661-11665 (1984).
16. Shardanand, "Nitrogen-Induced Absorption of Oxygen in the Herzberg Continuum," J. Quant. Spectrosc. Radiat. Transfer 18:525-530 (1977).
17. Frederick, J. E., and Hudson, R. D., "Predissociation Linewidths and Oscillator Strengths for the (2-0) to (13-0) Schumann-Runge Bands of O_2 ," J. Molec. Spectrosc. 74:247-258 (1979).
18. Yoshino, K., Freeman, D. E., and Parkinson, W. H., "Atlas of the Schumann-Runge Absorption Bands of O_2 in the Wavelength Region 175-205 nm," J. Phys. Chem. 13:207 (1984).
19. Bass, A. M., and Paur, R. J., "The Ultraviolet Cross-Sections of Ozone. I. Measurements," Atmospheric Ozone. Proceedings of the Quadrennial Ozone Symposium, Halkidiki, Greece, edited by C. Zerefos and A. Ghaz, pp. 606-616, D. Reidel, Inc., 1985.
20. Molina, L. T., and Molina, M. J., "Absolute Absorption Cross Sections of Ozone in the 185-350 nm Wavelength Range," J. Geophys. Res. 91:14501-14509 (1986).
21. Yoshino, K., Freeman, D. E., Esmond, J. R., and Parkinson, W. H., "Absolute Absorption Cross Section Measurements of Ozone in the Wavelength Region 238-335 nm and the Temperature Dependence," Planet. Space Sci. 36:395-398 (1988).
22. Cacciani, M., diSarra, A., and Fiocco, G., Laboratory Measurements of the Ozone Absorption Coefficients in the Wavelength Region 339-362 nm at Different Temperatures, Dept. of Physics, University of Roma - La Sapienza, Internal Note No. 882, 1987.
23. Anderson, G. P., Kneizys, F. X., Shettle, E. P., Abreu, L. W., Chetwynd, Jr., J. H., Huffman, R. E., and Hall, L. A., "UV Spectral Simulations Using LOWTRAN 7," Proc AGARD-Electromagnetic Wave Propagation Panel Symposium No. 45 on Atmospheric Propagation in the UV, Visible, IR, & MM-Wave Region and Related Systems Aspects, Copenhagen, Denmark, 9-13 October 1989.
24. Pierluissi, J. H., and Maragoudakis, C. E., Molecular Transmission Band Models for LOWTRAN, AFGL-TR-86-0272, AD A180655, 1986.
25. Clough, S. A., Kneizys, F. X., Shettle, E. P., and Anderson, G. P., "Atmospheric Radiance and Transmittance: FASCOD2," Sixth Conference on Atmospheric Radiation, May 13-16, 1986, American Meteorological Society, Boston, MA, 1987.

26. Rothman, L. S., Gamache, R. R., Goldman, A., Brown, L. R., Toth, R. A., Pickett, H. M., Poynter, R. L., Flaud, J.-M., Camy-Peyret, C., Barbe, A., Husson, N., Rinsland, C. P., and Smith, M. A. H., "The HITRAN Database: 1986 Edition," *Appl. Opt.*, 26: 4058-4097 (1987).
27. Longtin, D. R., Shettle, E. P., Hummel, J. R., and Pryce, J. D., "A Desert Aerosol Model for Radiative Transfer Studies, *Aerosols and Climate*, pp. 261-269, ed. by P. V. Hobbs and M. P. McCormick, A. Deepak Publishing, 1987.
28. Longtin, D. R., Shettle, E. P., Hummel, J. R., and Pryce, J. D., A Wind Dependent Desert Aerosol Model: Radiative Properties, AFGL-TR-88-0112, AD A206164, 1988.
29. Hummel, J. R., Shettle, E. P., and Longtin, D. R., A New Background Stratospheric Aerosol Model for Use in Atmospheric Radiation Models, AFGL-TR-88-0165, AD A210110, 1988.
30. Shettle, E. P., "Comments on the Use of LOWTRAN in Transmission Calculations for Sites with the Ground Elevated Relative to Sea Level," *Appl. Opt.* 28:1451-1452 (1989).
31. Shettle, E. P., "Models of Aerosols, Clouds and Precipitation for Atmospheric Propagation Studies," Proc. AGARD-EPP 45th Symposium on Atmospheric Propagation in the UV, Visible, IR and MM-Wave Region and Related System Aspects, Copenhagen, Denmark, 9-13 Oct. 1989.
32. Anderson, G. P., Clough, S. A., Kneizys, F. X., Chetwynd, Jr., J. H., and Shettle, E. P., AFGL Atmospheric Constituent Profiles (0-120 km), AFGL-TR-86-0110, AD A175173, 1986.
33. Isaacs, R. G., Wang, W.-C., Worsham, R. D., and Goldenberg, S., Multiple Scattering Treatment for Use in the LOWTRAN and FASCODE Models, AFGL-TR-86-0073, AD A173990, 1986.
34. Isaacs, R. G., Wang, W.-C., Worsham, R. D., and Goldenberg, S., "Multiple Scattering LOWTRAN and FASCODE Models", *Appl. Opt.* 26:1272-1281 (1987).
35. VanHoosier, M. E., Bartoe, J. D., Brueckner, G. E., and Prinz, D. K., "Solar Irradiance Measurements 120 nm - 400 nm from Spacelab 2 (Results from the SUSIM Experiment)," presented at IUGG XIX General Assembly, Canada, 9-22 Aug. 1987.
36. VanHoosier, M. E., and Brueckner, G. E., "Solar Ultraviolet Spectral Irradiance Monitor (SUSIM): Calibration Results from Spacelab 2," Proceedings of the 8th Workshop on Vacuum Ultraviolet Radiometric Calibration of Space Experiments, 19 March 1987.
37. Neckel, H., and Labs, D., "The Solar Radiation between 3300 and 12500 Å," *Solar Phys.* 90:205-258 (1984).
38. Wehrli, C., Extraterrestrial Solar Spectrum, Publication No. 615, Physikalisch-Meteorologisches Observatorium and World Radiation Center, CH-7260 Davos-Dorf, July 1985.
39. Thekeakera, M. P., "Extraterrestrial Solar Spectrum, 3000-6100 Å at 1 Å Intervals," *Appl. Opt.* 13:518-522 (1974).

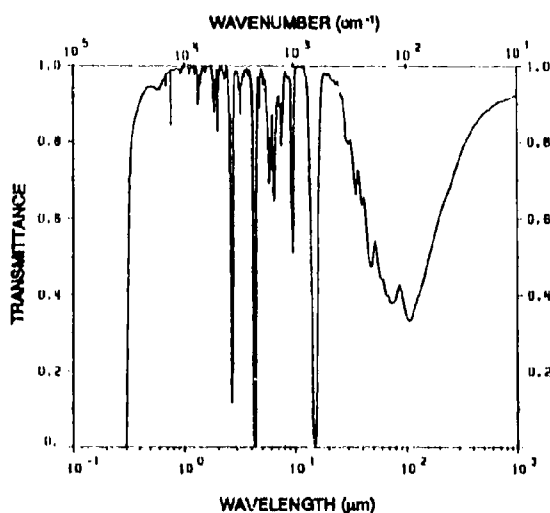


Fig. 1 Atmospheric Transmittance for a Vertical Path to space from 10 km Altitude for the 0.2 μm to 1000 μm Region (Midlatitude Summer Atmosphere, 23 km Rural Aerosol).

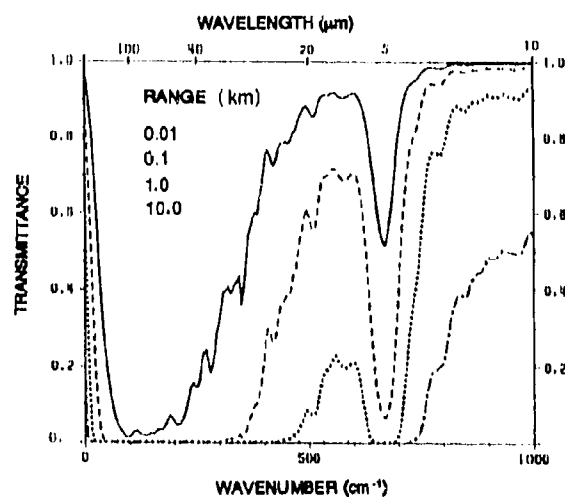


Fig. 2 Atmospheric Transmittance for Horizontal Path Lengths varying from 0.01 to 10 km at Sea Level (Midlatitude Summer Atmosphere, 23 km Rural Aerosol).

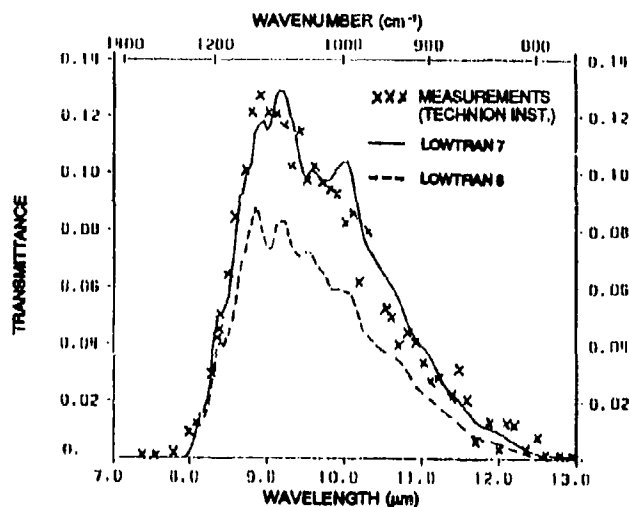


Fig. 3 Comparison of LOWTRAN 6 and 7 Calculations with a 6.6 km Atmospheric Transmittance Measurement in the 7-14 μm Region at Sea Level (for recorded meteorological conditions).

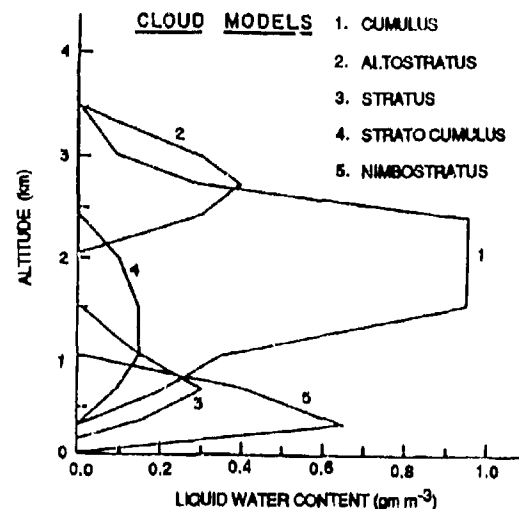


Fig. 4 Summary of Water Droplet Cloud Models in LOWTRAN 7

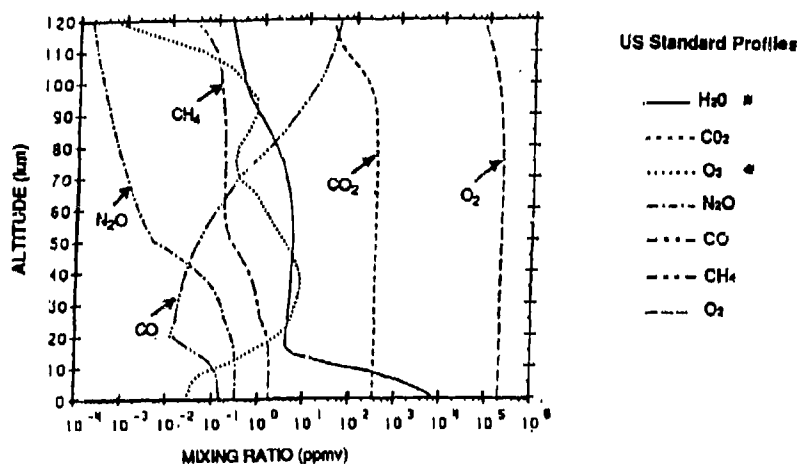


Fig. 5 Altitude Profiles of the Mixing Ratios of some Important Atmospheric Molecular Species.

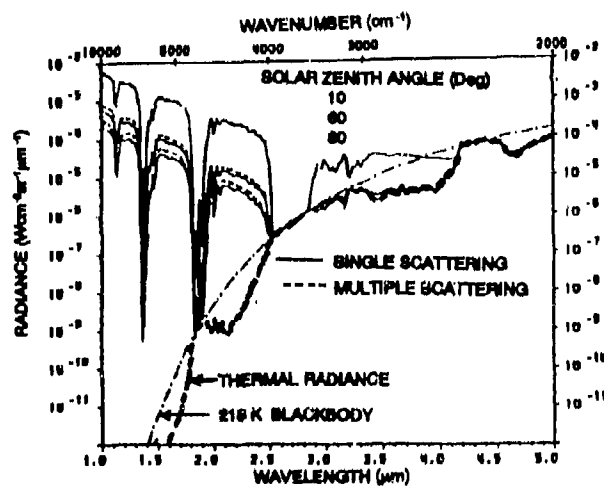


Fig. 6 Atmospheric Background Radiance for an Upward Viewing Scenario from Sea Level showing the contributions from Single and Multiple Scattering and Thermal Emission for 3 Solar Elevations, (US Standard Atmosphere, 23 km Rural Aerosol).

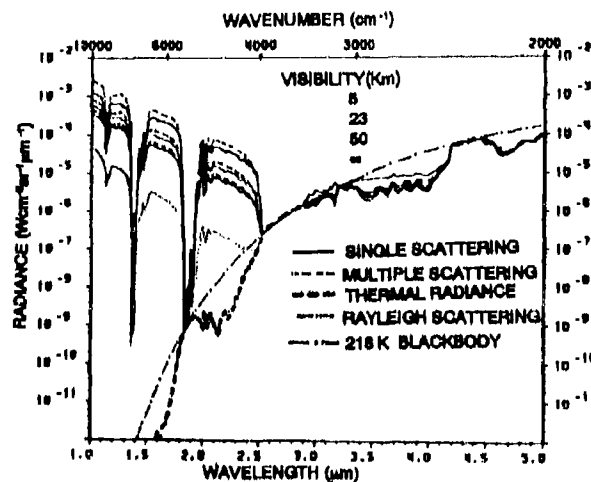


Fig. 7 Dependence of Atmospheric Background Radiance on Visibility for Single and Multiple Scattering for an Upward Viewing Scenario from Sea Level (Solar Zenith Angle = 60°, US Standard Atmosphere, 23 km Rural Aerosol Model).

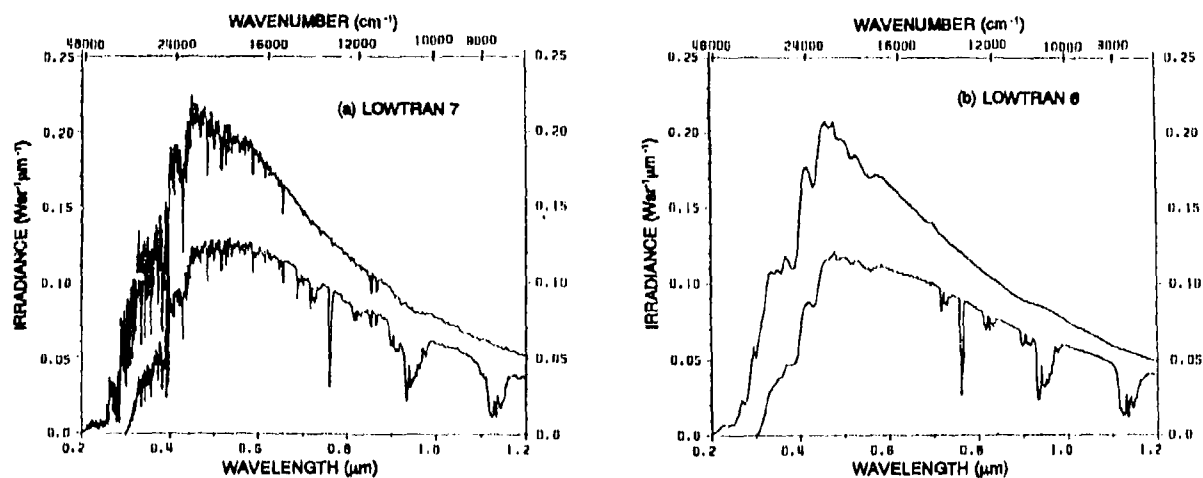


Fig. 8 Comparison between the extra-terrestrial Solar Irradiance and the Directly Attenuated Solar Irradiance at Sea Level for LOWTRAN 7, (Fig. a) and LOWTRAN 6, (Fig. b) for a Zenith Viewing Geometry (assuming a Midlatitude Summer Atmosphere and 23 km Rural Aerosol Model).

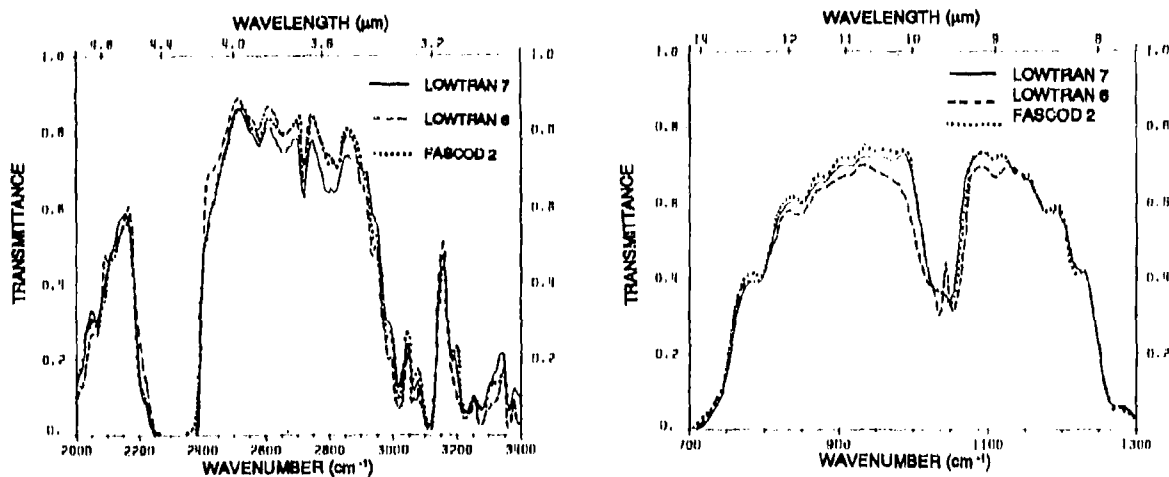


Fig. 9 Comparison of Atmospheric Transmission Calculations for a Vertical Path from Sea Level to Space in the 3-5 μm and 7-14 μm regions (Midlatitude Summer Atmosphere, no Aerosols).

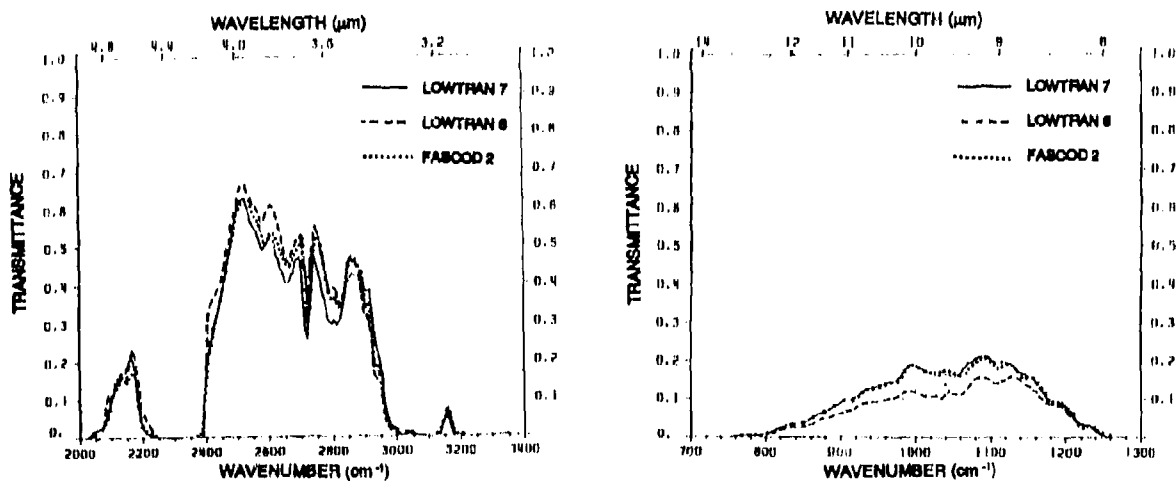


Fig. 10 Comparison of Atmospheric Transmission Calculations for a 10 km Horizontal Path at Sea Level in the 3-5 μm and 7-14 μm Regions (Midlatitude Summer Atmosphere, no Aerosols).

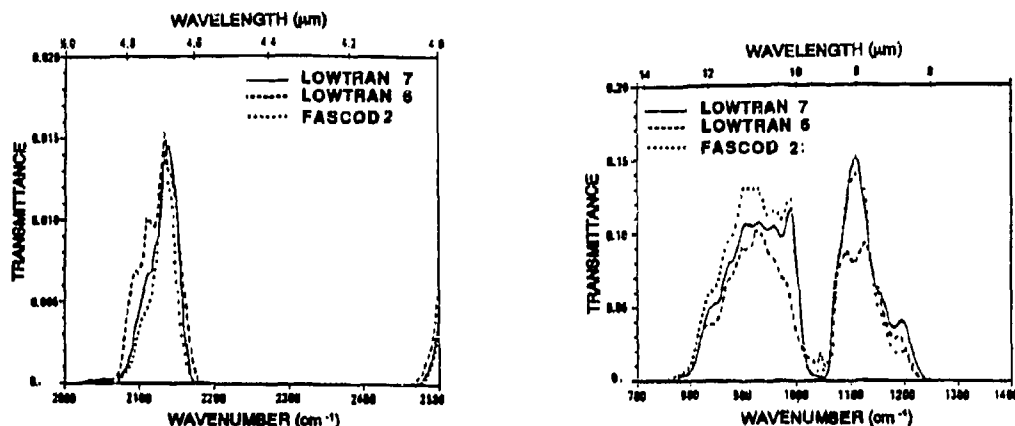


Fig. 11 Comparison of LOWTRAN 6, LOWTRAN 7 and FASCOD 2 Atmospheric Transmissions for a 500 km Slant Path from 36,000 ft. to 15,000 ft. Altitude in (a) 4-5 μm Region (b) 7-14 μm Region and (U.S. Standard Atmosphere).

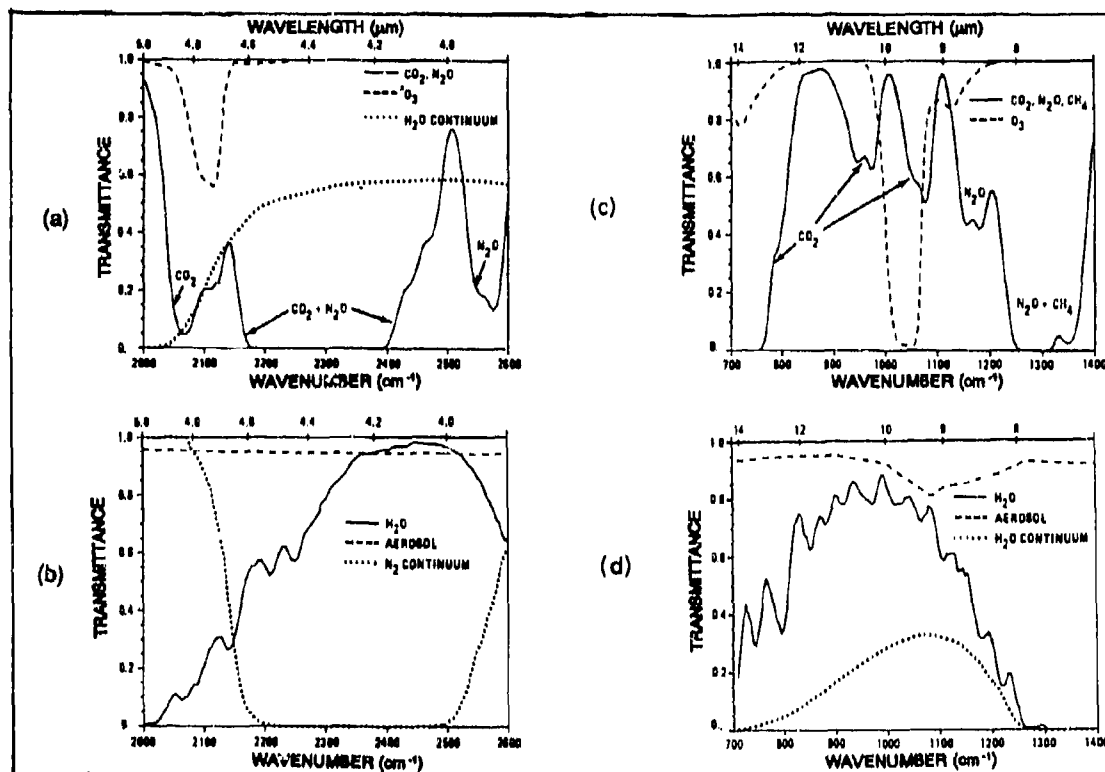


Fig. 12 Individual Atmospheric Transmission Components in the 4-5 μm and 7-14 μm Regions for the same path geometry given in Fig. 11.

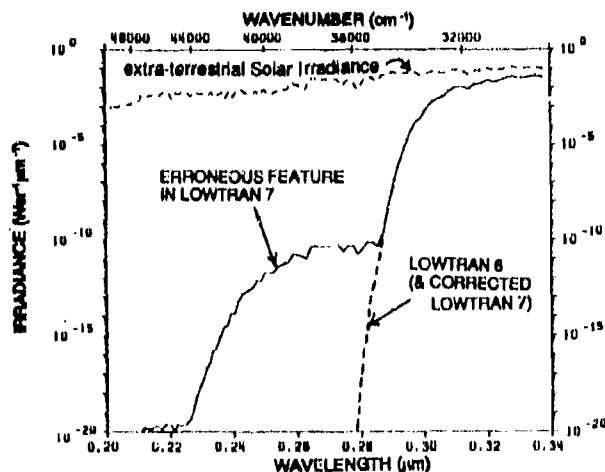


Fig. 13 Calculated Direct Solar Irradiance at Sea Level Indicating an Error in LOWTRAN 7 (version 3.6) for the UV Solar Blind Region.

PROPAGATION ENVIRONMENTS, EFFECTS, AND DECISION AIDS

by

F. E. Niles, M. G. Heaps, R. C. Shirkey, L. D. Duncan, and M. A. Seagraves
Atmospheric Sciences Laboratory
U.S. Army Laboratory Command
White Sands Missile Range, New Mexico 88002-5501
United States of America

SUMMARY

Reconnaissance, surveillance, target acquisition, communications, and weapon systems are becoming more sophisticated and are becoming more dependent on the propagation of electromagnetic or acoustic energy through the atmosphere. Weather and battle activity will constantly change the atmospheric conditions and hence the propagation environments when the systems are employed. The effects of these changing propagation environments must be understood for optimum system design, assessment of system performance, development of countermeasures, development of tactics and doctrine, and development of decision aids. In 1978 the U.S. Army Atmospheric Sciences Laboratory (ASL) began the development of the Electro-Optical Systems Atmospheric Effects Library (EOSAEL) in order to quantify some of the battlefield atmospheric effects. EOSAEL has had several releases; and the latest, EOSAEL 87, contains 26 modules that can be separated into six generic classes: (1) gases, (2) natural aerosols, (3) battlefield aerosols, (4) radiative transfer, (5) laser propagation, and (6) target acquisition and system performance. Combining information on weather and battle activity with an understanding of atmospheric effects has allowed ASL to produce tactical decision aids (TDAs) for many friendly and threat electro-optical systems. This developmental software is scheduled to be fielded on the Integrated Meteorological System (IMETS).

1. INTRODUCTION

Weather has always played a decisive role in warfare and, combined with the smoke, dust, and obscurants induced by battle activity, will continue to do so on future battlefields. The modern day battlefield will be filled with sophisticated reconnaissance, surveillance, target acquisition, communications, and weapon systems that exploit some part of the radiant energy spectrum. The full spectrum of radiant energy spans some 25 orders of magnitude from very low frequency acoustic energy at 1 Hz to hard gamma rays at 10^{25} Hz. The human eye sees only in the very narrow band around 5.4×10^{14} Hz (wavelengths between 0.4 and 0.7 μ m). Electro-optical (EO) systems have been built that extend the observer's capability into the infrared (IR), and even into the millimeter wave (MMW) region. Other EO systems enhance the capability of the observer to see under low light-level conditions. Radars function from the ultraviolet region using lasers (when lasers are used in this mode they are called lidars) to 300 MHz. Communications systems extend from the visible region, primarily using lasers, through the audio frequency region (approximately 10 Hz to 20 kHz). Acoustic sensors utilize the region from 1 Hz to about 1 kHz. The propagation environment through which the energy associated with or sensed by the various military systems travels is constantly changing and frequently is the determining factor in whether or not the systems perform satisfactorily.

The propagation environment is one of five parts in the target acquisition and smart weapons utilization picture that must be solved if advanced sensors and systems are to be utilized in the airland battle. The other parts are backgrounds, signatures, sensors and their platforms, and man-machine interfaces and automated analyses. The signal-to-noise (S/N) ratio is a major consideration in minimizing the false alarm or false target rate. If the backgrounds and propagation environments were uniform, then high S/N ratios could be routinely achieved. Unfortunately uniform conditions rarely exist, and the conduct of battle quickly increases clutter and obscuration.

2. SMART WEAPONS

Smart weapons (or the equivalent term, precision guided munitions) have the capability to search, detect, discriminate, select, and precisely engage a wide variety of ground and air targets. They employ rockets, missiles, or projectiles that may be fired from a variety of launch platforms (such as, tanks, armored combat vehicles, artillery, and helicopters) or delivered to the target vicinity by an aerial vehicle, ground robot, or other means. They may include submunitions that are dispersed from a carrier. Target engagement may be by either a guide to intercept (hit-to-kill) concept, or it may require the munition to aim and fire a warhead from a stand-off location (shoot-to-kill). Smart weapons may either require operator assistance as with a command guided system or be automatically guided by self-contained subsystems. There are currently three classes of smart weapons: (1) guided munitions, (2) smart munitions, and (3) brilliant munitions.

Guided munitions are characterized as one-on-one systems that require an operator in the loop either for target selection, as in the case of lock-on-before-launch, or for

assistance in guidance. Each munition is directed to a specific target by the operator or gunner. This procedure requires a line of sight (LOS) between the operator (or the sensor being used by the operator) and the target.

There are four principal forms of guidance: (1) command guidance, (2) beam rider guidance, (3) homing guidance, and (4) inertial guidance. In command guidance the target is tracked and the missile is directed to intercept. Information and guidance commands are received and transmitted by the missile in flight via a data link (such as wire, fiber optics, radio frequency, and IR). Examples include TOW and DRAGON. In beam rider guidance the missile travels along an encoded beam that has been directed at the target. The missile receives a unique guidance code, which it decodes and uses to maintain flight within the beam. In homing guidance the weapon homes in on a unique signature of or on the target. This could be heat generated by a tank engine or the unique laser designation required for COPPERHEAD or HELLFIRE. In inertial guidance preprogrammed information onboard the carrier is employed. This technique is more often used in long-range systems; however, it may be combined with other terminal guidance techniques for increased capabilities.

Smart munitions, in contrast with guided munitions, have the self-contained capability to search for, detect, acquire, and engage targets without reliance on an operator for specific target selection or terminal guidance. Autonomous operation is achieved by utilizing self-contained sensors or seekers that receive electromagnetic radiation emitted by targets and their surrounding environments. Smart munitions are delivered to the target area by projectiles, rockets, or missiles, with each carrier delivering from one to a few dozen munitions. By combining their autonomous operation with the means to rapidly deliver large quantities of munitions, smart munition weapon systems are most effective in the many-on-many situation. There are two types of smart munitions: sensor-fuzed munitions and terminally guided munitions. Sensor-fuzed munitions are designed for shoot-to-kill operations, normally from a top-attack position. Once delivered to and dispersed over the target area, an onboard sensor begins to search for targets. Upon detection, the sensor-fuzed munition immediately fuzes a lethal mechanism, usually an explosively formed penetrator, and directs it at the target. Terminally-guided munitions are hit-to-kill subsystems. They employ an onboard autopilot and flight control devices to steer to the target. An onboard warhead, usually a shaped-charge, is detonated upon impact.

Brilliant munitions are future systems that will combine the autonomous operation of a smart munition with enhanced navigation and target classification/identification capabilities. They may be assigned a mission to find and engage a specified class or type of targets.

A major consideration in the design of smart weapons is the environment in which they must operate. Target acquisition is significantly degraded by most adverse environmental conditions. Even in a benign environment, the signature of the target can vary widely, depending on its operating status and location. Other environmental factors that degrade acquisition include countermeasures, camouflage, and decoys designed to prevent or hinder acquisition and other phenomena such as weather, topography, and the clutter of battle.^{1 2}

3. ENVIRONMENTAL IMPORTANCE

Environmental factors can significantly affect the four basic tenets of airland battle doctrine--initiative, agility, depth, and synchronization. Initiative means setting or changing the terms of battle through action. Prediction of weather and environmental effects support this tenet by providing the force commander with timely, accurate information to assess the impact of environmental conditions on the battlefield. Computer-assisted tactical decision aids (TDAs) can assist in describing these impacts. Weather intelligence can indicate windows of opportunity within which the commander may seize the initiative and take advantage of conditions that adversely affect the enemy. Effective applications of environmental information will enhance the ability of the force commander to bring the required forces and firepower to bear at the optimum time and place on the battlefield. Agility is the ability to act faster than the enemy. The force commander's ability to create and exploit enemy vulnerabilities is enhanced through knowledge of the effects of anticipated environmental conditions. Depth is the extension of combat operations in space, time, and resources. Environmental effects analysis and accurate weather predictions support the commander's requirement to consider all environmental implications of the maneuver space. Accurate prediction of environmental effects across the battlefield can assist the commander in positioning his forces to maximize their ability to conduct operations while minimizing their vulnerabilities. Conversely, prediction of environmental conditions favorable to attack by enemy elements can significantly enhance preparedness across the battlefield. Synchronization is the process of organizing combat activities in time, space, and purpose to develop maximum combat power from available resources. Accurate environmental information enables the commander to better evaluate the capability of available forces. In deep operations it enables the commander to decide where to attack, how to detect the enemy, and when to deliver munitions. Accurate weather information can be the key to synchronizing a variety of forces with differing operational capabilities.

The importance of weather and environmental factors to all commanders will increase as more sophisticated weapons are introduced to the battlefield. For example, EO systems such as laser, television (TV), and IR systems and directed energy weapons may operate at different wavelengths and have different sensitivities to adverse weather conditions. Each system is, therefore, affected differently by environmental factors such as temperature contrast of the target and background, humidity, dust, and smoke. The commander who can best forecast future conditions and determine effects on opposing forces will have a decisive advantage on the battlefield.³

4. EOSAEL OVERVIEW

The Electro-Optical Systems Atmospheric Effects Library (EOSAEL) has been developed to quantify the propagation environments expected on future battlefields. The history of EOSAEL has been presented elsewhere.⁴ The U.S. Army Atmospheric Sciences Laboratory (ASL) started the development of EOSAEL in 1978. The latest version, EOSAEL 87, contains 26 computer modules that can be separated into 6 generic classes: (1) gases, (2) natural aerosols, (3) battlefield aerosols, (4) radiative transfer, (5) laser propagation, and (6) target acquisition and system performance.⁵ The 26 modules may be used under the control of an executive driver or in a stand-alone mode. The philosophy underlying the development of EOSAEL has been to include modules that give reasonably accurate results with the minimum in computer time for conditions that may be expected on the battlefield. This philosophy, along with the evolutionary nature of EOSAEL, has resulted in some redundancy within the library. While minor updates to EOSAEL 87 are planned, corrections for redundancy, upgrades of various modules, and expansion of wavelengths to cover ultraviolet and acoustic systems will be incorporated in the next edition, EOSAEL 92, to be distributed in early 1992.

Three modules for computing gaseous absorption are provided in EOSAEL 87. These are LOWTRN, LZTRAN, and MMMW. LOWTRN calculates atmospheric transmittance, radiance, and contrast due to specific molecules at 20 inverse centimeters spectral resolution on a linear wave number scale in the wavelength region 0.25 to 28.5 μm .⁶ LZTRAN calculates transmission through atmospheric gases for 97 laser lines in the wavelength region 0.5 to 11.0 μm for slant or horizontal paths.⁷ MMMW calculates transmission, backscatter, and refractivity due to gaseous absorption, fog, rain, and snow in the wavelength region 0.3 to 30.0 mm.⁸

For naturally occurring weather conditions, EOSAEL 87 contains three modules for transmission and statistical information. These are XSCALE, CLIMAT, and CLTRAN. XSCALE determines the transmission in the wavelength region 0.2 to 12.5 μm through haze and fog for both monochromatic and broadband wavelengths over arbitrary horizontal and slant paths and through rain and snow for horizontal paths.⁹ CLIMAT provides climatological data in terms of averages (usually over 11 years) and standard deviations or percentages of occurrence for 11 meteorological parameters (normally at a 2-m altitude) in each of 22 weather classes defined by obscuration type, visibility, absolute humidity, and cloud ceiling. The data are for different regions of Europe, the Mideast, Korea, Alaska, Scandinavia, Central America, India, Southeast Asia, South America, and Mexico.¹⁰ CLTRAN calculates slant path transmission in the wavelength regions 0.2 to 2.0 μm , 3.0 to 5.0 μm , and 8.0 to 12.0 μm through six different types of natural clouds that have been divided into stratiform and cumuliiform groups under the assumption of horizontal homogeneity and vertical variability in extinction coefficient.¹¹

EOSAEL 87 includes seven modules to address battlefield-generated aerosols. These are COPTER, COMBIC, SABRE, KWIK, GRNADE, FITTE, and MPLUME. COPTER accurately and realistically describes the obscuration in the wavelength regions 0.4 to 0.7 μm , 3.0 to 5.0 μm , 8.0 to 12.0 μm , and 0.3 to 30.0 mm resulting from helicopter downwash when a helicopter is operating near a surface covered with loose snow or dust.¹² COMBIC calculates the size, path length, concentration, and transmission in the wavelength regions 0.4 to 1.2 μm , 3.0 to 5.0 μm , 8.0 to 12.0 μm , and 3 mm for smoke clouds of white phosphorus, plasticized white phosphorus, hexachloroethane (HC), fog oil, and IR screeners and for artillery or vehicular-generated dust clouds.¹³ SABRE is a variant of COMBIC and calculates the effects of terrain for selected scenarios on windflow and smoke clouds.¹⁴ KWIK computes the number of initial and sustaining rounds, fire interval, and shell separations required to produce a smoke screen of specified length and duration for eight inventory munitions.¹⁵ GRNADE computes the obscuration produced in the wavelength regions 0.4 to 1.2 μm , 3.0 to 5.0 μm , 1.06 μm , 10.6 μm , and 3 mm produced by tube-launched LBA1 smoke grenades used for self-screening applications.¹⁶ FITTE calculates the LOS path-integrated, particle concentration; transmittance in the wavelength region 0.4 to 12.0 μm between target and observer; and both the attenuated thermal radiance from the target and the path radiance at the observer position for fires and smoke plumes from burning vegetation and real or simulated vehicle fires.¹⁷ MPLUME approximates the position and characteristics of missile smoke plumes and calculates the degradation of designation systems.¹⁸

EOSAEL 87 contains nine radiative transfer modules plus the radiative transfer driver (RTD) and an aerosol phase function data base (PFNDAT). The modules are FLOUD, OVRST, MSCAT, ASCAT, ILUMA, FASCAT, GSCAT, LASS, and REFRAC. RTD asks the user questions about the scenario, including relevant radiative transfer parameters, and then selects the radiative transfer code that will best fit the described situation.¹⁹

PFNDAT contains phase functions, extinction and scattering coefficients, and the single-scattering albedo for 38 natural and man-made aerosols at 16 wavelengths ranging from 0.55 to 12.0 μm .²⁰ FCLLOUD computes beam transmittance, path radiance, and contrast transmittance through a homogeneous ellipsoidal cloud for any wavelength included in the phase function file PFNDAT. OVRCAST computes beam transmittance, path radiance, and contrast transmittance along an arbitrary LOS under an overcast sky that is optically thick.²¹ MSCAT calculates the energy from a laser beam that arrives at a detector as a result of multiple scattering through an ellipsoidal aerosol cloud for wavelengths included in PFNDAT.²² ASCAT determines how much multiple-scattered radiation is detected for laser and transmissometer configurations for wavelengths included in PFNDAT.²³ ILUMA describes natural illumination under realistic atmospheric conditions that include clear skies, partly cloudy and overcast conditions, precipitation, and fog. Total illumination is computed as the sum of the contributions from the sun, the moon, and the background sky.²⁴ FASCAT utilizes fast computational techniques and approximations for treating single- and multiple-scattered radiation under partly cloudy conditions to compute path radiance and contrast at 0.55 and 1.06 μm .²⁵ GSCAT determines path radiance effects at visible wavelengths.²⁶ LASS determines the effectiveness at visible wavelengths of large area smoke screens deployed at large fixed and semifixed military installations.²⁷ REFRAC calculates the amount of curvature a ray of light at wavelengths between 0.4 and 2.0 μm experiences as it passes over a complex terrain surface.²⁸

Two modules in EOSAEL 87 address specific problems of the degrading effects of the atmosphere on laser beam propagation. These are IMTURB and NOVAE. IMTURB provides optical turbulence effects on propagation and imagery statistics for arbitrary slant paths in the surface boundary layer of the atmosphere for wavelengths from the visible through the IR.²⁹ NOVAE calculates linear and nonlinear effects on high-energy laser beam propagation from clear air, smokes, and aerosols for visible through IR wavelengths.³⁰

EOSAEL 87 has two system performance modules. These are TARGAC and RADAR. TARGAC evaluates the combined atmospheric and system effects to determine target acquisition ranges as a function of the probability of detection or recognition for visible and IR wavelengths.³¹ RADAR calculates absorption and backscatter at millimeter wavelengths (0.1 to 350 GHz) for rain, snow, and fog along the radar propagation path.³²

5. HANDBOOKS

EOSAEL has been used to aid in the preparation of several handbooks describing expected obscuration on the battlefield. In 1980 an ASL introductory monograph was published to describe qualitatively the obscuration factors that affect EO systems.³³ In 1981 a smoke obscuration primer was published.³⁴ This was followed in 1985 with a manual giving a convenient and concise reference for information on natural and combat-induced obscuration.³⁵ In 1986 the Combat Environments Obscuration Handbook was published.³⁶ Also in 1986 the standardization handbook, Quantitative Description of Obscuration Factors for Electro-Optical and Millimeter Wave Systems, was published.³⁷ This latter handbook was published to (1) provide data and methodology for Army design engineers to assess the effects of natural obscurants and battlefield-induced contaminants on EO and MMW systems, (2) provide the analytical community with information to calculate system performance, and (3) indicate to the test and evaluation community the effects that should be considered when a system is evaluated. In 1987 a primer on target visibility was published.³⁸ Also in 1987 a handbook was published to guide the operational tester in incorporating battlefield obscurants into the testing process.³⁹ Soon to be released will be the Smoke/Obscurants Handbook for the Electro-Optical, Millimeter Wave, and Radar Systems Developer.⁴⁰ It will provide useful examples of the realistic battlefield environment in which the sensors and systems must operate. This information will enable the materiel developer to make informed analyses and trade-offs. The handbook will also provide guidance for assessment of sensors and systems in realistic environments in developmental testing and a link between developmental testing and operational testing when realistic battlefield environments are to be specified. Also soon to be released is the Handbook for Assessment of Military Smokes and Smoke Screens.⁴¹ This handbook will provide standardized sets of definitions, performance criteria, and test methodologies. It will also identify questions and conclusions that should be addressed in future development and applications of smokes and obscurants.

These handbooks give qualitative and quantitative descriptions of battlefield atmospheric conditions. (Battlefield atmospheric has been defined as the branch of atmospheric sciences that deals with the presence of man-made as well as natural atmospheric conditions over potential battlefields and the effects of such realistic environments on materiel, personnel, tactics, or operations.)⁴² Specific purposes for the handbooks are listed in Table 1.

TABLE 1. PURPOSES OF BATTLEFIELD ATMOSPHERICS HANDBOOKS

To provide data and methodology for Army system proponents and designers to assess the effects of natural and battle-induced obscurants on EO components and systems.

To provide the analytic community with information to calculate system performance in obscured environments.

To indicate to the test and evaluation community the effects and levels of obscurants that should be considered for system evaluation.

To indicate to the training and doctrine community the effects of realistic battlefield environments on system deployment and the potential outcomes of conflicts in such environments.

The 11 rules-of-thumb given in Table 2 have been developed to estimate the effectiveness of smokes, obscurants, and weather on EO sensors. A reduction in transmittance is not the only reason for sensor defeat. Other important sensor defeat mechanisms include changes in illumination and contrast as well as attenuation of contrast caused by the obscurant cloud, scattering of light from or emission by the cloud, degradation of image resolution, and scene clutter.^{43 44}

TABLE 2. RULES OF THUMB FOR BATTLEFIELD ATMOSPHERICS

All conventional smokes (HC, fog oil, phosphorus, and anthracene) and dust at anticipated levels will screen visible and laser designator systems on at least some portions of the battlefield.

Phosphorus smokes and battlefield dust in large concentrations will screen thermal viewers (3 to 5 and 8 to 12 μ m wavelengths).

Conventional smokes other than phosphorus are not effective in the IR region unless large areas are screened so that lines of sight through these smokes are greater than 1 km.

Specially developed IR screeners will screen thermal viewers in areas where they are employed. Likewise, specially developed obscurants can screen MMW and radar systems. Visual systems may not always be screened, unless conventional smokes are also employed.

Top attack weapons offer an advantage over horizontal (ground level) line-of-sight weapons in battlefield smoke and obscurant environments.

Smoke and obscurants, acting in concert with natural reductions in visibility, can be much more effective than when used alone.

Natural reductions in visibility can defeat visual sensors (such as day sights, direct-view optics, and day TV) and laser rangefinders.

Thermal viewers provide an advantage over visual sensors in haze, fog, and light rain.

In very thick fog, as well as in snow, visual sensors and thermal viewers are both degraded about equally in performance.

Haze, fog, light rain, and snow provide much less attenuation for MMW and radar systems than for visual or IR systems; however, medium to heavy rain will adversely affect MMW systems.

Atmospheric factors will have a tremendous impact on the amounts of smokes and obscurants needed to effectively screen large areas.

6. TACTICAL DECISION AIDS (TDAs)

TDAs combine a knowledge of weather and battlefield-induced atmospheres and the effects they produce into a form that can aid the combat commander in decision-making. Weather-related TDAs have been developed and demonstrated as part of the AirLand Battlefield Environment program, the MICROFIX topographic workstation effort of the U.S. Army Forces Command, and proof-of-concept for the Integrated Meteorological System (IMETS). The plan is for IMETS to fuse and predict weather information and to automatically process the weather information into weather intelligence largely through the

use of TDAs.⁴⁵ Both weather data and weather intelligence will be disseminated from IMETS over the Army Tactical Command and Control System to automated systems throughout the battlefield.

7. CONCLUDING REMARKS

To field test each new weapon system or sensor in all conceivable battlefield weather conditions would be ideal; however, this procedure has been found both impractical and uneconomical. The operation of EO and other similar "seeing" devices follows a set of very predictable patterns, for example, Beers law of attenuation. By using computer simulation programs (models), the systems developer can predict the operational behavior of each of the sensing devices or weapon systems under varying weather conditions. Such a set of models may be found in EOSAEL. EOSAEL may be used to aid in the production of handbooks necessary for field and modeling use. Also, using EOSAEL in conjunction with handbooks and coupling these results with real-time weather have resulted in TDAs that will be operational with the fielding of the IMETS. IMETS will provide battlefield weather effects depictions in an easily understood form, automate reception of weather data from central facilities and local sensors, and fuse weather data from all sources into a comprehensive depiction of the atmosphere. Thus IMETS will provide battlefield commanders the ability to see the weather on the battlefield and to utilize environmental conditions as a force multiplier.

REFERENCES

1. Tactical Weapon Guidance and Control Information Analysis Center, U.S. Army Materiel Command, Smart Munitions Program Office, ATTN: AMSMI-RD-SM, Redstone Arsenal, Alabama 35898-5246, Smart Munitions: An Introduction to the Concepts, the Technologies, and the Systems, 1987, Primer and Briefing Manual, GACIAC SR-87-08.
2. Smart Weapons Management Office, U.S. Army Materiel Command, Smart Munitions Program Office, ATTN: AMSMI-RD-SM, Redstone Arsenal, Alabama 35898-5246, Smart Weapons Battlefield Employment, 31 January 1989, Briefing Manual.
3. TRADOC PAM 525-21 and MAC PAM 105-3, Headquarters, U.S. Army Training and Doctrine Command, Fort Monroe, Virginia 23651-5000, Joint Operational Concept for Weather and Environmental Support to Army Operations, 10 July 1987.
4. Niles, Franklin E., "EOSAEL: Past, Present, and Future," 1987, Proceedings of the Eighth Annual EOSAEL/TWI Conference, U.S. Army Atmospheric Sciences Laboratory, White Sands Missile Range, New Mexico 88002, Volume I, pp. xxxix-xlviii.
5. Shirkey, R. C., L. D. Duncan, and F. E. Niles, U.S. Army Atmospheric Sciences Laboratory, White Sands Missile Range, New Mexico 88002, EOSAEL 87: Executive Summary, 1987, ASL-TR-0221-1.
6. Pierluissi, Joseph H., and Christos E. Maragoudakis, U.S. Army Atmospheric Sciences Laboratory, White Sands Missile Range, New Mexico 88002, EOSAEL 87: Atmospheric Transmittance/Radiance Module LOWTRN, 1987, ASL-TR-0221-4.
7. Davis, Roger E., U.S. Army Atmospheric Sciences Laboratory, White Sands Missile Range, New Mexico 88002, EOSAEL 87: Laser Transmittance Module LZTRAN, 1987, ASL-TR-0221-5.
8. Brown, D. R., U.S. Army Atmospheric Sciences Laboratory, White Sands Missile Range, New Mexico 88002, EOSAEL 87: Near Millimeter Wave Module NMMW, 1987, ASL-TR-0221-6.
9. Duncan, L. D., M. A. Seagraves, and M. G. Heaps, U.S. Army Atmospheric Sciences Laboratory, White Sands Missile Range, New Mexico 88002, EOSAEL 87: Natural Aerosol Extinction Module XSCALE, 1987, ASL-TR-0221-7.
10. Avara, Elton P., and Bruce T. Miers, U.S. Army Atmospheric Sciences Laboratory, White Sands Missile Range, New Mexico 88002, EOSAEL 87: The Climatology Module CLIMAT, 1987, ASL-TR-0221-8.
11. Low, Richard D. H., and S. G. O'Brien, U.S. Army Atmospheric Sciences Laboratory, White Sands Missile Range, New Mexico 88002, EOSAEL 87: Cloud Transmission Module CLTRAN, 1987, ASL-TR-0221-9.
12. Burlbaw, Edward, U.S. Army Atmospheric Sciences Laboratory, White Sands Missile Range, New Mexico 88002, EOSAEL 87: Obscuration Due to Helicopter Lofted Snow and Dust Models COPTER, 1987, ASL-TR-0221-10.
13. Hoock, D. W., R. A. Sutherland, and D. Clayton, U.S. Army Atmospheric Sciences Laboratory, White Sands Missile Range, New Mexico 88002, EOSAEL 87: Combined Obscuration Model for Battlefield-Induced Contaminants COMBIC, 1987, ASL-TR-0221-11.
14. Maynard, Harry W., Donald W. Hoock, Frank V. Hansen, and Teizi Henmi, U.S. Army Atmospheric Sciences Laboratory, White Sands Missile Range, New Mexico 88002, EOSAEL 87: Simulation of Aerosol Behavior in Realistic Environments SABRE, 1987, ASL-TR-0221-12.

15. Peña, Ricardo, U.S. Army Atmospheric Sciences Laboratory, White Sands Missile Range, New Mexico 88002, EOSAEL 87: A Munitions Expenditures Module KWIK, 1987, ASL-TR-0221-13.
16. Davis, Roger E., and Robert A. Sutherland, U.S. Army Atmospheric Sciences Laboratory, White Sands Missile Range, New Mexico 88002, EOSAEL 87: Self-Screening Applications Module GRNADE, 1987, ASL-TR-0221-14.
17. Bruce, Dorothy, U.S. Army Atmospheric Sciences Laboratory, White Sands Missile Range, New Mexico 88002, EOSAEL 87: Fire-Induced Transmission and Turbulence Effects Module FITTE, 1987, ASL-TR-0221-15.
18. Manning, Joseph L., and Timothy J. Rogne, U.S. Army Atmospheric Sciences Laboratory, White Sands Missile Range, New Mexico 88002, EOSAEL 87: Missile Smoke Plume Obscuration Code MPLUME, 1987, ASL-TR-0221-16.
19. Miller, August, and Gary J. Garwood, U.S. Army Atmospheric Sciences Laboratory, White Sands Missile Range, New Mexico 88002, EOSAEL 87: Radiative Transfer Driver Module RTD, 1987, ASL-TR-0221-17.
20. Shirkey, R. C., R. A. Sutherland, and M. A. Seagraves, U.S. Army Atmospheric Sciences Laboratory, White Sands Missile Range, New Mexico 88002, EOSAEL 87: Aerosol Phase Function Data Base PFNDAT, 1987, ASL-TR-0221-26.
21. Turner, Robert E., U.S. Army Atmospheric Sciences Laboratory, White Sands Missile Range, New Mexico 88002, EOSAEL 87: Contrast Transmission Module FCLOUD and OVRCT, 1987, ASL-TR-0221-18.
22. O'Brien, S. G., U.S. Army Atmospheric Sciences Laboratory, White Sands Missile Range, New Mexico 88002, EOSAEL 87: Aerosol Multiple Scattering Module MSCAT, 1987, ASL-TR-0221-19.
23. Zardecki, A., S. A. W. Gerstl, and R. C. Shirkey, U.S. Army Atmospheric Sciences Laboratory, White Sands Missile Range, New Mexico 88002, EOSAEL 87: Approximate Multiple Scattering Module ASCAT, 1987, ASL-TR-0221-20.
24. Duncan, Louis D., David P. Sauter, and August Miller, U.S. Army Atmospheric Sciences Laboratory, White Sands Missile Range, New Mexico 88002, EOSAEL 87: Natural Illumination Under Realistic Weather Conditions ILUMA, 1987, ASL-TR-0221-21.
25. Hering, Wayne S., Richard W. Johnson, and August Miller, U.S. Army Atmospheric Sciences Laboratory, White Sands Missile Range, New Mexico 88002, EOSAEL 87: FASCAT Atmospheric Illumination Module, 1987, ASL-TR-0221-22.
26. Davis, Roger E., and Robert Sutherland, U.S. Army Atmospheric Sciences Laboratory, White Sands Missile Range, New Mexico 88002, EOSAEL 87: Single Scattering of Visible Radiation through Gaussian Clouds GSCAT, 1987, ASL-TR-0221-23.
27. Davis, R. E., and R. A. Sutherland, U.S. Army Atmospheric Sciences Laboratory, White Sands Missile Range, New Mexico 88002, EOSAEL 87: Large Area Screening Systems Applications Module LASS 87, 1987, ASL-TR-0221-24.
28. Tofsted, David H., U.S. Army Atmospheric Sciences Laboratory, White Sands Missile Range, New Mexico 88002, EOSAEL 87: Optical Path Bending Code Module REFRAC, 1987, ASL-TR-0221-25.
29. Miller, Walter B., and Jennifer C. Ricklin, U.S. Army Atmospheric Sciences Laboratory, White Sands Missile Range, New Mexico 88002, EOSAEL 87: A Module for Imaging through Optical Turbulence IMTURB, 1989, ASL-TR-0221-27.
30. Gebhardt, Frederick G., M. B. Richardson, Patti Gillespie, and Alan Wetmore, U.S. Army Atmospheric Sciences Laboratory, White Sands Missile Range, New Mexico 88002, EOSAEL 87: Nonlinear Aerosol Vaporization Breakdown Effects Module NOVAE, 1987 (to be published), ASL-TR-0221-28.
31. Davis, John M., U.S. Army Atmospheric Sciences Laboratory, White Sands Missile Range, New Mexico 88002, EOSAEL 87: Target Acquisition Model TARGAC, 1987, ASL-TR-0221-29.
32. D'Arcy, Edward M., U.S. Army Atmospheric Sciences Laboratory, White Sands Missile Range, New Mexico 88002, EOSAEL 87: Millimeter Wave System Performance Module RADAR, 1987, ASL-TR-0221-30.
33. Kays, Marvin D., Mary Ann Seagraves, Hubert H. Monahan, and Robert A. Sutherland, U.S. Army Atmospheric Sciences Laboratory, White Sands Missile Range, New Mexico 88002, Qualitative Description of Obscuration Factors in Central Europe, 1980, ASL Monograph No. 4.
34. Joint Technical Coordinating Group for Munitions Effectiveness, U.S. Army Material Systems Analysis Activity, Aberdeen Proving Ground, Maryland 21005, Smoke: An Obscuration Primer, 1981, 61 JTCG/ME-77-13.

35. Joint Technical Coordinating Group for Munitions Effectiveness, U.S. Army Materiel Systems Analysis Activity, Aberdeen Proving Ground, Maryland 21005, Smoke and Natural Aerosol Parameters (SNAP) Manual, 1985, 61 JTCG/ME-85-2.
36. Joint Technical Coordinating Group for Munitions Effectiveness, U.S. Army Materiel Systems Analysis Activity, Aberdeen Proving Ground, Maryland 21005, Combat Environments Obscuration Handbook (CEOH), Volume I - Natural and Combat-Induced Obscurants and Environments, 1986, 61 JTCG/ME-84-1-1.
37. Military Handbook, U.S. Army Atmospheric Sciences Laboratory, White Sands Missile Range, New Mexico 88002-5501, Quantitative Description of Obscuration Factors for Electro-Optical and Millimeter Wave Systems, 1986, DOD-HDBK-178(EK).
38. Joint Technical Coordinating Group for Munitions Effectiveness, U.S. Army Materiel Systems Analysis Activity, Aberdeen Proving Ground, Maryland 21005, A Primer on Target Visibility in Adverse Weather, 1987, 61 JTCG/ME-85-8.
39. Joint Technical Coordinating Group for Munitions Effectiveness, U.S. Army Materiel Systems Analysis Activity, Aberdeen Proving Ground, Maryland 21005, Handbook for Operational Testing of Electro-Optical Systems in Battlefield Obscurants, 1987, 61 JTCG/ME-87-10.
40. Joint Technical Coordinating Group for Munitions Effectiveness, U.S. Army Materiel Systems Analysis Activity, Aberdeen Proving Ground, Maryland 21005, Smoke/Obscurants Handbook for the Electro-Optical, Millimeter Wave, and Radar Systems Developer, to be published.
41. Joint Technical Coordinating Group for Munitions Effectiveness, U.S. Army Materiel Systems Analysis Activity, Aberdeen Proving Ground, Maryland 21005, Handbook for Assessment of Military Smokes and Smoke Screens (Fundamental Considerations), to be published.
42. Heaps, Melvin G., and Franklin E. Niles, U.S. Army Atmospheric Sciences Laboratory, White Sands Missile Range, New Mexico 88002, "Battlefield Atmospherics (U)," Army Science Conference Proceedings, 25-27 October 1988, Volume I, pp. 449-462.
43. Heaps, Melvin G., and Franklin E. Niles, U.S. Army Atmospheric Sciences Laboratory, White Sands Missile Range, New Mexico 88002, "Battlefield Obscuration Factors," Proceedings of the NATO/AGARD Electromagnetic Wave Propagation Panel, 15-19 May 1989, Naval Ocean Systems Center, San Diego, California.
44. Seagraves, Mary Ann, U.S. Army Atmospheric Sciences Laboratory, White Sands Missile Range, New Mexico 88002, Weather and Environmental Effects on Electro-Optical Devices: A Tutorial, ASL Technical Report (to be published).
45. Niles, Franklin E., and Bernard F. Engebos, U.S. Army Atmospheric Sciences Laboratory, White Sands Missile Range, New Mexico 88002, "Tactical Weather Intelligence: Past, Present, and Future," Proceedings for the Ninth Annual EOSAEL/TWI Conference, 29-30 November and 1 December 1988, pp. xi-xvii.

Models of Aerosols, Clouds and Precipitation for Atmospheric Propagation Studies

Eric P. Shettle
AFGL/OPA, Hanscom AFB, Bedford, MA 01731-5000, USA

SUMMARY

This paper will review a number of models for the atmospheric aerosols, clouds, and precipitation and their effects on the propagation of electromagnetic radiation at wavelengths from the ultraviolet through the microwave spectral regions. The focus will be on the models developed at AFGL and elsewhere primarily for use in the atmospheric propagation models LOWTRAN (Kneizys et al., 1983 & 1988) and FASCODE (Clough et al., 1986), but also will examine other particulate models.

The scattering and absorption properties of the different particulate models will be presented. Applications of the various models will be discussed with recommendations on when it is most appropriate to use which aerosol or cloud model. Sensitivities of calculated transmittances and background radiances to the different types of particulate models, will be examined for a range of wavelengths.

1. INTRODUCTION

Propagation of electromagnetic radiation at optical/infrared frequencies through the atmosphere is affected by absorption and scattering by air molecules and by particulates (e.g. haze, dust, fog, and clouds) suspended in the air. Scattering and absorption by haze or aerosols becomes the dominant factor in the boundary layer near the earth's surface, especially in the visible, and under reduced visibility conditions at all wavelengths. These atmospheric particles vary greatly in their concentration, size, and composition, and consequently in their effects on radiation.

This paper will describe the optical & infrared properties of the different types of particulates which are present in the atmosphere and provide summary of the various models developed at AFGL and elsewhere. The physical characteristics of the particulates which affect the propagation of radiation through the atmosphere will be considered. The greatest emphasis will be on the atmospheric aerosols, since they exhibit the largest degree of variability in their nature and properties. Further discussion of much of the material covered in this paper, particularly on the AFGL models, is given by Fenn et al. (1985), and the references therein.

2. AEROSOLS

Figure 1 summarizes the general characteristics of the atmospheric aerosols. Aerosols in the boundary layer of 1 to 2 kilometer thickness near the surface have the greatest variability. These aerosols consist of a variety of natural and man-made chemical compounds, inorganic as well as organic. Particles are transported from their source regions into the atmosphere, or maybe formed within the atmosphere by gas to particle conversion through chemical or photochemical processes.

Since over two-thirds of the earth's surface is covered by oceans, the marine aerosol component, which consists largely of sea salt solution particles and sulfates from the oxidation of dimethylsulphide (DMS) produced by the oceanic phytoplankton, is the most prevalent aerosol source. The wind blown dust advected from the desert regions is most important continental aerosol source. Table 1 gives a breakout of the global tropospheric aerosol composition. A recent review of the physical and chemical properties of the atmospheric aerosols is provided by Jaenicke (1988).

Figure 1 - Characteristics of the atmospheric aerosols as a function of altitude.

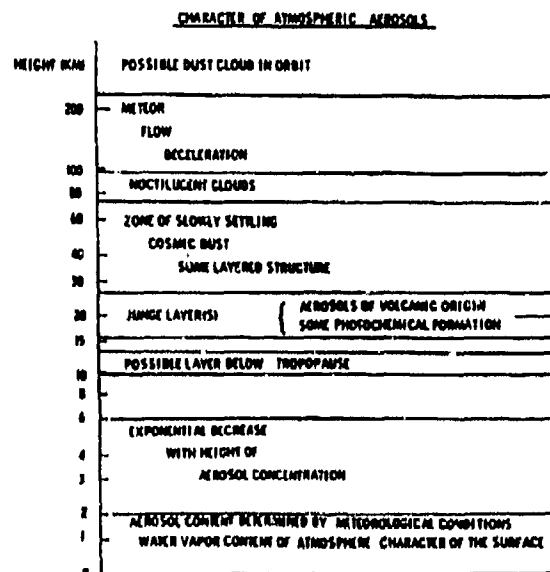


Table 1 - Estimated contribution of different sources to atmospheric particulates (10^6 metric tons/year) SMIC (1971)

| | |
|---|-----------------|
| Natural | |
| Soil and rock debris* | 100-500 |
| Forest fires and slash-burning debris* | 3-150 |
| Sea salt | 300 |
| Volcanic debris | 25-150 |
| Particles formed from gaseous emissions: | |
| Sulfate from H_2S | 130-200 |
| Ammonium salts from NH_3 | 80-270 |
| Nitrate from NO_x | 60-430 |
| Hydrocarbons from plant exudations | 75-200 |
| Subtotal | 773-2200 |
| Man-made | |
| Particles (direct emissions) | 10-90 |
| Particles formed from gaseous emissions: | |
| Sulfate from SO_2 | 130-200 |
| Nitrate from NO_x | 30-35 |
| Hydrocarbons | 15-90 |
| Subtotal | 185-415 |
| Total | 958-2615 |

*Includes unknown amounts of indirect manmade contributions.

2.1 Aerosol Models

A large number of aerosol models have been developed over the years describing the optical properties of the atmospheric aerosols and their effects on the propagation of radiation. Table 2 summarizes the models, developed during the last quarter century, which were intended for general use. Some of these neglected variations in the types of aerosol for different environments (Elterman and McClatchey et al.). Others did not specify the vertical distribution of the aerosols (Deirmendjian) or only described aerosols for the boundary layer (the work of Hänel & Bullrich, of Nilsson, and of d'Almeida & Koepke).

There have also been a number of different aerosol models developed to characterize the aerosol properties for a specific environment. These are given in Table 3 for the Marine, Desert and Stratospheric aerosols. Other versions of these specific aerosol types are also incorporated into the more general models discussed above and in Table 2.

Table 2 - General Aerosol Models

| MODEL | COMMENTS |
|---|---|
| Deirmendjian (1964 & 1969) | Attenuation Coeff. from Size Dist. & Ref. Index, for Continental, Maritime, & Stratospheric Aerosols, Clouds, and Rain |
| Elterman (1964, 1968, & 1970) | Vertical Profile & Empirical Wavelength Dependence |
| Ivlev (1967 & 1969) | Vertical Profiles, Size Distribution, & Ref. Index for Mixed Composition Aerosols |
| McClatchey et al. (1970) | Vertical Profile (from Elterman) - Single Size Dist. & Ref. Index |
| Shettle & Fenn (1976 & 1979) | Vertical Profiles (Seasonal & Volcanic dependence) - Rural, Urban, Maritime, Stratospheric, & Volcanic Aerosols - Size Dist. & Ref. Indices with Relative Humidity Dependence |
| Toon & Pollack (1976) | Boundary Layer, Tropospheric, & Stratospheric Aerosols - Size & Ref. Index - Primarily for Climate Studies |
| Hänel & Bullrich (1978) | Boundary Layer Models - Size Dist. & Ref. Index with Relative Humidity Dependence |
| Nilsson (1979) | Various Boundary Layer Aerosols with Size, Composition, & Relative Humidity Dependence |
| Kondratyev et al. (1981 & 1983) | Vertical Profiles - Various Tropospheric & Stratospheric Aerosols - Size, Composition, & Relative Humidity Dependence |
| I A M A P / Radiation Commission (1986) | Vertical Profiles - Tropospheric & Stratospheric Aerosols with Size & Ref. Index - Primarily Standard Models for Intercomparison of Radiation & Climate Models |
| d'Almeida & Koepke (1988a & 1988b) | Ten Different Types of Boundary Layer Aerosols with Size, Composition, & Relative Humidity Dependence, specified on a 5°x5° global grid |

Table 3 - Specific Aerosol Models

| MARINE AEROSOLS | DESERT AEROSOLS | STRATOSPHERIC AEROSOLS |
|--|---|--|
| Barnhardt & Streete (1970) | Joseph (1975) | Pinnick, Rosen, & Hoffmann (1976) |
| Hodges (1972) | Carlson & Caverly (1977) and Carlson & Benjamin (1980) | Turco et al. (1979) and Toon et al. (1979) |
| Wells, Gal, & Munn (1977) | Shettle (1985) and Longtin, Shettle, & Hummel (1987 & 1988) | Brogneiz & Lenoble (1987) |
| Gathman (1983a & 1983b) | d'Almeida (1987) | Hummel, Shettle, & Longtin (1988) |
| de Leeuw et al. (1989) Gathman, et al. (1989) | | |

2.2 Boundary Layer Aerosols

The boundary layer aerosol models include those representative of rural, urban, maritime, and desert environments, as well as fog models. Most of these models include a dependence on the relative humidity, and in the case of the maritime and desert models a dependence on the prevailing winds.

The effects of relative humidity become increasingly important as the atmosphere approaches saturation. For most atmospheric aerosols there is little accretion of water for relative humidities below 70 to 80%, (for some nitrates the critical relative humidity is as low as 50%, Pruppacher & Klett, 1978). This means the relative humidity effects are most important for the tropospheric aerosols where these relative humidities are frequently exceeded. The effect of increasing relative humidity is for the particles to grow through the accretion of water, which also means a change in the composition and effect refractive index of the aerosol particle.

The size distributions of atmospheric particulates are commonly represented by analytic functions. The most commonly used of these are the log-normal distribution:

$$n(r) = \frac{dN(r)}{dr} = \sum_{i=1}^2 \frac{N_i}{\ln(10) r \sigma_i \sqrt{2\pi}} \exp \left[-\frac{(\log r - \log r_i)^2}{2\sigma_i^2} \right] \quad (1)$$

where $N(r)$ is the cumulative number density of particles of radius r , σ_i is the standard deviation, r_i is the mode radius, and N_i is the total number, for the i^{th} mode; and the modified gamma distribution:

$$dN/dr = n(r) = a r^\alpha \exp(-b r^\gamma), \quad (2)$$

where a , α , b , and γ are parameters defining the size distribution.

Typical characteristics and sizes for the boundary layer models are given in Table 4, where the size parameters refer to the log-normal size distribution (eq. 1). The precise values of the parameters will change with variations in the relative humidity, and in the case of maritime aerosols with variations in the wind speed and duration of time since the air mass was over land (Gahman, 1983a & 1983b).

Table 4 - Representative Sizes and Composition for Boundary Layer Aerosols

| Aerosol Model | Size Distribution | | | Type |
|--------------------|-------------------|-------|------------|---|
| | N_i | r_i | σ_i | |
| Rural | 0.999875 | 0.03 | 0.35 | Mixture of Water Soluble and Dust-Like Aerosols |
| | 0.000125 | 0.5 | 0.4 | |
| Urban | 0.999875 | 0.03 | 0.35 | Rural Aerosol Mixtures with Soot-Like Aerosols |
| | 0.000125 | 0.5 | 0.4 | |
| Maritime | | | | |
| Continental Origin | 0.99 | 0.03 | 0.35 | Rural Aerosol Mixture |
| Oceanic Origin | 0.01 | 0.3 | 0.4 | Sea Salt Solution in Water |
| Tropospheric | 1.0 | 0.03 | 0.35 | Rural Aerosol Mixture |

For desert regions, in the absence of vegetation to hold the surface particles in place, the size distribution can be related to the prevailing wind velocities. Figure 2 shows the desert aerosol size distribution changes with wind speed for the models of d'Almeida (1987) and of Longtin et al. (1988a & 1988b).

Given the size distribution and complex refractive index for the atmospheric aerosols their radiative properties can be determined from Mie scattering calculations. Figure 3 illustrates the extinction coefficients for the rural aerosol model as a function of wavelength for several relative humidities. Figure 4 shows the angular scattering function (often referred to as the phase function) for marine aerosols for several wavelengths.

2.3 Stratospheric Aerosols

The aerosols normally present in the lower stratosphere (from the tropopause up to about 30 km), are largely sulfuric acid solution droplets. These are produced through photochemical reactions involving carbonyl sulfide (COS), sulfur dioxide (SO₂) and other gases (Whitten et al., 1980 and Toon & Farlow, 1981). The background stratospheric aerosols are often perturbed major volcanic eruptions (such as el Chichon) which can inject significant amounts of SO₂ and volcanic ash into the stratosphere. The larger volcanic ash particles will settle out in a short period of time but the sulfuric acid aerosols produced from the SO₂ will persist for several years, with a 1/e loss time of ≈ 12 months.

Representative values for the vertical distributions of the aerosol extinction are shown in Figure 5 for moderate, high, and extreme volcanic profiles in addition to the background conditions. Figure 6 illustrates the wavelength dependence of the different stratospheric aerosol models.

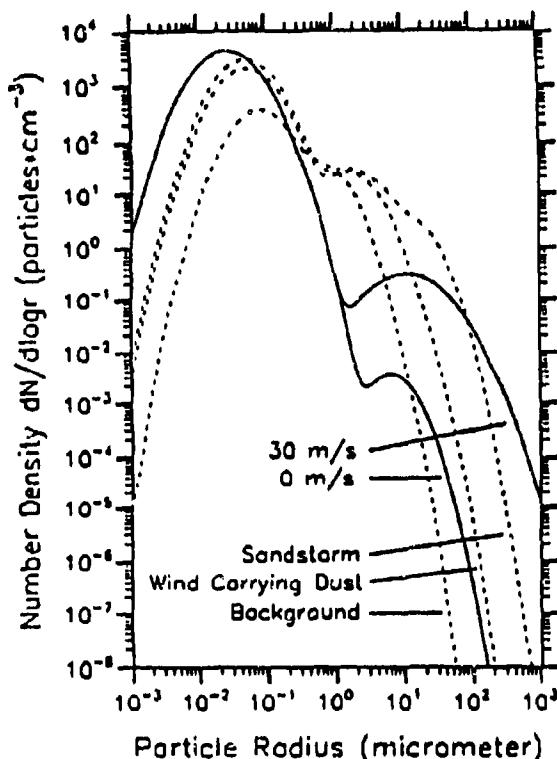


Figure 2. Number density distribution for the Longtin et al. (1988) desert model (solid lines) and that of d'Almeida (1987) (dashed lines).

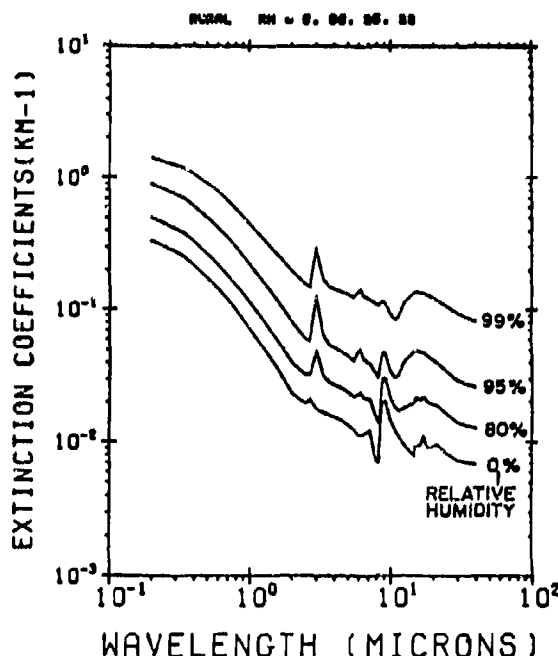


Figure 3. Extinction coefficients vs wavelength for the rural aerosol model with different relative humidities and a number density of $15,000 \text{ cm}^{-3}$.

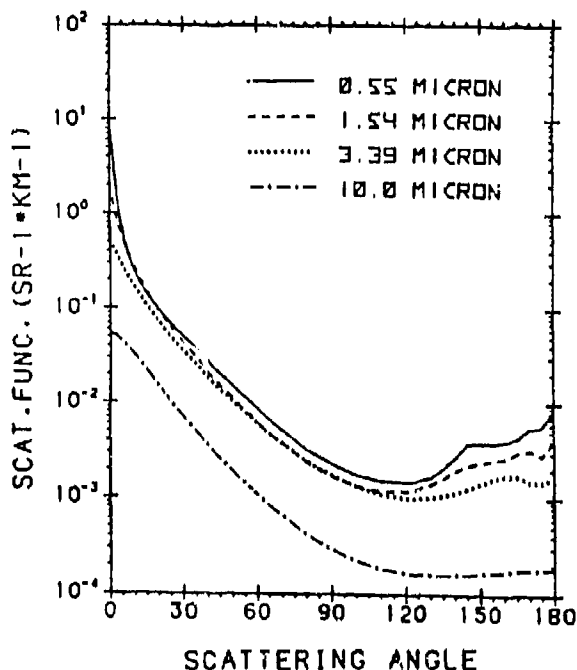


Figure 4. Angular scattering function for the Shettle & Fenn (1979) maritime aerosol model with a relative humidity of 80% and a number density of $4,000 \text{ cm}^{-3}$ for several wavelengths.

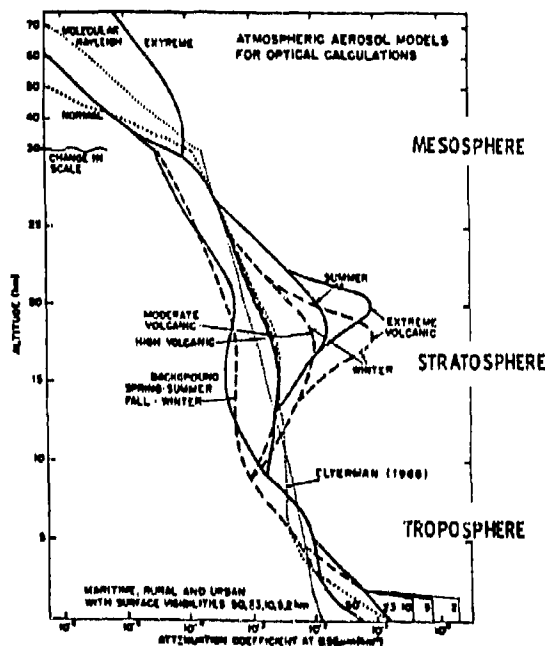


Figure 5. The vertical distribution of the aerosol extinction (at $0.55 \mu\text{m}$) for the Shettle & Fenn (1976) aerosol models. Also shown for comparison are the Rayleigh molecular scattering profile (dotted line) and Elterman's (1968) model. Between 2 and 30 km, where a distinction on a seasonal basis is made, the spring-summer conditions are indicated with a solid line and the fall-winter conditions a dashed line.

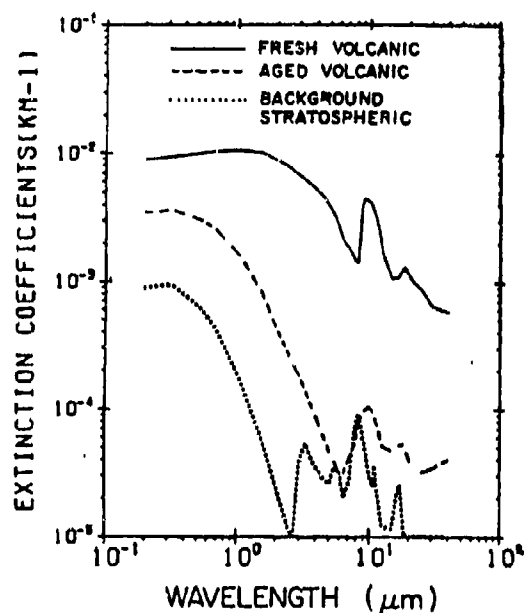


Figure 6. Extinction coefficients for the different stratospheric aerosol models. The extinction coefficients have been normalized to values near peak levels for these models.

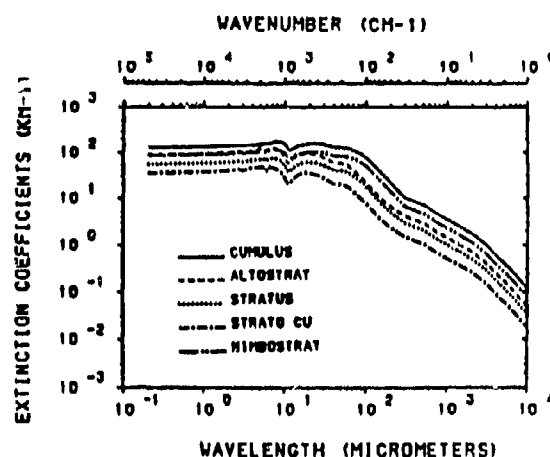


Figure 7. Spectral dependence of the extinction coefficients for the different water clouds.

3. FOG & CLOUD MODELS

There are five water cloud models (Cumulus, Stratus, Stratus/Strato-Cumulus, Alto-Stratus, & Nimbo-Stratus) which are included in LOWTRAN (Kneizys et al., 1988) & FASCODE (Clough et al., 1986 & 1988). These are based on a subset of the cloud models developed by Silverman and Sprague (1970), and discussed by Falcone et al. (1979) and Fenn et al. (1985). They were selected in part to encompass as wide a range as possible of the optical/IR properties of the ten cloud models developed by Silverman and Sprague, (the two extreme fog models of the four they developed are also used). The droplet size distributions for the models are represented by a modified gamma distribution (Eq. 2), with $\gamma = 1$. The values of the parameters characterizing the cloud droplet size distributions are summarized in Table 5.

Table 5 - Parameters for Fog & Cloud Size Distribution Models used in LOWTRAN & FASCODE

| Cloud Type | α | h | a | $N_0^* (\text{cm}^{-3})$ | $W^* (\text{g-m}^{-3})$ | $R_N (\mu\text{m})$ | $R_M (\mu\text{m})$ | $\text{Ext}^* (\text{km}^{-1}, \lambda=0.55\mu\text{m})$ |
|------------------------|----------|---------|-----------------------|--------------------------|-------------------------|---------------------|---------------------|--|
| Heavy Advection Fog | 3 | 0.3 | 0.027 | 20 | 0.37 | 10.0 | 20.0 | 28.74 |
| Moderate Radiation Fog | 6 | 3.0 | 607.5 | 20 | 0.02 | 2.0 | 3.0 | 8.672 |
| Cumulus | 3 | 0.5 | 2.604 | 250 | 1.00 | 6.0 | 12.0 | 130.8 |
| Stratus | 2 | 0.6 | 27.0 | 250 | 0.29 | 3.33 | 8.33 | 55.18 |
| Stratus/Strato-Cumulus | 2 | 0.75 | 52.734 | 250 | 0.15 | 2.67 | 6.67 | 35.65 |
| Alto-Stratus | 5 | 1.111 | 6.268 | 400 | 0.41 | 4.5 | 7.2 | 91.04 |
| Nimbo-Stratus | 2 | 0.425 | 7.676 | 200 | 0.65 | 4.7 | 11.76 | 87.08 |
| Cirrus | 6 | 0.09375 | $2.21 \cdot 10^{-12}$ | 0.025 | 0.06405 | 64.0 | 96.0 | 1.011 |
| Thin Cirrus | 6 | 1.5 | 0.011865 | 0.5 | $3.128 \cdot 10^{-4}$ | 4.0 | 6.0 | 0.0831 |

*Nominal values are shown for the number density, (N_0), the liquid water (or ice) content (W), and the visible extinction (Ext); they can be specified by the user in running the codes. R_N and R_M denote the mode radii for the number and mass distribution respectively.

Other cloud models are described by Carrier et al. (1967) and by Stephens (1978a & 1978b)). The latter were partially based on the size distributions of Carrier. Falcone et al. (1979) pointed out there are some inconsistencies between Carrier's size distributions and his original references. A review of fog properties is given by Stewart & Essenwanger (1982).

The radiative properties of the clouds were derived from Mie scattering calculations using the refractive index of water from Hale & Querry (1973) for wavelengths through 200 μm , and from Ray (1972) for the longer wavelengths. The resulting extinction coefficients for the cloud models are shown in Figure 7 as a function of wavelength.

There are three cirrus cloud models in LOWTRAN7, the NOAA model (Hall et al. 1983), which is retained for consistency with LOWTRAN6 and FASCOD2, and two new cirrus models, one for regular cirrus and the other for optically thin (or sub-visual) cirrus. The NOAA cirrus model was empirically based, assuming the extinction due to cirrus was independent of wavelength; it is only valid in the visible and IR and does not separate the scattering and absorption, so it can not be used for radiance calculations. To alleviate these limitations the new cirrus models were developed. The ice size distribution is similar to one used by Liou (1974) with different choices for the mode radius. The parameter values used for the two new cirrus models are given in Table 5.

For simplicity in the Mie calculations, the cirrus particles were assumed to be spherical, rather than cylindrical or platelets. The major spectral characteristics of the models should not be affected by this assumption, although the detailed values will be. The refractive index of ice was taken from Fenn et al. (1985) and from Warren (1984). The calculated values of the attenuation coefficients for the cirrus models are shown in Figure 8.

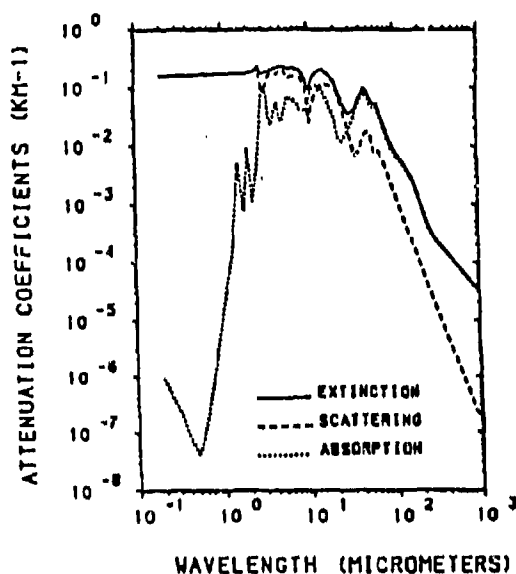


Figure 8a. Attenuation coefficients for the thin (sub-visual) cirrus cloud model with an ice crystal concentration of 1 cm^{-3} .

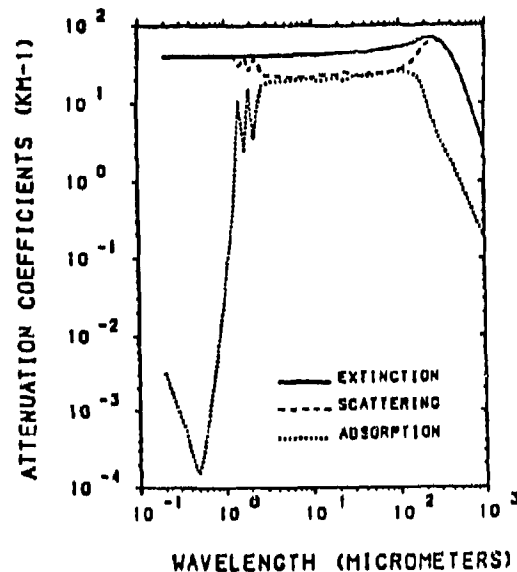


Figure 8b. Same as Fig. 8a for regular cirrus.

It should be recognized that real clouds can exhibit a very complex three-dimensional structure, unlike the LOWTRAN cloud models which only permit vertical variations in their concentration. The measurements of Eloranta & Grund (1989) presented at this symposium illustrate this very clearly.

4. PRECIPITATION MODELS

4.1 Rain Models

The most commonly used representation for the size distribution of raindrops is the exponential:

$$dN/dD = N_0 \exp(-\Lambda D), \quad (3)$$

where D is the diameter and N_0 and Λ are parameters. It dates back at least to Marshall & Palmer (1948), and is a special case of the modified gamma distribution (Eq. 2), with $\alpha=0$ and $\gamma=1$. They fit Eq. (3) to the measurements of Laws & Parsons (1943), finding $N_0 = 80,000 \text{ mm}^{-4}$ to be a constant and $\Lambda = 4.1 R^{-0.21} (\text{mm}^{-1})$, where R is the rain rate in mm/hr. More recently Joss & Waldvogel (1969) and Sekhon & Srivastava (1971) have used the exponential form where the choice of N_0 and Λ depend on the type of rainfall.

In the visible and IR it is possible to derive a analytic expression for the extinction, since the raindrops are large compared with the wavelength and the geometric optics limit applies. In this case the Mie extinction efficiency factor can be approximated as 2, independent of the wavelength. For rain size distribution the parameters are constants or have a power law dependence on the rainrate (as is the case for the size distributions discussed above), then the extinction coefficient, β_{ext} , can be related to the rainrate by a power law:

$$\beta_{\text{ext}} = AR^B. \quad (4)$$

The values for the parameters A and B corresponding to the various rain distributions are summarized in Table 6, where β has units of km^{-1} with R in mm/hr. The resulting extinction coefficients are shown in Figure 9 as a function of wavelength. Also shown for comparison, are some representative values of the extinction derived from various measured size distributions.

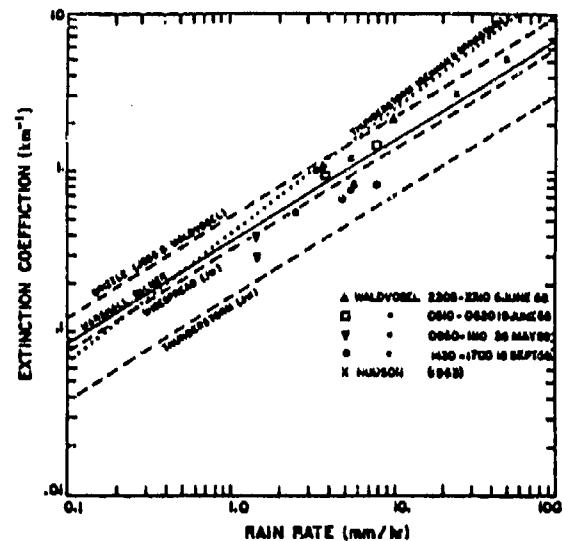


Figure 9. The visible and near IR extinction coefficients as a function the rainrate for several different rain models (see Table 6). The individual points were calculated from the measured size distributions for various rainfalls.

For longer wavelengths the assumption that the Mie extinction efficiency is 2, begins to breakdown and exact Mie scattering calculations should be used. For intermediate wavelengths (less than 0.3 mm) an empirical expression for the efficiency factor Q_{Ext} for water drops due to van de Hulst (1957) can be used:

$$Q_{\text{Ext}} = 2 + 1.84x^{-2/3}, \quad (5)$$

where $x = 2\pi r/\lambda$ is the size parameter. Using the van de Hulst approximation (Eq. 5) with the raindrop size distribution (Eq. 3) in integrating the extinction over the droplet size distribution leads to the following expression for extinction:

$$\beta_{\text{Ext}} = \pi N_0 \Lambda^3 + 0.46\pi^{1/3} N_0 \Lambda^{2/3} \Gamma(7/3), \quad (6)$$

where Γ is the Gamma Function. Evaluating this expression, it simplifies to:

$$\beta_{\text{Ext}} = A R^B + C \Lambda^{2/3} R^D, \quad (7)$$

where A, B, C, and D are parameters whose values are given in Table 6. Without the wavelength dependent correction (the term on the right-hand side of Eq. 7), Eq. (7) reduces to the power law approximation (Eq. 4) for the extinction due to rain.

Table 6 - Parameters Relating Size Distribution (Eq. 3) and Extinction Coefficient (Eq. 4 or 7) to the Rain Rate for Different Rain Models

| Type of Rain | N_0 ($\text{mm}^{-1}\text{m}^{-3}$) | Λ (mm^{-1}) | A* | B* | C* | D* |
|--|---|--------------------------------|-------|------|-------|-------|
| Marshall-Palmer (1948) | 8,000 | $4.1R^{-0.21}$ | 0.365 | 0.63 | 0.238 | 0.49 |
| Drizzle (Joss & Waldvogel, 1969) | 30,000 | $5.7R^{-0.21}$ | 0.509 | 0.63 | 0.415 | 0.49 |
| Widespread (Joss & Waldvogel, 1969) | 7,000 | $4.1R^{-0.21}$ | 0.319 | 0.63 | 0.319 | 0.49 |
| Thunderstorm (Joss & Waldvogel, 1969) | 1,400 | $3.0R^{-0.21}$ | 0.163 | 0.63 | 0.087 | 0.49 |
| Thunderstorm (Sekhon & Srivastava, 1971) | $7,000R^{0.37}$ | $3.8R^{-0.14}$ | 0.401 | 0.79 | 0.249 | 0.697 |

* The values for the parameters A, B, C, & D are for the rainrate R in mm/hr and the wavelength Λ in mm.

It might be noted that Nussenzweig and Wiscombe (1980) have derived a more accurate general expression, $\tau = \frac{1}{2} \pi x^3$ (Eq. 5), with the coefficient for $x^{3/2}$ equal to 1.992 instead of 1.84 plus higher order terms in x , with a dependence on the complex refractive index. However simply neglecting the higher order terms in the Nussenzweig and Wiscombe result does not do as well as using Eq. (5), which is accurate to better than 3% for wavelengths less than 0.3 mm.

4.2 Snow Models

Snow flakes present an interesting problem with regard to the optical effects because of their extremely complex shapes and dimensions. Under most conditions simple snow crystals have an approximate hexagonal symmetry. However their size and shape are influenced by the temperature and humidity conditions existent during their formation and growth. The standard classification scheme is that of Magno & Lee (1966). Further complicating the picture is the essentially infinite variety of agglomerates, (formed by collisions between individual snowflakes) that can exist, the fact that any of the basic crystals will be modified by the attachment of super-cooled waterdrops in a process called riming. A recent review of models for the effects of falling snow on atmospheric propagation is given by Koh (1989).

Studies by a number of investigators have addressed the question of the relationship between snow fall rate and extinction. The results as shown in Figure 10 (based on the work of Mason, 1978), vary widely, due to both variations in the crystal habit or the size distributions and to uncertainties in the measurement of the snow fall rate. It also should be noted that the attenuation due to snow (for all the data sets) is larger than the attenuation due to rain for the same mass precipitation rate, as was noted by Gibbons (1989) at this meeting. This is expected since the effective cross-sectional area of snowflakes will be larger than raindrops, since spheres have the minimum mean cross-section for a given volume and because ice is less dense than water.

The scatter in the extinction versus precipitation rate of Figure 10 can be reduced by using not the equivalent liquid water precipitation-rate but the actual rate of accumulated depth of precipitation, (which is much harder to accurately measure for snow). The results of the different studies in Figure 10 can be expressed as power-law identical to the relation between rainrate and extinction (Eq. 4), where R is generalized to the equivalent liquid water precipitation rate. Converting the equivalent liquid water, R , to snow depth, S , using the meteorological "rule-of-thumb" of 1 mm rain to 10 mm of snow (Miller & Thompson, 1970), this generalized expression for extinction (Eq. 4) as function of precipitation-rate becomes:

$$\beta = A'S^B \quad (8)$$

$$\text{where} \quad A' = A(1/10)^B, \quad (9)$$

and S is the rate of snow accumulation. The conversion from equivalent liquid water to actual snow depth will vary from less than 1 to 5 for wet-heavy snow to greater than 1 to 20 for dry-powdery snow.

The values for the parameters A and B given by Mason (1978), and the corresponding values of the parameter A' (calculated using Eq. 9), are given in Table 7. The resulting dependence of the extinction on the snow accumulation rate (Eq. 8) is shown in Figure 11, where the extinction for the Marshall-Palmer rain model is shown for comparison. The extinction due to rain now is bracketed by the different snow models.

Table 7 - Parameters Relating the Extinction Due to Snow to the Snow Precipitation Rate Expressed as Equivalent Liquid Water, in mm/hr. (Eq. 4), and Expressed as Accumulated Snow Fall, in mm/hr. (Eq. 8)

| Investigator | A | B | A' |
|-----------------------|-------|------|-------|
| Lillesaeter | 3.93 | 1.0 | 0.393 |
| Zel'manovich | 1.3 | 0.5 | 0.411 |
| Polyakova & Tretjakov | 3.2 | 0.91 | 0.394 |
| Mellor | 1.11 | 0.42 | 0.422 |
| Warner & Gunn | 2.53 | 1.0 | 0.253 |
| O'Brien | 1.393 | 0.69 | 0.284 |

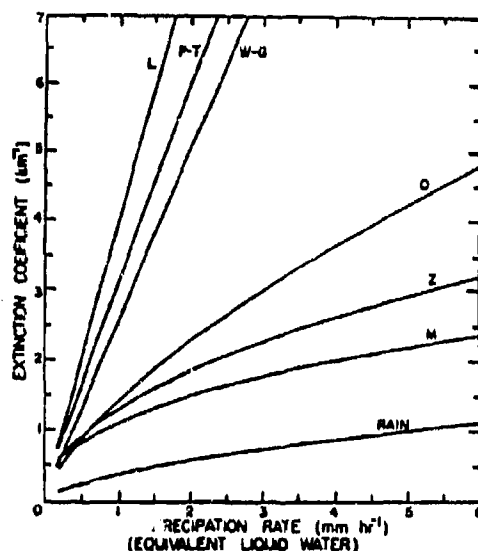


Figure 10. The extinction during falling snow as a function of precipitation rate as equivalent liquid water for several snow models (adapted from Mason, 1978)

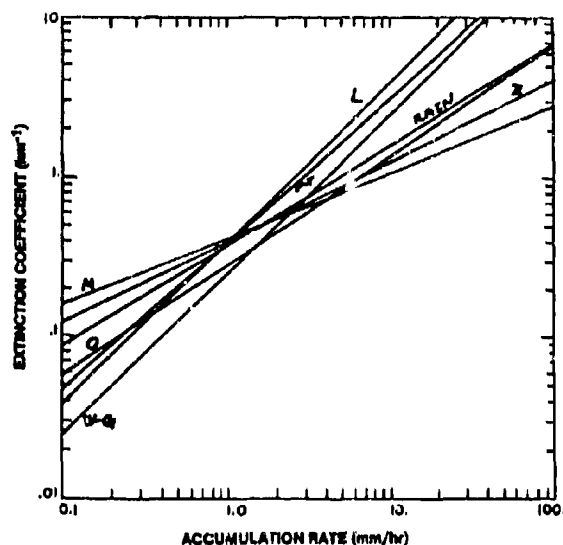


Figure 11. The same as Figure 10, only as a function of the actual accumulation rate, (Eq. 9).

4.3 Forward Scattering Corrections

For both rain and snow, where for visible and IR wavelengths the characteristic particle sizes are much larger than the wavelengths, the measured values of transmission will generally be higher than expected based on the extinction coefficients given in the previous two sections (4.1 & 4.2). Also they exhibit a stronger wavelength dependence than indicated by Eq. (7). Seagraves (1983) notes that snow transmittance measurements indicate the extinction is 30% to 50% higher in the 8-12 μm spectral region than the visible, instead of the less than 5% predicted by the wavelength dependence of Eq (7), (allowing for the difference between the size of snowflakes and raindrops).

Mill and Shettle (1983) have shown that this can be explained by the pronounced forward scattering lobes due to Fraunhofer diffraction for very large particles. The angular width of these diffraction peaks (which go inversely with the size parameter, x) can be comparable to the field-of-view for typical transmissometers. When this occurs, a significant fraction of the scattered light will be seen by the transmissometer and be indistinguishable from the directly transmitted light. They derived a relationship between the measured transmittance, τ_m , and the true transmittance, τ , (which would be measured by a transmissometer with zero receiver field-of-view, θ , or zero source divergence, ϕ :

$$\tau_m = \tau(1 + D' \ln \tau), \quad (10)$$

where D' is a function of the transmissometer f.o.v., the source divergence, and the particle size parameter. The values of D' are shown in Figure 12, (also see Fenn et al., 1985). Similar results have also been developed by Seagraves (1983 & 1986) and by Bohren & Koh (1985).

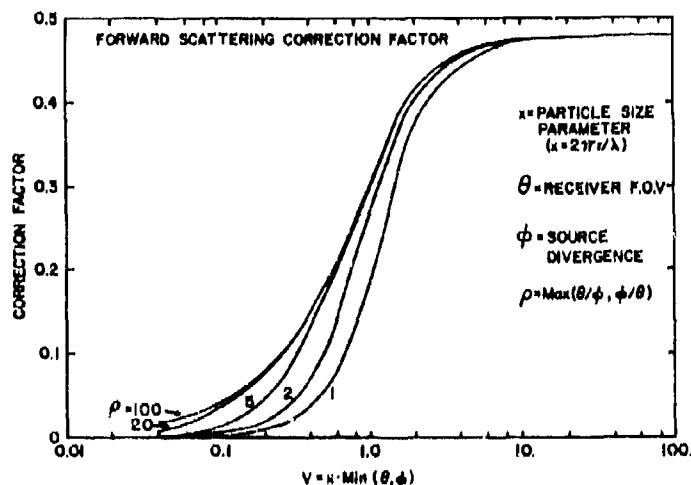


Figure 12. Correction factor, D' (Eq. 10), for forward scattering as a function of transmissometer geometry and particle size parameter.

5. REFERENCES

- d'Almeida, G.A. (1987) "On the variability of desert aerosol radiative characteristics", J. Geophys. Res., **92**, 3017-3026.
- d'Almeida, G.A. & P. Keopke (1988a) "An Approach to a Global Optical Aerosol Climatology", pg 125-138 in Aerosols and Climate, ed. P.V. Hobbs & M.P. McCormick, A. Deepak Publishing, Hampton, VA.
- d'Almeida, G.A. & P. Keopke (1988b) "An Optical Aerosol Climatology", pg 61-64 in Atmospheric Aerosols and Nucleation, ed. by P.E. Wagner & G. Vail, Lecture Notes in Physics, **309**, Springer, Berlin, FRG.
- Barnhardt, E.A. & J.L. Streets (1970) "A Method for Predicting Atmospheric Aerosol Scattering Coefficients in the Infrared", Appl. Opt., **9**, 1337-1344.
- Bohren, C.F. & G. Koh (1985) "Forward Scattering Corrected Extinction by Nonspherical Particles", Appl. Opt., **24**, 1023-1029.
- Brogniez, C. & J. Lenoble (1987) "Modeling of the Stratospheric Background Aerosols from Zonally Averaged SAGE Profiles", J. Geophys. Res., **92**, 3051-3060.
- Carlson, T.N. & S.G. Benjamin (1980) "Radiative Heating Rates for Saharian Dust", J. Atmos. Sci., **37**, 193-213.
- Carlson, T.N. & R.S. Caverly (1977) "Radiative Characteristics of Saharian Dust at Solar Wavelengths", J. Geophys. Res., **82**, 3141-3152.
- Carrier, L.W., G.A. Cate, & K.J. von Essen (1967) "The Backscattering and Extinction of visible and IR Radiation by Selected Major Cloud Models", Appl. Opt., **12**, 555-563.
- Clough, S.A., Kneizys, F.X., Shettle, E.P., and Anderson, G.P., 1986: "Atmospheric Radiance and Transmittance: FASCOD 2", Proc. of the Sixth Conference on Atmospheric Radiation, Williamsburg, VA, American Meteorological Society, Boston, MA, 141-144.
- Clough, S.A., F.X. Kneizys, G.P. Anderson, E.P. Shettle, J.H. Chetwynd, L.W. Abreu, L.A. Hall & R.D. Worsham (1989) "FASCOD3: Spectral Simulation", pg. 372-375, in IRS '88: Current Problems in Atmospheric Radiation, Ed. by J. Lenoble & J.F. Geleyn, A. Deepak Publishing, Hampton, VA.
- de Leeuw, G., K.L. Davidson, S.G. Gathman, & R.V. Noonkester (1989a) "Physical Models for the Aerosol in the Marine Mixed Boundary Layer", Proceedings, 44th Symposium of the Electromagnetic Wave Propagation Panel, Aids for Exploiting or Mitigating Electromagnetic Propagation Effects, pg. 40-1 to 40-8, AGARD CP 453, San Diego, CA, 15-19 May 1989.
- Deirmendjian, D. (1964) "Scattering and polarization properties of water, clouds, and hazes in the visible and infrared", Appl. Opt., **3**, 187-196.
- Deirmendjian, D. (1969) Electromagnetic scattering on spherical polydispersions, American Elsevier, New York, 290 pp.
- Eloranta, E.W. & C.J. Grund (1989) "Cirrus Cloud Optical Properties Measured with the University of Wisconsin High Spectral Resolution and Volume Imaging Lidars", to appear in the Proceedings of this conference - Fall 1989, Electromagnetic Wave Propagation Panel Symposium on Atmospheric Propagation in the UV, Visible, IR, & MM-Wave Region and Related Systems Aspects, Copenhagen, Denmark, 9-13 October 1989.
- Elterman, L. (1964) Atmospheric Attenuation Model, 1964, in the Ultraviolet, Visible, and Infrared Regions for Altitudes to 50 km, AFCRL-64-740, (Available from NTIS AD 607859)
- Elterman, L. (1968) UV, Visible, and IR Attenuation for Altitudes to 50 km, AFCRL-68-0153, (Available from NTIS ADA671933)
- Elterman, L. (1970) Vertical Attenuation Model with Eight Surface Meteorological Ranges 2 to 13 kilometers, AFCRL-70-0200, (Available from NTIS ADA671933)
- Falcone, V.J., L.W. Abreu and E.P. Shettle, 1979: Atmospheric Attenuation of Millimeter Waves, Models and Computer Code, AFGL-TR-79-0253 (NTIS, ADA 084485).
- Fenn, R.W., S.A. Clough, W.O. Gallery, R.E. Good, F.X. Kneizys, J.D. Mili, L.S. Rothman, E.P. Shettle & F.E. Volz, 1985: "Optical and Infrared Properties of the Atmosphere." Chap. 18 in Handbook of Geophysics and the Space Environment, A.S. Jursa Scientific Editor, Air Force Geophysics Laboratory, Hanscom AFB, MA 01731-5000, AFGL-TR-85-0315, (available from NTIS ADA167000)
- Gathman, S.G. (1963a) "Optical Properties of the Marine Aerosol as Predicted by the Navy Aerosol Model", Opt. Eng., **22**, 57-62.
- Gathman, S.G. (1983b) Optical Properties of the Marine Aerosol as Predicted by a BASIC Version of the Navy Aerosol Model, NRL Memorandum Report 5157, NRL, Washington, DC 20375.
- Gathman, S.G., G. de Leeuw, K.L. Davidson, & D.R. Jensen (1989) "The Naval Oceanic Vertical Aerosol Model: Progress Report", to appear in the Proceedings of this conference - Fall 1989, Electromagnetic Wave Propagation Panel Symposium on Atmospheric Propagation in the UV, Visible, IR, & MM-Wave Region and Related Systems Aspects, Copenhagen, Denmark, 9-13 October 1989.

Gibbins, C.J., (1989) "Millimetric, Infrared, and Optical Propagation Studies over a 500 m Path", to appear in the Proceedings of this conference - Fall 1989. Electromagnetic Wave Propagation Panel Symposium on Atmospheric Propagation in the UV, Visible, IR, & MM-Wave Region and Related Systems Aspects, Copenhagen, Denmark, 9-13 October 1989

Hale, George M., and Querry, Marvin R., 1973: "Optical constants of water in the 200-nm to 200 μ m wavelength region," Appl. Opt., 12, 555-563.

Hall, Jr., F.F. M.J. Post, R.A. Richter, G.M. Lefeld, V.E. Derr, 1983: "Cirrus Cloud Model," pg 58-67 in Kneizys et al. (1983).

Hänel, G. & K.Bullrich (1978) "Physico-Chemical Property Model of Tropospheric Aerosol Particles", Beitr. Phys. Atm., 51, 129-130.

Hodges, J.A. (1972) "Aerosol Extinction Contribution to Atmospheric Attenuation in Infrared Wavelengths", Appl. Opt., 11, 2304-2310.

Hudson, N.W. (1963) "Raindrop Size Distribution in High Intensity Storms", Rhodesian J. Agric. Res., 1, 6-11.

Hummel, J.R., E.P.Shettle, & D.R.Longtin (1988) A New Background Stratospheric Aerosol Model for use in Atmospheric Radiation Models, AFGL-TR-88-0166, (NTIS, ADA210110)

IAMAP/Radiation Commission (1986) A Preliminary Cloudless Standard Atmosphere for Radiation Computation, WCP-112, WMO/TD-No. 24, World Climate Research Programme, WMO, Geneva.

Ivlev, L.S. (1967) "Aerosol Model of the Atmosphere", pg. 125-160 in Prob. Fiz. Atmos., No. 7, Leningrad, USSR, Translated by Foreign Science & Technology Center, Dept. of the Army, (NTIS, AD 760393)

Ivlev, L.S. (1969) "Atmospheric Aerosol", pg. 28-42 in Radiation Characteristics of the Atmosphere and the Earth's Surface, ed. by K.Ya.Kondratyev, Amerind Publishing Co., New Delhi, (NTIS, TT-71-58003).

Jaenicke, R. (1988) "Aerosol Physics and Chemistry", Chap. 9, pg. 391-457 in Landolt-Boerstein Numerical Data and Functional relationships in Science and Technology, V, 4b, (Meteorology).

Joseph, J.H. (1975) "The Desert Aerosol" pg. 2-60, in The Evaluation of a Shuttle Borne Lidar Experiment to Measure the Global Distribution of Aerosols and their Effect on the Atmospheric Heat Budget, by S.T.Shipley, J.H.Joseph, J.T.Trauger, P.J.Guetter, E.W.Eloranta, W.J.Wiscombe, A.P.Odell, F.L.Roesler, & J.A.Weinman, Final Rpt. on NASA Grant NSG 1057, April 1975, (NTIS N76-16597)

Joss, J. & A.Waldvogel (1969) "Raindrop size distributions and sampling size errors", J. Atmos. Sci., 26, 566-569.

Kneizys, F.X., Shettle, E.P., Gallery, W.O., Chetwynd, J.H., Abreu, L.W., Selby, J.E.A., Clough, S.A. and Fenn, R.W. (1983) Atmospheric Transmittance/Radiance: Computer Code LOWTRAN 6, AFGL-TR-83-0187, (NTIS; AD A137796)

Kneizys, F.X., Shettle, E.P., Abreu, L.W., Anderson, G.P., Chetwynd, J.H., Gallery, W.O., Selby, J.E.A., and Clough, S.A. (1988) Users Guide to LOWTRAN 7, AFGL-TR-88-0177, (NTIS; AD A206773)

Koh, G. (1989) Physical and Optical Properties of Falling Snow, CRREL Rpt. 89-16, CRREL, 16 Lyme Rd, Hannover, NH.

Kondratyev, K.Ya. & D.V.Pozdnyakov (1981) Aerosol Models of the Atmosphere, Publishing House Nauka, Moscow, USSR, 104 pp.

Kondratyev, K.Ya., N.I.Moskalenko, & D.V.Pozdnyakov (1983) Atmospheric Aerosols, Leningrad, USSR, 224 pp.

Laws, J.O. & Parsons, D.A. (1943) "The relation of raindrop size to intensity", Trans. Amer. Geophys. Union, 24, 452-460.

Liou, K.N, 1974: "On the Radiative Properties of Cirrus in the Window Region and their Influence on Remote Sensing of the Atmosphere," J. Atmos. Sci., 31, 522-532.

Longtin, D.R., E.P.Shettle, J.R.Hummel, & J.D.Pryce (1988a) "A Desert Aerosol Model for Radiative Transfer Studies", pg 261-269 in Aerosols and Climate, ed. P.V.Hobbs & M.P.McCormick, A.Deepak Publishing, Hampton, VA.

Longtin, D.R., E.P.Shettle, J.R.Hummel, & J.D.Pryce (1988b) A Wind Dependent Desert Aerosol Model: Radiative Properties, AFGL-TR-0112, (NTIS, ADA 206164)

Magono, C. & C.Lee (1966) "Meteorological Classification of Natural Snow Crystals", J. Fac. Sci., Hokkaido Univ., Series VII, 2, 321-335.

Marshall, J.S. & W.M.K.Palmer (1948) "The Distribution of Raindrops with Size", J. Meteor., 5, 165-166.

Mason, J.B. (1978) Light Attenuation in Falling Snow, ASL-TR-0018, U.S.Army Atmospheric Sciences Laboratory, WSMR, NM.

McClatchey, R.A., R.W.Fenn, J.E.A.Selby, F.E.Volz, J.S.Garing (1970) Optical Properties of the Atmosphere, AFCRL-70-0527, (NTIS, AD 762904)

Mill, J.D. & E.P.Shettle (1983) A Preliminary LOWTRAN Snow Model, AFGL-TR-83-0148, (NTIS ADA 129826).

Miller, A. & J.C.Thompson (1970) Elements of Meteorology, C.E.Merrill Publishing Co., Columbus, Ohio.

- Nilsson, B. (1979) "Meteorological Influence on Aerosol Extinction in the 0.2-40 μm Wavelength Range" Appl. Opt., 18, 3457-3473.
- Nussenzveig, H.M. & W.J. Wiscombe (1980) "Efficiency Factors in Mie Scattering", Phys. Rev. Letters, 45, 1490-1494.
- Pinnick, R.G., J.M. Rosen, & D.J. Hofmann (1976) "Stratospheric Aerosol Measurements: III. Optical Model Calculations", J. Atmos. Sci., 33, 304-314.
- Pruppacher, H.R. & J.D. Klett (1978) Microphysics of Clouds and Precipitation, D. Reidel Publishing Co., Dordrecht, Holland, pp 714.
- Ray, P.S. 1972: "Broadband Complex Refractive Indices of Ice and Water," Appl. Opt., 11, 1836-1844.
- Seagraves, M.A. (1983) "Visible and Infrared Transmission and Precipitation Rate in Falling Snow", Ph.D. Thesis, Colorado State University.
- Seagraves, M.A. (1986) "Visible and Infrared Extinction in Falling Snow", Appl. Opt., 25, 1166-1169.
- Sekhon, R.S. & R.C. Srivastava (1971) "Doppler radar observations of drop-size distributions in a thunderstorm", J. Atmos. Sci., 28, 983-984.
- Shettle, E.P. & R.W. Fenn, "Models of atmospheric aerosols and their optical properties", in AGARD Conference Proceedings No. 183, Optical Propagation in the Atmosphere, AGARD-CP-183 (1976) (NTIS, ADA 028615).
- Shettle, E.P. and R.W. Fenn, 1979: Models for the Aerosols of the Lower Atmosphere and the Effects of Humidity Variations on Their Optical Properties, AFGL-TR-79-0214, (Available from NTIS ADA 085951).
- Silverman, B.S., and Sprague, E.D., 1970: "Airborne measurement of in-cloud visibility," pp 271-276, Second National Conference on Weather Modification, Santa Barbara, California, 6-9 April 1970, American Meteorological Society.
- SMIC (1971) Inadvertent Climate Modification: Report of the Study of Man's Impact on Climate, MIT Press, Cambridge, MA, 308 pp.
- Stephens, G.L. (1978a) "Radiation Profiles in Extended Water Clouds. I: Theory", J. Atmos. Sci., 35, 2111-2122.
- Stephens, G.L. (1978b) "Radiation Profiles in Extended Water Clouds. II: Parameterization Schemes", J. Atmos. Sci., 35, 2123-2132.
- Stephens, G.L., G.W. Paltridge, & C.M.R. Platt (1978) "Radiation Profiles in Extended Water Clouds. III: Observations", J. Atmos. Sci., 35, 2133-2141.
- Stewart, D.A. & O.M. Essenwanger (1982) "A Survey of Fog and Related Optical Propagation Characteristics", Rev. Geophys. & Space Sci., 20, 481-496.
- Toon, O.B. & N.H. Farlow (1981) "Particles above the Tropopause: Measurements and Models of Stratospheric Aerosols, Meteoric Debris, Nacreous Clouds, and Noctilucent Clouds", Ann. Rev. Earth Planet. Sci., 9, 19-58.
- Toon, O.B. & J.B. Pollack (1976) "A Global Average Model of Atmospheric Aerosols for radiative Transfer Calculations", J. Appl. Meteor., 15, 225-246.
- Toon, O.B., R.P. Turco, P. Hamill, C.S. Kiang, & R.C. Whitten (1979) "A One dimensional Model Describing Aerosol Formation and Evolution in the Stratosphere. II - Sensitivity Studies and Comparison with Observations", J. Atmos. Sci., 36, 718-736.
- Turco, R.P., P. Hamill, Toon, O.B., R.C. Whitten, & C.S. Kiang (1979) "A One dimensional Model Describing Aerosol Formation and Evolution in the Stratosphere. I - Physical Processes and Numerical Analogs", J. Atmos. Sci., 36, 699-717.
- van de Hulst, H.C. (1957) Light Scattering by Small Particles, Wiley Inc., New York, 470 pp.
- Waldvogel, A. (1974) "The N_0 Jump of Raindrop Spectra", J. Atmos. Sci., 31, 1067-1078.
- Warren, S.G., 1984: "Optical Constants of Ice from the Ultraviolet to the Microwave," Appl. Opt., 23, 1206-1255.
- Wells, W.C., G. Gal, M.W. Munn (1977) "Aerosol Distributions in Maritime air and Predicted Scattering Coefficients in the Infrared", Appl. Opt., 16, 654-659.
- Whitten, R.C., O.B. Toon, & R.P. Turco (1980) "The Stratospheric Sulfate Layer: Processes, Models, Observations, & Simulations" Pure Appl. Geophys., 118, 86-127.

DISCUSSION

A. KOHNLE

Land aerosol models are driven by parameters like wind velocity, humidity, etc. Are there any plans to relate these models to surface types and, in addition, to surface conditions?

AUTHOR'S REPLY

Other than for desert aerosols and the maritime aerosols which I discussed, I do not know of such modeling studies. For land surfaces with vegetation, the problem becomes more complicated, since in addition to variations in the soil composition, there are surface binding effects of plants and more variation in the moisture content of the ground surface than for desert regions. Also, there are less data available on the production of aerosols from such surfaces, than for desert or oceanic regions.

D. MÖHN

Can you give some more information on the wavelength dependence of transmission through falling snow, e.g., the higher measured values in the visible rather than the infrared at 10 μm ?

AUTHOR'S REPLY

The higher measured transmission for visible wavelengths than infrared (IR) in falling snow is an instrumental effect. For snow (and rain) where the particle sizes are much larger than the wavelength, much of the scattered light is in the forward direction within the so-called diffraction peak. The angular width of this diffraction peak is on the order of a few milliradians in the visible for falling snow, and goes inversely with the ratio of the particle size to the wavelength. This angular width of the scattered radiation is comparable to the field-of-view (FOV) of typical transmissometers. For the visible, much of the diffraction peak often falls within the FOV, so it appears not to be scattered. In the IR, the diffraction peak becomes broader with increasing wavelength, with the result that more of the scattered light falls outside of the FOV, and is not sensed by the transmissometer. With knowledge of the particle size distribution and the instrument characteristics this dependence on wavelength can be calculated. This is discussed further in the text of the talk.

J. SELBY

How do the optical properties of desert aerosols vary in different geographical desert areas and what has been used in LOWTRAN 7?

AUTHOR'S REPLY

Desert aerosols do have different optical properties depending on composition. This can be seen in the different colors of desert sands which range from white to yellows and browns or reds. LOWTRAN 7 uses the model of Longtin et al. (1988) which was developed to be representative of typical deserts. It treats the small particles as being background ammonium sulfate, with a slight contamination of carbon particles, and the large particles, or sand which is made up of quartz mixed with hematite. We have not attempted to model, within LOWTRAN, the variations in the composition which occur. However, the major variation with wavelength is driven by the size distribution, rather than the composition. The refractive index, which is a function of the composition, determines the spectral location of peaks and valleys in the scattering and absorption as a function of wavelength.

INTERPRETING METEOROLOGICAL DATA REPORTS FOR LOWTRAN 6
NAVY AEROSOL MODEL EXTINCTION CALCULATIONS

A.J. Beaulieu

Defence Research Establishment, Valcartier, 2459 Pie XI Blvd. North,
P.O. Box 8800, Courcellette, Québec, Canada, G0A 1R0

SUMMARY - To evaluate the aerosol extinction, one of the most advanced model is the LOWTRAN 6 Navy Aerosol model. However, to evaluate the extinction corresponding to weather conditions derived from meteorological reports is often difficult because these reports lack one critical parameter required by the model; the Air Mass parameter value. Using default values for this parameter can lead to substantial errors in the extinction at the longer wavelengths. Furthermore, the LOWTRAN model does not accept values of relative humidities greater than 98%. These deficiencies become serious when it is desired to derive statistics of the IR extinction from meteorological records. A meteorological data interpreter model has been developed to overcome these problems. This model uses the visibility to determine the effective Air Mass parameter as well as adjusting the RH, the wind velocities and the precipitation rates through a series of logical selections to arrive at a physically consistent solution with respect to the available data. This model was tested on a large number of weather scenarios which shows its validity and its effects on IR system performance assessment.

1. INTRODUCTION

The atmospheric extinction is the dominant factor affecting the performance of IR systems in the marine environment. To evaluate the performance of such systems in various regions of operation, the only data available is the meteorological records which have been accumulated by weather ships some 20 to 30 years ago. To estimate the IR extinction from such data, we presently rely on the LOWTRAN atmospheric propagation code¹. LOWTRAN 6 adequately accounts for the effects of molecular absorption and provide various models for calculating the aerosol extinction. One of these aerosol models, the Navy maritime model developed by Gathman² at NRL, is the most suitable one for ocean atmospheres.

In the Navy model, the particle size distribution mode (for radius r) is the sum of three log-normal distributions given by:

$$n(r) = \sum_{i=1}^3 A_i \exp \{ -(\ln(r/Fr_i))^2 \} \quad (\text{cm}^{-3} \mu\text{m}^{-1}) \quad (1)$$

where

$$A_1 = 2000(\text{AM})^2 \quad (2)$$

$$A_2 = 5.866(V_a - 2.2) \quad (3)$$

$$A_3 = 10^{(.006V_c - 2.8)} \quad (4)$$

Component A_1 represents the contribution by continental aerosols and AM is an Air Mass parameter that is allowed to range between integer values of 1 for open ocean and 10 for coastal areas. Components A_2 and A_3 represent equilibrium sea spray particles generated by surface winds. The first corresponds to small particles whose density is a function of the surface wind speed averaged over 24 h (V_a , in m/s) while the second depends on the current surface wind speed V_c . The expression for A_3 given here differs from the original one of Ref. (2) and is an improved value which is believed to be included in LOWTRAN 7³. For wind velocities less than 2.2 m/s, the density of the sea spray aerosols A_2 and A_3 are taken to be 0.5 and .000015 respectively.

In Eq. (1), r_i , the modal radius for each component, is allowed to grow with relative humidity (RH) according to the Fitzgerald formula⁴:

$$F = [(2 - \text{RH}/100) / .6(1 - \text{RH}/100)]^{1/3} \quad (5)$$

The contribution to the total extinction by each aerosol component can be written as:

$$B(\lambda)_i = (0.001 A_i / F) \int Q(\lambda, r, n) \exp \{ -(\ln(r/Fr_i))^2 \} r^2 dr \quad (\text{km}^{-1}) \quad (6)$$

where $Q(\lambda, r, n)$ is the cross section for the extinction normalized to the geometrical cross section of the spherical particle, and n is the complex refractive index, which is allowed to change from that of a dry sea salt as the particle deliquesces with increasing humidity. When an observed surface visibility is available as an input to the model, the model calculates the visibility at 0.55 μm predicted from the AM value, RH, V_a and V_c and takes the ratio (C) of the calculated to the observed visibility. It then uses this ratio to multiply all the A parameters such that the extinction at 0.55 μm is compatible with the observed visibility and the subsequent estimates of the extinction at any wavelength is made using these adjusted values of aerosol densities. Fundamentally, the input values of AM, RH and winds determines the ratio of visible to IR

extinctions and the visibility input adjusts the amplitudes of the extinctions to match the reported visibility. An error in the AM value will then strongly affect the IR extinction accuracy.

A number of difficulties were experienced when trying to estimate the aerosol extinction in the IR wavelengths using the available data from meteorological records. First there is no indication of what Air Mass parameter value to be used and in the absence of an input the program assumes a default value of 3 for AM. Secondly the wind values provided are only the current wind values and it is necessary to assume that the average wind is the same as the current value. Furthermore, a number of records indicate that the relative humidity is greater than 98% which the LOWTRAN code will not accept as valid. Finally the effects of precipitation on the visibility (and hence on the C ratio) is not taken into account. Even worse the precipitation rate is generally given by a simple descriptive such as "light rain" (which means anything from 0.1 to 2 mm/hr) which is generally assumed to mean something near the maximum. In the Northern seas, the occurrence of snow, which is much more effective in reducing the visibility, can significantly distort the extinction results.

2. METEOROLOGICAL DATA ANALYSIS

A number of representative weather reports were selected to represent the various conditions encountered in the North Atlantic⁵. Using the default value of 3 for the air mass parameter and limiting the RH value to 98%, the Navy aerosol model was used to evaluate the IR extinction corresponding to these scenarios. The C parameter values were also recorded as well as the "effective" air mass parameter and wind velocity. These effective parameter values are those which would be required to give the adjusted visible extinction as determined from the C ratio. Typically the effective wind (V_{eff}) is calculated from the relation:

$$5.866(V_{eff} - 2.2) = C * 5.866(V_a - 2.2) \quad (7)$$

Similarly the effective air mass parameter (AM_{eff}) value is estimated from the relation:

$$AM_{eff} = 3 (C)^{.5} \quad (8)$$

Particularly unrealistic values of effective air mass parameter in excess of 20 and winds in excess of 100 m/s were obtained when the RH was reported as greater than 98%. This has led to a reformulation of the way to calculate the effects of relative humidity which is described below.

3. EXTINCTION MODELING

Using the Navy aerosol model in LOWTRAN 6, it is possible to determine the normalized extinction (for $A_1/F = 1$) of the various types of aerosols as a function of their mean size which is given by Fr_1 where F is given by expression (5) and r_1 is the mean size of the aerosols at 80% relative humidity. In the limit of large particle size, this normalized extinction should vary as the cube of the mean particle size. A mathematical model⁶ was developed to replace the time consuming Mie calculations, and which respected the large size limit and the Anomalous Scattering approximation in the limit of small particles. When expressed in the same terms as the Navy aerosol model, this model is described by:

$$B(\lambda, r)_1 = (A_1/F)r^3 K_0 \{ [1 + K_1/(K_2 + r) + K_3/r] \{ r^2 / (K_2 K_4 + r^2) \} \} \quad (km^{-1}) \quad (9)$$

where the K_i s are to be determined for each wavelength except for K_0 which is the same for all wavelengths. Note that this model does not consider the effects of the changes in the refractive index of the aerosols as a function of the relative humidity. Plotting the normalized extinction obtained from LOWTRAN 6 against mean aerosol size for all three types of aerosols, best fit values of the K parameters were evaluated for the 40 reference wavelengths used in LOWTRAN. Typical results are shown in Figures 1 and 2.

The inaccuracies of this model are comparable to the interpolation inaccuracies of the Navy aerosol model. To obtain an improved accuracies the K constants should be replaced by variables which vary with the dielectric constant of the aerosols which change with RH. The added complexity was not judged worthwhile in view of the other inaccuracies inherent to the assumed size distribution model.

While this new approach allows the determination the extinction at high relative humidities, the accuracy of the measured values is critical and cannot be relied upon because of the small difference between the air temperature and the dew-point temperature and any small local air heating will give an RH error which will be magnified for RH values near 100% because the F function has a pole at this value. Furthermore the mean aerosol size varies as indicated by the Fitzgerald expression only in a system which is in equilibrium. For a natural environment with substantial air movement and a finite growth rate of the aerosol with increased RH, the value of relative humidity which should be used is some sort of average value over both space and time. Therefore for very high values of RH, some interpretation of the meteorological data is required. The same also applies to the determination of the Air Mass parameter and to that of the average wind. The method used in the Navy aerosol model to adjust the extinction to the observed visibility can lead to substantial errors in the estimation of the IR extinction. If the AM value used in the modeling is too small, changing equally the extinction from all types of aerosols in the visible will result in an

excessive change at the IR wavelengths because the small background aerosols have a much larger effect in the visible than at the long wavelengths while the wind-raised aerosols have a much more significant impact on the IR extinctions as can be seen from Figures 1 and 2. These considerations have led us to the development of an "Interpreter" model which will now be described.

4. METEOROLOGICAL DATA INTERPRETER

The basic concept of the interpreter is to use the visibility (however inaccurate it may be) to test the validity of the parameters used to calculate the extinction. Initially the Air Mass parameter is assumed to be low ($AM = 2$), the precipitation rate is taken near the upper limit of the reported range, the average wind is taken as equal to the reported current wind and finally if the RH value exceeds 98%, this exceedance is noted and the value decreased to 98% as this is within the range of errors possible. The extinction due to the precipitation, which is considered independent of wavelength, is calculated as in LOWTRAN 6 and is given by:

$$\beta_{rr} = 0.365(rr)^{.63} \quad (\text{km}^{-1}) \quad (10)$$

where rr is the precipitation rate in mm/h. This extinction is added to the aerosol extinction before calculating the ratio of the calculated to the observed visibility. This ratio is different from the C ratio used in the Navy aerosol model because it includes the effects of precipitations on the visibility, and to distinguish it clearly, it will be called F_1 . Figure 3 gives the logic diagram of the interpreter.

The modeling is based on the fact that all the variables which can be in error all operate in the same manner. An increase in any of the parameters AM , RH , wind or precipitation rate will lead to an increase of the extinction in the visible and hence decrease F_1 . If the F_1 ratio is close to unity, (i.e. $2/3 < F_1 < 3/2$), errors in the various parameters are equally probable except RH if it is not too high, and the number of each type of aerosol is multiplied by F_1 to adjust the visible extinction to the observed visibility as in the Navy aerosol model. The effective values of the parameters are then evaluated for further analysis.

If F_1 is greater than $3/2$, either the AM or the RH parameter is too low (wind and precipitation extinctions are unlikely to be significantly too low because of the high value selection of rr and the accuracy of wind measurements). If the reported RH is greater than 98%, it is the most likely cause of the high value of F_1 . In that case the value of AM is set to 4 to run a new evaluation of F_1 and if it is still greater than $3/2$, the value of F is increased in 10% increments until the value of F_1 drops below 1. Then the calculated RH is determined from the final F value by the inversion of expression (5). A final adjustment to the observed visibility is performed before determining the effective value of all the parameters and calculating the extinction at other wavelengths. When the reported value of RH is less than 98%, then the influence of small RH errors is generally not important and the Air Mass parameter is most likely to be too low. Then the value of the A_1 is stepped up in 10% increments until F_1 drops below 1. The final adjustments are performed as in the previous case.

If the F_1 parameter is below the value of $2/3$, it is unlikely that AM is too high as the initial default value was taken to be quite small. A reduction of the RH value would not be significant within the possible margin of error of the measurements except when the reported value is very close to 100% and these cases are already covered by the automatic decrease to 98% which occurs before the first evaluation of F_1 . Therefore, the most likely causes would be an excessive value or precipitation or of wind. The most probable source of error is the excessive precipitation rate inferred from the weather reports. However, a number of low F_1 cases were found when there was no precipitation. A second test is required to determine if the excessive calculated extinction could be due to an excessive wind estimate and F_1 is calculated again but taking $rr = 0$ such that if this new value of F_1 is still below 1, the average wind is decreased until F_1 becomes equal to 1 and the rain rate effective is then assumed to be zero. If this second value of F_1 is greater than 1, then the average wind is kept equal to the current wind and the precipitation rate is adjusted by a stepping iteration decreasing the rain rate in 10% increments until F_1 increases to a value greater than 1.

The interpreter logic is not absolutely perfect as it is limited to varying only one parameter at a time and the reliance on the visibility (which is not the most precisely measured parameter) is a source of uncertainty. In the cases of showers, it is well known that the visibility will vary depending on the direction of the observation and it is suspected that the reported values corresponds to directions where there is no precipitation. This explains why the calculated effective precipitation rates are sometimes very small. In complete performance evaluations, the spatial profile of the precipitation should be included in the extinction as a function of direction assuming that the values given by the interpreter apply in the directions of least precipitation. In spite of these restrictions, the merits of the interpreter have been tested on a large number of weather scenarios and the results summarized below.

5. APPLICATIONS OF THE INTERPRETER MODEL

As indicated earlier, a number of "typical" weather reports have been selected to represent the various weather conditions normally encountered in four separate regions of the North Atlantic. To evaluate the performance of the interpreter model, two

extreme regions were selected, the Canlant region covering from the East coast of Canada to the middle of the Atlantic, and the Westlant region covering from the East coast of the U.S. to the Canary Islands approximately. The calculated effective air mass parameter values for the 80 weather scenarios for the Westlant region, are illustrated in Fig. 4 while those for the 72 scenarios for the Canlant region are given in Fig. 5.

The most striking characteristics of these results is that large values of the AM parameter are obtained for the Gulf Stream sub-region of Westlant and, to a lesser extent, for the North American Basin sub-region of Canlant. The weather station of the first sub-region is Cape Hatteras which is essentially on the shore of the U.S. continent and it is normal to expect that the air mass will exhibit continental rather than oceanic properties. The North American Basin sub-region results are obtained from the Sable Island weather station which, although it is more remote from the North American continent, is also expected to display more frequently typically continental air mass properties. For the other weather stations which are all weather ships, except for the Canary Basin station of Lajes, the air mass parameter values as estimated by the interpreter is often near 2 which is comparable with the default value of 3 which is used for LOWTRAN. Values of the order of 6 are however frequently estimated in conditions where the visibility is reduced which are precisely the conditions of interest in performance assessment and where the higher AM values lead to a reduced estimation of the IR extinctions.

Another parameter behavior of interest is the estimation of the average wind velocity as a function of the reported wind. Figures 6 and 7 show the behavior of the estimated average wind as a function of the reported current wind as calculated by the interpreter (dark points) and the LOWTRAN 6 (light points) model, for the two regions. It can be seen that in general the interpreter results give average winds closer to the current wind than the LOWTRAN model. This is particularly important for the low current wind conditions where the LOWTRAN high values would seriously impact the IR extinction estimations.

The most important point for performance evaluations is the behavior of the extinction in the IR wavebands. Two wavelengths, 3.75 μm and 10.6 μm , were used for comparison purposes. For the 3.75 μm wavelength, the comparison between the LOWTRAN and the interpreter results is illustrated in Fig. 8 and Fig. 9 for the Central Atlantic (deep ocean) sub-region and the Gulf Stream sub-region (nearly continental) sub-region respectively. Both exhibit the LOWTRAN tendency to overestimate the IR extinction which is most significant in the Cape Hatteras results because of the higher values of the Air Mass parameter in this case. Another point of interest is that in these results, all the points above the 0.1 km^{-1} value in the LOWTRAN extinction estimates correspond to precipitation situations. The substantially smaller values obtained with the interpreter are generally due to an estimated reduction of the precipitation rate which is required for compatibility with visibility. This is most important in the estimation of the probability of experiencing large extinction due to precipitations.

Similar results are obtained for the longer wavelengths as indicated in Fig. 10 where a significant, although less important, reduction of the estimated extinction is shown by the interpreter model compared to the LOWTRAN results. However, the impact of these results on system performance evaluation is less significant for this wavelength because once the larger molecular extinction is added, the effects of the aerosol is much less significant on the total extinction except in the case of precipitations.

6. CONCLUSIONS

Using the same physical aerosol extinction model as that used in the Navy aerosol model of LOWTRAN 6, a meteorological data interpreter code has been developed to estimate the densities of various types of aerosols from the available meteorological records which contain no indication of the Air Mass parameter. The method for determining the effects of the relative humidity on the extinction has also been modified in order to be able to cover very high relative humidities and accompanying very low visibilities which are cases that the LOWTRAN 6 model cannot cover. The expected range of validity of this model is from 50 to 100% relative humidities and for visibilities greater than 200 m. For lower values of RH and visibilities the model is expected to produce IR extinction values which are lower than true. Using this model on a large number of weather reports has produced results which are consistent with physical interpretations and in general the IR extinctions are lower than those obtained with LOWTRAN, which can have a significant effect on the performance evaluation of IR systems at sea, especially in adverse weather conditions.

7.0 REFERENCES

1. F.X. Kneisys et al., "Atmospheric transmittance/radiance: computer code LOWTRAN 6", A.F. Geophys. Lab. Tech., Report No. 83-0187 (Aug. 1, 1983).
2. S.G. Gathman, "Optical properties of the marine aerosol as predicted by the Navy aerosol model", Opt. Eng., 22(1), 57-62 (1983).
3. S.G. Gathman, private communication
4. J.W. Fitzgerald, "Approximate formulas for the equilibrium size of an aerosol particle as a function of its dry size and composition and the ambient relative humidity", J. Appl. Meteorol., 14, 1044-1049 (1975).

5. T.B. Low and D.R. Hudak, "Summary Report on the Study for the Expansion of the Meteorological Module", KRL Research Corp., Report 97701-6-0764/01-SD, Mar 1989.

6. G. Fournier et al to be published.

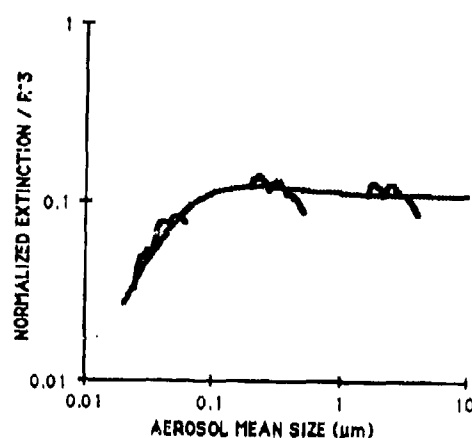


Fig. 1. Model match at 0.55 μm .

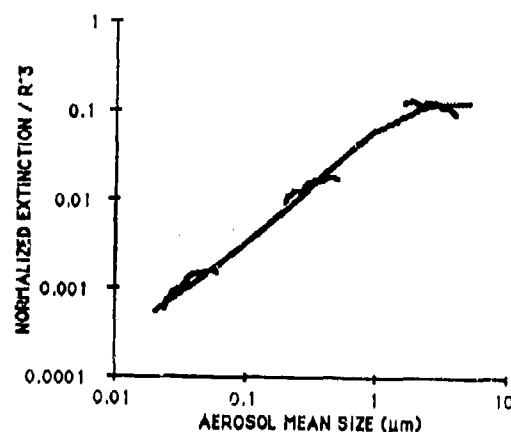


Fig. 2. Model match at 10.59 μm .

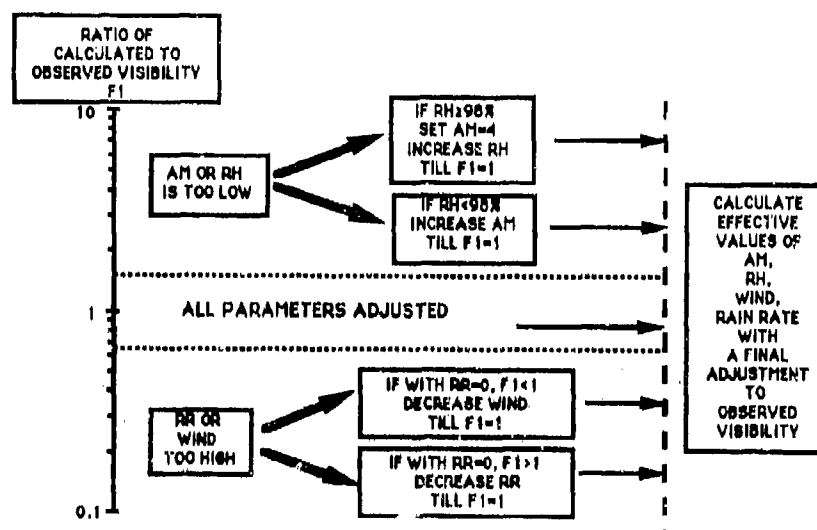


Fig. 3. Weather report interpretation logic.

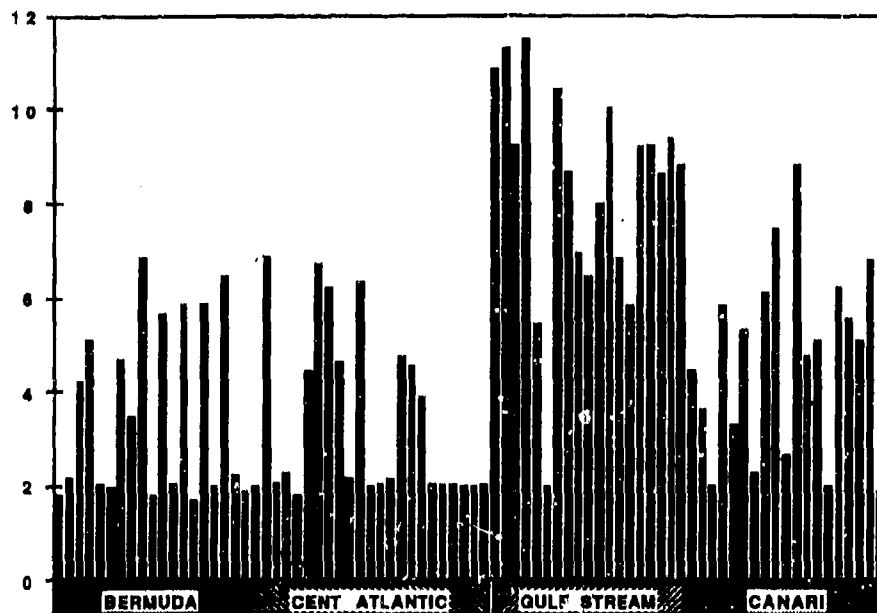


Fig. 4. Effective Air Mass Parameter values: Westlant region.

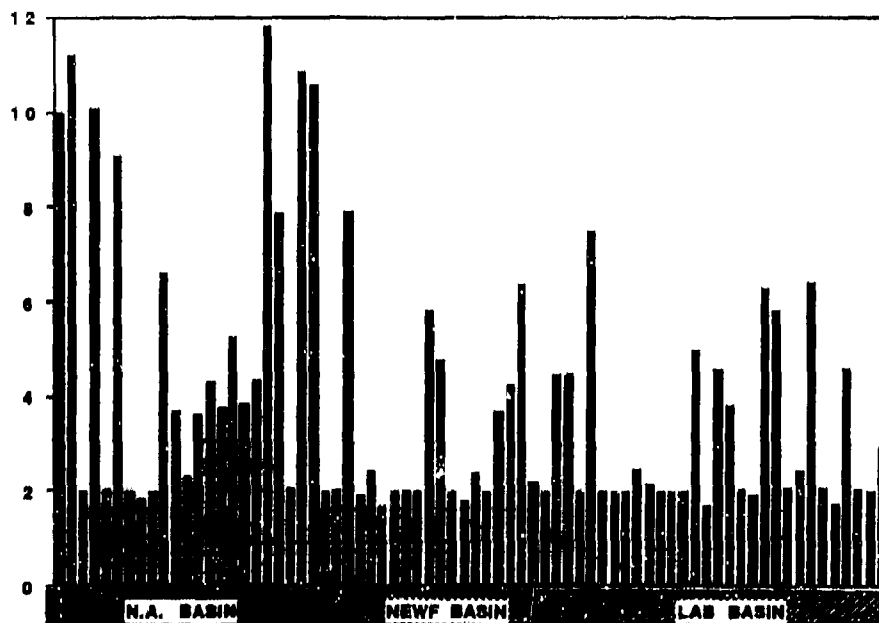


Fig. 5. Effective Air Mass Parameter values: Canlant region.

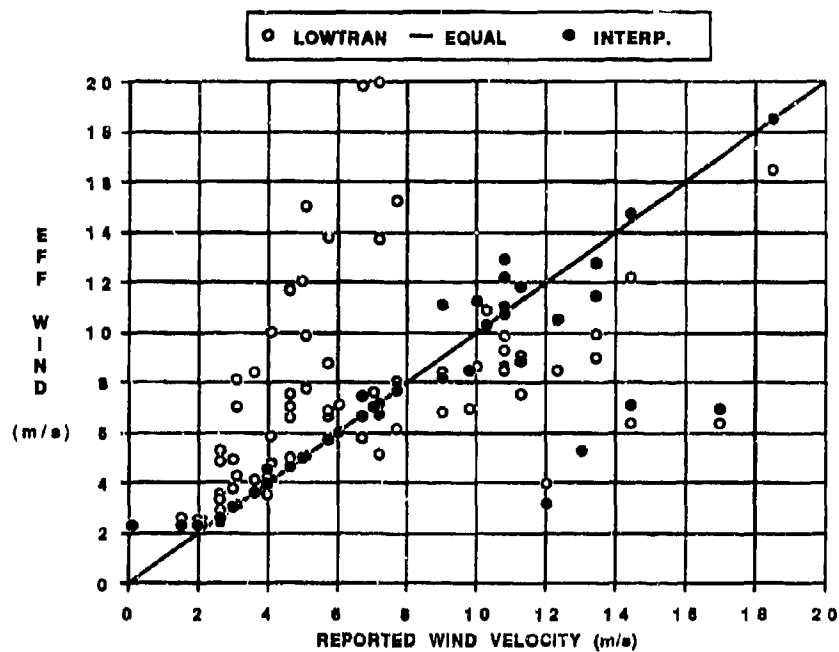


Fig. 6. Comparison of effective winds for the Westlant region.

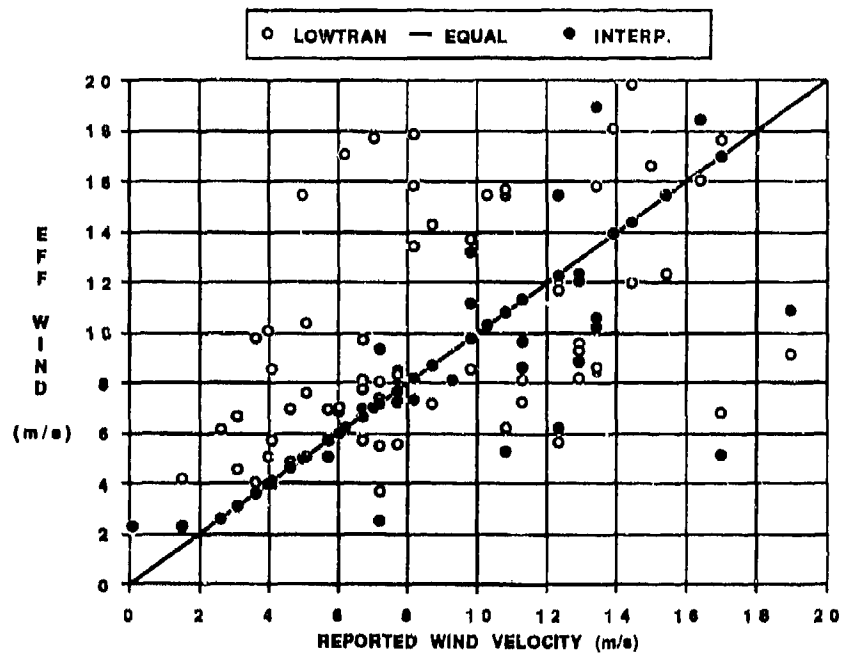


Fig. 7. Comparison of effective winds for the Canlant region.

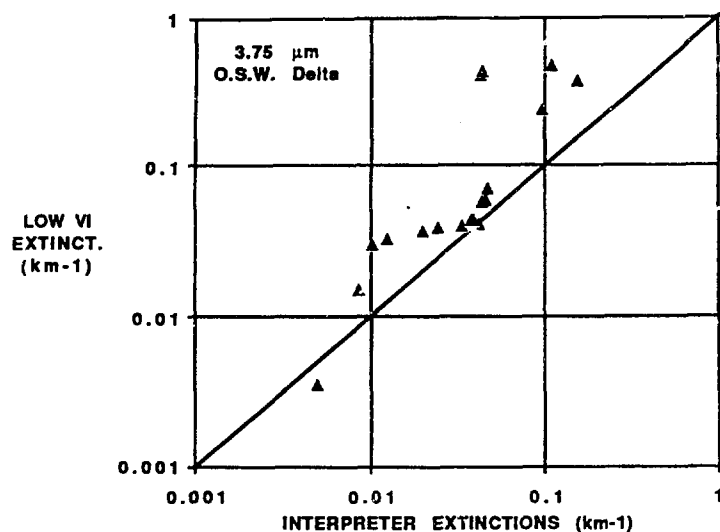


Fig. 8. Comparison of 3.75 μm extinctions for Central Atlantic sub-region.

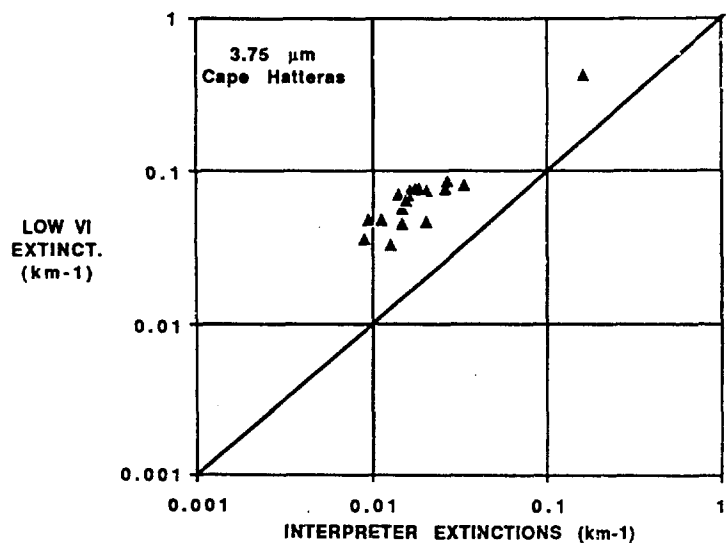


Fig. 9. Comparison of 3.75 μm extinctions for Cape Hatteras station.

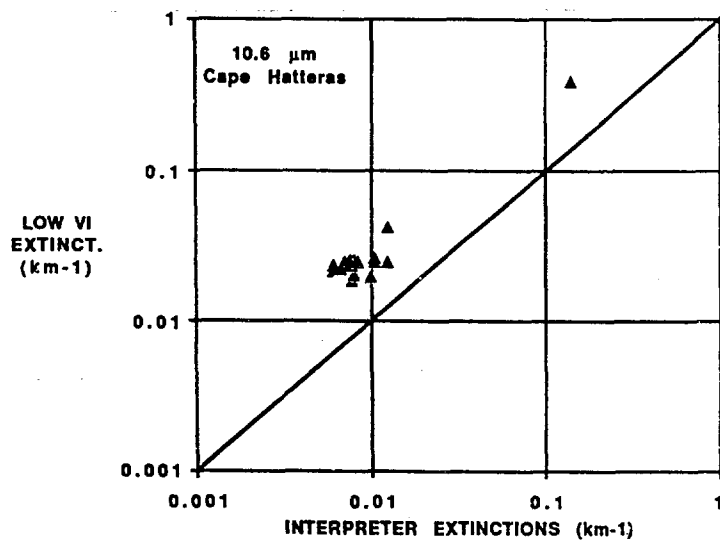


Fig. 10. Comparison of 10.59 μm extinctions for Cape Hatteras station.

DISCUSSION

E. SHUTTLE

Are the visibility data based on observer reports or instrumental measurements (such as a point visibility meter)? Given observer reports are notoriously poor, especially for open ocean with no landmarks, it is probably better to also consider the typical measurement errors for the other measurements, and try not to adjust the relative humidity and wind speed much beyond the expected error bars for those measurements to force agreement with the observed visibility.

AUTHOR'S REPLY

The only available data are meteorological observer reports from weather ships/stations. An error in visibility produces a much smaller IR error using the interpreter than if the same visibility is used with the Navy Aerosol Model visibility adjustment. This code modifies primarily the AM parameter. Relative humidity greater than 98% is the only case where it is adjusted. The precipitation rate and/or average wind is modified when the observed visibility is greater than the calculated one. A 50% error in estimated visibility has a much smaller effect on IR extinction than a change of the AM parameter by a factor of 2.

E. SHUTTLE (COMMENT)

I think the 50% error you used for the visibility is optimistic.

J. SELBY

I agree with Dr. Shuttle that visibility is one of the most difficult parameters to estimate on a ship (unless it is measured independently by an optical instrument). However, wind speed, temperature, and relative humidity are accurately measured. Would it not be better to put more weight on these parameters rather than visibility?

AUTHOR'S REPLY

Wind speed, relative humidity cannot give any clue on the value of the AM parameter. Average wind speed is also very difficult to measure as the data recording is only 2 points per day. Measurement uncertainties for relative humidities in the 98 - 100% range may have a very large effect.

THE NAVAL OCEANIC VERTICAL AEROSOL MODEL: PROGRESS REPORT

by

Stuart G. Gathman
Naval Research Laboratory, Code 4117
Washington D.C., 20375, U.S.A.

Garrit de Leeuw,* and Kenneth L. Davidson
Naval Postgraduate School, Department of Meteorology, Code 63
Monterey, California 93943-5000, U.S.A.

*permanent address: Physics and Electronics Laboratory TNO
P.O. Box 96864, 2509 JG The Hague, The Netherlands

Douglas R. Jensen
Naval Ocean Systems Center, Code 543
San Diego, California 92152-5000, U.S.A.

SUMMARY

The Naval Oceanic Vertical Aerosol Model (NOVAM) has been formulated to estimate the vertical structure of the optical and infrared extinction coefficients in the marine atmospheric boundary layer (MABL). NOVAM was designed to predict the non-uniform and non-logarithmic extinction profiles which are often observed. It is based on a combination of empirical and physical models which describe the aerosol dynamical behaviour. The extinction properties are calculated from the aerosol profiles using Mie theory. For the initial evaluation of NOVAM, data from the July 1987 FIRE experiment (conducted off the coast of southern California) was used. Aerosol particle size distributions, aerosol scattering and required meteorological parameters throughout the MABL were obtained from both airborne and surface based platforms (aircraft, ship and balloon instrumentation packages). The aerosol-derived extinction properties throughout the MABL are compared with the NOVAM estimates.

1. INTRODUCTION

NOVAM, the Naval Oceanic Vertical Aerosol Model,^{1,2,3} is being formulated to estimate the vertical structure of the extinction coefficients in the marine atmospheric boundary layer (MABL) for wavelengths between 0.2 and 40 μm . Its development is based on a combination of empirical and physical models^{4,5,6,7} which describe the aerosol dynamical behavior. The input to the empirical-dynamical model to calculate the profiles of the optical and infrared (IR) extinction coefficients is a given set of atmospheric parameters.^{1,2,3}

NOVAM was designed to describe the non-uniform but also non-logarithmic extinction profiles which are observed to exist throughout the MABL. It is mainly based on physical models for the processes that determine the aerosol vertical structure. The model is restricted to the marine atmosphere, hence the designation "Oceanic" in its title. The differences between this model and land-based models are the marine type of scaling used for the turbulent controlled processes near the sea surface, and the determination of the surface concentrations with the Navy Aerosol Model (NAM).⁴ The structure is a function of turbulent controlled processes and of particle growth due to height varying relative humidities. The turbulent processes produce, deposit and mix the aerosol and also determine the depth of the mixed layer itself.

NOVAM is a combination of models developed at the authors' institutes,^{4,5,6,7} which were merged by Gathman.³ In this paper the model is briefly summarized. A complete description of the model has been presented elsewhere.^{1,2,3} The NOVAM flow chart is shown in Figure 1. The kernel for NOVAM is NAM⁴ which has been extensively updated from the original. NAM produces a particle size distribution at a height of 10 m above the surface from the input data of wind speed (both current and the 24-hour average), visibility and relative humidity. This NAM-generated surface-layer particle size distribution is mixed throughout the MABL by turbulent-controlled processes, further modified by relative-humidity effects. The physics describing these processes are determined by the MABL vertical structure. Various models describing the atmospheric vertical structure are included in NOVAM, such as a simple mixed-layer model⁶ and a shallow convection case.⁵ Provision has been made to include other models such as for deep convection. The selection of the model is based on the input parameters describing the vertical stratification (thermal stability, the presence of an inversion and the inversion height), cloud cover, cloud type, wind speed, and the requested wavelength for the extinction calculation.

NOVAM will perform best when all of the above parameters, and those listed in section 2.1, are available. Thus the input files need to contain surface observations and the MABL vertical structure. The latter information can be obtained from a rawinsonde observation. If the information on the vertical structure is not available a default relative humidity profile, based on the surface observations,⁸ is generated. This

N.O.V.A.M

Dashed lines refer to input
Data flow during calculation.

Solid lines refer to program
logic flow.

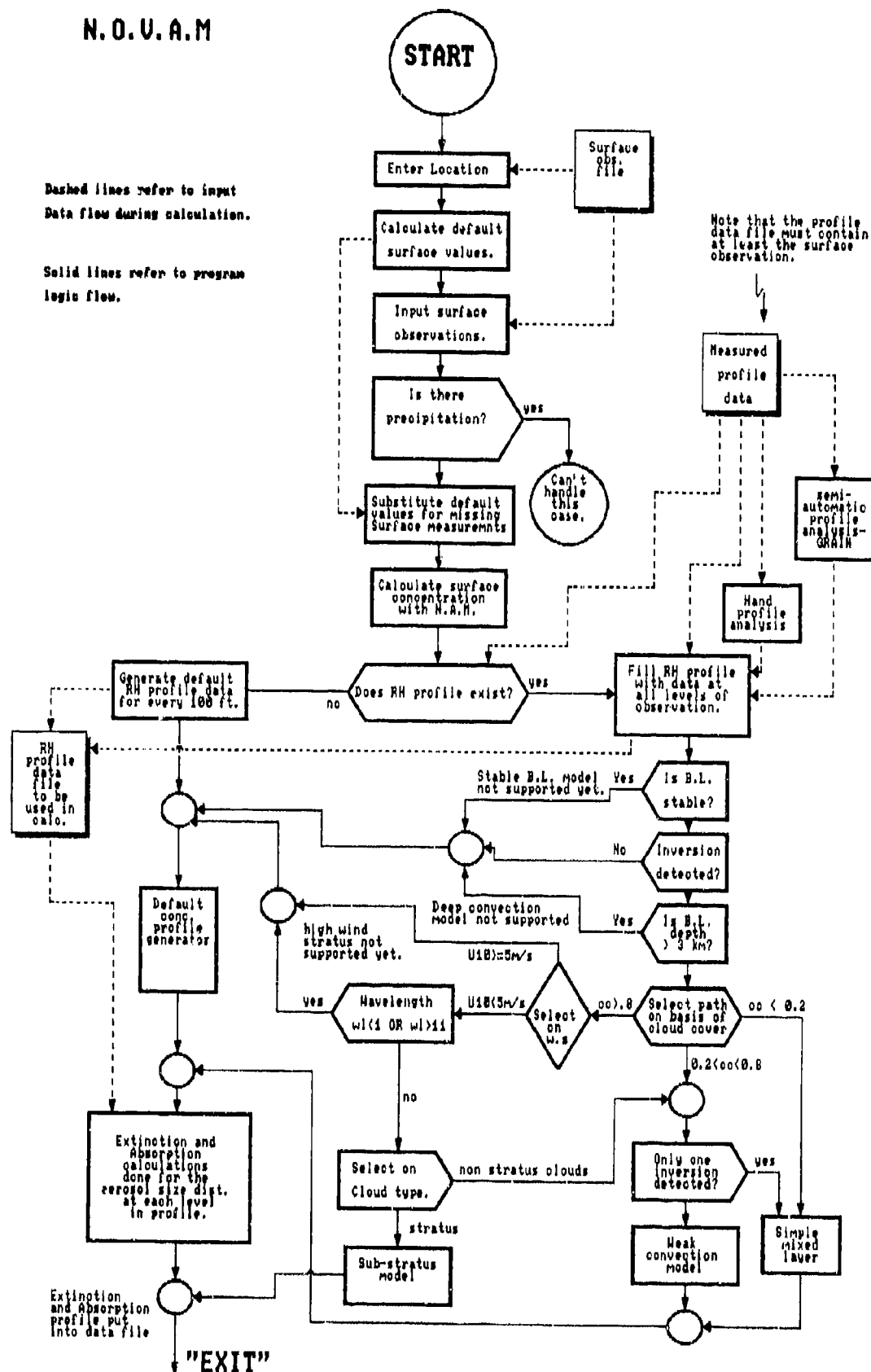


Figure 1. NOVAM flow chart.

default profile is also used when the required input parameters do not satisfy the presently supported models (mixed-layer, shallow convection or stratus). The stratus model is an empirical model that applies only to the marine stratus clouds for wind speeds less than 5 m/s and a desired extinction calculation for wavelengths between 1 and 11 μm .

A preliminary NOVAM-estimated profile comparison with one set of experimental data yielded favourable results.¹ This paper presents a more comprehensive initial evaluation of NOVAM utilizing an extended aerosol and extinction data base obtained during the project FIRE (First ISCCP Regional Experiment), see section 2. Results are compared with NOVAM predictions in section 3. Conclusions follow in section 4.

2. THE FIRE/ROMET EXPERIMENTS

2.1 APPROACH TO EVALUATION OF NOVAM

During June and July, 1987, the Marine Stratocumulus Intensive Field Observation Experiment of FIRE was conducted in the Southern Californian offshore area. FIRE is a cloud research program to validate/update the ISCCP (International Satellite Cloud Climatology Project) data base and cloud radiation parameterizations used in the general circulation models. Coordinated surface, aircraft, and satellite observations of marine stratocumulus clouds within and just above the marine boundary layer were made by a myriad of participants. A general overview of the FIRE project and the participants involved are outlined in reference 9. The Navy's ROMET (Electro-Optics METeorology program) participation in FIRE was both to be supportive of FIRE and to build a quality data base from which NOVAM could be evaluated.

The meteorological parameters required for the NOVAM evaluation are the mean surface-layer wind, temperature, humidity, aerosol size distributions, and visibility, Radon count or air mass parameter (AMP), the boundary layer profiles of temperature, humidity and either aerosol size distributions or optical/IR extinctions. Measurements were made from both airborne and surface based platforms (aircraft, ship, and balloon instrumentation packages). Rawinsonde launches were made from the ship.

2.2 MEASUREMENTS

Measurements were made from several platforms at different geographic locations during FIRE to characterize the stratocumulus topped MABL over spatial distances appropriate for satellite imagery (10 to 100 km). This scale corresponds to the meso-scale which is inherently three dimensional and has important temporal variations at intervals of hours. The measurements from San Nicolas Island (SNI), from aircraft and from the R/V Point Sur were designed to characterize meso-scale features. The measurements from the different platforms and locations were coordinated within intensive periods to describe the three dimensional nature of such features.

SNI is situated 102 km south-southwest of Point Mugu, California. The island is 14.5 km long and 5 km wide. It is an ideal location to make oceanic measurements.

2.2.1 R/V POINT SUR MEASUREMENTS

The R/V Point Sur, operated for the National Science Foundation by the California State University System for the Naval Postgraduate School (NPS), was an important platform because of its over water location and continuous (24 hour/day) measurement schedule for the period 7-16 July. The R/V Point Sur was generally located 30-40 km upwind (Northwest) of San Nicolas Island.

Several meteorological measurement systems were on board the R/V Point Sur to characterize surface layer stability and aerosol properties, and the mixed layer depth and turbulence. The quantities measured and the sensors are listed in Table 1.

2.2.2 AIRCRAFT MEASUREMENTS

The Naval Ocean Systems Center (NOSC) airborne platform was utilized to characterize the low level structure of the marine boundary layer. Flights were made in the vicinity of SNI and were coordinated with the R/V Point Sur, and the Naval Research Laboratories (NRL) Tethered Balloon Facility at SNI. NOSC evaluated one flight during the low stratus conditions on 15 July, and one during the clear sky conditions on 19 July. The former was the only flight when the R/V Point Sur was on station. The prescribed flight pattern for the NOSC aircraft consisted of spiral profiles taken near the NRL ground facility at SNI and upwind of SNI near the R/V Point Sur. Meteorological parameters recorded by the NOSC aircraft are shown in Table 1. Spiral climb rates were at 152 meters/minute. Meteorological data were recorded every 5 seconds and aerosol data every 4 to 8 seconds (depending on meteorological conditions). Each flight was scheduled to occur simultaneously with the NOAA-9 satellite overpass.

TABLE 1. Meteorological Measurements by the EOMET Group during FIRE.

| Measurement | Instrument | Frequency |
|---|---|------------|
| <u>I. NPS: R/V Point Sur</u> | | |
| <u>Mean Surface Layer:</u> | | |
| Radiation(short, total) | radiometers | continuous |
| Vector wind | propeller/vane | continuous |
| <u>Temperatures:</u> | | |
| Air | resistance therm. | continuous |
| Dew point | cooled mirror | continuous |
| Sea surface | floating thermistor | continuous |
| Waves | bridge observation | 1 per hour |
| <u>Turbulence</u> | | |
| Wind | hot-film anemometer | continuous |
| Humidity | Lyman-alpha Sensor | continuous |
| <u>Aerosol and Radon</u> | | |
| .08 to 1.5 μm radius | PMS ASASP | continuous |
| 0.5 to 12 μm radius | PMS CSASP | continuous |
| Radon concentration | HV filter | 1 per hour |
| <u>Mixed Layer and above:</u> | | |
| Vector wind | rawinsonde | 6 per day |
| Temperature | rawinsonde | 6 per day |
| Humidity | rawinsonde | 6 per day |
| Inversion height | rawinsonde/sodar | 6 per day/ |
| and strength | | continuous |
| Turbulence | sodar | continuous |
| <u>II. NRL Aerostat. SNI</u> | | |
| Air temperature | dry bulb thermometer | 5 Hz |
| Relative humidity | dry/wet bulb psychrometer | 5 Hz |
| | saturation hygrometer | 5 Hz |
| Liq. water conc. | forward scatt. meter | 5 Hz |
| Wind vector | bivane anemometer/ inclinometers/compasses | 5 Hz |
| Visual scattering | nephelometer | 1 Hz |
| Altitude | altimeter | 1 Hz |
| Aerosol, 0.5-16 μm radius | PMS CSASP | 1 Hz |
| Videorecordings | video recorder | continuous |
| <u>III. NOSC AIRBORNE PLATFORM</u> | | |
| <u>Temperatures:</u> | | |
| Air | Rosemont | continuous |
| Dew point | EG&G cooled mirror | continuous |
| Sea surface | Barnes IR | continuous |
| Cloud top | Barnes IR | continuous |
| Aerosol, 0.25-15 μm radius | PMS ASSP | continuous |
| 15-150 μm radius | PMS OAP | continuous |
| Altitude | Rosemont | continuous |

2.2.3 TETHERED BALLOON MEASUREMENTS

The NRL balloon facility¹⁰ was located at the northwest tip of SNI approximately 15 m above sea level. The NRL aerostat system consisted of a 538 m³ balloon, with a lifting capacity of 227 kg and a flat bed trailer which serves as a "mobile" mooring system. The instrument package hangs 35 meters below the balloon and the power source to eliminate exhaust contamination near the sensitive aerosol sensing devices. The platform is aligned with the wind by an aerodynamic mechanism. The instruments, listed in Table 1, were co-located on that platform to obtain the extinction in three independent ways. First, profiles of temperature and humidity were recorded for input to NOVAM calculations. Secondly, the aerosol size distributions were measured with an optical particle counter and extinction coefficients were calculated using Mie theory. Finally, a direct measurement of extinction (molecular and aerosol) was made at one wavelength by means of a spherical nephelometer.

3. EVALUATION

It is important to test NOVAM under real scenarios so that the applicability and accuracy of the model can be assessed. There is no better way of discovering model deficiencies, including software errors, than to actually exercise the model under a variety of natural input conditions. Weaknesses in the physical models can be determined by comparing the model estimates of extinction to measurements. In this way the adequateness of the model can be determined and the assumptions/default specifications can be assessed. The chosen approach to evaluate NOVAM is to compare the independently obtained experimental optical/IR extinction profiles with NOVAM estimates using only the simultaneously measured meteorological parameters.

In making such a comparison, one must consider the measurement accuracy of the input meteorological parameters required by NOVAM and the accuracy of the independently obtained optical/IR extinction data. Both of these are subject to instrumentation accuracies and errors introduced by statistical sampling of time and spaciouly varying fields. Although all precautions were taken to eliminate measurement and sampling errors, these types of errors still exist and must be considered when comparing data from different instruments. Therefore, in this evaluation, data envelopes were defined to show the most probable range of the extinction profiles.

Because of the significance of the meteorology to NOVAM, a description of the synoptic situation around SNI is given first. The R/V Point Sur measurements are used for comparison with the NAM. The simultaneous NOSC airborne and NRL Aerostat profile measurements provide the basis for the extinction comparisons with NOVAM.¹⁻³ Both stratus and clear-sky conditions are considered. Finally, a qualitative summary of the initial evaluation of NOVAM is presented.

3.1 SYNOPTIC SITUATION AND SURFACE MEASUREMENTS ON THE R/V POINT SUR, 14-16 JULY

The meteorological synoptic scale situation during the 14-16 July period was controlled by two pressure systems,¹¹ Figure 2. A stationary 1032-1036 mb closed surface high pressure system was located west of Washington State and British Columbia, Canada. A well-defined thermal low was located over Southern California. These two systems caused west to northwest winds in the vicinity of SNI due to the outflow from the high located to the northwest.

The time series of surface layer parameters and representative rawinsonde profiles obtained from the R/V Point Sur for 14-16 July are presented in Figures 3 and 4. Features of interest in the 3-day time series, Figure 3, are the steadily decreasing wind speeds and the diurnal variation of both the wind speed and direction. Steadily decreasing wind speeds are important to the production of marine aerosols. The diurnal variations in the MABL parameters due to the vicinity of the US Mainland, could imply a local circulation influenced by the land-sea proximity. Thus continental aerosol can be carried to the area, which influences the extinction.

The steady decrease in wind speed was associated with the thermal low which was moving northeast (more inland) from the Baja of California on 14 July to the California-Nevada border on 16 July (Figures 2a through f). The eastern Pacific surface high pressure systems remained nearly stationary during this period. The variations in wind speed and direction, during the 24-hour periods, were concluded to be due to the intensification of the thermal low, east of the area, during the local afternoon (1200 PDT is 1900 UT in Figures 2 and 3).

Evidence that there was a land-sea influence associated with the diurnal variation appears in the diurnal variation of the Radon concentration. Whether the Radon was advected horizontally or arrived in the mixed layer due to entrainment is unknown. The increase in temperature and decrease in humidity on the diurnal scale could be associated with entrainment of warm dry air from above the inversion. The entrainment of overlying air with continental aerosol is as important to NOVAM's performance as the horizontal advection of continental air.

The continental influence is obvious in the afternoon of 15 July. The increased Radon concentrations, a clear indication of continental influences, are followed by an increase in the extinction coefficients. The increase in the extinction coefficients is observed at all wavelengths from the visible to the far IR.

The vertical structure of the MABL is of crucial importance to the evaluation of NOVAM. The R/V Point Sur obtained this information from the rawinsonde launches. Profiles for 14, 15 and 16 July, around 2200-2300 UT, are shown in Figure 4. They exhibit differences as well as similarities. The differences are only in the depth of the mixed layer, which increases from the 14th to the 16th. The similarities are in the cloud cover, in the gradients within the mixed layer and in the features at the inversion.

Because of the importance to the stratus case presented in section 3.3.2, features in the rawinsonde profile for 15 July, 2253 UT, Figure 4b, are discussed. A stratus deck existed between 250 m and 650 m. Gradients are observed in the potential temperature and specific humidity throughout the boundary layer. This is not the case for the well-mixed boundary layers observed on 19 July (cf. Figure 6b). The large jumps in the potential temperature above the cloud tops are characteristic for the area. They are an effective lid on the boundary layer, preventing strong mixing of air between the boundary layer and the overlying free atmosphere. Moist layers due to advection are observed in the upper air. The vector winds are seen to be quite variable between the various layers. Changes in wind direction of 180 degrees over distances of less than 100 m are observed.

3.2 TIME SERIES OF SURFACE EXTINCTION

Figures 3d and 3e show the 3-day time series of surface extinction coefficients at 1.06 μm and 10.6 μm , calculated from the particle size distributions measured on the R/V Point Sur. The diurnal variation in the extinction coefficients follows the diurnal variations in the meteorological parameters, i.e. wind speed, Radon concentration and

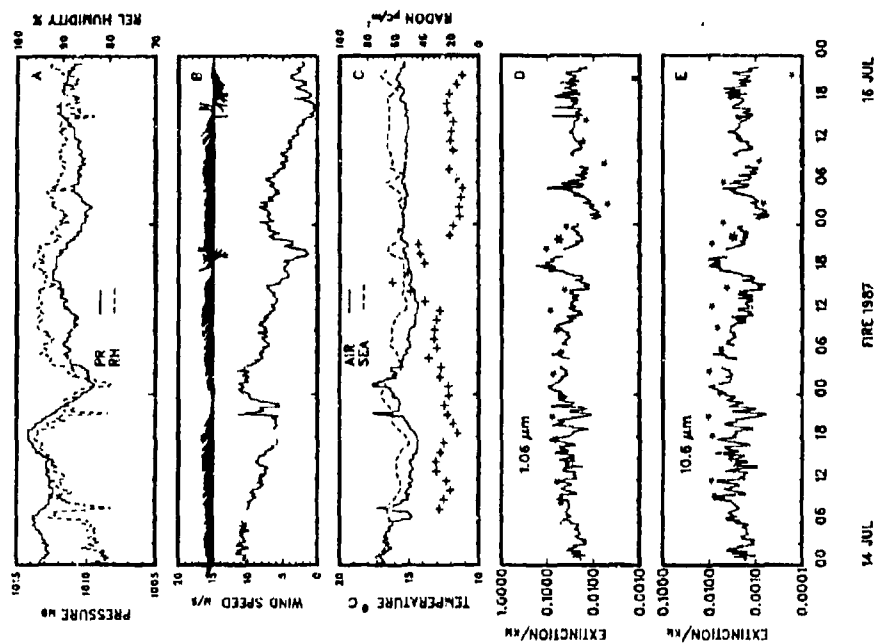


Figure 3. Time series of R/V Point Sur observations of
 a. atmospheric pressure and relative humidity
 b. wind speed and wind direction
 c. air and sea surface temperatures (line) and NOVAM-
 d. aerosol extinction coefficients (line) and NOVAM-
 estimated surface extinctions (*), both for 1.06 μm
 wavelength. The extinction derived from the NOSC
 airborne platform aerosol measurements on 15 July, at an
 altitude of 120 m, are indicated with *
 e. as panel d, for 10.6 μm wavelength.
 Note that the time is UT, i.e. 7 hours ahead of local time
 (PDT).

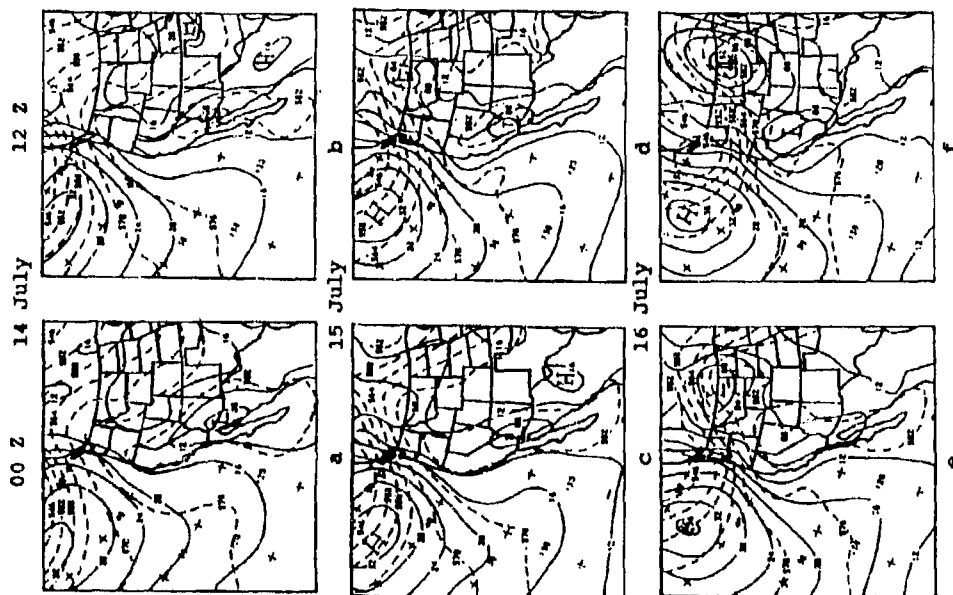


Figure 2. Synoptic weather maps for 14, 15 and 16 July,
 0000 and 1200 UT, i.e. 7 hours ahead of local time (PDT)
 (Figures reproduced from Reference 11).

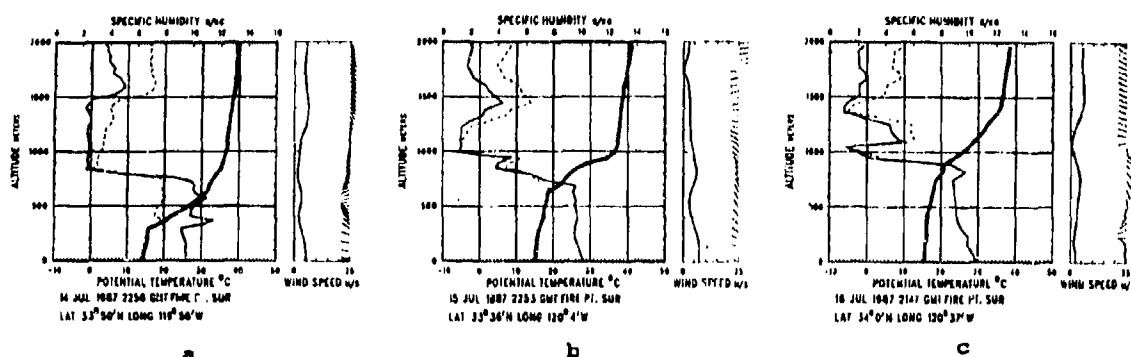


Figure 4. Rawinsonde profiles from the R/V Point Sur for 14, 15 and 16 July, for 2200-2300 UT.

relative humidity. Some of this variation is caused by the continental aerosol being advected from the US Mainland as seen in the afternoon of 15 July when the Radon concentrations peaked to 60 pCi/m^3 . In the far infra-red, the diurnal variation is caused in part by the variation in the sea-salt production in response to the wind speed. Overall, a slight decrease in the extinction coefficients is observed.

The extinction coefficients obtained from near-simultaneous (both in time and geographically) aerosol measurements by the NOSC airborne platform and the R/V Point Sur on 15 July are indicated. The airborne data are for an altitude of 120 m. The data are compared with NOVAM surface predictions, calculated every 3 hours from the observed meteorological parameters. Good agreement exists between the measured and NOVAM-estimated values.

3.3 SIMULTANEOUS AIRCRAFT AND BALLOON FLIGHTS

3.3.1 GENERAL COMMENTS ON EVALUATION

Simultaneous aircraft and balloon flights were considered under two different meteorological conditions, stratus and clear skies. The vertical structures of the meteorological and the optical/IR properties of the marine boundary layer were compared.

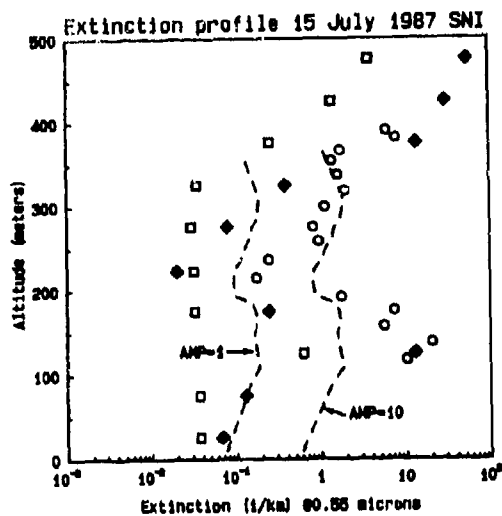
The purpose of having simultaneous flights is two fold. First, to see the variations between island-based and upwind measurements,¹² and second, to compare the two instrumentation packages in situ for data validation considering different system performance accuracies. This applies to both the meteorological instruments and the devices used to determine the optical/IR properties. These instrument accuracies influence both the NOVAM estimates and the data to which they are compared.

3.3.2 STRATUS CASE: 15 JULY 1987

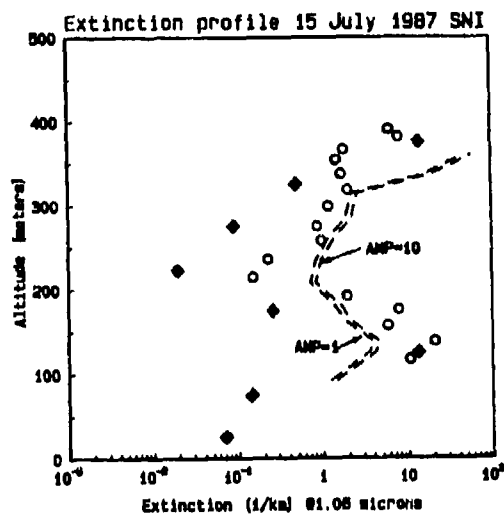
Evaluation of the NOVAM stratus model utilized the aircraft- and balloon-derived meteorological profiles and surface-based observations for the stratus conditions of 15 July 1987, 1500-1700 (PDT). A uniform stratus layer (100% cover) existed at and upwind of SNI with a base around 400 m and tops at 700 m. Winds were northwesterly at 5 m/s. Cloud base at SNI was determined at 320 m from the balloon liquid-water measurements. Drizzle was observed at the ground. Extinction coefficients fluctuated from 80 km^{-1} in the cloud, to low values (0.01 km^{-1}) above the cloud layer. The balloon RH instrument was pegged at 100% throughout the whole boundary layer. Upwind, however, the relative humidity below the clouds varied in the vertical between 95% and 100%, as determined from the aircraft data. The surface relative humidity at the R/V Point Sur, approximately 30 NM upwind from SNI, was 92% (Figure 3). This is a classic case of a stratus deck in which warm dry conditions existed above the moist marine stratus layer.

In Figures 5a through c we show the extinction profiles for wavelengths of 0.55, 1.06 and $10.6 \mu\text{m}$ from all available sources, including the NOVAM estimates below the cloud base. NOVAM presently incorporates two models for the stratus condition, the selection of which is determined by the desired wavelength. For wavelengths less than $1 \mu\text{m}$ or greater than $11 \mu\text{m}$ a mixed-layer model is used (Figure 5a). For wavelengths between 1 and $11 \mu\text{m}$ the sub-stratus model is used (Figures 5b and c). NOVAM does not support conditions of 100% relative humidity, nor does it support situations in which precipitation occurs. The NOVAM comparison of Figures 5a through c utilized the NOSC aircraft data because the NRL instrumentation at SNI recorded relative humidities of 100% and precipitation was observed.

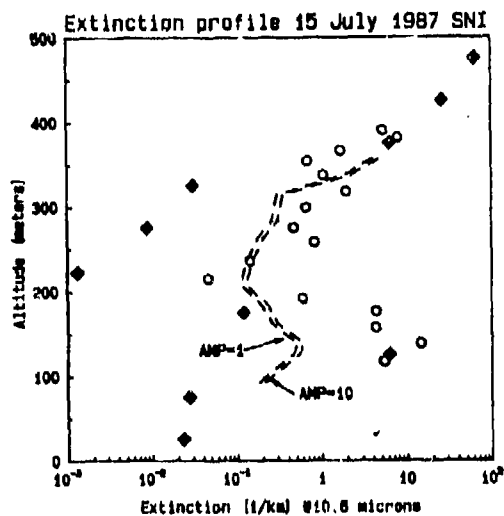
Figure 5a shows the AMP sensitivity of NOVAM for the visible wavelengths. Note that NOVAM selected the mixed-layer model for these calculations because the sub-stratus model does not apply to wavelengths smaller than $1 \mu\text{m}$. The fluctuations in the



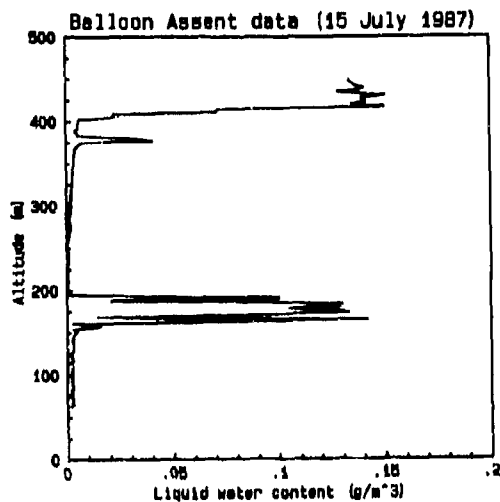
a



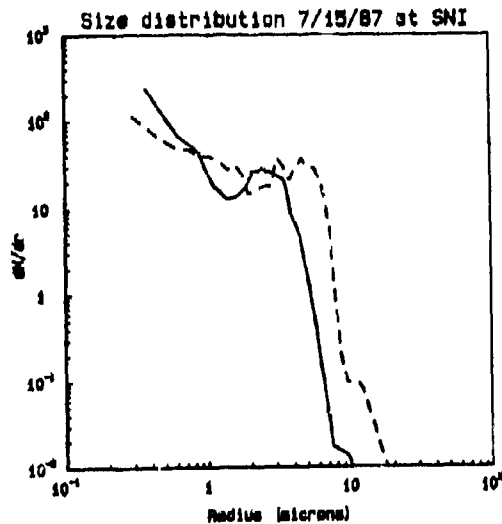
b



c



d



e

Figure 5. Stratus case for 15 July:

- extinction profiles for 0.55 μm , derived from the balloon (\circ) and aircraft (\square) aerosol measurements, the balloon nephelometer measurements (\square) and estimated with NOVAM for AMP's of 1 and 10. The NOVAM profile is estimated utilizing the mixed-layer model because the sub-stratus model does not apply to wavelengths smaller than 1 μm . The curves are further explained in the text.
- extinction profiles for 1.06 μm wavelength, derived from the balloon (\circ) and aircraft (\square) aerosol measurements and estimated with NOVAM (sub-stratus model) for AMP's of 1 and 10.
- as figure b, but for 10.6 μm wavelength.
- liquid water content profiles measured from the balloon.
- aerosol size distributions measured at a level of 125 m from the balloon (broken line) and at 120 m with the aircraft (line). The pronounced peak in the spectra is due to the growth of activated aerosols in supersaturated conditions (relative humidity slightly higher than 100%).

extinction coefficients determined from all sources are generally contained within the AMP limits. In the regions around 120 m and those above 320 m, where the extinction coefficients are outside the NOVAM bounds, the aircraft-observed relative humidities approached 100% - a region where NOVAM is not applicable. The problem here is that the hygroscopic aerosol (like sea salt droplets in the MABL) can be activated when relative humidities go slightly over 100%. The activated aerosols grow in size very fast and behave as cloud droplets, and cannot be described by equations that apply to subsaturated aerosol. This puts them into the arena of fog or cloud physics, and outside of the realm of aerosol modeling - including the capabilities of NOVAM. Figure 5d shows the liquid water concentration profile and Figure 5e the measured size distributions associated with this supersaturation phenomenon.

Figures 5b and c show the extinction profiles for 15 July for the sub-stratus model. The sub-stratus model is not as sensitive to the AMP as the mixed-layer model. Differences between the measured extinction coefficients and NOVAM estimates are in the high-humidity regions just described. The peak in the size distributions shown in Figure 5e affects the far IR more than the near IR.

The dilemma for model verification studies is how to avoid cases where activation is taking place but yet test the model at relative humidity values just below 100%. This dilemma arises because of the uncertainties in both measurement accuracies and horizontal variations of relative humidity. The activation problem can be avoided by excluding all cases where the apparent relative humidity is greater than some trigger value.

3.3.3 CLEAR SKY CONDITIONS: 19 JULY 1987

On 19 July 1987 the sky was clear and the visibility was essentially unrestricted. The winds were northwesterly at 6.5 m/s. The base of the inversion was at 400 meters and the top at 575 m. For clear sky conditions, NOVAM uses the mixed-layer model. Figure 6a shows, for the visible wavelength (0.55 μm), the NOVAM-estimated and aerosol calculated extinction profile. An excellent agreement between the NOVAM predicted and aerosol calculated extinction profiles could be obtained for an AMP between 1 and 10. The curves shown are for an AMP of 2.

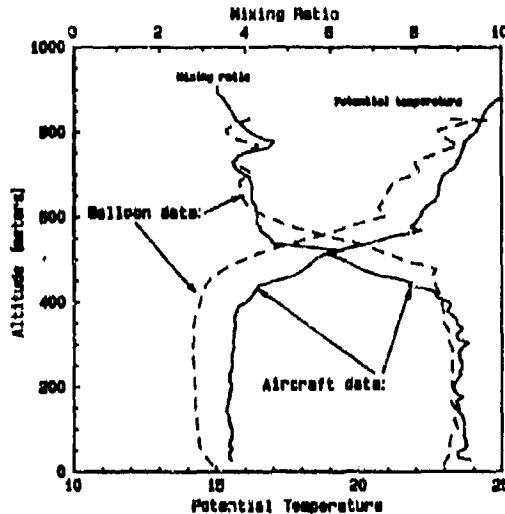
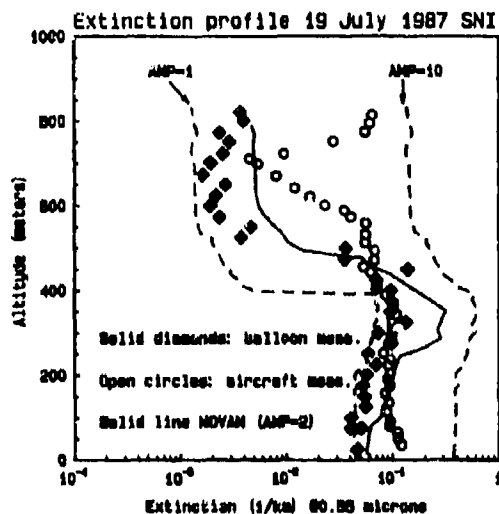


Figure 6. Profiles for clear air case of 19 July:

- extinction profiles at 0.55 μm , derived from the aerosol measurements with the balloon (\blacklozenge) and with the aircraft (\circ). The line is the NOVAM-estimated extinction profile for AMP=2, the broken lines are for AMP's of 1 and 10. The NOVAM-estimated extinction profile is within the envelope of the experimental data for 90% of the time. This profile would thus be graded "A" (see section 3.4).
- potential temperature and mixing ratio profiles.

3.4. INITIAL VALIDATION SUMMARY

In any model validation study certain criteria have to be established by which the performance of the model can be judged. For this initial NOVAM validation the criterium is how well the estimated extinction profiles compare to the experimental values. The envelope of experimental values define the acceptable limits for the NOVAM estimated values. If 90% of all data points in the estimated NOVAM profile were within this envelope, the profile was graded "A", 50% was graded "B". If 90% of all NOVAM-estimated data points was within twice the experimental envelope the profile was graded "C", 50% within twice the experimental envelope was graded "D". Everything outside these limits was graded "F". For the visible wavelengths, the results of this grading procedure for all the balloon and aircraft flights during the EOMET participation to FIRE, 15-25 July, are shown in Figure 7. In general a reasonable agreement existed for this initial evaluation in this West-Coast environment.

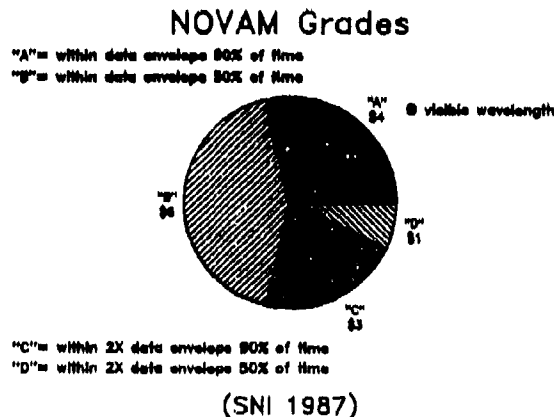


Figure 7. Summary of initial NOVAM validation for the visible wavelength.

4. CONCLUSIONS

NOVAM is an empirical model based on mean meteorological conditions and assumes a simplified marine boundary layer structure. Given a full set of meteorological inputs¹⁻³ it will estimate the extinction profiles for the visible and IR wavelengths. Based on a limited data base the following conclusions can be made:

1. The NOVAM estimates for visual wavelengths fall within the experimentally observed values for 71% of the cases (grades A and B in Figure 7). Reasonable agreement was observed in 22% of the cases and a real failure in only 7% (1 case).
2. NOVAM is not applicable for conditions where the relative humidity approaches 100%.
3. The NOVAM estimates are sensitive to the value of the AMP, a parameter which is not normally measured. Techniques are being incorporated which estimate the AMP from other meteorological inputs.
4. This initial evaluation does not include a study of the sensitivity of NOVAM for cases when only a few of the required meteorological input parameters are available. Also, it does not include the validation summaries for the IR wavelength regions.
5. The results from the initial evaluation of NOVAM are encouraging. However, NOVAM is not yet ready for distribution because the evaluation for other wavelengths, and in particular the evaluation of the default models, has not yet been completed.
6. For NOVAM to be generally applicable, similar evaluations must be made for other geographical areas with different meteorological and oceanographic characteristics.

5. REFERENCES

1. G. de Leeuw, K.L. Davidson, S.G. Gathman and R.V. Noonkester, "Physical models for aerosol in the marine mixed-layer," Proc. AGARD electromagnetic wave propagation panel specialists' meeting on "Operational decision aids for exploiting or mitigating electromagnetic propagation effects", San Diego, CA, USA, 15-19 May, 1989, pp. 40-1 to 40-8.
2. G. de Leeuw, K.L. Davidson, S.G. Gathman and R.V. Noonkester (1989). Modeling of aerosols in the marine mixed-layer. in: Propagation Engineering, Proc. SPIE, Vol. 1115 (1989) Paper 1127 (8 pp.), in press.

3. S.G. Gathman, Naval Research Laboratory, "A preliminary description of NOVAM, the Navy Oceanic Vertical Aerosol Model," 1989, NRL report 9200, Washington D.C.
4. S.G. Gathman, "Optical properties of the marine aerosol as predicted by the Navy aerosol model," Opt. Eng. 22 (1983) pp. 57-62.
5. K.L. Davidson and C.W. Fairall, "Optical properties of the marine atmospheric boundary layer: aerosol profiles," in: Ocean Optics VIII, Proc. SPIE, Vol. 637 (1986) pp. 18-24.
6. C.W. Fairall and K.L. Davidson, "Dynamics and modeling of aerosols in the marine atmospheric boundary layer," in: E.C. Monahan and G. Mac Niocaill, eds., Oceanic Whitecaps, Dordrecht, D. Reidel (1986) pp. 195-208.
7. V.R. Noonkester, "Profiles of optical extinction coefficients calculated from droplet spectra observed in marine stratus cloud layers" J. Atmos. Sci. 42 (1985) pp. 1161-1171.
8. S.G. Gathman, Naval Research Laboratory, "Model for estimating meteorological profiles from shipboard observations," 1978, NRL Report 8279, Washington D.C.
9. FIRE; Marine stratocumulus intensive field observations, June 29 - July 19, 1987, 1987 Operation Plan, May 1987.
10. J.E. James, H. Gerber, S.G. Gathman, M. Smith and I. Consterdine, Naval Research Laboratory, "Navy tethered balloon measurements made during the "FIRE" marine stratocumulus IFO July 1987," 1989, NRL Memorandum Report 6445, Washington D.C.
11. K.A. Klossel, B.A. Albrecht and D.P. Wylie, "FIRE marine stratocumulus observations - summary of observations and synoptic conditions," (1988) FIRE Technical Report No. 1, The Pennsylvania State University, Dept. Meteorology, University Park, PA 16802.
12. D.R. Jensen, "Horizontal variability of the marine boundary layer structure upwind of San Nicolas Island during FIRE," (1989), Naval Ocean Systems Center, Report NOSC TR 1292, San Diego.
13. N.H. Fletcher, "The physics of rain clouds," Cambridge at the Univ. press, 1962.

7. ACKNOWLEDGEMENTS

We wish to acknowledge other people who provided significant contributions to NOVAM. Thanks go to Dr. Juergen Richter (NOSC) who manages the EOMET applied research program under which NOVAM is developed, and Drs. Chris Fairall (Penn State) and Hermann Gerber (NRL) who were involved in numerous discussions on the direction of the formulation. Special thanks go to Mike H. Smith and Ian E. Consterdine of UMIST for making excellent aerosol measurements on the NRL Aerostat, and to Dr. Hermann Gerber for preparing the Aerostat. R.E. Larsen (NRL) made the Radon measurements, Peter Guest, Keith Jones (NPS) and Jeff James (NRL) assisted in data collection on the R/V Point Sur. Pat Boyle and Tamar Neta (NPS) assisted in the analysis. GdL participated in this program while he held a National Research Council Research Associateship at the Naval Postgraduate School.

MODELING MILLIMETER-WAVE PROPAGATION EFFECTS IN THE ATMOSPHERE

H. J. Liebe and G. A. Hufford

National Telecommunications and Information Administration
Institute for Telecommunication Sciences
325 Broadway
Boulder, CO 80303, U.S.A.

SUMMARY

Two millimeter-wave propagation models, called MPM and MZM, are discussed. The first one predicts, at frequencies up to 1000 GHz, loss and delay effects for a nonprecipitating atmosphere. Contributions from dry air and water vapor are addressed, as well as suspended water droplets that simulate fog or cloud conditions. For clear air, a local spectral line base is employed (44 O₂ + 30 H₂O lines) complemented by an empirical water-vapor continuum. Droplet effects are treated with the approximate Rayleigh scattering theory. Input variables are barometric pressure, temperature, relative humidity, and droplet concentration.

At heights between 30 and 100 km, the spectral lines of oxygen result in an anisotropic medium due to the geomagnetic Zeeman effect. The computer program MZM was developed to analyze propagation of plane, polarized radio waves in the vicinity (± 10 MHz) of O₂ line centers positioned in the 60-GHz band and at 119 GHz. Results are displayed that demonstrate many aspects of the unusual wave propagation through the mesosphere.

1. INTRODUCTION

The parameters of a radio wave are modified on propagation through the atmosphere. In general, such influences are due to refraction, absorption, and scatter. The complex refractive index, $n = n' + in''$, is a measure of the interaction of electromagnetic radiation with the medium and depends on frequency and atmospheric conditions. Its real part, n' , exceeds unity by a small amount ($n' - 1 \leq 0.0004$), slowing the propagation velocity to values less than speed of light in vacuum, while the positive imaginary part (n'') pertains to a loss of wave energy.

Complex refractivity, expressed in units of parts per million,

$$N = (n - 1)10^6 = N_0 + N'(f) + iN''(f) \quad \text{ppm}, \quad (1)$$

is a sensible measure of electromagnetic properties exhibited by the atmosphere. Frequency-independent contributions, N_0 , and respective refraction and absorption spectra, $N'(f)$ and $N''(f)$, can be specified.

Refractivity N is the center piece of models that characterize atmospheric radio-wave propagation. Two methods are discussed here to compute refractivity: In MPM, the standard case of an isotropic medium is dealt with [1]; on the other hand, in MZM a very special case is treated where, in the mesosphere, the medium behaves anisotropically and wave transmission depends on location, direction, and polarization [2].

1.1 Standard Atmospheric Propagation (MPM)

Free propagation of a plane wave in the z -direction is described by

$$E(z) = \exp[ikz(1 + N)] E_0 \quad (2)$$

where $E(z)$ is the electric field strength at a distance z along the path, which may be curved by refractive gradients $Re(dN/dz)$ according to Snell's law; $E_0 = E(z = 0)$ is the initial value; $k = 2\pi f/c$ is the free space wave number, and c is the speed of light in vacuum. Assuming the units for frequency f in GHz and for refractivity N in ppm, we have in more practical terminology the dispersive propagation rates of power attenuation α and phase lag β (or delay time τ); that is,

$$\begin{aligned} \alpha &= 0.1820 f N''(f) && \text{dB/km} \\ \text{and} \quad \beta &= 1.2008 f N'(f) && \text{deg/km, or} \\ \tau &= 3.3356 N'(f) && \text{ps/km,} \end{aligned} \quad (3)$$

where $0.1820 = (4\pi/c)10^{-6} \log e$, $1.2008 = (2\pi/c)(180/\pi)$, and $3.3356 = 1/c$.

Program MPM has five modules: (a) nondispersive refractivity N_0 , (b) contributions from 44 O₂ and 30 H₂O local (≤ 1 THz) line spectra, (c) the nonresonant dry air spectrum, (d) an empirical water vapor continuum that reconciles discrepancies with experimental absorption results, and (e) a refractivity due to suspended water droplets. Two additional modules estimate haze (i.e., reversible swelling or shrinking of hygroscopic aerosols when relative humidity varies between 80 and 99.9 %) and rain effects [1], but are not discussed here.

Section 2 gives the particulars how to compute refractivity N from five input parameters:

| | | | | |
|--|-----|-----------------|----------------------|-----|
| frequency | f | 1 - 1000 | GHz, | |
| barometric (total) pressure | P | 110 - 10^{-3} | kPa, | |
| temperature | T | -60 - 50 | $^{\circ}\text{C}$, | |
| relative humidity | U | 0 - 100 | %RH, | and |
| suspended water droplet concentr. at 100 %RH | W | 0 - 5 | g/m^3 . | (4) |

The spatial distribution of these variables along a radio path specifies an inhomogeneous propagation medium [3], a case not treated here. The O_2 Zeeman effect is approximated in MPM so that the height range can be extended to 100 km, but trace gas spectra (O_3 , CO, N_2O , CIO, etc.) are missing.

1.2 Anisotropic Propagation in The Mesosphere (MZH)

At high-altitude (30 - 100 km) pressures, the O_2 lines appear as isolated features and their spectral signature is governed by the Zeeman effect due to the geomagnetic field. The magnetic flux density B_0 varies with location and height and splits each line into three groups of Zeeman components [see (20)] that are spread, proportional to B_0 , over a range of a few megahertz. The spatial dependence of these three groups leads to anisotropic interactions with an electromagnetic field.

Following (2), the propagation of a plane, polarized wave is formulated by

$$E(z) = \exp[ikz(I_z + N_z)] E_0, \quad (5)$$

where z is the distance along a straight-line path. For the x/y -plane of polarization (orthogonal to z) we define $E(z)$, a two-dimensional field vector; $E_0 = E(z=0)$, the initial value; I_z , the 2×2 unit matrix; and N_z , a 2×2 refractivity matrix. Analysis of the complex field E implies a shorthand notation for $\text{Re}[\exp(-i2\pi ft) E]$. As the time t increases through one cycle, this real vector describes an "ellipse of polarization". The program MZH was developed [2] to solve (5) for a spherically stratified mesosphere (i.e., concentric height intervals of 1 km between 30 and 100 km [13]) as detailed in Section 3.

2. THE MPM MODEL

The concept of an atmospheric millimeter-wave propagation model in the form of $N(f)$ was introduced in [3]. Modular, quantitative relationships correlate meteorological conditions encountered in the neutral atmosphere with refractivity formulations. Contributions by dry air, water vapor, and suspended water droplets (haze, fog, cloud) are covered in [1]. Refractivity of air can be obtained, in principle, by considering all known resonant, far-wing, and nonresonant radio-wave interactions with the matter in a given volume element. Various degrees of approximations have been employed to reduce labor and computer time, as well as to bridge unknown spectroscopic information.

2.1 Atmospheric Model Parameters

Atmospheric input parameters are converted into internal model variables; that is, temperature T ($^{\circ}\text{C}$) into a relative inverse temperature variable

$$\theta = 300/(T + 273.15); \quad (6)$$

and relative humidity into

$$U = (e/e_s)100 \leq 100 \quad \%RH, \quad (7)$$

whereby the temperature dependence of the water vapor saturation pressure e_s (100 %RH) is approximated, and in turn, expressed as vapor pressure e or concentration v ; i.e.,

$$\begin{aligned} e &= 2.408 \cdot 10^5 U \theta^4 \exp(-22.64 \theta) \quad \text{kPa} \\ v &= 7.223 e \theta \quad \text{g/m}^3. \end{aligned} \quad (8)$$

Equation (8) allow one to correlate relative (U) and absolute (e or v) humidity and thus to separate the total pressure into partial pressures for dry air and water vapor ($P = p + e$).

Suspended water droplets representing fog or cloud conditions are described by a water droplet concentration W , which can be deduced from measured drop size spectra or estimated as path-average from optical visibility data. Cloud coverage is a frequent event that typically occurs half of the time with vertical extensions of up to 2 km. Whenever a concentration W is considered in MPM [i.e., (9) and (15)], the relative humidity has to be set to $U = 100\%$ ($e = e_s$).

2.2 Complex Refractivity

The total complex refractivity in MPM consists of nondispersive and dispersive parts, $N_t = N_s + N(f)$. Nondispersive refractivity is terms of $P = p + e(U)$, θ , and W follows from

$$N_s = [2.589p + (41.63\theta + 2.39)e]\theta + W[1.5 - 4.5/(\epsilon_s + 2)], \quad (9)$$

with $\epsilon_s = 77.66 + 103.3(\theta - 1)$ being the static permittivity of liquid water (see equation 16).

Dispersive complex refractivity is assumed to be the sum of four contributions,

$$N(f) = N_l(f) + N_a(f) + N_v(f) + N_w(f), \quad (10)$$

where N_l represents local (≤ 1 THz) line contributions, N_a and N_v are dry air and water vapor continuum spectra, and N_w is the refractivity spectrum due to suspended water droplets.

2.3 Local Line Absorption and Dispersion

A line-by-line summation of local spectra by the two principle absorber molecules, O_2 and H_2O , yields the the refractivity contribution

$$N_L = \sum_{j=1}^{44} S_j F_j(f) + \sum_{k=1}^{30} S_k F_k(f), \quad (11)$$

where S is a line strength in kHz, $F = F' + iF''$ is a complex shape function in GHz⁻¹, and j, k are the line indices. The Van Vleck-Weisskopf shape function, modified by Rosenkranz [5], [6] to include pressure-induced line interference, was selected to describe line broadening as follows:

$$F(f) = (f/\nu_0)[(1 - i\delta)/(\nu_0 - f - i\gamma) - (1 + i\delta)/(\nu_0 + f + i\gamma)] \quad (12)$$

defining dispersion [$\text{Re } F = F'(f)$] and absorption [$\text{Im } F = F''(f)$] spectra [1], and the parameters are:

| | Symbol | O ₂ Lines in Air (j) | H ₂ O Lines in Air (k) | |
|----------|-----------|--|--|-------|
| strength | S , kHz | $a_1 10^{-6} p \theta^3 \exp[a_2(1 - \theta)]$ | $b_1 \theta^{3.5} \exp[b_2(1 - \theta)]$ | (12a) |

| | | | | |
|-------|----------------|---|---|-------|
| width | γ , GHz | $a_3 10^{-3} (p \theta^{0.8 - 0.4}) + 1.1 \theta$ | $b_3 10^{-3} (p \theta^{0.4} + b_5 \theta^{0.6})$ | (12b) |
|-------|----------------|---|---|-------|

| | | | | |
|--------------|----------|---|---|-------|
| interference | δ | $(a_5 + a_6 \theta) 10^{-3} p \theta^{0.8}$ | 0 | (12c) |
|--------------|----------|---|---|-------|

A current set of line center frequencies ν_0 and spectroscopic coefficients a_1 to a_6 and b_1 to b_6 for strength S , pressure-broadened width γ and interference δ is given in Table 1 of reference [1]. The computing efficiency of MPM can be improved by approximating the temperature dependence of the width of water vapor lines by setting summarily $b_4 \approx 0.7$ and $b_5 \approx 0.9$.

Zeeman-splitting of O₂ lines has to be taken into account for altitudes above 30 km. Model MZM was developed to treat this special problem (see Section 3). A rough estimate of oxygen line behavior in the mesosphere is made in MPM by replacing the widths γ_j (12b) with

$$\gamma_j^h = [\gamma_j^2 + (25 \cdot B_0)^2]^{1/2} \quad \text{GHz}, \quad (12d)$$

where the geomagnetic flux density B_0 is in microtesla (μT). Doppler-broadening of H₂O lines at heights above 50 km is considered by substituting the widths γ_k with (ν_0 in GHz)

$$\gamma_k^h = [\gamma_k^2 + 2.14 \cdot 10^{-12} \nu_{0,k}^2 / \theta]^{1/2} \quad \text{GHz}. \quad (12e)$$

2.4 Nonresonant Dry Air Spectrum

Nonresonant refractivity terms of dry air make a small contribution [3],

$$N_b(f) = S_d \{1/[1 - i(f/\gamma_d)] - 1\} + iN_p'', \quad (13)$$

due to the O₂ Debye spectrum, $S_d = 6.14 \cdot 10^{-4} p \theta^2$ (kHz) and $\gamma_d = 5.6 \cdot 10^{-3} (p + 1.1 \theta) \theta^{1.05}$ (GHz) [4],

and pressure-induced nitrogen absorption, $N_p'' = 1.40 \cdot 10^{-10} f(1 - 1.2 \cdot 10^{-5} f^{1.5}) p^2 \theta^{3.5}$.

2.5 Water-Vapor Continuum

The real part of the water-vapor continuum spectrum, N_v' , is a theoretical estimate, while the loss term, N_v'' , is an empirical formulation leading to [1]

$$N_v'(f) = f^2(1 - 0.20 \cdot \theta) \theta^3 10^{-5} \quad \text{and} \quad N_v''(f) \approx f(b_e \theta + b_p p) \theta^3 10^{-5}, \quad (14)$$

where $b_e = 3.57 \cdot \theta^{7.5}$ and $b_p = 0.113$. Equation (14) supplements the H₂O line contribution $N_{L,k}$ (11).

Experimental attenuation rates α of moist air generally exhibit more water-vapor absorption than is contributed by the H₂O line base. The excess is most pronounced in atmospheric millimeter-wave window ranges. Continuum absorption N_v'' was determined by a series of accurate laboratory measurements in the 140-GHz window range where absolute attenuation $\alpha(P, T, U)$ was measured at $f = 138$ GHz for both pure water vapor and moist air conditions [7]. The b_p -term of (14) with its strong negative temperature dependence, so far, has not found a sound theoretical explanation. Hypotheses about its origin consider wing contributions from self-broadened H₂O lines above 1 THz, collision-induced absorption, and water dimers. These three effects may be involved separately or collectively [6].

2.6 Suspended Water Droplet Refractivity

Suspended water droplets in fogs or clouds are efficient millimeter-wave absorbers. Their maximum radii are below 50 μm , which allows the approximate Rayleigh scattering theory to be applied to formulate complex refractivity contributions [8],

$$N_d(f) = W[1.5 - 4.5/(\epsilon + 2)] \quad (15)$$

The complex permittivity spectrum of liquid water, ϵ , is given up to 1000 GHz by a double-Debye model,

$$\epsilon(f) = (\epsilon_\infty - \epsilon_1)/[1 - i(f/f_{D1})] + (\epsilon_1 - \epsilon_2)/[1 - i(f/f_{D2})] + \epsilon_2, \quad (16)$$

where ϵ_∞ is given at equation (9); the high frequency constants are $\epsilon_1 = 5.48$ and $\epsilon_2 = 3.51$, and the two relaxation frequencies are (in GHz)

$$f_{D1} = 20.09 - 142(\theta - 1) + 294(\theta - 1)^2 \quad \text{and}$$

$$f_{D2} = 590 - 1500(\theta - 1).$$

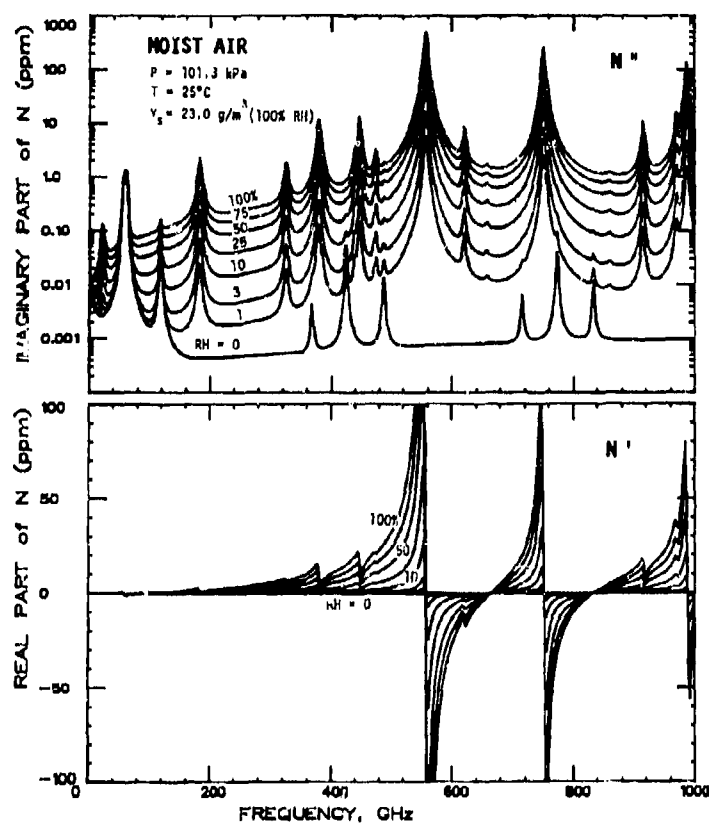
N'' N' 

Fig. 1. Atmospheric dispersive refractivity $N = N'(f) + jN''(f)$ over the frequency range from 0 to 1000 GHz for a sea level condition (P, T) at various relative humidities (U).

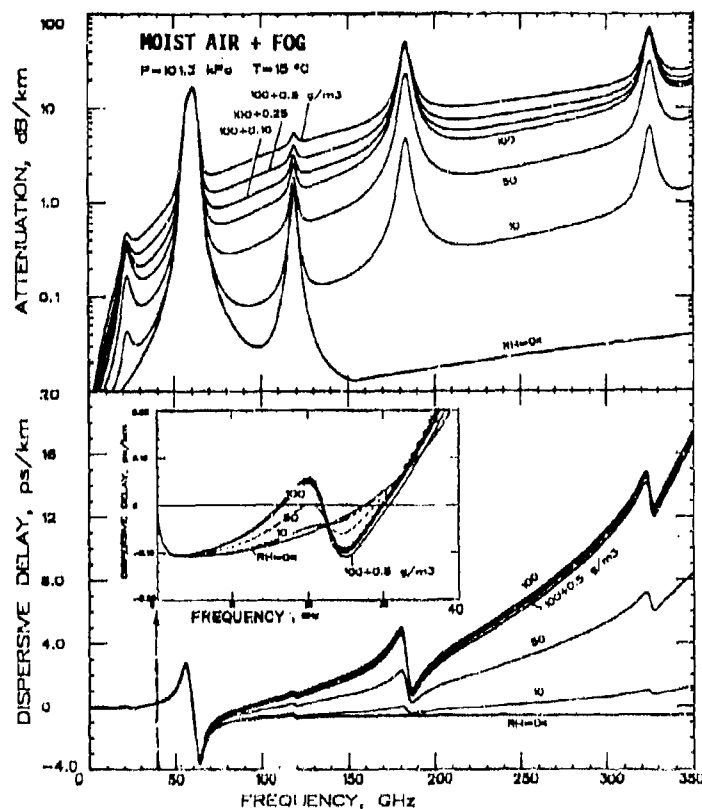
 α τ 

Fig. 2. Attenuation (α) and delay (τ) rates for fog cases ($W = 0.1, 0.25, 0.5 \text{ g/m}^3$) added to a saturated sea level condition. Also shown are dry air (0 %RH) and moist air (10, 50 %RH) characteristics.

The parameters in (16) are best fits to measured permittivity data reported for frequencies up to 1000 GHz over a temperature range from -10 to 30°C.

2.7 MPM Examples

Examples for a sea level condition exhibit spectra at various relative humidities ($U = 0$ to 100 %RH) in Figure 1. Molecular resonance absorption can be recognized in the 60-GHz band, at 119 GHz, and higher due to O_2 , as well as around 22, 183 GHz, and higher due to H_2O . Across the spectrum one notices more or less transparent window ranges separated by molecular resonance peaks. Above 120 GHz, relative humidity (7) is a key variable to describe the dominating water vapor effects of absorption and dispersive refractivity.

Systems designed for the millimeter-wave (90 - 350 GHz) range offer an attractive alternative to electro-optical schemes when operation has to be assured during periods of optical obscuration. Water droplet effects (15) of MPM are added to the state of saturated ($U = 100$ %RH) air by specifying a concentration W . Typical attenuation and delay rates due to fog are displayed in Figure 2.

3. THE MZM MODEL

The mesosphere lies between the stratosphere and thermosphere from somewhat above 30 km in altitude to about 100 km. Air is dry and the environmental parameters are pressure P (1.2 to $3 \cdot 10^{-5}$ kPa) and temperature T (-2 to -87°C) taken from the U.S. Standard Atmosphere 76 [13]. Oxygen line absorption is strong enough to affect radio propagation. Because the pressure is low, the lines are very sharp and new phenomena appear due to the Zeeman effect. The geomagnetic field (magnetic flux density B_0 can vary from 22 to 65 μT) splits each line into a number of sublines, and, furthermore, how these sublines react to an electromagnetic field depends on its polarization state. Over a few megahertz around the line centers, the medium is anisotropic, making radio waves subject to polarization discrimination and Faraday rotation. The physical reasons for this behavior and possible applications are discussed in references [9]-[12]. This background led to MZM, which shows how wave propagation in the mesosphere can be handled [2].

3.1 Oxygen Line Properties As Influenced By The Geomagnetic Field (Zeeman Effect)

The O_2 molecule interacts with radiation via its magnetic dipole moment. Rotational energy levels of the linear molecule have approximate values given by the formula $BK(K+1)$, where B is related to the moment of inertia of the molecule and the "quantum number" K is an odd integer. The microwave lines originate from the fine structure of the K levels caused by the electron spin. For each K , the "total angular momentum" quantum number takes on values $J = K-1, K, K+1$. Transitions can take place between the K and $K+1$ levels and between the K and $K-1$ levels and are labeled the K^+ and K^- absorption lines, respectively.

The program MZM is relevant only ± 10 MHz around isolated line centers $\nu_0(K^+)$ but operates in principle over ± 250 MHz. Each line strength and width is calculated with (12a,b). Center frequencies ν_0 and spectroscopic parameters a_1 , a_2 , and a_3 are listed in Table 1 for 40 O_2 absorption lines. Most of the 60-GHz lines are generally separated by about 500 MHz; since the line width above 30 km is 20 MHz or less, each line is well isolated. There are four cases where K^+ lines are separated by only about 100 MHz. These lines must be treated as "doublets" to account below $h = 50$ km for overlapping contributions.

Pressure decreases with altitude and the O_2 width approaches the Doppler width (ν_0 in GHz)

$$\gamma_0 = 1.096 \cdot 10^{-6} \nu_0 / \theta^{1/2} \quad \text{GHz}, \quad (17)$$

which is associated with a Gaussian shape function. The transition between pressure and thermal broadening is handled theoretically by a Voigt line shape (convolution of Lorentz and Gauss functions) [12]. Following [14], it is adequate to retain the Lorentz shape function (i.e., first term of equation 12) and to suppose that the width γ_i (12b) is replaced by

$$\gamma_h = 0.535\gamma + (0.217\gamma^2 + \gamma_0^2)^{1/2} \quad \text{GHz}. \quad (18)$$

Each of the fine structure J -levels is degenerate since the corresponding states have random azimuthal motion. The quantum number M of azimuthal momentum can be any integer from $-J$ to $+J$. When the O_2 molecule is subjected to a static magnetic field, a force is acting on the internal magnetic dipole. The resulting precession about the field affects the rotational energy in a manner directly related to the azimuthal quantum number M . The level then splits into $2J+1$ new levels. This elimination of degeneracy is called the Zeeman effect.

There are stringent selection rules for transitions between the many energy levels. When J changes by one, then simultaneously M can either remain fixed or else also change by one. Furthermore, each of those transitions can arise because of interaction with only one component of the electromagnetic field. The line components obtained when M is unchanged are called the π components and arise from interaction with a magnetic field vector that is linearly polarized in the direction of B . When M changes by ± 1 , the σ^+ or σ^- components are excited by a magnetic field vector which is circularly polarized in the plane perpendicular to B . The σ^+ (σ^-) components arise from a right (left) circularly polarized field. This anisotropic behavior is explained by noting that circularly polarized forces along the axis of rotation ought to change the azimuthal motion. Each set of components of the K^+ line contains $2K+1$ sublines, while the K^- line contains $2K-1$ sublines.

The line center frequency of a single Zeeman component is given by

$$\nu_0^{\pm} = \nu_0 + 28.03 \cdot 10^{-4} \eta_M B_0 \quad \text{GHz} \quad (19)$$

where ν_0 is the center frequency of the unsplit line, B_0 is in μT , and $\eta_M \leq \pm 1$ is a coefficient that depends on K^+ , M , and ΔM . A geomagnetic field of 50 μT spreads the Zeeman components over about $\nu_0 \pm 1.5$ MHz.

Table 1. Line Frequencies ν_0 and Spectroscopic Coefficients $a_{1,2,3}$ for Microwave Transitions of O_2 in Air

| $K\pm$ | ν_0 | a_1 | a_2 | a_3 |
|--------|------------|-----------------------------|--------|-----------------------------|
| | GHz | kHz/kPa $\times 10^{-6}$ | | GHz/kPa $\times 10^{-3}$ |
| 39- | 49.962257 | 0.34 | 10.724 | 8.50 |
| 37- | 50.474238 | 0.94 | 9.694 | 8.60 |
| 35- | 50.987749 | 2.46 | 8.684 | 8.70 |
| 33- | 51.503350 | 6.08 | 7.744 | 8.90 |
| 31- | 52.021410 | 14.14 | 6.844 | 9.20 |
| 29- | 52.542394 | 31.02 | 6.004 | 9.40 |
| 27- | 53.066907 | 64.10 | 5.224 | 9.70 |
| 25- | 53.595749 | 124.70 | 4.484 | 10.00 |
| 23- | 54.130000 | 228.00 | 3.814 | 10.20 |
| 21- | 54.671159 | 391.80 | 3.194 | 10.50 |
| 19- | 55.221367 | 631.60 | 2.624 | 10.79 |
| 17- | 55.783802 | 953.50 | 2.119 | 11.10 |
| 1+ | 56.264775 | 548.90 | 0.015 | 16.46 |
| 15- | 56.363389 | 1344.00 | 1.660 | 11.44 |
| 13- | 56.968206 | 1763.00 | 1.260 | 11.81 |
| 11- | 57.612484 | 2141.00 | 0.915 | 12.21 |
| 9- | 58.323877 | 2386.00 | 0.626 | 12.66 |
| 3+ | 58.446590 | 1457.00 | 0.084 | 14.49 |
| 7- | 59.164207 | 2404.00 | 0.391 | 13.19 |
| 5+ | 59.590983 | 2112.00 | 0.212 | 13.60 |
| 5- | 60.306061 | 2124.00 | 0.212 | 13.82 |
| 7+ | 60.434776 | 2461.00 | 0.391 | 12.97 |
| 9+ | 61.150560 | 2504.00 | 0.626 | 12.48 |
| 11+ | 61.800154 | 2298.00 | 0.915 | 12.07 |
| 13+ | 62.411215 | 1933.00 | 1.260 | 11.71 |
| 3- | 62.486260 | 1517.00 | 0.083 | 14.68 |
| 15+ | 62.997977 | 1503.00 | 1.665 | 11.39 |
| 17+ | 63.568518 | 1087.00 | 2.115 | 11.08 |
| 19+ | 64.127767 | 733.50 | 2.620 | 10.78 |
| 21+ | 64.678903 | 463.50 | 3.195 | 10.50 |
| 23+ | 65.224071 | 274.80 | 3.815 | 10.20 |
| 25+ | 65.764772 | 153.00 | 4.485 | 10.00 |
| 27+ | 66.302091 | 80.09 | 5.225 | 9.70 |
| 29+ | 66.836830 | 39.46 | 6.005 | 9.40 |
| 31+ | 67.369598 | 18.92 | 6.845 | 9.20 |
| 33+ | 67.900867 | 8.01 | 7.745 | 8.90 |
| 35+ | 68.431005 | 3.30 | 8.695 | 8.70 |
| 37+ | 68.960311 | 1.28 | 9.695 | 8.60 |
| 39+ | 69.489021 | 0.47 | 10.720 | 8.50 |
| 1- | 118.750343 | 945.00 | 0.009 | 16.30 |

Table 2. Relative Shift (η_M) and Strength (ξ_M) Factors for the Zeeman Components

| Zeeman transitions | K^+ - Lines | | K^- - Lines | |
|-----------------------------------|---------------------------|--|------------------------------|--|
| | $\eta_M(K)$ | $\xi_M(K)$ | $\eta_M(K)$ | $\xi_M(K)$ |
| | $M = -K, -K+1, \dots, K$ | | $M = -K+1, -K+2, \dots, K-1$ | |
| π ($\Delta M = 0$) | $\frac{M(K-1)}{K(K+1)}$ | $\frac{3((K+1)^2 - M^2)}{(K+1)(2K+1)(2K+3)}$ | $\frac{M(K+2)}{K(K+1)}$ | $\frac{3(K^2 - M^2)}{K(2K+1)(2K-1)}$ |
| σ^+ ($\Delta M = 1$) | $\frac{M(K-1)-K}{K(K+1)}$ | $\frac{3(K-M+1)(K-M+2)}{4(K+1)(2K+1)(2K+3)}$ | $\frac{M(K+2)-1}{K(K+1)}$ | $\frac{3(K-M+1)(K-M)}{4K(2K+1)(2K-1)}$ |
| σ^- ($\Delta M = -1$) | $\frac{M(K-1)+K}{K(K+1)}$ | $\frac{3(K+M+1)(K+M+2)}{4(K+1)(2K+1)(2K+3)}$ | $\frac{M(K+2)+1}{K(K+1)}$ | $\frac{3(K+M+1)(K+M)}{4K(2K+1)(2K-1)}$ |

Each of the three sets of Zeeman components leads to a refractivity spectrum,

$$N_i(f) = \sum_N S \xi_N F_N(f), \quad (20)$$

where the subscript $i = 0, +, -$ designates π and σ^\pm -components, respectively; the function F_N is a single Lorentzian [first term of (12), $\delta = 0$, and $f/\nu_0 = 1$] plus line strength S and line width γ_N , both independent of N , and equal to the values given by (12a) and (18). The scheme to calculate the coefficients η_N and ξ_N for the individual Zeeman components of each K^1 line is given in Table 2 [2], [12], based on the work by Lenoir [10]. Note that $\sum_N \xi_N$ equals 1 in the case of N_0 and 1/2 for the other two (N_\pm). When $B_0 = 0$ in (19) all the functions F_N are equal and the terms in (20) add so that $2N_+ = 2N_- = N_0 = N_L$.

Magnitude and direction of the geomagnetic vector \mathbf{B} are calculated with the geocentric model MAGFIN, which is updated with 1985 coefficients [15]. To allow for geodetic input coordinates (LATitude, LONgitude, and ALTitude above sea level), a small correction to latitude and altitude is applied to account for the flattening (1/298.25) of the Earth. It follows that path lengths traced through the mesosphere in N-S directions are slightly less than those in E-W directions (see Fig. 6).

The three spectra N_i are components of the constitutive properties in the mesosphere. Since it is the paramagnetic properties of oxygen that bring about the absorption lines, it is the magnetic permeability that is affected. The relative permeability of an anisotropic medium is formally a tensor of rank 2,

$$\mu_r = \mathbf{I} + 2\mathbf{N} \quad (21)$$

assuming \mathbf{N} is on the order of 10^{-6} , and \mathbf{I} is the unit tensor of a coordinate system for the basis $[\mathbf{e}_x, \mathbf{e}_y, \mathbf{e}_z]$ and \mathbf{N} is represented as a 3x3 matrix. When the z -axis is pointing in direction $\mathbf{e}_z = \mathbf{e}_0$ of the geomagnetic vector \mathbf{B} , we have

$$\mathbf{N} = \begin{pmatrix} N_+ + N_- & -i(N_+ - N_-) & 0 \\ i(N_+ - N_-) & N_+ + N_- & 0 \\ 0 & 0 & N_0 \end{pmatrix}, \quad (22)$$

where N_0, N_+, N_- are complex-valued functions of frequency expressed by (20). The shape of these functions is illustrated for an example in Figure 3.

3.2 Basic Equations For Plane-Wave Propagation

The tensor \mathbf{N} may be introduced in Maxwell's equations in the form of (22) and a plane-wave solution formulated [2]. Such solution takes the form of (5). The electric field strength \mathbf{E} is a 2-dimensional vector in the xy -plane and \mathbf{N}_2 is a 2x2 submatrix of \mathbf{N} . The real unit vectors $\mathbf{e}_x, \mathbf{e}_y$ define the plane of polarization which combines with \mathbf{e}_z , the direction of propagation, to form a righthanded orthogonal triad.

The refractivity tensor \mathbf{N} was represented as a 3x3 matrix of the anisotropic medium. It depends for its definition on \mathbf{e}_0 , the unit vector in the direction of the geomagnetic field. To obtain the 2x2 matrix \mathbf{N}_2 acting on the plane of polarization of the radio wave $\mathbf{E}(z)$, we let ϕ be the angle between the geomagnetic field and the direction of propagation, that is, between \mathbf{e}_0 and \mathbf{e}_z . Then the rotation of the "old" coordinate system with basis $[\mathbf{e}_x, \mathbf{e}_y, \mathbf{e}_0]$, in which \mathbf{N} is represented as in (22), and the "new" system with basis $[\mathbf{e}_x, \mathbf{e}_y, \mathbf{e}_z]$ gives \mathbf{N}_2 .

A physically natural approach was to treat refractivity and its propagation effects as associated with the magnetic wave vector \mathbf{H} , which was then changed via the impedance of free space to the corresponding electric field vector \mathbf{E} . The vector \mathbf{E} is not orthogonal to \mathbf{H} but the discrepancy is only of order N . It follows that the refractivity matrix in (5) is given by [2]

$$\mathbf{N}_2 = \begin{pmatrix} N_0 \sin^2 \phi + (N_+ + N_-) \cos^2 \phi & -i(N_+ - N_-) \cos \phi \\ i(N_+ - N_-) \cos \phi & N_+ + N_- \end{pmatrix}. \quad (23)$$

3.3 Characteristic Waves

The computation of the exponential in (5) may be carried out using the technique of spectral decomposition of the square matrix \mathbf{N}_2 [16]. We look for complex numbers ρ (the "eigenvalues") and vectors \mathbf{y} (the "corresponding eigenvectors") that satisfy

$$\mathbf{N}_2 \mathbf{y} = \rho \mathbf{y}. \quad (24)$$

To solve (24), we first treat the scalar equation (the "characteristic equation") [2]

$$\det(\rho \mathbf{I} - \mathbf{N}_2) = 0. \quad (25)$$

Since these are 2x2 matrices, this equation is quadratic in ρ and there should be two solutions ρ_1 and ρ_2 . Given these numbers, it is possible to find the corresponding eigenvectors \mathbf{y}_1 and \mathbf{y}_2 . Whenever the initial field \mathbf{E}_0 equals an eigenvector, then (5) becomes

$$\mathbf{y}_{1,2}(z) = \exp[ikz(1 + \rho_{1,2})] \mathbf{y}_{1,2}. \quad (26)$$

The two vector functions $\mathbf{y}_1(z)$ and $\mathbf{y}_2(z)$ are plane-wave solutions to Maxwell's equation called *characteristic waves*. They have the property that, while they may change in amplitude and phase, they always retain their original appearance and orientation. The two eigenvectors are linearly independent, and for any initial field we may find complex numbers E_1 and E_2 , so that

$$\mathbf{E}_0 = E_1 \mathbf{y}_1 + E_2 \mathbf{y}_2. \quad (27)$$

K= 5+ FQ= 59.59898 GHz B=30.07 μ T
 h= 75. km LAT= .0 deg LON= .0 deg

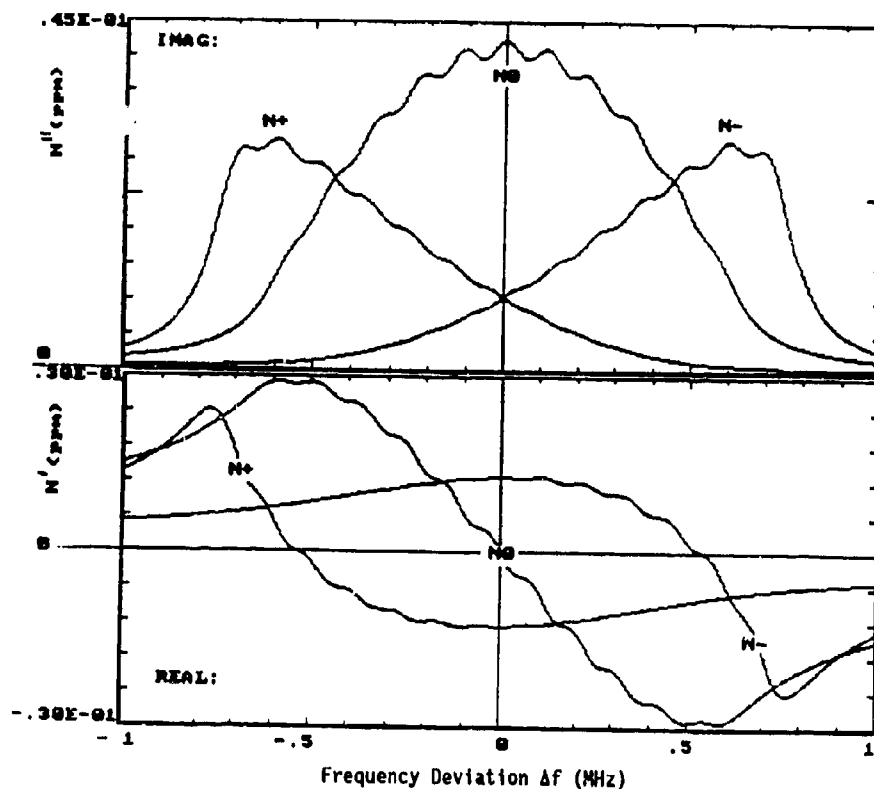


Fig. 3. Refractivity components N_0 , N_+ , and N_- (ppm) in the vicinity ($\Delta f = \pm 1$ MHz) of the $K = 5^+$ line for $h = 75$ km at $LAT=0^\circ$ (equator) and $LON=0^\circ$ (Greenwich) where the flux density is $B_0 = 30.07 \mu T$.

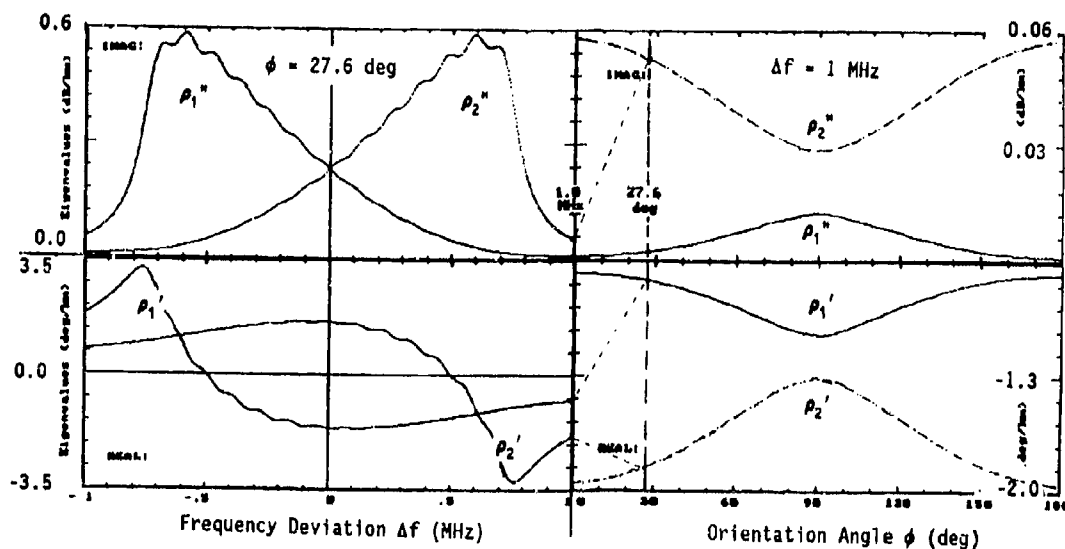


Fig. 4. Complex eigenvalues ρ_1 and ρ_2 for the 5^+ line at $h=75$ km and $LAT=0^\circ$, $LON = 0^\circ$ ($IMAG$ in dB/km, $REAL$ in deg/km): (a) around the line center ($\Delta f = \pm 1$ MHz) at an orientation angle $\phi = 27.6^\circ$ and (b) for orientation angles $\phi = 0$ to 180° at a frequency deviation $\Delta f = +1$ MHz.

Then the exponential in (5) becomes

$$\underline{E}(z) = e^{ikz} [E_1 \exp(ikz \rho_1) \underline{y}_1 + E_2 \exp(ikz \rho_2) \underline{y}_2] . \quad (28)$$

The field vector is now represented as a linear combination of the two characteristic waves.

The eigenvalues, ρ_1 and ρ_2 , have the same order of magnitude as the N_i values and have positive, generally differing, imaginary parts; hence, as z increases, $\underline{E}(z)$ decreases exponentially and one of the two components drops faster than the other. After some distance z , $\underline{E}(z)$ approaches the appearance of the remaining characteristic wave. Also, the real parts of the eigenvalues can differ. The two characteristic waves travel at different speeds through space and the phase relation between the two components in (28) varies continuously. In the process, the ellipse of polarization exhibits a "Faraday rotation."

Eigenvalues and eigenvectors are computed with

$$\rho_1 \rho_2 = \det(N_2) = 4N_0 N_+ \cos^2 \phi + N_0 (N_+ + N_-) \sin^2 \phi \quad (29)$$

and

$$\rho_1 + \rho_2 = \text{trace}(N_2) = 2(N_+ + N_-) + (N_0 - N_+ - N_-) \sin^2 \phi ,$$

from which ρ_1 and ρ_2 may be found. These complex-valued functions depend on frequency and orientation angle as demonstrated by the example in Figure 4. Let us suppose that ρ is one of these two and that we seek the corresponding eigenvector \underline{y} . Its components have the values v_x, v_y , so that (24) becomes a set of two equations in these two unknowns. The second of these equations is

$$i(N_+ - N_-) \cos \phi v_x + (N_+ + N_-) v_y = \rho v_y \quad (30)$$

and one solution is

$$v_x = \rho - N_+ - N_- \quad \text{and} \quad v_y = i(N_+ - N_-) \cos \phi . \quad (31)$$

Since ρ is an eigenvalue, the first equation is also satisfied. The two eigenvectors, v_1 and v_2 , of (27) are usually not orthogonal.

A special case occurs when $\phi = 0$. The solutions to (29) are $\rho_1 = 2N_+$ and $\rho_2 = 2N_-$, and when these are inserted into (31), the corresponding eigenvectors are, respectively, right circularly polarized and left circularly polarized and the z -axis is the direction of the geomagnetic field. When $\phi = \pi/2$, the eigenvalues are N_0 and $N_+ + N_-$, and the corresponding eigenvectors are linearly polarized with the \underline{E} vector pointing respectively along the x -axis and along the y -axis.

3.4 Polarization And Stokes Parameters

The polarization of a radio-wave field changes as it propagates through the Zeeman medium and we have to quantify the polarization. The vector \underline{E} (5) describes an "ellipse of polarization" that can be characterized by Stokes parameters. These are discussed in many texts (e.g., [17]) and here we summarize only some of their attributes.

Let \underline{E} lie in the x, y -plane and E_x, E_y be the complex-valued field components. Then the four Stokes parameters $g_{0,1,2,3}$ are real numbers given by

$$g_0 = |E_x|^2 + |E_y|^2 \quad g_1 = |E_x|^2 - |E_y|^2 \quad g_2 = 2 \operatorname{Re}[E_x^* E_y] \quad g_3 = 2 \operatorname{Im}[E_x^* E_y] \quad (32)$$

where the star indicates the complex conjugate. We note that g_0 is positive and equals the total field strength and recognize that

$$g_0^2 = g_1^2 + g_2^2 + g_3^2 .$$

In a three-dimensional space with g_1, g_2, g_3 axes, the Stokes parameters of a field vector lie on the surface of a sphere of radius g_0 . This is the *Poincaré* sphere and provides a geometric picture of the field vector polarization. Given the Stokes parameters, we can write for some phase angle ψ , that

$$E_x = [(g_0 + g_1)/2]^{1/2} e^{i\psi} \quad \text{and} \quad E_y = [(g_2 + ig_3)/[2(g_0 + g_1)]]^{1/2} e^{i\psi} . \quad (33)$$

The vector \underline{E} determines within the phase angle ψ the Stokes parameters and vice versa. Since the absolute phase of the field remains undefined, the Stokes parameters represent all the useful information for the field. What relates the parameters directly to the ellipse of polarization is the representation of the Poincaré sphere in spherical coordinates

$$g_1 = g_0 \cos 2\tau \cos 2\delta , \quad g_2 = g_0 \cos 2\tau \sin 2\delta , \quad g_3 = g_0 \sin 2\tau . \quad (34)$$

It turns out that δ ($0 \leq \delta < \pi$) is the angle between the major axis of the ellipse and the x -axis, while $\tan \tau = \pm b/a$ ($-\pi/4 \leq \tau \leq \pi/4$), where a and b are the major and minor semiaxes and the sign is chosen according to the sense of rotation. Thus the four Stokes parameters provide a complete description of the polarization.

If one limits the discussion to polarization, the Stokes parameters can be normalized by dividing them all by g_0 and the Poincaré sphere has unit radius. Treating this sphere as a globe, the northern hemisphere and the north pole correspond to right-hand polarization and right circular polarization (RC), while the southern hemisphere and the south pole correspond to left-hand polarization and to left circular polarization (LC). The equator corresponds to linear polarization with "east" at $(g_1, g_2, g_3) = (1, 0, 0)$ corresponding to polarization along the x -axis (HL) and "west" $(-1, 0, 0)$ to polarization along the y -axis (VL).

An alternate way to describe polarization uses the complex number p defined as a ratio of the two field components [18]. From (33) one obtains

$$p = E_y/E_x = (g_2 + ig_3)/(g_0 + g_1), \quad (35)$$

(when $E_x = 1$ then $p = |E_y|e^{i\psi}$) and, when the Stokes parameters are normalized,

$$g_1 = (1 - |p|^2)/(1 + |p|^2), \quad g_2 + ig_3 = 2p/(1 + |p|^2). \quad (36)$$

The real p -axis corresponds to linear, the upper half-plane to right-hand, and the lower half-plane to left-hand polarizations. The points $p = i, -i, 0$, and ∞ correspond respectively to right circular, left circular, linear along the x -axis, and linear along the y -axis polarizations. The advantage of notation (35) is the fact that the seemingly complicated polarization description has been reduced to a single number. The disadvantage is a lack of symmetry between small values of p (near $g_1 = 1$) and large values (near $g_1 = -1$).

3.5 MZM Model Features And Propagation Examples

Generally, a radio wave is defined as a linear combination of the two characteristic waves (28). Horizontal and vertical field components $[E_x(HZE) = 1, p = E_y(VTE) = |E_y|e^{i\psi}]$, where $\psi(POL)$ is the polarization angle (35)], or a matching set of Stokes parameters $[g_1, g_2, g_3]$ normalized to $g_0 = 1$ and $\psi = 0$ (33)] describe the polarization state. Typically, the imaginary parts (expressed in dB/km) of ρ_1 and ρ_2 differ (see Fig. 4), favoring after some propagation distance the characteristic wave with the lower value; simultaneously, different real parts (in deg/km) affect the polarization angle ψ . As a consequence, the polarization ellipse changes its axial ratio and "Faraday"-rotates approaching the polarization state of the dominant characteristic wave.

The mesospheric model MZM gives a solution to the problem introduced by (5). It analyzes the geomagnetic Zeeman effect of O_2 microwave lines to predict anisotropic propagation of polarized radio waves at about ± 10 MHz (Δf) from the line centers. Numerous input parameters are specified:

- frequency, defined as deviation from a particular (K^+) O_2 line center ($\Delta f = \nu_0 \pm f$)
- geodetic coordinates of the location where the wave originates (LATitude, LONgitude, and ALTitude)
- environmental parameters (pressure P and temperature T)
- geomagnetic field vector B [components B_n (north), B_e (east), B_u (up)] and flux density B_0
- polarization state of the launched plane radio wave [p (HZE=1, VTE) and $\psi(POL)$]
- direction and elevation angle [ϕ (AZI_muth, ELE_vation)] of the launched wave

The $K^+ = 5+$ line ($\nu_0 = 59.590983$ GHz) has been chosen as an example. Two cases are discussed:

- a) in a homogeneous atmosphere for given LAT, LON, and ALT(75 km), a radio wave propagates north at the frequency $\nu_0 + 1$ MHz covering a distance z of up to 1000 km, and
- b) at a location LAT, LON, ALT(100 km), a wave enters the inhomogeneous atmosphere, heads in either N, E, S, or W directions, descends to an altitude of 75 km, and then exits again at the 100 km level.

In the first case, path attenuation A and polarization state are followed along. Propagation effects are shown in Figure 5 as a function of distance z for a case where h (ALT), B (LAT, LON), and ϕ (AZI, ELE) are given to determine $\rho_1(y_1)$ and $\rho_2(y_2)$. At the frequency $\nu_0(5^+) + 1$ MHz, two initial polarizations are propagated along a path ranging at $h = 75$ km to a length of up to 1000 km. Results at $z = 1000$ km are

| Initial Polarization | A (dB) | Final Polarization | Figure |
|----------------------|--------|------------------------------|--------|
| 45°L | 10.9 | HZE=1, VTE =1.04, POL=87.4° | 5 |
| LC | 39.5 | 1 1.37 70.0° | 5 |
| RC | 8.0 | 1 1.04 88.0° | - |
| HL | 11.2 | 1 1.03 88.2° | - |
| VL | 10.8 | 1 1.05 87.8° | - |

Computations are more complicated for the second case, where a tangential path from outer space reaches a minimum height, $h_c = 75$ km. Starting at $h = 100$ km in a given direction (AZI) under an elevation angle, $ELV = -5.1^\circ$, a radio ray was traced through a homogeneous path cell via the coordinates LAT, LON, and ALT. Geodetic locations were transformed into geocentric coordinates to compute B , ϕ , and path increments Δz for 1-km height intervals; then a numerical integration was performed whereby the anisotropic behavior of each cell was evaluated analogously to the case exemplified in Fig. 5. The final polarization after traversing one cell served as starting polarization for the next. Total path attenuations A as a function of frequency deviation ($\nu_0 \pm 4$ MHz), initial polarization, and direction are given. Path attenuations for three different initial polarizations and four propagation directions are plotted in Figure 6 as a function of the frequency deviation Δf . Each curve represents the integration over fifty (100 \rightarrow 75 \rightarrow 100 km) 1-km thick cells performed at 100 frequencies between $\nu_0 \pm 4$ MHz. The path attenuations A (dB) at Δf (DFQ) = 1 MHz are

| AZI | Direction | HL | VL | Ratio | RC | LC | Ratio |
|------|-----------|------|-----|-------|------|------|-------|
| 0° | N | 6.4 | 6.7 | 1.05 | 3.5 | 27.6 | 7.89 |
| 90° | E | 13.5 | 8.7 | 1.55 | 12.6 | 9.1 | 1.39 |
| 180° | S | 7.1 | 7.6 | 1.07 | 22.7 | 4.4 | 5.16 |
| 270° | W | 11.9 | 8.5 | 1.40 | 8.5 | 12.3 | 1.45 |

4. CONCLUSIONS

Two parametric models of atmospheric refractivity N (1) have been discussed. Wave propagation described by (2) uses the isotropic model of $N(f; P, T, U; W)$, which is organized by MPM in five modules to control over 500 parameters. It was developed for applications in areas such as telecommunications, radar, remote sensing, and radio astronomy, which operate in the neutral atmosphere between 1 GHz and 1 THz. For MPM, various

shortcomings remain (e.g., empirical nature of H₂O continuum absorption and missing trace gas spectra). The physical origin of the water vapor spectrum in MPM is still not fully understood. Especially, the lack of a theoretical basis for the α -term of continuum absorption (14) is a source of concern. Its largely empirical origin can introduce modeling errors when predicting transmission effects in atmospheric window ranges. Research to uncover the true nature of the millimeter-wave water vapor continuum poses a challenge.

The anisotropic model of N₂(K⁴, Af; P, T; E; B; ϕ) is applied in MZM to a special propagation case that is described by (5) to treat the Zeeman effect of the O₂ lines listed in Table 1. The model predicts the transmission of polarized, plane waves through a spherically stratified (30 - 100 km) mesosphere at frequencies in close proximity of line center frequencies. For MZM, the experimental confirmation of the anisotropic geomagnetic Zeeman effect remains to be realized.

Programs for MPM and MZM were written to run efficiently on desk-top microcomputer (diskettes may be requested from ITS). Validation, error checking of predictions, and incorporation of new research results will continue to be critical and time consuming tasks.

5. REFERENCES

- [1] Liebe, H. J.: MPM - an atmospheric millimeter-wave propagation model, *Int. J. IR and MM Waves*, 10(6), 631-650, 1989.
- [2] Hufford, G. H. and H. J. Liebe: Millimeter-wave propagation in the mesosphere, NTIA Report 89-249, U.S. Dept. Commerce, Boulder, CO, September 1989.
- [3] Liebe, H. J.: An updated model for millimeter wave propagation in moist air, *Radio Sci.*, 20(5), 1069-1089, 1985.
- [4] Danese, L. and R. B. Fartridge: Atmospheric emission models: confrontation between observational data and predictions in the 2.5 - 300 GHz frequency range, *Astrophys. J.*, 342, 604-615, 1989.
- [5] Rosenkranz, P. W.: Interference coefficients for overlapping oxygen lines in air, *J. Quant. Spectr. Rad. Transf.*, 39(4), 287-297, 1988.
- [6] Rosenkranz, P. W.: Chapter 2 in *Atmospheric Remote Sensing By Microwave Radiometry* (M. A. Janssen, ed.), Wiley-Interscience, New York, N.Y., 1989.
- [7] Liebe, H. J. and D. H. Layton: Millimeter-wave properties of the atmosphere -- laboratory studies and propagation modeling, NTIA-Report 87-224, U.S. Dept. Commerce, Boulder, CO., October 1987.
- [8] Liebe, H. J., T. Manabe, and G. H. Hufford: Millimeter-wave attenuation and delay rates due to fog/cloud conditions, *IEEE Trans. Ant. Prop.*, AP-37(12), in press, 1989.
- [9] Townes, C. H. and A. L. Schawlow: *Microwave Spectroscopy* (Chapter 11), McGraw-Hill, New York, N.Y., 1955.
- [10] Lenoir, W. B.: Microwave spectrum of molecular oxygen in the mesosphere, *J. Geophys. Res.*, 73, 361-376, 1968.
- [11] Rosenkranz, P. W. and D. H. Staelin: Polarized thermal emission from oxygen in the mesosphere, *Radio Sci.*, 23(5), 721-729, 1988.
- [12] Liebe, H. J.: Modeling attenuation and phase delay of radio waves in air at frequencies below 1000 GHz, *Radio Sci.*, 16(6), 1183-1199, 1981.
- [13] COESA, U.S. Committee on Extension to the Standard Atmosphere: U.S. Standard Atmosphere 76, NOAA-S/T 76-1562; U.S. Gov. Printing Office, Washington, D.C., 1976.
- [14] Olivero, J. J. and R. L. Longbothum: Empirical fits to the Voigt line width -- a brief review, *J. Quant. Spectr. Rad. Transf.*, 17, 233-236, 1977.
- [15] Barracough, D. R.: International Geomagnetic Reference Field revision 1985, *Pure and Appl. Geophys.*, 123, 641-645, 1985.
- [16] Moler, C. and C. Van Loan: Nineteen dubious ways to compute the exponential of a matrix, *SIAM Rev.*, 20, 801-836, 78.
- [17] Born, M. and E. Wolf: *Principles of Optics* (Section 1.4), Pergamon Press, New York, N.Y., 1959.
- [18] Beckmann, P.: *The Depolarization of Electromagnetic Waves*, Golem Press, Boulder, CO., 1968.

6. ACKNOWLEDGMENTS

The authors acknowledge with gratitude the programming help provided by A. S. Katz in setting up MZM. Preparation of this paper was supported in part by the Naval Ocean Systems Center (Ref: RA35 G80).

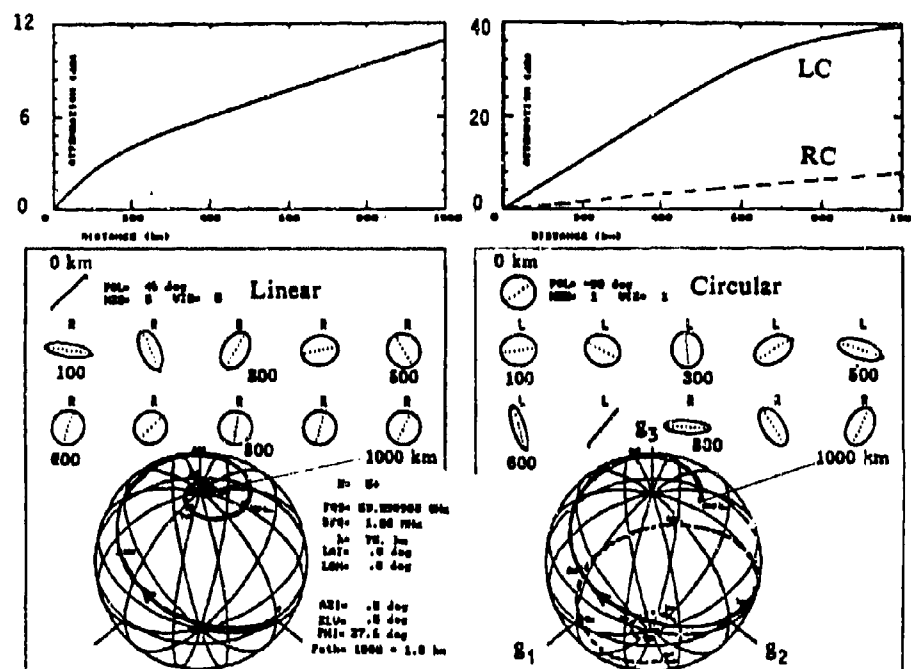


Fig. 5. Attenuation, Faraday rotation, and polarization state (Stokes parameters $g_{1,2,3}$ on Poincaré sphere) for initially linear ($45^\circ L$) and left-circular (LC) polarized radio waves propagating a distance of 1000 km at $h = 75$ km horizontally ($ELV = 0^\circ$) in the north direction ($AZI = 0^\circ$) under the computed orientation angle $\phi(PLI) = 27.6^\circ$ at a frequency $f = \nu_0(5^\circ) + 1$ MHz.

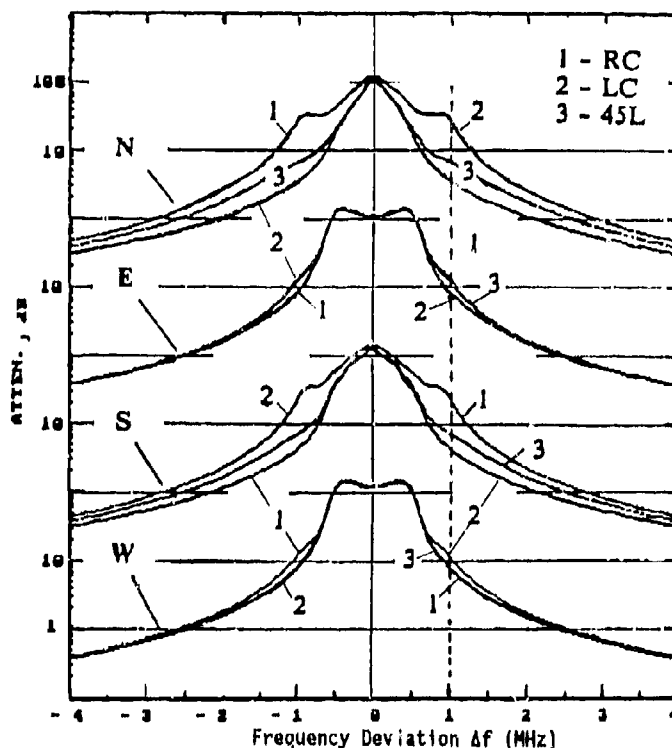


Fig. 6. Cumulative path attenuation A for tangential path through the U.S. Std. Atm. [13] in the vicinity $[\Delta f(DFQ) = \pm 4$ MHz] of the $K=5^\circ$ line. The radio wave enters the atmosphere at $LAT=0^\circ$, $LOH=0^\circ$, and $h(ALT)=100$ km with an elevation angle $ELV=-5.1^\circ$, propagates in either N, E, S, or W directions ($AZI=0^\circ, 90^\circ, 180^\circ, 270^\circ$), approaches a tangential height of 75 km, and leaves the atmosphere at $h = 100$ km. Path lengths: $z_{total} = 1129$ km for N or S, and 1140 km for E or W directions; initial polarizations: right-hand circular (RC), left-hand circular (LC), and 45° linear (45L).

DISCUSSION

J. SELBY

You showed good agreement between your calculations of atmospheric attenuation and some field measurements for your H_2O and O_2 line parameters and your H_2O continuum. How do your molecular line parameters and the H_2O continuum compare with those of AFGL (in HITRAN 86 and FASCOD 2)?

AUTHOR'S REPLY

I showed results from two experiments that confirmed MPM89 [1] predictions of atmospheric water vapor attenuation:

- a. about 1200 data (0.1-1.2 dB/km) from field measurements performed at 96.1 GHz (2-20 g/m³ H_2O , 5-35°C, 98 kPa) [Manabe et al., IEEE Trans AP-37(2), Feb 1989]; and
- b. about 180 data (2-20,000 dB/km) reported between 175 and 950 GHz for the monomer (proportional to ϵ_p) spectrum at 7.5 g/m³, 20°C, 101 kPa plus 35 data (0.3-1.2 dB/km) reported between 210 and 440 GHz to support a theoretical dimer spectrum as H_2O continuum, which is proportional to b_{02} (see equation (14) and reference [7]); [Furashov et al., IEE Conf. Publ. 301, 310-11, ICAP 89].

MPM89 uses from the AFGL HITRAN code only the line strength parameters of 30 H_2O lines -- all other spectroscopic information either originated from our laboratory work or the references given in [1].

Modelling of Optically and IR Effective Atmospheric Turbulence

V. Thiermann, A. Kohnle

Forschungsgesellschaft für Angewandte Naturwissenschaften (FGAN)
 Forschungsinstitut für Optik (FRO)
 (Doc. 1989/103)
 Schloss Kressbach
 D-7400 Tübingen 1
 F.R. Germany

Summary

This paper is devoted to the problem area of modelling atmospheric turbulence, which is limiting electro-optical, especially laser systems performance. We briefly and generally discuss the practical use of Monin-Oboukhov (MO) similarity for predicting the structure constant C_n^2 and the inner length scale l_n of refractive index fluctuations. Even though MO similarity originally was stated for an ideal surface layer which is nearly nowhere found, it can be expected to be helpful also in natural terrain under real meteorological conditions. A set of parameterizations of the surface fluxes, which are required in the MO similarity expressions, is proposed. These parameterizations need only very basic environmental input data.

Results of an experiment are presented showing reasonable agreement between model predictions and direct measurements at different heights. Model input parameters have been measured explicitly here. In many cases, input parameters have to be estimated or there are only simple, not fully representative measurements available. A sensitivity analysis with respect to all input parameters is performed. The overall model error in high refractivity turbulence level situations is found to be about half an order of magnitude for C_n^2 if we sum up over all contributions. For the inner scale l_n this is less than 40 %.

1. Introduction

The performance of electro-optical systems in the atmosphere is often degraded by the effects of turbulent refractivity fluctuations. The variability of the visible and IR window refractive index in the turbulent scale is mainly due to turbulent temperature fluctuations. In some cases a contribution of humidity might also be of importance, especially in the 8-13 μm band. The strongest refractivity turbulence occurs near the earth's surface where turbulence transports heat between atmosphere and ground in a daily cycle.

For many applications it is sufficient to describe refractivity turbulence by the inertial subrange spectral amplitude, the structure constant C_n^2 . For some others, where local angle of arrival fluctuations or, under the condition of a short propagation path or saturation, intensity fluctuations play a role, also the inner scale l_n has to be considered (Lee and Harp, 1969; Hill and Clifford, 1981). Observations have shown a large possible spread of these quantities for different geographical and meteorological conditions. This is especially true for C_n^2 , where values from less than 10^{-16} to about $10^{-12} \text{ m}^{-2/3}$ have been measured. Only recently, optical devices for measuring l_n were developed and applied systematically (Ochs and Hill, 1985; Azoulay et al., 1988; Thiermann and Azoulay, 1989). Values from 3 mm up to about 10 mm and more have been found.

Having the above mentioned variability in mind one understands the importance of a tool for predicting refractivity turbulence at a given location and weather. Since even the temporal variability at a certain location is very high, the simple assumption of climatological averages is not satisfying in most cases. Different prediction models have been developed, up to now being restricted to C_n^2 or to the in practice mostly equivalent structure constant of temperature fluctuations C_θ^2 . A group of models predict the height profile of C_n^2 with the help of statistically from regression analysis derived equations based on a set of meteorological input data (e.g. Eaton et al., 1985). Even though these models seem to be very successful at first view, an extrapolation to other locations than the one where the initial experiments were carried out is problematic.

A better way is to relate the quantities of interest to atmospheric turbulence theory which has always treated problems of deriving turbulence structure from less complex weather data. There are in principle three ways of doing this: the quantities can first be related to local gradients, as the Richardson number. Second, they can be related to the dissipation rates of turbulent kinetic energy and temperature variance, and third, through Monin-Oboukhov (MO) similarity to the height above ground and the turbulent fluxes of heat and momentum. For C_n^2 , the first method was invented by Tsvang (1960). The second method was used by Wesely and Alcaraz (1973). The last method, initially proposed by Wyngaard et al. (1971), is used here. It

can be regarded as the most direct one, because height profiles result directly from MO similarity and because the otherwise necessary derivation of local gradients or dissipation rates would mostly be based on MO similarity itself.

Application of MO similarity requires knowledge of the turbulent fluxes. These have to be obtained through parameterizations from available data. The set of available data is often quite limited and not covering quantities like soil heat diffusivity and heat capacity etc., which are explicitly required in models found in the literature (e.g. Kunkal and Walters, 1983). We tried to keep in mind the limited data base of a potential model user.

2. Similarity Equations

The considerations shall be limited to temperature fluctuations. Humidity fluctuations can be treated in a similar way because both potential temperature and humidity are passive conservative scalars and the respective diffusivities do not differ much. For the structure constant we have

$$C_n^2 = [a_1^2 (p/T^2)]^2 C_T^2 \quad (1)$$

where a_1 is about $79 \cdot 10^{-5}$ hPa/K for the visible and IR windows. p is the atmospheric pressure and T is the temperature in K. We assume the inner scales of refractivity l_n and temperature l_T to be equal (neglecting a shift due to humidity, see Hill, 1978a):

$$l_n = l_T. \quad (2)$$

The MO similarity equations used are those given by Wyngaard (1973):

$$\frac{C_n^2 z^{2/3}}{T_*^2} = 4.9 (1 - 7z/L)^{-2/3} \quad \text{for } z/L < 0, \quad (3a)$$

$$\frac{C_n^2 z^{2/3}}{T_*^2} = 4.9 [1 + 2.4(z/L)^{2/3}] \quad \text{for } z/L > 0, \quad (3b)$$

and Thierymann and Azoulay (1989):

$$\frac{l_T u_*^{3/4}}{(kz)^{1/4} \nu^{3/4}} = \frac{7.4}{(1 - 0.6z/L)^{1/4}} \quad \text{for } z/L < 0, \quad (4a)$$

$$\frac{l_T u_*^{3/4}}{(kz)^{1/4} \nu^{3/4}} = \frac{7.4}{1 + 0.7(z/L)^{1/4}} \quad \text{for } z/L > 0. \quad (4b)$$

z is the height above ground, $T_* = -Q_0/u_*$ is the temperature scale where Q_0 is the surface temperature flux and u_* is the surface friction velocity (square root of momentum flux), $L = -(u_*^3 T)/(k g Q_0)$ is the Monin-Obukhov length where k is the von Karman constant (0.4) and g is the gravitational acceleration. ν is the kinematic viscosity of air ($1.46 \cdot 10^{-5} \text{ m}^2/\text{s}$ at standard temperature and pressure).

The range of validity of the above equations is of course restricted to situations where MO similarity applies. This is in a strict sense only in the surface layer under temporally stationary and spatially homogeneous conditions. The surface layer may be defined by $z \leq |L|$. Above the surface layer we find during day (unstable density stratification, $z/L < 0$) the so called free convection layer, where u_* is no longer a scaling variable. The asymptotic behavior of Eqs. (3a) is such that for $z/L \rightarrow -\infty$ (through vanishing u_*) we get the appropriate free convection scaling. Even though the turbulent fluxes of heat and momentum already decrease noticeably for $z > L$, the upper validity limit of a scaling expression similar to Eq. (3a) was found by many investigators (Frisch and Och, 1975; Kaimal et al., 1976; Wyngaard and LeMone, 1980) to reach a height where entrainment effects between the boundary layer and the free atmosphere start to play a role. This is at about half the height of the boundary layer over land, typically at several hundred meters for days with strong surface heating after the morning hours. The asymptotic behaviour of Eq. (4a) in the limit $z/L \rightarrow -\infty$ ($u_* \rightarrow 0$) is such that l_T becomes a constant. This corresponds to a more or less constant dissipa-

tion rate (see Eq.(11)) in the free convection layer as observed by many researchers (Janschow, 1974; Kaimal et al., 1976; Guillouet et al., 1983). According to their results, the height limit of Eq.(4a) should not be lower than that of Eq.(3a).

At night the stable density stratification ($\alpha/L > 0$) tends to damp vertical turbulent transport, and the surface layer often does not cover more than the lowest several meters. In general the fluxes are assumed to decrease more or less well defined with a power of $(1-z/h)$ where h is the height of the nocturnal boundary layer. Nieuwstadt (1984) however has shown, that local MO similarity based on (the smaller) local fluxes Q_1 and u_1 instead of surface fluxes Q_0 and u_* still applies above the surface layer. Sortban (1986) postulated that the form of the MO functions for local scaling is the same as for surface layer scaling. This would lead to the fact that the errors which occur in the application of Eqs.(3b) and (4b) when leaving the surface layer are not very drastic. Additionally C_T^2 is scaled in the stable limit by a ratio of fluxes: $Q_1^{8/3}/u_1^4$. Both fluxes decrease with height and compensate partly. (Up to now it is not clear whether $Q_1^{8/3}$ or u_1^4 decreases more rapidly with height or, in other words, whether C_T^2 decreases or increases near the top of the boundary layer, see also Gijperts and Kohsiek, 1989.) L_T varies in the stable limit with $Q_1^{-1/4}$ which results in an error of less than 20% if Q_1 is $Q_0/2$. For practical purpose we are thus allowed to stress also Eq.(4b) to some extent into the boundary layer, and we might reach heights of several tenths of meters under moderate winds and even greater heights under stronger winds. For both, C_T^2 and L_T , low wind conditions remain very problematic due to the extremely rapid decay of the fluxes with height and the enhanced importance of radiative processes. Thus we cannot expect to obtain reliable results from Eqs.(3b) and (4b) here.

The problems of stationarity and homogeneity are very difficult to deal with. With regard to stationarity, we fortunately observe the turbulent time scale typically much smaller than the time scale of flux variations. Hence we will usually have the lower boundary layer to be sufficiently stationary to apply MO scaling. Periods of strong instationarity generally occur every day at least twice: after sunrise and before sunset, when the direction of the temperature flux changes sign. During these periods we additionally find the vertical extension of the required constant flux layer to be very limited. This causes problems especially at greater heights. For most practical applications, however, we expect all these effects to be of limited importance, because measurements have shown that the transition periods are characterized by typically low refractivity turbulence levels.

Inhomogeneity of a turbulent field mainly results from inhomogeneities of the underlaying surface with respect to roughness or temperature. Examinations of inhomogeneity effects on turbulence have been made for near neutral stratification by several authors (e.g. Rao et al., 1974). The required length scale for horizontal homogeneity of surface characteristics was found to be about hundred times the considered height. Such surfaces are in reality rarely found.

Let us get an impression of the effects of horizontal mean potential temperature inhomogeneity on C_T^2 . Temperature fluctuations are generated by the interaction of turbulent motion with the gradient of potential temperature. During day the vertical gradient of potential temperature decreases with height and reaches an order of magnitude of typically 10^{-3} K/m at 100m altitude. This does not seem to be much, but in the horizontal a gradient of mean temperature of 10^{-3} K/m = 1 K/km or more is rare. Thus the potential temperature gradient can be assumed to be in the vertical and to be unaffected by horizontal inhomogeneity. Only in a few extreme cases, e.g. near the coast line, we expect stronger effects. At night the vertical gradient is usually stronger than during day, so the situation is even better.

For estimating refractivity turbulence over inhomogeneous terrain in practice we can either use average ground properties or better make worst case calculations which should sufficiently give a range of possible values. We will later derive the model output sensitivity to surface parameters. If the sensitivity to one parameter is low, we also expect a low sensitivity to inhomogeneities of this parameter.

The effect of topography is another point we have to discuss. At daytime and above a certain height, convection is most important for producing temperature and velocity fluctuations. The strength of convection mainly depends on the surface temperature flux which is quite independent of the shape of the underlying surface. Thiernann and Kohnle (1988) have shown that even in the very extreme topography of a mountain valley, Eq.(3a) gives acceptable estimates. We are tempted to generalize these results also to Eq.(4a) even though we do not have any measurements. At night, turbulent friction is the most important mechanism for producing velocity fluctuations, which then produce temperature fluctuations through the vertical temperature gradient. Turbulent friction depends on wind shear and stability, and wind and temperature profiles are complex over non-flat terrain (e.g. Brost and Wyngaard, 1978). For practical applications, however, results might still be used in some cases, given data for a local flux estimate are available. We assume that, if the nearest elevation is further than, say, 100·z, we should have something like locally flat terrain. Or, if the height of upwind elevations within a distance of 100·z is less than, say, 0.1·z we could treat these elevations as roughness elements.

3. Flux Parameterizations

Eqs. (3) and (4) relate C_T^2 and I_T to the surface fluxes of heat and momentum. The used parameterizations of these fluxes are, little modified, those of Thiernann and Kohnle (1988). The momentum flux follows from the integrated flux profile relationship (Paulson, 1970; Dyer, 1974):

$$u_* = \frac{k u}{\ln \frac{z_u}{z_0} - \psi} \quad (5)$$

where

$$\psi = 2 \ln[(1 + y)/2] + \ln[(1 + y^2)/2] - 2 \tan^{-1} y + \pi/2$$

$$y = (1 - 16 z_u/L)^{1/4} \quad \text{for } z_u/L < 0$$

and

$$\psi = -5 z_u/L \quad \text{for } z_u/L > 0.$$

The needed input data are the windspeed u measured at the height z_u and the surface roughness length z_0 . The temperature flux Q_0 is estimated as follows.

For daytime a slightly simplified version of the parameterization scheme of Holtslag and Van Ulden (1983) provides Q_0 from solar irradiation R , surface albedo A , ground humidity parameter α and the temperature dependent temperature derivative of saturation specific humidity $s = \partial q_s / \partial T$:

$$Q_0 = \frac{\eta}{c_p \rho} \left(1 - \frac{\alpha}{1 + \gamma/s}\right) (1 - A)R - \beta. \quad (6)$$

γ is the ratio of the specific heat of air at constant pressure to the latent heat of water vapour c_p/r_w , ρ is the air density, and η and β are empirical constants. For η and β we choose 0.9 and 20 W/m² respectively. The humidity parameter α is 1 over wet surfaces, including midlatitude grassland, and 0 over dry surfaces like deserts. Intermediate values must be taken for partly vegetation covered terrain. The principle of Eq. (6) is an energy balance consideration. The system is driven by the absorbed fraction of the solar irradiation $(1 - A)R$. Part of this leaves the surfaces via IR radiation or ground heat conduction, the factor η and the offset β account for that. Following the Penman concept of equilibrium evapotranspiration, the remaining energy is partitioned between sensible heat flux $H_0 = c_p \rho Q_0$ and latent heat flux $E_0 = r_w W_0$, where W_0 is the surface water vapour flux. The temperature dependence of the sensible heat flux fraction for $\alpha = 1$ in Eq. (6) is shown in Fig. 1. A possible large reduction of the sensible heat flux due to ground humidity can be seen, especially for higher air temperatures.

This parameterization still contains the solar irradiation explicitly as a parameter, even though it cannot be considered to belong to standard weather data. However there is a variety of estimation schemes for R in the literature, mainly in terms of astronomical parameters and cloud cover. It is not our goal to improve such estimation techniques, the reader should refer to Holtslag and Van Ulden (1983) or others.

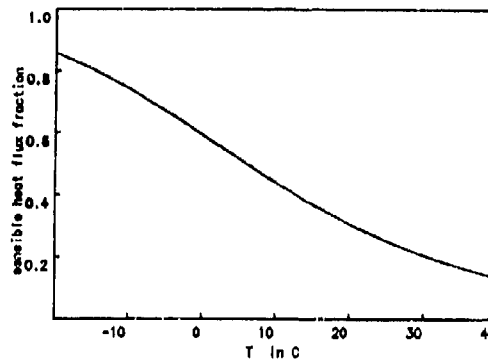
A difficult task is the parameterization of the nighttime temperature flux. There is a complex equilibrium at the surface between ground heat storage, the processes of radiative cooling, latent cooling or heating (due to evaporation or dew production), ground heat conduction and sensible turbulent heat flux. None of these processes is generally dominant making simple assumptions on the energy balance impossible. Our approach to proceed here is trying to isolate the effect of one important parameter: the wind speed. At night, the wind shear is driving the temperature flux against the buoyancy forces. To see which functional dependence on wind speed Q_0 has, we examine the dependence of Q_0 on u_* in Eq. (5) for $z_u/L > 0$. We see that there is a maximum value of possible Q_0 , which is in terms of u , z_u and z_0 :

$$Q_{0m} = c u^3 \quad (7)$$

with

$$c = -\frac{4}{27} \cdot \frac{k^2 T}{5 z_u g [\ln(z_u/z_0)]^2}.$$

Fig.1. Partitioning between sensible and latent heat flux. Temperature dependence of the factor $[1 - 1/(1+\gamma/s)]$ in Eq.(6).



(The derivation of Eq.(7) is based on some premises which are not fully true under real conditions. However a discussion of this would be beyond the scope of this paper.) An example of an observed wind speed dependence of Q_0 is given in Fig.2. Here Q_0 is obtained by an optical measurement of c_T^2 and a measurement of wind velocity via Eqs.(3b) and (5) with a known roughness length. The upper curve represents Eq.(7). We see that for low wind velocities the measured Q_0 is very close to the one predicted by Eq.(7). (The fact that the "maximum possible" Q_0 is observed under low wind conditions might be explained by a negative feedback mechanism near the turbulence collapse involving the whole lower boundary layer.)

It is clear that, if the wind speed goes to infinity, Q_0 can not increase further with u^3 because this would force a contradiction with energy balance considerations. It is even plausible that the u dependence of Q_0 reaches more or less early saturation, since under strong winds and near neutral conditions it is especially the IR radiative flux component, which limits Q_0 . This upper limit of the sensible heat flux $H_{Omax} = c_p \cdot \rho \cdot Q_{Omax}$ shall be an empirical parameter and enter the parameterization equation in a way that provides a smooth transition from the low wind to the saturation regime, such as:

$$Q_0 = \frac{c u^3}{1 + \frac{c}{Q_{Omax}} u^3} \quad (8)$$

The value of H_{Omax} mainly depends on the radiative situation and the ground heat conductivity. Phenomena which reduce surface cooling, like cloud cover, high air humidity, or high ground conductivities (moist ground) lead to low values of H_{Omax} . Clear sky in a dry atmosphere over well isolated ground (desert) should give the highest values of H_{Omax} . We don't have systematic measurements but we expect low values for cloud covered sky of about 5 to 10 W/m² and high values for clear sky of 20 to 100 W/m² depending on air humidity and soil type. In Fig.2, Eq.(8) is drawn in for three values of H_{Omax} . The measurements were taken under clear sky (Heppen experiment, see next section). The curve corresponding to H_{Omax} equal -40 W/m² fits the points reasonably well.

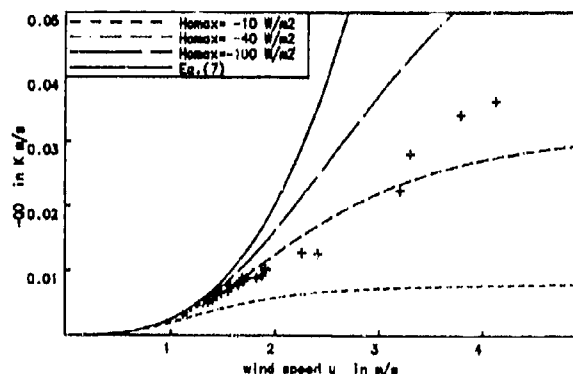


Fig.2. Wind speed dependence of nocturnal temperature flux Q_0 . Crosses denote measurements, curves are Eqs.(7) and (8).

4. Comparison with measurements

Data taken during the turbulence experiment in Meppen (northern F.R. Germany) in late summer 1988 were used to compare model predictions of C_T^2 and I_n with measured values. The experiment is described in Thiermann and Azoulay (1989). The experimental site was flat agricultural land with single groups of trees at distances of 150m and more. At a height of 2m, C_T^2 and I_n were measured by a bichromatic scintillometer. The evaluation of the optical data was based on the turbulence spectrum of Hill (1978b). Additionally, at heights of 48m and 80m, a meteorological tower was equipped with ultrasonic anemometer thermometers taking spectra of temperature $\Phi_T(\kappa)$ and velocity $\Phi_{u_i}(\kappa)$ which were related through Taylor's hypothesis to the spatial wavenumber κ . From these spectra we computed C_T^2 and the dissipation rate ϵ using the inertial subrange expressions:

$$\Phi_T(\kappa) = 0.25 C_T^2 \kappa^{-5/3} \quad (9)$$

and

$$\Phi_{u_i}(\kappa) = (4/3) \alpha_u \epsilon^{2/3} \kappa^{-5/3} . \quad (10)$$

The Kolmogorov constant α_u was chosen to be 0.5 following Champagne et al. (1977). The dissipation rate finally was related to the inner scale via (Hill and Clifford, 1978):

$$I_n = I_T = 7.4 \nu^{3/4} \epsilon^{-1/4} . \quad (11)$$

In parallel to the turbulence measurements, low resolution data of all basic meteorological quantities were recorded. Wind speed at 2m height and solar irradiation were used as model input. The roughness length z_0 was determined from the wind profile to be 9mm and the albedo A was measured to be 0.2. The ground humidity parameter a was estimated to be 0.7 except after rain when it was set to 1.

Time series of solar irradiation and wind speed during the comparison period of about four and a half days are shown in Figs.3 and 4. The time scale is given in days (date) and flat numbers correspond to midnight according to local time. The first day was prevailingly cloudy with occasional rain showers, the second day was characterized by broken clouds, and the last two days were nearly constantly sunny. Nights were clear in most cases and, as Fig.2 suggested, we fixed H_{0max} to -40 W/m^2 . The wind speed ranged during day from about 2 to 5 m/s and during night from around 1 to 3 m/s, except during the third night which for many hours did not show any measurable wind velocity.

In Fig.5 the model prediction of C_T^2 at heights of 2m (upper curve) and 48m (lower curve) is given. This prediction is based on 10 min means of the input parameters and the output has been smoothed by a sliding 30 min average. Optically (at 2m) measured values of C_T^2 are marked by circles (10 min means) and tower measurements (at 48m) by stars (30 min means). Periods of missing symbols correspond to times where the optical system was not operated or the wind direction was such that tower flow distortion could not be excluded.

Predictions and measurements show good agreement. Discrepancies occurred at 48m mainly in the morning or evening hours when the stationarity requirement was not fulfilled (see Section 2). It is interesting and of considerable importance for applications that during these instationarity periods C_T^2 did not significantly exceed the values before or after these periods. Generally we see values of C_T^2 near the ground during sunny days about one order of magnitude larger than during night. At 48m we find less variation between day and night. The lowest values were observed during the first day where the sky was cloudy and the ground was wet. Cloudy nights have not been examined.

Fig.6 compares model predictions of I_n with measured values, now for 2m (lower curve) and 80m (upper curve). Again there is a good general agreement between model prediction and measurement except for the instationarity periods. At 2m we observed inner scale values between 3mm and 6mm during day and between 5mm and 8mm during night. As for C_T^2 , the magnitudes itself are of minor importance compared to the fact that the model predicts these values quite well. Different environmental parameters could lead to quite different results. At 80m, values between 8mm and 20mm occurred. In the calm night we determined values even up to about 50mm. Here the model is principally in doubt (see section 2). Also the measurements cannot be regarded with too much confidence here, because the wind fluctuations in the undisturbed flow are very small and sensor flow distortion might have a large effect. Such effects would lead to too small values of derived I_n , so we can rather expect even higher values of I_n in the undisturbed flow.

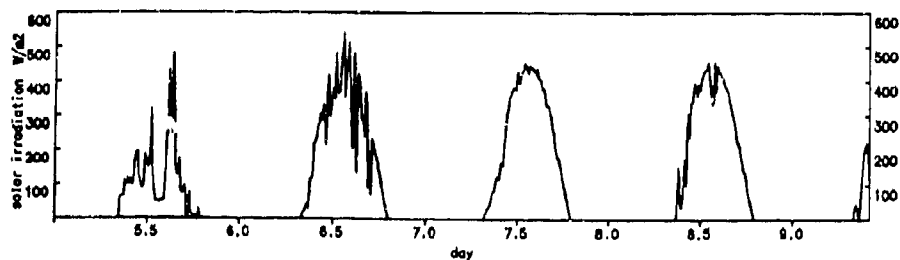


Fig.3. Time series of solar irradiation during the measurement period of four and a half days.

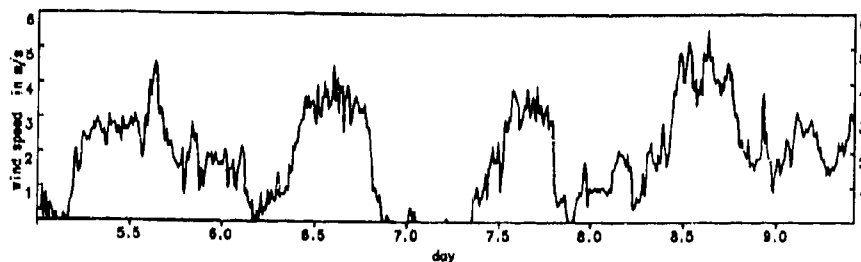


Fig.4. Same as Fig.3 but for wind velocity.

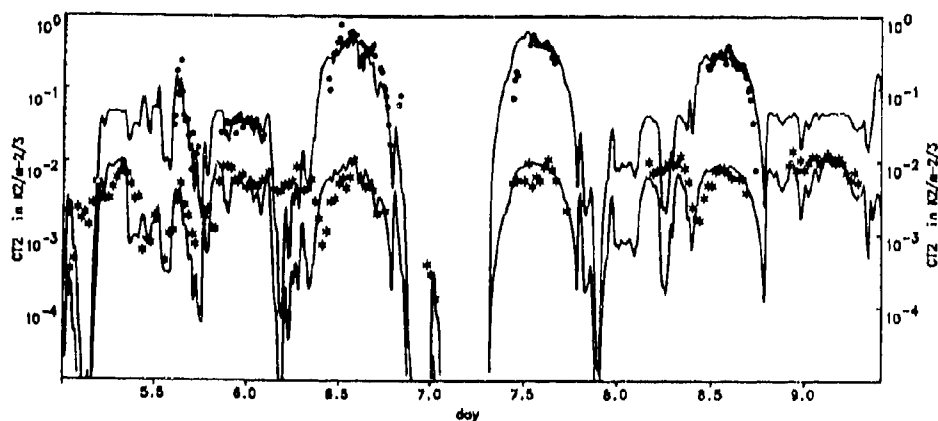


Fig.5. Comparison of model prediction of C_T^2 (curves) with measurements (symbols). Upper curve, circles: height 2m; lower curve, stars: height 48m.

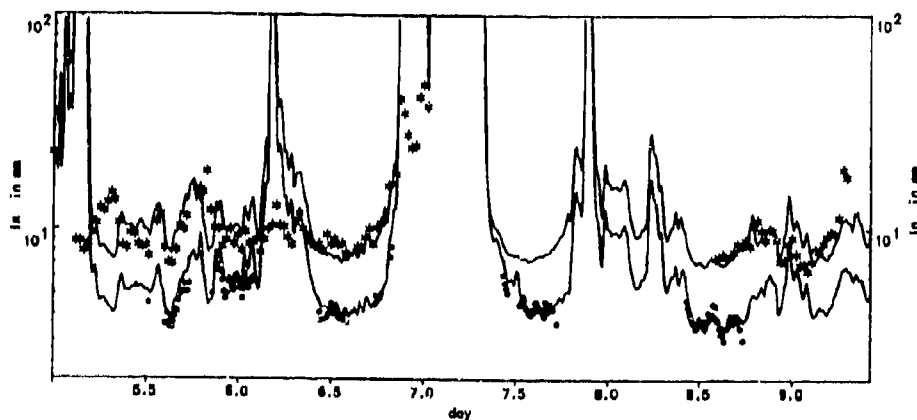


Fig.6. Same as Fig.5 but for the inner scale l_n . Lower curve, circles: height 2m; upper curve, stars: height 80m.

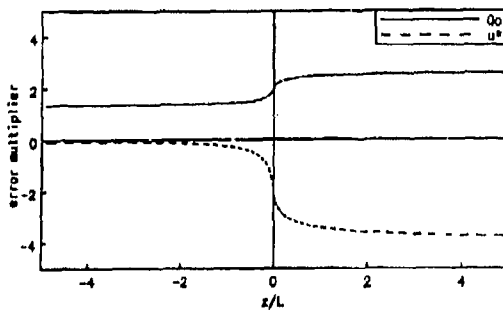


Fig.7. Differential error multiplier of C_T^2 with respect to Q_0 and u_*

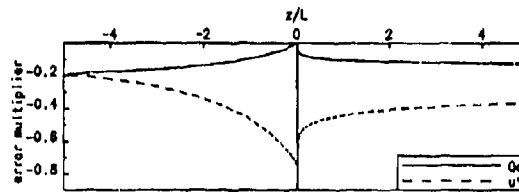


Fig.8. Same as Fig.7 but for the inner scale l_n .

5. Model Sensitivity

The comparisons above were made for quantitatively well characterized environment, all meteorological input data and surface parameters were carefully determined. However, we often don't know exactly how large the roughness length or the wind speed really is or if the ground is rather dry or wet, etc.. This is because we might have to predict input parameters in time. Moreover natural surfaces are never homogeneous, so we have to extrapolate spatially. And even if we want to make a model run for 'here and now', we often have to estimate many input quantities because their measurement is complicated or not possible at the moment. In general, the model input parameters are chosen to be as few as possible and as 'easy to guess' as possible. But some of them are more important than others for a certain application. To see the weight of the different input parameters we examined the respective model response.

Some general features can be understood when analysing the sensitivity of the similarity equations (3) and (4) to changes in heat and momentum flux. Even though the uncertainty of these fluxes might be quite large, it is helpful to look at small changes via the derivatives of Eqs.(3) and (4) with respect to Q_0 and u_* . Fig.7 gives the differential error multipliers of C_T^2 with respect to Q_0 and u_* , i.e. the fractional (or relative) error in C_T^2 divided by the fractional errors in Q_0 and u_* respectively, as a function of non-dimensional height z/L . We see that the sensitivity to changes in Q_0 is not too different for all heights and does not even differ very much under stable and unstable conditions. The value of the error multiplier is about 2. The friction velocity on the other hand has a totally different influence during day and night. During day, if we are not too close to the ground, the effect is negligible. At night the error multiplier is in the region -3 to -4, which is considerable. u_* and $-Q_0$ are positively correlated for fixed H_{Omax} and varying u (Eqs.(5) and (8)), so the respective error multipliers cancel partly. For fixed u and varying H_{Omax} however, they are anticorrelated (Eq.(5)), which will result in a strong H_{Omax} dependence of C_T^2 .

The error multipliers of the inner scale are demonstrated in Fig.8. They all have negative sign. This means an overestimation of the absolute fluxes always leads to an underestimation of l_n . The importance of the friction velocity is always larger than that of the heat flux except for very large values of $-z/L$. The value of the error multiplier with respect to u_* is typically around 0.5 and decreases for higher instability as the Q_0 impact increases.

The next four figures explicitly show the model dependence on the dynamic input quantities u and R for daytime in Figs.9 and 10, and u and H_{Omax} for nighttime in Figs.11 and 12. One set of parameters R and H_{Omax} has been chosen for cloud free ($R = 800 \text{ W/m}^2$, $H_{Omax} = -40 \text{ W/m}^2$) and one for cloudy conditions ($R = 200 \text{ W/m}^2$, $H_{Omax} = -10 \text{ W/m}^2$). The computations were done for two heights: 2m and 50m. All other model input quantities were fixed at the values used in the above experimental verification.

For C_T^2 the radiative situation is very important at all altitudes. At night this dominates even the height dependence. The cloud free and cloudy cases differ by up to one order of magnitude during day, and even more at night if the wind speed is not very low. The effect of the radiative situation on the inner scale is very weak at night but of importance during day for lower and moderate winds, especially at greater altitudes. The wind speed is quite unimportant for C_T^2 during day. Only very close to the ground, we observe a noticeable decrease with increasing u . At night, in contrast, the wind speed dependence is remarkable at all heights. For very low winds C_T^2 is predicted to be very small and to increase very rapidly as u increases. A maximum is reached at about 2 m/s followed by a moderate slope down. Such a behaviour was already qualitatively observed and reported by Ryznar (1963). The position and shape of the maximum depends

only slightly on H_{Omax} and altitude. The height variation of C_T^2 is strongest during day: we count up to two orders of magnitude decrease from 2m to 50m. At night this is less than half of it. The height variation of the inner scale is small for low winds. Under stronger winds we observe a factor of two increase from 2m to 50m. At 2m the largest values of C_T^2 occur on sunny calm days, whereas at 50m the maximum possible daytime and nighttime values do not differ very much. The smallest values of l_n can be found under strong winds day and night, the largest values during calm nights.

In the following figures we investigate the importance of the static input parameters: z_0 , A , α and T . We have selected variation ranges of these quantities according to typical uncertainties. The uncertainty in the roughness length z_0 might be large because z_0 is hard to estimate and difficult to measure. We allowed z_0 to be in the range 5mm to 5cm. The albedo A was varied between 0.1 and 0.4 which corresponds to dark and bright soil respectively, and the surface humidity parameter α was varied from 0.5 to 1, all still midlatitude values e.g. for dry and moist vegetation. A temperature change of 10 K was finally considered. The computations are done for the "cloud free sky" values of R and H_{Omax} . As a measure of the model sensitivity to the respective changes we use the relative response defined as

$$X = (x_{\text{max}} - x_{\text{min}}) / (x_{\text{max}} + x_{\text{min}}), \quad (12)$$

where x_{max} and x_{min} are the respective maximum and minimum values of C_T^2 or l_n .

Comparing the effects of the variations in all four parameters for daytime C_T^2 in Fig.13, the dominance of the surface humidity parameter α is striking. A change of the lower limit to the desert value of $\alpha = 0$ could lead to an order of magnitude variation in C_T^2 . This is the main reason for the often reported difference between C_T^2 values in the desert and the summer midlatitudes. Compared to the effect of α that of the albedo is in practice nearly negligible. The temperature is mainly important through its effect on s in Eq.(6) according to Fig.1. Hence a rough knowledge of temperature is necessary over wet ground, but 10 K uncertainty is not enough to have noticeable consequences. However a temperature higher than the 290 K used here, would lead to an even larger effect of α . In that way α becomes especially important for high temperatures. A significant effect of a change in z_0 can only be observed at 2m for at least moderate wind speed. The magnitude, however, is even here lower than the overall effect of the other contributions.

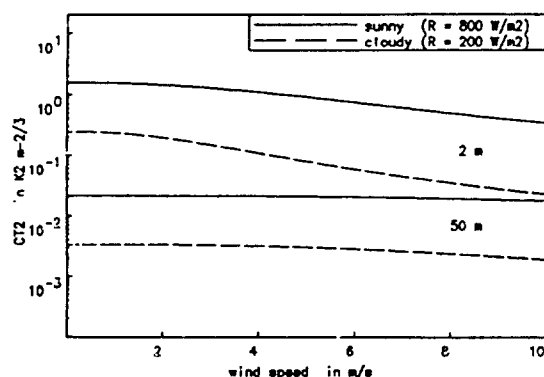


Fig.9. Example of a wind speed dependence of model C_T^2 at 2m and 50m height for a sunny and a cloudy day.

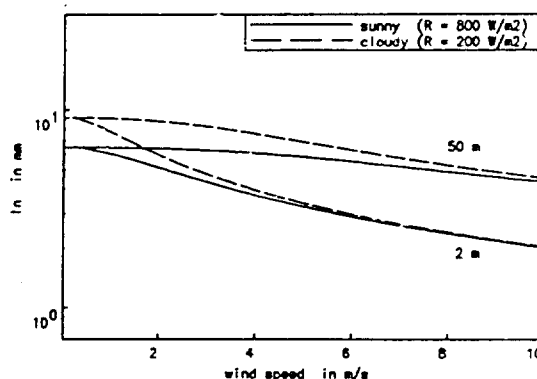


Fig.10. Same as Fig.9 but for model l_n .

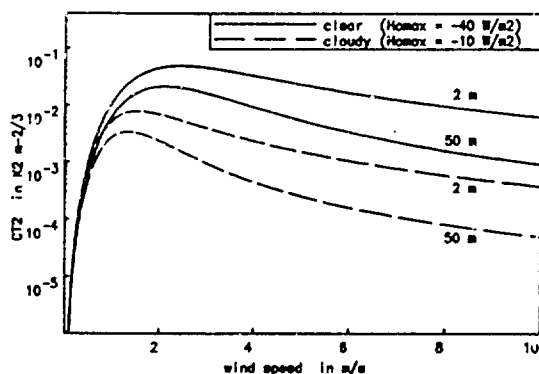


Fig.11. Same as Fig.9 but for a clear and a cloudy night.

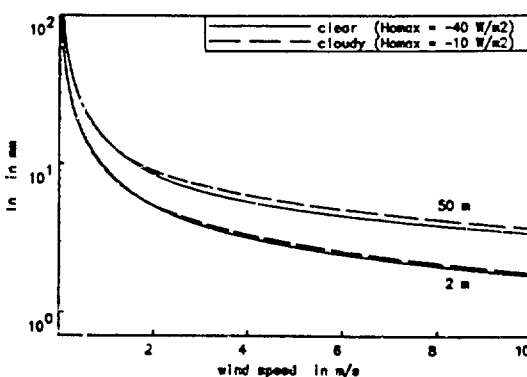


Fig.12. Same as Fig.10 but for a clear and a cloudy night.

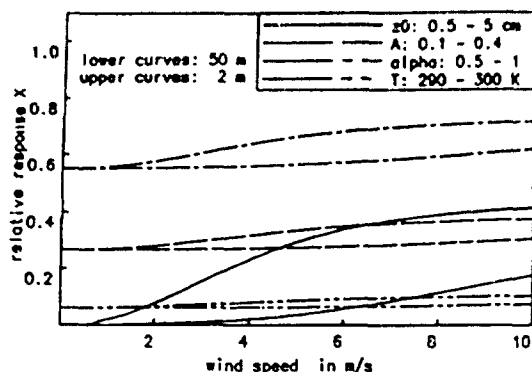


Fig. 13. Sensitivity of daytime model C_T^2 to static-input-parameter variations. Relative response X defined in Eq. (12).

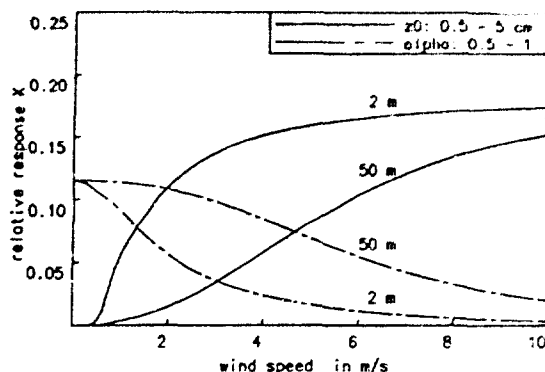
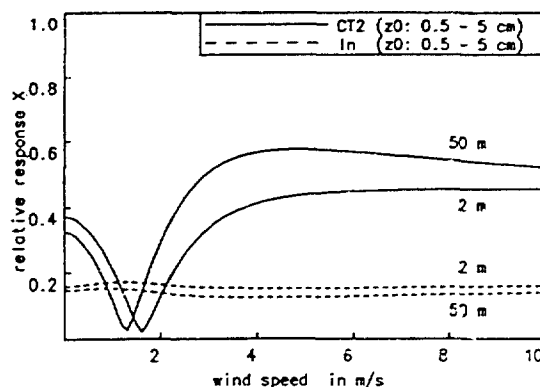


Fig. 14. Same as Fig. 13 but for l_n .

Fig. 15. Sensitivity of nighttime model C_T^2 and l_n to roughness length variation. Relative response X defined in Eq. (12).



Comparing Figs. 7 and 8 it is clear that the relative importance of the parameters effecting Q_0 for daytime, i.e. α , A and T , is much lower for the inner scale than for C_T^2 . Thus for analysing the inner scale sensitivity we reduce this set of parameters to the most important one: α . (The effect of A and T might be estimated as a fraction of that of α , as it can be seen in Fig. 13) In Fig. 14 we find two regions: a low wind speed region where α is most important and a moderate to high wind speed region where z_0 dominates. The transition wind speed increases with increasing altitude. However, it should be noted that, if we sum up the uncertainties, it is unlikely to exceed about $\pm 20\%$.

At night, the only relevant static parameter is z_0 . The sensitivity of C_T^2 and l_n to z_0 is shown in Fig. 15. There is a response minimum of C_T^2 to variations in z_0 at a wind speed little below 2 m/s. A considerable sensitivity can be found especially for higher wind speeds. The response of the inner scale to z_0 is quite independent of wind speed. Its magnitude is close to that of the daytime l_n uncertainty.

6. Conclusion

It was demonstrated that a combination of Monin-Oboukhov similarity expressions with simple flux parameterizations can provide very useful predictions of C_n^2 and l_n in the lower boundary layer under natural conditions. Considerable experimental disagreement between model prediction and measurement occurred only at greater heights in the morning and early evening hours, when the turbulence system changed between daytime and nighttime regime. However C_n^2 and l_n did not show any extreme values here. Problematic are nighttime low wind situations from both, the measurement and the modelling point of view. l_n values up to 50 mm have been observed here at a height of 80 m. (This did not necessarily belong to the boundary layer at that time, however.)

For C_T^2 the most important input quantities are the solar irradiation and the ground humidity parameter α on daytime and the wind speed together with a heat flux classification (H_{max}) at night. The surface roughness is important on daytime close to the ground and generally at night. l_n is mostly determined by the windspeed and the surface roughness except during day at greater heights, where the same parameters as for C_T^2 have importance: the solar irradiation and the ground humidity.

It is difficult to generally estimate the overall error of a prediction according to the proposed scheme. This error may contain a contribution resulting from the fact that the considered lower boundary layer deviates in its structure from the ideal case. Another contribution follows directly from an inaccuracy of the Eqs. 3 and 4. A next reason for model errors are the approximations contained in the flux parameterization expressions, and finally we have an uncertainty in the dynamic and static model input parameters. Only for the last point we can simply make quantitative calculations as it was done here. We find a possible error range of about a factor of two to three for C_T^2 and of about 20 to 30% for l_n . Concerning the remaining error, i.e. the error if all input quantities are well known, we can get an impression from our experimental results indicating again a similar error magnitude. Together this leads to an error of about half an order of magnitude for C_T^2 and up to about 30 to 40 % for l_n . From this we have to exclude the critical situations in the morning or evening hours as well as nocturnal low wind conditions. However, these periods do not show the highest refractivity turbulence levels.

References

- Azoulay, E., V. Thiermann, A. Jetter, A. Kohnle and Z. Azar, "Optical measurements of the inner scale of turbulence", *J. Phys. D: Appl. Phys.* 21 (1988), S41-S44.
- Brost, R.A., and J.C. Wyngaard, "A model study of the stably stratified planetary boundary layer", *J. Atmos. Sci.* 35 (1978), 1427-1440.
- Chapagne, F.H., C.A. Friehe, J.C. LaRue and J.C. Wyngaard, "Flux measurements, flux estimation techniques, and fine scale turbulence measurements in the unstable surface layer over land", *J. Atmos. Sci.* 34 (1977), 515-530.
- Cuijpers, J.W.M., and W. Kohlsiek, "Vertical profiles of the structure parameter of temperature in the stable, nocturnal boundary layer", *Boundary-Layer Meteorol.* 47 (1989), 111-129.
- Dyer, A.J., "A review of flux-profile relationships", *Boundary-Layer Meteorol.* 7 (1974), 363-372.
- Eaton, F.D., D.M. Garvey, E. Dewan and R. Beland, "Transverse coherence length (r_0) observations", *SPIE 551 Adaptive Optics* (1985), 42-51.
- Frisch, A.S., and G.R. Ochs, "A note on the behavior of the temperature structure parameter in a convective layer capped by a marine inversion", *J. Appl. Meteor.* 14 (1975), 415-419.
- Guillemet, B., H. Isaka and P. Mascart, "Molecular dissipation of turbulent fluctuations in the convective mixed layer, part I: height variations of dissipation rates", *Boundary-Layer Meteorol.* 27 (1983), 141-162.
- Hill, R.J., "Spectra of fluctuations in refractivity, temperature, humidity and the temperature-humidity co-spectrum in the inertial and dissipation ranges", *Radio Sci.* 13 (1978a), 953-961.
- Hill, R.J., "Models of the scalar spectrum for turbulent advection", *J. Fluid Mech.* 88 (1978b), 541-562.
- Hill, R.J., and S.F. Clifford, "Modified spectrum of atmospheric temperature fluctuations and its application to optical propagation", *J. Opt. Soc. Am.* 68 (1978), 892-899.
- Hill, R.J., and S.F. Clifford, "Theory of saturation of optical scintillation by strong turbulence for arbitrary refractive-index spectra", *J. Opt. Soc. Am.* 17 (1981), 675-686.
- Holtslag, A.A.M., and A.P. van Ulden, "A simple scheme for daytime estimates of the surface fluxes from routine weather data", *J. Climate Appl. Meteor.* 22 (1983), 517-529.
- Kaimal, J.C., J.C. Wyngaard, D.A. Haugen, O.R. Coté, Y. Izumi, S.J. Caughey and C.J. Readings, "Turbulence structure in the convective boundary layer", *J. Atmos. Sci.* 33 (1976), 2152-2168.
- Kunkel, K.E., and D.L. Walters, "Modeling the diurnal dependence of the optical refractive index structure parameter", *J. Geophys. Res.* 88 (1983), C10999-C11004.
- Lee, R.W., and J.C. Harp, "Weak scattering in random media, with applications to remote probing", *Proceedings of the IEEE* 57 No. 4 (1969), 375 pp.
- Lenschow, D.H., "Model of the height variation of the turbulence kinetic energy budget in the unstable planetary boundary layer", *J. Atmos. Sci.* 31 (1974), 465-474.
- Nieuwstadt, F.T.M., "The turbulent structure of the stable nocturnal boundary layer", *J. Atmos. Sci.* 41 (1984), 2202-2216.
- Ochs, G.R., and R.J. Hill, "Optical-scintillation method of measuring turbulence inner scale", *Appl. Opt.* 24 (1985), 2430-2432.
- Paulson, C.A., "The mathematical representation of wind speed and temperature profiles in the unstable atmospheric surface layer", *J. Appl. Meteor.* 9 (1970), 857-861.
- Rao, K.S., J.C. Wyngaard and O.R. Coté, "The structure of the two-dimensional internal boundary layer over a sudden change of surface roughness", *J. Atmos. Sci.* 31 (1974), 738-746.
- Ryznar, E., "Visual resolution and optical scintillation in stable stratification over snow", *J. Appl. Meteor.* 2 (1963), 526-530.
- Sorbjan, Z., "On similarity in the atmospheric boundary layer", *Boundary-Layer Meteorol.* 34 (1986), 377-397.
- Thiermann, V., and E. Azoulay, "Modeling of structure constant and inner scale of refractive index fluctuations - an experimental investigation", *Proceedings of the SPIE 1115 Propagation Engineering* (1989).
- Thiermann, V., and A. Kohnle, "A simple model for the structure constant of temperature fluctuations in the lower atmosphere", *J. Phys. D: Appl. Phys.* 21 (1988), 837-840.
- Tsvang, L.R., "Measurements of temperature-fluctuation frequency spectra in the surface layer of the atmosphere", *Izv. Akad. Nauk. SSSR, Ser. Geofiz.* 8 (1960), 1252-1262.
- Wesely, M.L., and E.C. Alcaraz, "Diurnal cycles of the refractive index structure function coefficient", *J. Geophys. Res.* 78 (1973), 6224-6232.
- Wyngaard, J.C., "On surface-layer turbulence", *Workshop on Micrometeorology*, D.A. Haugen ed., *Am. Meteor. Soc.* (1973), p.128.
- Wyngaard, J.C., Y. Izumi and S. Collins, "Behavior of the refractive-index-structure parameter near the ground", *J. Opt. Soc. Am.* 61 (1971), 1646-1650.
- Wyngaard, J.C., and M.A. LeMone, "Behavior of the refractive index structure parameter in the entraining convective boundary layer", *J. Atmos. Sci.* 37 (1980), 1573-1585.

DISCUSSION

J. SELBY

What caused the dip in your C_T^2 curve (in Figure 15) at a wind speed of 2 m/s?

AUTHOR'S REPLY

Under stable conditions, an increase of Z_0 leads to two competing processes. On one hand, it increases u_* in Eq. (5) tending to decrease C_T^2 in Eq. (3b). On the other hand it also increases Q_0 in Eq. (8) tending to increase C_T^2 . For light winds, the net effect is an increase of C_T^2 . For stronger winds, it is the other way because the value of Q_0 is closer to Q_{0max} and less variable. Consequently, we must find a transmission range at moderate wind speed when the Z_0 influence is low. This range corresponds to the dip in Fig (15).

High Intensity Laser Beam Interactions with Single Droplets

Richard K. Chang and Alfred S. Kwok
Yale University

Department of Applied Physics and Center for Laser Diagnostics
P. O. Box 2157, Yale Station
New Haven, Connecticut 06520-2157, USA

SUMMARY

High intensity laser beam propagation in the atmosphere requires knowledge of the linear and nonlinear optical interactions of the UV, visible, and IR radiation with individual water droplets. The spherical water-air interface of droplets (with radii larger than the wavelength) can (1) enhance the incident laser intensity inside the droplet and in the air, (2) provide optical feedback which can lower the threshold for stimulated nonlinear emission when the wavelength is in the transparent range of water, and (3) modify the internal intensity distribution and, thereby, distort the droplet shape when the incident radiation is in the transparent or absorbing range of water. We review our nonlinear optical research with single micrometer-size water droplets irradiated by high intensity laser radiation in the transparent and absorbing regions of water.

RESEARCH RESULTS

Internal Field Distribution

The Lorenz-Mie formalism can be used to calculate the internal and near-field distribution of a sphere (with radius a and complex index of refraction n) when a monochromatic plane wave from a laser (with wavelength λ) is incident on the droplet (specified by its size parameter $x = 2\pi a/\lambda$) [1]. Figure 1 shows the internal field distribution within the equatorial plane of four droplets with $x = 29.64$, $\text{Re}(n) = 1.38$, and four different $\text{Im}(n) = 10^{-4}$, 10^{-3} , 10^{-2} , and 10^{-1} . The incident laser intensity is I_0 . The direction of the plane wave of the incident laser beam is designated by the arrow.

At the lowest $\text{Im}(n)$ value, the intensity is concentrated in two regions, one just within the droplet shadow face and the other just within the droplet illuminated face. Both intensity maxima at these two regions are $> I_0$. The intensity "ripples" throughout the equatorial plane result from the standing wave of two oppositely traveling reflected waves, one from the droplet illuminated face and the other from the droplet shadow face.

As $\text{Im}(n)$ is increased from 10^{-4} to 10^{-2} , Fig. 1 shows that the intensity ratio of the maximum near the illuminated face and of the maximum near the shadow face decreases rapidly. The more rapid decrease of the intensity maximum ratio suggests that the intensity maximum near the illuminated face results from reflected rays which have traversed the droplet at least twice. In contrast, the intensity maximum near the shadow face results from refracted rays which have traversed the droplet only once. When $\text{Im}(n) = 10^{-1}$, the absorption length [defined as α^{-1} , where the absorption coefficient $\alpha = 4\pi\text{Im}(n)/\lambda$] is less than the droplet radius. Consequently, the rays are greatly attenuated before reaching the shadow face, and the internal intensity is localized in the form of a crescent at the droplet illuminated face and decreases exponentially toward the droplet center.

Figure 2 shows the intensity distribution in the equatorial plane for four different water droplets [with $x = 5, 10, 15$, and 30 and $\text{Im}(n) = 0.0662$] irradiated by a CO_2 laser beam (with $\lambda = 10.6 \mu\text{m}$). Even for a water droplet with $x = 5$, the attenuation of the rays traveling along the droplet diameter is reduced by $\exp(-1.3)$. For droplets with $x = 5$ and 10 , the opposing effects of absorption and of intensity concentration cause the internal intensity distribution to be fairly uniform. For droplets with $x = 15$ and 30 , absorption dominates, and the internal intensity distribution is localized in the form of a crescent at the droplet illuminated face.

Nonlinear Source Polarization (PNLS)

The electromagnetic field (E) internal to the droplet can induce both a linear and nonlinear polarization, which can be expressed as:

$$P_L + P_{NLS} = [\chi^L + (\delta\chi/\delta E) E + (\delta^2\chi/\delta E\delta E) EE + (\delta\chi/\delta Q) Q] E, \quad \text{Eq. (1)}$$

where the linear susceptibility $\chi^L = (n^2 - 1)/4\pi$ is complex if $\text{Im}(n) \neq 0$.

The nonlinear source polarization PNLS generates electromagnetic waves within the droplet which have a different frequency from that of the incident laser frequency. Equation 1 shows that PNLS has the following terms: (1) $(\delta\chi/\delta E) E$, which is zero inside the droplet because liquid has an inversion symmetry and, thus, no second harmonic frequency generation is expected; (2) $(\delta^2\chi/\delta E\delta E) EE$, which gives rise to third harmonic frequency generation if all three E's in Eq. 1 have the same frequency and, more generally, gives rise to third-order sum frequency generation if the E's in Eq. 1 have different frequencies [2]; and (3) $(\delta\chi/\delta Q) Q$, which gives rise to Raman scattering when Q is the vibrational coordinate of the H_2O molecule (usually the O-H stretching mode) and to Brillouin scattering when Q is the sound wave amplitude in water.

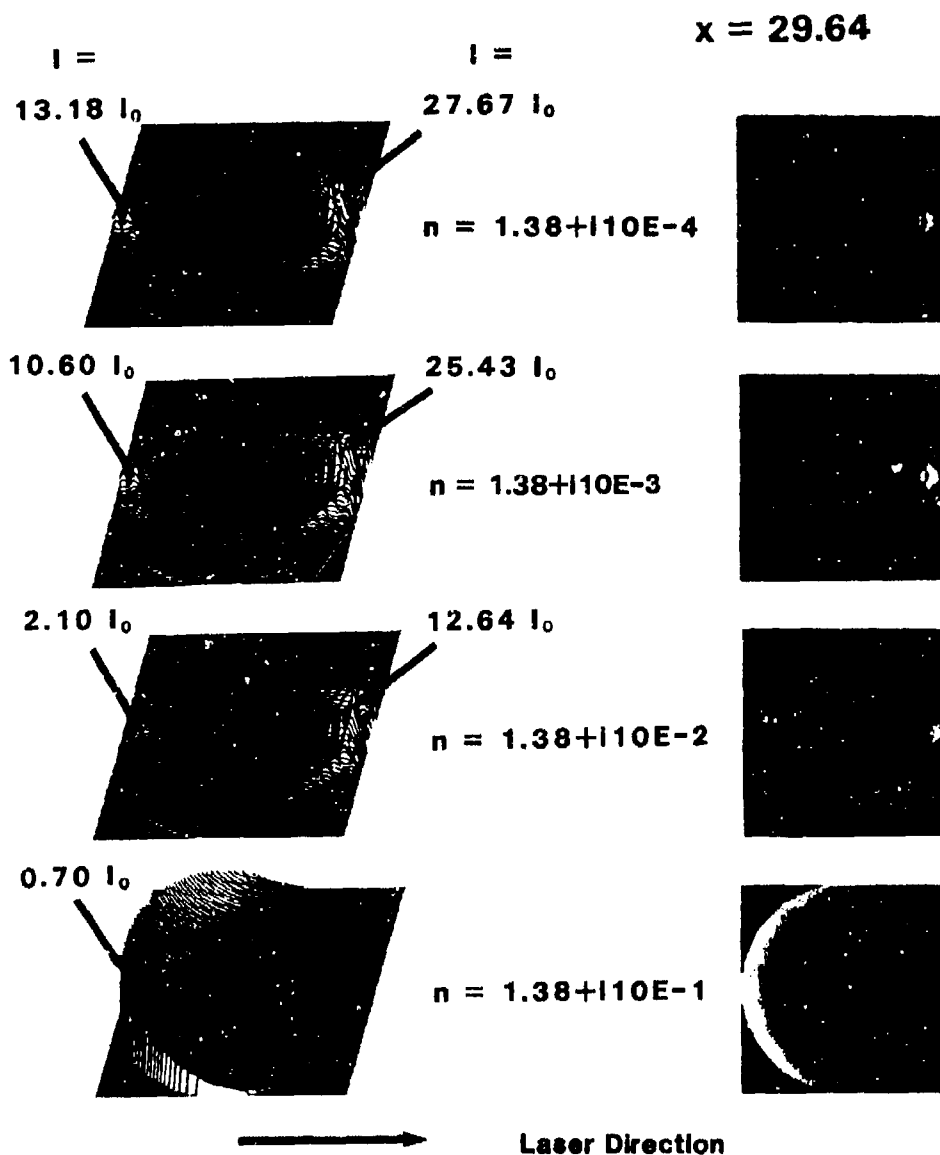


Fig. 1. The internal intensity distribution within the equatorial plane of four droplets with increasing absorption. Three-dimensional plots are shown in the left column and the gray scale plots are shown in the right column. The real part of the index of refraction for the droplet is 1.38 and the imaginary part varies from 10^{-4} to 10^{-1} . The droplet size parameter $x = 2\pi a/\lambda$ is 29.64, where a is the droplet radius and λ is the incident laser wavelength. The incident laser beam intensity is I_0 . The beam direction is indicated by the arrow.

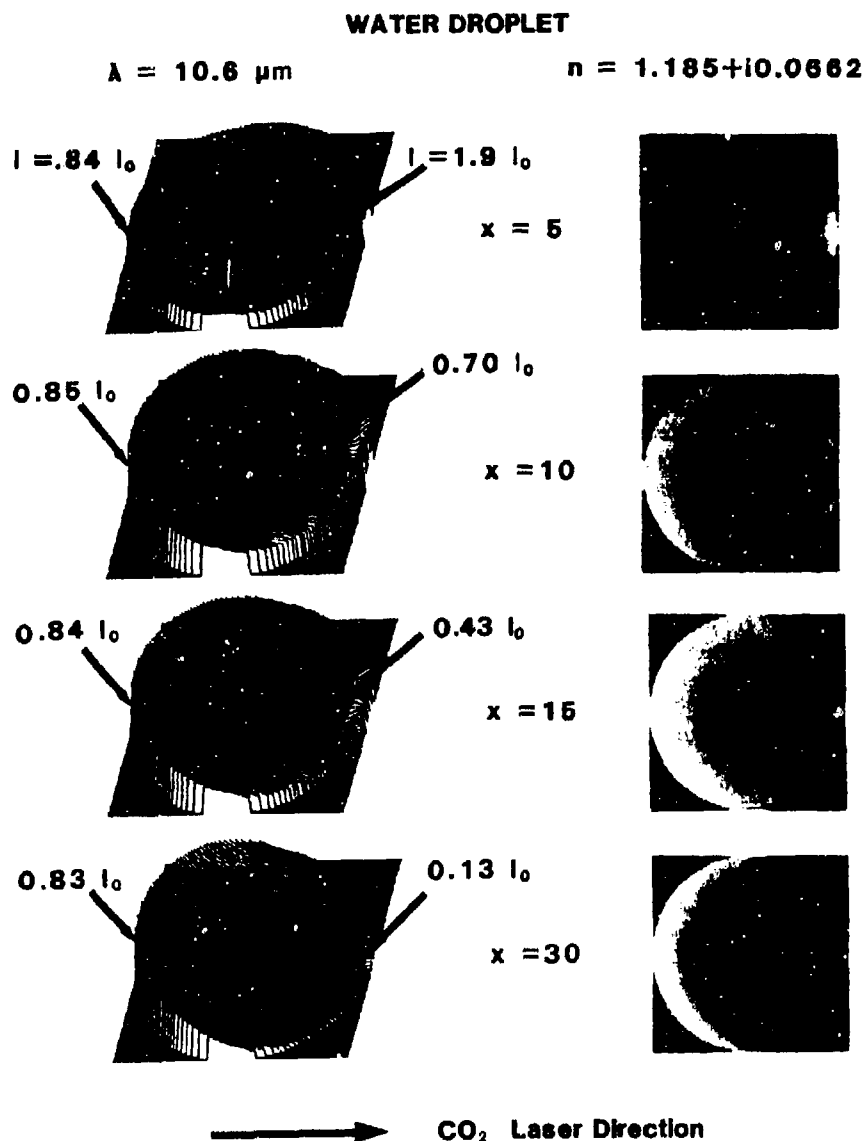


Fig. 2. Same as in Fig. 1 except that the droplet size parameter varies from $x = 5$ to $x = 30$. The index of refraction is selected to be that of water, $n = 1.185 + i0.0662$. The CO_2 laser wavelength is $10.6 \mu\text{m}$. The beam direction is indicated by the arrow.

Stimulated Raman scattering (SRS) occurs when the amplitude of the vibrational mode Q (with vibrational frequency ω_{vib}) is coherently driven by $E(\omega_1)$ and $E^*(\omega_2)$ (where $\omega_1 - \omega_2 = \omega_{\text{vib}}$) [3]. Stimulated Brillouin scattering (SBS) occurs when the sound wave amplitude Q (at ω_{sound}) is coherently driven by $E(\omega_1)$ and $E^*(\omega_2)$, [where $\omega_1 - \omega_2 = \omega_{\text{sound}}$ and $\vec{k}(\omega_1) - \vec{k}(\omega_2) = \vec{k}(\omega_{\text{sound}})$] [4].

Nonlinear Optical Signals

When $x \gg 1$ and $\text{Im}(n) \approx 0$, the nonlinear radiation generated by PNLs is initially produced in a region within the droplet where the input laser intensity is the largest, i.e., just within the droplet shadow face (see Fig. 1). The nonlinearly generated radiation is usually frequency shifted from the laser frequency and has a linewidth larger than the laser linewidth. The spherical shape of the droplet can efficiently trap some of the internally produced nonlinearly generated radiation. At specific wavelengths within the linewidth of the nonlinearly generated radiation, the droplet can be envisioned as a high Q -factor optical resonator which can provide

feedback at specific λ 's or x 's corresponding to the morphology-dependent resonances (MDR's) of a sphere [1]. The Q-factor of the MDR's and the number of MDR's within a wavelength interval have been calculated using the Lorenz-Mie formalism [5,6]. The Q-factor of MDR's has been determined by measuring, after the incident laser beam is off, the decay time of the nonlinearly generated radiation which is trapped within the droplet [7,8].

Spontaneous Raman scattering and spontaneous Brillouin scattering are produced mainly just within the droplet shadow face where the laser intensity is largest. At specific wavelengths within the spontaneous Raman and Brillouin linewidths which correspond to MDR's, part of the spontaneous Raman and Brillouin radiation is trapped by the droplet interface and propagates around the droplet rim. SRS and SBS occur when the round-trip gain for the amplified spontaneous Raman and Brillouin emission is larger than the round-trip loss. There is no phase-matching requirement for the amplified spontaneous Brillouin and Raman emission processes leading to SBS and SRS.

For SBS, the gain is provided by the internal intensity of a single-mode or multimode laser, which is maximized just within the droplet shadow face. For first-order SRS, the gain can be provided by the following two internal intensities: (1) the internal intensity of the multimode laser, which is maximized just within the droplet shadow face and (2) the internal intensity of SBS (pumped by the single-mode laser), which is distributed around the droplet rim because SBS in the droplet needs optical feedback [9]. For n th-order SRS radiation, the gain is provided by the internal intensity of the $(n - 1)$ th-order SRS radiation which is also distributed around the droplet rim [10]. The depletion of SBS as a result of first-order SRS being generated and the depletion of the first-order SRS as a result of multiorder SRS being generated have been observed [9]. However, the depletion of the internal laser intensity (with single-mode or multimode operation) has not been reported.

The third-order sum frequency signal is many orders of magnitude weaker than SRS and SBS. Unlike SRS and SBS, the third-order sum frequency process requires phase-matching, which cannot be satisfied in a liquid. When a near-IR laser beam ($\lambda = 1.064 \mu\text{m}$) is used to irradiate a droplet, very weak signals resulting from the nonlinear mixing of the electric fields of the laser, first-order SRS, and multiorder SRS have been observed throughout the UV and the visible [2].

Additional nonlinear optical signals which have been observed from single droplets can also be related to the various terms in Eq. 1. Both the observed coherent anti-Stokes Raman scattering (CARS) and the more general four-wave mixing effect (commonly referred to as coherent Raman mixing) [11] are related to $(\delta\chi/\delta Q)$ Q in Eq. 1. The observed phase-modulation broadening of the elastically scattered light and of the SRS [12] is related to $(\delta^2\chi/\delta E\delta E)$ EE in Eq. 1.

Laser-Induced Breakdown

Laser-induced breakdown (LIB) is also a consequence of nonlinear optical processes. The intensity threshold for LIB is considerably higher than that for other nonlinear processes such as SBS, SRS, and third-order sum frequency generation. However, once LIB occurs, the nonlinear optical signals such as SBS, SRS, and CARS are quenched by the strong absorption associated with the plasma [13].

There is some controversy regarding the initiation of LIB in water, i.e., whether the "seed electrons" already exist in the water or need to be generated by the laser radiation via the multiphoton ionization process. Regardless of the origin of the seed electrons, the electric field of the laser radiation causes avalanche multiplication of electrons and the generation of a dense plasma. After the initiation of LIB and the increase in plasma density, a transparent water droplet is transformed into a strongly absorbing droplet. Spatially resolved spectroscopy has been used to determine the location of LIB initiation [14]. LIB is initiated just within the shadow face of a water droplet with a $< 60 \mu\text{m}$ and in air just outside the shadow face of a water droplet with a $> 60 \mu\text{m}$ [14]. The addition of salt, such as NaCl or NaNO_3 , lowers the LIB threshold inside the water droplets [15].

Spatially and temporally resolved plasma emission diagnostics have been used to study the ejection of the plasma (in the form of a packet) from the water droplet shadow face and the propagation of the plasma (as an optical detonation wave) from the shadow face toward the illuminated face and then from the illuminated face toward the laser [16-18]. These experimental results were found to be in quantitative agreement with a one-dimensional hydrodynamic and thermodynamic model of a slab of water irradiated by a laser beam, which heats the plasma initially introduced within the slab shadow face [19,20].

Spatially and temporally resolved diagnostic techniques have also been used to determine the transmission through the plasma created by the LIB process [20]. The expanding plasma plume can attenuate the laser pulse. The decrease of the transmission (from numerous resolvable points along a line parallel to the laser beam) was measured during the laser pulse, and the recovery of the transmission was measured after the laser pulse [21].

Laser-Induced Droplet Shape Distortions

(1) In the transparent region of water:

Once the rising portion of the input laser pulse (with wavelength in the visible) exceeds the LIB threshold, the rapidly developing plasma strongly absorbs the remaining portion of the laser pulse and the laser radiation is converted into heat. At higher intensity, laser heating occurs throughout the droplet and the air behind the droplet illuminated face. At lower intensity, laser heating occurs mainly within the water droplet shadow face. For the latter case, the resultant temperature and pressure increase produces convective forces and cavitation which expel material initially from the droplet shadow face and then from the rest of the highly distorted droplet.

Using the shadowgraph technique, we photographed the temporal evolution of droplet shape distortion with a framing camera long after the initiation of LIB by a visible laser beam [22]. Both the shape deformation rate and the recoil velocity of the remaining droplet (as a result of material ejected from the shadow face) have been deduced from the framing camera photographs [22].

A high energy laser beam (with wavelength in the transparent region of water) may not have the intensity needed to initiate LIB. Nevertheless, a high energy laser beam can distort the droplet shape via electrostrictive forces. Shape distortion and the ejection of smaller droplets from a single water droplet irradiated by a high energy laser pulse (with pulse duration of 400 nsec and fluence of $\sim 300 \text{ J/cm}^2$) have been photographed with a framing camera [23]. The distortion amplitude and shape have been compared with a recent calculation which includes the electromagnetics and hydrodynamics for a water droplet of the same size and for a laser beam with the same energy used in our experiment [24].

(2) In the absorbing region of water:

When the laser wavelength is in the absorbing region of water, the laser radiation can directly heat the water droplet without the need to first produce a plasma that can then absorb the laser radiation. At laser energy below the explosive vaporization threshold, direct heating of the droplet can lead to droplet shape distortion without any vaporization. For example, direct heating of the illuminated face of a water droplet with $x = 30$ (see Fig. 2 for the internal intensity distribution) by a CO_2 laser beam can cause droplet bulging at the illuminated face as a result of lowering the surface tension of the illuminated face and of thermal expansion in the crescent-shaped region in which the laser heating is initially localized. Although the electrostrictive force observed for the transparent case [23,24] is still present in the absorbing case, the electrostrictive effect is smaller than the hydrodynamic and thermodynamic effects in the nonuniformly heated water droplet.

A framing camera has been used to record the time evolution of the shadowgraphs of a water droplet irradiated by a CO_2 laser pulse with an energy exceeding the explosive vaporization threshold [25,26]. The ejected vapor plume and the liquid streaming from the illuminated face of the laser heated water droplet cannot be distinguished in the shadowgraphs. Both the ejected vapor and the liquid (in the form of smaller droplets and irregularly shaped fragments) produce a dark image when the shadowgraph configuration is used.

A new fluorescence imaging technique has been developed [27] to provide a greater contrast between the ejected vapor plume and the liquid droplets. The experimental configuration for the new fluorescence technique is shown in Fig. 3. A CO_2 laser beam (idealized in the form of a Gaussian spatial profile and propagating horizontally along the x axis) irradiates three to five water droplets flowing downward in a linear stream along the z axis. A cationic dye, Rhodamine 6G (R6G), with a concentration of $\sim 10^{-4} \text{ M}$ is dissolved in the water droplets. R6G fluoresces in the green when excited by a UV probe laser (N_2 laser emitting at $\lambda = 0.3371 \mu\text{m}$) which is propagating along the $-x$ axis in the direction opposite to the CO_2 laser beam. Among the dyes with high quantum yield in water, R6G is specifically selected because its quantum yield is nearly independent of the water temperature. Thus, the fluorescence intensity from the original droplet heated by the CO_2 laser and from the numerous ejected/shattered droplets is less dependent on the water temperature. The fluorescence image of the droplet and the ejected/shattered material is detected by a CCD camera placed along the y axis at 90° to the N_2 and CO_2 laser beam directions. The CO_2 laser pulse shape as a function of time is shown in Fig. 3 (upper left).

Figures 4 and 5 show the fluorescence images recorded at different time delays after the start of the CO_2 laser pulse. Each fluorescence image has five or seven droplets, referred to as droplets 1 through 5 or droplets 1 through 7, counting the droplets from the top of each image. Each fluorescence image corresponds to a different CO_2 laser pulse, and each pulse unavoidably has a different spatial distribution. The highest intensity is centered at droplet 2, 3, or 4.

In Figs. 4 and 5, the fluorescence intensity from R6G in the liquid phase is higher than that from R6G in the vapor phase for the following reasons: (1) the quantum yield of R6G in the vapor phase is $\sim 18\%$ and that of R6G dissolved in water is $\sim 95\%$; (2) the vapor pressure of R6G is much lower than that of water and, thus, there

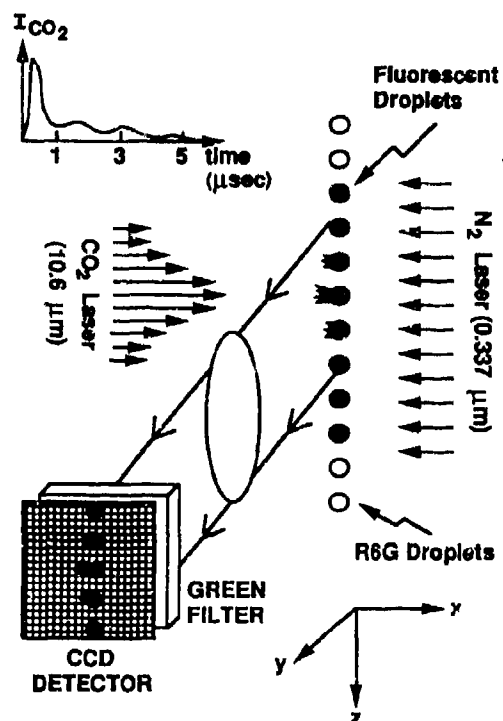


Fig. 3. Schematic of the experimental arrangement used to record the fluorescence image of droplets flowing in a linear stream (vertically along the z axis). The CO_2 laser used to heat the water droplets propagates along the x axis, the N_2 laser used to excite the dye fluorescence propagates along the $-x$ axis, and the two-dimensional CCD detector used to record the fluorescence image is located along the y axis. A green filter is used to block the scattered N_2 laser radiation and to transmit the dye fluorescence. The temporal pulse shape of the CO_2 laser radiation is shown in the upper left.

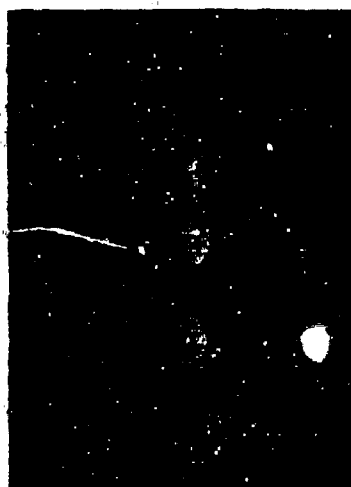
are fewer R6G molecules than water molecules in the vapor phase as a result of the thermal vaporization process; and (3) even if there are R6G molecules in the vapor phase as a result of an explosive vaporization process, the density of R6G molecules in the vapor phase is much lower than in the liquid phase, since the volume of the vapor plume is much larger than that of the droplet. Therefore, the combination of the lower R6G quantum yield in the vapor phase, the lower vapor pressure of the R6G compared to water, and the lower density of R6G in the vapor plume makes the fluorescence imaging technique particularly advantageous for the study of droplet shape distortion and material ejection/shattering in the liquid phase without interference from the fluorescence of R6G in the vapor plume. When the shadowgraph technique is used, both the ejected vapor plume and the liquid produce a dark image. We are, therefore, unable to distinguish the ejected/shattered liquid from the vapor plume or to distinguish the distorted shape of the original droplet from the ejected liquid material emerging from the water droplet illuminated face [25,26].

The water droplets shown in Figs. 4 and 5 are irradiated with an average CO_2 laser fluence of $\approx 3 \text{ J/cm}^2$. Assuming that the geometric cross section of the droplet is πa^2 (where $a = 50 \text{ } \mu\text{m}$), the estimated laser energy intercepted by the droplet is $\approx 2.4 \times 10^{-4} \text{ J}$. The estimated temperature rise within the crescent-shaped volume (shown in Fig. 2) is $\approx 390^\circ\text{C}$. This temperature exceeds the superheated temperature of water (generally accepted to be 305°C), the temperature in which water can exist in the metastable liquid state before spontaneous nucleation of bubbles occurs when there is no nucleation site [28].

Figures 4 and 5 show the fluorescence images of water droplets (containing 10^{-4} M R6G) at $\Delta t = 1, 3, 7, 10, 12, 15, 25$, and $45 \text{ } \mu\text{sec}$ after the onset of the CO_2 laser pulse. A gray scale is used to represent the fluorescence intensity. The scale is chosen to display the weaker fluorescence intensity from the ejected/shattered droplets and, thereby, to allow the fluorescence image inside the parent droplet to be saturated.



$\Delta t = 1 \mu\text{sec}$



$\Delta t = 3 \mu\text{sec}$



$\Delta t = 7 \mu\text{sec}$



$\Delta t = 10 \mu\text{sec}$



$\Delta t = 12 \mu\text{sec}$

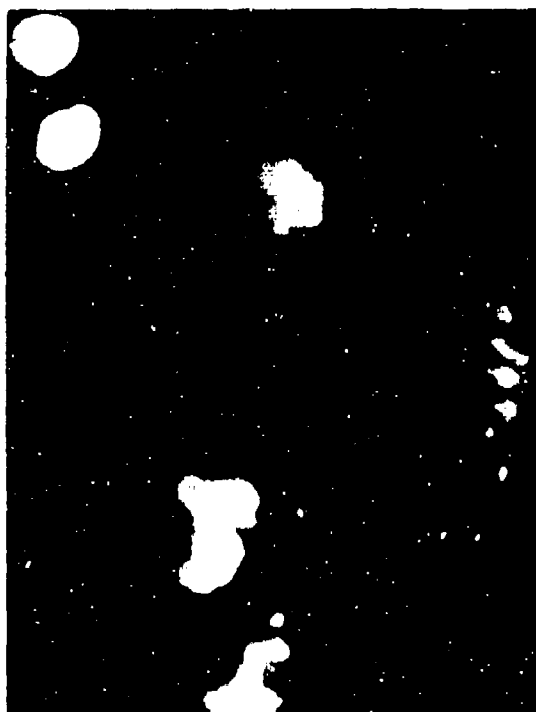


$\Delta t = 15 \mu\text{sec}$

Fig. 4. Fluorescence images of five water droplets (containing 10^{-4} M R6G dye) recorded at six time delays ($\Delta t = 1, 3, 7, 10, 12$, and $15 \mu\text{sec}$) after the initiation of the CO_2 laser pulse. The different images correspond to different CO_2 laser pulses which have their highest intensity at either droplet 2 or droplet 3 (counting from the top of each image). The CO_2 beam direction is from left to right. The fluorescence intensity within the droplets is allowed to saturate in order to display the fluorescence image from the ejected material.



$\Delta t = 25 \mu\text{sec}$



$\Delta t = 45 \mu\text{sec}$

Fig. 5. Same as Fig. 4 except that the fluorescence images are of seven water droplets (containing 10^{-4} M R6G dye) recorded at $\Delta t = 25$ and $45 \mu\text{sec}$ after the initiation of the CO_2 laser pulse.

At $\Delta t = 1 \mu\text{sec}$, Fig. 4 shows that the water droplets remain nearly spherical. The higher fluorescence intensity at the droplet rim indicates that the droplets are lasing upon excitation by the N_2 laser pulse [29].

For the fluorescence image taken at $\Delta t = 3 \mu\text{sec}$, the CO_2 laser radiation is most intense for droplet 2. Figure 4 shows that the illuminated face of droplet 2 is flattened as a result of significant material removal by explosive vaporization. The fact that it takes $3 \mu\text{sec}$ before significant material removal is evidence that nucleation and subsequent cavitation require an incubation time of several microseconds even though the illuminated face is superheated. The shapes of droplets 1, 3, 4, and 5 which receive less CO_2 laser radiation appear to be distorted without much material removal. Shape bulging of the illuminated face can result from lowering of the water surface tension and from thermal expansion in the crescent-shaped region in which most of the CO_2 laser radiation is absorbed (see Fig. 2).

For the fluorescence image taken at $\Delta t = 7 \mu\text{sec}$, the CO_2 laser radiation is most intense for droplet 3. At $\Delta t = 7 \mu\text{sec}$, Fig. 4 shows that material is now being ejected for all the droplets. Droplet 1 indicates significant material removal from its illuminated face, which is tilted because of the intensity gradient in the spatial profile of the focused CO_2 laser beam. Material ejection in the form of long fragments is observed. The long Δt needed before material ejection for droplet 1 supports the premise that, when less heat is deposited in the crescent-shaped region, explosive vaporization for a water droplet requires a longer incubation time. The three central droplets (droplets 2, 3, and 4) are propelled as a result of material ejection. Furthermore, these three droplets become elongated in the direction perpendicular to the CO_2 laser beam, start to bend toward the droplet shadow face, and develop a "skirt" at the droplet shadow face. Discrete images of small droplets behind the illuminated faces of droplets 2, 3, and 4 are discernible. The fuzzy image behind the illuminated face of these three droplets can be either fluorescence from smaller droplets outside the image plane or Rayleigh scattering by the water vapor of the bright fluorescence radiation from the highly distorted droplets 2, 3, and 4. The fuzzy image in front of the shadow face of droplet 3 can be from the skirt, which is partially outside the image plane.

At $\Delta t = 10 \mu\text{sec}$, most of the fuzzy images present at $\Delta t = 7 \mu\text{sec}$ are no longer observable behind the illuminated faces of droplets 2, 3, and 4. The disappearance of the fuzzy images suggests that the vapor and/or the small droplets are displaced from the field of view by the subsonic pressure wave associated with explosive vaporization at the droplet illuminated face. Furthermore, the smaller droplets can also be vaporized. Discrete droplets of a larger size can be clearly observed behind the illuminated faces of droplets 2 and 4. For droplets 3 and 4, skirts have developed.

At $\Delta t = 12 \mu\text{sec}$, droplet propulsion continues with droplet 3 having recoiled the most and droplets 2 and 4 having recoiled less than droplet 3. Small droplets behind droplets 1 and 5 are readily observed. For the fluorescence image at $\Delta t = 15 \mu\text{sec}$, the CO_2 laser radiation is most intense for droplet 2, which has recoiled the most. The irregularity of the recoil distance among the five droplets is illustrative of the irregular spatial profile of the CO_2 laser beam. Droplet ejection from the skirts of droplets 1 and 5 is noted.

For the two fluorescence images at $\Delta t = 25$ and $45 \mu\text{sec}$, a total of seven droplets is shown in Fig. 5. Droplets 1 and 2, which are barely irradiated by the CO_2 laser beam, remain nearly spherical and experience no recoil. In fact, droplets 1, 2, and 7 provide a convenient reference of the size and spacing of water droplets in a linear stream. At $\Delta t = 25 \mu\text{sec}$, the elongated droplets 3, 4, 5, and 6 are beginning to break up into many fragments because of hydrodynamic instability. It is now difficult to assign the origin of these fragments to each of the original droplets. By $\Delta t = 45 \mu\text{sec}$, the original droplets are completely shattered into fairly large fragments, which are propelled ~ 15 droplet diameters away from the vertical line defined by the linear stream of water droplets.

CONCLUSIONS

A large number of nonlinear optical interactions have been observed when a high intensity laser beam (with wavelength in the visible region of water) irradiates a single water droplet with a $\gg \lambda$. The most dominant nonlinear effects are SBS and SRS, which have intensity thresholds well below that for LIB. Once LIB is initiated during the rising portion of the laser pulse, a normally transparent droplet becomes absorbing and, thus, quenches SRS and SBS. The remaining portion of the laser pulse causes explosive vaporization of the entire droplet. When a high energy laser beam (with wavelength in the visible region of water) irradiates a single water droplet, electrostrictive forces distort the droplet shape and cause droplet shattering.

Direct laser heating can result when the laser wavelength is in the absorbing region of water. A new fluorescence imaging technique which can provide a greater contrast between the liquid and vapor phases of the ejected material has been applied to the study of water droplets irradiated by a CO_2 laser pulse. We have observed droplet shape distortion, ejection and shattering of small liquid fragments, droplet propulsion, and total disintegration of the original droplets into several large liquid fragments.

REFERENCES

1. C. F. Bohren and D. R. Hoffman, Absorption and Scattering of Light by Small Particles (Wiley, New York, 1983).
2. W.P. Acker, D.H. Leach, and R.K. Chang, "Third-Order Optical Sum Frequency Generation in Micrometer-Size Liquid Droplets," *Opt. Lett.* **14** (1989) 402.
3. J.B. Snow, S.-X. Qian, and R.K. Chang, "Stimulated Raman Scattering from Individual Water and Ethanol Droplets at Morphology-Dependent Resonances," *Opt. Lett.* **10** (1985) 37.
4. J.-Z. Zhang and R.K. Chang, "Generation and Suppression of Stimulated Brillouin Scattering in Single Liquid Droplets," *J. Opt. Soc. Am. B* **6** (1989) 151.
5. P.R. Conwell, P.W. Barber, and C.K. Rushforth, "Resonant Spectra of Dielectric Spheres," *J. Opt. Soc. Am. A* **1** (1984) 822.
6. S.C. Hill and R.E. Benner, "Morphology-Dependent Resonances Associated with Stimulated Processes in Microspheres," *J. Opt. Soc. Am. B* **3** (1986) 1509.
7. J.-Z. Zhang, D.H. Leach, and R.K. Chang, "Photon Lifetime within a Droplet: Temporal Determination of Elastic and Stimulated Raman Scattering," *Opt. Lett.* **13** (1988) 270.
8. R.K. Chang, D.H. Leach, and J.-Z. Zhang, "The Q-Factor of Micrometer-Size Droplets as Optical Cavities," in Proceedings of the U.S.-Mexico Workshop on Electrodynamics of Interfaces and Composite Systems, Taxco, Mexico, August 10-14, 1987, R.G. Barrera and W.L. Mochan, eds. (World Scientific Publ. Co., 1988), p. 373.
9. J.-Z. Zhang, G. Chen, and R. K. Chang, "Pumping of Stimulated Raman Scattering by Stimulated Brillouin Scattering within a Single Liquid Droplet: Input Linewidth Effects," to be published in *J. Opt. Soc. Am. B*.
10. S.-X. Qian and R.K. Chang, "Multiorder Stokes Emission from Micrometer-Size Droplets," *Phys. Rev. Lett.* **56** (1986) 926.
11. S.-X. Qian, J.B. Snow, and R.K. Chang, "Coherent Raman Mixing and Coherent Anti-Stokes Raman Scattering from Individual Micrometer-Size Droplets," *Opt. Lett.* **10** (1985) 499.
12. S.-X. Qian and R.K. Chang, "Phase-Modulation-Broadened Line Shapes from Micrometer-Size CS₂ Droplets," *Opt. Lett.* **11** (1986) 371.
13. W.-F. Hsieh, J.-B. Zheng, and R.K. Chang, "Time Dependence of Multiorder Stimulated Raman Scattering from Single Droplets," *Opt. Lett.* **13** (1988) 497.
14. J.H. Eickmans, W.-F. Hsieh, and R.K. Chang, "Laser-Induced Explosion of H₂O Droplets: Spatially Resolved Spectra," *Opt. Lett.* **12** (1987) 22.
15. J.H. Eickmans, W.-F. Hsieh, and R.K. Chang, "Plasma Spectroscopy of H, Li, and Na in Plumes Resulting from Laser-Induced Droplet Explosion," *Appl. Opt.* **26** (1987) 3721.
16. W.-F. Hsieh, J.-B. Zheng, C.F. Wood, B.T. Chu, and R.K. Chang, "Propagation Velocity of Laser-Induced Plasma inside and outside a Transparent Droplet," *Opt. Lett.* **12** (1987) 576.
17. J.-B. Zheng, W.-F. Hsieh, S.-C. Chen, and R.K. Chang, "Temporally and Spatially Resolved Spectroscopy of Laser-Induced Plasma from a Droplet," *Opt. Lett.* **13** (1988) 559.
18. J.-B. Zheng, W.-F. Hsieh, S.-C. Chen, and R. K. Chang, "Laser-Induced Breakout and Detonation Waves in Droplets: I. Experiments," submitted to *J. Opt. Soc. Am. B*.
19. J.C. Carls and J. R. Brock, "Propagation of Laser Breakdown and Detonation Waves in Transparent Droplets," *Opt. Lett.* **13** (1988) 273.
20. J.C. Carls, Y. Soo, and J.R. Brock, "Laser-Induced Breakout and Detonation Waves in Droplets: II. Model," submitted to *J. Opt. Soc. Am. B*.

21. W.-F. Hsieh, J.-B. Zheng, and R.K. Chang, "Transmission through Plasma Created by Laser-Induced Breakdown of Water Droplets," to be published in Opt. Lett.
22. J.-Z. Zhang, J.K. Lam, C.F. Wood, B.T. Chu, and R.K. Chang, "Explosive Vaporization of a Large Transparent Droplet Irradiated by a High Intensity Laser," Appl. Opt. **26** (1987) 4731.
23. J.-Z. Zhang and R.K. Chang, "Shape Distortion of a Single Water Droplet by Laser-Induced Electrostriction," Opt. Lett. **13** (1988) 916.
24. H.M. Lai, P.T. Leung, K.L. Poon, and K. Young, "Electrostrictive Distortion of a Micrometer-Sized Droplet by a Laser Pulse," to be published in J. Opt. Soc. Am. B.
25. C.F. Wood, D.H. Leach, J.-Z. Zhang, R.K. Chang, and P.W. Barber, "Time-Resolved Shadowgraphs of Large Individual Water and Ethanol Droplets Vaporized by a Pulsed CO₂ Laser," Appl. Opt. **27** (1988) 2279.
26. R.K. Chang, J.H. Eickmans, W.-F. Hsieh, C.F. Wood, J.-Z. Zhang, and J.-B. Zheng, "Laser-Induced Breakdown in Large Transparent Water Droplets," Appl. Opt. **27** (1988) 2377.
27. A.S. Kwok, C.F. Wood, and R.K. Chang, "Fluorescence Imaging of CO₂ Laser Beam Heated Droplets," submitted to Opt. Lett.
28. V.P. Skripov, Metastable Liquids (Wiley, New York, 1974).
29. H.-M. Tzeng, K.F. Wall, M.B. Long, and R.K. Chang, "Laser Emission from Individual Droplets at Wavelengths Corresponding to Morphology-Dependent Resonances," Opt. Lett. **9** (1984) 499.

ACKNOWLEDGEMENTS

We gratefully acknowledge the partial support of this research by the U.S. Army Research Office (Contract No. DAAL03-88-K-0040) and the U.S. Air Force Office of Scientific Research (Grant No. 88-0100).

DISCUSSION

F. NILES

In nature, rain drops are not spherical. What happens when a high intensity laser beam interacts with a rain drop?

AUTHOR'S REPLY

This is an astute question. For falling rain droplets, especially those with radii $>1 \mu\text{m}$, the inertia effect causes each droplet shape to deviate from a sphere to an oblate spheroid or even a flat-bottom droplet. The inertia effect is dependent on the Weber and Reynolds numbers of the droplet. The droplet shape can be calculated as long as the Weber number is <5 and the Reynolds number is <500 . Dr. David Dandy of Sandia is an expert in this area. The morphology-dependent resonances (MDRs) of a sphere can be readily calculated by the Mie formalism. Each MDR is specified by the mode order (affects the radial distribution) and the mode number l (affects the θ distribution, where θ is the zenith angle). For a sphere, the azimuthal distribution (the ϕ angle), which is described by index m , is degenerate since all the great circles of a sphere are the same. By symmetry, $m=1$. However, for a prolate spheroid, the perimeter length depends on θ and m can take on values from $m = 0, 1, 2, \dots, l$, analogous to a magnetic system with angular momentum l and magnetic quantum numbers m .

A high degeneracy MDR of a sphere will split into numerous MDRs of a prolate or oblate spheroid. Profs. Peter Barber and Steven Hill of Clarkson University have used the T-matrix formalism to calculate such splitting for small droplets (with size parameters <100). Prof. Kenneth Young of the Chinese University of Hong Kong has recently developed a perturbation approach that can calculate the MDR splittings which are independent of the droplet size parameter. The MDR splittings are dependent only on the ratio of the droplet semi-major to semi-minor axes ratio and the MDR mode number l .

The degeneracy split MDRs give rise to more spectral peaks in the linear and nonlinear spectra and thereby cause complications. However, once we are more comfortable dealing with spheroids, the degeneracy split MDRs in the stimulated Raman spectra can be used to provide both size and shape information, in addition to species identification. Experimentally, we have indeed observed degeneracy split MDR peaks in the stimulated Raman scattering spectra and are in the process of documenting our observations of these closely spaced (in cm^{-1}) spectral peaks of nonspherical droplets with $l = 450$.

C. GIBBINS

You may have already answered my question from your response to the previous question, but could you envisage application of your technique to the measurement of the distribution of drop-sizes in rain, which is very hard to measure accurately.

AUTHOR'S REPLY

High accuracy droplet sizing can be deduced from the frequency spacing (in cm^{-1}) of the stimulated Raman scattering peaks, which are related to the morphology-dependent resonances of a sphere of a specific radius. To determine the size distribution of rain by this technique, it is important that only one droplet be sampled by the collection optics for each laser firing. This limitation is no different from that required in other optical sizing instruments. However, the additional requirements of the morphology-dependent resonance peak sizing technique are that the rain droplet circumference-to-wavelength ratio (size parameter) must be >10 (better if >50) and the rain droplet shape must not be too nonspherical.

Path Calculations

C.W.Lui, M.W.P.Cann and R.W.Nicholls
 Centre for Research in Earth and Space Science,
 York University, 4700 Keele Street, Ontario M3J 1P3, Canada
 and
 Institute for Space and Terrestrial Science,
 4850 Keele Street, North York, Ontario M3J 3K1, Canada

SUMMARY

The computation of aerosol absorption and scattering coefficients is normally a lengthy process, so that atmospheric slant path calculations rely on selections from pre-calculated data. This paper describes an investigation in which the calculated coefficients are stored in a parameterised form. The object was to encompass a wide variety of cloud and rain types in a data set of manageable proportions.

Atmospheric aerosols and rain are characterised by the mass density, size distribution $n(r)$, and shapes of the constituent water drops or ice crystals. Particle shapes may be irregular - in ice clouds, snow and rain for example - but for the calculations reported here are assumed to be spheres of equivalent volume. We adopt the modified gamma function, first proposed by D. Deirmendjian, as $n(r)$. The original form of the function contains four parameters. To facilitate the parameterization, we regroup them into two physically meaningful parameters r_c (critical radius) and $\delta = \alpha\gamma$, proportional to the slope of $n(r)$ around r_c . Then we express the absorption and scattering coefficients calculated from Mie theory as a polynomial in temperature and frequency. These coefficients in the polynomials are stored for retrieval and interpolation during a slant path calculation. The parameterization is quite general and includes the Marshall-Palmer relation for rain, the Laws and Parsons and inverse power distributions.

1. INTRODUCTION

For the calculation of attenuation, or radiance, along a slant path the atmosphere is subdivided into several homogeneous horizontal layers, each of which is assigned mean values for temperature, pressure and species concentrations. Layer properties and boundaries are determined with a pre-selected atmospheric model, which includes cloud and rain selections. Cloud (rain) attenuation properties are altitude dependent and must be calculated or retrieved from tables for each atmospheric layer in which they contribute. In general the computation of extinction coefficients for hydrometeors (clouds, rain, etc.) is a lengthy procedure requiring Mie theory and cannot be considered during a slant path calculation.

Many different types of rain and cloud occur in nature and some limited expression of these must be selected for inclusion in practical computer codes. Since the calculation of the absorption and scattering properties of these particulates is computationally intensive it is usual to use pre-calculated values in practical radiance computations, but tables of coefficients for all the conditions found in the atmosphere would be too extensive for general use. This paper describes an investigation into using generalised pre-calculated coefficients to obtain the attenuation for a variety of particle types and drop-size distributions. When this study began our interest lay in the microwave region (up to 300 GHz) so it is to this part of the spectrum that this paper relates, although the method should apply generally and we expect to extend it in the future. In the microwave region the absorption and scattering by clouds is negligible but attenuation by rain, and beam depolarisation by both rain and ice clouds, can be important.

We consider a group of water or ice particles with size distribution given by Deirmendjian's modified gamma function [1]. The particles are assumed to be spherical: small cloud drops are nearly so while raindrops tend to be oblate, if large [2], and ice crystals [3] have many shapes. Although Deirmendjian's modified gamma function is quite popular, there exist other functions, such as the inverse power law (e.g. for continental aerosols [4]), Laws and Parsons [5] distribution, and bimodal distributions [6]. Yet a summation of several Deirmendjian distributions, assuming no interaction between them, will approximate these other polydispersions. With some simplification the four parameters of the Deirmendjian distribution can be reduced to two. Mie theory is then used to calculate the absorption and scattering coefficients which are then fitted by a polynomial in temperature and frequency. The coefficients for the fitted polynomials are tabulated for various distribution parameters.

2. MIE CALCULATION AND POLYNOMIAL REPRESENTATION

The absorption and scattering coefficients are computed from the expressions

$$\mu_a = \int \pi r^2 Q_{abs}(x) n(r) dr, \quad \text{in 1/length,} \quad (1a)$$

$$\mu_s = \int \pi r^2 Q_{sca}(x) n(r) dr, \quad (1b)$$

The Q_{abs} and Q_{sca} are the absorption and scattering efficiency factors respectively for a single particle of radius r , expressed in terms of Mie Coefficients for the size parameter $x = 2\pi r/\lambda$ [1], where λ is the wavelength. $n(r)$ is the dropsize distribution function, which is discussed in the next section. The coefficients μ_a and μ_s are fitted to Eqs. (2a) and (2b) by means of least squares.

$$\mu_a = \sum_{i=0}^{n_t} \sum_{j=0}^{n_s} a_{ij} t^i f^j, \quad (2a)$$

$$\mu_s = \sum_{i=0}^{n_t} \sum_{j=0}^{n_s} s_{ij} t^i f^j, \quad (2b)$$

Here t is the temperature in Kelvin and f the frequency. These calculations are carried out for various $n(r)$, t and frequency and the polynomial parameters a_{ij} and s_{ij} are tabulated for use in atmospheric path calculations.

3. THE SIZE DISTRIBUTION $n(r)$

In a particular frequency range, we assume that the dropsize distribution for either water or ice is given by the modified gamma function with the four parameters first proposed by Deirmendjian [1]:

$$n(r) = a r^\alpha \exp(-b r^\gamma), \quad a, \gamma > 0, b \geq 0, \alpha > -4, \quad (3)$$

This form of monomodal distribution is in fact quite general. It includes the well-known Marshall-Palmer distribution [7] for rain

$$n(r) = 16000 \exp(-8.2 R^{-.21} r) \quad \text{in } \text{mm}^{-1} \text{m}^{-3}, \quad (4)$$

where R is the rain rate in mm/hr, and also the inverse r distribution with $\alpha > -4, \gamma = 1, b = 0$. The alternate form of the distribution is

$$n(r) = a r^\alpha \exp \left[-(\alpha/\gamma) (r/r_c)^\gamma \right], \quad (5)$$

where the critical radius r_c (radius of maximum occurrence) is given by

$$r_c = (\alpha/b\gamma)^{\frac{1}{\gamma}}. \quad (6)$$

For finite range of radii between two cut-off values, negative values [8] of α and γ can be used in Eq. (3). For the present application the conditions given in Eq. (3) are more suitable. In general Eq. (5) is physically more meaningful, except for $\alpha < 0$, when r_c is not defined. In this case either the meaning of r_c has to be re-defined for Eq. (5), Eq. (3) used with re-defined b , or Eq. (4) used for $\alpha = 0$. Here we use Eq. (5) and reduce the number of size-distribution parameters to two, by means of the quantities liquid (or solid) water mass density, M , total number density N , and dn/dr :

$$M = \int F \rho (4/3) \pi r^3 n(r) dr$$

$$= a F \rho \left(\frac{4\pi}{3\gamma} \right) \left(\frac{r_c}{r} \right)^{\frac{d+4}{\gamma}} r_c^{d+4} \Gamma\left(\frac{d+4}{\gamma}\right), \quad (7)$$

$$N = a \Gamma\left(\frac{d+4}{\gamma}\right) / \gamma (\alpha/\gamma r_c^\gamma)^{\frac{d+4}{\gamma}}, \quad (8)$$

$$dn/dr = \frac{\alpha n}{r} \left[1 - \left(\frac{r}{r_c} \right)^\gamma \right] = \frac{-\delta n \Delta r}{r^2}, \quad (9)$$

where $\delta = \alpha\gamma$ and $\Delta r = r - r_c$.

The F and ρ are respectively the conversion factor and the density of the hydrometeor.

Eqs. (6)-(9) enable us to choose a new set of parameters in place of a, b, α, γ . The critical radius, r_c , is a good new parameter since it shows the location of the maximum of $n(r)$. The other parameter is $\delta = \alpha\gamma$, which describes the behaviour of $n(r)$ around r_c - Eq. (9) gives the slope of $n(r)$. For large δ , the drops are more concentrated around r_c , but for small δ they are more widespread, Figure 1. For example, with $\delta = 10$, an 80% change in r will drop $n(r)$ by 90%, but with $\delta = 20$ a change of 50% in r has the same effect. For $\delta = 0$, the Marshall-Palmer distribution is obtained, with r_c in the tables for computer access (see below) re-defined as the rain rate. For negative δ , r_c is not defined, but $b = 0$. The remaining parameter, " a ", is a normalization constant which is fixed by normalizing to $M=1 \text{ g/m}^3$ in (7). Alternatively we could have chosen to normalize N instead of M , but this is less convenient as N may vary over many orders of magnitude, depending on the type of hydrometeor.

4. CALCULATION OF COEFFICIENTS AND POLYNOMIAL FITTING

We first tested the effect of varying α for fixed δ and it was found that the behaviour was about the same for both the absorption and scattering coefficients. Thus it is usually sufficient to characterize a distribution with just the two parameters δ and r_c and in our calculations we adopt the following values of

$$\begin{aligned} \alpha &= 0 & \text{for } \delta &= 0, \\ \alpha &= 2 & \text{for } \delta &< 8, \\ \alpha &= 8 & \text{for } \delta &> 8. \end{aligned} \quad (10)$$

For greater accuracy, a small correction may be applied to the absorption and scattering coefficients which takes into account the differences arising with other values of α , see Section 6. With α determined by (10) then, for a given δ and r_c , the values of parameters a, α, γ and r_c (or alternatively a, b, α, γ) are fixed. For the special case $\delta = 0$, we obtain the Marshall-Palmer distribution, in which the only other parameter needed is the rain rate; for this one case, in our computed tables of a_1 and a_2 the parameter r_c is the rain rate, not the critical radius (see Tables 1 and 2).

For a given set of size-distribution parameters, δ and r_c , the absorption and scattering coefficients are calculated over the frequency range of interest. These coefficients are then fitted by least squares to polynomials, Eqs. (2a) and (2b). If necessary the frequency range is broken down into smaller, overlapping, ranges to improve the quality of fit. Alternatively the orders of the polynomials may be increased. Calculations for water drops and for ice crystals are separate on account of their different refractive indices.

Absorption and scattering coefficients were computed for various selections of δ , and r_c for a frequency range of 1 to 300 GHz. Temperatures were selected between 253.2 K and 308.2 K, for water, and between 253.2 and 273.2 K for ice. The resulting coefficients vary over several orders of magnitude. For example, with $\delta = 6$ and $r_c = 250 \mu\text{m}$, characteristic of moderate rain, the absorption coefficients vary from 4.10×10^{-9} at 1 GHz to 1.01×10^{-6} at 300 GHz, and those for scattering from 1.61×10^{-9} at 1 GHz to 1.73×10^{-6} at 300 GHz. For some $n(r)$ the coefficients vary over seven orders of magnitude, and it was found necessary to divide the frequency interval into two ranges: 1 to 15.4 GHz and 15 to 300 GHz (for both liquid water and for ice hydrometeors). In each range $n_c = 8$ and

$n_s = 9$, for absorption and scattering respectively, Eqs. (2a, 2b). On the other hand the variation with temperature is much less, so that the range in temperature encountered in the Earth's atmosphere can be accommodated with one quadratic polynomial each for μ_a and μ_s . Thus for these calculations there are a total of 27 polynomial parameters for absorption and 30 for scattering, for each size distribution. Table 1 is an example of the results and shows some tabulated parameters for scattering which, with Eq. (2b), can be used to generate scattering coefficients for particle size distributions specified by $\delta = 6$ and $r_c = 0.05, 0.10$, microns, etc. Figures 2 to 4 show examples of the differences found between the Mie calculations and the computations from Eqs. (2a, 2b). In general the accuracy is quite good, at most a few percent, except for some cases near the ends of the frequency range. Near 300 GHz the discrepancy rises to over 10% in some cases.

5. PARAMETER USE IN ATMOSPHERIC SLANT PATH CALCULATIONS

For retrieval and use by our slant path computer program the polynomial parameters are organized into a tree-structure as shown in Figure 5. Retrieval of the required set of parameters then follows down the links, e.g. the sequence CLOUD-->TABLE-->CUNB collects any default values that may be required for δ , r_c , and also the altitude profile for cumulonimbus cloud; then the parameters required for the calculation of absorption and scattering coefficients with Eqs. (2a, 2b) are obtained with the sequence PARAM-->WATER-->FREQn-->[ABSO-->delta(*)-->cr.radius(*); SCAT-->delta(*)-->crit.radius(*)]. Interpolations are indicated by (*) and the appropriate frequency member FREQn is selected for the calculation, or more than one if required. For the case where the specified δ and r_c coincide exactly with the tabulated values the appropriate parameters are retrieved and the absorption (or scattering) coefficients calculated. In other cases interpolations are carried out over r_c and again over δ , using a 3-point Lagrangian scheme. At the present time these interpolations have to be performed on the calculated absorption coefficients, rather than over the polynomial parameter sets, which would be more efficient. This process provides absorption coefficients for the specified temperature, for unit path and unit mass. Multiplication by the appropriate water (or ice) mass density and path length then follows.

Table 2 shows parameters for certain types of cloud and rain. A table like this is stored in the parameter data set (TABLE in Figure 5). By means of the acronym a user can select default values for a particular hydrometeor. The parameters for ice and water are different, on account of their different refractive indices, and are stored separately, Figure 5.

Program instructions then take the form

```
CLOUD,CUNB
CLOUD ,delta,crit.radius,liq.wat.mass,base,top,cover
RAIN,HE    ,rain-rate,,top
CLOUD,CUNB ; ,liq.wat.mass,base,,cover
etc
```

The program uses any parameter specifications that are given. If the cloud or rain type is specified with a recognisable acronym then any missing parameters are obtained from the appropriate TABLE, for clouds or rain respectively, which also contains default values for base and top altitudes. Provision is also provided in the data set for altitude structure in specified clouds, which are stored as members bearing the cloud name (acronym).

Each set of stored parameters has stored with it any instructions which will be required by the program, such as the number of terms in the polynomial for temperature, for frequency, and sometimes, if required, the interpolation scheme to be employed. Similar data sets are used by the program for molecular continua, spectral line shapes, aerosol absorption and scattering coefficients. A current change being introduced in the program instruction list is recognition of the generic name PARTICLE, so that a cloud instruction could also be entered as

```
PARTICLE,CLOUD,CUNB ; etc
```

The program then looks for a member name CLOUD in the data set, and proceeds as before. At this point it is clear that one can introduce cloud data under different names (CLOUD1, CLOUD2, etc), or something quite different, e.g. SMOKE, which the program does not have to recognise but will find in the data set.

6. CORRECTION TERMS FOR DIFFERENT VALUES OF

As mentioned in Section 4, we need some correction if we are concerned with the attenuation results when α values are different from our those given in (10). To first order no correction is required for absorption. The first order correction to the scattering coefficients obtained using Eq. (2b) is independent of temperature and frequency,

$$\frac{\mu_s(\delta, \alpha')}{\mu_s(\delta, \alpha)} = \left(\frac{\alpha}{\alpha'}\right)^{3/\gamma} \frac{\Gamma\left(\frac{\alpha'+7}{\gamma'}\right) \Gamma\left(\frac{\alpha+4}{\gamma}\right)}{\Gamma\left(\frac{\alpha'+7}{\gamma}\right) \Gamma\left(\frac{\alpha+4}{\gamma'}\right)} \quad (11)$$

where γ' is obtained from $\gamma' = \delta/\alpha'$ and on the left-hand side the parameters in the denominator are the conditions of the stored data and in the numerator those for the desired type of cloud. Higher order corrections can be considered but these depend on both frequency and temperature and are to be avoided if possible.

7. CONCLUSIONS

This paper describes a method for including clouds and rain in atmospheric radiation attenuation calculations. Hydrometeor extinction properties are stored in parametric form which permits flexibility in specifying a particular cloud or rain for inclusion in atmospheric calculations. The study was made for the 1 - 300 GHz spectral range and extensions to higher frequencies are planned. Future work will also seek to improve the parameterization and interpolation schemes, with a view to greater accuracy, smaller data sets and less computing.

Some work has also been done on including beam de-polarization, as cross polarization discrimination, with some preliminary consideration of the plate and needle shapes of ice crystals. This is incomplete but is of special importance in the microwave region where ice clouds, which do not attenuate significantly, can cause appreciable beam depolarization. Other aspects which can be considered in the future include wind effects, on rain for example, multiple scattering and the extension to non-spherical particles.

REFERENCES

1. Deirmendjian D.
Scattering on Spherical Polydispersions.
American Elsevier Pub. Co. Inc., New York, 1969.
2. Green A.W.
An Approximation for the Shapes of Large Raindrops.
J. Appl. Meteorol. 14, 1578-1583 (1975).
3. Magono C., Lee C.W.
Journal of Faculty of Science, Hokkaido University, Japan,
Series VII, Vol. II, No. 4, p.324-325, 1966.
4. Junge C.E.
"Aerosol" in Handbook of Geophysics, C.F. Campan et al., eds.,
Macmillan, New York, 1960.
5. Laws J.O., Parsons D.A.
The relation of raindrop size to intensity.
Trans. Am. Geophys. Union 24, 452-460 (1943).
6. Mason B.J., Jonas P.R.
The evolution of droplet spectra and large droplets by
condensation in cumulus clouds.
Quart. J. Roy. Meteor. Soc. 100, 23-28 (1974).
7. Marshall J.S., Palmer W.
The distribution of raindrops with size.
J. Meteorol., 5, 165-166 (1948).
8. Mallow J.V.
Empirical Fog Droplet Size Distribution Functions with Finite
Limits.
J. Atmos. Sci., 32, 440-443 (1975).
9. Welch R.M., Cox S.K., Davis J.M.
Solar Radiation and Clouds.
Meteorol. Mon., Vol 17, No. 39, American Meteorological
Society, Boston, 1980.

10. Falcone V.J., Abreu L.W., Shettle E.P.
 Atmospheric Attenuation of Millimeter and Submillimeter
 Waves: Models and Computer Code.
 Air Force Geophysics Laboratory, U.S. Air Force, Hanscom
 AFB, Mass. Technical Report AFGL-TR-79-0253, 1979.

Table 1. Example of Coefficients for the Fitted
 Formulae - Scattering by Cloud ($\delta = 6$)

| | n_s | n_t | δ | r_c | Freq. Range (GHz) |
|----------------|----------------|----------------|----------------|----------------|----------------------|
| CLOUD SCAT | 9 | 2 | 6.00 | 0.05 | 1.00 15.40 |
| -1.8843779E-23 | 4.4453726E-23 | -4.0153285E-23 | 1.8689932E-23 | -3.6342072E-24 | |
| 8.3739242E-25 | -9.1734958E-26 | 5.0781565E-27 | -1.6693780E-28 | 2.3650991E-30 | |
| 1.1867653E-25 | -2.8102622E-25 | 2.5571114E-25 | -1.2005028E-25 | 3.2645043E-26 | |
| -5.4718505E-27 | 6.0419985E-28 | -3.3628904E-29 | 1.1115008E-30 | -1.5832584E-32 | |
| -2.1927926E-28 | 5.1893085E-28 | -4.7199189E-28 | 2.2153221E-28 | -6.1004012E-29 | |
| 1.0084202E-29 | -1.1052746E-30 | 6.2066713E-32 | -2.0542993E-33 | 2.9252039E-35 | |
| CLOUD SCAT | 9 | 2 | 6.00 | 0.10 | 1.00 15.40 |
| 1.3517840E-22 | -3.2497515E-22 | 2.9297562E-22 | -1.3654296E-22 | 4.8115454E-23 | |
| -6.0031423E-24 | 5.5574625E-25 | -3.8013198E-26 | 1.2990014E-27 | -1.8282985E-29 | |
| -1.2007875E-24 | 2.8699012E-24 | -2.5752112E-24 | 1.1929423E-24 | -3.2024213E-25 | |
| 5.1949695E-26 | -4.8898129E-27 | 3.2413728E-28 | -1.0987481E-29 | 1.5416340E-31 | |
| 2.2364802E-27 | -5.3401138E-27 | 4.7865923E-27 | -2.2142365E-27 | 5.8731908E-28 | |
| -9.6218220E-29 | 9.1111081E-30 | -5.9788097E-31 | 2.0219819E-32 | -2.8347340E-34 | |

Table 2 Some Cloud and Rain Default Parameters

| Name | Acronym | δ | r_c (μ m) | M (g/m^3) | Ref | Remarks |
|-----------------|---------|----------|------------------|---------------|-----|-------------------|
| Mist | MI | 0.5 | 0.05 | 4.948E-5 | 1 | |
| Drizzle | DR | 0.5 | 50 | 0.4948 | 1 | |
| Light rain | LI | 1 | 70 | 0.117 | 1 | |
| Moderate rain | MO | 4 | 333.3 | 0.509 | 9 | |
| Heavy rain | HE | 6 | 600 | 2.110 | 9 | |
| Marshall-Palmer | MP | 0 | 10 | 0.6153 | | r_c = rain rate |
| Continuous rain | CO | 0 | 5 | 0.3437 | | r_c = rain rate |
| Nimbostratus | NS | 2.41 | 9.67 | 1.034 | 9 | |
| Stratus | ST | 3.9 | 6.75 | 0.379 | 9 | |
| Altostratus | ALST | 5 | 4.5 | 0.41 | 10 | |
| Alto cumulus | ALCU | 5 | 4 | 0.39 | | |
| Stratocumulus | STCU | 5.95 | 5.33 | 0.141 | 9 | |
| Cumulus | CU | 6 | 4 | 0.06255 | 1 | |
| Cumulonimbus | CUNB | 3 | 5 | 0.16 | 10 | |
| Nacreous | NA | 24 | 2 | 0.00377 | 1 | |
| Cumuliiform | CUFM | 4 | 4.5 | 0.08 | | |
| Heavy Fog | HF | 3 | 10 | 0.37 | 10 | |
| Moderate Fog | MF | 6 | 4 | 0.06 | 10 | |
| Land Haze | LH | 1 | 0.07 | 1.167E-5 | 1 | |
| Noctilucent | NO | 7 | 50 | 0.06 | | Ice cloud |
| Cirrus | CI | 6 | 110 | 0.916 | | Ice cloud |
| Cirrocumulus | CICU | 6 | 100 | 0.6 | | Ice cloud |
| Cirrostratus | CIST | 6 | 75 | 0.39 | | Ice cloud |
| Hail | HA | 2 | 1000 | 0.2878 | | Ice cloud |

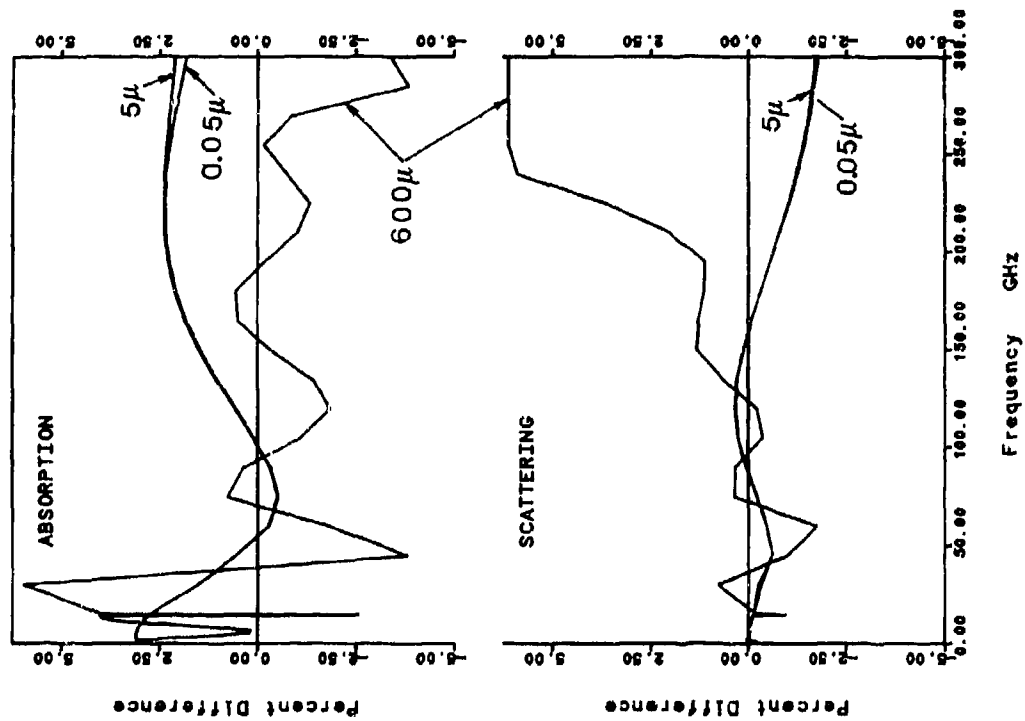
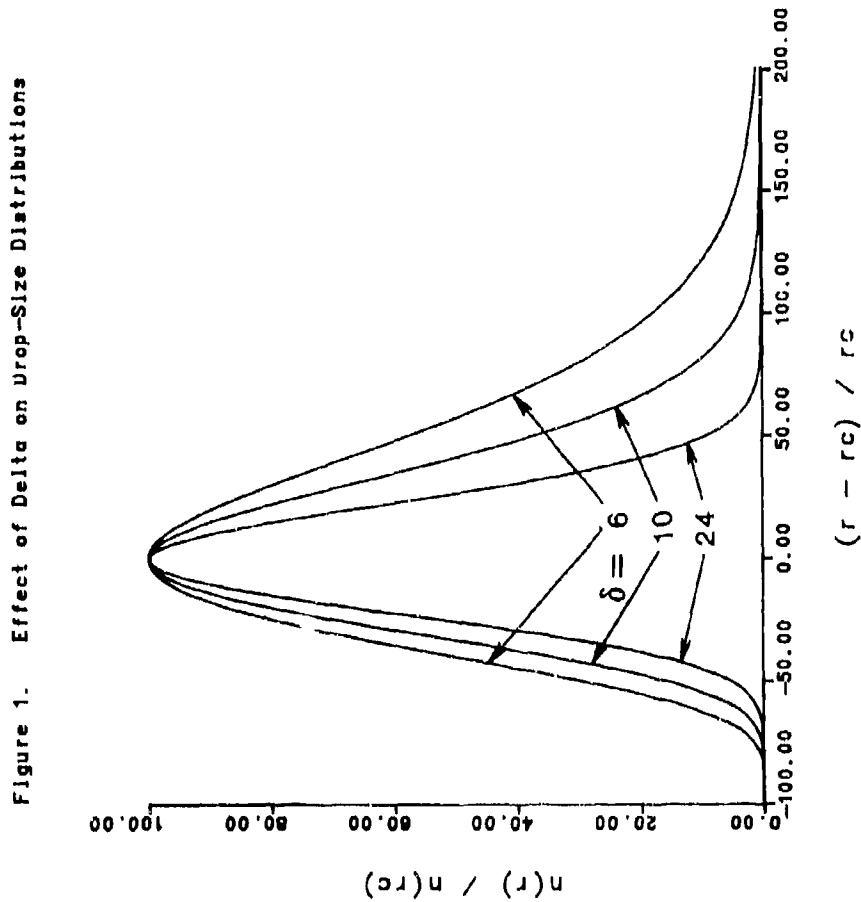


Figure 3. Comparison with Initial Mie Calculations.
B: Variation with Temperature
Delta = 6; Critical radius = 5 microns

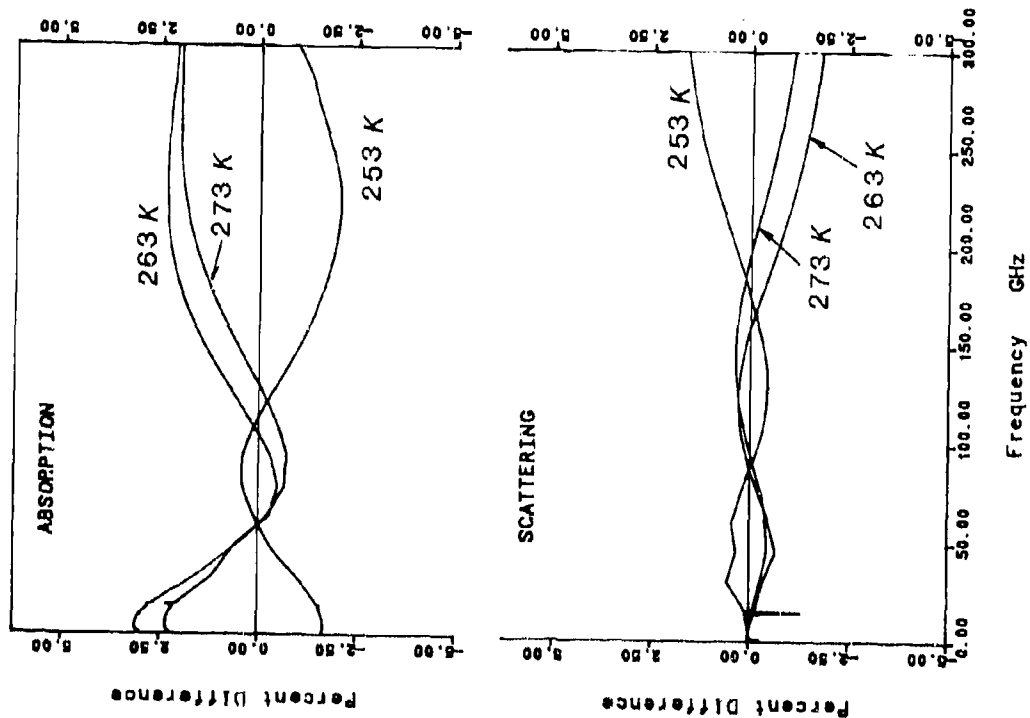


Figure 4. Comparison with Initial Mie Calculations
C: Variation with Delta
Critical radius = 5 microns; Temperature = 263 K

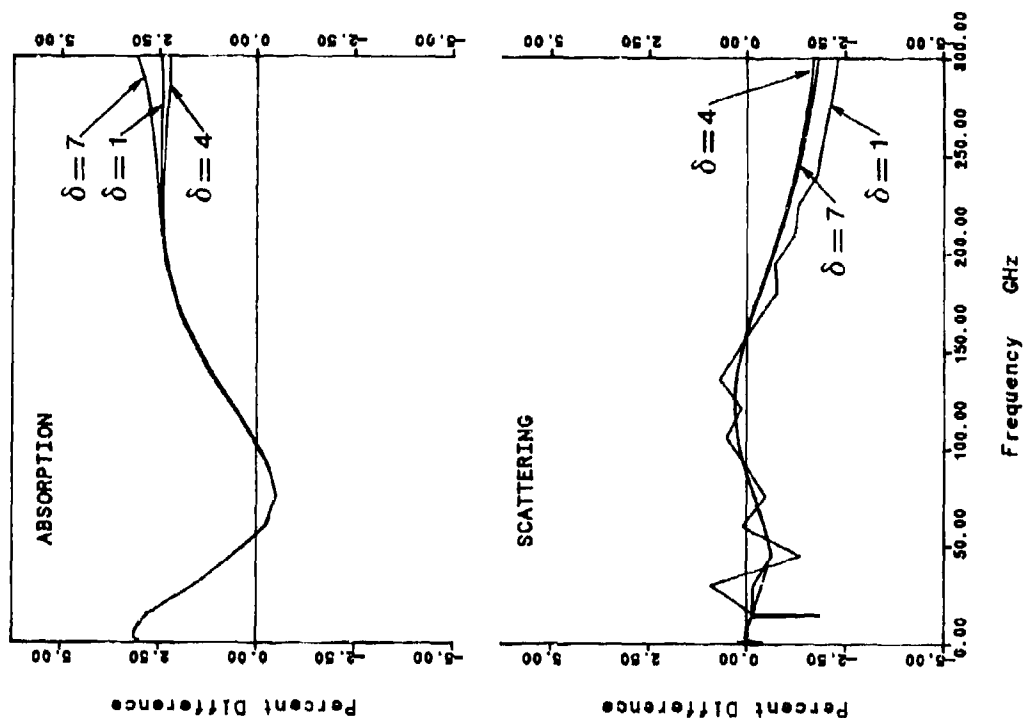
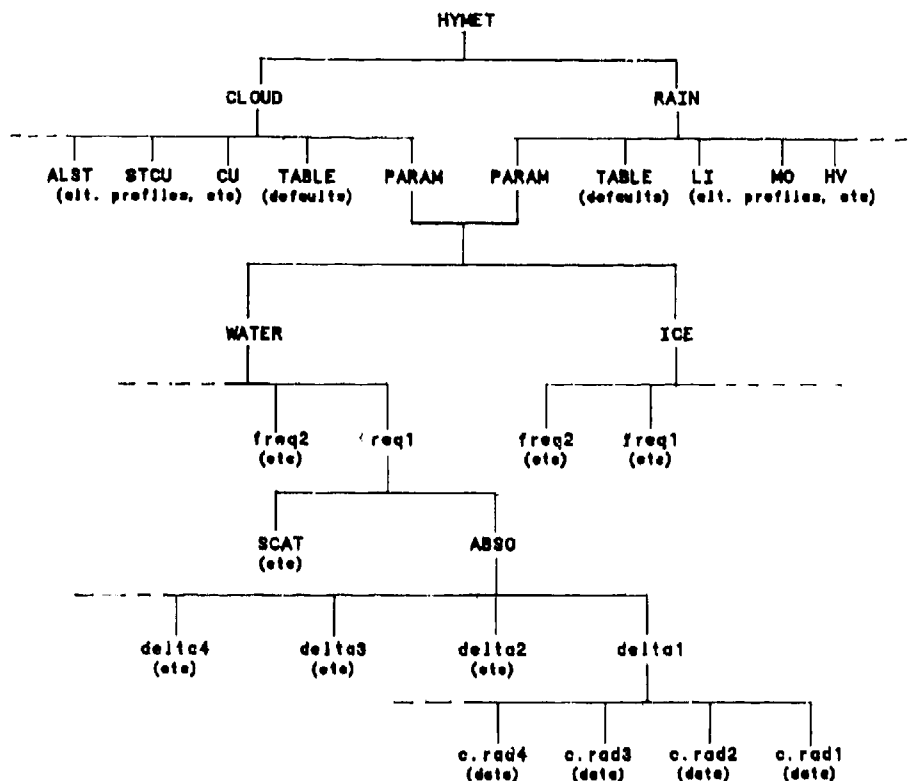


Figure 5. Data Set Organisation for Clouds and Rain

(Member lists for members with lower case names contain numeric entries for interpolation, etc.)



DISCUSSION

F. MILES

Are you making an assumption that the rain particle size distribution is constant with altitude?

AUTHOR'S REPLY

No. Provision is made in the data set for storing altitude profile information - under member names with the acronym for the particular cloud or rain type.

E. SHETTL

I have a comment and a question. First, a comment, for clouds LOWTRAN and FASCODE already do an analytic calculation for wavelengths longer than 0.2 mm. This uses the liquid content of the cloud, since you are in the Rayleigh limit, details of size are not important and analytic expressions for the refractive index exist for water and ice. Second, for rain, several others have developed analytic expressions for millimeter wavelength rain scattering and absorption. One recent one was by R. Issacs, et al. in Applied Optics a year or two ago based on earlier work of R. Savage. Have you compared your expressions with any others?

AUTHOR'S REPLY

In response to your first point, we are aware that the Rayleigh approximation can be applied at these frequencies. In fact, absorption and scattering by clouds are not too important. But our prime objective was to develop a procedure for our computation which could also be applied at higher frequencies, in the infrared and visible. Regarding your question, these calculations were done by my colleague Dr. Lui and I do not know whether he has made such comparisons. I rather think not. Thank you for your comment, I'll inform him.

INFRARED PROPAGATION IN THE AIR-SEA BOUNDARY LAYER

R. Larsen and K.A. Proedy
GEC-Marconi Research Centre,
Great Baddow, Chelmsford,
Essex, CM2 8HN, U.K.

G. Drake
Future Systems Laboratory, GEC Sensors Ltd.,
Christopher Martin Road,
Basildon, Essex, SS14 3EL, U.K.

1 INTRODUCTION

Over the oceans and other large bodies of water the structure of the lowest layers of the atmosphere is often strongly modified by evaporation of water vapour from the water surface. At radio wavelengths this layer will usually be strongly refracting or ducting, and the layer is commonly known as the evaporation duct. However, the refractive index of air at infrared wavelengths differs from that at radio wavelengths, and this paper examines the effects of the marine boundary layer on the propagation of infrared radiation.

Meteorological models of the air-sea boundary layer are used to compute vertical profiles of temperature and water-vapour pressure. From these are derived profiles of atmospheric refractive index at radio wavelengths and at infrared wavelengths in the window regions of low absorption.

For duct propagation to occur it is necessary that the refractivity of air decreases rapidly with increasing height above the surface. At radio wavelengths this usually occurs when there is a strong lapse of water vapour pressure with increasing height. By contrast, at infra-red wavelengths the refractive index is almost independent of water vapour pressure, and it is found that an infra-red duct is formed only when there is a temperature inversion.

2 REFRACTIVITY OF AIR AT INFRA-RED AND RADIO WAVELENGTHS

a) Infra-red wavelengths

The complex refractive index of air in the infra-red (IR) region of the electromagnetic spectrum is dominated by the effects of water vapour. In this region there are a large number of vibrational and rotational resonances of the polar water molecule. These resonances affect both the real and imaginary parts of the refractive index.

The imaginary part of the complex refractive index determines absorption, the real part - i.e. that which is usually implied by the simple term "refractive index" - determines refraction. The resonances cause intense absorption of IR at particular wavebands, but clear window regions of low absorption occur between resonances. The resonances also contribute an anomalous term to the atmospheric refraction (i.e. to the real part of the complex refractive index).

The refractivity, N , at IR can be written as the sum of three terms, a dry term N_d accounting for the atmospheric gas contribution, a wet term N_w accounting for the water vapour contribution and an anomalous term N_a accounting for resonant effects. Thus

$$N = N_d + N_w + N_a \quad \text{..... (1)}$$

Formulae for these terms at IR are given by Hill [1]. When converted to appropriate units:-

$$N_d = 0.284N_0 \frac{P}{T} \quad \text{and} \quad N_w = -12.79 \frac{e}{T} \quad \text{..... (2)}$$

and thus

$$N = 0.284N_0 \frac{P}{T} - 12.79 \frac{e}{T} + N_a \quad \text{..... (3)}$$

where

P = pressure in mb
 T = Temperature °K
 e = Water vapour pressure (mb)
 N_0 = Refractivity at $T=288^\circ\text{K}$, $P=1013$ mb

The refractivity N_a varies with wavelength [1] according to:-

$$N_a = 64.328 + \frac{29498.1}{146 - \lambda^{-2}} + \frac{255.4}{41 - \lambda^{-2}} \quad \text{..... (4)}$$

where λ is the wavelength in μm .

It can be seen from Equations 3 and 4 that at infra-red wavelengths the continuum value $N_c (= N_d + N_w)$ is only weakly dependent on wavelength. It can also be seen from Equation 3 that the dry term dominates the wet term under normal conditions. For example, if $\lambda = 10 \mu\text{m}$, $P = 1013$ mb, $T = 288^\circ\text{K}$ and $e = 17$ mb (i.e. air is saturated) then

$$N_c = 272.6, \quad N_d = 272.3 \quad \text{and} \quad N_w = -0.75$$

In the window regions between absorption resonances (i.e. in the 3-5 μm and 8-14 μm bands) the anomalous term N_a is found to be small [1], e.g. in the 8-14 μm region its value is approximately ~ 2 N-units.

b) Radio wavelengths

At radio wavelengths the resonances of the water vapour molecule are no longer important, and the refractivity of air may be considered to have a value that is independent of frequency up to millimetre wave frequencies. The refractivity again depends on atmospheric pressure, temperature and water vapour content, and is given [2] by:-

$$N = \frac{77.6P}{T} + 373256 \frac{e}{T^3} \quad \text{.....(5)}$$

where P, T and e are as defined above. In this expression the first term is the dry term N_d and the second term is the wet term N_w .

Under normal conditions (P = 1013 mb, T = 288°K and e = 17 mb, as above) we find

$$N_d = 272.9 \quad \text{and} \quad N_w = 76.5$$

Note that the dry term is essentially the same as for the IR case, but the wet term N_w is very much larger than in the IR case. Although the dry term is still numerically larger than the wet term, it is found in practice that the normally encountered variations in water vapour pressure exert a stronger influence on variations in refractivity than do variations in temperature, i.e. N_w fluctuates more widely than N_d .

The conclusion from Equations (3) and (5) is that at IR the refractive effects will be dominated by the vertical temperature profile of the atmosphere, whilst at radio wavelengths the water vapour profile is of greater importance. For ducting to occur it is necessary that the refractivity of the air decreases rapidly with increasing height above the surface. At IR this occurs when air temperature increases with increasing height (described as a temperature inversion). At radio wavelengths it is usually necessary to have a strong lapse of water vapour pressure with height to form a duct. However, the temperature profile is still important in the radio case, and a temperature inversion will reinforce the refractivity gradient caused by a water vapour lapse, whilst a temperature lapse will weaken it.

3 METEOROLOGICAL ANALYSIS

3.1 Structure of the Air-Sea Boundary Layer

Prediction of electromagnetic propagation close to the sea surface requires a detailed knowledge of the refractivity structure of the lowest layers of the atmosphere. Practical measurements of the required parameters in close proximity to the sea are extremely difficult to accomplish, and most studies of oversea propagation have made use of theoretical models of the structure of the boundary layer.

The Monin-Obukhov similarity theory concerns the structure of the surface layer of atmosphere, and it was used successfully to model the radio evaporation duct [3]. The basis of the theory is that air in contact with the sea surface is saturated and in thermal equilibrium. The atmosphere is considered to be fully turbulent above the surface. Heat and vapour are transported by turbulence to the higher layers. The theory of Monin and Obukhov is valid for the lowest few tens of metres of the atmosphere where the vertical fluxes of momentum, heat and water vapour are approximately constant.

For this boundary region we may derive the following practical height profiles of temperature and water vapour pressure [3]

$$e = e_s + C \left[\ln \left(\frac{h + h_0}{h_0} \right) + \psi \left(\frac{h}{L} \right) \right] \quad \text{..... (6a)}$$

$$T = T_s + D \left[\ln \left(\frac{h + h_0}{h_0} \right) + \psi \left(\frac{h}{L} \right) \right] \quad \text{..... (6b)}$$

where

- e_s - surface value of saturated vapour pressure (mb)
- T_s - sea surface temperature °K
- h_0 - effective sea surface roughness (m)
- L - Monin-Obukhov stability length (m)
- C, D - experimental constants
- ψ - the integrated Monin-Obukhov function

The integrated Monin-Obukhov function is a tabulated function. In conditions of neutral stability it is purely logarithmic. (It should be noted that h_0 represents the surface roughness of a calm sea surface, it is not an effective waveheight. This figure was taken as 0.15 mm as this was found to be appropriate from other radio studies.)

An important limitation of the theory is the requirement for fully developed turbulence. In stable atmospheric conditions turbulence is damped out by buoyancy effects, and in these conditions the theory breaks down. In general, if the inverse stability length $1/L$ becomes appreciably larger than zero (say $1/L > 1$) then this would indicate that the theory is no longer valid.

3.2 Example Profiles in the Boundary Layer

The meteorological parameters required to deduce vertical profiles of temperature, T and water vapour pressure, e are as follows:-

- T_s - sea temperature °C
- T_h - air temperature °C at height h
- e_h - water vapour pressure (mb) at height h
- U_h - horizontal wind speed (m/s) at height h
- h - the measurement height (m) above the sea surface.

From these parameters the experimental constants (C and D in Equations 6(a) and 6(b)) may be deduced. Equation 6 may then be used to calculate the vertical profiles of air temperature and water vapour pressure in the air-sea boundary layer. Some example profiles are shown in Figures 1 and 2. These were computed from meteorological data collected in the German Bight by Brooks et al [4]. The profiles shown are representative of average meteorological conditions in this sea area; for the great majority of the time the air is cooler than the sea surface, leading to a vertical lapse of both temperature and water vapour pressure.

The computed profiles of T and e were used in conjunction with Equations (3) and (5) to generate vertical profiles of atmospheric refractivity N at both IR and radio wavelengths; the results are shown in Figure 3. The surface atmospheric pressure was assumed to be 1013 mb, and the pressure lapse rate was taken as -0.1 mb.m^{-1} . The meteorological theory employed here applies only to the air-sea boundary layer, and at large heights above the surface the temperature and water vapour profiles tend towards those of the normal atmospheric lapse rate.

At IR the refractivity profile close to the surface is dominated by the air temperature gradient; the strong lapse of temperature in the lowest few metres leads to a strong increase of refractivity. At greater heights (above about 5 metres in the example shown) the temperature lapse rate is much smaller, and the refractivity gradient here results principally from the lapse of atmospheric pressure with height. In this region the refractivity profile tends towards the IR refractivity lapse rate in a normal atmosphere of about -24 N/km .

At radio wavelengths the dry term in the expression for atmospheric refractivity is almost identical to that for IR. However the wet term exerts a stronger influence, and the strong lapse of water vapour pressure in the lowest few metres results in a strong refractivity lapse. At greater heights the refractivity gradient tends towards the normal atmosphere radio refractivity lapse rate of about -40 N/km .

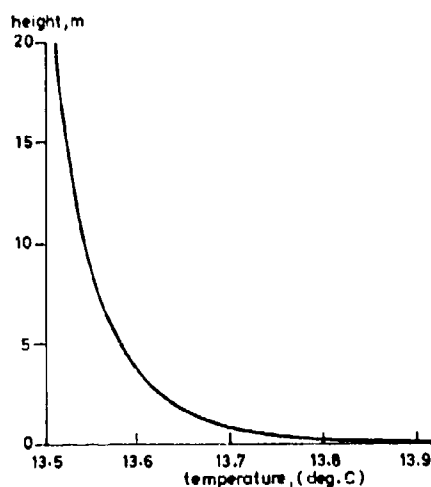


Figure 1 Vertical profile of atmospheric temperature.

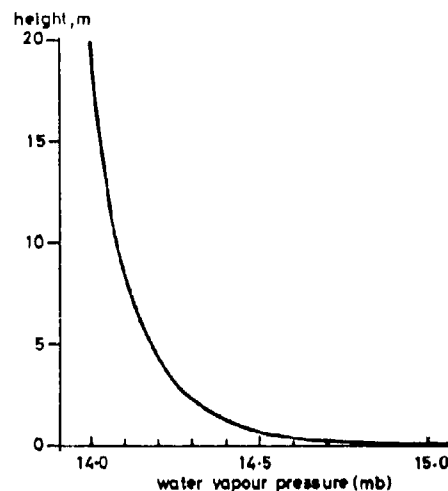


Figure 2 Vertical profile of water vapour pressure.

In conditions of strong refraction close to the surface it is often more convenient to work in terms of modified refractivity M (rather than refractivity N), defined as

$$M = N + h \cdot 10^6 / a$$

where M is modified atmospheric refractivity
 N is conventional atmospheric refractivity
 h is height above the surface of the Earth (km)
 a is true Earth radius (km)

Taking the Earth radius as $a = 6370$ km this becomes:-

$$M = N + 157 h$$

$$\text{and } \frac{dM}{dh} = \frac{dN}{dh} + 157$$

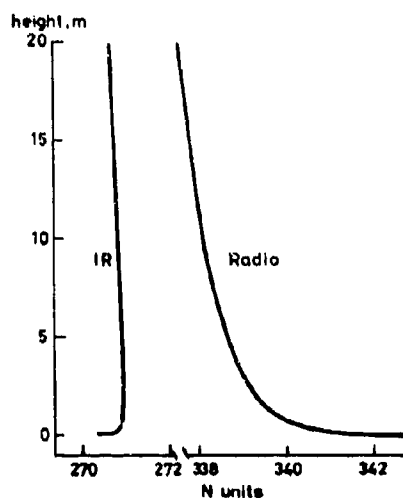


Figure 3 Vertical profiles of atmospheric refractivity N , infrared and radio wavelengths.

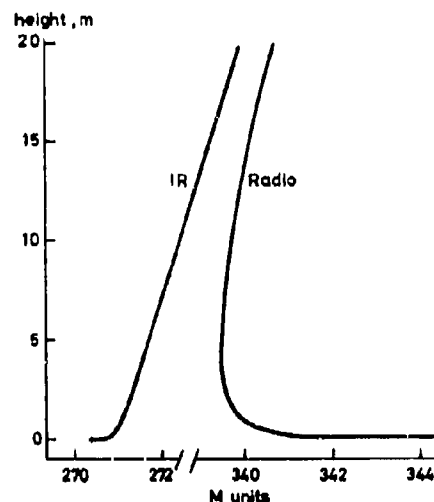


Figure 4 Vertical profiles of modified refractivity M , infrared and radio wavelengths.

The vertical profiles of modified refractivity M for IR and radio wavelengths are shown in Figure 4 (these curves are again for average meteorological conditions in the German Bight, as for Figure 3). Figure 4 clearly shows that at radio wavelengths there is a significant surface duct (the evaporation duct); the height of the duct is the height at which $dM/dh = 0$, it is about 5 metres in this example. Above the duct the gradient of radio modified refractivity becomes that of a normal atmosphere ($dM/dh = +117$ M-units/km).

At IR wavelengths the same meteorological structure is seen to be strongly subrefractive (i.e. dM/dh is large and positive at the surface). It is thus found to be inappropriate to describe the surface layer as an "evaporation duct" when considering IR propagation. Well above the boundary layer the gradient of IR modified refractivity again becomes that of a normal atmosphere ($dM/dh = +117$ M-units/km).

(It may be noted that in normal atmospheric conditions both IR and radio waves are refracted such that near-horizontal ray paths acquire a downward curvature. However the curvature at IR is little more than half that at radio wavelengths. Thus in a normal atmosphere the effective Earth radius factor, k , is 1.34 at radio wavelengths, but is about 1.18 at IR wavelengths.)

4 EFFECTS OF ATMOSPHERIC REFRACTION

A raytracing program has been used to calculate the paths of infra-red radiation and radio waves propagating through the refractivity structures described above. The methods employed in the raytracing program are described in Reference [5], and the results are shown in Figures 5 and 6.

In each case a family of rays with different launch angles has been drawn with respect to a flattened Earth, and the maximum and minimum launch angles are indicated. It should be noted that the vertical and horizontal scales of the diagrams are very different, leading to a great exaggeration of angles in the vertical plane. In fact the diagrams include only rays at very small angles (fractions of a degree) to the horizontal.

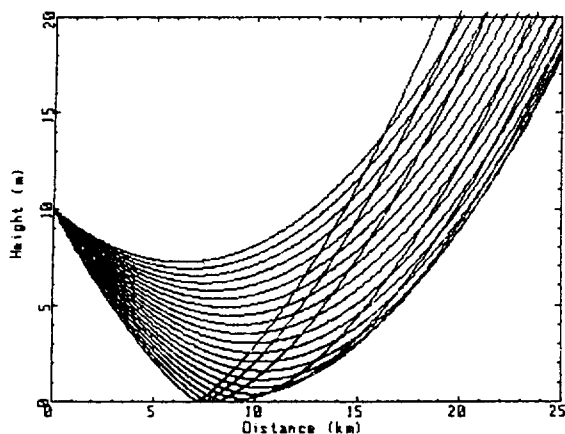


Figure 5 Raytrace through infrared profile of Figure 4; transmitter height 10 metres.

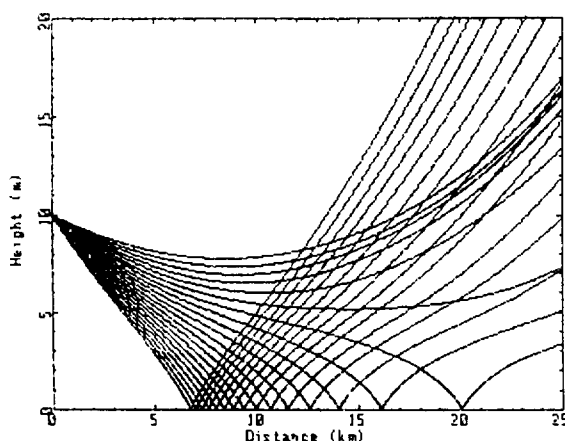


Figure 6 Raytrace through radio profile of Figure 4; transmitter height 10 metres.

The horizon distance (i.e. the maximum range at which an object on the sea surface is visible) is readily deduced from the raytrace diagrams. It is the maximum distance at which a ray path just touches the abscissa of the graph. At distances beyond the horizon range the ray paths are refracted upwards before they reach the surface, and the surface is not visible. The envelope of the ray paths to the lower right of Figure 5 in fact represents the "horizon line" of an IR sensor, below which nothing is visible.

In the case of radio propagation (Figure 6) the same atmospheric structure is now ducting, and the horizon line coincides with the surface of the Earth. This means that for any distance from the sensor it is possible to find a ray path that reaches the sea surface at that distance, and (in principle at least) the surface is visible to very large distances. In practice the ray picture of Figure 6 implies that radio terminals may be able to communicate with low propagation losses, even when separated by distances well beyond the horizon ranges for IR terminals at the same heights above sea level.

5 RELATIONSHIP BETWEEN IR AND RADIO PROPAGATION

The refractivity of air was shown above to depend on the atmospheric pressure, temperature and water vapour concentration. The relative importance of these terms depends on the wavelength of electromagnetic radiation under consideration. For the case of IR it was found that in the window regions the refractivity N is almost independent of water vapour pressure.

At radio wavelengths the refractivity depends strongly on water vapour pressure e as well as on temperature T , and the vertical gradients of e are usually the major factor in determining the vertical profile of refractivity N . (It may be noted that in a perfectly dry atmosphere, i.e. $e = 0$ mb, the refractivity profiles at IR and radio wavelengths would be essentially identical, and hence the propagation behaviour would also be the same.)

Typical profiles of T and e in the boundary layer (Figures 1 and 2) display a vertical lapse of both temperature and humidity. In the case of IR propagation the temperature lapse causes refractivity to increase with height and hence creates subrefractive conditions. In the case of radio propagation the temperature lapse also creates a tendency to subrefraction, but this is outweighed by the effects of the humidity lapse. The decrease of e with height causes refractivity to decrease sharply, and the combined effect of the T and e profiles is a decrease of refractivity with increasing height, causing super-refraction or ducting at radio wavelengths.

Studies of maritime meteorological data have suggested that there is a fairly strong tendency (but not an invariable rule) for negative e gradients to occur with negative T gradients and vice versa. Thus the conditions that give rise to ducting at IR (positive T gradients or temperature inversions) tend to be associated with positive e gradients. Depending on the strength of the e gradients this may cause the radio refractivity profile to be either mildly or strongly subrefractive. Thus suggests that conditions causing subrefraction and reduced system ranges at IR will usually cause super-refraction and extended ranges for radio systems, while super-refraction at IR usually coincides with subrefraction at radio wavelengths.

In order to illustrate this behaviour a database of meteorological observations collected during the HEXOS experiment [6] was examined. For each observation the surface gradients of modified refractivity dM/dh were computed for both IR and radio wavelengths. A scatter diagram of the two gradients is shown in Figure 7. Evidently there is a fair degree of irregularity in the results (as would be expected unless the T and e profiles were perfectly correlated). However the diagram demonstrates a fairly clear trend for dM/dh at IR to become larger in a positive direction (i.e. more subrefractive) as dM/dh at radio wavelengths becomes larger in a negative direction (i.e. more strongly superrefracting).

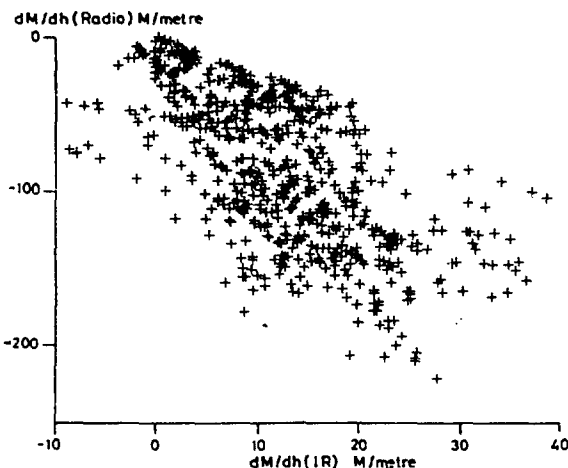


Figure 7 Surface gradients of modified refractivity dM/dh , radio vs. IR (HEXOS data).

The diagram also illustrates the fact that for the great majority of cases the boundary layer is more or less strongly superrefractive at radio wavelengths, whilst it is usually subrefractive at IR. (Note that the axes are scaled in M-units/metre. Thus in a normal atmosphere the modified refractivity gradient would be +0.117 M-units/metre at radio wavelengths and +0.133 M-units/metre at IR. The gradients in Figure 7 are very strong, but they occur only at the extreme lower limit of the atmospheric boundary layer.)

6 SUMMARY AND CONCLUSIONS

The refractivity of air at IR wavelengths has been examined and compared with that at radio wavelengths. At radio wavelengths the refractivity depends on atmospheric pressure, temperature and quite strongly on water vapour pressure. However at IR wavelengths the refractivity depends essentially on atmospheric pressure and temperature alone.

Models of the structure of the air-sea boundary layer lead to the conclusion that there is a semi-permanent duct (the evaporation duct) at radio wavelengths, whilst at IR the same meteorological structure appears to be subrefractive. This leads to reduced horizon ranges for IR systems whilst radio systems experience reduced propagation losses and increased system ranges.

There is a fairly well marked negative correlation between the surface gradients at IR and at radio wavelengths. For the majority of time the atmospheric boundary layer over the sea is subrefractive at IR and superrefractive at radio wavelengths.

7 ACKNOWLEDGEMENTS

The studies reported here were supported by Procurement Executive, Ministry of Defence, UK. The data from the HEXOS experiment used to generate Figure 7 were supplied by the Department of Pure and Applied Physics, UMIST, Manchester.

8 REFERENCES

1. R.J. Hill et al, "Refractive Index and Absorption Fluctuations in the Infra-red Caused by Temperature, Humidity and Pressure Fluctuations", J. Opt. Soc. Am., Vol. 70, No. 10, October 1980, pp 1192-1205.
2. Recommendations and Reports of the CCIR, 1986, Geneva, Vol. 5, Rec 453-1.
3. S. Rotherham, "Radiowave Propagation in the Evaporation Duct", Marconi Review, First Quarter 1974.
4. K. Brocks et al, "Meteorologische Beobachtungen in der Helgolander Bucht 1956-1961", Geophysikalischen Instituts der Universitat Hamburg 1963.
5. R.N. Herring, "General Raytracing Techniques for Predicting Fields in an Arbitrarily Varying Troposphere", IEE International Conference on Antennas and Propagation, ICAP 85, April 1985, pp 279-282.
6. K.B. Katsaros, S.D. Smith, and W.A. Oost, "HEXOS - Humidity Exchange Over the Sea A Program for Research on Water-Vapour and Droplet Fluxes from Sea to Air at Moderate to High Wind Speeds", Bulletin American Meteorological Society, Vol. 68, No. 5, May 1987, pp.466-476.

DISCUSSION

J. RICHTER

You may be interested in actual data consisting of 10.6 and 0.63 micron measurements which we took some ten years ago to investigate refractive bending effects over an 8.5 km over-water path; we were specifically interested in range reductions under subrefractive conditions. (Feinberg, R., H. V. Hitney and H. G. Hughes, "Marine Boundary Layer Effects in the Infrared," NOSC TN 555, 1978).

AUTHOR'S REPLY

I would be interested in your data.

J. RIDOUT

You stated that subrefraction is normal for the HEXOS measurements. Is this expected to be the same for other geographic areas?

AUTHOR'S REPLY

I showed here only the results for the HEXOS data, but we have also examined other data sets from the North Sea and various parts of the North Atlantic, and found essentially the same conclusion. Dr. Richter has just stated that he also found subrefraction (at IR) in his studies off the coast of California.

E. ELORANTA

The sense of the refractive effect must depend on the sign of the air-sea temperature difference. Both lapse and inversion conditions exist so why don't your results show this?

AUTHOR'S REPLY

I showed only results for surface refractivity gradients simply as a matter of convenience. In fact, the surface gradients are very strongly correlated with the values the air-sea temperature difference. In all the data bases that we examined the great majority of measurements showed a negative air-sea temperature difference.

K. ANDERSON (COMMENT)

We have a database of air-sea temperature difference covering most ocean areas - the preponderance is for air temperature less than sea temperature.

A TEMPERATURE-DEPENDENT REGULAR INFRARED BAND MODEL FOR ABSORPTION AND DISPERSION

P.L. Roney
Defence Research Establishment, Valcartier, 2459 Pie XI Blvd. North,
P.O. Box 8800, Courcellette, Québec, Canada, G0A 1R0

SUMMARY - A temperature-dependent infrared band model for the absorption and refraction of spectral lines, simultaneously broadened by Doppler and collisional effects, is developed. The model also takes into account the effects of line-coupling. The case of a simple diatomic molecule, in the rotating oscillator approximation is treated. The result is given in the form of an infinite series which converges rapidly and is appropriate for efficient computation.

LIST OF SYMBOLS -

$\chi = \chi' - i\chi''$ = complex susceptibility, $\eta = N - iK$ = complex refractive index, ϵ = dielectric constant, μ = permeability, J = rotational quantum number, S_J = line strength, ν = wavenumber, ν_J, ν_0 = line centre wavenumber, B', B'' = rotational spectroscopic constants, $d = B' + B''$, $I(J)$ = intensity, L_J, L = line-coupling coefficients, $S(T)$ = effective band strength, α_c = collision half-width, α_D = Doppler half-width, $b = \ln 2 / \alpha_D^2$, $x = (\nu - \nu_0) / d$, $y = \alpha_c / d$, $z = x + iy$, $a = b d^2$, $E(x, a) = G(x, y, a) - iF(x, y, a)$ = oscillatory line-shape function, $W(z, a)$ = complex error function.

1. INTRODUCTION

In an earlier paper, Ref. 1, henceforth referred to as I, a temperature dependent band model for the absorption or emission of spectral lines, simultaneously broadened by Doppler and collisional effects, was developed. The purpose of this model was to provide a rapid and efficient means of computation of the absorption of regular or symmetrical molecules (e.g. CO, CO₂, N₂O and CH₄), as opposed to the random line model which is strictly applicable only to asymmetric molecules such as H₂O. The purpose of the present paper is to extend the scope of the model to include refractive index variations within an absorption band, and also to include the effects of line-coupling.

2. COMPLEX SUSCEPTIBILITY AND REFRACTIVE INDEX FOR COMBINED DOPPLER AND COLLISIONAL LINE-BROADENING

In order to introduce the refractive index contribution and the effects of line coupling into the infrared band model developed in I, it is necessary to recall some of the relationships between the complex susceptibility $\chi = \chi' - i\chi''$, the refractive index $\eta = N - iK$ and the dielectric constant ϵ . From Maxwell's classical electromagnetic wave theory, for a medium with permeability μ equal to unity, we have the following relationships:

$$\epsilon = 1 + 4\pi\chi \quad (1)$$

$$\eta^2 = \mu\epsilon = \epsilon. \quad (2)$$

Equations 1 and 2 give an equation for the susceptibility χ in terms of the real and imaginary parts of the refractive index, $N - iK$. For a gas, where $N=1$ and $N^2-1 \gg K^2$, we obtain

$$2\pi\chi = N-1-iK, \quad (3)$$

In terms of the absorption coefficient per unit length κ

$$\kappa = 4\pi\nu K = 8\pi^2\chi''. \quad (4)$$

The theory of combined Doppler and collisional line broadening in the impact approximation^{2,3}, neglecting collisional shifts, line narrowing and line-coupling

effects, gives the following expression for the complex susceptibility χ

$$2\pi\chi = (N-1-iK) = \sum_J \frac{s_J b^{1/2}}{\pi^{3/2}} \int_{-\infty}^{\infty} \frac{dv e^{-bv^2} [(v-v_J-v)-i\alpha_J]}{(v-v_J-v)^2 + \alpha_J^2},$$

$$= \sum_J \frac{s_J b^{1/2}}{\pi^{3/2}} \int_{-\infty}^{\infty} \frac{dv e^{-bv^2}}{(v-v_J-v + i\alpha_J)}, \quad (5)$$

where s_J is the strength of the line located at wavenumber v_J , α_J is the collision half-width, α_D is the Doppler half-width and $b = \ln 2/\alpha_D^2$. In the present case J is the lower state rotational quantum number.

The theory of Rosenkrantz ⁴ can be used to account for line-coupling effects. This is a first-order theory which is valid at low pressures. The theory was originally given only in terms of the absorption coefficient K for collisional broadening. Gentry and Strow ⁵ have shown that for the case of combined Doppler and collisional broadening Rosenkrantz's approximation can be expressed as

$$K = \sum_J \frac{s_J b^{1/2}}{\pi^{3/2}} \int_{-\infty}^{\infty} \frac{dv e^{-bv^2} [\alpha_J + L_J (v-v_J-v)]}{(v-v_J-v)^2 + \alpha_J^2}, \quad (6)$$

where L is the first-order line coupling coefficient. More details on the line-coupling theory can be obtained from Ref. 4. In order to extend the regular infrared band model of I to include the refractive index and line-coupling it is necessary to derive the expression for the quantity $(N-1-iK)$ corresponding to eq. 6. This is accomplished through the application of the Kramers-Kronig dispersion relation ⁶ which relates the real and imaginary parts of the susceptibility via a Hilbert transform. This is straightforward since the Hilbert transform is relative to the wavenumber v and therefore it is only necessary to perform the transform over the frequency dependent part of the integrand of eq. 6. The result for the complex refractive index is

$$(N-1-iK) = \sum_J \frac{s_J b^{1/2}}{\pi^{3/2}} \int_{-\infty}^{\infty} \frac{dv e^{-bv^2} \{[(v-v_J-v)-L_J\alpha_J]-i[\alpha_J+L_J(v-v_J-v)]\}}{(v-v_J-v)^2 + \alpha_J^2},$$

$$= \sum_J \frac{s_J b^{1/2}}{\pi^{3/2}} \int_{-\infty}^{\infty} \frac{dv e^{-bv^2} (1-iL_J)}{(v-v_J-v + i\alpha_J)}, \quad (7)$$

3. DERIVATION OF THE TEMPERATURE-DEPENDENT BAND MODEL

We now apply the methods of I to derive the regular band model for a infrared vibration-rotation band. For simplicity we treat the case of the P and R branches of a diatomic molecule in the rotating harmonic oscillator approximation. The expression for $(N-1-iK)$ of eq. 7 for this case can be written

$$(N-1-iK) = S(T) \sum_J \left\{ \frac{I_R(J)}{I_P(J)} \right\} \frac{b^{1/2}}{\pi^{3/2}} \int_{-\infty}^{\infty} \frac{dv e^{-bv^2} (1-iL_J)}{(v-v_C-v + i\alpha_J)}, \quad (8)$$

where S_J has been split up into a band-strength factor $S(T)$ and intensity $I(J)$ which is different for each branch. The effective band strength $S(T)$ is treated as a constant which does not play a role in the following discussion. The intensity factors $I(J)$ and the line-centre wavenumbers v_C , which are also different for each branch, are given below in terms of J (and a related number m) and vibration constants B'' (lower), B' (upper state).

$$I_R(J) = (J+1) \exp[-J(J+1)hcB''/kT]$$

$$= m \exp[-m(m-1)hcB''/kT], \quad m = J+1 \quad (9a)$$

$$\begin{aligned}
 v_C &= v_0 + (B' + B'')(J+1) + \dots \\
 &= v_0 + (B' + B'')m + \dots, \quad m = J+1,
 \end{aligned} \tag{10a}$$

$$\begin{aligned}
 I_P(J) &= J \exp[-J(J+1)hcB''/kT] \\
 &= -m \exp[-m(m-1)hcB''/kT], \quad m = -J,
 \end{aligned} \tag{9b}$$

$$\begin{aligned}
 v_C &= v_0 - (B' + B'')J + \dots \\
 &= v_0 + (B' + B'')m + \dots, \quad m = -J,
 \end{aligned} \tag{10b}$$

Defining the following variables x , y and z in terms of the line spacing parameter d , we put

$$x = (v - v_0)/d, \quad y = \alpha_C/d, \quad z = x + iy, \quad a = bd^2, \quad d = (B' + B''),$$

where it is assumed that all $\alpha_J = \alpha_C$ and all $L_J = L$. (Note that the variable y differs from that in I by a factor of 2π). Equation 8 now takes the form

$$(N-1-iK) = S(T) \sum_m \left\{ \frac{I_R(m)}{I_P(m)} \right\} \frac{a^{1/2}}{d\pi^{3/2}} \int_{-\infty}^{\infty} \frac{du e^{-au^2} (1-iL)}{(z - m - u)}, \tag{11}$$

The retention of only terms linear in m , in the denominators of the Voigt integrals in eq. 11, is the first approximation of the model i.e. neglect of interaction between rotation and vibration. This approximation is essential for a simplification of the mathematical expressions. The next approximation is the replacement of the discrete numbers m by the continuous variable x in the intensity factors $I(m)$ of eq. 11. As discussed in I, the justification for this approach is that these line intensity factors $I(m)$ are slowly varying compared to the rapid fluctuations due to the alternating peaks and troughs of the individual spectral lines (represented by the Voigt integral terms). The intensity terms $I(x)$ can then be removed from under the summations over m .

The last approximation is to extend the summations over m to run from $-\infty$ to $+\infty$. There are two consequences to this extension of the summations. On the one hand, it allows a considerable simplification of the mathematical form of the equations, which in turn greatly reduces the computational time and complexity. On the other hand, the contributions of the R and P branches must be carried out separately and independently. Nevertheless, a good approximation is obtained for the overlap contribution from one branch to the other, as demonstrated in I. The extended summation also introduces a spurious nonphysical spectral line. This is due to a mathematical artifact which arises through the introduction of the value $m = 0$ which is not allowed by the physics of the situation. Applying these approximations to eq. 11 we obtain

$$(N-1-iK) = S(T) \left\{ \begin{array}{l} I_R(x), \quad x > 0 \\ I_P(x), \quad x < 0 \end{array} \right\} [E(z, a) + iW(z, a)](1-iL)/d, \tag{12}$$

$$I_R(x) = -I_P(x) = x \exp[-x(x-1)hcB''/kT], \tag{13}$$

where

$$E(z, a) = \frac{a^{1/2}}{\pi^{3/2}} \sum_{-\infty}^{\infty} \int_{-\infty}^{\infty} \frac{du e^{-au^2}}{(z - m - u)}, \tag{14}$$

$$W(z, a) = i \frac{a^{1/2}}{\pi^{3/2}} \int_{-\infty}^{\infty} \frac{du e^{-au^2}}{(z - u)}, \tag{15}$$

In the R-branch calculations x is always positive and in the P-branch calculations x is always negative. The function $W(z,a)$ of eq. 14 is the complex error function and is introduced to remove the spurious central line produced by the term at $m = 0$ mentioned above.

The complex function $E(z,a)$ is a monophasic function of x , whose imaginary part produces a repeated pattern of Voigt line-profiles and whose real part gives a corresponding pattern of refractive index profiles. The line spacing is 1 in the x domain, for both the P and the R branches. $E(z,a)$ is a generalized extension into the complex plane of the oscillatory line-profile function $Fv(x,\beta,a)$ of eqs. 25 and 33 of I. The function $E(z,a)$ can be expressed in the form of a rapidly convergent infinite series, which is more convenient for computation than eq. 14, by a method analogous to that employed in I. The details of this derivation are treated in Appendix A. The result is

$$E(z,a) = G(x,y,a) - iF(x,y,a), \quad (16a)$$

$$G(x,y,a) = 2 \sum_{k=1}^{\infty} e^{-\pi k(2y+\pi k/a)} \sin(2\pi kx), \quad (16b)$$

$$F(x,y,a) = [1 + 2 \sum_{k=1}^{\infty} e^{-\pi k(2y+\pi k/a)} \cos(2\pi kx)]. \quad (16c)$$

The limit of $E(x,y,a)$ for pure Doppler broadening follows directly from eq. 16 by putting $y = 0$, since the function is well-behaved in this limit. The limit for pure collisional broadening is derived in Appendix A and gives simple analytical functions. The real and imaginary parts of eq. 12 have been separated and the resulting equations for the refractive index and the absorption coefficient are summarized in Table I.

4. CALCULATIONS

In order to illustrate the model some sample calculations have been made. Figure 1 shows the oscillatory line profile function, $(F-f)$, for absorption in the case of pure collisional broadening, with a half-width of $.1 \text{ cm}^{-1}$, and a line spacing of 1 cm^{-1} . Figure 2 shows the corresponding oscillatory refraction profile function $(G-g)$. In the latter case it is apparent that the removal of the spurious line, by the subtraction of g , is not perfect. The reason for this is that the subtraction of the spurious single line at the centre does not exactly compensate entirely for line wing overlap contributions. Figures 2 and 3 illustrate the P and R branch absorption and refraction respectively, both without line-coupling. The conditions are the same as for Figs. 1 and 2 and a temperature of 100K. This low temperature has been chosen in order to show a large part of the band using relatively few lines. Figures 5 and 6 show some of the effects of line coupling. For these figures a relatively large value of $L = .5$ has been chosen in order to exaggerate the effects. For the case of absorption, Fig. 4, the effect is fairly small. The line peaks are not affected which is to be expected since $(N-1)$ is zero at the line centres. The main effect is a reduction of the underlying continuum absorption in the line troughs. The effect of line coupling is more dramatic for the refraction spectrum of Fig. 6. The refraction line "peaks" are all depressed to lower values and the whole shape of the band in refraction is changed. Again this is to be expected since, for positive L , the effect of coupling is negative and is a maximum at the absorption line centres where the refraction $(N-1)$ is normally zero without line-coupling.

5. CONCLUSIONS

The model gives a reasonable representation of absorption and refraction in a simple diatomic molecule. The calculation is very rapid and efficient and should provide a useful tool for examining specific problems as well as considerably simplifying calculations in atmospheric transmission models involving the Voigt profile. Limitations of the model are the fixed spacing between lines and the use of an average value for the line-coupling coefficient. The latter limitation can be overcome if the variation of L with J is uniform and can be functionalized simply.

A more important problem is the representation of Q branches. Here the model must be improved to take into account the very rapid variation of line spacing within a Q branch. This will be the subject of future investigations.

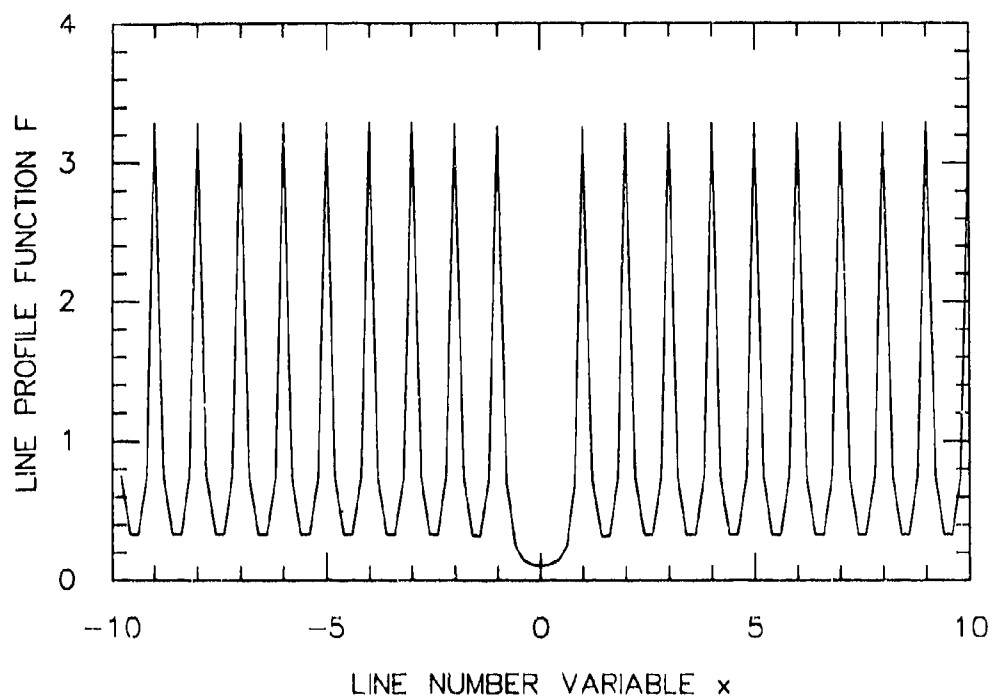


Fig.1 The oscillatory function F: Lorentz profile with $d = 1 \text{ cm}^{-1}$, $\alpha_e = 0.1 \text{ cm}^{-1}$

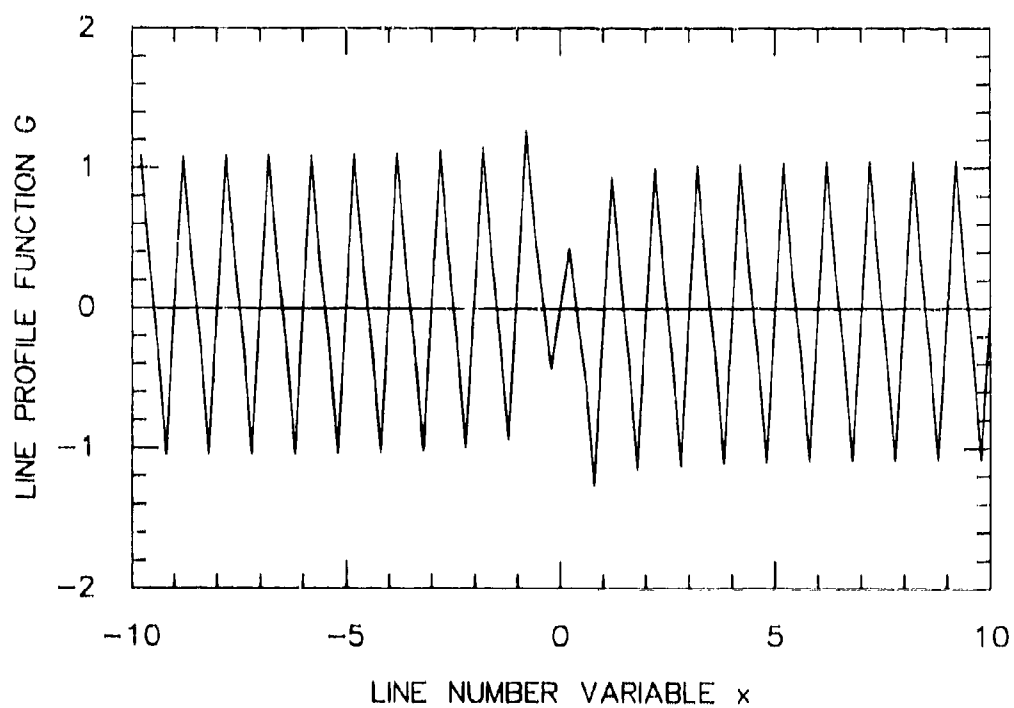


Fig.2 The oscillatory function G: Lorentz profile with $d = 1 \text{ cm}^{-1}$, $\alpha_e = 0.1 \text{ cm}^{-1}$

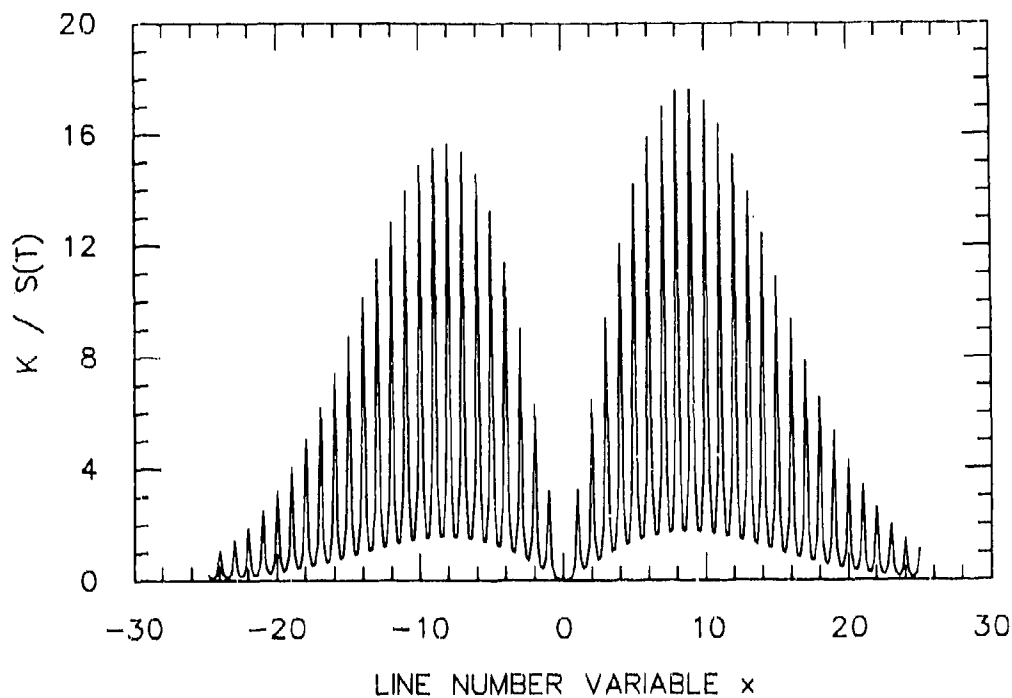


Fig.3 The normalized absorption coefficient for a diatomic molecule:
Lorentz profile with $\alpha_c = 0.1 \text{ cm}^{-1}$, $d = 1 \text{ cm}^{-1}$, $T = 100\text{K}$, $L = 0$

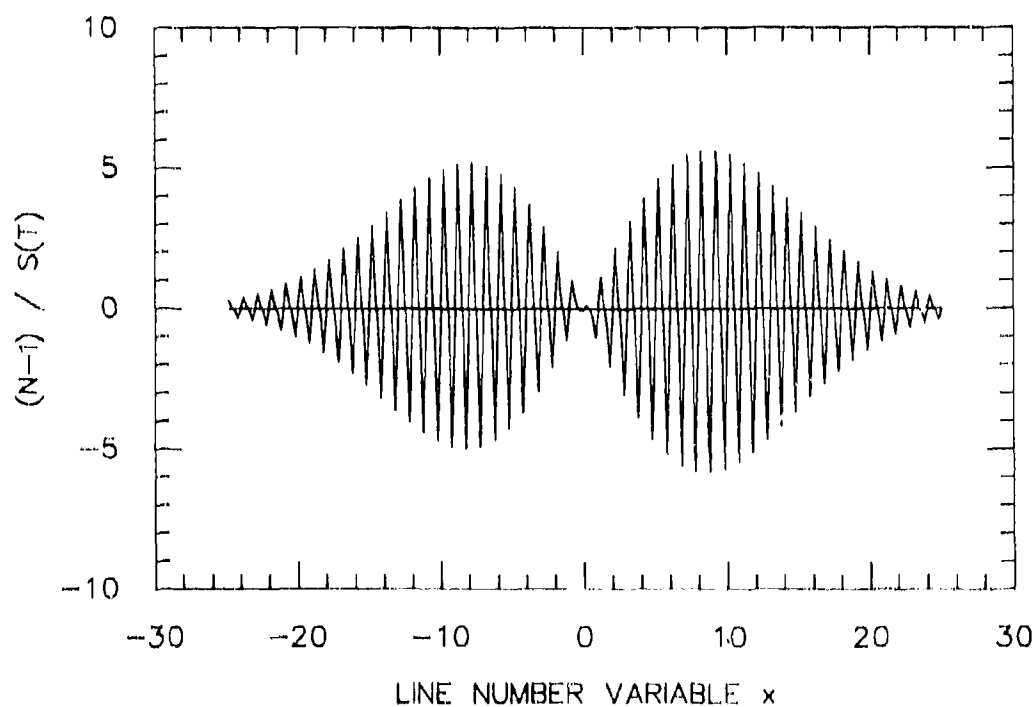


Fig.4 The normalized refractive index for a diatomic molecule:
Lorentz profile with $\alpha_c = 0.1 \text{ cm}^{-1}$, $d = 1 \text{ cm}^{-1}$, $T = 100\text{K}$, $L = 0$

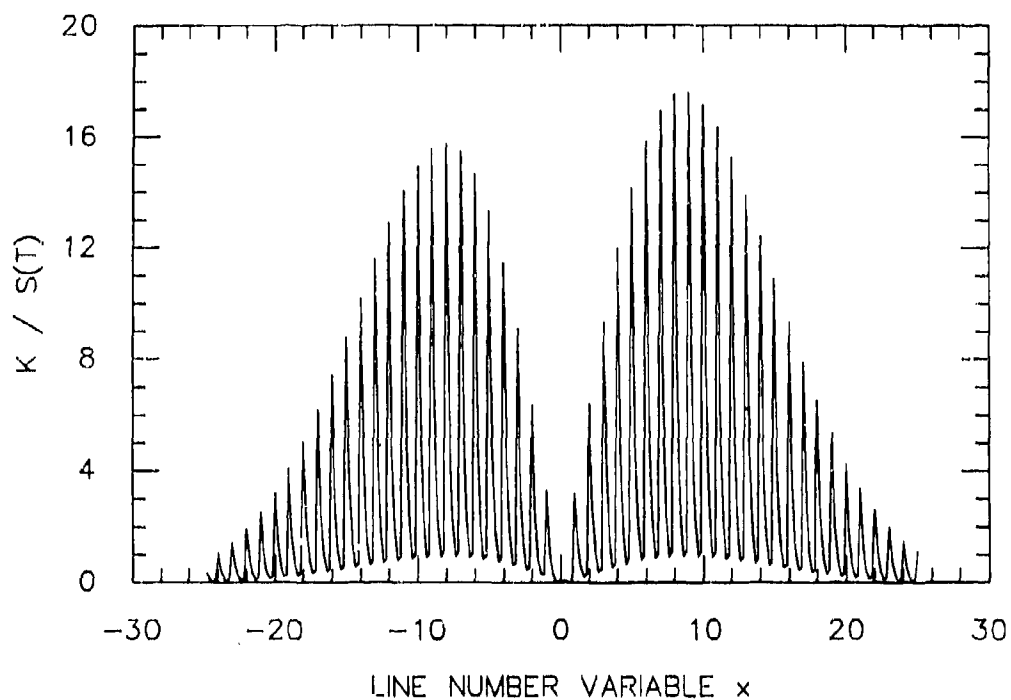


Fig.5 The normalized absorption coefficient for a diatomic molecule:
Lorentz profile with $\alpha_c = 0.1 \text{ cm}^{-1}$, $d = 1 \text{ cm}^{-1}$, $T = 100\text{K}$, $L = 0.5$

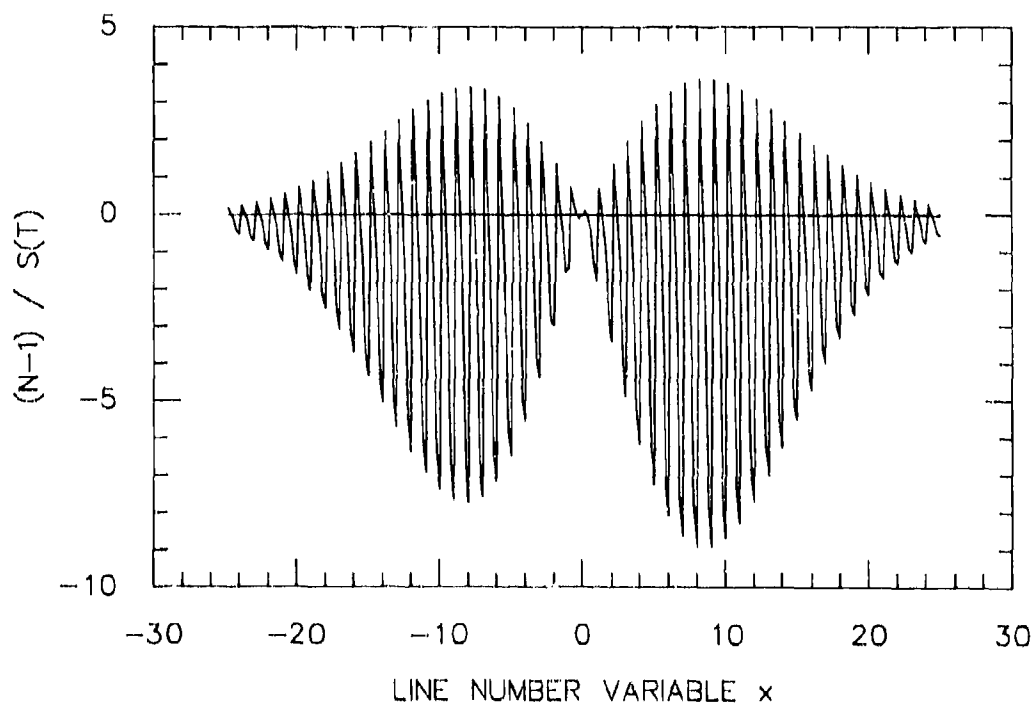


Fig.6 The normalized refractive index for a diatomic molecule:
Lorentz profile with $\alpha_c = 0.1 \text{ cm}^{-1}$, $d = 1 \text{ cm}^{-1}$, $T = 100\text{K}$, $L = 0.5$

TABLE I

Equations for the refractive index and the absorption coefficient for a diatomic molecule

$$(N-1) = S(T) \begin{cases} I_R(x), & x > 1 \\ I_P(x), & x < 1 \end{cases} [(G - g) - L (F - f)] / d$$

$$K = S(T) \begin{cases} I_R(x), & x > 1 \\ I_P(x), & x < 1 \end{cases} [(F - f) + L (G - g)] / d$$

$$I_R(x) = -I_P(x) = x \exp[-x(x-1)hcB''/kT],$$

$$G = 2 \sum_{l=1}^{\infty} e^{-\pi k(2y+\pi k/a)} \sin(2\pi kx),$$

$$+ \frac{\sin(2\pi x)}{[\cosh(2\pi y) - \cos(2\pi x)]}, \quad (\text{collision broadening})$$

$$F = [1 + 2 \sum_{l=1}^{\infty} e^{-\pi k(2y+\pi k/a)} \cos(2\pi kx)],$$

$$+ \frac{\sinh(2\pi y)}{[\cosh(2\pi y) - \cos(2\pi x)]}, \quad (\text{collision broadening})$$

$$g = \frac{a^{1/2}}{\pi^{3/2}} \int_{-\infty}^{\infty} \frac{du e^{-au^2} y}{(x-u)^2 + y^2} + \frac{y}{\pi(x^2 + y^2)}, \quad (\text{collision broadening})$$

$$f = \frac{a^{1/2}}{\pi^{3/2}} \int_{-\infty}^{\infty} \frac{du e^{-au^2} (x-u)}{(x-u)^2 + y^2} + \frac{x}{\pi(x^2 + y^2)}, \quad (\text{collision broadening})$$

$$x = (v - v_0)/d, \quad y = a_G/d, \quad z = x + iy,$$

$$a = \ln 2 (d/a_D)^2, \quad d = (B' + B'').$$

REFERENCES

1. P.L. Roney, "A Temperature-Dependent Regular Infrared Band Model", JQSRT 42, No. 3, 169 (1989).
2. P.L. Roney, "A Theory of Doppler and Binary Collision Broadening by Foreign Gases - I", JQSRT 15, 361 (1975).
3. P.L. Roney, "A Theory of Doppler and Binary Collision Broadening by Foreign Gases - II", JQSRT 15, 181 (1975).
4. P.W. Rosenkrantz, "Shape of the 5 mm Oxygen Band in the Atmosphere", IEEE Trans. Antennas Propag. AP-23, 498 (1975).
5. B. Gentry and L.L. Strow, "Line Mixing in a N₂-Broadened CO₂ Q Branch Observed with a Tunable Diode Laser", J. Chem. Phys. 86, 5722 (1987).
6. P. Roman, "Advanced Quantum Theory", 1st Ed., Reading, Massachusetts, Addison-Wesley Pub. Co., 1965, pp 200-209.
7. I.S. Gradshteyn and I.M. Ryzhik, "Tables of Integrals, Series and Products", 4th Ed., New York, Academic Press, 1965, p 42.

EVALUATION OF THE FUNCTION $E(z, a; q)$

From eq. 14 we have $E(z, a; q)$ in the form

$$E(z, a) = \frac{a^{1/2}}{\pi^{3/2}} \sum_{-\infty}^{\infty} \int_{-\infty}^{\infty} \frac{du e^{-au^2}}{(z - m - u)}. \quad (A1)$$

The summation over the denominator of the integrand of eq. A1 can be expressed in the form of a cotangent as follows.

$$\begin{aligned} \sum_{-\infty}^{\infty} \frac{1}{(z-m-u)} &= \frac{1}{2} \sum_{-\infty}^{\infty} \left[\frac{1}{(z-u-m)} + \frac{1}{(z-u+m)} \right], \text{ on changing the sign of } m, \\ &= (z-u) \sum_{-\infty}^{\infty} \frac{1}{(z-u)^2 - m^2}, \text{ on recombining terms,} \\ &= \frac{1}{(z-u)} + 2(z-u) \sum_{1}^{\infty} \frac{1}{(z-u)^2 - m^2} = \pi \cot [\pi(z-u)] \end{aligned} \quad (A2)$$

where the last form follows from the expansion of cotangent as a partial fraction. Writing the complex variable $z = x + iy$, and expanding the cotangent in terms of sines and cosines we obtain from eq. A2

$$\begin{aligned} \frac{1}{\pi} \sum_{-\infty}^{\infty} \frac{1}{(z-m-u)} &= \cot [\pi(z-u)] = \cot [\pi(x+iy-u)], \\ &= \frac{[\sin 2\pi(x-u) - i \sinh 2\pi y]}{[\cosh 2\pi y - \cos 2\pi(x-u)]}, \end{aligned} \quad (A3)$$

$$= \left\{ 2 \sum_{1}^{\infty} e^{-2\pi k y} \sin 2\pi k(x-u) - i \left[1 + 2 \sum_{1}^{\infty} e^{-2\pi k y} \cos 2\pi k(x-u) \right] \right\}. \quad (A4)$$

This last expression follows from the following two formulae to be found in Ref. 7

$$\frac{\sin x}{\cosh t - \cos x} = 2 \sum_{1}^{\infty} e^{-kt} \sin kx, \quad \frac{\sinh t}{\cosh t - \cos x} = 1 + 2 \sum_{1}^{\infty} e^{-kt} \cos kx.$$

Recombining the real and imaginary parts of eq. A4 we obtain

$$\frac{1}{\pi} \sum_{-\infty}^{\infty} \frac{1}{(z-m-u)} = -i \left[1 + 2 \sum_{1}^{\infty} e^{i2\pi k(z-u)} \right]. \quad (A5)$$

Substituting for eq. A5 in eq. A1 for $E(z, a)$ the integration is now straightforward. We obtain

$$\begin{aligned} E(z, a) &= i(a/\pi)^{1/2} \left[\int_{-\infty}^{\infty} du \exp(-au^2) + 2 \sum_{1}^{\infty} \exp(i2\pi kz) \int_{-\infty}^{\infty} du \exp(-au^2 - i2\pi ku) \right], \\ &= -i \left[1 + 2 \sum_{1}^{\infty} \exp(i2\pi kz - \pi^2 k^2/a) \right]. \end{aligned} \quad (A6)$$

Separating the real and imaginary parts of eq. A6 we obtain

$$E(z, a) = G(x, y, a) - iF(x, y, a), \quad (A7)$$

$$G(x, y, a) = 2 \sum_{1}^{\infty} e^{-\pi k(2y + \pi k/a)} \sin(2\pi kx), \quad (A8)$$

$$F(x, y, a) = \left[1 + 2 \sum_{k=1}^{\infty} e^{-\pi k(2y + \pi k/a)} \cos(2\pi kx) \right]. \quad (A9)$$

The limits of $G(x, y, a)$ and $F(x, y, a)$ for pure Doppler broadening follow directly from eqs. A10 and A11 by putting $y = 0$. The limits for pure collisional broadening can be most conveniently obtained by substituting for eq. A3 in eq. A1 and carrying out the integration in the limit $a \rightarrow \infty$, (i.e. $a_D \rightarrow 0$). The result is

$$G(x, y) \rightarrow \frac{\sin(2\pi x)}{[\cosh(2\pi y) - \cos(2\pi x)]}, \quad (A10)$$

$$F(x, y) \rightarrow \frac{\sinh(2\pi y)}{[\cosh(2\pi y) - \cos(2\pi x)]}. \quad (A11)$$

DISCUSSION

A. KOHNLE

The absorption coefficients are normalized with respect to the effective band strength $S(T)$. How do you calculate $S(T)$?

AUTHOR'S REPLY

The effective band strength $S(T)$ is composed basically of the dipole strength factor, and the vibrations and rotational position sums. The latter is temperature dependent. Also $S(T)$ does have a weak wavenumber dependence which has been neglected in the formulation of the model.

UV SPECTRAL SIMULATIONS USING LOWTRAN 7

G.P. Anderson, F.X. Kneizys, E.P. Shettle, L.W. Abreu,
J.H. Chetwynd, R.E. Huffman, and L.A. Hall

Air Force Geophysics Laboratory, Hanscom AFB, MA 01731, USA

SUMMARY

LOWTRAN 7¹ is a low-resolution propagation model and computer code for predicting atmospheric transmittance and background radiance from 0 to 50,000 cm⁻¹ (wavelengths greater than 0.2μm). The current model, released in February 1989, is a major extension of the LOWTRAN 6² model. In addition to incorporating new and improved molecular band models (primarily influencing IR calculations), LOWTRAN 7 has been particularly adapted for basic ultraviolet transmittance and radiance calculations. It now contains a 0.2nm resolution extra-terrestrial solar source function along with temperature-dependent O₃ (Hartley-Huggins) and pressure-dependent O₂ (Herzberg continuum) absorption cross sections. The O₂ Schumann-Runge band absorption has been patterned after the IR band model. As with past versions of LOWTRAN, the line-of-sight viewing and solar incidence geometry can be arbitrarily configured for either direct or backscattered calculations. Both solar and thermal multiple scattering are accommodated.

Initial validations of the UV portions of LOWTRAN 7 have been made against two separate AFGL spectrometers. Excellent agreement has been found with UV data from a balloon-borne spectrometer designed to measure in situ solar irradiance within the stratosphere. These direct solar observations, all at high sun angles, were made at stratospheric altitudes. Ultraviolet background measurements in the 0.2-0.29μm wavelength region were made from the S3-4 satellite in a polar, sun-synchronous, nadir-viewing orbit. For moderate to high solar incidence angles, the backscatter comparisons with LOWTRAN 7 are again reasonable (generally within 10%). With the sun on the horizon, however, the twilight airglow becomes a dominant feature; such emission sources are not incorporated into LOWTRAN.

1. INTRODUCTION:

Spectroscopic data describing the ultraviolet absorption properties of molecular oxygen and ozone have been collected for incorporation into both FASCOD³ and LOWTRAN. The data include the O₂ Herzberg continuum and Schumann-Runge bands and the O₃ Hartley and Huggins bands. All of these systems result in the dissociation of the parent molecule and the creation of atomic oxygen. The non-dissociative Herzberg bands are not currently part of the data set although they may be important for accurate transmittance calculations near the surface. In addition, LOWTRAN 7 provides a new solar irradiance and the ability to calculate its direct and scattered components. [NOTE: The scattering algorithms (single and multiple) are also designed for thermal radiation.]

2. MOLECULAR PROPERTIES:

The dissociation of oxygen allotropes is of paramount importance to the chemical makeup of the earth's atmosphere. The strongly absorbing O₂ Schumann-Runge and weaker Herzberg systems influence different altitude regimes in the atmosphere because of the relative strengths of their respective transition probabilities. Figure 1 (after Watanabe⁴) shows the approximate depth of penetration of solar irradiance throughout the UV spectral range. In general, solar radiation in the 0.175 to 0.2μm spectral region is completely absorbed by the Schumann-Runge system at altitudes above 40 Km. Towards longer wavelengths (greater than 0.2μm) absorption by ozone begins to compete with the residual Schumann-Runge and Herzberg absorption; the combination does not allow solar energy at wavelengths less than 0.3μm to penetrate to the surface. In addition to this shielding of high energy solar radiation, the UV absorption properties of ozone provide the dominant source of stratospheric heating.

2.1. HERZBERG CONTINUUM:

While the Herzberg continuum absorption is small relative to both the Schumann-Runge and ozone contributions, it is very important to the maintenance of stratospheric photochemical balance. Until recently the Herzberg continuum was thought to be almost 40% stronger than the current estimate. Because it lacks any detailed spectral structure, the absorption properties are readily described by an analytic function proposed by Johnston et.al.⁵. After fitting the combined measurements of U.S. and French laboratories⁶ to a function of this form, the cross section can be expressed as:

$$\sigma(\text{cm}^2) = 6.88 \times 10^{-24} R \exp[-69.7374 \{ \ln(R) \}^2]$$

where: $R = 0.20487/(\mu)$

and: μ = wavelength in μm

This equation generally reproduces both data sets to within 5%.

The longevity of the erroneously large Herzberg values can be traced to their pressure dependence, related to dimer formation. The cross sections are so small that laboratory determinations must rely on high pressure techniques to create the necessary opacities. Historically, extrapolation to zero pressure was attempted, but with poor success. In fact, long-path, low pressure stratospheric measurements of attenuation of solar irradiance provided the first verification that the laboratory estimates were seriously wrong^{7a}.

Accurate determination of the pressure dependence of O_2 within an O_2 environment is still a necessary part of the laboratory procedure when measuring the cross section. Yoshino et.al.⁶ provide an equation of the form:

$$\sigma(p, \mu m) = \sigma(0, \mu m) (1 + (\Gamma(\mu m) / \sigma(0, \mu m)) \times P_{O_2}(\text{Torr}))$$

where $\Gamma(\mu m)$ represents the pressure dependent term. However, because of coding considerations, the FASCODE/LOWTRAN formulations replace the spectrally dependent Γ with a proportionality constant,

$$\Gamma(\mu m) / \sigma(0, \mu m) = 1.81e-3$$

that is good to within 10% for most of the Herzberg spectral range (between 0.20 and 0.23 μm); see Fig. 2. The errors gradually increase to 30% at 0.24 μm . The magnitude of this wavelength-dependent error is generally tolerable because the pressure contribution is often a fractionally small portion of the diminishing O_2 cross section which is, in turn, overwhelmed by the ozone cross section. However, near the surface (high pressures and low ozone mixing ratios) the errors can become significant.

Atmospheric pressure dependence is also governed by interaction with N_2 (O_2 - N_2 dimer formation). Shardanand⁹ has provided an estimate of this effect, N_2 being approximately 45% as efficient as pure O_2 . Fig. 2 shows the degree of spectral similarity between the N_2 dimer effect and the pure Herzberg absorption, $\sigma(0, \mu m)$, so it has similarly been scaled to $\sigma(0, \mu m)$. The pressure dependence of the Herzberg continuum for a combination of 21% O_2 and 78% N_2 , including the 45% efficiency factor is then:

$$\sigma(p, \mu m) = \sigma(0, \mu m) (1 + .83 (P/P_0)(T_0/T))$$

The total pressure has been replaced by a normalized density function with P_0 and T_0 at STP.

As mentioned above, the Herzberg bands are not included explicitly in FASCODE and LOWTRAN. While they would not contribute to the photochemical production of odd oxygen, some contribution is expected in the total transmittance calculations¹⁰. This has been approximated in LOWTRAN 7 and FASCOD3 by extending the Herzberg analytic equation to longer wavelengths (0.277 μm or 36000 cm^{-1}) with a linearly smooth damping to zero absorption at that arbitrary cutoff. The errors introduced by this approximation are potentially serious for transmittance calculations for ozone-poor lines of sight (such as solar-blind calculations at the surface¹¹). However, for most general cases the effect of the omission is not discernible. Eventually a more correct band model approximation will be developed within the context of LOWTRAN.

2.2. SCHUMANN-RUNGE BANDS:

The O_2 Schumann-Runge band analysis has been addressed in two ways: (1) a line-by-line spectroscopic atlas, similar in format to the HITRAN database¹², has been calculated from published energy levels; and (2) a one parameter 20 cm^{-1} resolution band model has been generated for incorporation into LOWTRAN. Using the new atlas, line-by-line syntheses of the Schumann-Runge cross sections, including temperature dependence of the vibronic population levels, have been created using FASCOD3; this effort will be described elsewhere. It is important to note, however, that while the Schumann-Runge system exhibits very rich spectral structure, including rotational splitting at fractions of a wavenumber separation, the half widths of the lines are sufficiently broadened by predissociation to be independent of pressure and temperature. Figure 3 shows a portion of the new database, giving line positions and relative strengths at line center; the triplet structure is not depicted. Individual band groupings are easily identified.

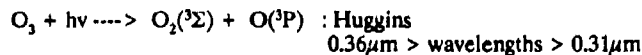
The 20 cm^{-1} band model for the Schumann-Runge system (as currently available in LOWTRAN 7) was developed from a similar line-by-line formulation¹³ with additional laboratory input¹⁴. The band model is both preliminary and inadequate for detailed spectroscopic calculations because it does not properly simulate the strong temperature dependence of the O_2 cross sections brought about by the change in population of the first excited state ($v''=1$). This effect is strongest in the spectral regions away from the $v''=0$ band heads (i.e. in the window regions). Solar energy penetrates deepest into the atmosphere in just these window regions so improvement in the formulation is mandatory if it is to be used for photochemical calculations.

Given these stated inaccuracies, the band model does show reasonable agreement with in situ measurements of the depleted solar irradiance. In Figure 4 data from the 1983 balloon flight of a single dispersion half-meter Fbert-Fastie spectrometer¹⁵ is compared to simulated data using the new Schumann-Runge band model. These calculations also include other major portions of the LOWTRAN 7 algorithm, particularly the Herzberg continuum and ozone cross sections. The only exception to LOWTRAN 7 compatibility is the solar irradiance; the lack of solar spectral signature can be seen near 0.199 μm (199 nm) in the simulated data. The band model algorithm is patterned on that developed for the IR¹⁶, including the use of their fitting parameters for O_2 . A single spectral function $C(\mu m)$ has been calculated for the wavelength range from 0.1875 to 0.203 μm . When a more sensitive band model is developed, the wavelength range for LOWTRAN will be

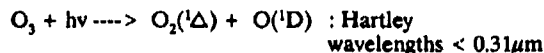
extended to include the entire Schumann-Runge system. It is expected that this new band model will separate the $v''=0$ from the $v''=1$ bands, with the treatment of the ground state transitions remaining as described here. [NOTE: while the preliminary band model parameters are available within the LOWTRAN 7 coding, they are not directly accessible for wavelengths smaller than $0.2\mu\text{m}$. This limitation is imposed by an "if-test" related only to the nonavailability of the aerosol functions for these wavelengths; the solar irradiance, Rayleigh scattering coefficients and an estimated Herzberg continuum are all provided.]

2.3. OZONE:

Absorption by ozone, the remaining UV-active oxygen allotrope, is described in both FASCODE and LOWTRAN by a temperature-dependent (quadratic) continuum. This continuum includes two major bands, the spectrally-overlapping Huggins and Hartley systems. [NOTE: Steinfeld, et.al.¹⁷ present an excellent review.] The Hartley band is by far the more efficient at production of the first excited state of atomic oxygen, $\text{O}({}^1\text{D})$, with approximately 88% efficiency, while the Huggins band fragmentation generally leads to the ground state product for atomic oxygen, $\text{O}({}^3\text{P})$:



and:



The atomic oxygen excitation state is critical to subsequent photochemical reactions because $\text{O}({}^1\text{D})$ is the energetically preferred partner. The Hartley band absorption is very strong, exhibiting only marginal structure and generally no temperature dependence. The Huggins system has a much more pronounced band structure and moderate to strong temperature dependence, although the features are still broad enough not to be amenable to detailed line-by-line representation (Figure 5). [Note: Katayama¹⁸ has established definitive vibrational assignments and inferred a band origin.]

Studies of the ozone absorption cross section have been available since the early 1900's. The relatively recent measurements of Bass and Paur¹⁹ form the basis of LOWTRAN 7-FASCOD3 formulation. Their values, including quadratic temperature dependence, are provided at 5cm^{-1} intervals from 41000 to 30000cm^{-1} (0.24 to $0.33\mu\text{m}$). Subsequent measurements of Molina and Molina²⁰ have been used in combination with those of Yoshino, et.al.²¹ to expand the temperature dependent range to $0.34\mu\text{m}$, with a final extension to $0.36\mu\text{m}$ using the values of Cacciani, et.al.^{22,23}. At wavelengths less than $0.24\mu\text{m}$, the temperature-independent values of Molina and Molina were again adopted (between 0.18 and $0.24\mu\text{m}$). The various data sources agree very well (usually better than 3%) in the regions of overlap. All feature replication is real and suitable; that is, the small spectral features are represented at their natural resolution such that a line-by-line calculation would not provide significantly greater detail.

3. SOLAR IRRADIANCE:

The LOWTRAN 7 Transmittance/Radiance program now includes a new solar spectrum for calculating scattered (single or multiple) and directly transmitted solar irradiances. The recent values of VanHoosier et.al.²⁴ have been adopted in the UV (0.2 to $0.35\mu\text{m}$) with a resolution compatible with LOWTRAN (20cm^{-1}). These data were obtained from the Shuttle platform (the Solar Ultraviolet Spectral Irradiance Monitor (SUSIM) on Spacelab 2) at 0.15nm resolution and subsequently converted to frequency for smoothing. The data, as stored in LOWTRAN 7, actually start at $0.174\mu\text{m}$, recognizing that the code may well be extended further into the UV at some future time. In the near UV to visible range (0.35 to $0.86\mu\text{m}$), the data of Neckel & Labs²⁵ have been adopted. Because these data have a resolution of $1\text{-}2\text{nm}$, they underrepresent the actual variability in the solar Fraunhofer structure at the stated 20cm^{-1} resolution. Estimated accuracy of the composite LOWTRAN compilation is $5\text{-}10\%$ for the SUSIM spectral range (including feature replication at 20cm^{-1} resolution) and 5% for the near UV and visible range when degraded to 100cm^{-1} resolution. [NOTE: Because of general calibration difficulties in the UV, measured solar irradiances differ by as much as 10% in absolute magnitude²⁶, while relative spectral detail is reproducible to much higher accuracy.]

4. MULTIPLE SCATTERING:

An efficient and reasonably accurate multiple scattering parametrization^{27,28} has been implemented in the LOWTRAN 7 model based on the two stream approximation and an adding method for combining atmospheric layers. LOWTRAN includes both solar and thermal sources for its general scattering algorithm; only the solar portion will be discussed here. In general, the multiple scattering algorithm uses the single scattered solar solution as the primary stream. However, because it scales the vertical path opacity using the secant approximation for a plane parallel atmosphere, the algorithm loses accuracy for sun angles much larger than 80° . While this scaling is efficient, it should ultimately prove unnecessary because the "true" line-of-sight geometry calculations for a spherically refractive atmosphere are available in LOWTRAN 7 and are used correctly for the single-scattered solution. A more accurate, multi-stream solar scattering approximation is now being developed.

Briefly, (after Kneizys, et.al.²) the single scattering algorithm requires the scattering angle and the equivalent absorber amounts for the primary solar paths from each scattering point along the line-of-sight. This calculation involves tracking two optical paths for each scattering point. One path leg extends from the observer to the scattering point, and the other from the scattering point toward the sun (or moon), ending at the top of the atmosphere. Each path is, in general,

bent by refraction but each remains in a fixed vertical plane containing the path endpoints and the center of the earth. The intersection of the two planes at each scattering point defines the scattering angle. There are, of course, an infinite number of scattering points along the path; LOWTRAN specifically uses only the intersections of the line-of-sight with the model atmospheric layer boundaries. Therefore, care must be taken in selection of atmospheric layering, particularly for limb-viewing configurations. If the individual layers are too optically thick, the algorithm cannot properly calculate the scattered contribution. [NOTE: a layer thickness of no more than 1/2 the atmospheric or ozone scale height (2-3km) at the tangent height is recommended.]

The multiple scattering algorithm must determine the layer fluxes across each boundary, along with the composite transmissivity and reflectivity. The multiply scattered flux at a given layer will, in part, be determined by radiation from all atmospheric layers, even those above or below the stated line-of-sight, necessitating contributions from the surface to space and back again. It is at this juncture that the vertical path scaling and the plane parallel atmosphere have been adopted. Resultant error from this approximation can be greater than 30% for large zenith angles, with the solution ill-defined for sun angles below the horizon. However, for higher sun angles ($<75^\circ$), the LOWTRAN 7 radiance is well within 20% of that calculated with more exact multiple scattering codes.

5. COMPARISONS:

Comparisons of the final LOWTRAN 7 ultraviolet simulation capability to actual measurements show it to be generally adequate for calculations of UV transmittance and direct solar observations. Figure 6 provides data from two different sources, a "top of the atmosphere" solar irradiance spectrum measured from a rocket platform²⁹ and a larger portion of the AFGL balloon-borne irradiance data, again at 40km¹⁵. The LOWTRAN 7 simulations for both cases show very good agreement. Where differences arise, as in the absolute magnitude of the solar irradiances (attributed to calibration) or in the ozone depletion at 40km (the simulation used a US Standard profile), they appear to be related to physical rather than modeling problems.

A second set of comparisons (Figure 7) have been made with data from a dual spectrometer flown on a nadir sensing, sun-synchronous satellite³⁰. The LOWTRAN 7 simulations include multiple scattering and, again, are in excellent agreement with the data for medium to high solar zenith angles. The small scale spectral differences arise almost entirely from resolution differences and instrumental scattered light contamination. However, for larger zenith angles, two sources of divergence between measurement and LOWTRAN 7 arise: (a) the multiple scattering two-stream approximation breaks down and (b) large airglow features (primarily NO bands) appear against the weakened solar background. The multiple scattering corrections will be addressed in the near future (see previous discussion). However, successful modeling of the airglow phenomena will require major coding evolution.

6. CONCLUSIONS:

As an adjunct to the preparation of LOWTRAN 7 and FASCOD3, a set of UV spectroscopic data has been compiled. In addition to a new composite solar spectrum, the data set includes an analytic function which describes the O₂ Herzberg continuum absorption (0.19-0.244 μ m) with an extension of that function to approximate the Herzberg bands. The analytic expression for the continuum allows for an atmospheric (O₂ and N₂) pressure dependent term, providing a combined estimated accuracy of 10-15%. In addition to calculating a preliminary line atlas for the O₂ Schumann-Runge bands, a 20cm⁻¹ band model developed for portions of that system has been incorporated into LOWTRAN 7. The band model is adequate (10-20%) for frequency ranges dominated by transitions to the ground level ($v''=0$) but only approximates the behavior of the weaker temperature dependent $v''=1$ transitions in the window regions. The Hartley-Huggins O₂ absorption cross section has been collated from 4 different sets of measurements. The resultant continuum formulation incorporates a quadratic T-dependence for the wavelength range from 0.19-0.36 μ m with an expected accuracy of 3-5% for the Hartley system and 3-10% for the Huggins. The LOWTRAN 7 Transmittance/Radiance Program incorporates all of these features in a user-friendly environment for UV spectral simulations; total end-to-end accuracy for simulations not involving multiple scattering is 10-15%. However, for lines of sight which may be dominated by multiple scattering signatures, the errors can increase dramatically. Minor, but occasionally important atmospheric absorption signatures, particularly SO₂ and N₂O, are currently missing from the LOWTRAN 7 UV formulation. Similarly, airglow contributions, as might appear at twilight, are not now available within the LOWTRAN algorithm.

7. REFERENCES:

1. Kneizys, F.X., E.P. Shettle, L.W. Abreu, J.H. Chetwynd, G.P. Anderson, W.O. Gallery, J.E.A. Selby, S.A. Clough, Users Guide to LOWTRAN 7, AFGL-TR-88-0177, AD A206773, 1988.
2. Kneizys, F.X., E.P. Shettle, W.O. Gallery, J.H. Chetwynd, L.W. Abreu, J.E.A. Selby, S.A. Clough, and R.W. Fenn, Atmospheric Transmittance/Radiance: Computer Code LOWTRAN 6, AFGL-TR-83-0187, AD A137796, 1983.
3. Clough, S.A., F.X. Kneizys, E.P. Shettle, and G.P. Anderson, "Atmospheric Radiance and Transmittance: FASCOD2", Sixth Conference on Atmospheric Radiation, May 13-16, 1986, American Meteorological Society, Boston, Mass, 1987.
4. Watanabe, K., "Ultraviolet Absorption Processes in the Upper Atmosphere", Advances in Geophysics, 5, 153-221, 1958.
5. Johnston, H.S., M. Paige and F. Yao, "Oxygen absorption Cross Sections in the Herzberg Continuum and Between 206 and 327K", J. Geophys. Res., 89, 11661-11665, 1984.

6. Yoshino, K. A.S.-C. Cheung, J. R. Esmond, W.H. Parkinson, D.E. Freeman, S.L. Guberman, A. Jenouvieu, B. Coquart and M.F. Merienne, "Improved Absorption Cross Sections of Oxygen in the Wavelength Region 205-240nm of the Herzberg Continuum", Planet. Space Sci., **36**, 1469-1475, 1988.
7. Frederick, J.E. and J.E. Mentall, "Solar irradiance in the Stratosphere: Implications for the Herzberg Continuum Absorption of O₂", Geophys. Res. Lett., **9**, 461-464, 1982.
8. Anderson, G.P. and L.A. Hall, "Attenuation of Solar Irradiance in the Stratosphere: Spectrometer measurements Between 191 and 207nm", J. Geophys. Res., **88**, 6801-6806, 1983.
9. Shandanaand, "Nitrogen-Induced Absorption of Oxygen in the Herzberg Continuum", J. Quant. Spectrosc. Radiat. Transfer, **18**, 525-530, 1977.
10. Cann, M.W.P., J.B. Shin, and R.W. Nicholls, "Oxygen Absorption in the Spectral Range 180-300nm for Temperatures to 3000K and Pressures to 50 Atm.", Can. J. Phys., **62**, 1738-1751, 1984.
11. Trakhovsky, E., A. Ben-Shalom, U.P. Oppenheim, A.D. Devir, L.S. Balfour, and M. Engel, "Contribution of Oxygen to Attenuation in the Solar Blind UV Spectral Region", Appl. Opt., **28**, 1588-1591, 1989.
12. Rothman, L.S., R.R. Gamache, A. Goldman, L.R. Brown, R.A. Toth, H.M. Pickett, R.L. Poynter, J.-M. Flaud, C. Camy-Peyret, A. Barbe, N. Husson, C.P. Rinsland, and M.A.H. Smith, "The HITRAN Database: 1986 Edition", Appl. Opt., **26**, 4058-4097, 1987.
13. Frederick, J.E. and R.D. Hudson, "Predissociation Line Widths and Oscillator Strengths for the (2-0) to (13-0) Schumann-Runge Bands of O₂", J. Molec. Spectrosc., **74**, 247-258, 1979.
14. Yoshino, K., D.E. Freeman, and W.H. Parkinson, "High Resolution Absorption Cross Section Measurements and Band Oscillator Strengths of the (1-0)-(12-0) Schumann-Runge Bands of O₂", Planet. Space Sci., **31**, 339-353, 1983.
15. Anderson, G.P. and L.A. Hall, "Stratospheric Determination of O₂ Cross Sections and Photodissociation Rate Coefficients: 191-215nm", J. Geophys. Res., **91**, 14509-14514, 1986.
16. Pierluissi, J.H. and C.E. Maragoudakis, Molecular Transmission Band Models for LOWTRAN, AFGL-TR-86-0272, AD A180655, 1986.
17. Steinfeld, J.I., S.M. Adler-Golden and J.W. Gallagher, "Critical Survey of Data on the Spectroscopy and Kinetics of Ozone in the Mesosphere and Thermosphere", J. Phys. Chem. Ref. Data, **16**, 911-942, 1987.
18. Katayama, D.H., "New Vibrational Quantum Number Assignments for the UV Absorption Bands of Ozone Based on the Isotope Effect", J. Chem. Phys., **71**, 815-820, 1979.
19. Bass, A.M. and R.J. Paur, "The Ultraviolet Cross Sections of Ozone, I: Measurements", in Atmospheric Ozone Proceedings of the Quadrennial Ozone Symposium, Halkidiki, Greece, C. Zeferos and A. Ghazi, editors, 606-616, D. Reidel, Hingham, Mass., 1985.
20. Molina, L.T. and M.J. Molina, "Absolute Absorption Cross Sections of Ozone in the 185-350nm Wavelength Range", J. Geophys. Res., **91**, 14501-14508, 1986.
21. Yoshino, K., D.E. Freeman, J.R. Esmond, and W.H. Parkinson, "Absolute Cross Section Measurements of Ozone in the Wavelength Region 238-335nm and the Temperature Dependence", Planet. Space Sci., **36**, 395-398, 1988.
22. Cacciani, M., A. diSarra, and G. Fiocco, Laboratory Measurements of the Ozone Absorption Coefficients in the Wavelength Region 339-362nm at Different Temperatures, Dept. of Physics, University of Roma - La Sapienza, Italy, Internal Note No. 882, 1987.
23. Cacciani, M., A. diSarra, G. Fiocco, and A. Amoroso, "Absolute Determination of the Cross Sections of Ozone in the Wavelength Region 339-355nm at Temperatures 220-293K", J. Geophys. Res., **94**, 8485-8490, 1989.
24. VanHoosier, M.E., J.D. Bartoe, G.E. Brueckner, and D.K. Prinz, "Absolute Solar Spectral Irradiance 120nm-400nm (Results from the Solar Ultraviolet Spectral Irradiance Monitor-SUSIM-Experiment on Board Spacelab 2)", Astro. Lett. and Communications, **27**, 163-168, 1988.
25. Neckel, H. and D. Labs, "The Solar Radiation Between 3300 and 12500A", Solar Phys., **90**, 205-258.
26. G.P. Anderson and L.A. Hall, "Solar Irradiance Between 2000 and 3100A with Spectral Band Pass of 1A", J. Geophys. Res., **94**, 6435-6441, 1989.
27. Isaacs, R.G., W.-C. Wang, R.D. Worsham, and S. Goldenberg, Multiple Scattering Treatment for Use in the LOWTRAN and FASCODE Models, AFGL-TR-86-0073, AD A173990.
28. Isaacs, R.G., W.-C. Wang, R.D. Worsham, and S. Goldenberg, "Multiple Scattering LOWTRAN and FASCODE Models", Appl. Opt., **26**, 1272-1281, 1987.
29. Mentall, J.E., J.E. Frederick, and J.R. Herman, "The Solar Irradiance from 200-330nm", J. Geophys. Res., **86**, 9881-9884, 1981.
30. Huffman, R.E., F.J. LeBlanc, J.C. Larrabee, and D.E. Paulson, "Satellite Vacuum Ultraviolet Airglow and Auroral Observations", J. Geophys. Res., **85**, 2201-2215, 1980.

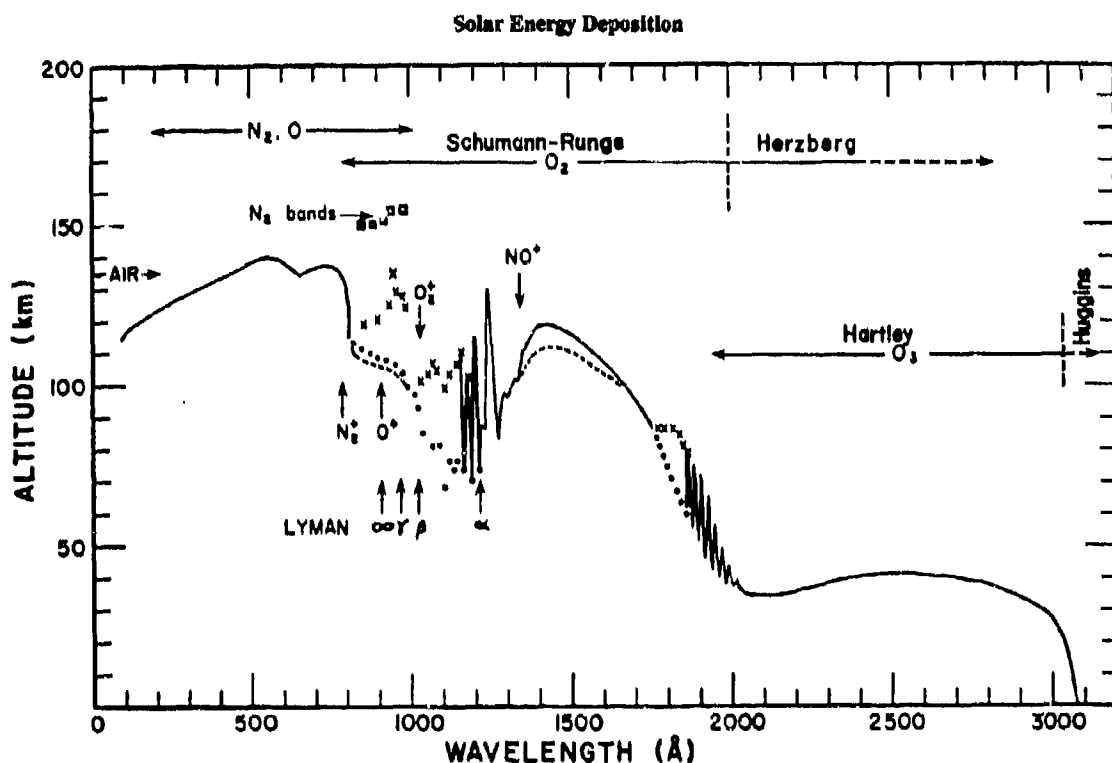


Figure 1: The approximate altitude at which $1/e^{\text{th}}$ of the solar irradiance is deposited; after Watanabe⁴. In the ultraviolet wavelength spectral range, LOWTRAN 7 includes the effects of the ozone Hartley and Huggins bands plus portions of the molecular oxygen Schumann-Runge and Herzberg systems. See text for additional discussion.

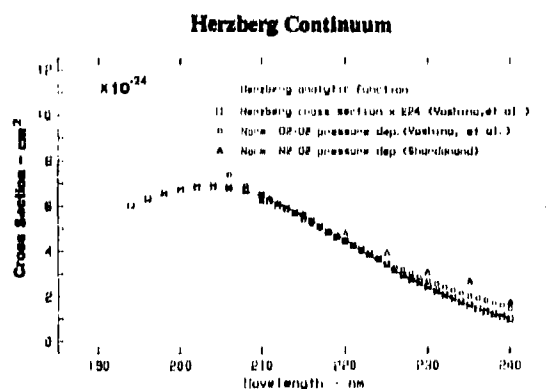


Figure 2: The form of the analytic function used to express the Herzberg Continuum within LOWTRAN 7, plus the supporting measurements for that continuum and its normalized pressure-dependent terms; see text.

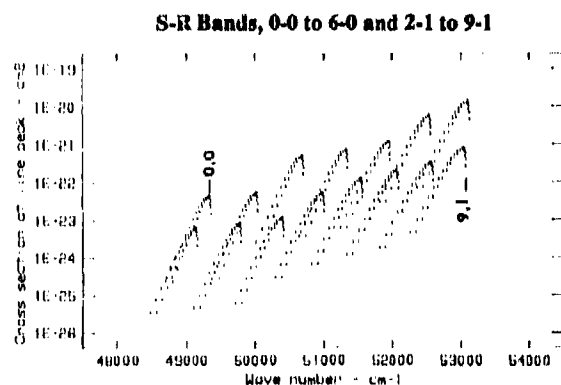


Figure 3: Calculated line positions and strengths for a portion of the Schumann-Runge Band System. LOWTRAN 7 directly accesses only those bands with frequencies less than 50,000 cm⁻¹, although coding for the entire depicted range is embedded.

S-R Band Model Simulation:

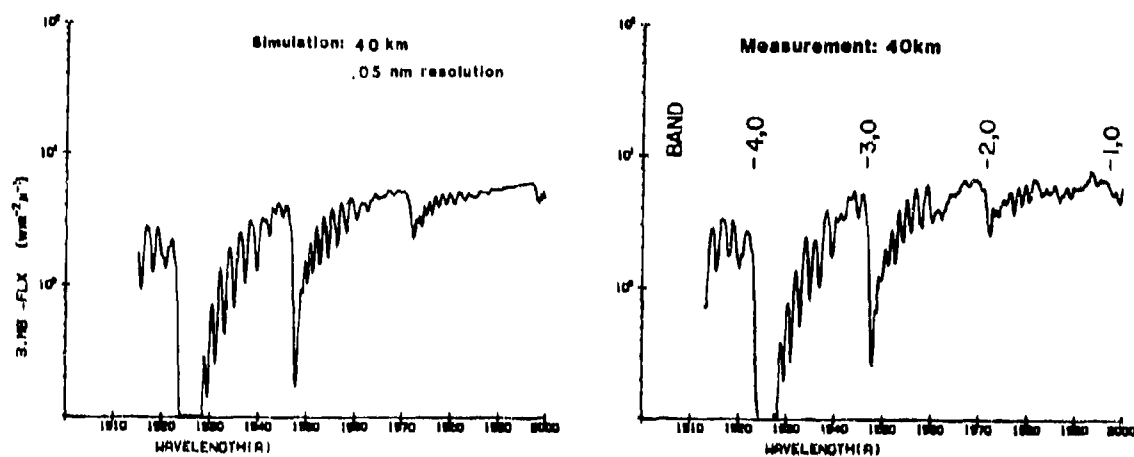


Figure 4: A comparison of the LOWTRAN 7 Schumann-Runge Band Model algorithm and an actual balloon-borne measurement of in situ solar irradiance. The balloon altitude was approximately 40 km with the sun at 24° zenith angle. The model easily reproduces the 4-0, 3-0, 2-0 and 1-0 band heads.

Ozone Absorption Properties in the UV

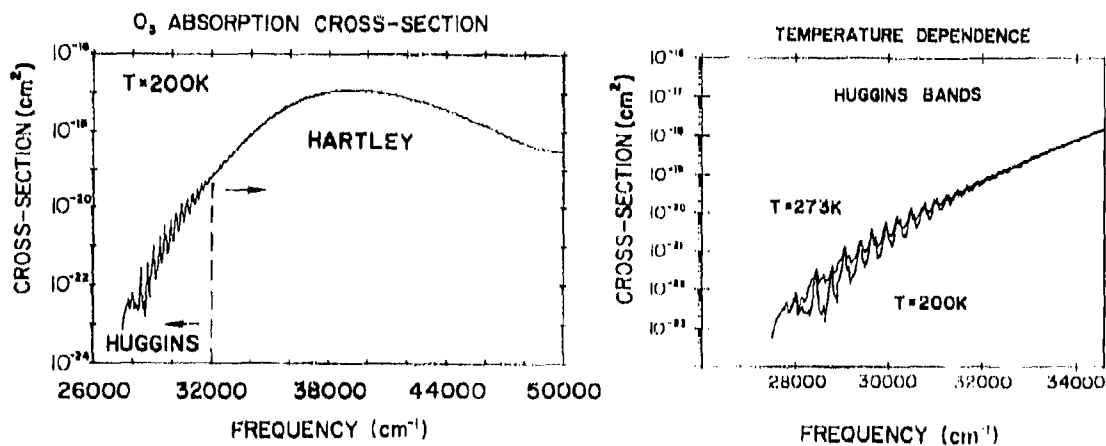


Figure 5: The ozone absorption cross sections as available in LOWTRAN 7. Structure at the center of the Hartley system does not appear in this logarithmic representation but is provided in the code. See the text for source references.

Comparisons: Direct Observations of Solar Irradiance

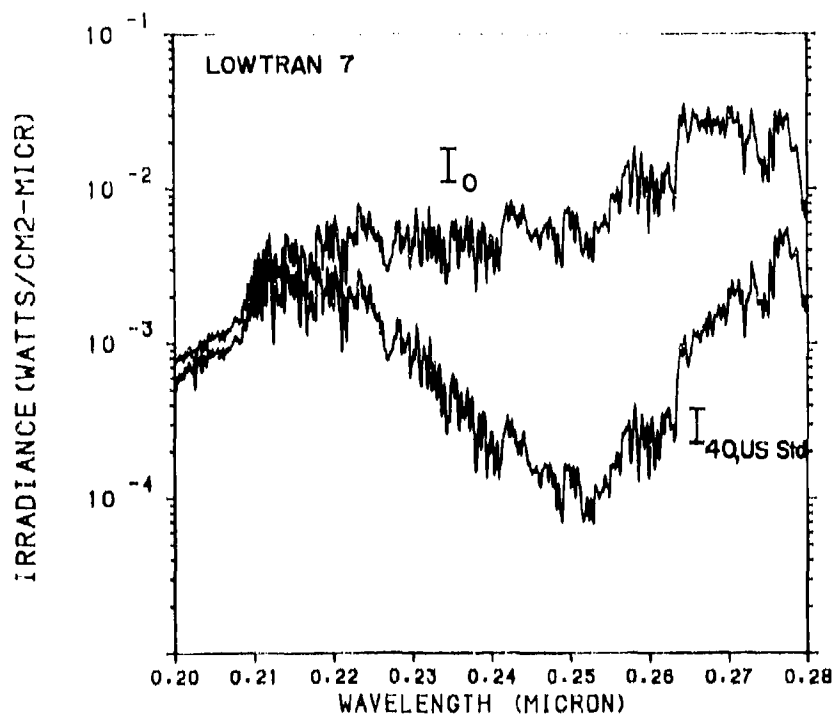
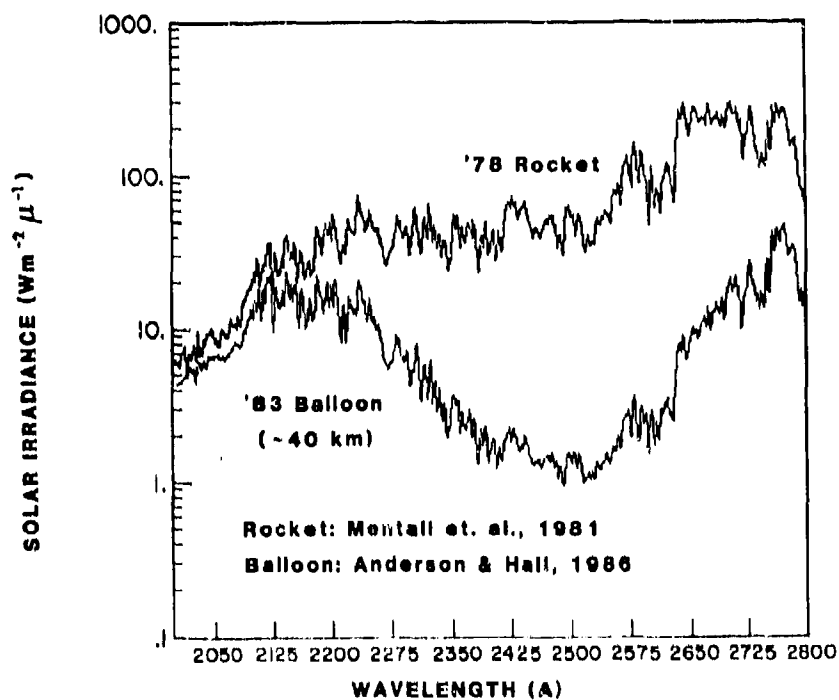
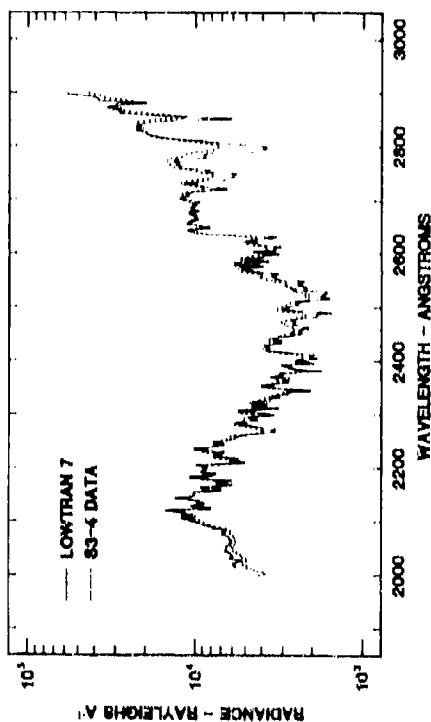


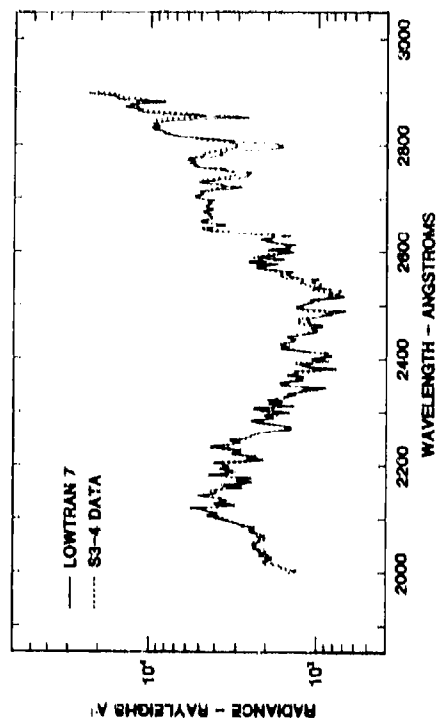
Figure 6: Comparisons of measured incident and in situ solar irradiances (see text) with LOWTRAN 7 simulations. The LOWTRAN 7 values for I_0 are based on Spacelab 2 measurements²⁴. While the geometric conditions (40km altitude and 24° solar zenith angle) for the balloon simulation have been incorporated into the calculation, the requisite temperature and ozone profiles are those of the U.S. Standard Atmosphere rather than the actual flight.

Comparisons: Backscattered Observations of UV Radiance

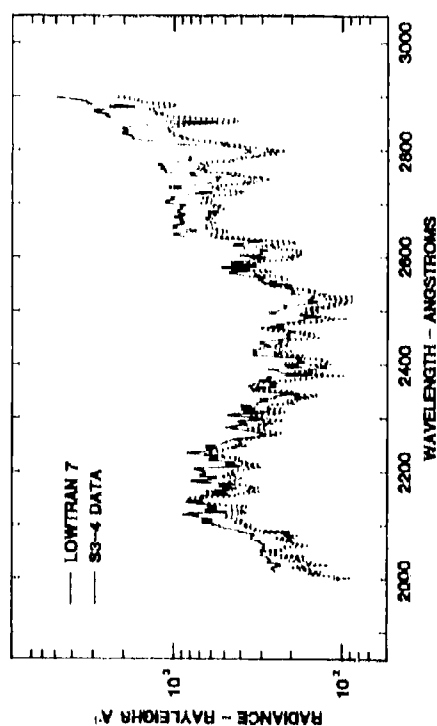
EARTH RADIANCE - SZA 24 DEG



EARTH RADIANCE - SZA 70 DEG



EARTH RADIANCE - SZA 90 DEG



EARTH RADIANCE - SZA 94 DEG

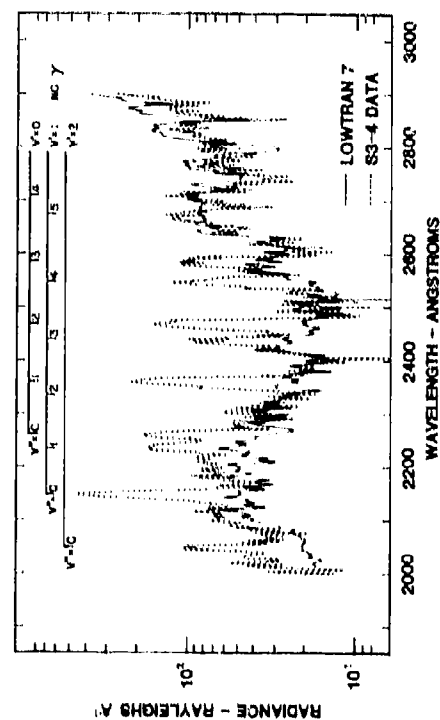


Figure 7: Comparisons of backscattered UV radiance as observed from space (nadir view)³⁰ with corresponding LOWTRAN 7 simulations. As the solar zenith angle varies from 24° to 95°, the measured and predicted radiances decrease by two orders of magnitude. The small scale spectral features are mostly solar Fraunhofer lines; however, at low sun angles, large airglow emission signatures can be readily identified. Again, the calculations were based on U.S. Standard temperature and ozone profiles.

MILLIMETRE-WAVE PROPAGATION IN THE EVAPORATION DUCT

by

M.F. Levy and K.H. Craig
Radio Communications Research Unit
Rutherford Appleton Laboratory
Chilton, Didcot, OX11 0QX
United Kingdom

SUMMARY

Recent developments in propagation modelling based on the Parabolic Equation Method allow the forecasting of two-dimensional antenna coverage diagrams at millimetre wavelengths, in a dispersive atmosphere with arbitrary two-dimensional variation of the refractive index. The model has been applied successfully to mm-wave propagation in the evaporation duct. The evaporation duct height is not sufficient to characterize mm-wave propagation, and information on the water vapour content is essential for the correct modelling of atmospheric absorption. Turbulence simulations have been carried out, showing marked scintillation effects in the evaporation duct. The method can be applied to arbitrary refractivity spectra, and gives a complete numerical description of the field statistics.

1. INTRODUCTION

Increasingly sophisticated radar systems at millimetre wavelengths require a good understanding of the propagation medium, especially over the sea where several complex processes are involved. For microwaves, propagation over the sea is dominated by the evaporation duct which results from the steep humidity gradient in the boundary layer. For mm-waves, ducting effects are counterbalanced by atmospheric absorption, and the water-vapour content plays an important role. A model based on the Parabolic Equation Method has been implemented, with the aim of providing a tool for assessment of mm-wave systems performance in the evaporation duct. A full calculation of the frequency dependent refractive index is carried out, and specular reflection from the rough sea surface is modelled. The main features of the model are presented in section 2, with examples of output for 35 GHz and 95 GHz antennas.

Atmospheric turbulence in the boundary layer is rather stronger than in the free atmosphere, causing important scintillation effects. Because of the complex refraction effects in the evaporation duct, it is not clear whether the usual models for estimating amplitude fluctuations of the signal are valid, and numerical simulations may be the only way of gaining some insight into the statistical characteristics of the field. The Parabolic Equation Method is particularly well adapted to the study of electromagnetic wave propagation in a turbulent medium. This is the object of section 3, where the principles of turbulence simulations are outlined. The main problem is to obtain a good statistical description of the medium. Turbulence in the air-sea boundary layer is fairly well understood, and examples based on the accepted model for the spectrum of refractivity fluctuations in the evaporation duct are presented.

2. PARABOLIC EQUATION METHOD FOR MM-WAVES

The parabolic equation approximation to the Helmholtz wave equation has been used extensively for predicting radiowave propagation in the troposphere, because it can cope with essentially arbitrary two-dimensional refractivity structures, and is numerically tractable [3,5]. If a scalar field component $\Phi(x, z)$ is written as

$$\Phi(x, z) \sim u(x, z) \frac{e^{ikz}}{\sqrt{x}}, \quad (1)$$

where k is the free space wave number, then u satisfies the parabolic equation,

$$\frac{\partial^2 u}{\partial z^2} + 2ik \frac{\partial u}{\partial x} + k^2 (m^2 - 1) u = 0, \quad (2)$$

provided that the refractive index variations are small on the scale of a wavelength and that $\log \frac{\partial u}{\partial x}$ is a slowly varying function of range over a wavelength. These assumptions hold for millimetre waves if the backscattered field is neglected. As usual, $m(x, z)$ denotes the modified refractive index $m(x, z) = n(x, z) + z/a$, where a is the Earth's radius. The Earth flattening approximation gives accurate results for angles of propagation of less than about 20° from the horizontal. This is not a restriction for the very low altitudes of interest here.

The solution of equation 2 can be marched forward in range, by using either a split-step Fourier transform method or a finite difference scheme. The results of this paper have been obtained with a split-step implementation on an IBM-PC compatible computer with a transputer card (the hardware has been described in [4]). It takes about 3 minutes to generate a coverage diagram for a typical case of mm-wave propagation in the evaporation duct, for a frame of 20 m by 20 km. Since the troposphere is dispersive and absorptive at millimetre wavelengths, the program needs temperature and humidity data to work out the complex refractivity structure at each frequency. The model is robust enough cope with measured data [8], but in this paper, a simple log-linear model for meteorological profiles the boundary layer has been used, corresponding to Battaglia's model for near-neutral conditions [1]. In particular, the duct height d (m) is given by

$$d = .96(T_a - T_s) - 3.4(e_a - e_s), \quad (3)$$

where T_a ($^\circ\text{K}$) is the air temperature measured at 10 m above mean sea level, T_s ($^\circ\text{K}$) is the sea surface temperature, e_a (mb) is the water vapour pressure at 10 m and e_s (mb) is the water vapour pressure at sea level. The non-dispersive modified refractivity is of the form

$$M(z) - M(0) = \alpha \left(z - d \log \frac{z + z_0}{z_0} \right), \quad (4)$$

where z_0 is the momentum roughness length, here taken to be 1.5×10^{-4} m, and α is a coefficient depending on surface conditions. For standard conditions, $\alpha \approx .120$ M-units/m. A line by line calculation of refractive dispersion and absorption is carried out using Liebe's model [9], and these are added to the non-dispersive modified refractivity to obtain the complex modified refractivity profile. The model is valid for frequencies up to 300 GHz. The examples given here assume horizontal homogeneity of the refractivity structure, but variation with range could be considered without added complexity.

Boundary conditions at the sea surface are modelled with an approximate image theory. The angular spectrum of the source field is added to that of the image field, modified by a Fresnel reflection coefficient which is a function of the angle of incidence. This corresponds to a decomposition of the field into its plane wave components, with the appropriate Fresnel reflection formula applied to each component. The advantage of this method is that surface roughness is easily incorporated in the model by multiplying the Fresnel coefficient for each angle of incidence by the corresponding roughness reduction factor. Simple fits to the curves in CCIR recommendation 527-1 [2] give the conductivity and permittivity of the sea as functions of frequency. The surface roughness reduction factor, which depends on frequency, rms wave height and incidence angle, is given in [12]. This method only models specular reflection. The noise introduced by diffuse reflection could be modelled by statistical simulations with a finite-difference implementation using a realistic description of the sea surface.

Figure 1 and 2 show basic transmission loss contours for a 35 GHz antenna, for the 0 m duct and 20 m evaporation duct A respectively, for a smooth sea. The parameters for the different evaporation ducts used in the paper are shown in Table 1.

Figure 3 shows attenuation in dB/km as a function of height, at 95 GHz, for three of the evaporation ducts described above. When there is no duct, humidity is constant and so is attenuation. In the presence of a duct, attenuation decreases very rapidly immediately above the surface and then more slowly, by about .1 dB/km between 2 m and 20 m. Note the higher attenuation for 20 m duct B, which is due to the higher temperature and hence higher water vapour content. Figures 4, 5 and 6 show basic transmission loss contours for a 95 GHz antenna for the 0 m duct and the two 20 m ducts, for a smooth sea. The stronger attenuation for the second 20 m duct has obvious consequences on the contours.

Table 1: Evaporation duct examples

| | T_s | T_a | e_s | e_a |
|-------------|-------|-------|---------|---------|
| 0 m duct | 20°C | 20°C | 23.4 mb | 23.4 mb |
| 20 m duct A | 20°C | 20°C | 23.4 mb | 17.6 mb |
| 20 m duct B | 28°C | 28°C | 37.9 mb | 32.0 mb |
| 30 m duct | 25°C | 25°C | 31.8 mb | 22.9 mb |

The main point here is that the duct height is not sufficient to characterize propagation at millimetre wavelengths.

3. MODELLING TURBULENCE

There are two approaches in modelling turbulence effects on electromagnetic wave propagation. The first one formulates an approximate equation satisfied by the successive moments of the phase and amplitude of the field. This approach has been used extensively in the literature. (see [7], chapters 17 and 20 for an excellent survey). For simple line-of-sight cases, the variance σ_χ^2 (dB) of the log-power of the received signal is approximately

$$\sigma_\chi^2 = 42.25k^{7/6} \int C_n^2(r)r^{5/6}dr, \quad (5)$$

where k is the wavenumber, and C_n^2 ($m^{-2/3}$) is the refractive index structure constant [13]. However this equation assumes weak fluctuations in the medium, and no coherent multipath, and its validity for mm-wave propagation in the evaporation duct is not clear. With less restrictive assumptions, the equation satisfied by the fourth moment of intensity fluctuations becomes extremely difficult to solve numerically, although some progress has been made in recent years [10].

The second approach consists in running numerical simulations on a computer. This approach has become very popular for turbulence studies in fluid dynamics, because it permits the visualization of features of turbulence which were not previously modelled. It has been used for statistical purposes in [11]. For propagation studies, the turbulent medium is represented as a sequence of thin phase-screens. This lends itself very well to the parabolic equation method: at each step, the deterministic refractive index is simply modified by the addition of a random term W . The main problem is the generation of successive realizations of this random process that will represent accurately the physical atmospheric turbulence.

Since many simulations are needed to obtain meaningful statistics, it is impractical to use full simulations of atmospheric turbulence to produce a grid of refractive index values, and some sort of spectral representation must be sought. If the process is homogeneous, it can be represented as the convolution of its correlation function with white noise. For a process that is only locally homogeneous, the correlation function does not exist and has to be replaced with the structure function. Unfortunately, the turbulent refractive index is not even locally homogeneous, since the intensity of the turbulence varies with height and range. To handle this, we make the simplifying assumption that $V(x, z) = W(x, z)/C_n(x, z)$ is isotropic and locally homogeneous (we assume that W does not depend on time). If the range step size used for the numerical solution of the parabolic equation is greater than the correlation length of the medium, the realizations of $V(x, z)$ can be generated independently at each range. A horizontal step size of 100 m probably satisfies this requirement for independence, and is small enough to obtain accurate solutions for mm-wave propagation in the evaporation duct.

The problem is now reduced to that of generating a realization of a random process $V(z)$ with a known power spectrum Φ at points $0, \Delta z, 2\Delta z, \dots, (N-1)\Delta z$. This is done in the spectral domain by filtering the sample spectrum of discrete white noise by $\sqrt{\Phi}$. An inverse Fourier transform gives V , and W is obtained by multiplying V by the refractive index structure constant C_n .

Here, we have assumed a Kolmogorov spectrum for V . The one dimensional spectrum is then

$$\Phi(\kappa) = \frac{\pi}{40} \kappa^{-5/3}. \quad (6)$$

The profile of C_n^2 ($\text{m}^{-2/3}$) for an evaporation duct of height d in neutral conditions is given by [6]

$$C_n^2(z) = a^2 K^{4/3} (0.120d)^2 z^{-2/3}, \quad (7)$$

where $a^2 \approx 2.8$ and $K \approx 0.4$ is Von Karman's constant. Hence the strength of the turbulence is proportional to the height of the evaporation duct. Figure 7 shows the profile of C_n^2 for a 20 m duct.

Figure 8 shows an example of basic transmission loss contours for a 95 GHz antenna in the turbulence associated with 20 m duct A, for a smooth sea. It is easy to see how scintillation effects occur, since the amplitude along a lobe now presents peaks and troughs which will vary in time and space.

Figures 9 and 10 show the standard deviation σ_x (dB) of the log-power as a function of range, at three different heights, for the 10 m duct and the 30 m duct respectively, calculated from 100 simulations. The rms wave height is 0.25 m, corresponding to a wind speed of 7 m/s. Similar simulations were carried out with a rougher sea, showing that the lobing effects are in fact due to interference with the reflected signal, which weaken when coherent reflection becomes less important. However after discarding these effects, the remaining trend seems independent of surface roughness, and the strength of the turbulence is not affected. As expected, the scintillation effects are much stronger for the higher duct, leading to serious degradation of the signal-to-noise ratio.

4. CONCLUSIONS

The behaviour of millimetre waves in the evaporation duct can be predicted with a model based on the parabolic equation method, taking into account atmospheric absorption and dispersion, as well as surface roughness effects on specular reflection. The model is implemented on a desk-top computer with a transputer card. It allows the forecasting of antenna coverage diagrams for frequencies up to 300 GHz, for arbitrary two-dimensional refractivity structures. It takes about 3 minutes to generate a prediction for a typical frame of 20 m by 20 km. The model has been applied successfully to mm-wave propagation in the evaporation duct in near-neutral conditions. It is clear that duct height is not a sufficient parameter to characterize mm-wave propagation, because information on the water-vapour content is essential for the absorption calculations.

The effects of atmospheric turbulence on propagation can be studied by running numerical simulations with a randomly varying refractive index. The method can be applied to arbitrary refractivity spectra, and gives a complete description of the field statistics. Some examples based on boundary layer theory show marked scintillation effects in the evaporation duct. Although the lobing pattern has a influence on the fluctuations of the log-amplitude of the received signal, their intensity is essentially independent of surface roughness.

5. ACKNOWLEDGMENTS

We wish to thank our colleague C.J. Gibbins for his implementation of Liebe's model, and for many useful discussions.

References

- [1] Battaglia, M.R., Modelling the radar evaporative duct, *RANRL Technical Note 3/85*, Department of Defence, Defence Science and Technology Organisation, Weapons Systems Research Laboratory, RAN Research Laboratory, Australia, 1985.
- [2] CCIR Recommendation 527-1, Electrical characteristics of the surface of the Earth, 1986.
- [3] Craig, K.H., Propagation modelling in the troposphere: parabolic equation method, *Elec. Lett.*, **24**, 1136-1139, 1989.
- [4] Craig, K.H. and Levy, M.F., A forecasting system using the parabolic equation method—application to surface-to-air propagation in the presence of elevated layers, *AGARD CP*, 44th

Symposium of the Electromagnetic Wave Propagation Panel, on Operational Decision Aids for Exploiting or Mitigating Electromagnetic Propagation Effects, 1989, to appear.

- [5] Dockery, G.D., Modeling electromagnetic wave propagation in the troposphere using the parabolic equation, *IEEE Trans. AP-36*, 1464-1470, 1989.
- [6] Gossard, E.E., Clear weather meteorological effects on propagation at frequencies above 1 GHz, *Radio Science*, **16**, 589-608, 1981.
- [7] Ishimaru, A., *Wave propagation and scattering in random media, Vol.2, Multiple scattering, turbulence, rough surfaces, and remote sensing*, Academic Press, New York, 1978.
- [8] Levy, M.F. and Craig, K.H., Assessment of anomalous propagation predictions using minisonde refractivity data and the parabolic equation method, *AGARD CP*, 44th Symposium of the Electromagnetic Wave Propagation Panel, on Operational Decision Aids for Exploiting or Mitigating Electromagnetic Propagation Effects, 1989, to appear.
- [9] Liebe, H.J. , An updated model for millimeter wave propagation in moist air, *Radio Science*, **20**, 1069-1089, 1985.
- [10] Macaskill, C., An improved solution to the fourth moment equation for intensity fluctuations, *Proc. R. Soc. Lond. A* **386**, 461-474, 1983.
- [11] Macaskill, C. and Ewart, T.E., Computer simulation of two-dimensional random wave propagation, *IMA Journal of Appl. Math.* **33**, 1-15, 1984.
- [12] Miller, A.R., Brown, R.M. and Vegh, E., New derivation for the rough-surface reflection coefficient and for the distribution of sea-wave elevations, *IEE Proc.*, Vol. 131, Part H, **2**, 114-116, 1984.
- [13] Tatarski, V.I., *The effects of the turbulent atmosphere on wave propagation*, U.S. Dept of Commerce, NSF Rep. TT 68-50464, NTIS, 1971.

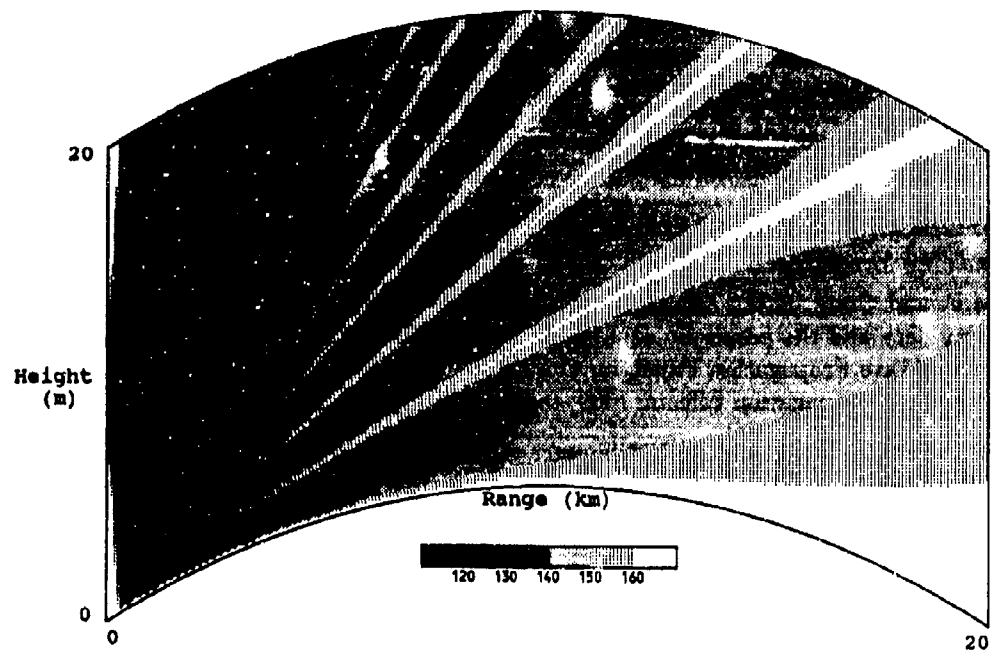


Figure 1. Basic transmission loss (dB) for a 35 GHz antenna in a 0 m evaporation duct.

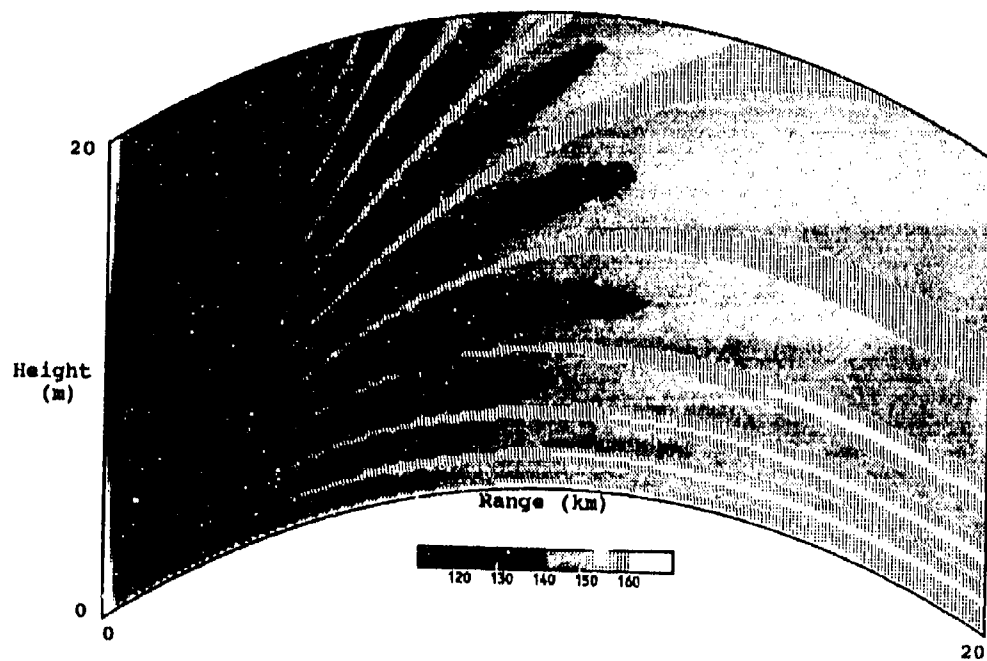


Figure 2. Basic transmission loss (dB) for a 35 GHz antenna in 20 m evaporation duct A.

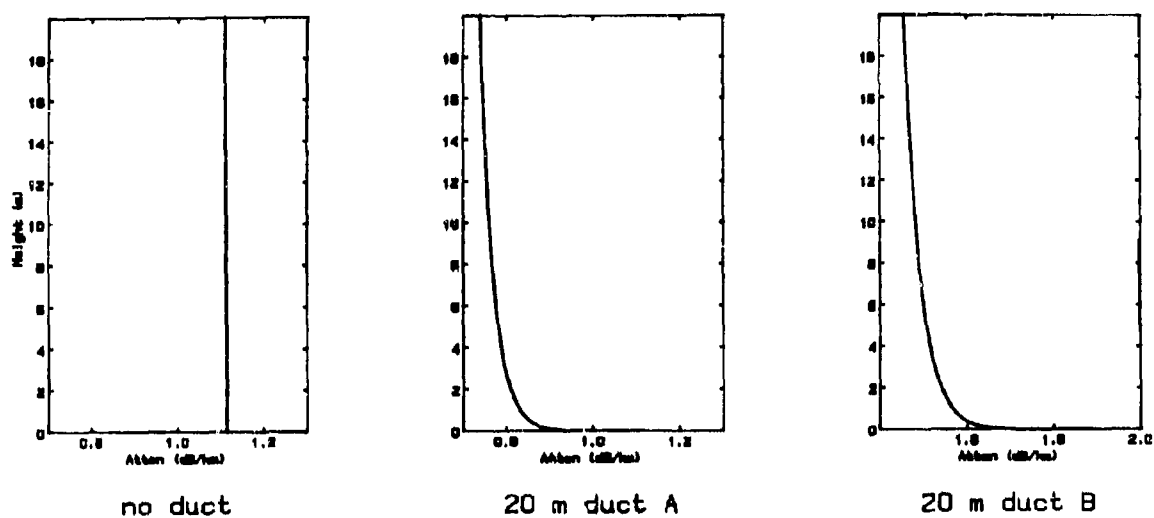


Figure 3. Atmospheric absorption at 95 GHz.

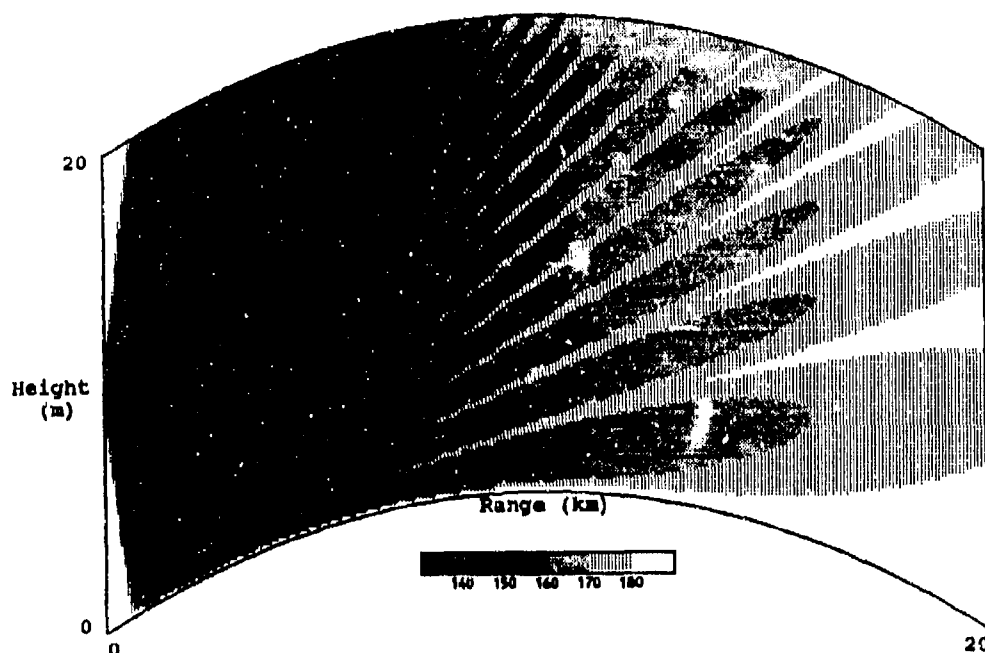


Figure 4. Basic transmission loss (dB) for a 95 GHz antenna in a 0 m evaporation duct.

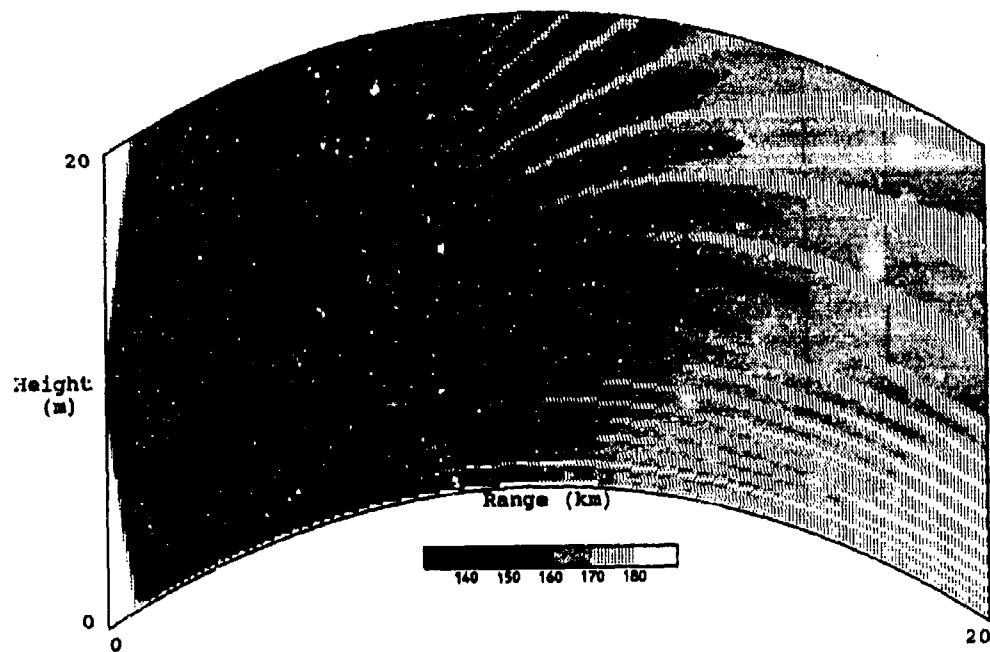


Figure 5. Basic transmission loss (dB) for a 95 GHz antenna in 20 m evaporation duct A.

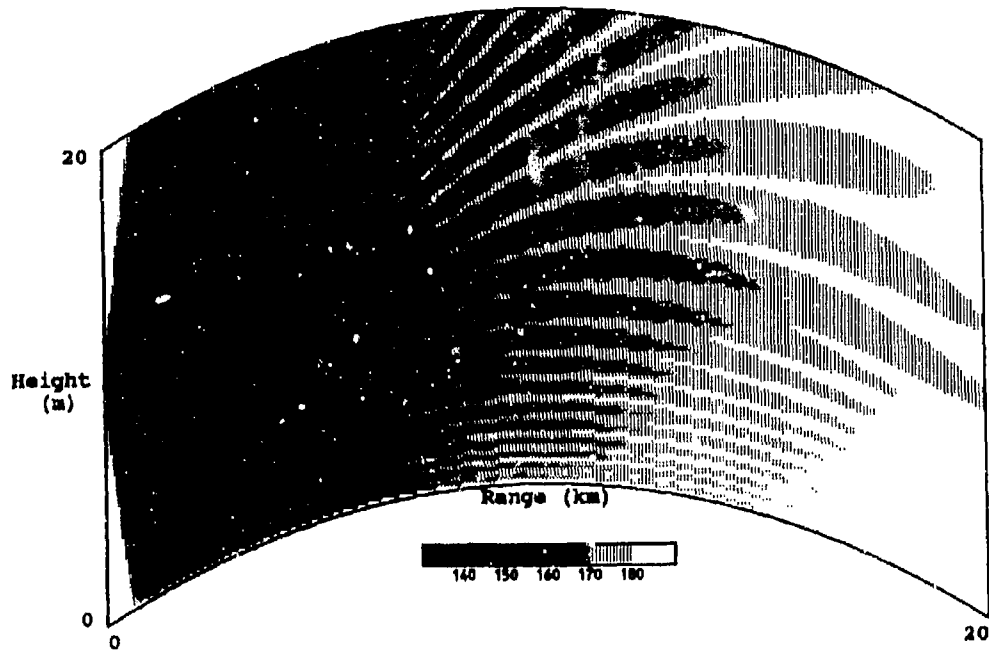


Figure 6. Basic transmission loss (dB) for a 95 GHz antenna in 20 m evaporation duct B.

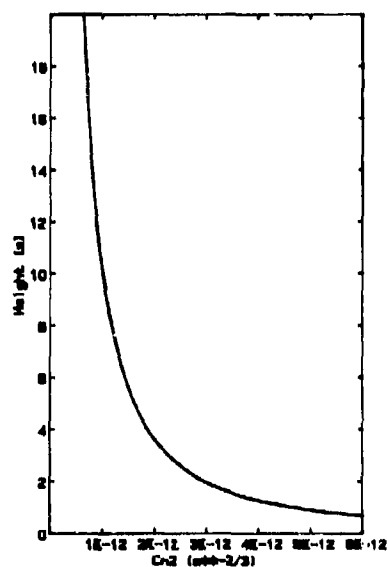


Figure 7. Structure constant of the refractive index for 20 m duct A.

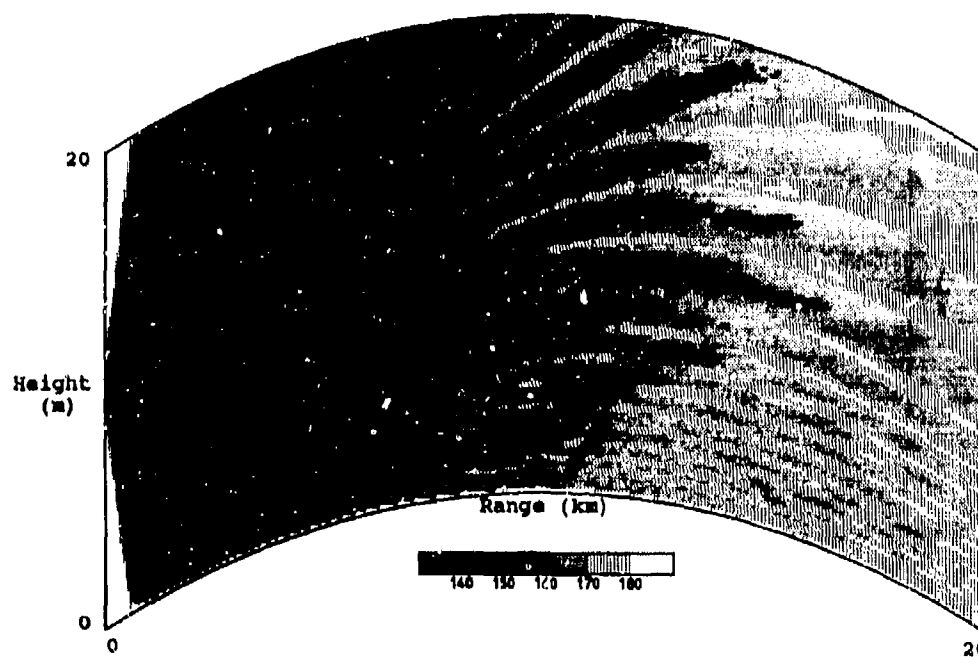


Figure 8. Basic transmission loss (dB) for a 95 GHz antenna in 20 m duct A, for a turbulent atmosphere.

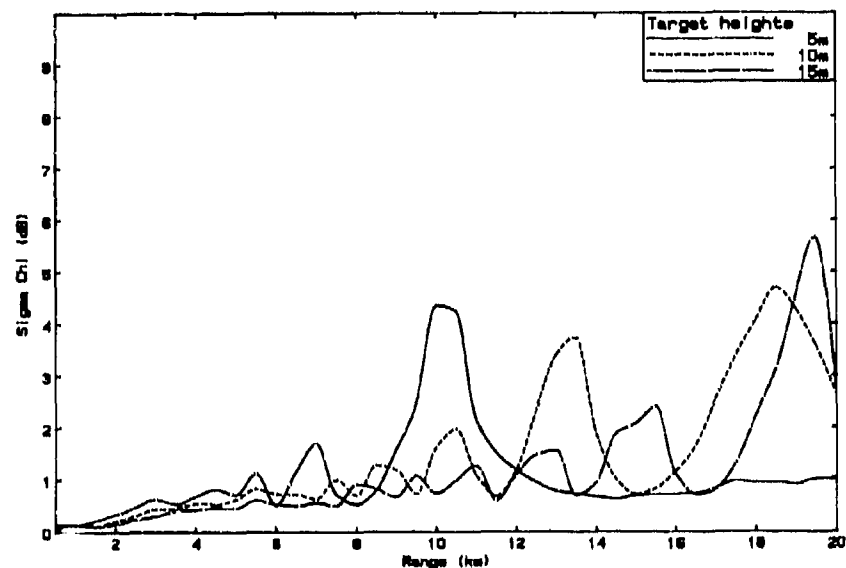


Figure 9. Standard deviation of the log-amplitude fluctuations for a 95 GHz antenna in a 10 m duct.

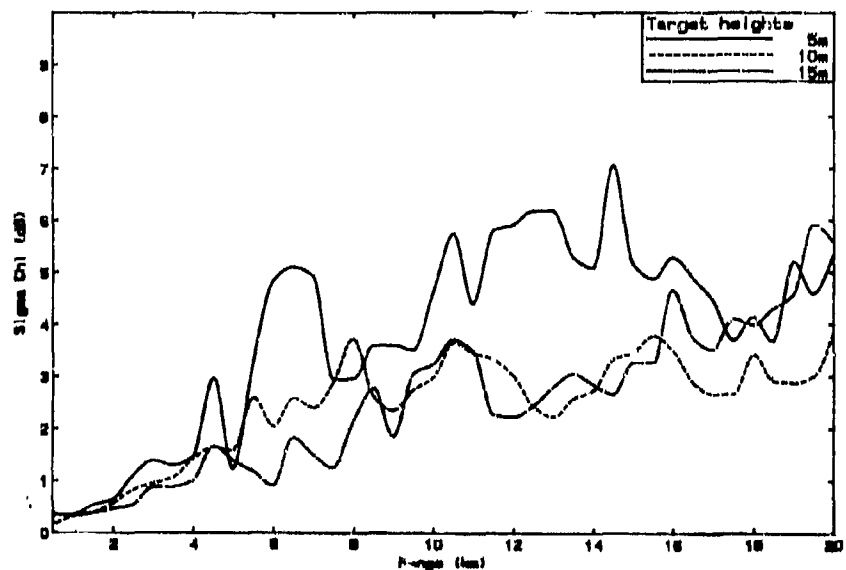


Figure 10. Standard deviation of the log-amplitude fluctuations for a 95 GHz antenna in a 30 m duct.

LIDAR MEASUREMENTS OF THE OPTICAL PROPAGATION ENVIRONMENT*

Thomas D. Wilkerson, Upendra N. Singh, Anthony Notari, and W. Charles Braun
Institute for Physical Science and Technology
University of Maryland
College Park, Maryland 20742-2431
U.S.A.

SUMMARY

Results of lidar measurements are reported, particularly the layering of tropospheric haze and extinction/backscatter by cirrus clouds at visible wavelengths. This work includes the operation of a fixed lidar at College Park, and a transportable lidar for geographic locations of interest to DoD. A sensitivity baseline for these lidars has been established using Rayleigh backscatter from the high altitude molecular atmosphere. Profiles of temperature and density cover the altitude range 30-80 km. For cirrus clouds, measured relationships between extinction and backscatter make it possible to estimate the long-range horizontal visibility through cirrus layers via calibrated backscatter observations. Inversion of tropospheric haze measurements to vertical profiles of extinction is reported. Applicability of lidar probe methods to energy and information transfer through the atmosphere is summarized. Upper atmosphere observations are discussed, relevant to the prediction of atmospheric effects on re-entry vehicles.

1. INTRODUCTION

This presentation discusses the goals, methods and results of atmospheric lidar measurements at the University of Maryland, specifically our research that uses untuned Nd:YAG lasers to observe Mie scattering by particulates and Rayleigh scattering by the molecular atmosphere.

The relevance of lidar for this Symposium lies in the unique capabilities for remote probing of the atmosphere afforded by pulsed lasers. Using the radar principle of converting time-of-return into distance along the laser beam direction, coupled with the narrowness of the beam itself, one can carry out remote mapping of large portions of the atmosphere with a time resolution limited only by the pulse repetition frequency of the laser (typically 10-1000 Hz). As a support for studies of electromagnetic propagation, lidar is attractive because the propagation phenomena of interest (e.g., light scattering and extinction) are directly addressed by lidar measurements. Other important parameters of the environment, such as temperature and humidity, can also be measured remotely by means of lidar. Excellent references on lidar are the book by Measures¹ and the March 1989 special issue of Proceedings of the IEEE.^{2,3} Table 1 outlines the parts of the Maryland program to be discussed here.

TABLE 1. UNIVERSITY OF MARYLAND LIDAR PROGRAM (SDIO/ONR)

-
- Middle atmosphere measurements (ground-based),
from various geographical locations
 - Tropospheric measurements
 - Fixed lidar site at College Park (operational)
 - Transportable lidar (testing), for observations from
desert, mountain, Arctic, and oceanic sites
 - Current observations at College Park
 - Tropospheric haze layers } Mie scattering
 - Cirrus clouds (10-13 km) }
 - Clear air Rayleigh scattering (to 85 km)
 - Temperature and density profiles
(stratosphere, mesosphere)
-

2. APPLICATIONS

Table 2 indicates capabilities in our Atmospheric Lidar Observatory (ALO) for making useful measurements in support of DoD programs, specifically infrared search and track (IRST), high energy laser weapon systems (HELWS), reentry of high speed vehicles (HSV), and cloud free line-of-sight (CFLOS). The third heading on density structure in the upper atmosphere is also of interest to NASA for Shuttle re-entry and the National Aerospace Plane.^{4,5} The fourth main heading mentions our interest in setting up lidar operations at sites other than College Park.

*Research supported by the University of Maryland, and by SDIO and ONR through contract number N00014-85-K-0582.

TABLE 2. ALO CAPABILITIES RELEVANT TO DoD PROGRAMS
(IRST, HELWS, HSV RE-ENTRY, CFLOS)

-
- CIRRUS (thin, very thin, "subvisible")
 - Optical extinction data vital for validation of long range sensor capabilities (visible, IR)
 - AEROSOL
 - Optical background (IR)
 - Visibility layering
 - Mass loading of atmosphere: implications for ablation of high speed vehicles
 - Impact of uniform/non-uniform layering on nonlinear (high power) optical propagation
 - PROFILES OF UPPER ATMOSPHERE DENSITY
 - Influence of large gas density fluctuations on HSV flight
 - Climatology of density perturbations for avoidance of effects
 - INTEREST IN OTHER LIDAR SITES
 - Clear weather
 - High altitude
 - Airborne platforms
-

3. EQUIPMENT

Table 3 describes the equipment used in the work reported here. The fixed system in the ALO at College Park currently looks only at the zenith, and could be tilted to approximately 45° elevation in any direction. The transportable system also looks vertically, and will soon have the capability of viewing at all elevation angles in a plane.

TABLE 3.

| <u>LASER SOURCES</u> | | <u>FREQUENCY DOUBLED Nd:YAG LASERS</u> |
|---|--|--|
| * | WAVELENGTH | 532 nm |
| * | ENERGY | 400 mJ |
| * | BEAM DIVERGENCE | 0.6 m rad |
| * | PULSE WIDTH | 10-15 ns |
| * | REPETITION RATE | 10 Hz |
| <u>RECEIVERS</u> | | |
| * | CASSEGRAIN TELESCOPE | 60 cm diam. (FIXED) |
| * | NEWTONIAN TELESCOPE | 44 cm diam. (TRANSPORTABLE) |
| <u>DETECTOR AND DATA ACQUISITION SYSTEM</u> | | |
| * | SINGLE CHANNEL DETECTORS FOR ROUTINE BACKSCATTER MEASUREMENTS | |
| * | DUAL CHANNEL DETECTOR SYSTEM USING WOLLASTON PRISM FOR DEPOLARIZATION MEASUREMENTS | |
| * | TRANSLAC 2012 DIGITIZERS | |
| * | LASER INTERFACE DATA ACQUISITION SYSTEMS | |
| * | 12 MHz, 80286 COMPUTERS & DATA STORAGE | |
| * | PHOTON COUNTING SYSTEM FOR MIDDLE ATMOSPHERE MEASUREMENTS | |
| * | SOFTWARE SYSTEMS FOR DATA STORAGE AND MULTI-LEVEL ANALYSIS | |

4. TROPOSPHERIC HAZE LAYERS

This section describes the visualization of haze layers in the troposphere and some results on optical extinction derived from backscatter data. Figure 1 shows the observed lidar backscatter intensity as a function of altitude z (vertical) and time (horizontal).^{*} The time span is about 50 minutes in the early morning of August 11, 1988, when the air was very stable and polluted for several days. The haze layers extend upward to about 3.7 km altitude.

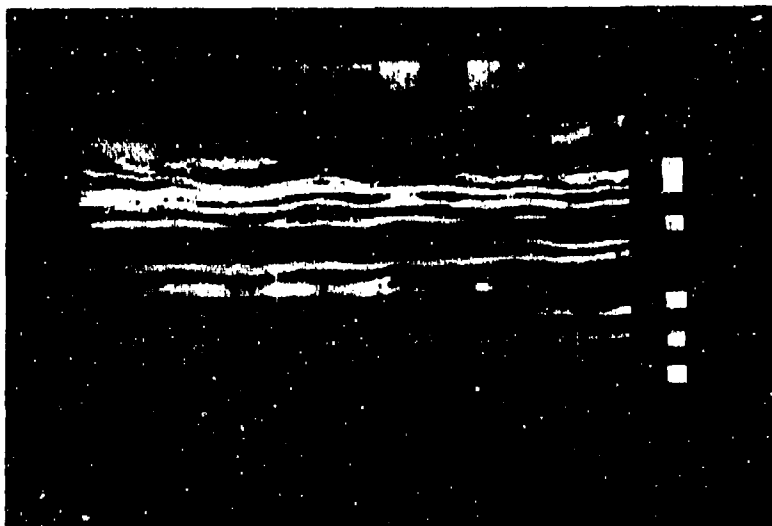


Figure 1. Lidar image of haze layers over College Park, MD, August 11, 1988. Altitude is vertical; time runs horizontally and increases to the right.

Figure 2 shows an example of reducing the backscatter data for August 14, 1988 to optical extinction κ vs altitude, using the inversion method suggested by Kaestner.⁶ The accuracy of extinction inferred from backscatter depends on some assumptions. The results given in Figure 2 show that optical extinction varies dramatically with altitude in such layered hazes. Lidar inversions for cirrus clouds are discussed in the next section. For the interested reader we have listed many of the useful references on lidar inversions.^{2,6-14}

Figure 3 demonstrates a situation bearing on CFLOS (Cloud Free Line-of-Sight). The intrusion of a thin layer of low lying, patchy clouds produces a highly variable total extinction between the ground and any altitude above about 800 meters. At times, the layers above this cloud are easily located; at other times the vertical visibility goes to zero. This situation suggests an approach to high energy laser applications requiring good transmission between the ground and space; namely that probe lidars be used as control systems to locate and characterize aerosol layers that can affect non-linear beam propagation at high power, and/or identify moments of good and bad transmission due to variable cloudiness. Spatially scanning lidars, such as the University of Wisconsin system, can rapidly map the overhead sky transmission for the same purpose.

^{*}Lidar returns are corrected for the $1/z^2$ decrease in solid angle and signal. Figures 1, 3, 4, and 5 are black-and-white renditions of a false color scale which is not possible to reproduce here. Reliable data start at about 1 km altitude, because of the setting of the overlap of the field of view of the telescope and the laser transmitter.

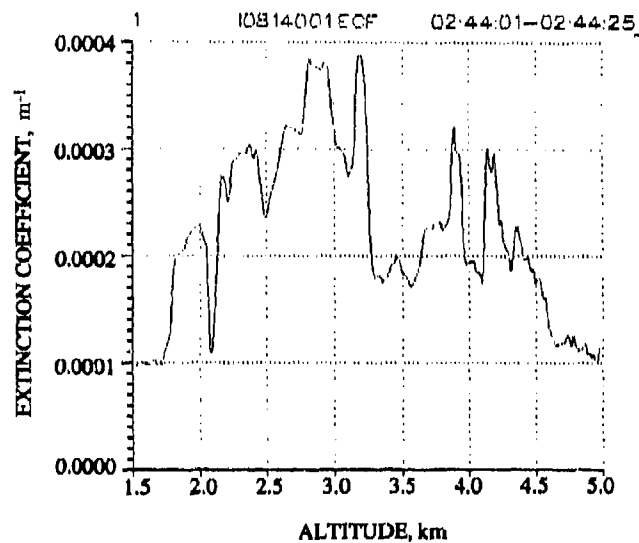


Figure 2. Optical extinction coefficient ($\lambda = 532$ nm) as function of altitude, calculated by inverting lidar backscatter returns.

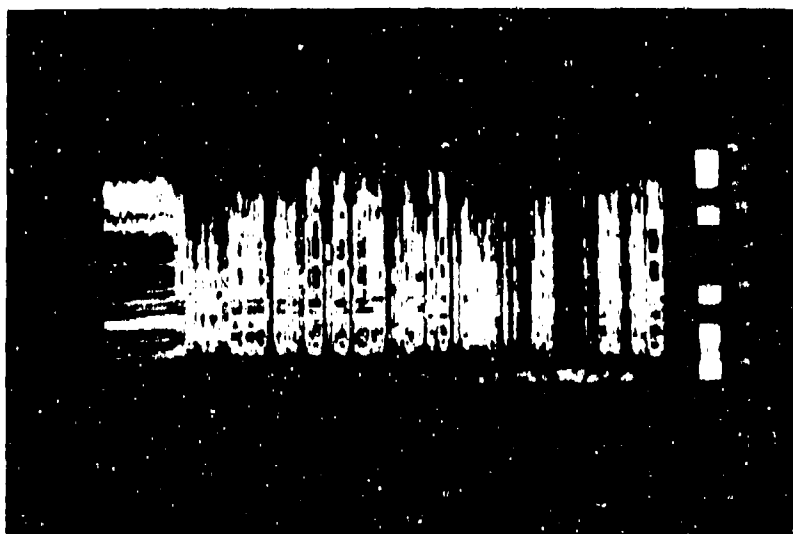


Figure 3. Tropospheric haze layers, with interference by low lying clouds.

5. CIRRUS CLOUDS

Figures 4 and 5 are altitude-time plots of the backscatter intensity from cirrus clouds on August 16, 1988. Figure 4 shows the entire record from the ground to 15 km altitude, including layers at 7 km and cirrus at 11-12 km. Figure 5 expands the altitude scale, so as to display greater detail in the cirrus clouds.

Figure 6 indicates how one can use the numerical data from which the pictures are derived to evaluate the extinction by the clouds and the scattering from the clouds, independent of one another. Extinction at any given time is given by the decrease of return signal from the relatively constant, clear air regions (z_1) above the tropopause. Backscatter intensity is calibrated by assuming Rayleigh scattering from clear air, near or at the cloud level (e.g., z_2). Results of our analysis for a few cirrus clouds will be given below.

Also one can invert the cirrus cloud backscatter profile alone to obtain an extinction profile and a mean extinction for the cloud, so as to compare results with the completely empirical method just described. The essential point of these lidar observations and analyses is to detect cirrus clouds even when they are "thin" or "subvisible", and to estimate their optical extinction properties from backscatter data.

Figure 7 summarizes the results of many of our cirrus observations to indicate the approximate range they fall into. For a given extinction, the backscatter coefficient is of order $1/4$ to $1/10$ the value that would apply for Rayleigh scattering. This is consistent with the highly forward scattering expected for Mie scattering, and the consequent reduction of intensity expected in the backward direction.

Data from a particular cirrus cloud pattern for about one hour on the night of August 16, 1988 are shown in Figure 8. The numbers associated with sample data points are extinction optical depth, $\tau = \langle \sigma_e \rangle h$, of the cirrus cloud at various times during the observing period. That there is a systematic relationship between extinction and backscatter is evident even at small optical depths.

Figure 9 shows similar data for September 15, 1988; Figure 10 is a re-plot using linear scales for the variables. A non-linear relationship is certainly suggested--which is not to say that the processes are intrinsically so related, but possibly that at least one important property of the cloud, such as the particle size distribution, may be varying along with the total extinction. We are also looking into other possibilities, such as subtle effects leading to detector saturation, that may have gone undetected so far. Taking these data at face value for the present, we are carrying out the inversions mentioned above. Figure 11 shows the results of inverting the backscatter profile to obtain the mean extinction, using Kaestner's inversion method with a non-linear relationship derived from the data in Figure 10. Good agreement between Figs. 9 and 11 is obtained. Our study of these optical properties and inversion methods is continuing.

We are also investigating the characterization of cirrus clouds in terms of their geometric properties and the dependence of optical properties on temperature.

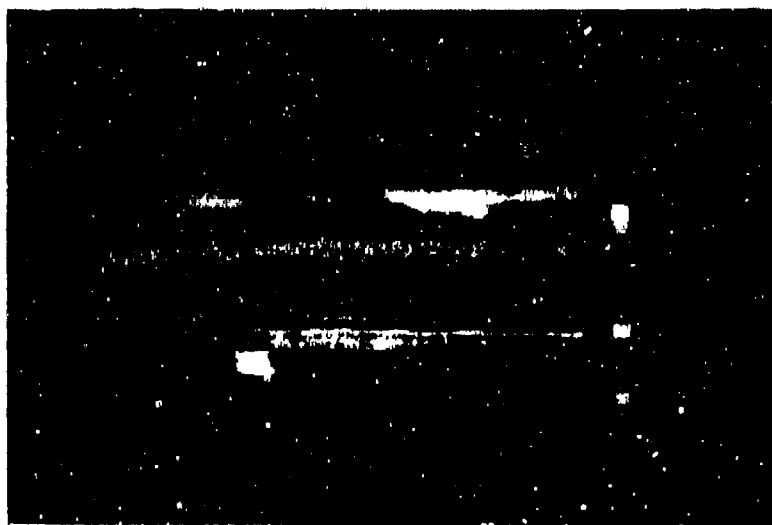


Figure 4. Altitude-time picture of cirrus cloud layer (11-12 km) and lower lying cloud layers (7 km).

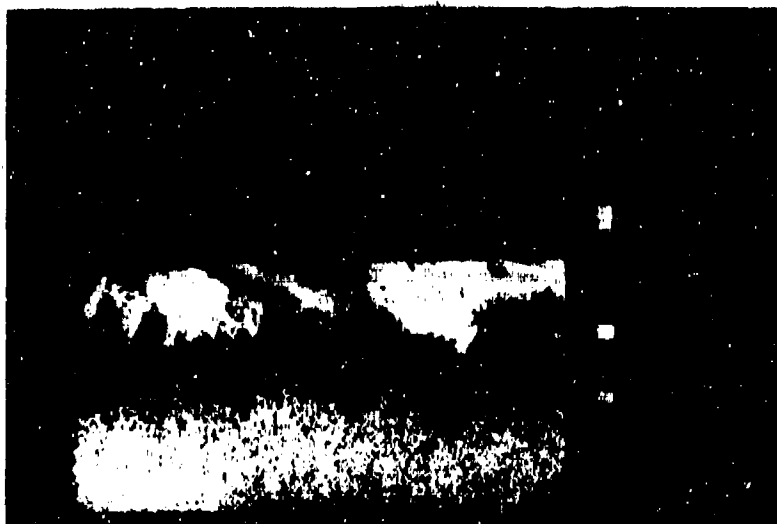


Figure 5. Expanded plot of cirrus shown in Figure 4.

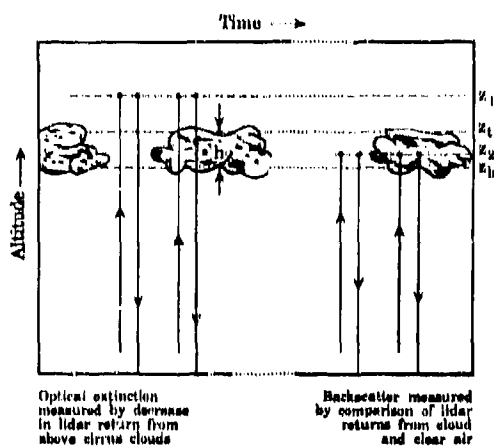


Figure 6. Principles of obtaining independent data on extinction (left) and scattering (right), using clear air lidar return for comparison or as a standard.

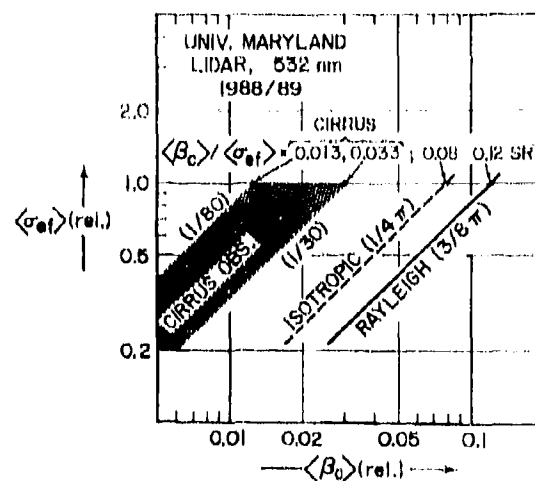


Figure 7. Illustration of the range of extinction/backscatter relationships expected for ideal Rayleigh and isotropic scattering, and observed for various cirrus clouds.

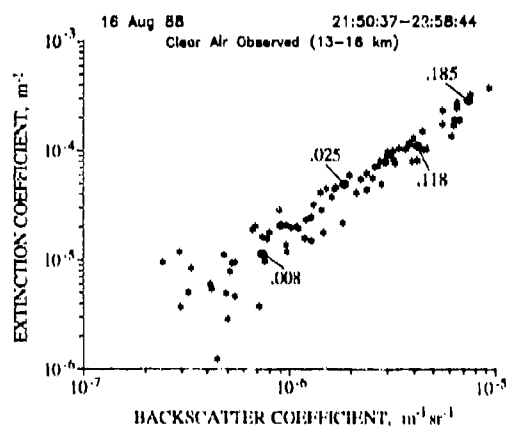


Figure 8. Empirical relationship between extinction $\langle\beta_{\text{ext}}\rangle$ and backscatter $\langle\beta_{\text{b}}\rangle$ for cirrus cloud on August 16, 1988, using method described in text and in Figure 6.

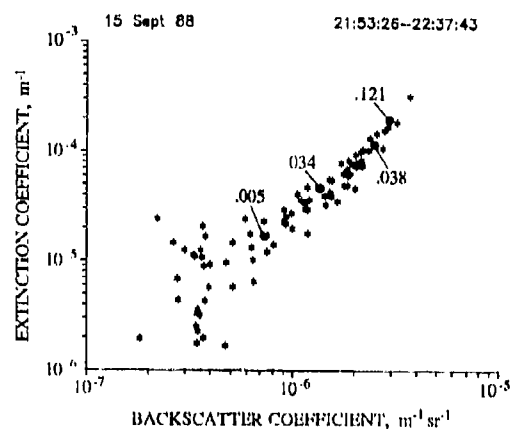


Figure 9. Empirical plot of $\langle\beta_{\text{ext}}\rangle$ vs $\langle\beta_{\text{b}}\rangle$ for cirrus cloud, September 15, 1988.

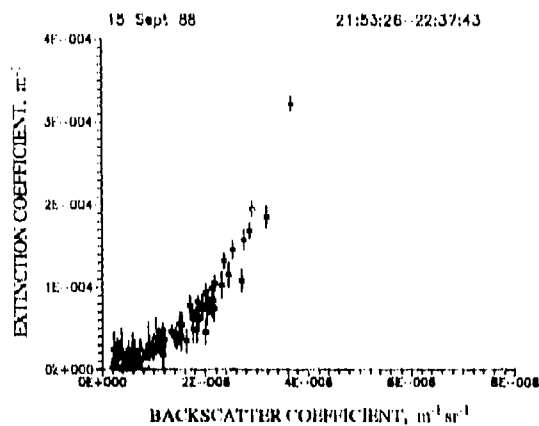


Figure 10. Linear representation of extinction data from Figure 9.

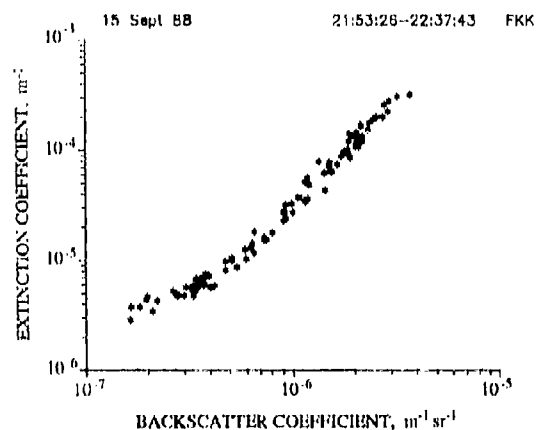


Figure 11. Prediction of mean extinction from backscatter profile alone, using non-linear fit to results of Figure 9 to carry out inversion of lidar backscatter by the method of Kaestner.⁶

Histograms showing distributions of cloud base height and cloud geometric depth are presented in Figs. 12 and 13 for observations made on the nights of September 15 and August 16, 1988. Cloud base heights were observed on September 15 in the range 8.9-9.7 km; on August 16, the heights were in the range 10.4-11.3 km. Cloud geometric depths measured on September 15 were 100 to 800 m, while on August 16 they were 100 m to 1.3 km.

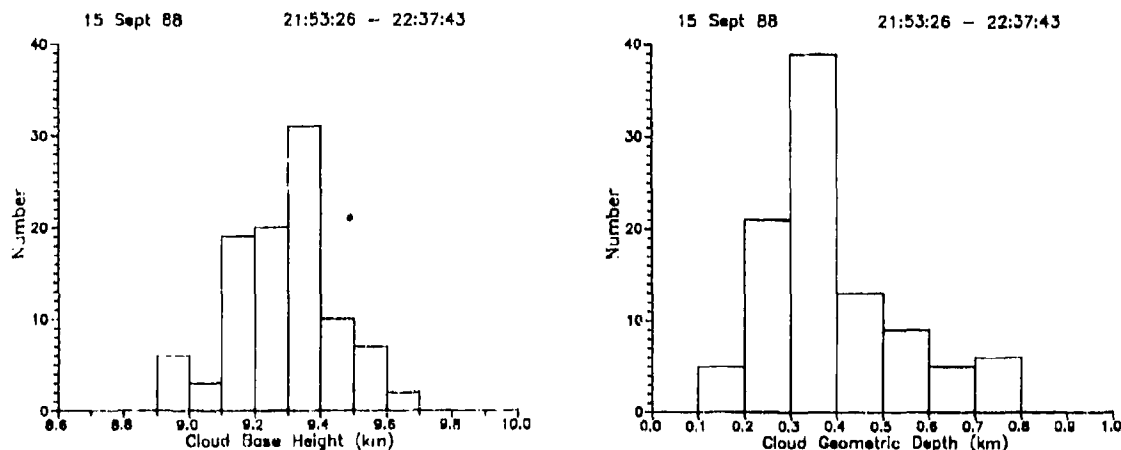


Figure 12. Histograms of cloud base height (left) and cloud thickness (right) for September 15, 1988 (College Park, MD).

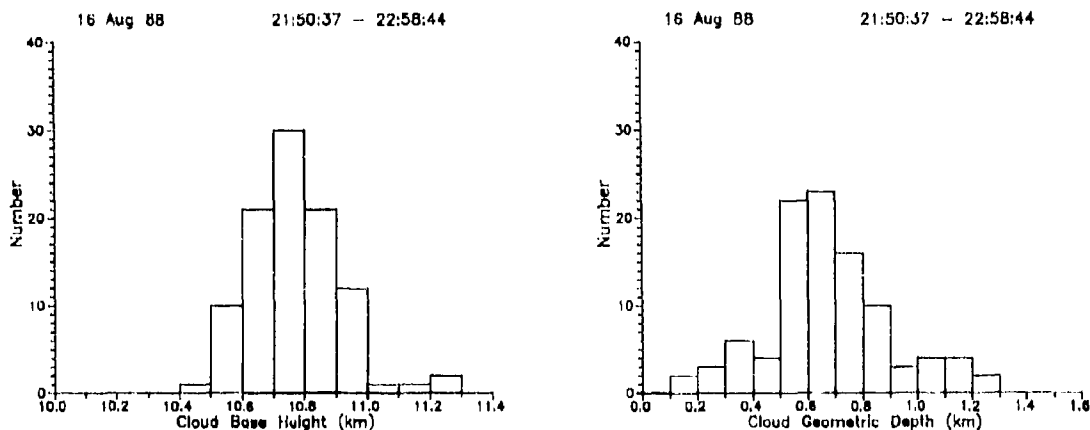


Figure 13. Histograms of clouds base height (left) and cloud thickness (right) for August 16, 1988 (College Park, MD).

Figure 14 compares the effective backscatter-to-extinction ratio of September 15 to the mid-cloud temperatures estimated from radiosonde data. The square in Figure 14 gives the position of the average values for the sample. The value of effective backscatter-to-extinction ratio at -36°C is the same as a value reported previously for this temperature.¹⁵ After accounting for their use of an isotropic backscatter coefficient ($= 4\pi$), the value given by these authors is 0.035, while the average value from Figure 14 is 0.035. Here we have ignored possible effects from multiple scattering inside the cloud, which is justified considering the narrow field of view of the receiver (1.2 mrad full angle).

The backscatter-to-extinction ratio is dependent on the cloud particle phase and crystal habit. Larger polycrystalline forms have been seen to predominate in cirrus clouds at temperatures greater than -40°C , while smaller and simpler crystal forms are more numerous¹⁶ at temperatures below -40°C to -50°C . Supercooled water droplets certainly exist in cirrus clouds at temperatures above -40°C , and there have been reports¹⁷ of manifestations of their presence at temperatures as low as -55°C . Since the backscatter-to-extinction ratio is thought to be greater for water droplets than ice crystals, and to be larger for the more complex ice crystals found at warmer tempera-

tures than for the simpler crystals found at lower temperatures, one expects greater values of this ratio at higher temperatures. Indeed, Platt and Dillely have found this to be the case in their observations,¹⁵ and have also noticed a sharp jump in the ratio at temperatures of -40°C and -50°C , where one might expect a change due to changing particle phase and crystal habit. Our observations will be geared toward increasing the number of results such as these presented, in order to enable us to draw more definitive conclusions on the microphysical properties of cirrus clouds.

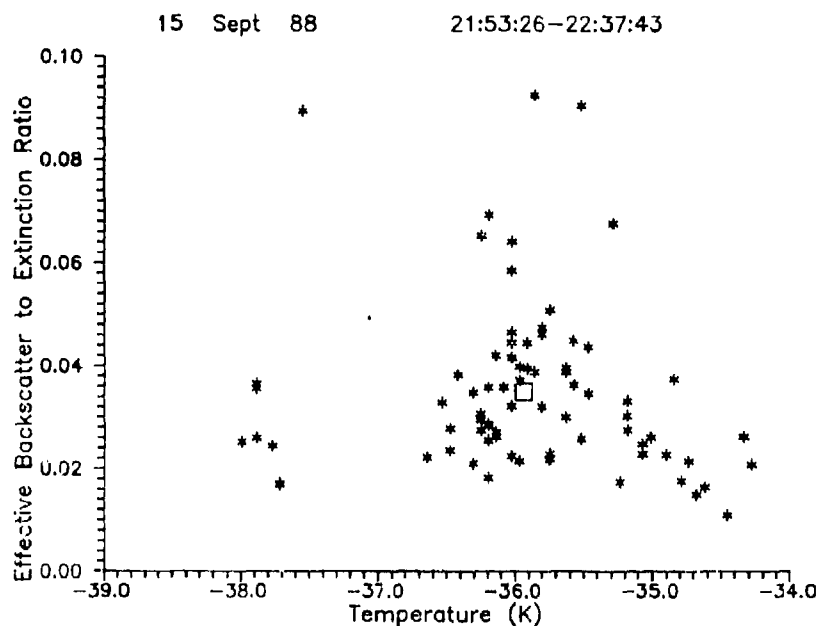


Figure 14. Observed values of the effective backscatter-to-extinction ratio for different values of mid-cloud temperature. Temperature is inferred from radiosonde profiles.

6. UPPER ATMOSPHERE OBSERVATIONS BY MEANS OF RAYLEIGH SCATTERING

This section reports examples of the measurement of thermal properties and fluctuations in the stratosphere and mesosphere, using Rayleigh backscatter intensity as a function of altitude.¹⁸⁻²³ This method employs the linear dependence of Rayleigh scattering on gas density, plus the ideal gas law and the hydrostatic pressure equilibrium of the atmosphere. Integration of these equations from high altitude downward yields profiles of the absolute temperature and the relative density.

Figure 15 shows plots of absolute temperature and relative density vs altitude for a 50-minute period on the night of March 16, 1989. The dashed curves represent climatological averages²⁴ for the month of March at our local latitude. The relative density is normalized to unity at 35 km altitude. Below this, the data are problematic because of saturation in the photon counter and possible aerosol contributions to the lidar return. The regions that we currently monitor with the greatest reliability are the upper stratosphere (35-50 km) and most of the mesosphere (50-70 km). While the stratosphere is relatively quiescent, the regions above the stratopause (~ 47 -50 km) display great variability in the density and temperature. Large density fluctuations can occur,^{4,5} the medium often appears "turbulent" with a dominant fluctuation scale size of order 1-3 km, and propagating gravity waves are frequently seen. In some cases, these atmospheric density fluctuations can have serious effects on high speed vehicle flight through the upper atmosphere.

Figure 16 is a similar presentation for November 21-22, 1988. Our data around this time showed large fluctuations and heating at altitudes above 60 km. This was just prior to a stratospheric warming event that peaked on December 12-13 and was detected by ground based lidar and passive satellite instruments. Analysis of our stratwarm data is continuing, and will be reported in the near future. For fundamental studies of the atmosphere for geophysics and meteorology, lidar offers convenient and frequent access to atmospheric regions that are difficult to monitor by other means.

7. CONCLUSION

We conclude by briefly addressing three main points. First, we summarize the results we have obtained in the Maryland lidar program. Secondly, we stress that our accomplishments are a small part of a mature lidar technology base that has undergone steady, international development over the past twenty years. Thirdly, we urge the defense R&D community to incorporate this technology more and more into atmospheric propagation projects.

Table 4 summarizes the Maryland results described in this presentation. We are continuing and broadening this work, and intend to use the transportable lidar at other sites of interest to DoD programs.

The capabilities of lidar systems in general extend well beyond the above topics to include atmospheric winds, temperature, pressure, humidity, turbulence, concentrations of minor species and pollutants, and atom/ion species and motions in the upper atmosphere. While scientists and engineers in the United States have played a major role in lidar developments, much of the initiative, excellence, and accomplishment in this field comes from other countries.

As a result of all this work, it is now possible to carry out, by means of lidar, almost any remote measurement of the atmosphere that would be required for electromagnetic propagation experiments. We suggest that atmospheric lidar is still a greatly underutilized technology, having the potential for long-awaited improvements in the efficiency, reliability and decisiveness of R&D programs in electromagnetic propagation.

TABLE 4. RESULTS - UNIVERSITY OF MARYLAND LIDAR (SEPTEMBER 1989)

-
- Atmospheric backscatter (aerosol/molecules) to 85 km altitude
 - Backscatter intensity (altitude - time plots)
 - Molecular temperature/density profiles (Rayleigh scattering) in stratosphere/mesosphere
 - Detection and morphology of optically thin cirrus ($\tau \geq .01$)
 - Depolarization by clear air and cirrus clouds
 - Independent backscatter and extinction coefficients for high clouds
 - Linear/non-linear relationships between backscatter and extinction
 - Extinction determined by inversion of lidar backscatter
 - Statistics on cirrus height, thickness, and optical properties vs temperature
-

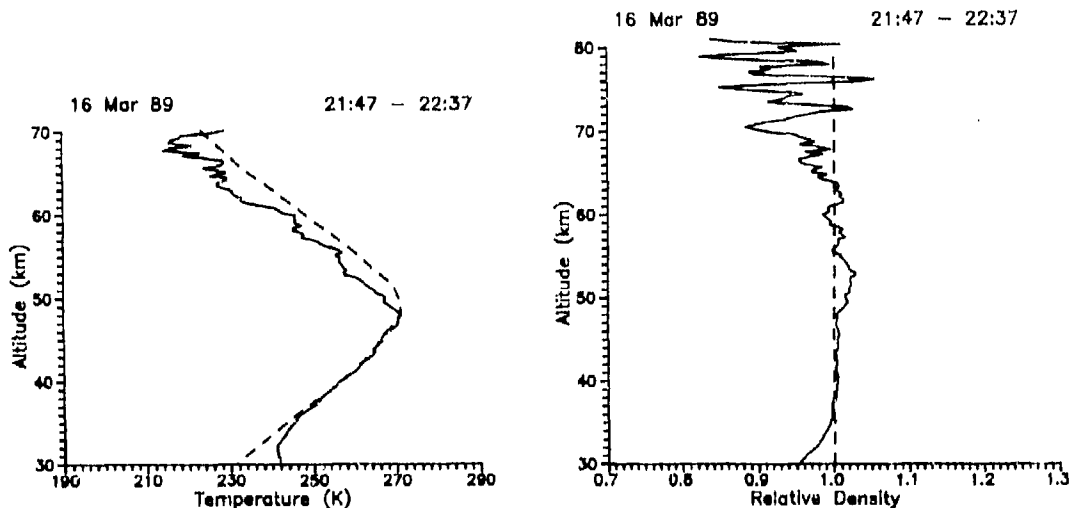


Figure 15. Vertical profiles of atmospheric temperature and density measured by lidar (March 16, 1989, College Park, MD). Altitude range of reliable data is 35-70 km.

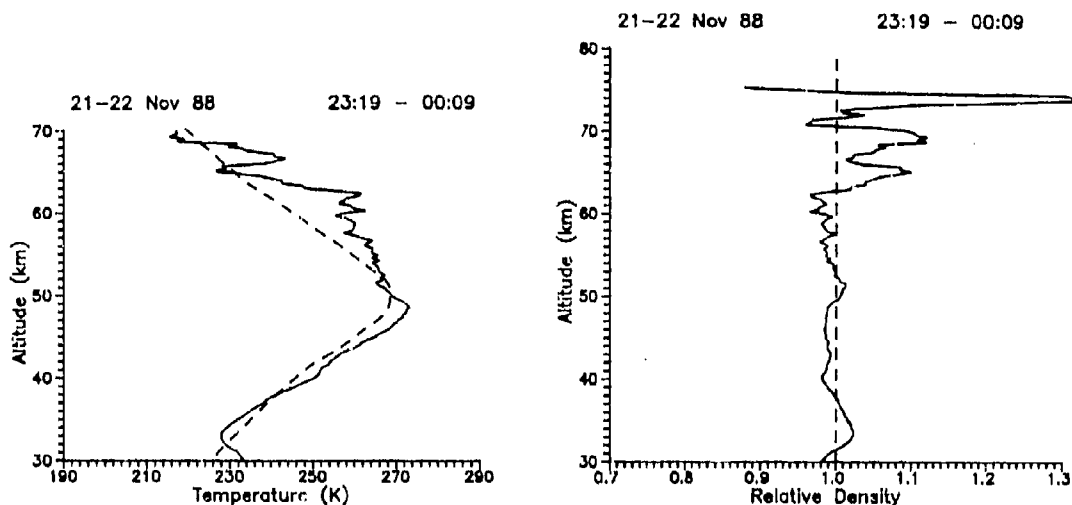


Figure 16. Lidar profiles of temperature and density (November 21-22, 1988, College Park, MD). Evidence of mesospheric heating and large density fluctuations above 60 km.

REFERENCES

1. R. M. Measures, *Laser Remote Sensing*, John Wiley & Sons, 1984, 510 pp. (1984).
2. J. A. Reagan, M. P. McCormick, and J. D. Spinhirne, "Lidar Sensing of Aerosols and Clouds in the Troposphere and Stratosphere", *Proc. IEEE*, 77, 433-448 (1989).
3. C. S. Gardner, "Sodium Resonance Fluorescence Lidar Applications in Atmospheric Science and Astronomy", *Proc. IEEE*, 77, 408 (1989).
4. L. J. Ehnberger, "High Altitude Turbulence for Supersonic Cruise Vehicles", NASA Technical Memorandum 88285 (1987).
5. R. C. Blanchard, P. W. Henson, and V. Nicholson, "Shuttle High Resolution Accelerometer Package: Experimental Results", *J. Spacecraft*, 26, 173 (1989).
6. M. Kaestner, "Lidar Inversion with Variable Backscatter/Extinction Ratios: Comment", *Appl. Opt.*, 25, 833-835 (1986).
7. F. G. Fernald, B. M. Herman, and J. A. Reagan, "Determination of Aerosol Height Distributions by Lidar", *J. Appl. Met.*, 11, 482-489 (1972).
8. J. D. Klett, "Stable Analytical Inversion Solution for Processing Lidar Returns", *Appl. Opt.*, 20, 211-220 (1981).
9. J. A. Ferguson, and D. H. Stephens, "Algorithm for Inverting Lidar Returns", *Appl. Opt.*, 22, 3673-3675 (1983).
10. F. A. Fernald, "Analysis of Atmospheric Lidar Observations: Some Comments", *Appl. Opt.*, 23, 652-654 (1984).
11. J. M. Mulders, "Algorithm for Inverting Lidar Returns: Comment", *Appl. Opt.*, 23, 2855-2856 (1984).
12. J. D. Klett, "Lidar Inversion with Variable Backscatter/Extinction Ratio", *Appl. Opt.*, 24, 1638-1643 (1985).
13. W. C. Braun, "General Formula for the Errors in Aerosol Properties Determined from Lidar Measurements at a Single Wavelength", *Appl. Opt.*, 24, 925-927 (1985).
14. W. Garnuth, and R. Reiter, "Cloud Extinction Profile Measurements by Lidar using Klett's Inversion Method", *Appl. Opt.*, 25, 2899-2907 (1986).
15. C. M. R. Platt and A. C. Dilley, "Remote Sounding of High Clouds: IV: Observed Temperature Variations in Cirrus Optical Properties", *J. Atmos. Sci.*, 38, 1069-1081 (1982).
16. A. J. Heymsfield and C. M. R. Platt, "A Parameterization of the Particle Size Spectrum of Ice Clouds in Terms of the Ambient Temperature and the Ice/Water Content", *J. Atmos. Sci.*, 41, 846-855 (1984).

17. K. Sassen, D. O'C. Starr, and T. Uttal, "Mesoscale and Microscale Structure of Cirrus Clouds: Three Case Studies", J. Atmos. Sci., 46, 371-396 (1989).
18. A. Hauchecorne and M.-L. Chanin, "Density and Temperature Profiles Obtained by Lidar between 35 and 70 km.", Geophys. Res. Lett., 7, 565 (1981).
19. A. Hauchecorne and M.-L. Chanin, "Mid Latitude Ground-Lidar Study of Stratospheric Warmings", J. Atmos. Terr. Phys., 44, 577 (1982).
20. M.-L. Chanin, "Review of Lidar Contributions to Understanding of the Middle Atmosphere", J. Atmos. Terr. Phys., 46, 3843 (1983).
21. A. Hauchecorne and M.-L. Chanin, "Mid-Latitude Lidar Observations of Planetary Waves in the Middle Atmosphere During the Winter of 1981-1982", J. Geophys. Res., 88, 3843 (1983).
22. M.-L. Chanin, A. Hauchecorne and N. Smires, "Contributions to the CIRA Model from Ground-based Lidar", MAP Handbook, 16, 305 (1985).
23. T. Shibata, T. Kukuda and M. Maeda, "Density Fluctuations in the Middle Atmosphere over Fukuoka Observed by a Xef Rayleigh Lidar", Geophys. Res. Lett., 13, 1121 (1986).
24. A. S. Jursa, Ed., Handbook of Geophysics and the Space Environment, Air Force Geophysics Laboratory, NTIS, Springfield, VA 22161 (1985).

ACKNOWLEDGMENTS

The authors express their appreciation for the following: to M. Martins, B. Bloomer, G. Treacy, A. Chu and S. Yang for contributions to the results reported here; to L. Cotnoir and G. Schwemmer for past contributions to the program; and to J. Yorke, P. Twitchell, W. Hoppel, and M. Salinas for their continued interest and support; to NASA's Langley Research Center for the donation of the 60 cm. diameter telescope.

DISCUSSION

B. EVANS

Do you have any physical insight as to your non-linear relationship between β (backscatter) and σ (extinction)?

AUTHOR'S REPLY

We do not believe that there is any intrinsic non-linear relationship between the amounts of β and σ in any given scattering event, but rather that some unmeasured cloud property (e.g. particle distribution function) changes as we go from thin to thick clouds within a given set of observations. Multiple scattering (MS) is not responsible for the non-linear relationship between the effective extinction and the effective backscatter; MS would cause the logarithmic curves to bend the other way, i.e., to have a slope less than unity.

J. RICHTER

A relationship between backscatter and extinction holds only for aerosols of the same compositions and origin. If you have overlying air masses of unknown aerosols, you don't know the backscatter - extinction relationship and, therefore, can't infer extinction profiles through such layers.

AUTHOR'S REPLY

What we have done is to establish some approximate calibrations of high cloud extinction in terms of the easily-measured lidar quantity - namely the backscatter profiles. In so doing, we find systematic - and to some degree non-linear - relationships between the observed total extinction and the observed mean backscatter. This is very useful, because we can infer extinction from backscatter in future observations, at least to within certain error bounds. Also, it is a fact that, when we employ two aforesaid non-linear relationships in a Fernald-Klett-Kaestner inversion of the backscatter alone, we obtain good agreement between the calculated total extinction by these high clouds and the empirical total extinction. I am sure there are situations in which the β - σ relations (along the lidar line of sight) are so variable that the inversion process would not be reliable. However, I suggest that, even there, the use of data from the total extinction versus mean backscatter method may bound the β - σ relationship sufficiently that the extinction profiles (derived from the resulting inversion) are satisfactory for some purposes. Further, I suggest that experiments of this type be carried out for the

Lidar Measurement of Concentration and Turbulence in Battlefield Obscurants

by

B.T.N. Evans and G. Roy

Defence Research Establishment, Valcartier

2459, Pie XI Blvd., North (P.O. Box 8800)

Courcelette, Quebec, G0A 1R0

Canada

ABSTRACT

Concentration inhomogeneities, caused by turbulence, in obscurant clouds are studied by using a rapidly scanning lidar. Spatial correlograms in the three spatial directions are derived and are related to atmospheric stability. Implications of these inhomogeneities for obscurant effectiveness and interdevice comparison are discussed.

1. INTRODUCTION

It is known that obscurant clouds, produced in the field, have significant concentration inhomogeneities. Large concentrations can give excellent screening against enemy threats, however, low concentrations may give the enemy significant time to lock on to a friendly target. It is therefore important to have an understanding of the statistical size of the concentration inhomogeneities under different atmospheric conditions.

To date the rapid changes in concentrations have not been studied to any great extent since it is extremely difficult to model or measure these fluctuations in realistic conditions. This paper is an early attempt to directly measure some of the statistical behaviour of these fluctuations. To do so, the results obtained by the Laser Cloud Mapper (LCM) from Smoke Week IX (SWIX) have been used. The Smoke Weeks are large obscurant events operated by the PM Smoke/Obscurant office of the US Army. SWIX was held from 4-17 May 1987 at Eglin Air Force Base in Florida (see (1)). During this set of trials the LCM measured the smoke concentration for many obscurant types and different atmospheric stabilities (Pasquill stabilities). Furthermore, since the LCM rapidly scans the entire cloud, details of the concentration and transmission inhomogeneities can be obtained. Also, LCM derived concentrations were compared with 20 90°-nephelometers that were placed *in situ* in a line in the cloud. It was found during the comparison, that the concentration inhomogeneities can be extreme, especially in the vertical direction, hence detailed knowledge of the correlation lengths in the region of the comparison is required to perform a fair comparison.

2. BRIEF DESCRIPTION OF THE LASER CLOUD MAPPER

The LCM was originally developed by OPTECH Inc., Downsview, Ontario in 1980 for DREV. It is a rapidly scanning Lidar system that operates a 1.06 μm Nd:YAG laser with a 100 Hz repetition frequency. The nominal pulse length is about 10 ns. The direction of the laser beam is constrained by a rotating mirror to form laser fire positions in a raster scan pattern. This scan pattern as well as the pulsing laser allows the LCM to interrogate the cloud in the three spatial dimensions as well as time. A typical 'snapshot' of the cloud takes

about 2.0 s to perform and can be repeated every 4 s. A schematic of the LCM operation is shown in Fig. 1.

A typical trial setting for the LCM is to fire 30 – 40 shots horizontally over 90° of azimuth for 5 – 6 different elevation angles. Thus between 150 to 240 shots may be involved in scanning a cloud at one time. More or less shots and/or more or less elevation angles can be used to vary the azimuthal and vertical resolution. The radial resolution can be varied from 1.5 m to very coarse distance intervals. The best radial resolution is usually preferred. For the SWIX trials the LCM was usually set to 36 shots for each horizontal sweep with 6 sweeps making up a full scan. Thus 216 shots comprised a scan. More information of the LCM can be found in (2) and (3).

3. TRIAL SETUP AND DATA REDUCTION

A schematic of the trial layout for the LCM at SWIX is shown in Fig. 2. Shown are the smoke release area, typical positions of the smoke generators and the line of nephelometers and the position of the LCM. For this trial the LCM was set up to scan the laser over 90° in azimuth and between 5° to 10° in elevation. Usually the radial resolution was set to about 1.5 m with 100 bins (radial resolution elements) to each shot. The electronic delay, or the point from the LCM where the data was collected, was varied so that the obscurant cloud was near the front part of each shot. As the wind direction varies this positioning of the cloud with respect to the LCM data collection was imperfect and hence was not always ideal.

Most of the SWIX trials lasted for 1-2 minutes. In this time the LCM collected 9 statistically independent whole volume samples of the cloud concentration.

The cloud concentration is obtained by inversion of the lidar equation and using the ancillary relations that relate backscatter to extinction and extinction to concentration. The monostatic Lidar equation is

$$P = P_0 F(r) \frac{c\tau}{2} \frac{A}{r^2} \beta(r) e^{-2 \int_0^r \sigma(r') dr'} \quad [1]$$

where P is the return power, P_0 is the initial laser pulse power, $F(r)$ is a system specific function, c is the speed of light, τ is the laser pulse length, A is the receiver area, β is the backscatter coefficient, and σ is the extinction coefficient. The backscatter to extinction relation used is the linear relation

$$\beta(r) = \Re \sigma(r) \quad [2]$$

where \Re is the Lidar ratio. The final relation required is

$$C(r) = \alpha \sigma(r) \quad [3]$$

where $C(r)$ is the range resolved concentration and α is the volume or linear extinction coefficient.

The method of inversion employed is similar to, but not the same as, the now often used inversion method of Klett (4). Unlike in (4), this inversion method requires only one boundary term for a whole set of trials as opposed to a new boundary condition for each Lidar shot.

The inversion method and validity of [1] can be found in (5) and the range of validity of [2] is discussed in (6). As of yet the validity of [3] has not been detailed in the literature but it is known to be valid for aerosols not changing in particle size distribution and for some combinations of wavelength and water aerosols (7). The mass extinction coefficients have been obtained in the field (8) and in aerosol chambers (9) and (10) for a variety of obscurants.

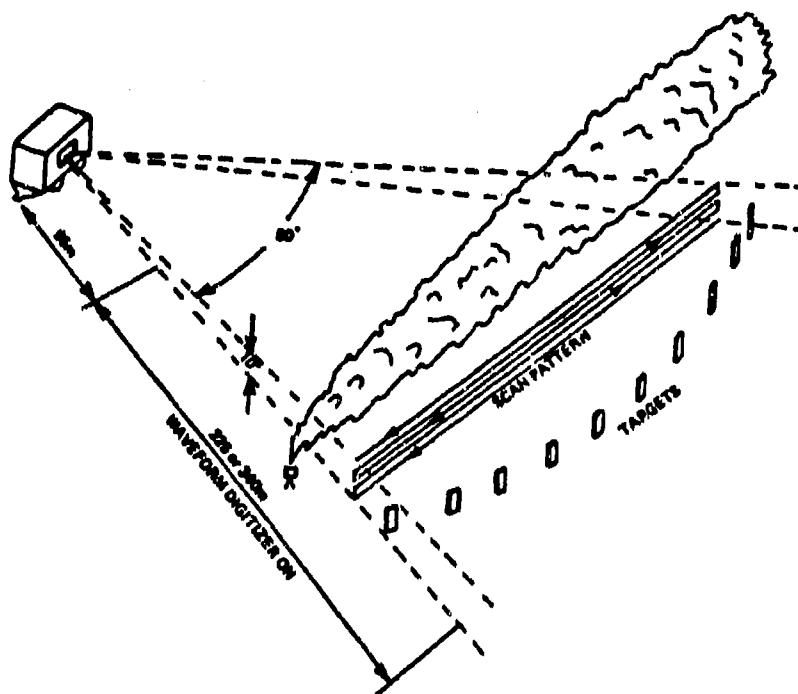


Fig. 1- Schematic of the Laser Cloud Mapper operation.

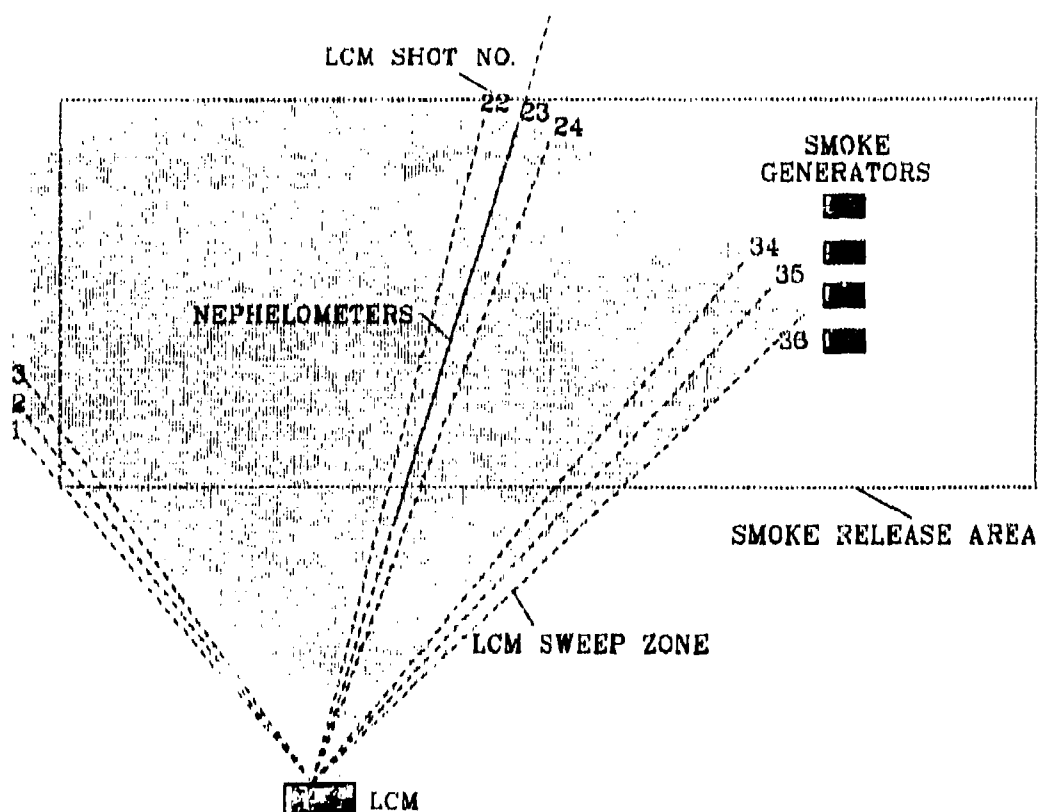


Fig. 2- Schematic of trial layout of the LCM at SWIX.

4. CORRELATION LENGTHS

The statistical parameter used to analysis the data from the LCM to indicate the extent of concentration inhomogeneities is defined here as the correlation length. It is defined, in analogy to the scale of turbulence (11) and (12), as

$$\ell_\delta = \int_0^\infty R_\delta(x) dx \quad [4]$$

where ℓ is the correlation length, r is the distance between any two points in the δ direction, and R is the correlation function defined as

$$R_\delta = \overline{C_i C_j} / \overline{C^2}. \quad [5]$$

Here, C_i is the aerosol concentration at point i and $\overline{C^2}$ represents the average of the concentration squared over time. It is assumed here that $\overline{C^2}$ is independent of small changes in the cloud. This is consistent with the assumptions inherent in [5], i.e. of statistical homogeneity and isotropy. The different directions that will be considered here are the radial, r , azimuthal, θ and vertical, v , directions. Since for a majority of trials the wind direction was perpendicular to the central LCM shot direction, the radial direction can be considered the same as the cross wind direction.

Since the LCM obtains information on C_i over a great many different positions and times, it is possible, using the above definition to estimate R , and hence, ℓ at any point inside the cloud within the spatial resolution of the LCM of the particular direction.

Again, in analogy with the scale of turbulence (11), the correlation function R can be modeled by a gaussian curve. Here we will use the average \overline{R} instead of R since we want a statistical average of the concentration scale. Thus we have

$$\overline{R}_\delta = e^{-\frac{x^2}{2\sigma_\delta^2}}. \quad [6]$$

With this model we then have

$$\overline{\ell}_\delta = \sqrt{\pi}/2\sigma_\delta. \quad [7]$$

This means that an estimate of $\overline{\ell}_\delta$ is given approximately by $\overline{\ell} = x'$ where $\overline{R}_\delta(x') = .5$. This will be made more clear in the following section discussing results.

5. RESULTS AND DISCUSSION

For many types of obscurants and atmospheric stability conditions \overline{R}_δ and consequently $\overline{\ell}_\delta$ have been derived from the LCM data. Attempts to relate these quantities to atmospheric stability, obscurant type and distance into the cloud are discussed in this section.

Examples of \overline{R}_δ versus distance from the point in question, for fog oil are given in Figs. 3-5. Plotted in the diagrams are \overline{R}_θ in Fig. 3, \overline{R}_r in Fig. 4 and \overline{R}_v in Fig. 5. These plots are sometimes called correlograms. Shown, in Figs. 3-4, are three different trials, each curve being an average over 9 statistically independent samples at the same position. Note that \overline{R}_δ rapidly decreases from 1 to values less than .5. Figure 5 is for only one fog oil trial but shows the variation with distance from the LCM instead. In Fig. 3, $\overline{\ell}_\theta \approx 20 - 30$ m using the criterion in the last paragraph of the last section. From the latter two diagrams we can estimate $\overline{\ell}_r \approx 15 - 40$ m and $\overline{\ell}_v \approx 1 - 2.5$ m. Although $\overline{\ell}_r \approx \overline{\ell}_\theta$ for these cases $\overline{\ell}_v$ is much smaller. This shows, as is generally known, that ℓ is an anisotropic quantity.

No discernible relationship between $\overline{\ell}_r$ or $\overline{\ell}_v$ and the various obscurant types could be found. This is shown in Figs. 6-7. Figure 6 shows $\overline{\ell}_r$ for 8 different obscurant types and Fig. 7 shows $\overline{\ell}_v$ for the same obscurant types. It is surprising at first that the generator

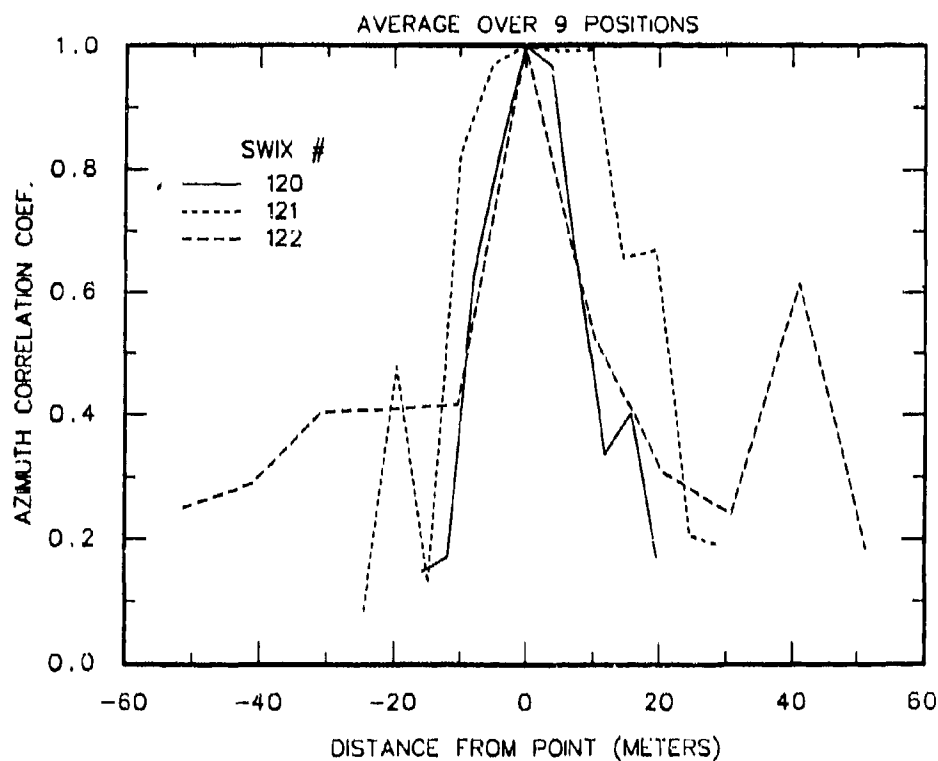


Fig. 3- Correlogram of the azimuthal correlation coefficient versus distance from point in question for fog oil trials SWIX 120, 121, and 122.

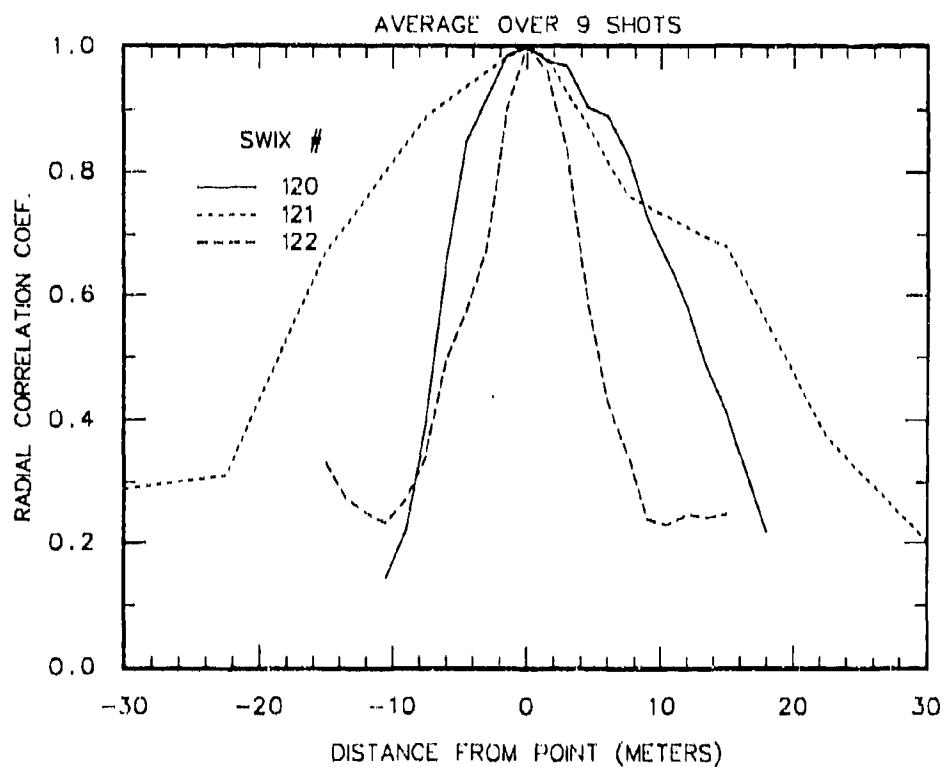


Fig. 4- Same as Fig. 3 but the radial correlation coefficient is plotted.

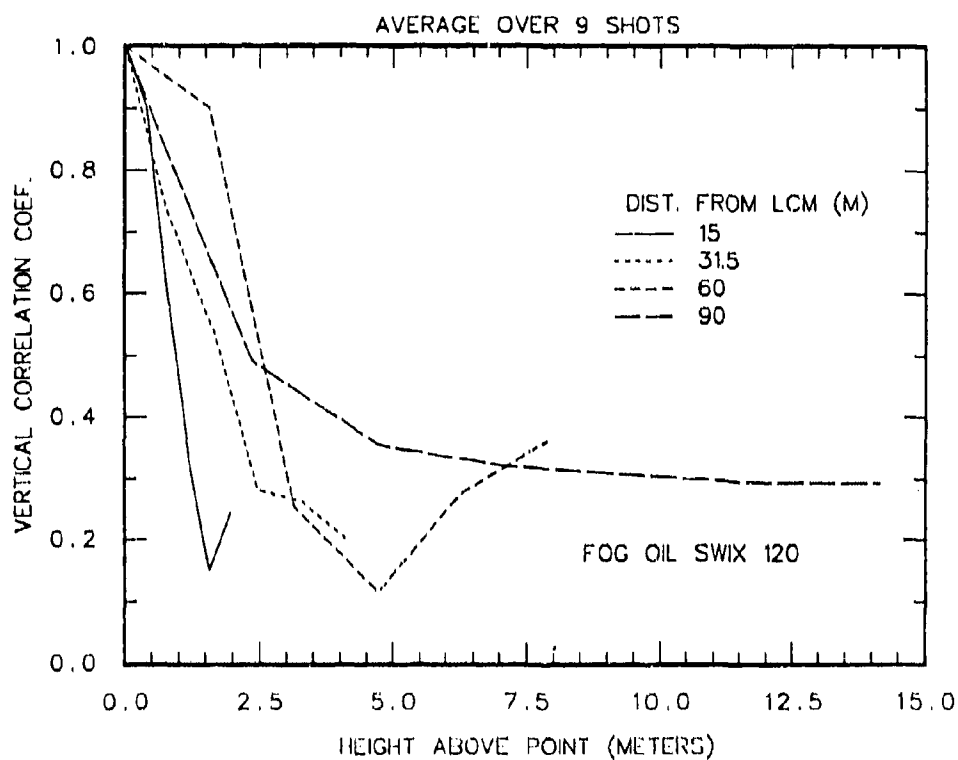


Fig. 5- Correlogram of the vertical correlation coefficient versus height above point in question for difference distances from the LCM. The trial is a fog oil smoke SWIX 120.

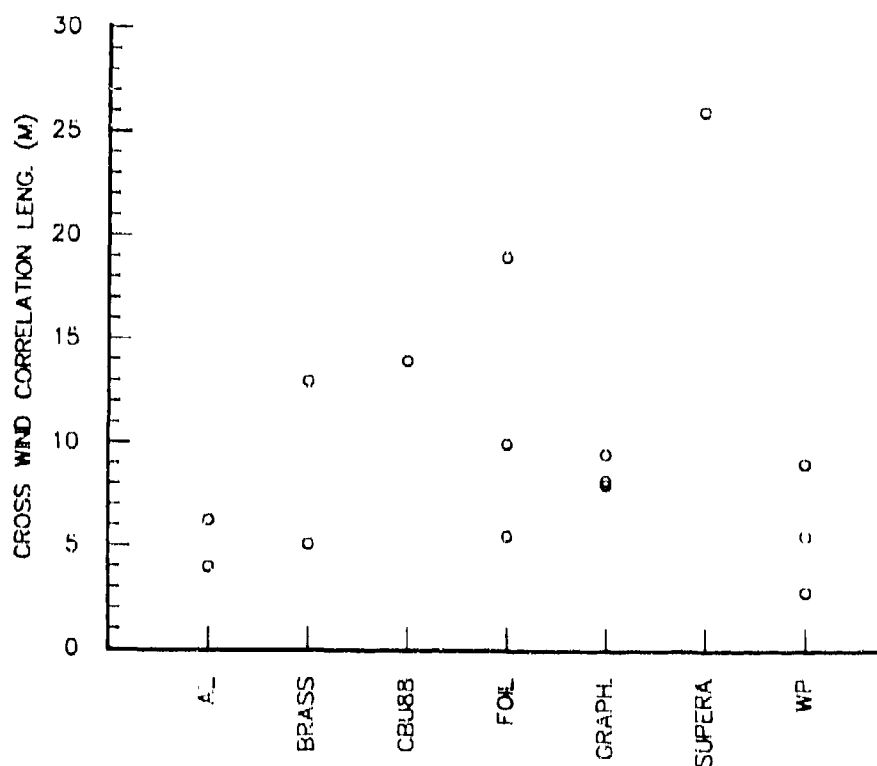


Fig. 6- Cross wind (or radial) correlation length versus obscurant type.

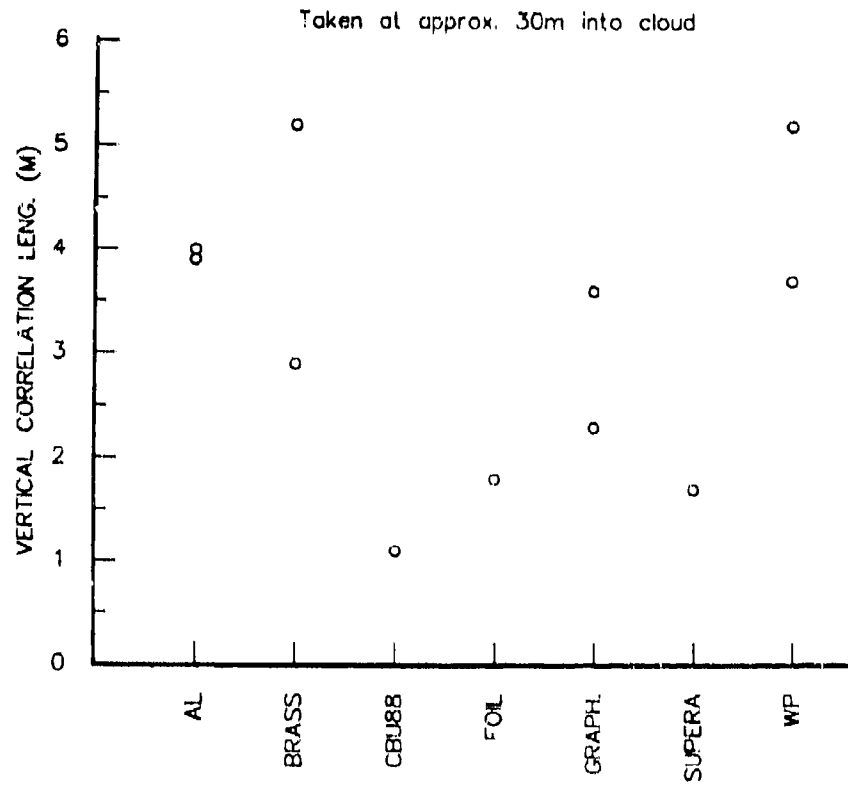


Fig. 7- Vertical correlation length versus obscurant type.

trials (those for aluminum, brass, graphite flakes and fog oil) are not different from the pyrotechnically produced phosphorous trials (white phosphorous, super arboc and CBU88). The explanation may be that the aerosols were thermalized to the ambient temperature before reaching the particular point used for this study. Also there was a tendency to have generator trials under slightly unstable or neutral conditions whereas many phosphorous trials were held under more unstable or more stable conditions.

During the SWIX trials many different atmospheric stability categories were encountered. This allows for a study to see if there is any trend between the correlation length and atmospheric stability (here summarized by the Pasquill category). The categories, A-G vary in the degrees of stability from very unstable to extremely stable, category D being the neutral condition. The data set from the SWIX trials did not have any cases with A or E stability categories. In the cross wind or radial direction a trend with the Pasquill category can be seen in Fig. 8. The results from 15 different trials including different obscurant types. It is evident that the correlation length in the cross wind direction increases with increasing atmospheric stability. This is not surprising since the more stable conditions produce layering of the atmosphere whereas the unstable conditions are more turbulent and thus break up the layering. Note that $\bar{z}_r \approx 3 - 5$ m for B stability, $\bar{z}_r \approx 8 - 15$ m for neutral stability D, and $\bar{z}_r \approx 10 - 25$ m for the very stable conditions F and G. The point for G stability should be considered tentative since there is only one point and the obscurant used (Super Arboc) is created by many sub-source points.

A similar plot to Fig. 8 is Fig. 9 that shows the vertical correlation length plotted against the Pasquill category. Note in this case that, although the trend is less obvious, there is a tendency for this length to decrease with increasing atmospheric stability. This is presumably since as the atmosphere is more layered in very stable conditions there is little connection between the variations between the concentration in one layer and another. This connection is increased with increasing turbulence. Here $\bar{z}_v \approx 3.6 - 5.2$ m for the unstable conditions, $\bar{z}_v \approx 1.8 - 3.6$ m for neutral stabilities, and $\bar{z}_v \approx 0.8 - 2$ m for the very stable conditions. It is interesting to note that $\bar{z}_r \approx \bar{z}_v$ for category B. It is desirable to know the trend for category A. Again the point for G should be considered tentative. Since, in general, $\bar{z}_v \leq \bar{z}_r$, an interdevice comparison should be performed at the same vertical height.

From the preceding two diagrams, Fig. 8 and 9, a lesson can be drawn in any attempt to compare two instruments that measure the same quantity that involves concentration. If the distance between the measuring points of the two instruments is of the order of \bar{z}_s or less it should not be expected that the two devices will agree at all points even if each is a perfect measuring system. Furthermore since it appears that \bar{z}_s is a function of atmospheric stability this factor must be included in the analysis of the comparison.

In order to see if there is any link between the distance into the cloud and \bar{z}_r or \bar{z}_v the point for the same stability category were averaged and then plotted. The averaging being performed as an attempt to amplify any tendency. The result is Figs. 10 and 11. These are plots of \bar{z}_r or \bar{z}_v respectively with distance into cloud separated into the different Pasquill categories. No apparent trend is noticeable in Fig. 10. However, in Fig. 11, \bar{z}_v appears to increase about 30 m into the cloud and then decrease for the unstable conditions and does not change for the neutral and stable categories. It should be pointed out that the typical generator width was about 30 m (as measured by the LCM) and thus the behaviour of \bar{z}_r or \bar{z}_v into the cloud may be explained by this. However the two trials used for Pasquill category B were white phosphorous clouds. This makes the interpretation difficult.

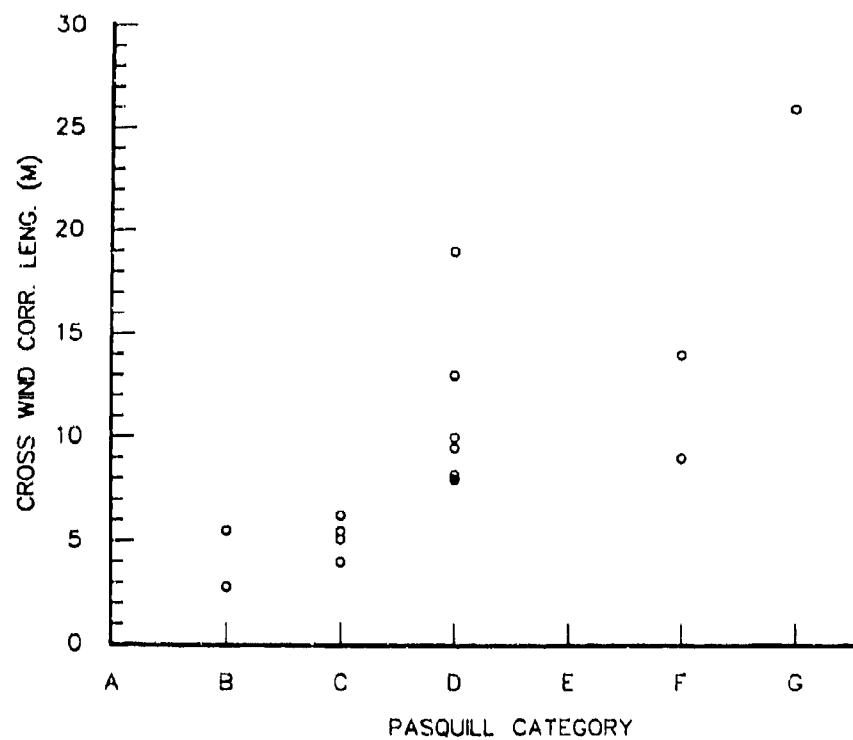


Fig. 8- Cross wind (or radial) correlation length versus Pasquill stability category.

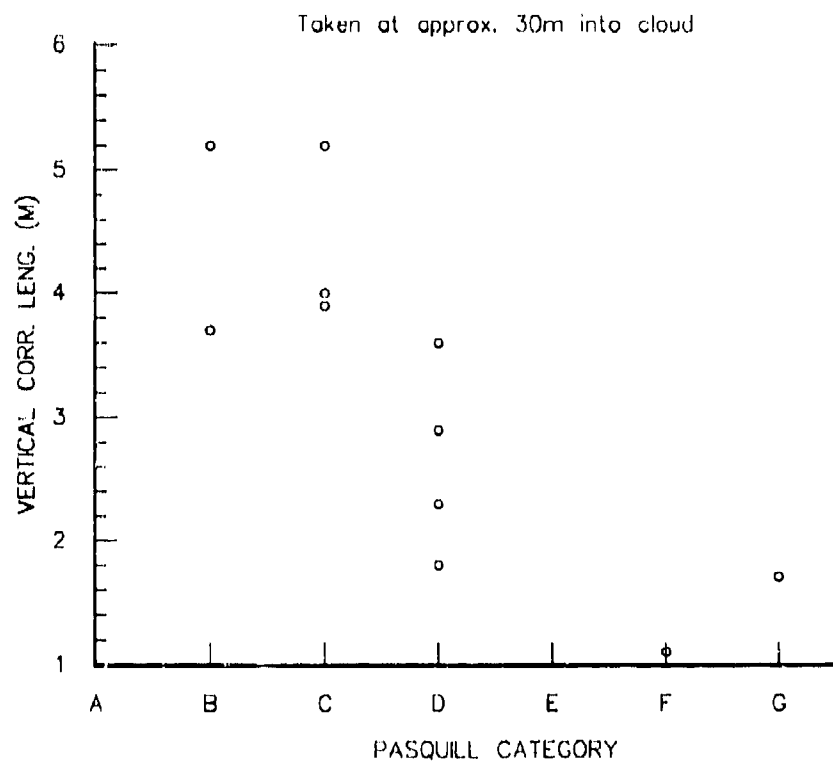


Fig. 9- Vertical correlation length versus Pasquill stability category.

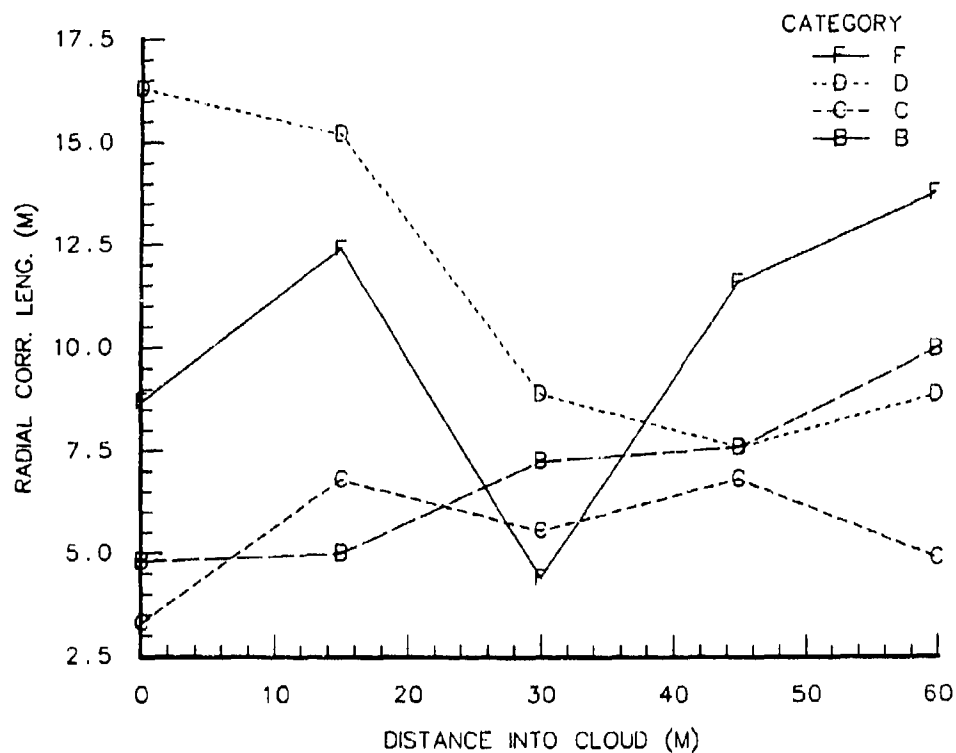


Fig. 10- Averaged radial correlation length versus distance into cloud for various Pasquill categories.

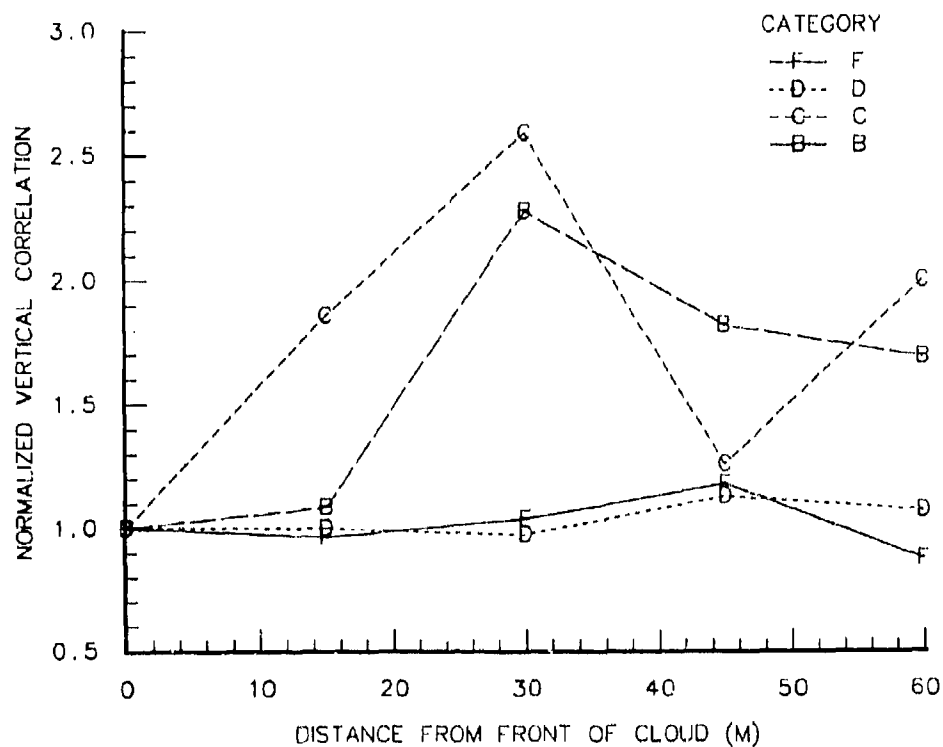


Fig. 11- Normalized and averaged vertical correlation length versus distance from front of cloud for various Pasquill categories.

5. SUMMARY

Result of the LCM obtained from Smoke Week IX were analyzed to obtain information on the statistical spatial extent of concentration inhomogeneities in obscurant clouds under realistic conditions. Seven different obscurant types are included in the discussion as well as five different Pasquill stability categories. It is tentatively shown that the average cross wind correlation length, $\bar{\ell}_r$, increases and the average vertical correlation length, $\bar{\ell}_v$, decreases with atmospheric stability. This is probably due to the amount of layering or turbulence occurring under a given atmospheric stability. As the atmospheric stability increased, $\bar{\ell}_r$ varied from ≈ 3 m to over 15 m and $\bar{\ell}_v$ went from ≈ 5 m to 0.8 m.

No effect on these correlation lengths was found by changing the obscurant type. This is possibly due to the selectiveness of performing generator trials under more neutral conditions than the pyrotechnically produced events.

Very preliminary results indicate that the vertical correlation lengths may increase with increasing by distance into the cloud.

6. REFERENCES

1. Farmer, W.M., Soto, R.F., Locke B.A. and Steedman, J.E., "Evaluation of Electro-Optical System Performance in Luminous and Emissive Smoke and Obscurant Environments", Science and Technology Corp., STC 2179, July 1987.
2. Evans, B.T.N., Kluchert R.E., Levesque, R.J., Evans, A. and Roy, G., "Field Evaluation of a Canadian Laser Cloud Mapper and Candidate IR Screening Aerosols", Defence Research Establishment, Valcartier, DREV R-4271/82, November 1982.
3. Evans, B.T.N. and Roy, G., "Laser Cloud Mapper and Its Applications", Proceedings of SPIE, Vol 663, pp174-181, 1986.
4. Klett, J.D., "Stable Analytical Inversion Solution for Processing Lidar Returns", Applied Optics, Vol. 20, No. 2, pp. 211-220, 1981.
5. Evans, B.T.N., "On the Inversion of the Lidar Equation", Defence Research Establishment, Valcartier, DREV R-4343/84, November 1984.
6. Evans, B.T.N., "Sensitivity of the Backscatter/Extinction Ratio to Changes in Aerosol Properties: Implications for Lidar", Applied Optics, Vol. 27, No. 15, pp.3299-3305, 1988.
7. Pinnick, R.G., Jennings, S.G., Chylek, P., Ham, C. and Grandy, Jr, W.T., "Backscatter and Extinction in Water Clouds", J. Geophys. Res. Vol. 88, p6787, 1983.
8. Shirkey, R.C., Sutherland, R.A. and Seagraves, M.A., "EOSAEL 87, Aerosol Phase Function Data Base PFNDAT", Vol. 26, Atmospheric Sciences Labs., ASL TR-0221-26, 1987.
9. Huffman, D.R., "Extinction Measurements on Aluminum and Carbon Smoke Particles from Far Infrared to Far Ultraviolet", Chemical Research, Development and Engineering Center, Aberdeen Proving Ground, CRDEC-CR-98059, 1987.
10. Roy, G. and Vallée, G., "Laboratory Evaluation of Potential Infrared Screening Powders", Defence Research Establishment, Valcartier, DREV R-4427/86, 1986.
11. Pasquill, F., "Atmospheric Diffusion", D. Van Nostrand Co. Ltd., Toronto, 1968.
12. Taylor, G.I., "Statistical Theory of Turbulence, Part I", Proc. of the Royal Society, A, Vol. 151, pp421-44, 1935.

DISCUSSION

W. CARNUTH

How do you get the data in grams per m^3 in your lidar-nephelometer comparison from the data in optical units?

AUTHOR'S REPLY

I first obtain the volume or linear extinction coefficient by using lidar inversion. To obtain the concentration from this, I use independent experimental or field measured values of the mass extinction coefficient. Thus the concentration is obtained by dividing the volume extinction by the mass extinction coefficients.

Cirrus Cloud Optical Properties Measured with the University of
Wisconsin High Spectral Resolution and Volume Imaging Lidars

E.W. Eloranta and G.J. Grund
University of Wisconsin
1225 W. Dayton
Madison, WI 53706
USA

The High Spectral Resolution Lidar (HSRL) provides calibrated range-resolved measurements of atmospheric optical parameters. These measurements include: the optical backscatter cross section, extinction cross section, optical depth and, when the absorption cross section is negligible, the backscatter phase function. Calibrated measurements are achieved by partitioning the lidar signal into separate aerosol and molecular scattering components. The separation is possible because the molecular signal is spectrally broadened by Doppler shifts from the thermal velocities of the molecules while the aerosol return spectrum is nearly unaffected by the slow Brownian motions of the aerosols. Details of the HSRL system can be found in Grund (1987) and Shipley et. al. (1983).

Visible and subvisible cirrus cloud optical properties measured at a wavelength of 510 nm with the HSRL are presented in this paper. Backscatter cross sections between 5×10^{-5} (km sr^{-1}) to 0.18 (km sr^{-1}) have been measured along with backscatter phase functions in the range between $.02 \text{ sr}^{-1}$ and $.065 \text{ sr}^{-1}$ (phase function values are presented in normalized form: i.e. divided by 4π). The highest values of both backscatter cross section and back-scatter phase have been observed in layers where cirrus is forming by the glaciation of altocumulus clouds; these values are likely to represent the dominate optical effect of liquid water in mixed phase clouds. Clouds with optical depths ranging from .003 to 2.9 have been observed; at the low end of this range the clouds are not visible to the eye. These subvisible clouds often occur at the same altitude as visible cirrus and in spaces between visible clouds. Figure 1 presents an example of the tenuous enhanced backscattering often observed with the HSRL at cirrus altitudes. While we refer to these clouds as subvisible "cirrus" it is possible that at least some of them are aerosol dense regions rather than ice clouds. Since 2.9 is largest optical depth we can currently observe with the HSRL this does not represent the maximum optical depth of cirrus; however, most cirrus optical depths are smaller than this limit. Table 1 provides examples of the mid-cloud altitudes, the optical thickness, and the backscatter phase function observed in cirrus clouds with the HSRL. The mid-cloud temperatures reported in this table were derived from radiosonde data. Figure 2 plots optical thickness of cirrus clouds as a function of their mid-cloud temperature. It is clear that maximum optical thickness increases in warmer clouds as might be expected because of the potentially larger total water content of air at higher temperatures. Platt and Dillay (1984) present evidence of an abrupt change in the backscatter phase function of cirrus clouds at a temperature of -40°C . Figure 3 presents their results along with measurements obtained from the HSRL. Although the error bars on the HSRL observations are still quite large and the scatter could possibly obscure evidence of a sharp transition, cirrus clouds over Madison, Wis. do not appear to show the same behavior. Figure 4 shows a comparison of cirrus cloud optical depths measured with the HSRL and thermal emissivities measured by satellite with the CO_2^{-2} slicing method (for details of the method see Menzel et. al. (1983)). These preliminary observations lend support to the model results of Hansen (1971) which are also plotted in the figure.

The University of Wisconsin also operates a Volume Imaging Lidar (VIL) optimized for three-dimensional mapping of atmospheric structure. This lidar couples a 0.6J, 30Hz Nd-YAG laser, with a 0.5 m diameter receiver, a 20 degree/sec beam scanning unit and data system capable of acquiring, displaying and storing data at sustained high rates. In a single thirty second scan this lidar can produce a high resolution picture, composed of 900 lidar profiles, depicting a 200 km long segment of a cirrus cloud.

Images of cirrus clouds obtained with the volume imaging lidar show diverse cirrus morphologies. The thickness of cirrus layers vary from less than 100 meters to over 8 kilometers. In the cirrus anvils of thunderstorms, thin stable layers (order of 100 meters) are interspaced with chaotic apparently turbulent layers. Other clouds show multiple thin horizontal layers distributed over many kilometers of depth with occasional shafts of wind sheared ice crystal virga falling through the entire depth of the cloud region. In some cases, wind sheared cirrus cells overlap to produce a venetian blind effect so as to provide frequent holes when the cloud is viewed at small elevation angles in one direction and continuous coverage when viewed in other directions. Specular reflections from horizontally oriented, flat faced crystals are frequently observed when the lidar is pointed vertically. The scattering cross section often increases by more than a factor of ten within a degree of the zenith. The crystal forms in the cirrus clouds appear to be spatially and temporally variable. Images show specular reflections in thin layers separated by less than 100 meters in altitude from cirrus layers showing no evidence of enhanced reflection. Time lapse video movies generated from these lidar scans show regions of specular reflection which appear and disappear as the cloud is advected by the lidar. This indicates that the crystal forms orientation also vary in the horizontal.

References

- Hansen, J.E., "Multiple scattering of polarized light in planetary atmospheres. Part I: The doubling method.", *J. Atm. Sci.*, 120-125 (1971).
- Platt, C.M.R. and A.C. Dilley, "Determination of cirrus particle single-scattering phase function from lidar and solar radiometer data", *App. Optics*, 23, 380-386, 1984.
- Grund, C.J., "Measurement of cirrus cloud optical properties by high spectral resolution lidar", Ph.D. Thesis Univ. of Wisconsin-Madison, (1987).
- Shipley, S.T., D.H. Tracey, E.W. Eloranta, J.T. Trauger, J.T. Sroga, F.L. Rossler, and J.A. Weinman (1983) "High spectral resolution lidar to measure optical scattering properties of atmospheric aerosols. 1: Theory and instrumentation". *App. Opt.*, 22, pp. 3716-3742.
- Grund, C.J., and E.W. Eloranta 1989: the 27-28 October 1986 FIRE IFO cirrus cloud study: Cloud optical properties determined by the High Spectral Resolution Lidar. *Mon. Weather Review*. Accepted for publication.
- Menzel, W.P., W.L. Smith, T.R. Steward (1983), Improved Cloud Motion Wind Vector and Altitude Assignment Using VAS. *J. Clim. App. Meteor.* 22, 377.

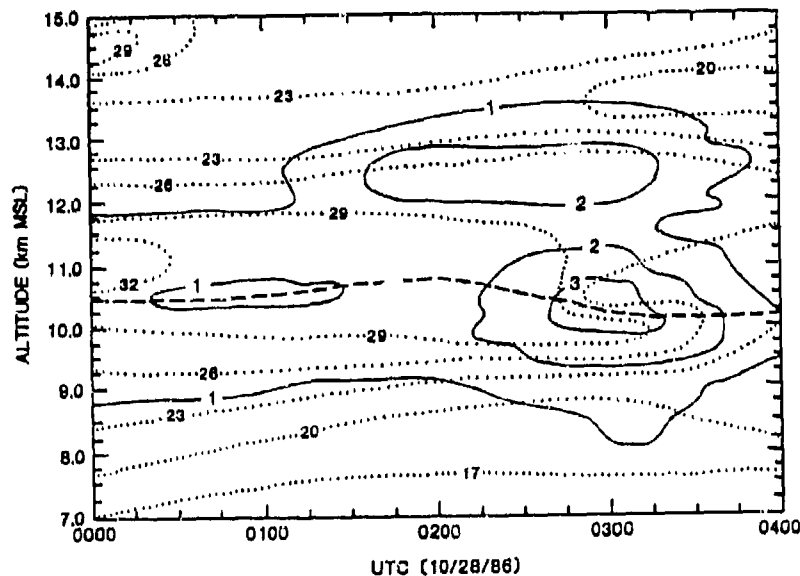


Fig. 1. Background veil of enhanced particulate backscatter may persist at cirrus cloud altitudes even when cirrus are not apparent. The range resolution has been reduced to 900 m to improve the noise statistics of this low backscatter data.

Cloud Optical Thickness vs. Temperature

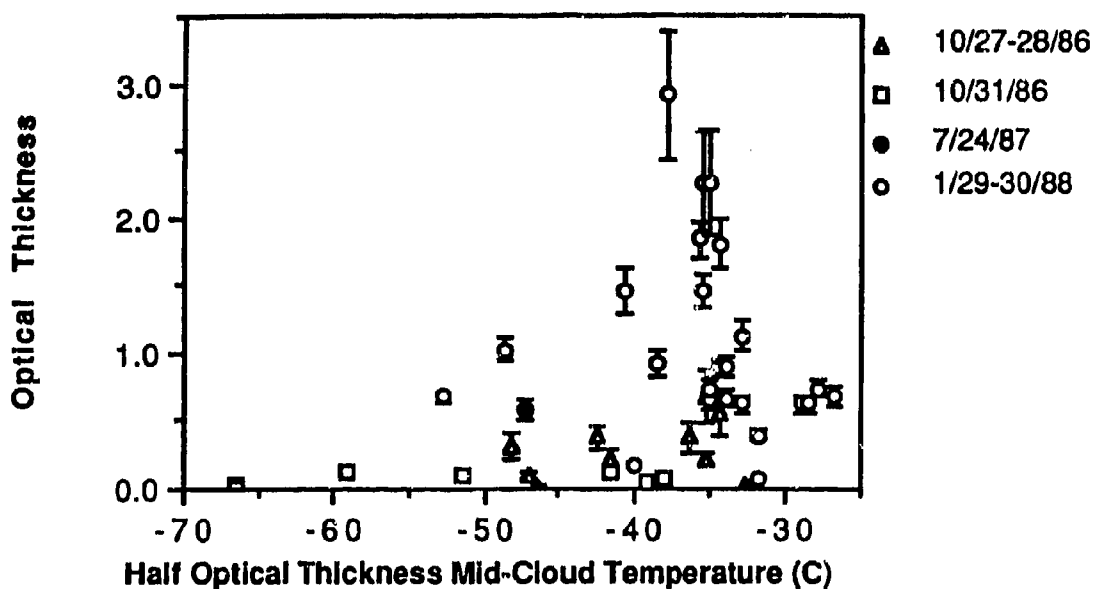


Fig. 2. As the mid-cloud temperature decreases, the maximum cirrus cloud layer optical thickness also decreases, while the minimum observed cloud optical thicknesses do not seem to depend on temperature.

Backscatter Phase Function vs. Temperature

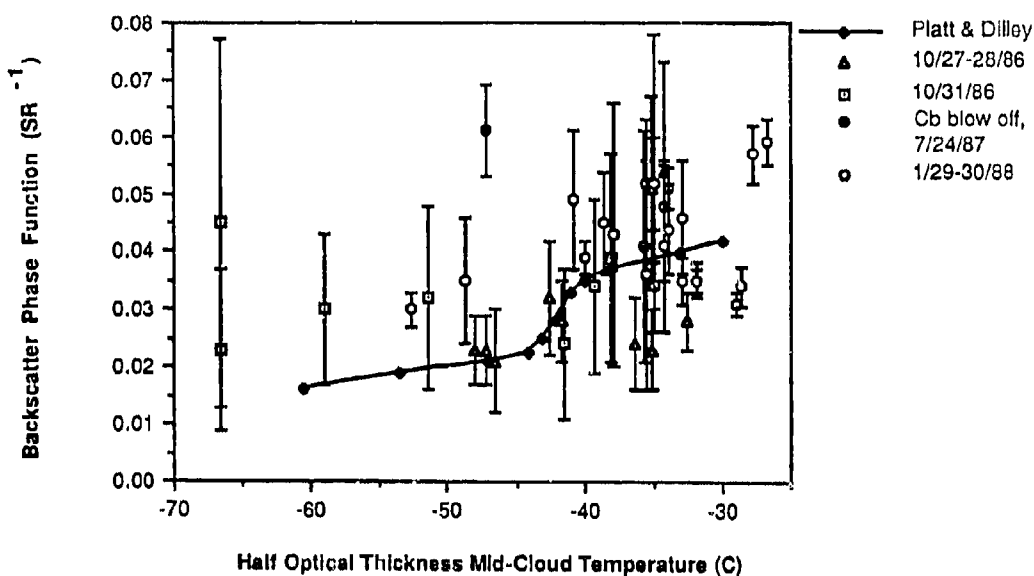


Fig. 3. HSRL determined backscatter phase function as a function of mid-cloud temperature.

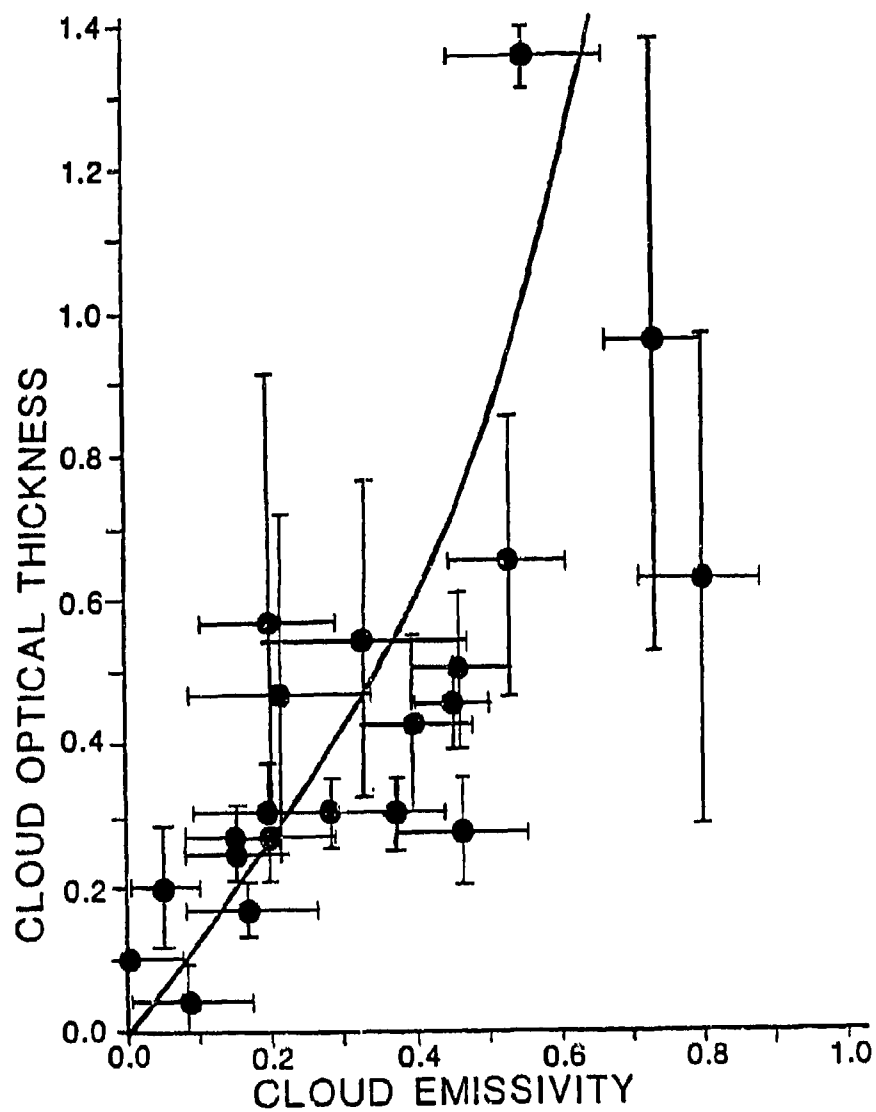


Figure 4. The cloud optical thickness from the HSRL lidar as a function of the IR emissivity measured from GOES/VAS satellite imagery.

DISCUSSION

J. SELBY

You showed that you measured specular reflections in the top layers of cirrus clouds when you looked vertically. Did you find evidence of specular reflections at other elevation angles, which might indicate that the ice crystals are oriented at other angles in lower levels in the cloud (in particular in the venetian blind like cloud formation which you observed)? Also, did you find evidence of horizontally oriented ice platelets at lower levels in the cloud or were they only near the top of the clouds?

AUTHOR'S REPLY

We have not observed specular reflections at pointing directions other than the zenith. I don't have any reason to expect systematic orientation at other angles. Specular reflections are frequently seen at many different altitudes, however they appear most frequently at high altitudes in the cases we have observed.

V. THIERMANN

You mentioned your lidar is capable of detecting invisible cirrus clouds. What was the probability of detecting a structure you would call a "cirrus cloud" in your lidar observations?

AUTHOR'S REPLY

At this point, we have not analyzed a sufficient number of cases to state a percentage probability with much reliability. On days where cirrus is visible anywhere in the sky, we find a high probability of observing "subvisible" cirrus in regions of the sky which appear clear to the eye. My general impression is that more than 10% of the clear sky days have thin layers of enhanced optical scattering at cirrus altitudes. Again, it is not clear whether these layers are composed of ice crystals or other aerosols.

E. LAMBERTON

Recent results from an airborne CW CO₂ laser backscatter measuring system show very high ($\beta = 10^{-7} - 10^{-8}$) scatter from extremely thin incipient cirrus layers approximately tens of meters thick which are difficult, if not impossible, to detect from ground or satellite, but which would have a major effect on airborne IR systems.

AUTHOR'S REPLY

We also often observe very thin layers of subvisible "cirrus". At times, these may exhibit relatively high scattering cross sections and persist for many hours. Not all subvisible "cirrus" is confined to thin layers; at times layers with very small scattering cross sections per unit volume can extend over several kilometers of altitude. Even though these subvisible layers often exist at the same altitude as visible cirrus it is not clear whether these layers are composed of ice crystals or other aerosols.

S. CLIFFORD

Can you measure temperature with your lidar using molecular scattering?

AUTHOR'S REPLY

You can in principle, but it's very difficult.

Verification of Klett's Method by Comparison of Lidar and Transmissometer Measurements (NATO unclassified)

Walter Carnuth, Fraunhofer Institute for Atmospheric Environmental Research (IfU),
Kreuzerbahnstrasse 19, D-8100 Garmisch-Partenkirchen (FRG)

Summary

Lidar measurements are performed in 532 nm wavelength along a slant path from ground level at 730 m MSL to a 1780 m mountain peak at 7 km horizontal distance, and extinction profiles derived from them by Klett's inversion method. This method, proceeding in the backward direction, avoids the instabilities occurring with the classical forward inversion, but requires a reference extinction value at the end of the lidar path. In our case it is derived from visual range data obtained by an integrating nephelometer which is operated continuously at the mountain peak. Parallel to the lidar the optical depth is measured by a broadband optical transmissometer (350 to 900 nm). The data are compared with those calculated by integration of the lidar extinction profiles.

List of symbols

| | |
|---------------|--|
| A | aperture area of lidar receiving telescope, m^2 |
| B | backscatter/extinction ratio (β/σ), sr^{-1} |
| B_A | aerosol backscatter/extinction ratio (β_A/σ_A), sr^{-1} |
| B_M | molecular backscatter/extinction ratio (β_M/σ_M), sr^{-1} |
| $B(r)$ | total backscatter coefficient, $m^{-1} \cdot sr^{-1}$ at range r |
| $B_A(r)$ | aerosol backscatter coefficient, $m^{-1} \cdot sr^{-1}$ at range r |
| $B_M(r)$ | molecular backscatter coefficient, $m^{-1} \cdot sr^{-1}$ at range r |
| B_m | boundary value for B at range r_m for Klett solution, $m^{-1} \cdot sr^{-1}$ |
| c | velocity of light, $m \cdot s^{-1}$ |
| C | lidar calibration factor, $A \cdot W^{-1}$ or $V \cdot W^{-1}$ |
| δ | optical depth |
| k | exponent in backscatter/extinction relation |
| p(r) | received radiation power at the lidar telescope from range r, Watts |
| Q | transmitted laser pulse energy, Joules |
| r | range, m |
| $\sigma(r)$ | total optical extinction coefficient, m^{-1} , at range r |
| $\sigma_A(r)$ | aerosol extinction coefficient, m^{-1} at range r |
| $\sigma_M(r)$ | molecular extinction coefficient, m^{-1} at range r |
| σ_0 | boundary value for σ at range r_0 for standard solution, m^{-1} |
| σ_m | boundary value for σ at range r_m for Klett solution, m^{-1} |
| τ | transmissivity |
| V | visual range, m |
| y(r) | lidar signal amplitude from range r, Amps or Volts. |

1. Introduction

The lidar is regarded as an effective tool for range-resolved remote sensing of atmospheric optical parameters, e.g. the extinction coefficient σ , which is related to the visual range V by Koschmieder's formula,

$$V = -\ln(0.02)/\sigma \quad (1)$$

However, the quantitative derivation of those parameters from the lidar signals is encountered by some fundamental difficulties. One of them are instabilities which most inversions of the lidar equation, which relates the range-dependent radiation power received by the lidar detector from range r to the optical parameters, exhibit at higher optical depths. J. D. Klett (Refs. 1, 2) published an inversion method which delivers stable solutions, if a reference extinction value at the end of the regarded range interval is known or can be estimated. The method is described in more detail in chapter 3. We take advantage of the visual range data recorded continuously at an observatory which is located at a 1800 m MSL mountain top at 7 km horizontal distance from the institute (730 m MSL), to calculate boundary values for Klett's inversion. The extinction profiles obtained by this method are stable, but are still influenced besides by measurement errors by the particular choice of the backscatter-to-extinction (β/σ) ratio, which is the key parameter for any solution of the lidar equation. It seems to be interesting, therefore, to verify the lidar-derived extinction or optical depth data by comparison with direct transmissivity measurements. Such measurements have been started late in 1987. Some results will be presented here.

2. Instrumentation

For the backscatter measurements a mobile lidar system is used containing a Nd:YAG laser with second and third harmonic generation (SHG and THG), delivering pulse energies of 300, 125 and 60 mJ at 1064, 532 and 355 nm wavelength, respectively. The maximum pulse repetition frequency (PRF) is 10 Hz. This laser was installed in the system early in 1989, replacing two older ruby and Nd:glass lasers. The backscattered radiation is collected by a 30 cm Cassegrain telescope and detected by a bialkali photomultiplier (532 and 355 nm) or a PIN diode detector (1064 nm). The detector field-of-view is 10 mrad with the PIN diode and 4 mrad with the photomultiplier. The amplified signals are

digitized by a 12-bit, 10-MHz transient recorder and transferred to a personal computer. Recently a fast hardware averager with 24 bit memory has been purchased allowing signal averaging at the full 10 Hz PRF.

The visual range is recorded at the mountain observatory as well as in the valley at 400 m distance from the lidar site by commercial AEG-Ruppersberg visibility meters. In these instruments the scattered light from a flashlamp which is ignited every 10 seconds is measured by a photodiode detector. For normalization a second detector measures the light intensity of the flashlamp itself. The range of scattering angles is 10 to 130°, thus rendering data quite independent of the size distribution of the aerosol particles. For calibration a light-scattering opal glass plate can be introduced into the beam of the flashlamp, giving a scattering signal which has been determined by eye observation to be equal to 230 m visual range. The measurement range of the instrument is 50 m to 40 km.

The optical transmissivity of the path between institute and mountain observatory is measured by a broad-band Barnes transmissometer. The light source, consisting of a 150 watts halogen lamp, a 1 kHz chopper and an off-axis collimator with 12 cm aperture diameter and 65 cm focal length, is installed at the mountain peak. The chopped radiation is transmitted to the institute and measured by a detector containing an 11 cm dia. Cassegrain telescope, a 350 to 900 nm optical filter and a Si diode radiation sensor. The detector-FOV is 2.5 mrad. The signals are amplified by a lock-in amplifier. The chopper frequency of the source is telemetered to the detection site and fed to the reference input of the lock-in. The system is calibrated by measurements during extreme atmospheric clearness. The maximum measurable optical depth at a pathlength of 7.07 km is at least 6. The analog signals are digitized by a home-made digitizer and transferred to a personal computer. The digitizer incorporates an automatic, computer-controlled gain switch.

3. Data evaluation

The backscattered power $p(r)$ collected by the lidar telescope from range r as function of the atmospheric scattering parameters is described by the so-called lidar equation, which reads in its most widely using form, neglecting close-range geometric attenuation, multiple scattering and effects due to finite laser pulse length:

$$p(r) = \frac{c}{2} \cdot A \cdot Q \cdot r^{-2} \cdot B(r) \cdot \exp \left[-2 \int_0^r \sigma(x) \cdot dx \right] \quad (2)$$

with c denoting velocity of light, Q the laser pulse energy, A the telescope aperture area and B and σ the backscatter- and extinction coefficients, respectively. If the electrical signal delivered by the detector is proportional to $p(r)$, this equation can be expressed in terms of the signal amplitude $y(r)$:

$$y(r) = C \cdot p(r) \quad (3)$$

with C = lidar calibration constant. In Eq. (2) two unknowns occur, $B(r)$ and $\sigma(r)$, which cannot be independently inverted from the measured return signals $p(r)$. Therefore, a relationship between B and σ must be known or assumed. In practice this relation depends on the nature, i.e. size distribution, refractive index and shape of the scattering particles (see Ref. 3). If an exponential relation of the form

$$B(r) = B \cdot \sigma(r)^k \quad (4)$$

with B and k = const, is assumed, which includes the simple proportionality with $k' = 1$, Eq. (3) is known to have the following analytical solution:

$$\sigma(r) = \frac{\left[y(r) \cdot r^2 \right]^{1/k}}{\left[y(r_0) \cdot r_0^2 \right]^{1/k} / \sigma_0 - \frac{2}{k} \cdot \int_{r_0}^r \left[y(x) \cdot x^2 \right]^{1/k} \cdot dx} \quad (5)$$

σ_0 , the extinction coefficient at the reference range r_0 , usually chosen as close to the lidar site as possible, is the reference or boundary value. It can be derived from the lidar signal $y(r)$ itself, if the system is calibrated, i.e. if the constant C is known, and if the constants B and k in Eq. (4) are known. The expression (5) becomes unstable with increasing optical depth because the denominator then becomes a small difference of two increasingly large numbers. Even small measurement errors or errors in the choice of σ_0 may then have a large influence on the calculated extinction coefficient $\sigma(r)$. Klett (Ref. 1) avoided these instabilities by choosing the reference value at the remote end r_m instead of the close end r_0 of the range interval, thus inverting the lidar equation in the backward direction:

$$\sigma(r) = \frac{[y(r) \cdot r^2]^{1/k}}{[y(r_m) \cdot r_m^2]^{1/k} / \sigma_m + \frac{2}{k} \cdot \int_r^{r_m} [y(x) \cdot x^2]^{1/k} \cdot dx} \quad (6)$$

In this equation the difference in the denominator of Eq. (5) is replaced by a sum, and the instabilities are eliminated. Furthermore, in contrary to Eq. (5), the influence of the boundary value upon the resulting σ decreases with increasing optical depth, since then the second term in the denominator of Eq. (6) becomes large compared to the first one. Both Eqs. (5) and (6) are used here in a slightly different notation than in Klett's paper. It becomes more simple in the frequently used case $k = 1$.

The remote extinction coefficient is generally more difficult to obtain than that at close range. Especially it cannot be derived from the lidar signal itself. We have the opportunity to use experimental extinction coefficients as boundary values, derived from visibility data obtained at the mountain observatory. However, even with ideal errorless reference values the solution still depends on the β - σ relation. For example, Eq. (4) is definitely not fulfilled in clear atmospheres where molecular scattering cannot be neglected against aerosol scattering. For this case Klett (Ref. 2) published an extension of his inversion algorithm. However, the exponent k in (4) must then be set to unity and the constant B be known. The modified expression for the total extinction coefficient $\sigma = \sigma_A + \sigma_M$ reads:

$$\sigma(r) = \frac{y(r) \cdot r^2 \cdot \exp[I_M(r)]}{y(r_m) \cdot r_m^2 \cdot B_A/B_M + 2 \cdot \int_r^{r_m} y(x) \cdot x^2 \cdot \exp[I_M(x)] \cdot dx} = (B_M/B_A - 1) \cdot \sigma_M(r) \quad (7)$$

with $B_A = B_A/\sigma_A$, $B_M = B_M/\sigma_M = 3/8\pi$ and $I_M(r) = 2 \cdot (1/B_A - 1/B_M) \cdot \int_r^{r_m} B_M(x) \cdot dx$

In this expression, besides that of B_A , the knowledge of the molecular scattering coefficient $\sigma_M(r)$ is additionally required. If the atmospheric density variations along the lidar path are not too large, they can be calculated from a standard atmosphere or even, as in our case, by linear interpolation between two known values at the ends of the range interval (atm. pressure and temperature are recorded at both sites). For molecular scattering becoming small compared to aerosol scattering, i.e. $B_M \rightarrow 0$ and $\sigma_M \rightarrow 0$, $\exp[I_M(r)]$ becomes unity, the factor B_A cancels out and Eq. (6) is recovered with $k = 1$.

In addition to the external parameters just mentioned, some error sources may influence the calculated extinction profiles. One of them are measurement errors. For example, the first terms in the denominators of Eqs. (6) and (7) are equally influenced by errors in the signal amplitudes at the reference range r_m , $y(r_m)$, and by errors in the reference values σ_m . Due to the geometric attenuation term r^2 in the lidar equation (2) or (3), the amplitudes at the remote end of the interval may become small and the errors large even with low extinction losses along the lidar path. Finally the single scattering lidar equation (2) itself may become invalid if the optical depth is sufficiently large and multiple scattering no longer negligible. Due to the extreme mathematical complexity of multiple scattering, most authors neglect it even in cases where this is in principle not allowed. Up to now we also used the expressions (6) and (7), based on the single scattering lidar equation, up to optical depths of 1 and more. Erroneous extinction data can then no longer be excluded.

For these reasons comparative lidar and transmission measurements seem to be interesting and desirable.

4. Measurements and results

Verification measurements for Klett's method are only meaningful if the aerosol is inhomogeneously distributed along the lidar path. Under homogeneous conditions the evaluation of the return signals is trivial, since the extinction coefficient can then be derived from the slope of the logarithmic range-normalized profiles (slope method). Measurements under homogeneous conditions, however, are useful for a check of the calibration status of transmission and visibility meters. Inhomogeneous conditions occur especially in the winter half-year, when the top of the planetary boundary layer remains below the level of our mountain observatory. The catabatic wind system frequently occurring under fine weather conditions in mountain valleys which are open to the plains outside, gives then rise to additional strong diurnal aerosol variations. During nighttime the wind blows downhill and transports clear air from higher altitudes into the valley, where the institute is located and which is in our case oriented approximately from SSW to NNE. In the forenoon the wind direction usually reverses, and polluted air from the industrialized region in the north outside the mountains is advected in a ground-based layer with increasing vertical extent, until the wind reverses again in the evening and a new cycle is started. Within the daytime aerosol layer frequently quite low visual ranges, sometimes even fog, are observed.

A measurement series during such atmospheric conditions was performed, for example, on January 19 and 20, 1989. The diagram Fig. 1 shows the visual range measured at 730 m MSL, during the 48-hour period from Jan. 19 to 20. Fig. 2 illustrates the course of windspeed and wind direction during the same period. Both visual range and wind data are measured at an unmanned station at 400 m distance from the transmissometer path. In the early morning hours of Jan. 19 the visibility is still increasing due to advection of clear air by the downhill blowing wind. With the wind reversal at about 7 AM the visibility begins to decrease until 5 PM, with an interruption between 10 and 12 AM, when temporarily the wind was blowing again downhill. After 5 PM (17:00 CET) the visibility increases, again interrupted by a period with ground fog and very high extinction from 10 PM (22:00 CET) on January 19 and 7 AM on January 20. On this day the reversal of the wind direction was obviously suppressed, as indicated in Fig. 2, by a superposed southwesterly geostrophical foehn wind. So the near-ground air remained clear except a few interruptions. The 1800 m station remained within the clear air above the boundary layer throughout this period, and thus the visual ranges at this altitude remained beyond the 40 km measuring range of the visibility meter.

The measured transmissivities τ are shown in Fig. 3. The transmissometer was running only during a part of the time period, but on order to make comparisons easier the same time scale was chosen than in the previous diagrams. The data show in general a similar behavior than the ground visual ranges, Fig. 1. Occasional differences, e.g. the peak in the visibility between 9:30 and 12:00 on Jan. 19 which does not show up in the τ curve, may be attributed to the spatial distance between transmissometer path and location of the visibility meter.

Lidar measurements were performed in the wavelengths 1064 and 532 nm. For this comparison, however, only the data in the wavelength 532 nm, which is close to the center of the visible range, are considered. For laser safety reasons the lidar cannot be pointed directly to the mountain observatory site. Therefore, an elevation angle of 11 instead of 8.1 degrees was chosen, and a slightly different azimuth angle. The laser beam thus passed accessible terrain at least in a distance of 300 m. The reference range for the Klett inversion, r_m , was set, therefore, to 5.3 instead of 7.07 km, resulting in an altitude equal to that of the observatory. The resulting horizontal difference of both points is 2 km, but it was reasonable to assume that the horizontal homogeneity of the atmosphere was sufficient for neglecting any differences of the scattering coefficients. Since at least partially the molecular scattering could not be neglected against aerosol scattering, the lidar returns were evaluated by the extended Klett method, Eq. (7), assuming $B_A = 0.022$. For comparison, however, the "standard" Klett formula, Eq. (6), was also used.

Since the visual range V at 1800 m MSL exceeded the 40 km measuring range of the nephelometers, an estimated value $V = 100$ km was used. The example Fig. 4 shows a range-normalized lidar return from January 19, 17:42 CET. The near-ground aerosol layer with an upper boundary at range 1.8 km (340 m above ground level) clearly shows up. The text block at the left side of the diagram contains all important measurement and housekeeping data. It is created automatically by the computer program except the last line, which is a manually typed-in comment. The curves denoted by "sig" in Figs. 5 and 6 present profiles of the extinction coefficient, calculated from the signal Fig. 4 by the extended and standard Klett method, Eq. (7) and (6), respectively. The continuously ascending "del" curves are the integrals of the extinction coefficients, i.e. the optical depths δ . In order to get δ values comparable to the transmissometer data, the curves must be extrapolated to range zero due the geometric compression of the lidar signals in the close range, and multiplied by the path length correction factor $7.07/5.3 = 1.334$.

All lidar returns from the period Jan. 19/20 were evaluated. However, they cannot be presented completely in this paper (for the future a three-dimensional plot is planned). Only four extinction profiles calculated using Eq. (7) are shown in Figs. 7 to 10 to illustrate the time behavior of the aerosol situation. The abscissae present the extinction coefficients in units km^{-1} , the ordinates the altitudes above ground. Figs. 7 and 10 show the clear, nearly aerosol-free atmosphere before (Jan. 19, 11:42 CET) and after (Jan. 20, 08:10 CET) the influx of the aerosol layer, Figs. 8 and 9 this layer at 11:57 and 18:03 CET on Jan. 19. The noise in the upper parts of some of the profiles is caused by the skylight background during daytime. The measurements were done before the installation of the averager, and thus only 16 single shots were averaged. In the meantime typically 200 shots can be averaged within 30 seconds, and a considerably better S/N ratio obtained also during daytime.

The optical depths measured by transmissometer and lidar are presented in Fig. 11 for the total period and in Figs. 12, 13 and 14 for three partial periods in a stretched time scale. From the curves it becomes immediately clear that the standard Klett method results throughout in too small δ 's. The optical depths calculated by Eq. (7) generally agree much better with the transmissometer data, but deviations are still observed in some cases. The largest deviations occur during the fog period from 16 and 19 PM on Jan. 19 and are then certainly due to local aerosol inhomogeneities. In the other cases they may be caused a) by wrong signal amplitudes at range r_m due to noise, b) by erroneous boundary values since estimated data are available, c) by errors in the choice of B_A or generally non-proportionality between B_A and σ_A , and finally d) by the neglect of multiple scattering. The noise in the signal amplitudes at the reference point has already been reduced by spatial averaging in addition to temporal averaging (averaging of more shots) but the possibilities of spatial averaging are limited to about 20 data points maximum around r_m . The influence of the boundary values upon the calculated δ 's is too small (one of the benefits of Klett's method) for an explanation of the discre-

pancies. They can be removed, however, by a proper choice of B_A , for example $B_A = .012$ instead of .022 in the measurement at 18:27 CET on Jan. 19.

It is possible, finally, to "align" the extinction profiles obtained by Klett's standard method by choosing a suitable exponent k different from unity. In our case, $k = .6$ would give good results. However, this method is not justified physically, and looks, therefore, somewhat artificial.

The most severe error source, finally, is the influence of multiple scattering. It results in apparently reduced extinction coefficients and influences both transmissivity and lidar backscatter measurements. Since its mathematical treatment is extremely complex, we neglected it in our computations so far, although this is not justified in those cases where the optical depth approaches values of one and more. An easily applicable inversion algorithm for a multiple scattering lidar equation does not exist yet, but some authors, e.g. L. C. Bissonette from DREV, Courcellette, Québec, Canada, published methods for calculation of backscatter signatures from given distributions of scattering coefficients (Ref. 4). In the future we will calculate theoretical return signals by Bissonette's TFMSCAT algorithm from the extinction profiles obtained using the single scattering lidar equation and Klett's method. By comparison with the original measured signals it should then be possible to estimate the error resulting from the neglect of multiple scattering.

On March 30 and July 13, 1989, the aerosol was at times quite homogeneously distributed along the slant path, especially in the afternoon and during the maximum vertical mixing activity. Logarithmic range-corrected lidar returns were quite exactly linear, as shown in the examples Figs. 15 and 16, and extinction coefficients could be derived from them by the slope method. These extinction data are correlated with those obtained by the transmissometer in the diagram Fig. 17. The agreement is sufficient, especially no systematic deviation is observed. The calibration of the transmissometer may be regarded, therefore, as correct. On July 13 the visibility was within the range of the visibility meter. The extinction coefficient derived from the lidar returns by the slope method turned out to be .64 smaller than that calculated from the measured visual range by Eq. (1). Obviously the visibility meter is not calibrated correctly.

The diagrams Fig. 18 presents optical depths obtained during aerosol conditions characterized by comparably high extinction coefficients within the total altitude range covered by the measuring path. The visual range thus remained within the range if the nephelometers also at 1800 m MSL. The lidar data were evaluated by Klett's standard method using the uncorrected extinction coefficients from 1800 m MSL as reference values. The diagram now clearly shows, in addition to some random errors, an average systematic deviation between the lidar and transmissometer optical depths, the former being distinctly larger. The deviations are eliminated, if the corrected extinction coefficients are used as reference values (Fig. 19). The remaining random deviations may be attributed to the error sources mentioned above.

5. Preliminary conclusions

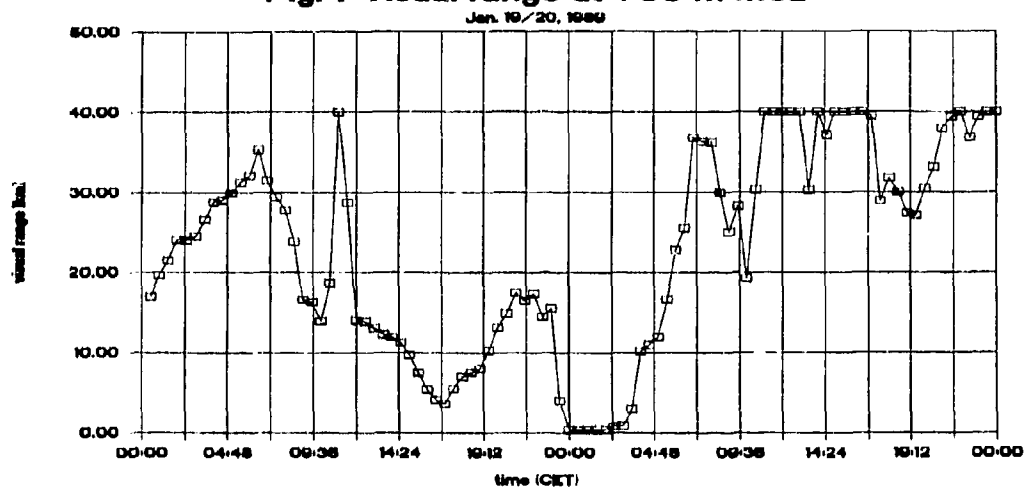
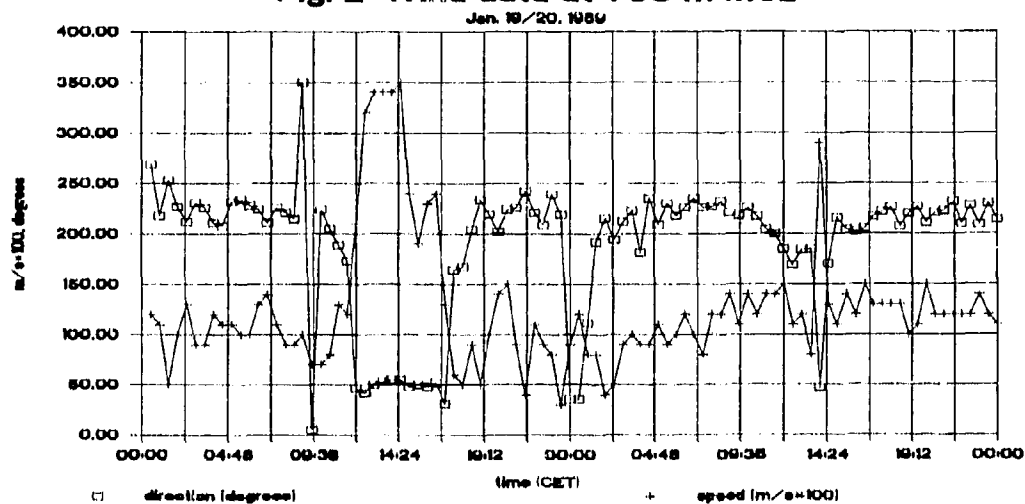
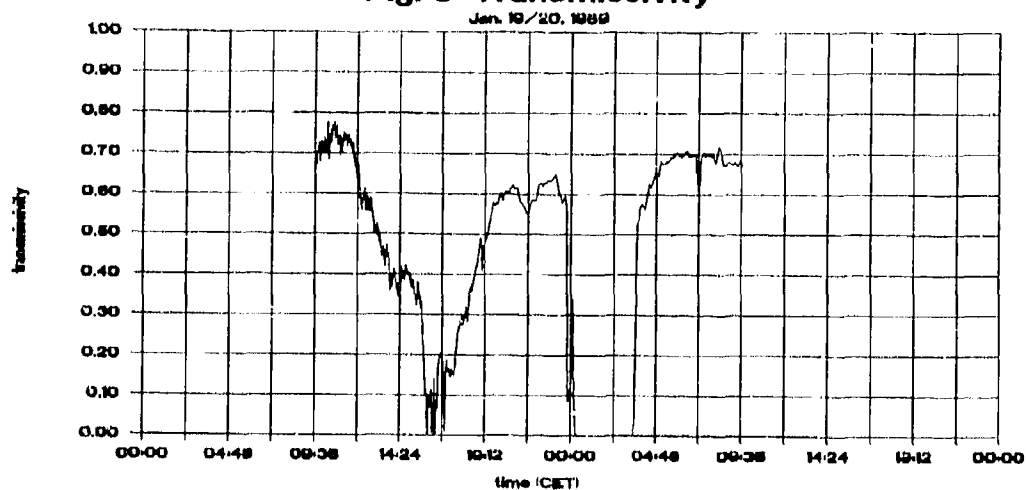
From the data available so far it may be concluded that sufficient agreement can be expected between lidar- and transmissometer-derived optical depths in many cases, if Klett's stable inversion method is applied using correct boundary extinction values at the far end of the range interval and if the lidar returns itself from that point are also sufficiently accurate. In other cases, however, discrepancies are observed which may be attributed, besides to measurement errors and multiple scattering effects, to the still variable parameter in Klett's inversion, namely the backscatter/extinction function or ratio. Further measurements are required in order to find the best choice for these parameters.

6. Acknowledgments

The research work presented here is supported by the German Defense Ministry, Division RüFo3, under contract No. T/RF35/G0056/G1237.

7. References

1. Klett, J.D., "Stable Analytical Inversion Solution for Lidar Returns." Appl. Opt. 20, 211, (1981).
2. Klett, J.D., "Lidar Inversion with Variable Backscatter/Extinction Ratios." Appl. Opt. 24, 1638, (1985).
3. Reagan, J.A., M.V. Apte, A. Ben-David, and B.M. Herman, "Assessment of Aerosol Extinction to Backscatter Ratio Measurements Made at 694.3 nm in Tucson, Arizona." Aerosol Sci. Technol. 8, 215 (1988).
4. Bissonnette, L.R., "Multiscattering Model for Propagation of Narrow Light Beams in Aerosol Media." Appl. Opt. 27, 2478 (1988).

Fig. 1: Visual range at 730 m MSL**Fig. 2: Wind data at 730 m MSL****Fig. 3: Transmissivity**

FILE:04060100
 SERP: 0
 DTIME: 1.00
 T1: 45:44-45:48
 T2: 45:45-45:47
 T3: 45:46-45:48
 T4: 45:48-45:50
 T5: 45:50-45:52
 T6: 45:52-45:54
 T7: 45:54-45:56
 T8: 45:56-45:58
 T9: 45:58-45:59
 T10: 45:59-46:00
 T11: 46:00-46:01
 T12: 46:01-46:02
 T13: 46:02-46:03
 T14: 46:03-46:04
 T15: 46:04-46:05
 T16: 46:05-46:06
 T17: 46:06-46:07
 T18: 46:07-46:08
 T19: 46:08-46:09
 T20: 46:09-46:10
 T21: 46:10-46:11
 T22: 46:11-46:12
 T23: 46:12-46:13
 T24: 46:13-46:14
 T25: 46:14-46:15
 T26: 46:15-46:16
 T27: 46:16-46:17
 T28: 46:17-46:18
 T29: 46:18-46:19
 T30: 46:19-46:20
 T31: 46:20-46:21
 T32: 46:21-46:22
 T33: 46:22-46:23
 T34: 46:23-46:24
 T35: 46:24-46:25
 T36: 46:25-46:26
 T37: 46:26-46:27
 T38: 46:27-46:28
 T39: 46:28-46:29
 T40: 46:29-46:30
 T41: 46:30-46:31
 T42: 46:31-46:32
 T43: 46:32-46:33
 T44: 46:33-46:34
 T45: 46:34-46:35
 T46: 46:35-46:36
 T47: 46:36-46:37
 T48: 46:37-46:38
 T49: 46:38-46:39
 T50: 46:39-46:40
 T51: 46:40-46:41
 T52: 46:41-46:42
 T53: 46:42-46:43
 T54: 46:43-46:44
 T55: 46:44-46:45
 T56: 46:45-46:46
 T57: 46:46-46:47
 T58: 46:47-46:48
 T59: 46:48-46:49
 T60: 46:49-46:50
 T61: 46:50-46:51
 T62: 46:51-46:52
 T63: 46:52-46:53
 T64: 46:53-46:54
 T65: 46:54-46:55
 T66: 46:55-46:56
 T67: 46:56-46:57
 T68: 46:57-46:58
 T69: 46:58-46:59
 T70: 46:59-47:00
 T71: 47:00-47:01
 T72: 47:01-47:02
 T73: 47:02-47:03
 T74: 47:03-47:04
 T75: 47:04-47:05
 T76: 47:05-47:06
 T77: 47:06-47:07
 T78: 47:07-47:08
 T79: 47:08-47:09
 T80: 47:09-47:10
 T81: 47:10-47:11
 T82: 47:11-47:12
 T83: 47:12-47:13
 T84: 47:13-47:14
 T85: 47:14-47:15
 T86: 47:15-47:16
 T87: 47:16-47:17
 T88: 47:17-47:18
 T89: 47:18-47:19
 T90: 47:19-47:20
 T91: 47:20-47:21
 T92: 47:21-47:22
 T93: 47:22-47:23
 T94: 47:23-47:24
 T95: 47:24-47:25
 T96: 47:25-47:26
 T97: 47:26-47:27
 T98: 47:27-47:28
 T99: 47:28-47:29
 T100: 47:29-47:30
 T101: 47:30-47:31
 T102: 47:31-47:32
 T103: 47:32-47:33
 T104: 47:33-47:34
 T105: 47:34-47:35
 T106: 47:35-47:36
 T107: 47:36-47:37
 T108: 47:37-47:38
 T109: 47:38-47:39
 T110: 47:39-47:40
 T111: 47:40-47:41
 T112: 47:41-47:42
 T113: 47:42-47:43
 T114: 47:43-47:44
 T115: 47:44-47:45
 T116: 47:45-47:46
 T117: 47:46-47:47
 T118: 47:47-47:48
 T119: 47:48-47:49
 T120: 47:49-47:50
 T121: 47:50-47:51
 T122: 47:51-47:52
 T123: 47:52-47:53
 T124: 47:53-47:54
 T125: 47:54-47:55
 T126: 47:55-47:56
 T127: 47:56-47:57
 T128: 47:57-47:58
 T129: 47:58-47:59
 T130: 47:59-48:00
 T131: 48:00-48:01
 T132: 48:01-48:02
 T133: 48:02-48:03
 T134: 48:03-48:04
 T135: 48:04-48:05
 T136: 48:05-48:06
 T137: 48:06-48:07
 T138: 48:07-48:08
 T139: 48:08-48:09
 T140: 48:09-48:10
 T141: 48:10-48:11
 T142: 48:11-48:12
 T143: 48:12-48:13
 T144: 48:13-48:14
 T145: 48:14-48:15
 T146: 48:15-48:16
 T147: 48:16-48:17
 T148: 48:17-48:18
 T149: 48:18-48:19
 T150: 48:19-48:20
 T151: 48:20-48:21
 T152: 48:21-48:22
 T153: 48:22-48:23
 T154: 48:23-48:24
 T155: 48:24-48:25
 T156: 48:25-48:26
 T157: 48:26-48:27
 T158: 48:27-48:28
 T159: 48:28-48:29
 T160: 48:29-48:30
 T161: 48:30-48:31
 T162: 48:31-48:32
 T163: 48:32-48:33
 T164: 48:33-48:34
 T165: 48:34-48:35
 T166: 48:35-48:36
 T167: 48:36-48:37
 T168: 48:37-48:38
 T169: 48:38-48:39
 T170: 48:39-48:40
 T171: 48:40-48:41
 T172: 48:41-48:42
 T173: 48:42-48:43
 T174: 48:43-48:44
 T175: 48:44-48:45
 T176: 48:45-48:46
 T177: 48:46-48:47
 T178: 48:47-48:48
 T179: 48:48-48:49
 T180: 48:49-48:50
 T181: 48:50-48:51
 T182: 48:51-48:52
 T183: 48:52-48:53
 T184: 48:53-48:54
 T185: 48:54-48:55
 T186: 48:55-48:56
 T187: 48:56-48:57
 T188: 48:57-48:58
 T189: 48:58-48:59
 T190: 48:59-49:00
 T191: 49:00-49:01
 T192: 49:01-49:02
 T193: 49:02-49:03
 T194: 49:03-49:04
 T195: 49:04-49:05
 T196: 49:05-49:06
 T197: 49:06-49:07
 T198: 49:07-49:08
 T199: 49:08-49:09
 T200: 49:09-49:10
 T201: 49:10-49:11
 T202: 49:11-49:12
 T203: 49:12-49:13
 T204: 49:13-49:14
 T205: 49:14-49:15
 T206: 49:15-49:16
 T207: 49:16-49:17
 T208: 49:17-49:18
 T209: 49:18-49:19
 T210: 49:19-49:20
 T211: 49:20-49:21
 T212: 49:21-49:22
 T213: 49:22-49:23
 T214: 49:23-49:24
 T215: 49:24-49:25
 T216: 49:25-49:26
 T217: 49:26-49:27
 T218: 49:27-49:28
 T219: 49:28-49:29
 T220: 49:29-49:30
 T221: 49:30-49:31
 T222: 49:31-49:32
 T223: 49:32-49:33
 T224: 49:33-49:34
 T225: 49:34-49:35
 T226: 49:35-49:36
 T227: 49:36-49:37
 T228: 49:37-49:38
 T229: 49:38-49:39
 T230: 49:39-49:40
 T231: 49:40-49:41
 T232: 49:41-49:42
 T233: 49:42-49:43
 T234: 49:43-49:44
 T235: 49:44-49:45
 T236: 49:45-49:46
 T237: 49:46-49:47
 T238: 49:47-49:48
 T239: 49:48-49:49
 T240: 49:49-49:50
 T241: 49:50-49:51
 T242: 49:51-49:52
 T243: 49:52-49:53
 T244: 49:53-49:54
 T245: 49:54-49:55
 T246: 49:55-49:56
 T247: 49:56-49:57
 T248: 49:57-49:58
 T249: 49:58-49:59
 T250: 49:59-50:00
 T251: 50:00-50:01
 T252: 50:01-50:02
 T253: 50:02-50:03
 T254: 50:03-50:04
 T255: 50:04-50:05
 T256: 50:05-50:06
 T257: 50:06-50:07
 T258: 50:07-50:08
 T259: 50:08-50:09
 T260: 50:09-50:10
 T261: 50:10-50:11
 T262: 50:11-50:12
 T263: 50:12-50:13
 T264: 50:13-50:14
 T265: 50:14-50:15
 T266: 50:15-50:16
 T267: 50:16-50:17
 T268: 50:17-50:18
 T269: 50:18-50:19
 T270: 50:19-50:20
 T271: 50:20-50:21
 T272: 50:21-50:22
 T273: 50:22-50:23
 T274: 50:23-50:24
 T275: 50:24-50:25
 T276: 50:25-50:26
 T277: 50:26-50:27
 T278: 50:27-50:28
 T279: 50:28-50:29
 T280: 50:29-50:30
 T281: 50:30-50:31
 T282: 50:31-50:32
 T283: 50:32-50:33
 T284: 50:33-50:34
 T285: 50:34-50:35
 T286: 50:35-50:36
 T287: 50:36-50:37
 T288: 50:37-50:38
 T289: 50:38-50:39
 T290: 50:39-50:40
 T291: 50:40-50:41
 T292: 50:41-50:42
 T293: 50:42-50:43
 T294: 50:43-50:44
 T295: 50:44-50:45
 T296: 50:45-50:46
 T297: 50:46-50:47
 T298: 50:47-50:48
 T299: 50:48-50:49
 T300: 50:49-50:50
 T301: 50:50-50:51
 T302: 50:51-50:52
 T303: 50:52-50:53
 T304: 50:53-50:54
 T305: 50:54-50:55
 T306: 50:55-50:56
 T307: 50:56-50:57
 T308: 50:57-50:58
 T309: 50:58-50:59
 T310: 50:59-51:00
 T311: 51:00-51:01
 T312: 51:01-51:02
 T313: 51:02-51:03
 T314: 51:03-51:04
 T315: 51:04-51:05
 T316: 51:05-51:06
 T317: 51:06-51:07
 T318: 51:07-51:08
 T319: 51:08-51:09
 T320: 51:09-51:10
 T321: 51:10-51:11
 T322: 51:11-51:12
 T323: 51:12-51:13
 T324: 51:13-51:14
 T325: 51:14-51:15
 T326: 51:15-51:16
 T327: 51:16-51:17
 T328: 51:17-51:18
 T329: 51:18-51:19
 T330: 51:19-51:20
 T331: 51:20-51:21
 T332: 51:21-51:22
 T333: 51:22-51:23
 T334: 51:23-51:24
 T335: 51:24-51:25
 T336: 51:25-51:26
 T337: 51:26-51:27
 T338: 51:27-51:28
 T339: 51:28-51:29
 T340: 51:29-51:30
 T341: 51:30-51:31
 T342: 51:31-51:32
 T343: 51:32-51:33
 T344: 51:33-51:34
 T345: 51:34-51:35
 T346: 51:35-51:36
 T347: 51:36-51:37
 T348: 51:37-51:38
 T349: 51:38-51:39
 T350: 51:39-51:40
 T351: 51:40-51:41
 T352: 51:41-51:42
 T353: 51:42-51:43
 T354: 51:43-51:44
 T355: 51:44-51:45
 T356: 51:45-51:46
 T357: 51:46-51:47
 T358: 51:47-51:48
 T359: 51:48-51:49
 T360: 51:49-51:50
 T361: 51:50-51:51
 T362: 51:51-51:52
 T363: 51:52-51:53
 T364: 51:53-51:54
 T365: 51:54-51:55
 T366: 51:55-51:56
 T367: 51:56-51:57
 T368: 51:57-51:58
 T369: 51:58-51:59
 T370: 51:59-52:00
 T371: 52:00-52:01
 T372: 52:01-52:02
 T373: 52:02-52:03
 T374: 52:03-52:04
 T375: 52:04-52:05
 T376: 52:05-52:06
 T377: 52:06-52:07
 T378: 52:07-52:08
 T379: 52:08-52:09
 T380: 52:09-52:10
 T381: 52:10-52:11
 T382: 52:11-52:12
 T383: 52:12-52:13
 T384: 52:13-52:14
 T385: 52:14-52:15
 T386: 52:15-52:16
 T387: 52:16-52:17
 T388: 52:17-52:18
 T389: 52:18-52:19
 T390: 52:19-52:20
 T391: 52:20-52:21
 T392: 52:21-52:22
 T393: 52:22-52:23
 T394: 52:23-52:24
 T395: 52:24-52:25
 T396: 52:25-52:26
 T397: 52:26-52:27
 T398: 52:27-52:28
 T399: 52:28-52:29
 T400: 52:29-52:30
 T401: 52:30-52:31
 T402: 52:31-52:32
 T403: 52:32-52:33
 T404: 52:33-52:34
 T405: 52:34-52:35
 T406: 52:35-52:36
 T407: 52:36-52:37
 T408: 52:37-52:38
 T409: 52:38-52:39
 T410: 52:39-52:40
 T411: 52:40-52:41
 T412: 52:41-52:42
 T413: 52:42-52:43
 T414: 52:43-52:44
 T415: 52:44-52:45
 T416: 52:45-52:46
 T417: 52:46-52:47
 T418: 52:47-52:48
 T419: 52:48-52:49
 T420: 52:49-52:50
 T421: 52:50-52:51
 T422: 52:51-52:52
 T423: 52:52-52:53
 T424: 52:53-52:54
 T425: 52:54-52:55
 T426: 52:55-52:56
 T427: 52:56-52:57
 T428: 52:57-52:58
 T429: 52:58-52:59
 T430: 52:59-53:00
 T431: 53:00-53:01
 T432: 53:01-53:02
 T433: 53:02-53:03
 T434: 53:03-53:04
 T435: 53:04-53:05
 T436: 53:05-53:06
 T437: 53:06-53:07
 T438: 53:07-53:08
 T439: 53:08-53:09
 T440: 53:09-53:10
 T441: 53:10-53:11
 T442: 53:11-53:12
 T443: 53:12-53:13
 T444: 53:13-53:14
 T445: 53:14-53:15
 T446: 53:15-53:16
 T447: 53:16-53:17
 T448: 53:17-53:18
 T449: 53:18-53:19
 T450: 53:19-53:20
 T451: 53:20-53:21
 T452: 53:21-53:22
 T453: 53:22-53:23
 T454: 53:23-53:24
 T455: 53:24-53:25
 T456: 53:25-53:26
 T457: 53:26-53:27
 T458: 53:27-53:28
 T459: 53:28-53:29
 T460: 53:29-53:30
 T461: 53:30-53:31
 T462: 53:31-53:32
 T463: 53:32-53:33
 T464: 53:33-53:34
 T465: 53:34-53:35
 T466: 53:35-53:36
 T467: 53:36-53:37
 T468: 53:37-53:38
 T469: 53:38-53:39
 T470: 53:39-53:40
 T471: 53:40-53:41
 T472: 53:41-53:42
 T473: 53:42-53:43
 T474: 53:43-53:44
 T475: 53:44-53:45
 T476: 53:45-53:46
 T477: 53:46-53:47
 T478: 53:47-53:48
 T479: 53:48-53:49
 T480: 53:49-53:50
 T481: 53:50-53:51
 T482: 53:51-53:52
 T483: 53:52-53:53
 T484: 53:53-53:54
 T485: 53:54-53:55
 T486: 53:55-53:56
 T487: 53:56-53:57
 T488: 53:57-53:58
 T489: 53:58-53:59
 T490: 53:59-54:00
 T491: 54:00-54:01
 T492: 54:01-54:02
 T493: 54:02-54:03
 T494: 54:03-54:04
 T495: 54:04-54:05
 T496: 54:05-54:06
 T497: 54:06-54:07
 T498: 54:07-54:08
 T499: 54:08-54:09
 T500: 54:09-54:10
 T501: 54:10-54:11
 T502: 54:11-54:12
 T503: 54:12-54:13
 T504: 54:13-54:14
 T505: 54:14-54:15
 T506: 54:15-54:16
 T507: 54:16-54:17
 T508: 54:17-54:18
 T509: 54:18-54:19
 T510: 54:19-54:20
 T511: 54:20-54:21
 T512: 54:21-54:22
 T513: 54:22-54:23
 T514: 54:23-54:24
 T515: 54:24-54:25
 T516: 54:25-54:26
 T517: 54:26-54:27
 T518: 54:27-54:28
 T519: 54:28-54:29
 T520: 54:29-54:30
 T521: 54:30-54:31
 T522: 54:31-54:32
 T523: 54:32-54:33
 T524: 54:33-54:34
 T525: 54:34-54:35
 T526: 54:35-54:36
 T527: 54:36-54:37
 T528: 54:37-54:38
 T529: 54:38-54:39
 T530: 54:39-54:40
 T531: 54:40-54:41
 T532: 54:41-54:42
 T533: 54:42-54:43
 T534: 54:43-54:44
 T535: 54:44-54:45
 T536: 54:45-54:46
 T537: 54:46-54:47
 T538: 54:47-54:48
 T539: 54:48-54:49
 T540: 54:49-54:50
 T541: 54:50-54:51
 T542: 54:51-54:52
 T543: 54:52-54:53
 T544: 54:53-54:54
 T545: 54:54-54:55
 T546: 54:55-54:56
 T547: 54:56-54:57
 T548: 54:57-54:58
 T549: 54:58-54:59
 T550: 54:59-55:00
 T551: 55:00-55:01
 T552: 55:01-55:02
 T553: 55:02-55:03
 T554: 55:03-55:04
 T555: 55:04-55:05
 T556: 55:05-55:06
 T557: 55:06-55:07
 T558: 55:07-55:08
 T559: 55:08-55:09
 T560: 55:09-55:10
 T561: 55:10-55:11
 T562: 55:11-55:12
 T563: 55:12-55:13
 T564: 55:13-55:14
 T565: 55:14-55:15
 T566: 55:15-55:16
 T567: 55:16-55:17
 T568: 55:17-55:18
 T569: 55:18-55:19
 T570: 55:19-55:20
 T571: 55:20-55:21
 T572: 55:21-55:22
 T573: 55:22-55:23
 T574: 55:23-55:24
 T575: 55:24-55:25
 T576: 55:25-55:26
 T577: 55:26-55:27
 T578: 55:27-55:28
 T579: 55:28-55:29
 T580: 55:29-55:30
 T581: 55:30-55:31
 T582: 55:31-55:32
 T583: 55:32-55:33
 T584: 55:33-55:34
 T585: 55:34-55:35
 T586: 55:35-55:36
 T587: 55:36-55:37
 T588: 55:37-55:38
 T589: 55:38-55:39
 T590: 55:39-55:40
 T59

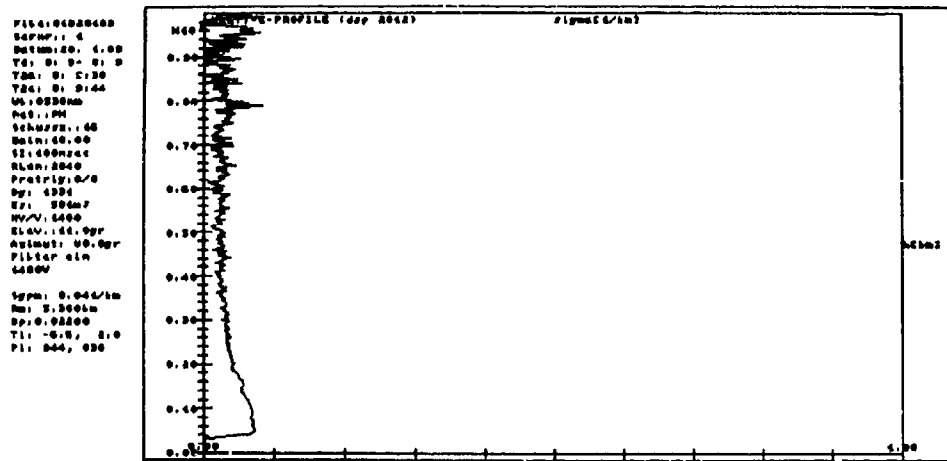


Fig. 10: Extinction coefficient profile in 532 nm from January 20, 1989, 08:10 CET

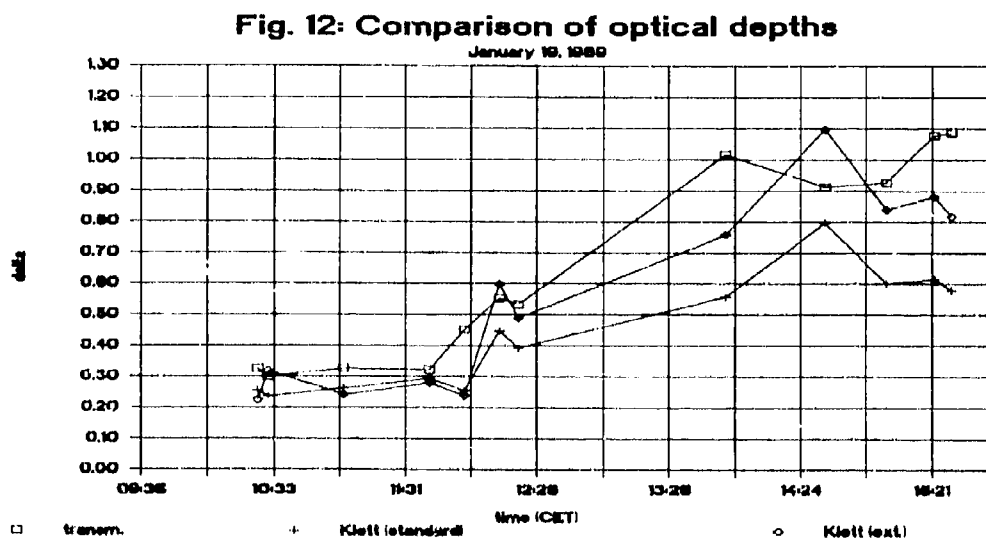
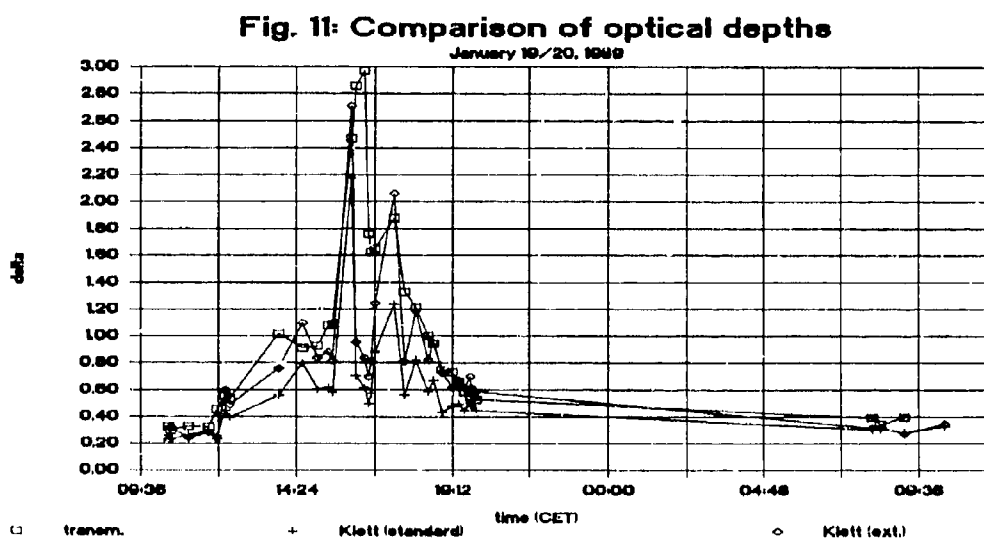


Fig. 13: Comparison of optical depths

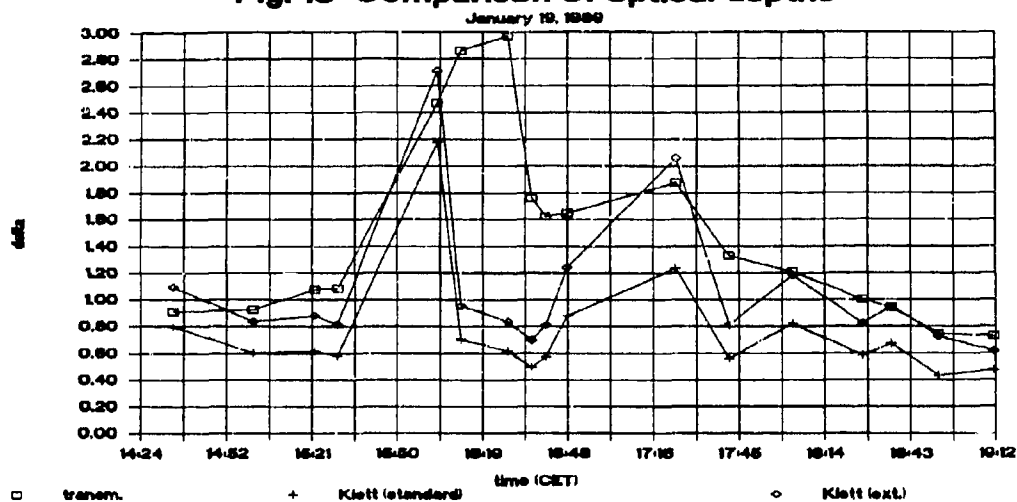


Fig. 14: Comparison of optical depths

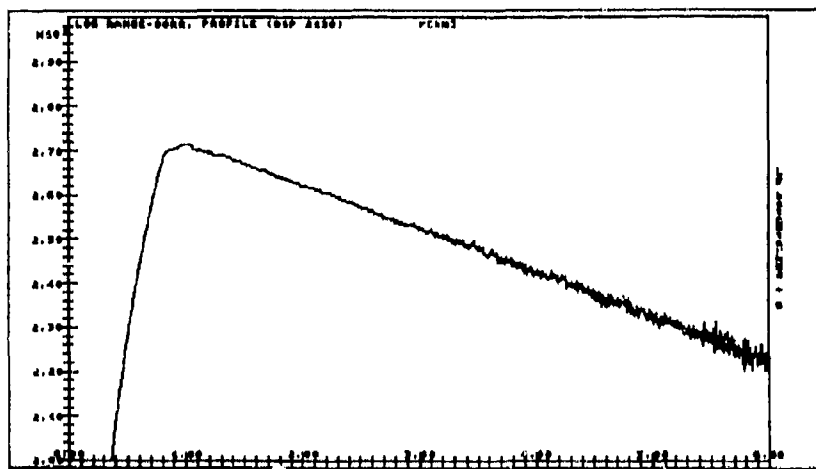
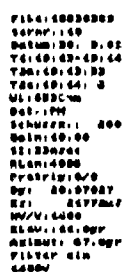
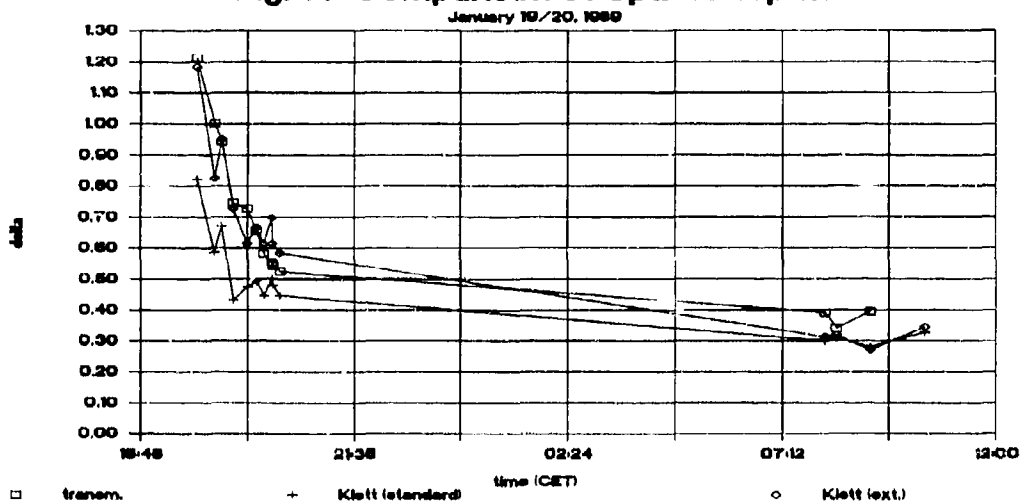
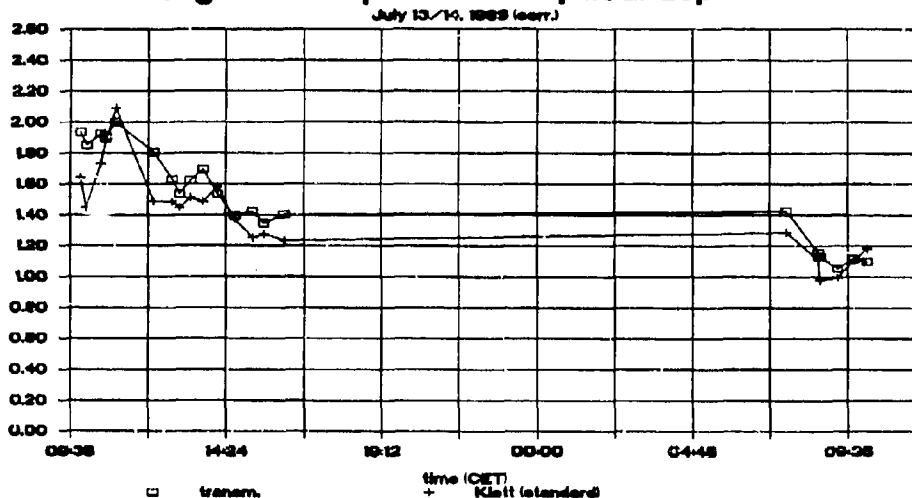


Fig. 15: Logarithmic range-corrected lidar return in 532 nm from March 30, 1989, 19:14 CET

Fig. 19: Comparison of optical depths



DISCUSSION

E. SHETTLÉ

The results of the Klett Method are somewhat sensitive to the choice of the extinction coefficient at the maximum range. This is particularly true for smaller optical depths (≤ 1) where the Klett solution does not have sufficient range to converge to the correct solution. How did you choose this extinction coefficient and how sensitive are your results to this choice?

AUTHOR'S REPLY

Generally, we calculate the extinction coefficient at the reference range from the measured visual range data at that point. In the particular case presented here, the visual range at the mountain station was beyond the measuring range of the nephelometer and was thus estimated to about 100 km. The sensitivity of the Klett extinction profiles to the choice of the boundary value is not sufficient in this case to explain the deviations observed in some cases.

E. ELORANTA

How did you select values of $p(180)/4\pi$ for aerosols?

AUTHOR'S REPLY

For the measurements presented here we have chosen $\beta_A \sim p(180)/4\pi (= \beta/\sigma)$ equal to 0.022, a value found in the literature. The β_A values can be used to bring the lidar-derived δ values closer to the transmittometer δ s. The best choice for β_A should be found from further measurements.

TECHNIQUE FOR SELECTING AN AEROSOL MODEL USEFUL FOR INFRARED ATMOSPHERIC TRANSMITTANCE CALCULATIONS

Herbert G. Hughes
Ocean and Atmospheric Sciences Division
Naval Ocean Systems Center
San Diego, California 92152-5000

SUMMARY

Vertical profiles of meteorological parameters are used with the LOWTRAN 6¹ atmospheric transmittance/radiance computer code to model measurements of near horizon infrared radiances. It is shown that calculations with the Navy Maritime Aerosol Model can exactly reproduce the measured horizon pixel radiance using non-unique combinations of air mass factors and surface visibilities. This feature is the result of the visibility scaling factor of the size distribution remaining nearly constant for any appropriate combination of the two factors, and the relative insensitivity of the calculated extinction coefficients for the far infrared wavelengths to the air mass factor term. Using measurements taken on two consecutive days during low wind speed conditions, it is shown that any appropriate combination of the two factors will allow the calculated and measured radiances at other angles above the horizon to differ less than 2%. These agreements place confidence in using the selected aerosol model in transmittance calculations for the far infrared wavelength bands over other propagation paths.

INTRODUCTION

In the absence of size distribution measurements, we must presently rely on the models in the LOWTRAN 6¹ code to calculate the effects of aerosols on infrared (IR) atmospheric transmittances and background radiances using measured meteorological parameters as inputs. These aerosol models were developed to be as representative as possible of different atmospheric conditions. However, they cannot be expected to exactly reproduce the optical properties in a given location at any specific time. A method is needed for selecting the input parameters so that the model best represents a particular situation. Of particular interest to Navy applications, is the Navy Maritime Aerosol Model for use in electro-optical systems performance prediction codes. This model (see Appendix) is the sum of three log normal size distributions, and, in addition to the surface wind speeds (current and 24-hour averaged) and relative humidity, requires the input of an air mass factor which identifies the origin of the aerosols as either marine or continental which is allowed to range between integer values of 1 for open ocean conditions and 10 for coastal regions. Also, when an observed surface visibility is available as an input, the model is adjusted so that the visibility calculated at a wavelength of 0.55 μm is the same as the observed value. The accuracy to which this model can predict atmospheric transmission or radiance for a given wavelength band is sensitive to the selection of the appropriate visibility and air mass factor². The air mass factor may be determined by either the measurement of atmospheric radon or by an air mass trajectory analysis to determine the time the air mass has been over land. The second option is extremely difficult, and requires a large data set of synoptic flow patterns. Neither of these techniques are presently available for shipboard use. Also, radiance contrast measurements between the sky background and objects at known distances in the open ocean are rarely available, and visibilities inferred from point scattering measurements onboard ship are most apt to be contaminated by ship influences. In this paper, a remote sensing technique is presented whereby an appropriate aerosol size distribution model can be selected which is applicable to transmittance and radiance calculations in the far infrared wavelength bands. In this method, nonunique combinations of the air mass factor and visibility for different meteorological conditions are inferred from LOWTRAN 6 calculations which allow agreement with measurements of 8-12 μm horizon radiances.

MEASUREMENTS

For this study, a Piper Navajo aircraft, equipped with Rosemount temperature and pressure probes, and an EG&G dewpoint sensor, made vertical spirals over the ocean to obtain the profile of temperature, relative humidity and pressure which are required inputs to the LOWTRAN 6 computer code for calculating the sky radiances. The vertical profiles of temperature and relative humidity, measured at 1430 PST on 9 November and 1424 PST 10 November 1968 off the coast of San Diego, California, are shown in Figures 1 and 2, respectively. The current and 24 h averaged wind speeds ($V_c = 3.7 \text{ m/s}$ and $\bar{V} = 2.1 \text{ m/s}$ for 9 November, and $V_c = 4.8 \text{ m/s}$ and $\bar{V} = 2.8 \text{ m/s}$ for 10 November) measured on shore during both days were from a westerly direction. At the time the meteorological parameters were obtained, measurements of IR (8 to 12 μm) horizon radiances were also made with a calibrated thermal imaging system (AGA THERMOVISION, model 780) using a 2.95° field of view lens. For these measurements the scanner was located at an elevation of 33 m on the Point Loma peninsula in San Diego and was directed over the ocean in a southerly direction. The response of the system is determined by placing a blackbody of known temperature ($\pm 0.1^\circ\text{C}$ for temperatures $< 50^\circ\text{C}$) in front of the lens aperture. The digitized video signal transfer function of the system then allows the blackbody temperature to be reproduced to within $\pm 0.2^\circ\text{C}$. The data processing software of the AGA system also allows the thermal scene to be displayed on a computer terminal in a format consisting of 128 pixels (0.023°/pixel). The effective blackbody temperature corresponding to each pixel can then be displayed on the screen by positioning a cursor at the appropriate position.

CALCULATION OF BACKGROUND RADIANCE SCENES

These measurements can be modeled with LOWTRAN 6 calculations to aid in selecting an appropriate aerosol model for radiance calculations on each day. In these calculations the meteorological profiles were divided into 33 layers as allowed by LOWTRAN 6. The lower layers of the profiles are also divided into sublayers containing the same amount of absorbing and scattering material and the temperature as the original layer. This artificial layering has been found necessary to remove the anomalous dip which occurs when aerosols are included in the LOWTRAN 6 radiance calculations for zenith angles close to 90° . As the ACA scanner could not be accurately plumbed, the zenith angle of the infrared horizon (the pixel corresponding to the maximum radiance) in each thermogram was taken to be one-half of a pixel less than the angle ($\theta = 90.177^\circ$ on 9 November and $\theta = 90.175^\circ$ on 10 November) for which the LOWTRAN calculations indicated the refracted ray path first struck the earth. Using these zenith angles with the measured profiles of meteorological parameters, the visibility required to match the measured horizon pixel radiance, for each integer value of air mass factor, must be determined by iteration from several different LOWTRAN calculations. The locus of points which allow the LOWTRAN calculations to exactly match the measured horizon pixel radiances ($3.27 \text{ mW/cm}^2 \text{ sr}$ on 9 November and $3.281 \text{ mW/cm}^2 \text{ sr}$ on 10 November) with nonunique combinations of air mass factor and visibility are shown in Figure 3 for the two days. This feature is the result of the visibility scaling factor (see Appendix) of the size distribution remaining nearly constant for any appropriate combination of the two factors, and the relative insensitivity of the calculated extinction coefficients for the far infrared wavelengths to the air mass factor term (AM) as shown in Figure 4. Any appropriate combination of the two factors will allow the radiances calculated at other angles above the horizon to be nearly identical as seen in Figures 5 and 6. Using widely different combinations of air mass factors and visibilities as shown in the figures, the calculated and measured values for 9 November differ by less than 2% over an elevation angle of approximately 1° . These radiance differences correspond to equivalent blackbody temperature differences of less than 0.7°C near the elevation angles of 0.4° and 0.8° . On 10 November the calculated and measured radiances with elevation are in excellent agreement below 0.8° elevation angle. Above that angle, the radiance differences amount to less than 0.5°C in equivalent blackbody temperature.

The variations in calculated transmittances (τ) to the infrared horizons ($R_{\text{hor}} = 19.491 \text{ km}$ on 9 November and $R_{\text{hor}} = 18.073 \text{ km}$ on 10 November), corresponding to the zenith angles where the refracted ray path first hit the earth, are shown in Figure 7 for the different combinations of air mass factor (AM) and required visibility. The resulting extinction coefficient (determined from the relation $\sigma = (-\ln \tau)/R_{\text{hor}}$) are shown in Figure 8. Both the calculated transmittances and resulting extinction coefficients show little variation for the different combinations of air mass factor and required visibility. These calculations are also summarized in Table 1. In the table, N_c , N_m and V_r refer to the calculated and measured radiances, and required visibility, respectively.

DISCUSSION

The results of this study have shown that in the absence of radon and visibility measurements, appropriate combinations of these two inputs to the Navy Aerosol Model can be inferred from LOWTRAN 6 calculations using standard meteorological inputs to match measured infrared horizon pixel radiances. In a practical sense, sophisticated instruments with the temperature resolution (0.1°C) and instantaneous field-of-view (0.87 mrad) similar to the ACA would have to be mounted on stabilized platforms for shipboard use. Such instruments are not presently available. However, horizon radiance measurements with hand-held instruments with wider fields-of-view of 1° or better could possibly be matched by calculated radiances integrated over the instrument's field-of-view as demonstrated in Figures 5 and 6.

The approach here is limited to the far infrared wavelengths. For shorter wavelengths the transmittances and extinction coefficients calculated with the model will depend more strongly on the air mass factor in the first component of the distribution. In earlier work, it was demonstrated that an appropriate aerosol size distribution could be selected which is applicable to transmittance and radiance calculations in both the visible and IR wavelength bands by including calculations which also matched the visible atmospheric optical depths determined from satellite detected upwelling solar radiances. This approach, however, is limited to cloud-free sky conditions during the daytime and requires a favorable position of the satellite to avoid sun glint from the ocean. An alternative approach is to incorporate a visible or near-infrared LIDAR system with the infrared measurements and model the backscattered power as a function of range.

ACKNOWLEDGEMENTS

Appreciation is extended to Dr. Douglas R. Jensen who provided the airborne measurements of meteorological parameters, and to Merle R. Paulson who assisted in the ACA measurements. Dr. Juergen H. Richter was responsible for providing the funding for this work effort. This work was sponsored by the Office of Navy Technology under Program Element 62435N, Project RM35G80, and Task N02G.

REFERENCES

1. Kneizys, F. X., E. P. Shettle, W. O. Gallery, J. H. Chatwynd, Jr., J. H. Abreu, J. E. A. Selby, S. A. Clough and R. W. Fenn, "Atmospheric transmittance /Radiance: Computer Code LOWTRAN 6, Air Force Geophysics Laboratory Technical Report No. 83-0187, August 1983.
2. Gathman, S. G. and B. Ulfers, "On the Accuracy of IR Predictions Made by the Navy Aerosol Model," in American Meteorological Society Ninth Conf. on Aerospace and Aeronautical Meteorology, pp. 194-198 (1983).

3. Wollenweber, F. G., "Effects of Atmospheric Model Layering on LOWTRAN 6 Calculations of 8 to 12 μ m Near Horizon Sky Radiances," NOSC TD 1193, January 1988.
4. Hughes, H. G., "Evaluation of the LOWTRAN 6 Navy Maritime Aerosol Model Using 8 to 12 μ m Sky Radiances," Opt. Eng., 26, 1155 (1987).
5. Hughes, H. G. and D. R. Jensen, "Aerosol Model Selection Using Surface Measurements of IR Horizon Radiances and Satellite Detected Visible Radiances," Appl. Opt., 27, 4367 (1988).
6. Fitzgerald, J. W., "Approximate Formulas for the Equilibrium Size of an Aerosol Particle as a Function of its Dry Size and Composition and the Ambient Relative Humidity," J. Appl. Meteorol., 14, 1044 (1975).

APPENDIX: DESCRIPTION OF THE LOWTRAN 6 NAVY MARITIME AEROSOL MODEL

The particle size distribution model (at radius r) is the sum of three log-normal distributions given by

$$n(r) = \sum_{i=1}^3 A_i \exp\left[-\left(\ln \frac{r}{r_i}\right)^2\right] \quad (\text{cm}^{-3} \cdot \mu\text{m}^{-1}), \quad (1)$$

where

$$A_1 = 2000(AM)^2, \quad (2)$$

$$A_2 = 5.866(\bar{V} - 2.2), \quad (3)$$

$$A_3 = 10 \quad (0.06V_c - 2.8) \quad (4)$$

Component A_1 represents the contribution by continental aerosols. AM is an air mass parameter that is allowed to range between integer values of 1 for open ocean and 10 for coastal areas and is given by

$$AM = \text{INT}(Rn/4) + 1, \quad (5)$$

where Rn is the measured atmospheric radon content expressed in pCi/m^3 . In the absence of radon measurements, the air mass factor can be related to the elapsed time, $T(\text{days})$ for the air mass to reach the point of observation:

$$AM = \text{INT}[9\exp(-T/4)] + 1 \quad (6)$$

Components A_2 and A_3 represent equilibrium sea spray particles generated by the surface wind speed averaged over 24 h (\bar{V} , in m/s) and the current surface wind speed (V_c , in m/s), respectively. (It should be noted that the current wind speed component is different from the value published in LOWTRAN 6. This modification was found to be necessary in order to match previously published measurements of IR sky radiances and near surface aerosol size distributions using the model). In Equation (1), r_i , the modal radius for each component referenced to a relative humidity of 80% ($r_1 = 0.03 \mu\text{m}$, $r_2 = 0.24 \mu\text{m}$ and $r_3 = 2.0 \mu\text{m}$) is allowed to grow with relative humidity (RH) according to the Fitzgerald⁶ formula:

$$f = [(2 - RH/100)/6(1 - RH/100)]^{1/3}, \quad (7)$$

The contribution to the total extinction or absorption by each component can then be written as

$$\sigma_{e,a}(\lambda)_i = (SF) \left(C_i \int_r Q_{e,a}(\lambda, r, m) \exp\left[-\left(\ln \frac{r}{r_i}\right)^2\right] r^2 dr \right) \quad (8)$$

where $C_i = (0.001\pi/f)A_i$. The factor f^{-1} in the expression for C_i ensures a constant total number of particles as the relative humidity increases. $Q_{e,a}(\lambda, r, m)$ is the cross section for either the extinction or absorption normalized to the geometrical cross section of the spherical particle, and m is the complex refractive index, which is allowed to change from that of dry sea salt as the particle deliquesces with increasing humidity. LOWTRAN 6 provides precalculated values in tabular form of the parameter $\sigma_{e,a}(\lambda)_i/C_i$ at discrete wavelengths for four relative humidities (50%, 85%, 90% and 99%), from which the average extinction for a specific wavelength band and relative humidity can be readily determined by interpolation. When an observed surface visibility (VIS) is available as an input to the model, the amplitudes of the three components are adjusted by a scaling factor (SF) so that the calculated aerosol extinction coefficient, σ_o , at a wavelength of $0.55 \mu\text{m}$ is the same as the observed extinction, σ_o , determined from the relationship

$$\text{VIS}_o = \frac{3.912}{\sigma_o + \sigma_r} \quad (9)$$

where σ_r is the Rayleigh contribution to extinction at $0.55 \mu\text{m}$.

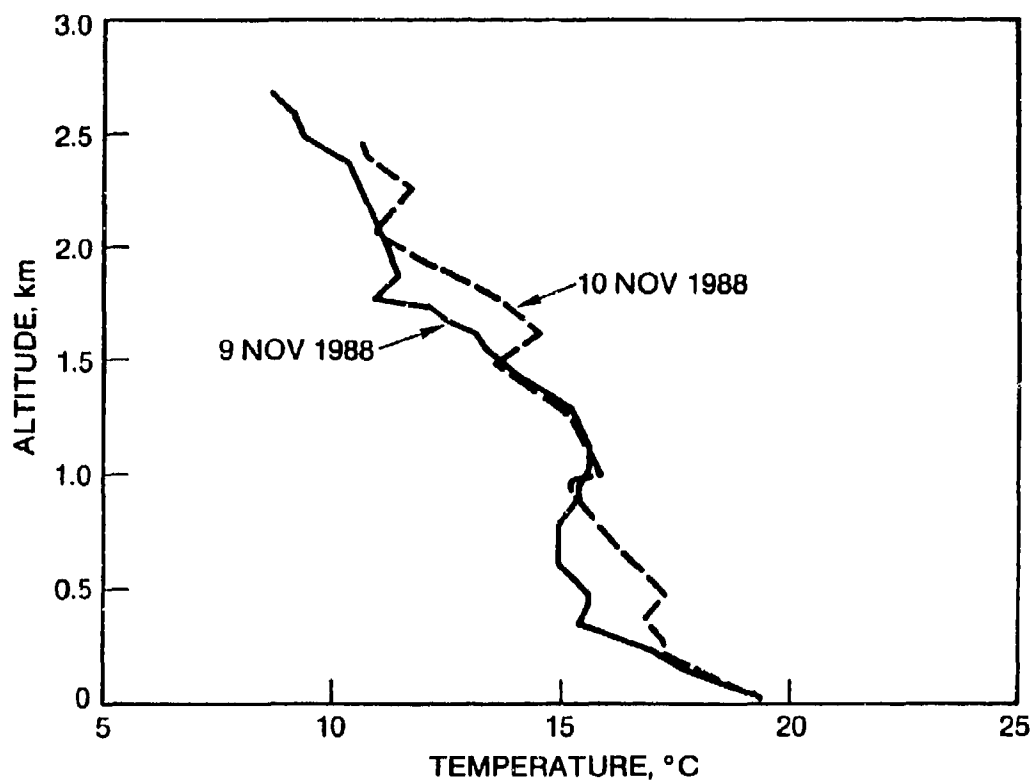


Figure 1. Profiles of air temperature measured with altitude on 9 and 10 November 1988 off the coast of San Diego, California.

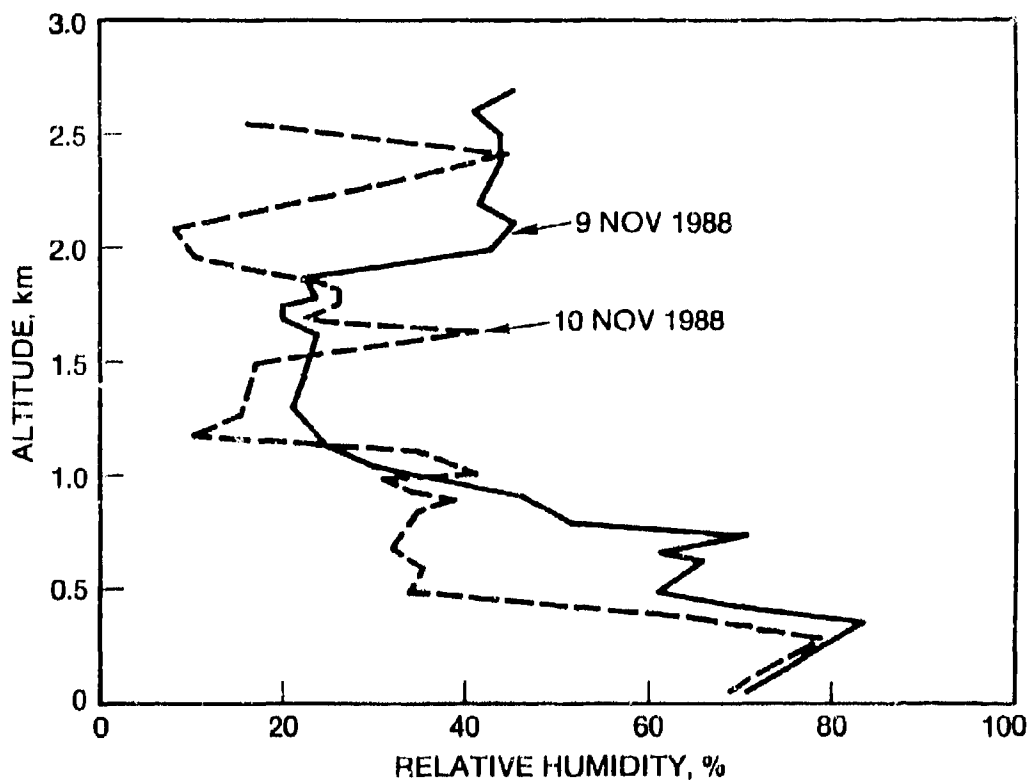


Figure 2. Profiles of relative humidity measured with altitude on 9 and 10 November 1988 off the coast of San Diego, California.

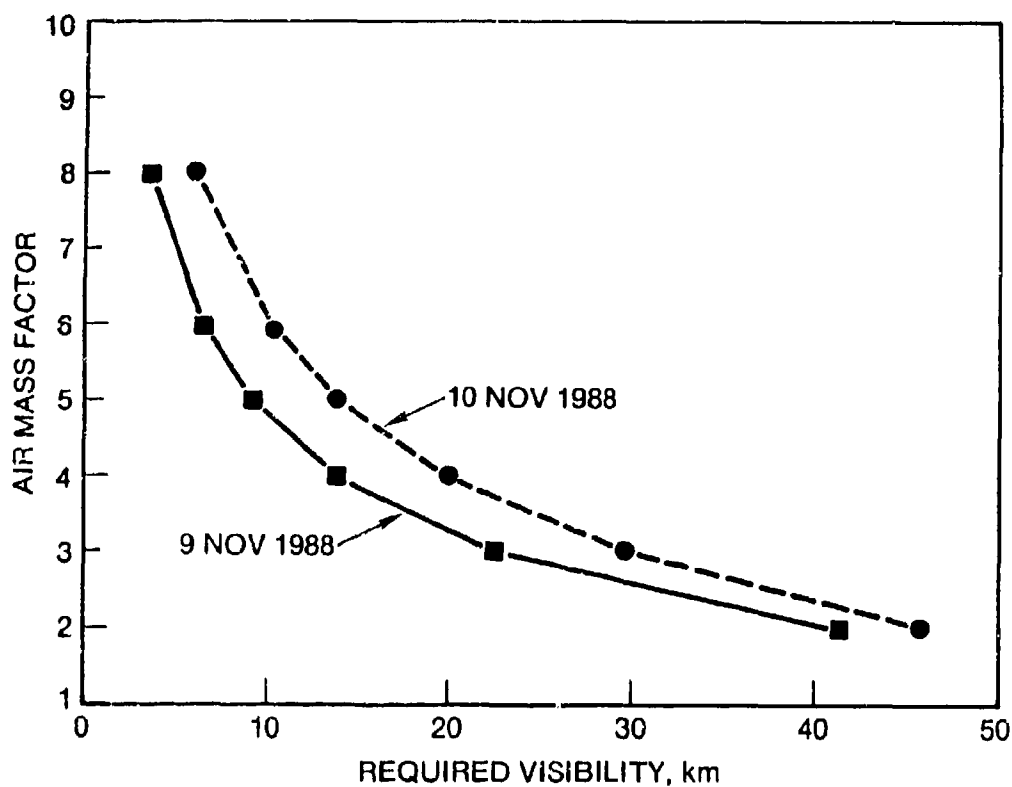


Figure 3. Loci of points of LOWTRAN 6 calculations with different combinations of air mass factors and visibilities which match measured values of IR (8 to 12 μ m) horizon radiances 9 and 10 November 1988.

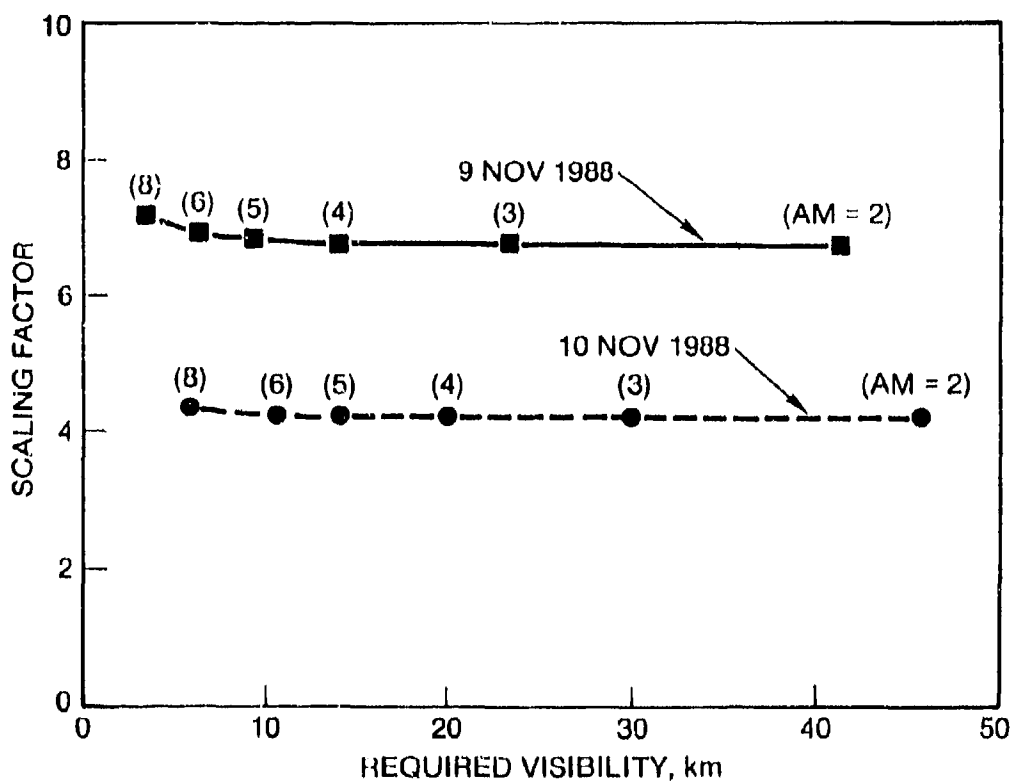


Figure 4. Aerosol size distribution scaling factor (SF) versus the required surface visibility to match the measured infrared horizon pixel radiance for fixed values of air mass factors (AM).

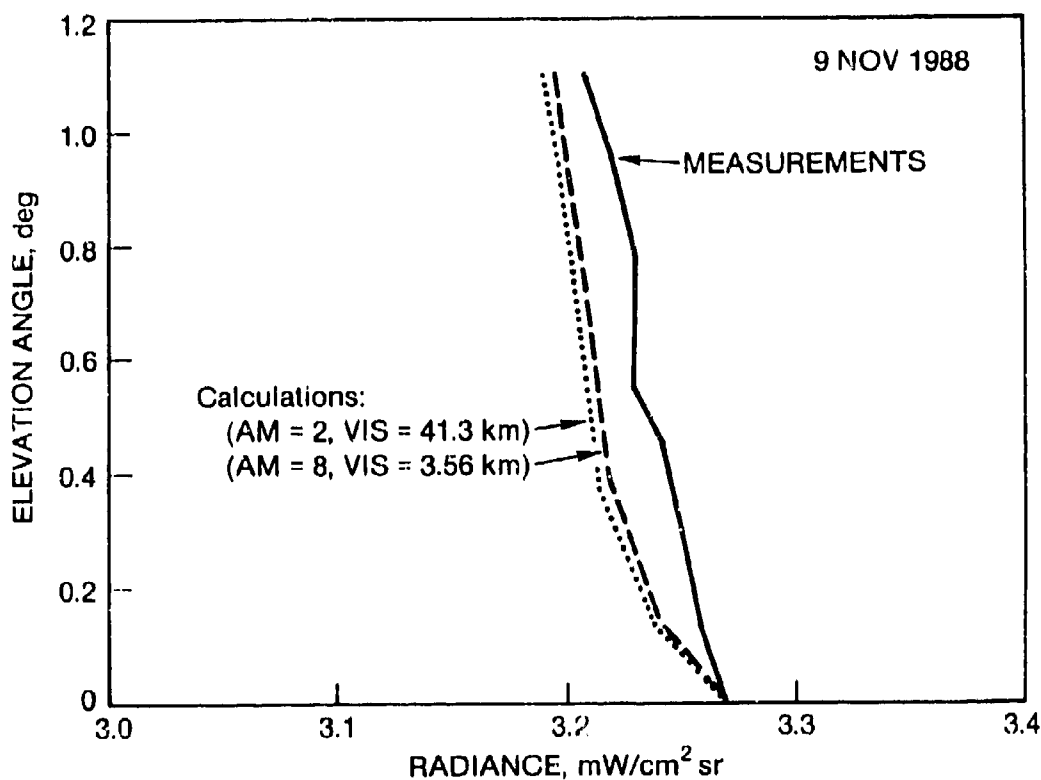


Figure 5. Comparison of the measured and calculated IR (8 to 12 μm) radiances for zenith angles about 1° above the horizon using different combinations of air mass factors and visibilities determined for 9 November 1988.

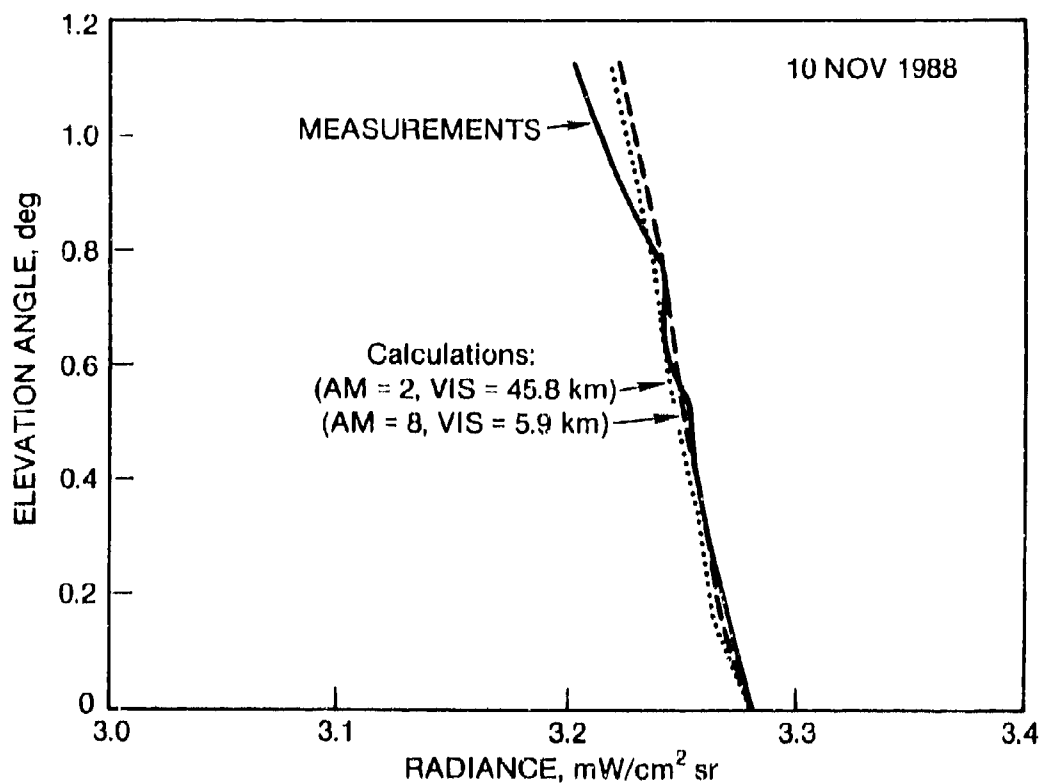


Figure 6. Comparison of the measured and calculated IR (8 to 12 μm) radiances for zenith angles about 1° above the horizon using different combinations of air mass factors and visibilities determined for 10 November 1988.

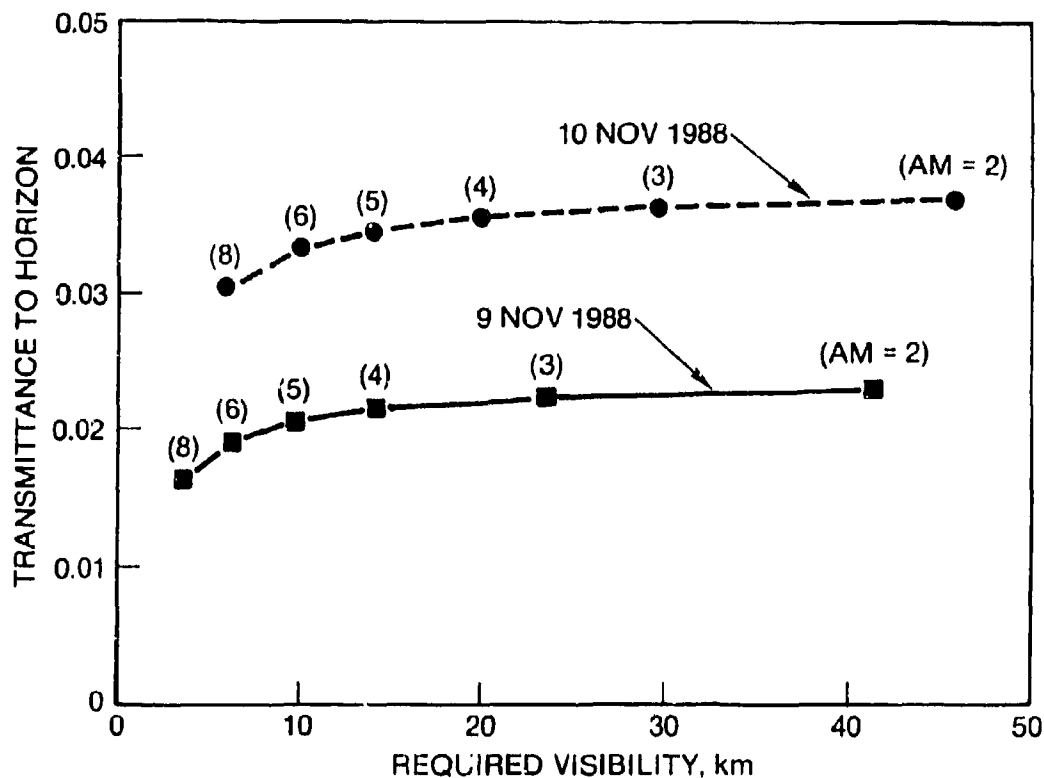


Figure 7. Calculated values of IR (8 to 12 μm) transmittances to the horizon using different combinations of air mass factors (AM) and required surface visibility.

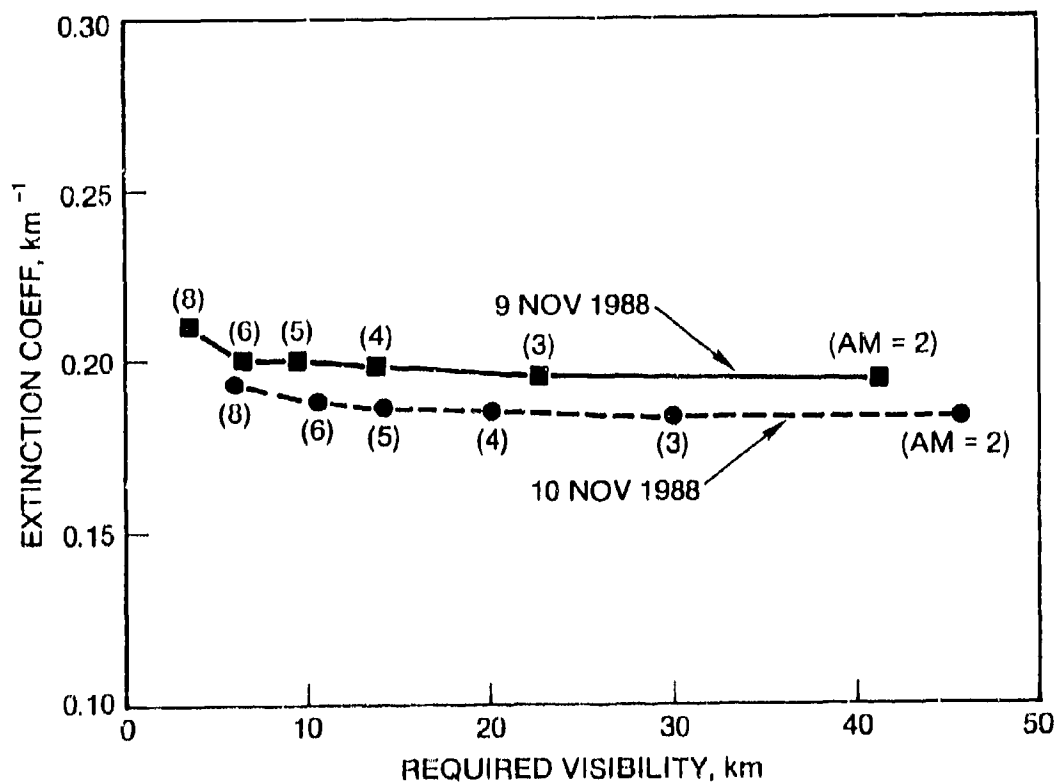


Figure 8. Extinction coefficients corresponding to the calculated transmittances shown in Figure 7.

| | AM | V_r (km) | SF | N_c (mW/cm ² sr) | τ | σ (km ⁻¹) |
|-------------------------------------|----|---------------|------|----------------------------------|--------|---------------------------------|
| 9 Nov 1988 | 2 | 41.3 | 6.71 | 3.270 | 0.023 | 0.194 |
| $N_m = 3.270$ mW/cm ² sr | 3 | 22.5 | 6.75 | 3.270 | 0.022 | 0.195 |
| $R_{hor} = 19.491$ km | 4 | 13.8 | 6.74 | 3.270 | 0.021 | 0.198 |
| | 5 | 9.1 | 6.82 | 3.270 | 0.020 | 0.200 |
| | 6 | 6.4 | 6.89 | 3.270 | 0.019 | 0.200 |
| | 8 | 3.56 | 7.14 | 3.270 | 0.016 | 0.210 |
| 10 Nov 1988 | 2 | 45.8 | 4.16 | 3.281 | 0.037 | 0.183 |
| $N_m = 3.281$ mW/cm ² sr | 3 | 29.6 | 4.18 | 3.281 | 0.036 | 0.183 |
| $R_{hor} = 18.073$ km | 4 | 19.8 | 4.19 | 3.281 | 0.036 | 0.185 |
| | 5 | 13.1 | 4.22 | 3.281 | 0.035 | 0.186 |
| | 6 | 10.1 | 4.22 | 3.281 | 0.033 | 0.188 |
| | 8 | 5.9 | 4.31 | 3.281 | 0.030 | 0.193 |

Table 1. Summary of LOWTRAN 6 calculations of scaling factors, horizon pixel radiances, transmittances and extinction coefficients using different combinations of air mass factors and required surface visibilities.

DISCUSSION

M. SHETTLER

Some of your measurements of radiance as a function of elevation angle, showed alternating increases and decreases in the radiance. Can you explain these?

AUTHOR'S REPLY

I can't give a definite answer. It may be related to low-level aerosols entrained by the inversion.

Radar Scatterometry and Polarimetry at 220 GHz

Robert E. McIntosh, Professor and James B. Mead, Research Assistant
University of Massachusetts
Microwave Remote Sensing Laboratory
Amherst, MA 01003, U.S.A.
Tel.: 413/545-0779; FAX: 413/545 0724

Summary

The University of Massachusetts has developed two high-power portable radars operating in the 220 GHz absorption window. The first, an incoherent 215 GHz scatterometer has been used for reflectivity measurements of foliage, fallen snow, clouds and fog between ranges of .1 and 2 km. We have also developed an incoherent 225 GHz polarimetric radar capable of fully characterizing the Stokes scattering matrix of distributed targets. Both radars employ an Extended Interaction (Klystron) Oscillator (EIO) as the transmitting source. These tubes produce a 60 W pulse of 50-600 ns duration and operate at a maximum duty cycle of .005. High efficiency Schottky barrier diode mixers are attached directly to the feed horns of the receiver antennas to minimize loss. This paper will summarize our work at 215 GHz, including a review of the hardware and measurements of clouds and fog. The 225 GHz polarimeter will be discussed in greater depth, including a review of the theory of polarimetry, a description of the hardware and a novel calibration technique requiring only a single in-scene reflector. Preliminary polarimetric measurements of a dihedral reflector and foliage are presented and discussed.

215 GHz System Description

A block diagram of the 215 GHz radar system is given in Figure 1. Table 1 summarizes the important parameters for estimating overall system performance. The transmitter employs a Varian VKY2429M1 EIO capable of producing 60 W pulses at a duty cycle up to 0.005. The modulator consists of an internal Pulse Repetition Frequency (PRF) generator, a Field Effect Transistor (FET) switch, and a high voltage triode switch. The triode acts as a hard-tube modulator that is capable of providing the high peak currents to rapidly charge the EIO stray capacitance, while providing a flat pulse to minimize EIO frequency drift. The receiver front end employs a single ended Schottky diode mixer driven by a 71.2 GHz InP Gunn diode local oscillator through a frequency tripler. An automatic frequency control (AFC) loop operating between 1.2 and 1.6 GHz down converts the signal to 160 MHz, where a logarithmic amplifier is used prior to detection. Separate 6-inch Gaussian optics lens antennas with scalar feed horns are used to achieve high isolation (> 100 dB) between transmitter and receiver. A dual antenna scheme was chosen due to inefficiency of circulators and transmit/receive switches at this wavelength.

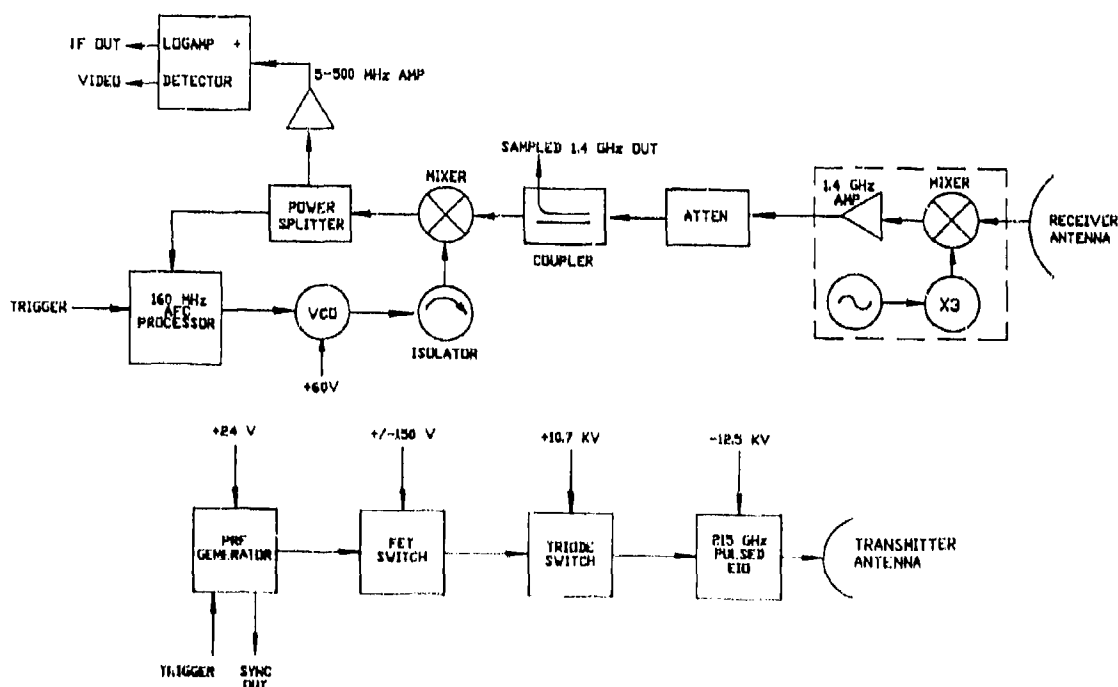


Figure 1. 215 GHz radar block diagram.

Range Capability

An approximate model for equivalent reflectivity factor, Z_e , of clouds and fog has been computed using Mie scattering theory and an appropriate particle distribution model. Using Deirmendjian's distributions several cloud types have been modeled at 215 GHz [1]. Values for $\text{dB}(Z_e)$ are given in Table 2, along with extinction coefficient, K_e , for several cloud varieties and fog. Atmospheric loss due to water vapor, L_w , is typically 2 to 6 dB/km. Total atmospheric attenuation, L_a , can be approximated by $K_e + L_w$.

The radar range equation may be solved for Z_e using the parameters given and assuming 10 dB of integration gain (100 samples). Solving for the minimum Z_e as a function of range yields

$$\text{dB}(Z_e)_{\min} = 20 \log R + (L_a)R/500 - 80.2 \quad (1)$$

where Z_e is the effective reflectivity factor in mm^6/m^3 , R is range in meters and L_a is atmospheric attenuation in dB-km. Figure 2 plots minimum $\text{dB}(Z_e)$ versus range for two atmospheric loss conditions.

Table 1. Characteristics of UMass 214 GHz wavelength radar system.

| Transmitter | |
|-------------------|-----------------|
| Center Frequency | 215 GHz Nominal |
| Peak Output Power | 60 W |
| Pulsewidth | 100-500 nsec |
| PRF | 700 Hz-20 KHz |
| Tuning Bandwidth | 300 MHz |
| Max Duty Cycle | .005 |

Table 2. $\text{dB}(Z_e)$ and K_e for Various Cloud Varieties and Fog

| Antenna | | Cloud Type | $\text{dB}(Z_e)$ | K_e (db-km) |
|----------------|----------|-------------------|------------------|---------------|
| | 6" Lens | Stratocumulus | -8 | 2.8 |
| 3 dB beamwidth | 0.64 deg | Fog Layer | -14 | 1.6 |
| Gain | 48 dB | Low-Lying Stratus | -16 | 2.6 |
| | | Cumulus Congestus | +14 | 22.5 |

| Receiver | |
|---------------|--------------------|
| Noise Figure | 10 dB DSB |
| 1st IF | 1.4 GHz |
| 2nd IF | 160 MHz |
| Bandwidth | Variable, 5-40 MHz |
| Dynamic Range | 70 dB |

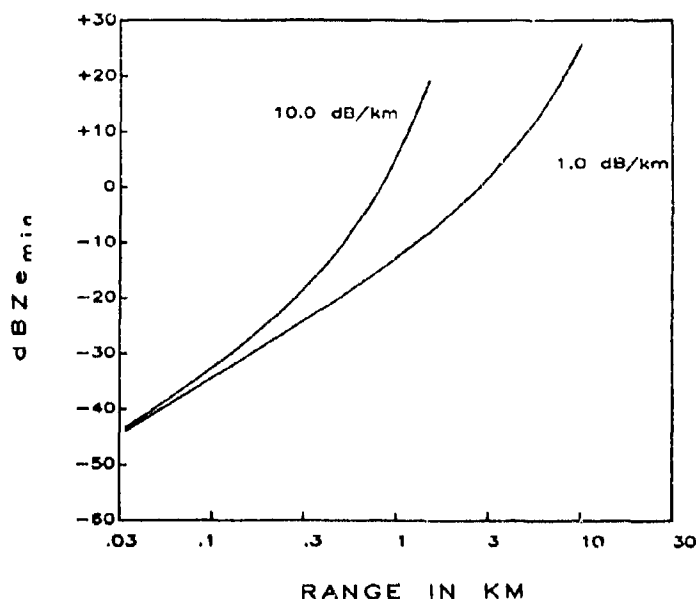


Figure 2. Minimum detectable reflectivity versus range for two atmospheric loss conditions.

Measurements

Measurements of fog and clouds show good agreement with predicted performance. Near horizontal measurements of fog with visibility varying between 300 and 800 meters were made over a period of one hour. A range vs. time diagram of fog reflectivity is shown in figure 3. Figure 4 is a map of stratocumulus reflectivity versus altitude over a period of 20 minutes. Significant backscatter was measured down to ground level, indicating the presence of small numbers of non-precipitating hydrometeors far below the apparent cloud base.

In addition to atmospheric measurements, we have made extensive radar cross section measurements of foliage and fallen snow. Measurements of foliage were made during the 1987 growing season [2], which indicated that the largest contribution to σ° was due to scattering from the leaves and that coniferous trees were more depolarizing than deciduous trees.

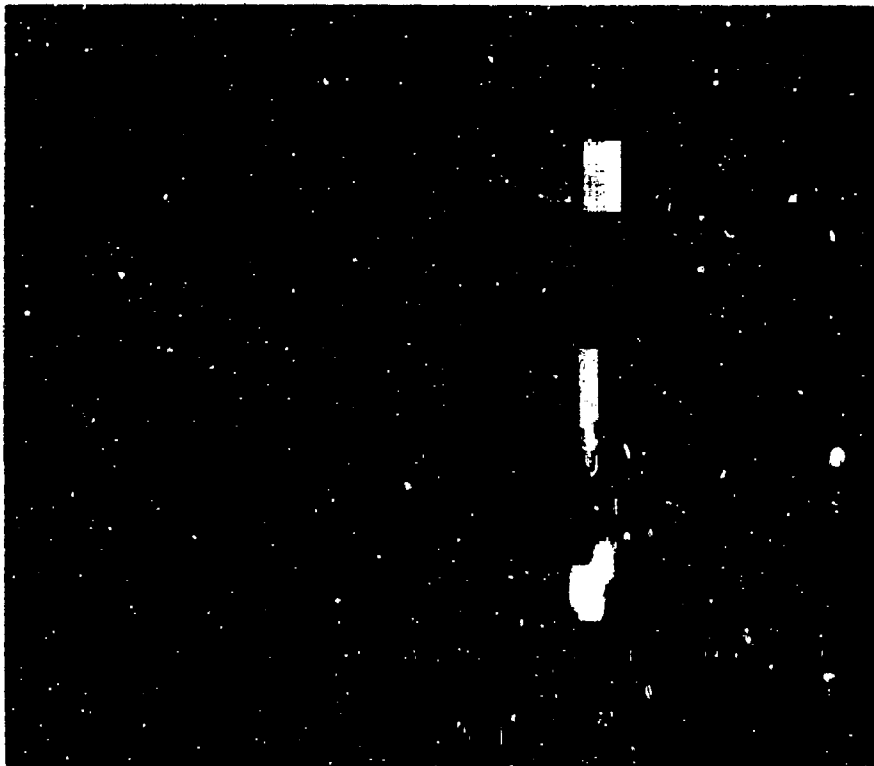


Figure 3. Range-time diagram of fog reflectivity for near horizontal path.

225 GHz Polarimeter

Polarimetric radars capable of fully characterizing the polarization transformation matrix of a target can provide significantly more insight into scattering mechanism than ordinary single polarization radars. Microwave measurements of the monostatic target scattering matrix are typically made by alternately transmitting two orthogonally-polarized waves and measuring the phase and magnitude of the response with orthogonally-polarized receiver channels. Such coherent measurement techniques are capable of rapidly characterizing the instantaneous complex scattering matrix of a target. Recent measurements using a polarimetric synthetic aperture radar (SAR) [3] have proven effective in classifying target homogeneity, scattering mechanisms, and in determining optimal polarizations.

The design, construction and system evaluation of a portable, *incoherent* 225 GHz polarimetric radar capable of measuring the average Stokes scattering matrix of natural and man-made targets is described below. The transmitter employs an EIO which produces a 60 W output pulse of 50-600 ns duration. The measurement of the average Stokes matrix, which characterizes the mean polarization transformation behavior of a target, is achieved by transmitting waves having vertical, horizontal, -45 linear, right hand circular polarization, and simultaneously receiving both the vertical and horizontal components of the scattered wave simultaneously. A brief review of the theory of polarimetry is presented next in order to clarify the hardware requirements.

Principles of Incoherent Polarimetry

The quasi-instantaneous polarization state of a TEM wave traveling in the $\pm Z$ direction can be described in terms of the ellipse traced out by the electric field vector as measured at $Z = Z_0$, as shown in Figure 5. The ellipse parameters, ϕ and r completely specify the polarization state of the wave and are expressed in terms of electric field quantities by

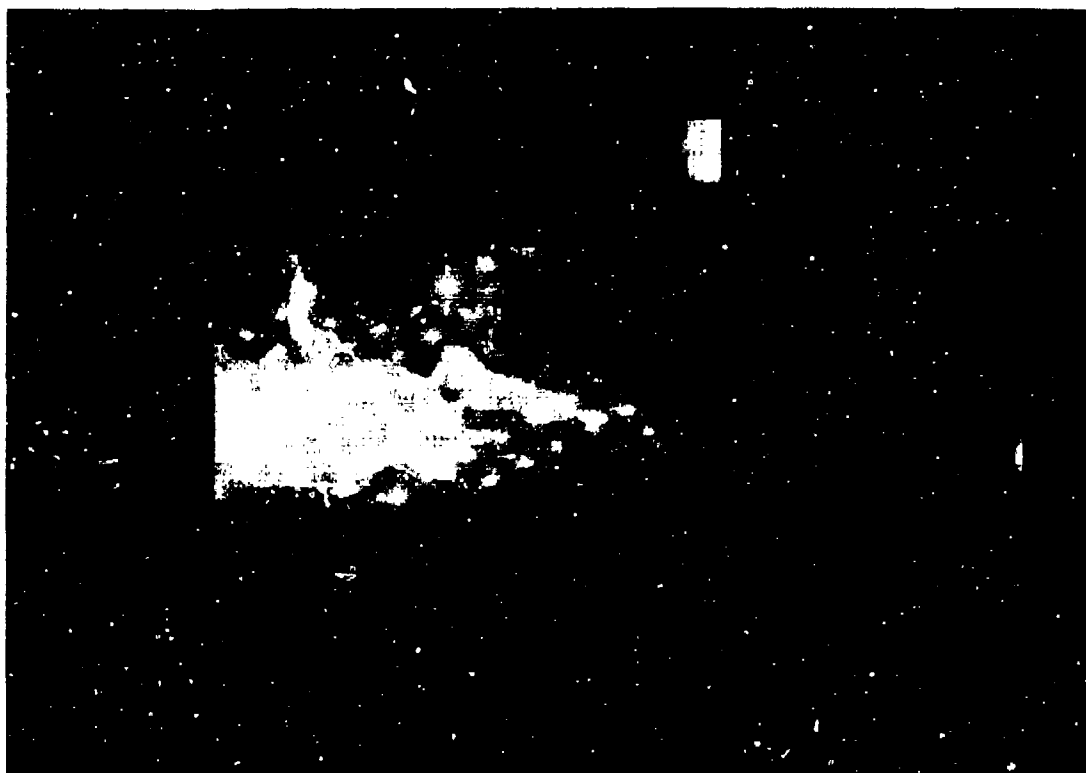


Figure 4. Range time diagram of stratocumulus reflectivity for vertically pointed radar.

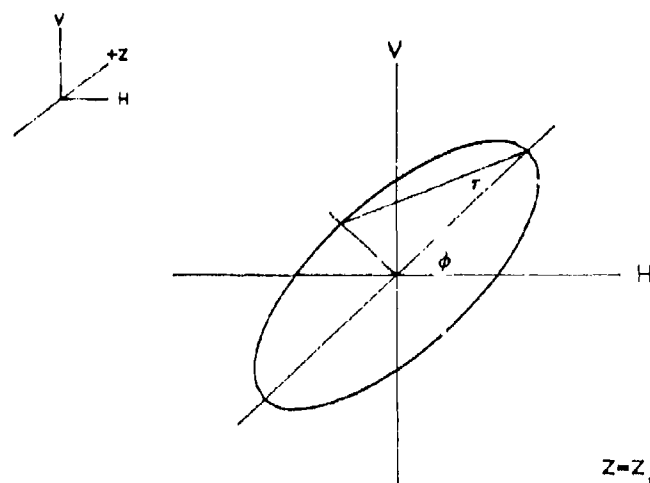


Figure 5. Polarization ellipse parameters ϕ (orientation) and r (ellipticity).

$$r = \frac{1}{2} \sin^{-1} \left(\frac{2|V||H|\sin \delta}{|V|^2 + |H|^2} \right) \quad (2)$$

$$\phi = \frac{1}{2} \tan^{-1} \left(\frac{2|V||H|\cos \delta}{|V|^2 - |H|^2} \right) \quad (3)$$

where $|V|$ and $|H|$ represent the magnitude of the electric field in the vertical and horizontal planes respectively, and δ is the phase difference between the vertical and horizontal fields. For this treatment, $r > 0$ represents right-hand sense waves where the right-hand rule is applied to the rotating field vector at $Z = Z_0$ with the thumb in the direction of propagation. A receiver capable of measuring $|V|$, $|H|$ and δ is sufficient to measure the polarization state of an incoming wave. A more general description of wave polarization, one which may account for partially polarized waves, is given by the Stokes vector \mathbf{g} where

$$\begin{aligned}
 g_0 &= |H|^2 + |V|^2 \\
 g_1 &= |H|^2 - |V|^2 \\
 g_2 &= 2|V||H|\cos\delta \\
 g_3 &= 2|V||H|\sin\delta
 \end{aligned} \quad (4)$$

The scattering behavior of an arbitrary distributed target or point target may be characterized in terms of the average Stokes matrix (Mueller matrix), M . The power received by an antenna whose polarization state is given by g_{rc} from a target with Stokes matrix M illuminated by a transmit antenna with Stokes vector g_{tr} is given by

$$P_{rec} = k g_{rc} \cdot M g_{tr} \quad (5)$$

where k is a lumped constant representing all propagation factors.

The average Stokes matrix may be measured by illuminating a target with vertical, horizontal, 45 degree linear, and right hand circular polarization. The Stokes vectors for these polarizations are

$$\begin{aligned}
 g_v &= \begin{bmatrix} 1 \\ -1 \\ 0 \\ 0 \end{bmatrix} & g_h &= \begin{bmatrix} 1 \\ 1 \\ 0 \\ 0 \end{bmatrix} & g_{45} &= \begin{bmatrix} 1 \\ 0 \\ 1 \\ 0 \end{bmatrix} & g_{RHCG} &= \begin{bmatrix} 1 \\ 0 \\ 0 \\ 1 \end{bmatrix}
 \end{aligned} \quad (6)$$

Suppose a receiver is capable of measuring the instantaneous Stokes vector, $r_i = (r_{0i}; r_{1i}; r_{2i}; r_{3i})$ of an incoming wave corresponding to transmit polarization i . Using the transmit Stokes vectors from Equation (6), a set of equations may be written which relates the elements of the Stokes scattering matrix, M , to the measured values of r_i

$$\begin{bmatrix} r_{01} & r_{02} & r_{03} & r_{04} \\ r_{11} & r_{12} & r_{13} & r_{14} \\ r_{21} & r_{22} & r_{23} & r_{24} \\ r_{31} & r_{32} & r_{33} & r_{34} \end{bmatrix} = \begin{bmatrix} 1 & 0 & 0 & 0 \\ 0 & 1 & 0 & 0 \\ 0 & 0 & 1 & 0 \\ 0 & 0 & 0 & 1 \end{bmatrix} \begin{bmatrix} M_{01} & M_{02} & M_{03} & M_{04} \\ M_{11} & M_{12} & M_{13} & M_{14} \\ M_{21} & M_{22} & M_{23} & M_{24} \\ M_{31} & M_{32} & M_{33} & M_{34} \end{bmatrix} \begin{bmatrix} 1 & 1 & 1 & 1 \\ 1 & 1 & 0 & 0 \\ 0 & 0 & 1 & 0 \\ 0 & 0 & 0 & 1 \end{bmatrix} \quad (7)$$

which may be solved for M .

215 GHz Polarimeter System Description

The 225 GHz polarimeter consists of a multiple polarization transmitter, a dual polarization receiver, a Polarimetric Radar Control and Data Acquisition (PRACDA) subsystem, and a data logging computer. Much of the transmitter circuitry, including the modulator, driver and pulse generator were built at the Georgia Tech Research Institute [4]. The transmitter is functionally equivalent to the 215 GHz transmitter shown in Figure 1, except the modulator incorporates a tailbiter circuit to reduce power supply loading. The transmitter employs a Gaussian Optics Lens Antenna with two quarter-wave plates mounted between the feed and the lens that can be independently rotated to control the polarization state. The quarter wave plates are rotated by a chain drive system powered by stepper motors and controlled by PRACDA in order to automate the measurement process.

Figure 6 is a block diagram of the receiver showing its major functional components. The antenna, mixers, local oscillator and phase-lock circuitry were provided as an integrated subsystem by Millitech Corporation. The dual polarization antenna uses a six inch diameter TPX[®] lens with $f/d = 1$. The incoming field is separated into vertical and horizontal polarization (V and H) using a linear array of 0.001 inch diameter wires spaced at 300 wires per inch. Scalar feed horns are attached directly to the input of the harmonic mixers to minimize losses. The second harmonic mixers are pumped with an LO of 112.717 GHz at a power level of approximately 10 mW. The overall double sideband noise figure of the receiver was measured radiometrically to be 11.0 dB.

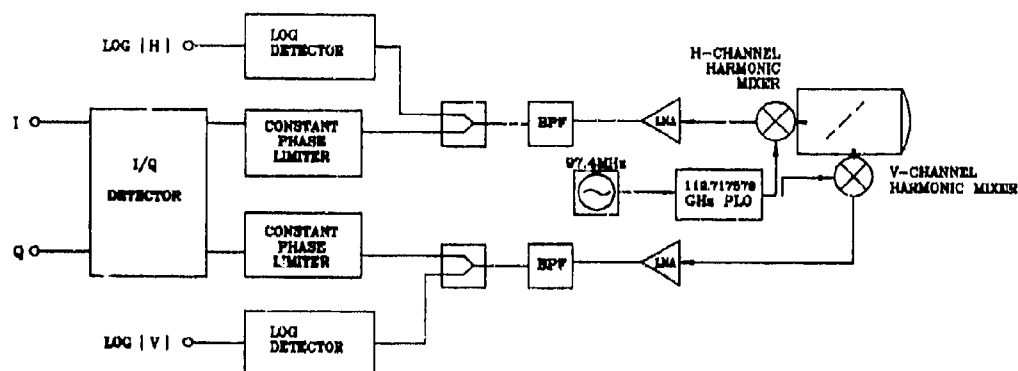


Figure 6. 225 GHz polarimetric receiver block diagram.

The receiver IF consists of separate magnitude and phase detection channels. The magnitude of V and H are sampled independently by log detectors having a dynamic range of 70 dB. The relative phase between V and H is measured by an In-phase and Quadrature (I-Q) detector which is preceded by matched constant phase limiters that provide a constant 10 dBm output over more than 65 dB dynamic range. Table 3 summarizes the salient features of the 225 GHz polarimeter.

Table 3 Specifications for 225 GHz Polarimetric Radar

| <u>Transmitter</u> | |
|---------------------|---|
| Center Frequency | 225.63 GHz |
| Output Power, Peak | 60 W |
| Duty Cycle, Maximum | .005 |
| PRF, Maximum | 20 KHz |
| Pulse Width | 50-500 ns |
| <u>Receiver</u> | |
| SSB Noise Figure | 15 dB |
| F_{IF} | 194.8 MHz |
| IF Bandwidth | Up to 50 MHz |
| Outputs | $\log V , \log H , I_{rel}, Q_{rel}$ |
| Dynamic Range | 70 dB |
| <u>Antennas</u> | |
| Receiver | Dual Polarization, H and V Channels, .61° Beamwidth |
| Transmitter | Multiple Polarization, Manually Switchable, .61° Beamwidth |

The control and data acquisition system, PRACDA, consists of six 20 MHz, 8-bit A/D converters, a 150 bit status register that stores the various radar states, and circuitry to interface with the data logging computer. The status registers are used to control the radar's PRF, number and position of the range gates, and the transmitter polarization. The maximum data rate is limited by the computer interface to 120 Kbytes·sec⁻¹. This constrains the PRF range gate product to 30,000.

Calibration

Calibration of an incoherent polarimeter has been described previously by Wood [5]. Wood's procedure involves using four in scene reflectors, three of which scatter waves having known polarization and the fourth being an odd-bounce reflector, such as a trihedral corner reflector. Fixed errors are removed from the receiver so it may accurately measure the polarization state of an incoming wave, and then the calibrated receiver is used to measure the state of the four transmitted polarizations used in making Stokes matrix measurements. An alternative technique which is equivalent to Wood's procedure requires placing a polarizing grid in front of the receiver antenna which can be rotated to three different positions. This modification has several advantages. Firstly, only a single odd bounce reflector is required, and secondly, it eliminates the errors which arise from clutter in the return signal from an in-scene polarized target.

Preliminary Measurements

Measurements of foliage, terrain, rain as well as various artificial targets were carried out during the summer of 1989. Measurements of a vertically oriented dihedral corner reflector made at a range of 200 meters are presented in Figure 7, as a function of the orientation angle, ϕ and ellipticity angle, τ , of the transmitter polarization. For the co-polarized signature, the receiver antenna is assumed to have the same polarization state as the transmitter, while the receiver and transmitter polarizations are orthogonal in the cross-polarized signature. The minima/maxima in the co-/cross-polarized signatures at $\phi = 45^\circ$ and 135° , $\tau = 0^\circ$ are characteristic of this type of target [6]. Co-polarized signatures for a deciduous tree (Eastern Cottonwood) and a conifer (White Pine) are compared in Figures 8a-b. The pedestal at $\tau = \pm 45^\circ$ is a measure of the degree of depolarization (randomness) in the scattered wave. Our data indicates that the height of the pedestal at $\tau = \pm 45^\circ$ decreases with increasing leaf/needle size. The greater depolarization displayed by the White Pine is shown more dramatically in Figures 8c-d where a histogram of the receive polarization state ϕ and τ is plotted for vertical transmit polarization. The power-weighted standard deviation of ϕ and τ are given in Table 4.

Table 4. Standard deviations of the received polarization ellipse angles ϕ and τ for vertical transmit polarization.

| | σ_ϕ | σ_τ |
|------------|---------------|---------------|
| Cottonwood | 11.3° | 9.2° |
| White Pine | 22.8° | 14.0° |

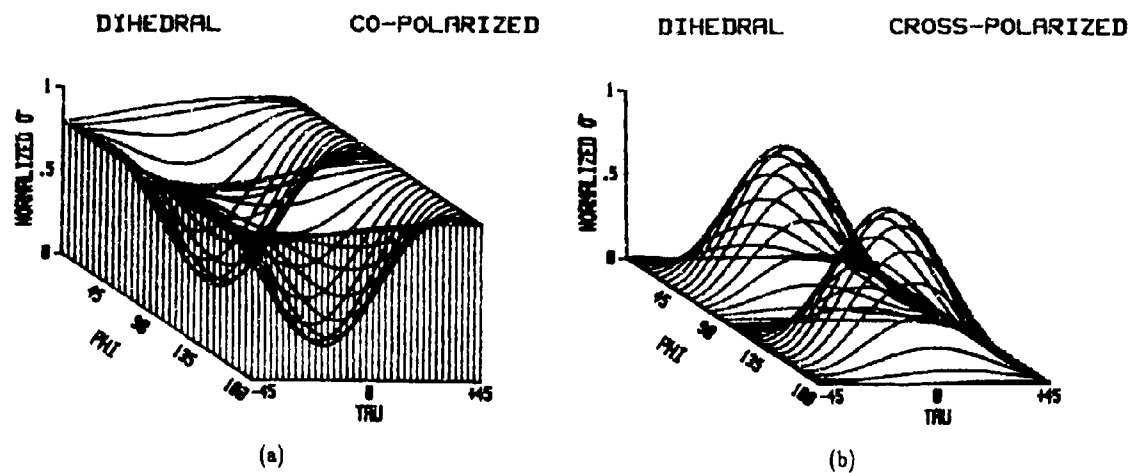


Figure 7. Co- and cross-polarized polarization signatures for a dihedral corner reflector.

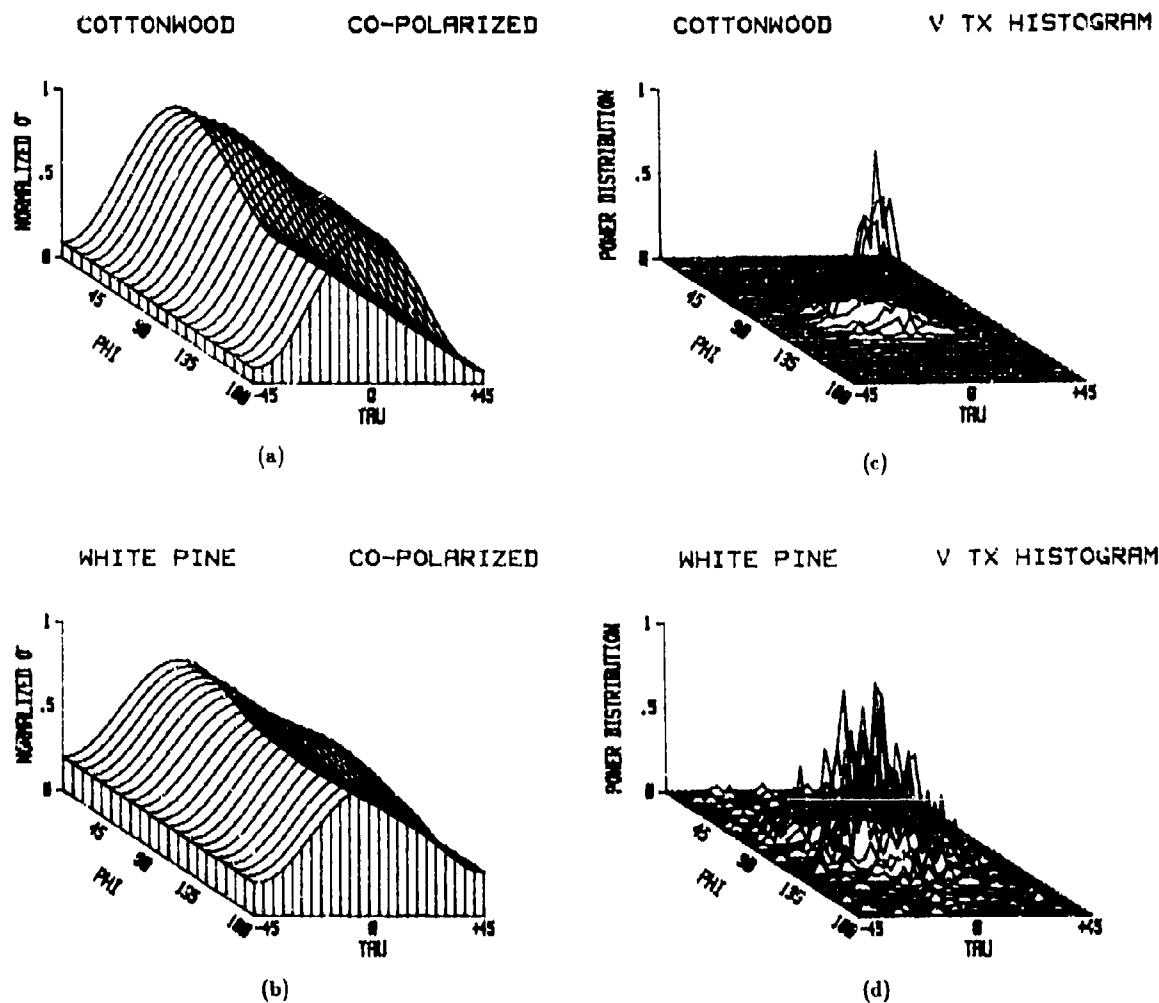


Figure 8. Co-polarized signatures for a) Eastern Cottonwood and b) White Pine. Scatter plot of received pol state for c) Eastern Cottonwood and d) White Pine with vertical transmit polarization.

References

- [1] Ulaby, F. T., R. K. Moore, A. K. Fung, *Microwave Remote Sensing, Active and Passive, Volume I*, pp. 290-309.
- [2] Narayanan, R. M., C. C. Borel, R. E. McIntosh, "Radar Backscatter Characteristics of Trees at 215 GHz, *IEEE Trans. on Geosci. Remote Sens.*, Vol. 26, No. 3, May 1988, pp. 217-228.
- [3] Evans, D. L., T. G. Farr, J. J. Van Zyl, H. A. Zebber, "Radar Polarimetry: Analysis Tools and Applications," *IEEE Trans. Geosci. Remote Sens.*, Vol. 26, No. 6, November 1988, pp. 774-789.
- [4] McMillan, R. W., et al., *Near Millimeter-Wave Radar Technology, Volume I*, Interim Technical Report, Phase III, GT/Project No. A-2445, Contract No. DAAK70-79-C-0108, October 11, 1982.
- [5] Wood, M. A., *A Theoretical Study of Calibration Procedures for Coherent and Non-Coherent Polarimetric Radars*, RSRE Report No. 86011, June 1986.
- [6] Huynen, J. R., "Phenomenological Theory of Radar Targets," Ph.D. Dissertation, Drukkerij Bronder Offset, N.V., Rotterdam, 1970.

MILLIMETER-WAVE BISTATIC SCATTERING BY TERRAIN

Fawwaz T. Ulaby

Department of Electrical Engineering and Computer Science
The University of Michigan
Ann Arbor, MI 48109-2122

SUMMARY

(NU) Interference caused by bistatic and forward scattering by terrain can often lead to degradation in performance for electromagnetic sensors and communications systems. This paper describes the results of a study conducted to evaluate the directional distribution of bistatic scattering from terrain surfaces at 35 GHz. A calibrated radar system was used in a bistatic mode to measure the scattering from a variety of smooth and rough surfaces and from standing trees for all four linear polarization combinations HH, HV, VH, and VV. The measurements were made as a function of the azimuth and elevation angles of the receive antenna direction for fixed directions of the transmit antenna.

(NU) The scattering data for trees were used to develop a new model for the phase matrix of foliage which can then be used in conjunction with transport theory to compute bistatic scattering by forest canopies for any incident and scattered directions. This approach was found to give excellent agreement with backscatter measurements conducted at 35 GHz, 94 GHz, and 140 GHz.

I INTRODUCTION

(NU) Over the past few years, concerted efforts have been devoted by several organizations in the U.S.A. and Europe to acquire millimeter-wave backscatter data of terrain. Bistatic data, on the other hand, is almost nonexistent. The only bistatic data of note were measured in the late 1950's at 1.15 GHz [1] and in the mid-1960's at 10 GHz [2]. The scarcity of bistatic data is due, in part, to the fact that bistatic radar measurements are more difficult to make than monostatic measurements, and this is especially true at millimeter wavelengths. Understanding the nature of bistatic scattering by terrain is important, however, for two major applications: (1) interference caused by bistatic, and particularly forward, scattering can often lead to degradation in performance for electromagnetic sensors and communication systems, and (2) bistatic scattering in vegetation media plays a critical role in modeling and understanding the backscatter from vegetation canopies, particularly at millimeter wavelengths, because the backscatter is strongly influenced by multiple scattering in the vegetation volume.

(NU) This paper documents the results of an experimental investigation conducted to examine the bistatic scattering behavior of trees and smooth and rough ground surfaces, all made at 35 GHz. The scattering data for trees were then used to develop a new model for the phase matrix of foliage, which was used in conjunction with radiative transfer theory to develop a general bistatic scattering model for foliage. Model results are compared with backscatter data measured at 35, 94, and 140 GHz.

II MEASUREMENT SYSTEM

(NU) The data reported in this paper were acquired by the University of Michigan's millimeter-wave polarimeter (MMP), which operates at 35, 94, and 140 GHz [3]. An additional channel was recently added at 215 GHz. The system operates in a backscatter mode from a 20-m high truck mounted platform, and can be arranged to operate in a bistatic mode in laboratory- or laboratory-like conditions. The bistatic data were acquired by the 35-GHz channel of the MMP (Fig.1). The MMP includes a swept-frequency source driven by a HP 8510A vector network analyzer. It sweeps in frequency from 2 to 4 GHz. The signal is sent to the transmitter section and is upconverted to 34-36 GHz using a mixer and fixed-frequency Gunn source operating at 32 GHz. The RF signal is transmitted by a lens-corrected horn antenna with a beamwidth of 4.2°. The transmitter section also contains a fixed-frequency source operating at 10.7 GHz. Part of the swept 34-36 GHz transmitted signal is sampled by a directional coupler and then mixed with the third harmonic of the 10.7 GHz using a harmonic down-converter to produce a 2-4 GHz swept frequency signal for the reference port of the HP 8511A frequency converter (port a, in Fig.1). The receiver section consists of another antenna and another harmonic downconverter. A sample of the 10.7-GHz signal transmitted from the transmitter section to the receiver section through a 10-m-long low-loss coaxial cable serves as the local oscillator signal at the receiver. Thus,

all cables connecting the transmitter section and the receiver section with the HP 8510A (and associated peripherals) carry 2-4 GHz signals and the cable connecting the transmitter to the receiver carries a 10.7-GHz signal. This design arrangement makes it possible to operate the radar system in a bistatic mode while maintaining phase coherence between the transmitted and received signals. A summary of the system characteristics is given in Table 1.

III BISTATIC SCATTERING FOR SAND AND GRAVEL

(NU) The arrangement used for making measurements of the bistatic scattering coefficient of sand and gravel surfaces is illustrated in Fig. 2; the incidence angle θ_i is between the surface normal and the boresight direction of the transmit antenna, a similar definition applies to the scattering angle θ_s , and the azimuth angle ϕ is defined as the azimuth angle of the boresight direction of the receive antenna. The $\phi = 0$ direction (x-axis) is chosen to coincide with the azimuth direction of the transmit antenna. When using narrow-beam transmit and receive antennas, it is difficult to achieve perfect overlap of their footprints on the target surface. To avoid measurement inaccuracies that may be caused by imprecise pointing of the transmit and receive antennas, a broad-beam antenna was used for reception and a narrow-beam antenna was used for transmission. The transmit antenna had a beamwidth of 4.2° , compared to 15° for the beam of the receive antenna. Thus, the power arriving at the receive antenna is essentially the result of scattering by the area illuminated by the transmit antenna.

(NU) The bistatic scattering measurements were comprised of two major experiments. In the first experiment, both θ_i and θ_s were maintained constant at 66° and the azimuth angle ϕ was varied from 10° to 180° . At a nominal range of 3.2 m between the target and the transmit and receive antennas, the area illuminated by the transmit antenna was an ellipse with minor and major axes of 24 and 50 cm, respectively. The target material (sand or gravel) was placed in a "sandbox" at the center of a circle approximately 5 m in diameter. The sandbox, whose surface had dimensions of 1.2 m x 1.2 m, was much larger in surface area than the footprint of the transmit antenna. The floor area surrounding the sandbox was covered with absorbing material.

(NU) The purpose of the second experiment was to extend the results of the first experiment by examining the variation of the bistatic scattering coefficient $\sigma^0(\theta_i, \theta_s, \phi)$ as a function of both θ_s and ϕ for a fixed value of θ_i , namely 60° .

3.1 Calibration

(NU) The radar equation of the bistatic scattering case is given by

$$P = P_t \frac{G_{t0} G_{r0} \lambda^2}{(4\pi)^3} \int \frac{g_t(\theta_t) g_r(\theta_r)}{R_t^2 R_r^2} \sigma^0 dA \quad (1)$$

where P_t is the transmitted power; G_0 is maximum gain of the (transmit or receive) antenna; $g(\theta)$ is the normalized radiation pattern; R is the range to the target; the subscripts t and r stand for transmit and receive, respectively; θ is the antenna angle relative to the boresight direction; and dA is an element of area. Assuming σ^0 is approximately constant over the angular range of the transmit antenna beamwidth, the preceding equation may be rewritten as

$$P = P_t \frac{G_{t0} G_{r0}}{(4\pi)^3} \lambda^2 \sigma^0 I \quad (2)$$

where

$$I = \int \frac{g_t(\theta_t) g_r(\theta_r)}{R_t^2 R_r^2} dA \quad (3)$$

is the illumination integral, which is readily computable from knowledge of the antennas' radiation patterns and the measurement geometry. Because the beamwidth of the transmit antenna is much smaller than that of the receive antenna, the illumination integral is governed primarily by $g_t(\theta_t)$.

(NU) The system was calibrated by measuring the power received with the transmit and receive antennas pointing at each other along their boresight directions. This provides the reference level P_0 given by

$$P_0 = P_t G_{t0} G_{r0} \left(\frac{\lambda}{8\pi R} \right)^2 \quad (4)$$

where R is the distance between the two antennas. Combining (4) with (2) provides the expression

$$\sigma^0 = \left(\frac{\pi}{R^2 I} \right) \left(\frac{P}{P_0} \right). \quad (5)$$

3.2 Target Characteristics

(NU) The targets examined in this investigation included two sand surfaces and a coarse gravel surface. The first sand surface was prepared to be flat and smooth and the second one was artificially roughened to generate a randomly distributed, slightly rough surface. Based on measurements of two transects of the surface height profile, the rms height is estimated to be smaller than 0.1 cm for the smooth surface and about 1.67 cm for the slightly rough surface. The latter surface consisted of smooth undulations with no significant small scale structure; the undulations looked like randomly oriented plane facets approximately 10 cm in diameter. The gravel consisted of stones that had relatively smooth surfaces and ranged in size from 1-2 cm in diameter.

(NU) The depth of the material placed in the wooden box was selected such that it was equal to twice the penetration depth δ_p . The complex dielectric constant of the sand material was measured at 10 GHz as $\epsilon = 2.5 - j0.03$. The sand was totally dry. Hence, its ϵ at 35 GHz is not expected to be different from its value at 10 GHz. This leads to $\delta_p = 7.5$ cm at 35 GHz. The sandbox was filled with sand to a depth of 15 cm, or two penetration depths. The two-way attenuation for a depth equal to $2\delta_p$ is 17 dB. Thus, contributions from depths greater than 15 cm may be neglected. This conclusion was verified experimentally by measuring the received power from the sand layer as a function of layer thickness.

3.3 Bistatic Scattering From Smooth Sand

(NU) The first question that needed to be addressed was: "How close to a specular surface is a visually smooth sand surface at 35 GHz?" The scattering function for a specular surface is a delta function; for a given incidence angle θ_i , power is reflected only in the direction corresponding to $\theta_s = \theta_i$ and $\phi = 180^\circ$. Moreover, the reflected signal is totally coherent in nature. As the surface departs from perfectly smooth, the magnitude of the coherent scattering component decreases and incoherent scattering becomes present in addition.

(NU) To answer the question we posed above, we first computed the Fresnel reflectivity Γ for sand (with $\epsilon = 2.5 - j0.03$) as a function of the incidence angle θ_i for both H and V polarizations. We wanted to choose θ_i such that the ratio $\Gamma_H(\theta_i)/\Gamma_V(\theta_i)$ is large so it would be easy to measure, and yet we did not want θ_i to be too large because that would make the pointing geometry difficult to arrange. In our first experiment we chose $\theta_i = 66^\circ$; at this angle, $\Gamma_H(66^\circ) = 0.27$ (or -5.7 dB) $\Gamma_V(66^\circ) = 0.014$ (or -18.5 dB) and the ratio $\Gamma_H/\Gamma_V = 19.3$ (or 12.8 dB).

(NU) With $\theta_i = 66^\circ$, the received power was measured along the specular direction first for the smooth sand surface and then for a perfectly conducting flat plate placed on top of the sand surface. The signal reflected from the sand surface was lower than that reflected from the metal plate by 6.4 dB for H polarization and by 18.4 dB for V polarization. Thus, the measured reflectivity Γ_H and Γ_V of the smooth sand surface are respectively only 0.7 and 0.1 dB lower in level than their theoretical counterparts for a specular surface. In other words, a "visually" smooth sand surface is also electromagnetically smooth with regard to reflection along the specular direction at 35 GHz.

(NU) Fig. 3 shows measured values of the bistatic scattering coefficient $\sigma^0(\theta_i, \theta_s, \phi)$ plotted as a function of ϕ for $\theta_i = \theta_s = 66^\circ$. The plots cover the range from 10° to 350° , although the actual measurements covered only the range from 10° to 180° and the remaining part is a mirror image. We observe that in the specular direction, σ_{HH}^0 is larger than σ_{VV}^0 by 12 dB, but outside the main lobe region, σ_{VV}^0 tends to be slightly larger than σ_{HH}^0 .

(NU) In our second experiment, we fixed θ_i at 60° and measured $\sigma^0(\theta_i, \theta_s, \phi)$ as a function of ϕ for $\theta_s = \theta_i$ (i.e., essentially replicating the previous experiment) and as a function of θ_s at each of two values of ϕ , namely 180° and 270° . Also, the measurements included observations with HV polarization, in addition to HH and VV polarizations. The polarization orientation is defined with respect of the frame of reference of the transmit or receive antennas. This means that at $\phi = 90^\circ$ we should expect stronger cross-polarized scattering than like-polarized scattering. Our expectation was confirmed by the results shown in Fig. 4(a); σ_{HV}^0 is much smaller than σ_{HH}^0 for ϕ between 150° and 210° (actually σ_{HV}^0 could not be measured at $\phi = 180^\circ$ because it is lower than σ_{HH}^0 by more than the 30-dB depolarization isolation factor of the antenna), but σ_{HV}^0 is larger than σ_{HH}^0 for $\phi = 60^\circ - 90^\circ$ (and $270^\circ - 300^\circ$). Fig. 4 depicts the variation of $\sigma^0(\theta_i, \theta_s, \phi)$ with θ_s at $\phi = 180^\circ$, and Fig. 5 shows a contour plot of σ^0 as a function of both θ_s and ϕ . The plot was generated using simple interpolation between the various one-dimensional profiles.

3.4 Bistatic Scattering From Rough Sand and Gravel

(N^r) The HH-polarized bistatic scattering patterns of the rough sand and gravel surfaces exhibit significantly lower levels in the specular direction compared to the smooth sand surface (Fig. 6), but exhibit higher levels at off-specular directions (Fig. 7).

IV BISTATIC SCATTERING MEASUREMENTS OF FOLIAGE

(NU) Two types of measurements were conducted for trees: 1) transmission measurements to determine the attenuation rate versus the number of trees in the transmission path, and 2) bistatic scattering measurements to evaluate the azimuthal variation of the bistatic scattering coefficient. The configurations used are sketched in Fig. 8. In both cases, the transmitter and receiver antennas were mounted on poles at the same height above the ground and the transmitter remained stationary throughout both experiments. Because the beamwidths of both transmit and receive antennas were on the order of 4.2°, an infrared beam was used (prior to placing the trees in the transmission path) to insure proper antenna alignment.

(NU) Two distinctly different types of trees were selected for examination in this study: Ficus and Arbor Vitae (Fig. 9(a)). The Ficus tree (Ficus Nitida-Green Gem) has small, flat, simple leaves approximately 10 cm² in area (Fig. 9(b)). The Arbor Vitae had a branching trunk arrangement and a conical crown of short upwardly spreading branches. Its needles were approximately 1.5-3 mm in length. The complex dielectric constants of the leaves and trunk at 35 GHz were estimated by extending 1-20 GHz dielectric measurements that were made using a coaxial probe [4] to 35 GHz by applying a dielectric model that was recently developed for vegetation [5]. Over the experiment duration, the trees were kept in pots and did not undergo major changes; however, differences as large as ± dB were observed between transmission measurements made a week apart. These variations are attributed to the loss of a few leaves and to possible changes in moisture content.

(NU) When considering an elementary volume of a vegetation medium containing N randomly distributed particles (leaves, needles, branches) per unit volume, one can characterize bistatic scattering by the volume in terms of the bistatic scattering cross section per unit volume (or bistatic scattering coefficient) κ_{rt} ,

$$\begin{aligned}\kappa_{rt}(\hat{\mathbf{r}}, \hat{\mathbf{t}}) &= N \langle \sigma_{rt}(\hat{\mathbf{r}}, \hat{\mathbf{t}}) \rangle \\ &= 4\pi N \langle |S_{rt}(\hat{\mathbf{r}}, \hat{\mathbf{t}})| \rangle\end{aligned}\quad (6)$$

where $r, t = v$ or h denote the polarizations (vertical or horizontal) of the receive and transmit antennas, respectively, $\hat{\mathbf{r}}$ and $\hat{\mathbf{t}}$ denote the scattered and incident directions, σ_{rt} is the bistatic radar cross section of an individual particle, and S_{rt} denotes the scattering amplitude of that particle. The symbol $\langle \rangle$ denotes ensemble average.

(NU) For both types of trees examined in this investigation, the measured like-polarized scattering patterns, $\kappa_{vv}(\psi)$ and $\kappa_{hh}(\psi)$, were observed to be approximately equal, and a similar results was observed for $\kappa_{vh}(\psi)$ and $\kappa_{hv}(\psi)$. Thus,

$$\kappa_{hh}(\psi) \simeq \kappa_{vv}(\psi) \triangleq \kappa_1(\psi) \quad (7)$$

$$\kappa_{hv}(\psi) \simeq \kappa_{vh}(\psi) \triangleq \kappa_2(\psi) \quad (8)$$

(NU) Figure 10 shows plots of the measured values of $\kappa_1(\psi)$ and $\kappa_2(\psi)$ for the Ficus tree. Similar patterns were observed for the other tree. Also shown are plots calculated using the expressions discussed below.

(NU) The bistatic scattering coefficients can each be expressed as the product of the average scattering coefficient κ_s and a pattern function $g(\psi)$,

$$\kappa_1(\psi) = \kappa_s g_1(\psi), \quad (9)$$

$$\kappa_2(\psi) = \kappa_s g_2(\psi). \quad (10)$$

In view of the shapes of the measured patterns (Fig 10), $g_1(\psi)$ and $g_2(\psi)$ can each be described as the sum of a relatively weak isotropic component and a Gaussian-shaped, strong and narrow forward-scattering lobe $f(\psi)$,

$$\begin{aligned}g_1(\psi) &= [\alpha_1 f_1(\psi) + (1 - \alpha_1)] C \\ &= \left[\alpha_1 \left(\frac{2}{\beta_1} \right)^2 \exp \left[- \left(\frac{\psi}{\beta_1} \right)^2 \right] + (1 - \alpha_1) \right] C\end{aligned}\quad (11)$$

$$\begin{aligned}
 g_2(\psi) &= [\alpha_2 f_2(\psi) + (1 - \alpha_2)](1 - C) \\
 &= \left[\alpha_2 \left(\frac{2}{\beta_2} \right)^2 \exp \left[- \left(\frac{\psi}{\beta_2} \right)^2 \right] + (1 - \alpha_2) \right] (1 - C)
 \end{aligned} \quad (12)$$

where β_1 and β_2 are the effective beamwidths of the like- and cross- polarized forward scattering lobes.

(NU) The "calculated" plots shown in the Fig. 10 are based on (9) - (12) with the values of the parameters selected to provide good agreement between the measured and calculated plots.

V PHASE MATRIX

(NU) The random nature of tree foliage supports the use of radiative transfer theory [6,7] for modeling millimeter wave propagation in the canopy [8,9]. In the radiative transfer model, the formulation is given in terms of the phase matrix $\mathbf{P}(\theta_s, \phi_s; \theta_i, \phi_i)$ relating the specific intensity scattered by a unit volume of the scattering medium into the direction (θ_s, ϕ_s) to the specific intensity incident upon the unit volume from the direction (θ_i, ϕ_i) , with both sets of orientation angles being defined with respect to a reference coordinate $(\hat{x}, \hat{y}, \hat{z})$. The phase matrix represents the average Stokes matrix of the particles constituting the unit volume.

(NU) Upon applying the definition of the phase matrix [7] and making certain assumptions regarding the phase relationships between the four elements of the scattering matrix, S_{vv}, S_{hh}, S_{hv} , and S_{vh} , we obtain the following result for the phase matrix $\mathbf{P}(\psi)$ for scattering in the principal plane ($\phi_i = \phi_s = 0$),

$$\mathbf{P}(\psi) = \frac{\kappa_s}{4\pi} \begin{bmatrix} g_1 & g_2 & 0 & 0 \\ g_2 & g_1 & 0 & 0 \\ 0 & 0 & g_1 + g_2 & 0 \\ 0 & 0 & 0 & g_1 - g_2 \end{bmatrix} \quad (13)$$

where $\psi = \theta_s - \theta_i$, and g_1 and g_2 are as given by (11) and (12).

(NU) For the general case where the incident and/or scattered directions are outside the principal plane, the phase matrix $\mathbf{P}(\theta_s, \phi_s; \theta_i, \phi_i)$ can be related to $\mathbf{P}(\psi)$ through

$$\mathbf{P}(\theta_s, \phi_s; \theta_i, \phi_i) = \mathbf{L}(\pi - \gamma_2) \mathbf{P}(\psi) \mathbf{L}(-\gamma_1) \quad (14)$$

where $\mathbf{L}(\pi - \gamma_2)$ and $\mathbf{L}(-\gamma_1)$ are angular transformations [10] and the angles γ_1 and γ_2 are related to the incident and scattered angles.

VI RESULTS OF RADIATIVE TRANSFER CALCULATIONS

(NU) Given the phase matrix expressions outlined in the preceding section, it is a relatively straightforward task to compute the radar bistatic scattering coefficient for a forest canopy using radiative transfer theory [7]. This was implemented by Ulaby et al. [9] for the backscattering case in order to compare the model results with experimental observations made at 35, 94, and 140 GHz. A summary of their comparison is shown in Fig. 11 which contains experimental measurements for a canopy of Spruce trees at 35 GHz and for a canopy of Bur Oak trees at 94 GHz and 140 GHz. The calculated curves, which are in good agreement with the experimental observations, are based on a second-order solution of the radiative transfer equation using the phase function expressions given in the preceding section.

VII CONCLUSIONS

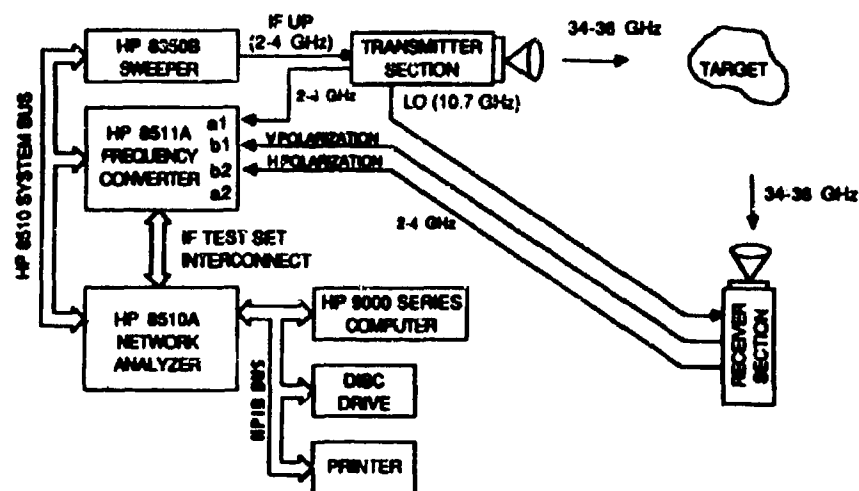
(NU) In addition to examining the character of the bistatic scattering pattern of various surfaces, this study has shown that a visually smooth sand surface acts like a specular surface in the specular direction, even at millimeter wavelengths, but when the rms roughness of the surface becomes comparable to the wavelength, reflection along the specular direction can decrease by 10 dB or more. For tree canopies, bistatic scattering is characterized by a narrow Gaussian-like lobe in the forward direction, superimposed on a relatively weak isotropic pattern. Measurements of the scattering pattern led to a formulation of a phase matrix appropriate for tree foliage at millimeter wavelengths, which was then used in a radiative transfer model to compute the radar scattering coefficient for tree canopies.

References

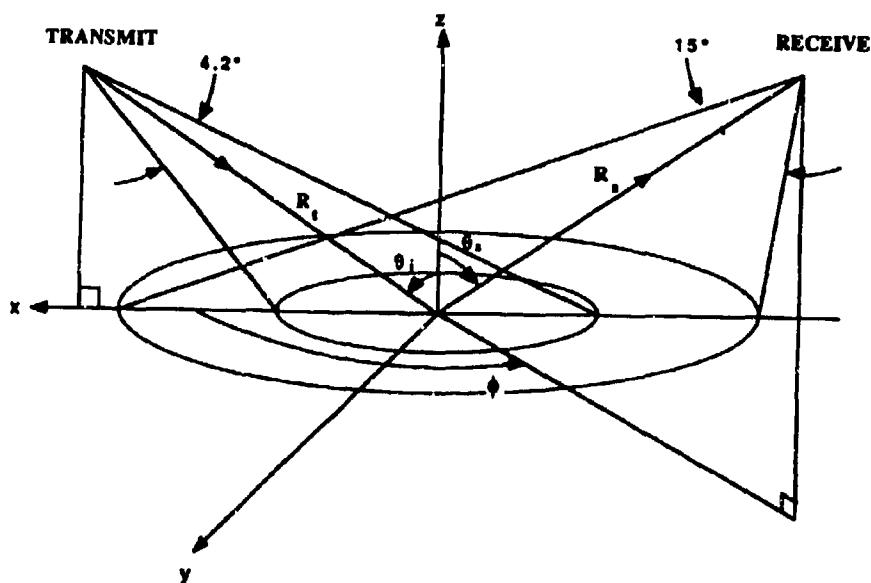
- [1] R.L. Cosgriff, W.H. Peake, and R.C. Taylor, "Terrain Scattering Properties for Sensor System Design," Ohio State University, Report 181, 1960
- [2] W.H. Peake and T.L. Oliver, "The Response of Terrestrial Surfaces at Microwave Frequencies," Air Force Avionics Lab, Wright-Patterson AFB, OH, TR AFAL-JR-70-301, 1971.
- [3] F.T. Ulaby, T.F. Haddock, J. East, and M.W. Whitt, "A Millimeterwave Network Analyzer Based Scatterometer," *IEEE Trans. Geosci. Remote Sensing*, Vol. GE-26, No. 1, pp. 75-81, Jan. 1988.
- [4] M. El-Rayes and F.T. Ulaby, "Microwave Dielectric Spectrum of Vegetation Part I: Experimental Observations," *IEEE Trans. Geosci. Remote Sensing*, Vol. GE-25, NO. 5, pp. 550-557, Sept. 1987.
- [5] F.T. Ulaby and M. El-Rayes, "Microwave Dielectric Spectrum of Vegetation Part II: Dual Dispersion Model," *IEEE Trans. Geosci. Remote Sensing*, Vol. GE-25, No. 5, pp. 550-557, Sept. 1987.
- [6] A. Ishimaru, *Wave Propagation and Scattering in Random Media*, Vol. 1, Academic Press, New York, 1978, Ch. 7.
- [7] F.T. Ulaby, R.K. Moore, and A.K. Fung, *Microwave Remote Sensing*, Vol. III, ARtech House, Dedham, Massachusetts, 1986, Ch. 13.
- [8] F.K. Schwering, E.J. Violette, and R.H. Espeland, "Millimeter-Wave Propagation in Vegetation: Experiments and Theory," *IEEE Trans. Geosci. Remote Sensing*, Vol. GE-26, pp. 355-367, May 1988.
- [9] F.T. Ulaby, T.H. Haddock, and Y. Kuga, "Measurement and Modeling of Millimeter-Wave Scattering from Tree Foliage," submitted to *Radio Science*, August 1989.
- [10] S. Chandrasekhar, *Radiative Transfer*, Dover Publications, New York, 1960, pp. 34-35.

(NU) Table 1. Parameters of the University of Michigan
Millimeter Wave Polarimeter

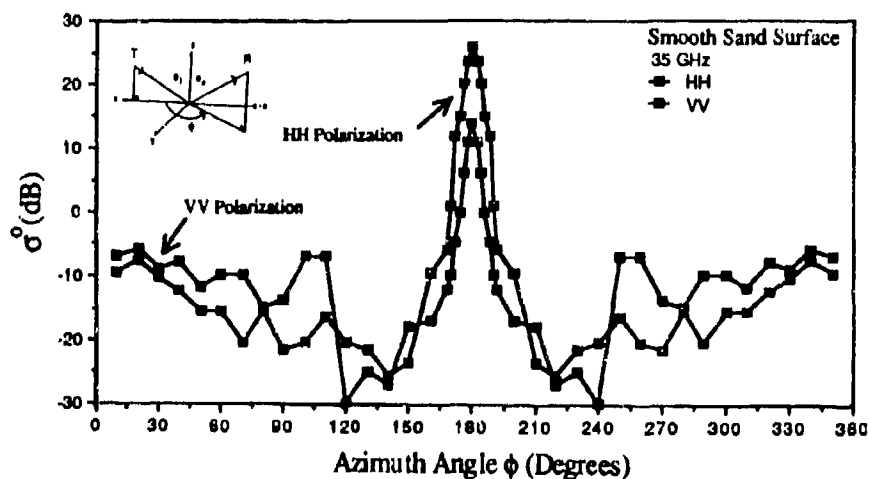
| | | | |
|---|---|--------------------------|----------------|
| FREQUENCIES: | 35, 94, 140, 215 GHz | | |
| IF BANDWIDTH: | 0 to 2.0 GHz | | |
| SWEEP RATE: | 1 ms/freq., 51, 101, 201, 401 freq./sweep | | |
| POLARIZATION: | HH, HV, VV, VH | | |
| INCIDENCE ANGLES: | 0 to 70 degrees | | |
| PLATFORM HEIGHT: | 3 meters minimum, to 18 meters maximum | | |
| NOISE EQUIV. σ': | 35 GHz: | -22 dB | |
| | 94 GHz: | -28 dB | |
| | 140 GHz: | -21 dB | |
| | 215 GHz: | -30 dB | |
| CROSSPOL ISOLATION: | 35 GHz: | 23 dB | |
| | 94 GHz: | 20 dB | |
| | 140 GHz: | 15 dB | |
| | 215 GHz: | 20 dB | |
| PHASE STABILITY: | 35 GHz: | ~1 degree/hour | |
| | 94 GHz: | ~1 degree/minute | |
| | 140 GHz: | ~10 to 50 degrees/second | |
| | 215 GHz: | ~20 degrees/hour | |
| NEAR FIELD DIST: | 35 GHz: | 2.7 m | |
| | 94 GHz: | 7.3 m | |
| | 140 GHz: | 2.7 m | |
| | 215 GHz: | 4.4 m | |
| BEAMWIDTH: | 35 GHz: | R: 4.2 deg | T: 4.2 deg |
| | 94 GHz: | R: 1.4 deg | T: 2.8 deg |
| | 140 GHz: | R: 2.2 deg | T: 11.8 deg |
| | 215 GHz: | R: 1.1 deg | T: 2.3 deg |
| ANTENNA DIAMETER: | 35 GHz: | R: 6 inches | T: 6 inches |
| | 94 GHz: | R: 6 inches | T: 3 inches |
| | 140 GHz: | R: 3 inches | T: 0.36 inches |
| | 215 GHz: | R: 3 inches | T: 1.5 inches |



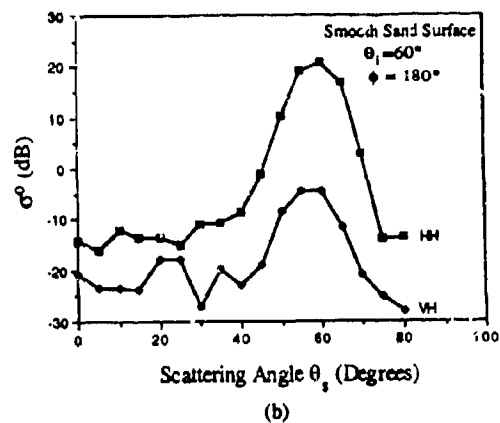
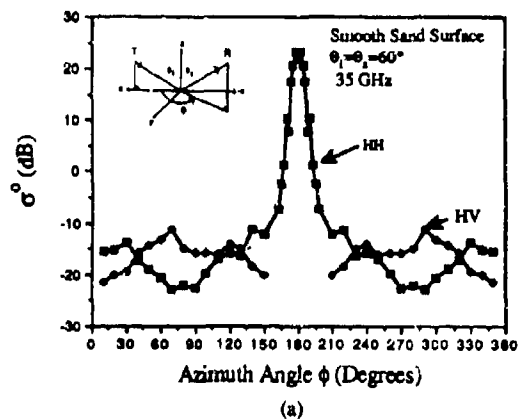
(NU) Fig. 1. Block diagram of the 35-GHz channel of the MMP when operated in the bistatic mode.



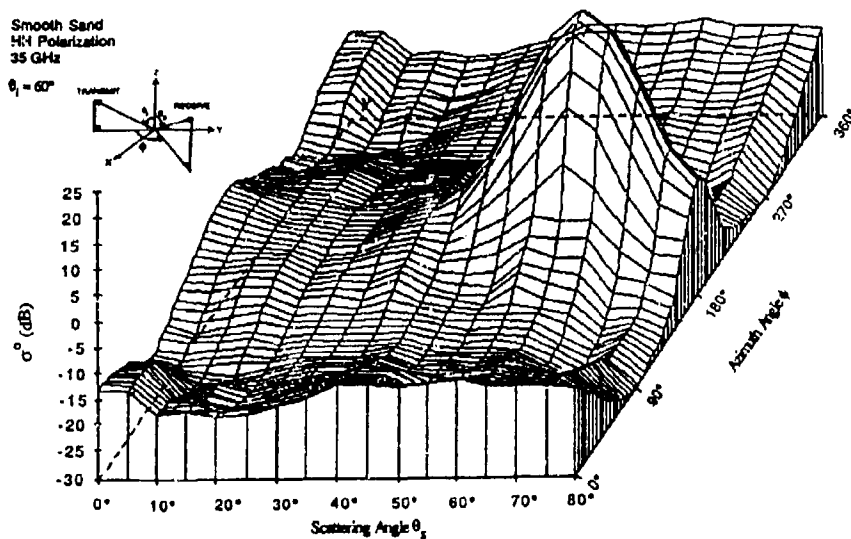
(NU) Fig. 2. Geometry of the bistatic scattering arrangement.



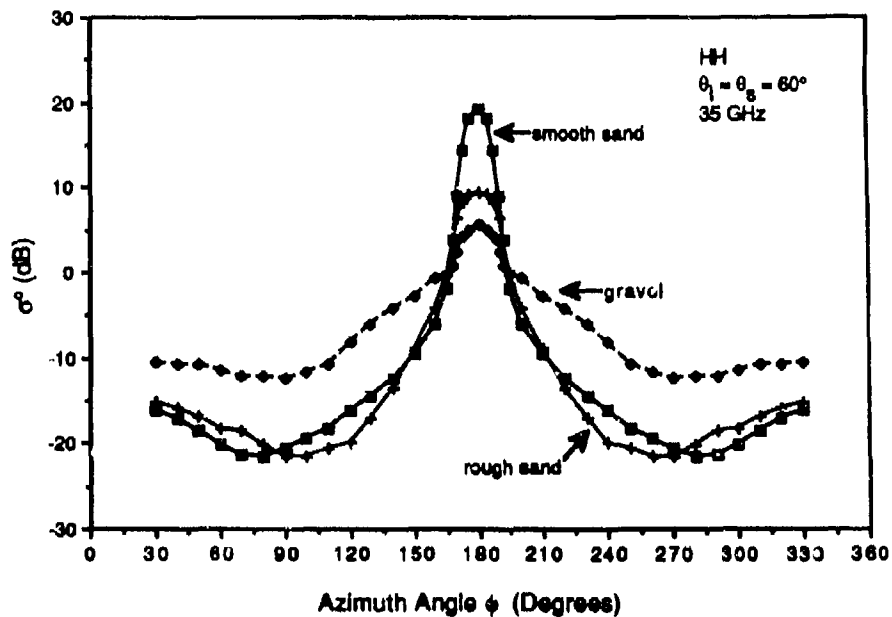
(NU) Fig. 3. Measured bistatic scattering pattern of a smooth sand surface with $\theta_i = \theta_s = 66^\circ$.



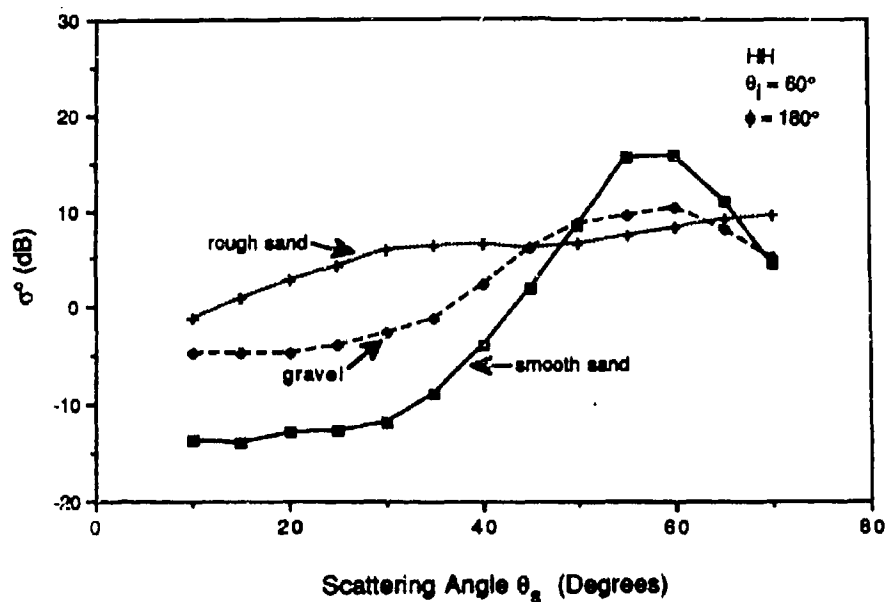
(NU) Fig. 4. Bistatic scattering from a smooth sand surface with $\theta_i = 60^\circ$, (a) azimuth variation with $\theta_s = 60^\circ$ and (b) scattering angle variation with $\phi = 180^\circ$.



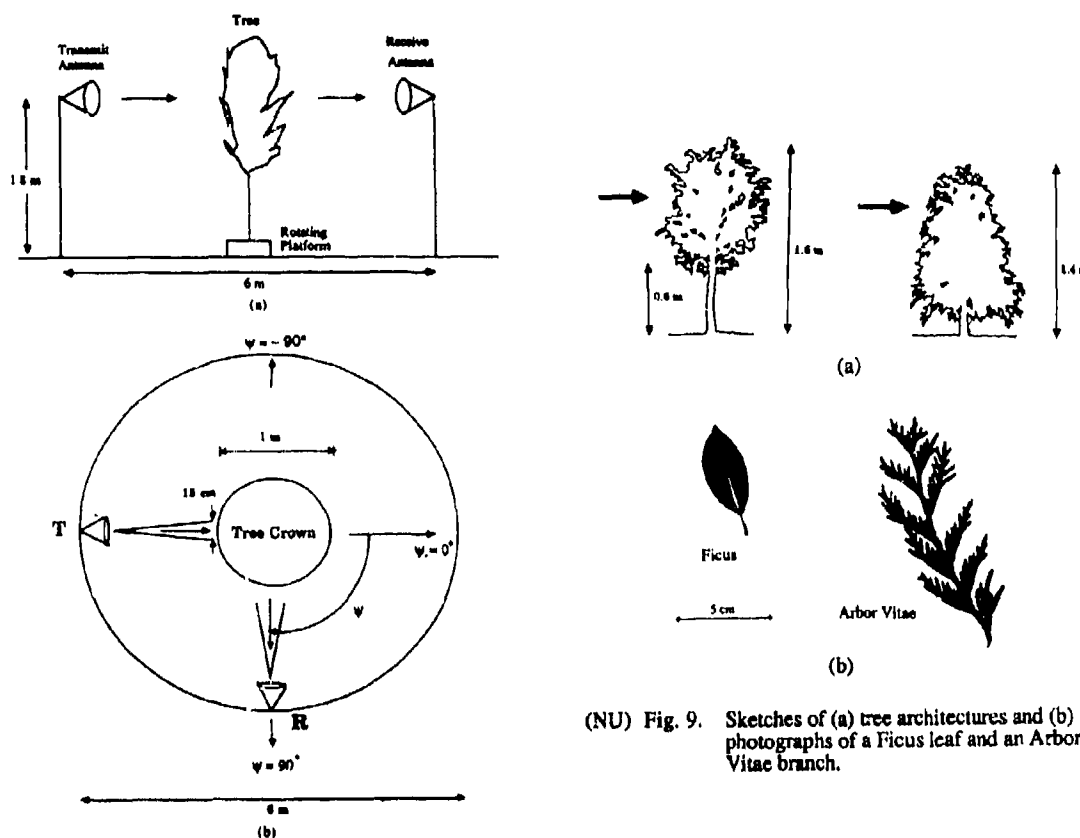
(NU) Fig. 5. Three dimensional contour plot of bistatic scattering from smooth sand surface.



(NU) Fig. 6. Bistatic scattering as a function of the azimuth angle ϕ for smooth sand, rough sand, and gravel surfaces.



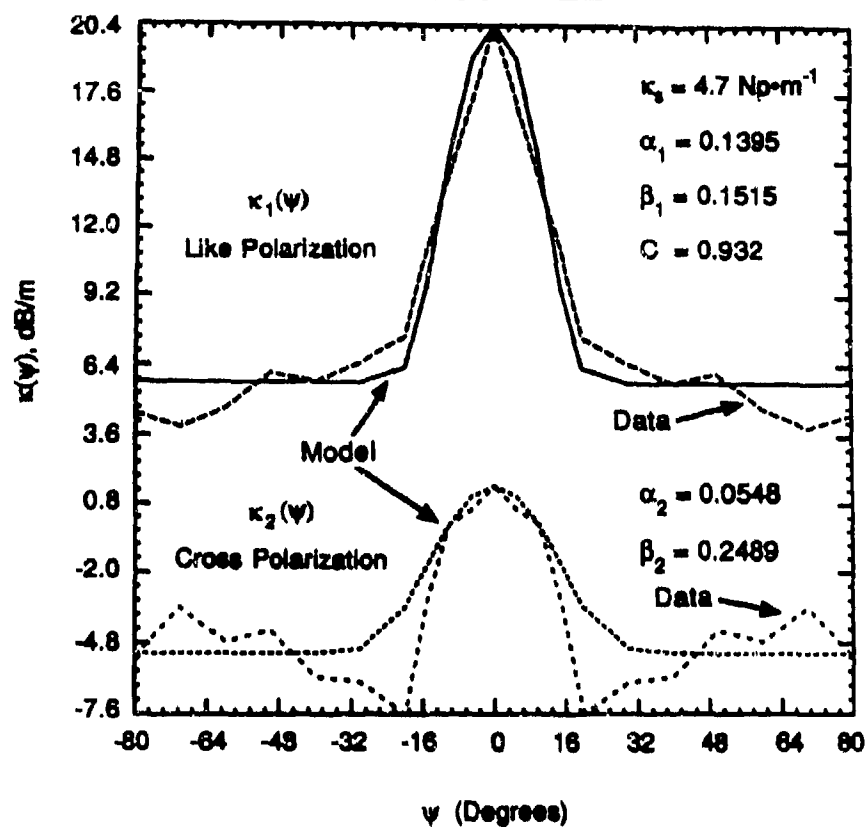
(NU) Fig. 7. Bistatic scattering in the elevation plane with fixed incidence and azimuth angles.



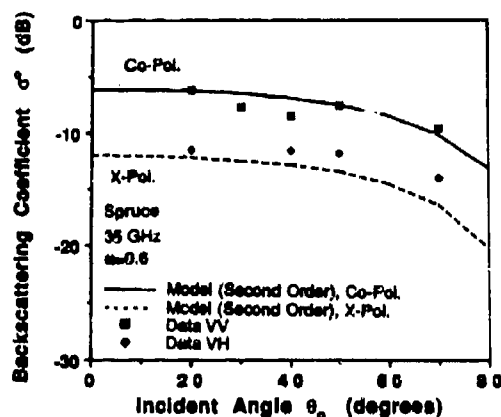
(NU) Fig. 9. Sketches of (a) tree architectures and (b) photographs of a Ficus leaf and an Arbor Vitae branch.

(NU) Fig. 8. Configurations used for measuring (a) foliage attenuation and (b) bistatic scattering from trees. For measurements involving more than one tree in the transmission path, the distance between the transmitter and receiver antennas was increased to 8 m.

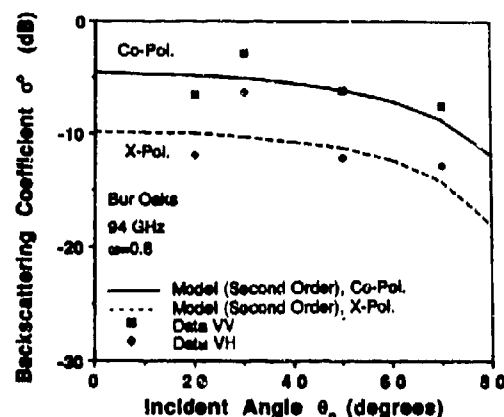
FICUS TREE



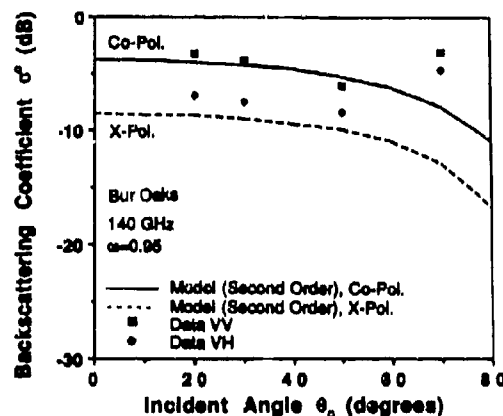
(NU) Fig. 10. Comparison of measured bistatic scattering cross section per unit volume for Ficus tree foliage with calculations based on the modal functions given in the text.



(a) 35 GHz



(b) 94 GHz



(c) 140 GHz

(NU) Fig. 11. Comparison of theory with experimental observations at (a) 35 GHz for a canopy of Spruce trees at (b) 94 GHz and (c) 140 GHz for a canopy of Bur Oak trees.

DISCUSSION

M. LEVY

Is it possible to make bistatic scatter measurements over the sea?

AUTHOR'S REPLY

It could be done, but deployment of equipment is not easy.

M. SHETTL

In your measurements of the phase function for a tree, there appears to be a symmetric scattering pattern even to detailed features. Most trees, I have seen, are not that uniformly symmetric. Can you explain or comment on this?

AUTHOR'S REPLY

The tree was rotated 360° for each measurement resulting in a statistical averaging of aspect dependency.

M. AMBERTON

Could you please comment on the relative backscatter properties of coniferous and deciduous trees. Are there any major differences which might have impact on system requirements for applications, such as MMW terrain following radar.

AUTHOR'S REPLY

The water content of the foliage appeared to be the major factor, more so than the distinction between deciduous and coniferous trees.

Modelling UV-Visible Radiation Observed from Space

D.E. Anderson, Jr.
Code 4141
Naval Research Laboratory
Washington, D.C. 20375 USA

and

D.J. Strickland
Computational Physics Inc.
P.O. Box 360
Annandale, VA 22003 USA

SUMMARY

Development of space-based passive remote systems for observing and tracking artificial radiation sources in the earth's atmosphere requires the characterization of the natural radiation background. Recent advances in detector technology and theoretical modelling have led to improved understanding of the UV-visible (1000-3000 Å) atmospheric background radiation. There are two principal sources of naturally occurring UV-visible atmospheric radiation: (1) Rayleigh and mie scattering of sunlight; and (2) auroral and airglow emission. The first source is generated primarily in the troposphere, but is affected by the presence of aerosols and ozone in the stratosphere up to 40 km. In addition, clouds, surface reflection and multiple scattering can have a significant affect on the radiation field. The relative importance of these sources to nadir emission are shown. In particular, we find that for wavelengths greater than 3000 Å as much as 60% of the nadir emission can be due to multiple scattering. The second source, auroral and airglow emission, emanates from the mesosphere above 50 km and the thermosphere below 1000 km altitude and exhibits remarkable geographic and geomagnetic variability. A description of these radiation fields and models developed to analyse satellite remote sensing data in the UV-visible region of the spectrum are presented. Emission levels from both sources are compared and expected geographic and solar cycle variability identified.

1. INTRODUCTION

UV-visible optical backgrounds observed from space naturally fall into two categories: those excited by Rayleigh and mie scattering in the atmosphere below 100 km; and atomic and molecular line emission from the atmosphere. Except at very high spectral resolution or at night, the latter are observed only when the altitude above the surface of the line-of-sight, or tangent altitude, rises above 90 km. Below this altitude Rayleigh scattering overwhelms other emission sources. We will show, however, that at very high spectral resolution (± 1 Å) molecular emissions may be observed down to tangent altitudes as low as 40 km tangent.

For optical backgrounds below 90 km, models such as LOWTRAN¹ provide a representation of earth radiance, irradiance and atmospheric transmission over the electromagnetic spectrum longward of 2000 Å. LOWTRAN is best suited for limb observations below 50 km altitude. The model results described here are based on algorithms developed at the Naval Research Laboratory which provide a description of the contribution to limb emission of Rayleigh and mie scattering below 100 km in the wavelength region 2000-10000 Å.^{2,3,4} Although there is very little variation in the solar flux with solar cycle in this wavelength region ($<10\%$ at 2000 Å decreasing rapidly with wavelength to $<1\%$ at 3000 Å), there is a large variability in the limb emission profiles due to climatological effects. This natural variability must be included in any optical backgrounds model which hopes to predict background scenes.

Above 90 km, solar energy at wavelengths shortward of 2000 Å and particle precipitation from the magnetosphere induce not only a myriad of emissions from atomic and molecular constituents, but large global, seasonal and solar cycle variability in the distribution of these constituents. User friendly optical backgrounds models similar to LOWTRAN have not been developed for this region of the atmosphere. Recent advances in our understanding of emission sources above 90 km may soon lead to such models, but in order to predict optical backgrounds in this region it will be necessary to incorporate a thermosphere climatology as a source for the constituent distributions.

In the next section, an optical backgrounds model for altitudes below 90 km is described and examples of optical backgrounds are shown. Thermosphere emissions are then described for the dayglow followed by a description of auroral emissions.

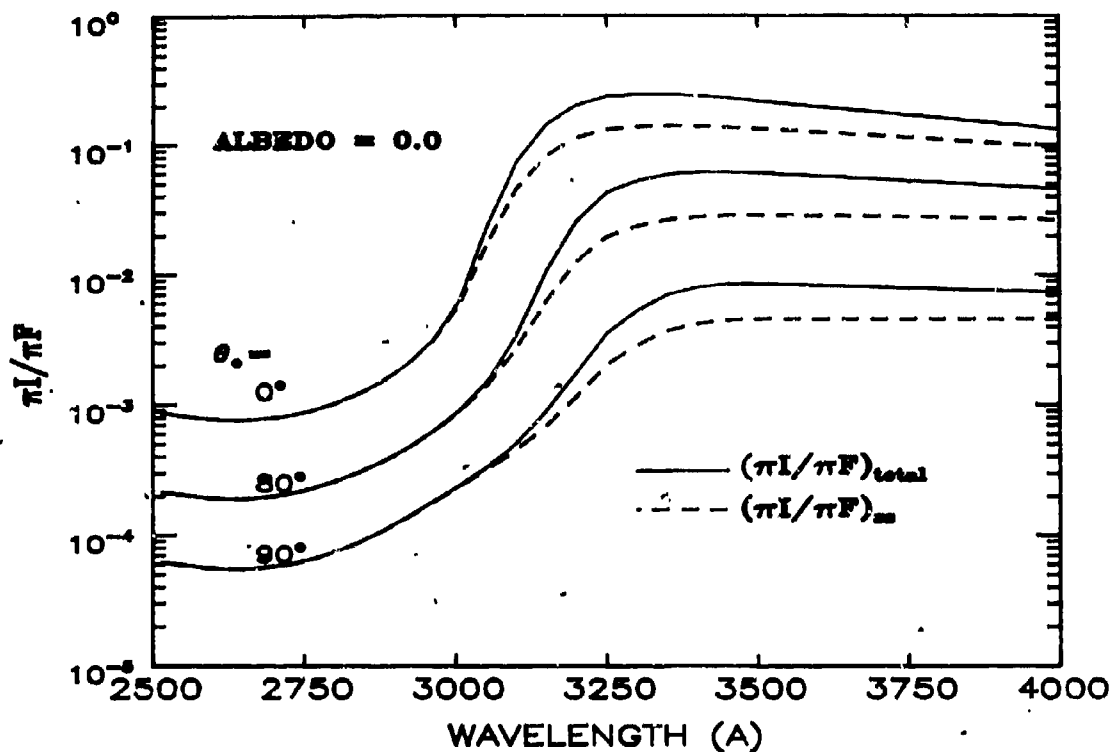


Figure 1. Earth albedo for three solar zenith angles. $(\pi I / \pi F)_{\text{total}}$ and $(\pi I / \pi F)_{\text{ss}}$ refer to the earth albedo with and without multiple scattering, respectively.

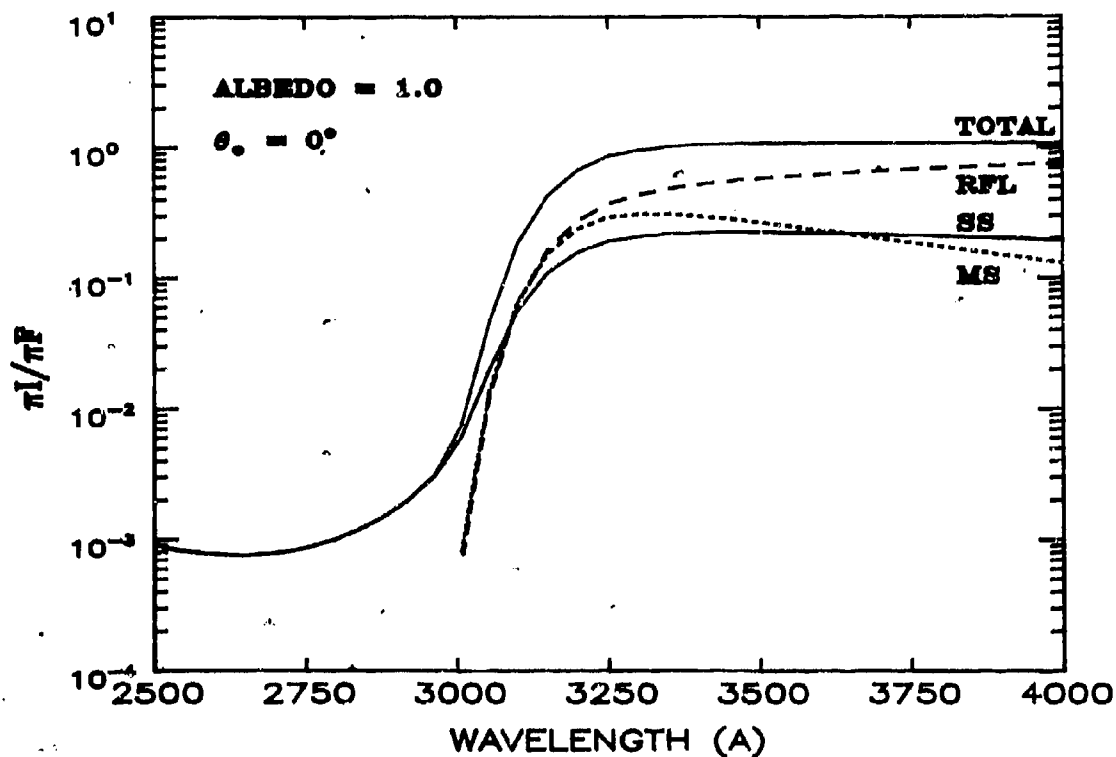


Figure 2. Earth albedo with ground reflection included. **TOTAL**, **RFL**, **SS** and **MS** refer to the earth albedo with multiple scattering, and the reflected, single scattered and multiple scattered components, respectively.

2. OPTICAL BACKGROUNDS FROM THE ATMOSPHERE BELOW 90 KM

Observed UV-visible emission for tangent altitudes less than 90 km is dominated by Rayleigh and aerosol (mie) scattering from the troposphere and stratosphere.⁵ During periods of high volcanic activity, the emission is often enhanced above the normal background.⁶ In addition, during late spring and summer at high latitude in both the northern and southern hemisphere, polar mesosphere clouds centered at 85 km are observed as an enhancement in the emission in the vicinity of 85 km tangent altitude.⁷ Thus, both seasonal variations of the aerosol scattering and variations caused by injection of aerosols into the stratosphere (volcanic or artificial) cause emission rate fluctuations. Sporadic signatures of clouds have been observed throughout the stratosphere and at a wide variety of latitudes. Finally, the seasonal-latitudinal variation in the ozone distribution results in a modulation of the UV-visible radiance, because ozone absorbs radiation that would otherwise contribute to the radiation field.

The calculated earth albedo (solar energy backscattered to space) is shown for the 2500-4000 Å wavelength range in Figure 1 for solar zenith angle $\theta_0 = 0, 80$ and 90 degrees. The model utilizes the 1976 U.S. Standard Atmosphere for molecular nitrogen N_2 , oxygen O_2 and ozone O_3 and a clear atmosphere with a ground albedo of 0.0. The curves show the total earth albedo as well as earth albedo when multiple scattering is not included. The effects of non-zero ground albedo are emphasized in Figure 2, where the results for a ground albedo of unity are shown. Comparison of the two figures shows that ground reflection produces, in the extreme case, a factor of five increase in earth albedo. Multiple scattering increases because of increased trapping of radiation in the atmosphere. Multiple scattering is not important below about 3000 Å because of absorption by ozone in the stratosphere. As noted earlier, when aerosols, clouds and ozone variability are included, emission levels will change. At large solar zenith angles (>80 degrees) the earth albedo due to Rayleigh scattering is reduced so that atomic and molecular emissions from the thermosphere above 90 km can often be seen even at relatively low spectral resolution.

Limb emission profiles for an observation platform above 100 km altitude and for tangent altitudes less than 75 km are shown in Figure 3 for a solar zenith angle of 50 degrees. Wavelength intervals of 100 Å were integrated to yield the column emission rate in megaRayleighs, where one megaRayleigh is the radiance in units of photons $cm^{-2} s^{-1} sr^{-1}$ and scaled by $4\pi \times 10^{-12}$. The emission profiles for wavelengths less than 3000 Å reach a maximum at the tangent altitude where absorption due to ozone and molecular oxygen begins to attenuate the signal. In this wavelength region, limb emission variations with latitude and season are expected. For wavelengths greater than 3000 Å, the limb emission profile continues to increase until the solid earth is encountered (tangent altitude = 0 km), indicating that contributions from the ground are possible. In fact, the variability of ground albedo and multiple scattering due to aerosols and molecules in this spectral region leads to considerable variability in observed emissions. The theoretical emission profiles shown are accurate to better than 20%, based on the combined uncertainty in the solar flux and in the model calculation. Thus, the model of optical backgrounds emitted from the troposphere, stratosphere and mesosphere may be utilized to assist in-flight instrument calibration throughout the UV-visible range.⁸ In addition, the model limb profiles can be utilized to assist in determining the pointing accuracy by comparison with limb observations. Finally, although not discussed in detail here, radiance measurements in this spectral range may be inverted to yield planetary-scale circulation patterns in the stratosphere and global variability of ground albedo, aerosol content and mesosphere cloud distributions.

At very high spectral resolution (<1 Å) molecular emissions from the stratosphere and mesosphere are observable throughout the day and the observed radiances may be inverted to yield the altitude distribution of the emitting molecules. A new and exciting investigation of observation and analysis of limb emissions, the Middle Atmosphere High Resolution Spectrograph (MAHRS) experiment, promises to establish new remote sensing techniques for investigation of the D and E region of the ionosphere, and the chemistry and dynamics of the stratosphere and mesosphere.⁹ The emission models described above will be directed to the MAHRS shuttle-based data set to be obtained in the early 1990's. The MAHRS will obtain spectral data in 35 Å segments from 1900 to 3200 Å in first order at 0.1 Å spectral resolution and <5 km altitude resolution. A theoretical MAHRS spectrum 35 Å wide and centered at 3083 Å is shown in Figure 4 for a tangent altitude of 75 km and a spectral resolution of 0.1 Å. The low level background represents Rayleigh scattering of the incident solar radiation (dotted line). The solid vertical lines represent molecular emissions arising from solar resonance scattering by the hydroxyl radical (OH) present in the atmosphere below 90 km. The OH spectral features shown have been integrated over 0.1 Å so that most of the features shown represent the sum of several rotational lines. The feature indicated by the vertical arrow, however, is the emission from a single transition. Emission from this line was calculated for a range of tangent altitudes and Figure 5 shows the resultant limb profile together with the Rayleigh background. The solid curves represent Rayleigh background reduced by 90% due to the presence of a polarizer in the MAHRS spectrograph which will filter out much of the highly polarized Rayleigh background. At these wavelengths the emission is sensitive to the ozone concentration and the difference in the two solid curves arises because of the different ozone distributions calculated for December (lower intensity) and April. The dashed and dotted curves represent the OH emission and are based on a 1500 hrs local time OH distribution calculated with a chemical-diffusion model of the stratosphere and mesosphere for December and April.¹⁰ Thus, at high spectral resolution the background from Rayleigh scattering is reduced and optical signatures from natural and artificial sources can be investigated to at least 40 km tangent altitude. When MAHRS flies, a new generation of space observations will begin. The MAHRS investigation is a joint venture between the Naval Research Laboratory and the West German ASTRO SPAS/CRISTA shuttle investigation to investigate chemistry, radiation and dynamics in the stratosphere, mesosphere and lower thermosphere. This investigation emphasizes the continued importance of maintenance and support of high spectral resolution radiance codes. In the next section we describe theoretical limb emission profiles from the thermosphere (tangent altitude > 100 km) observed during the day.

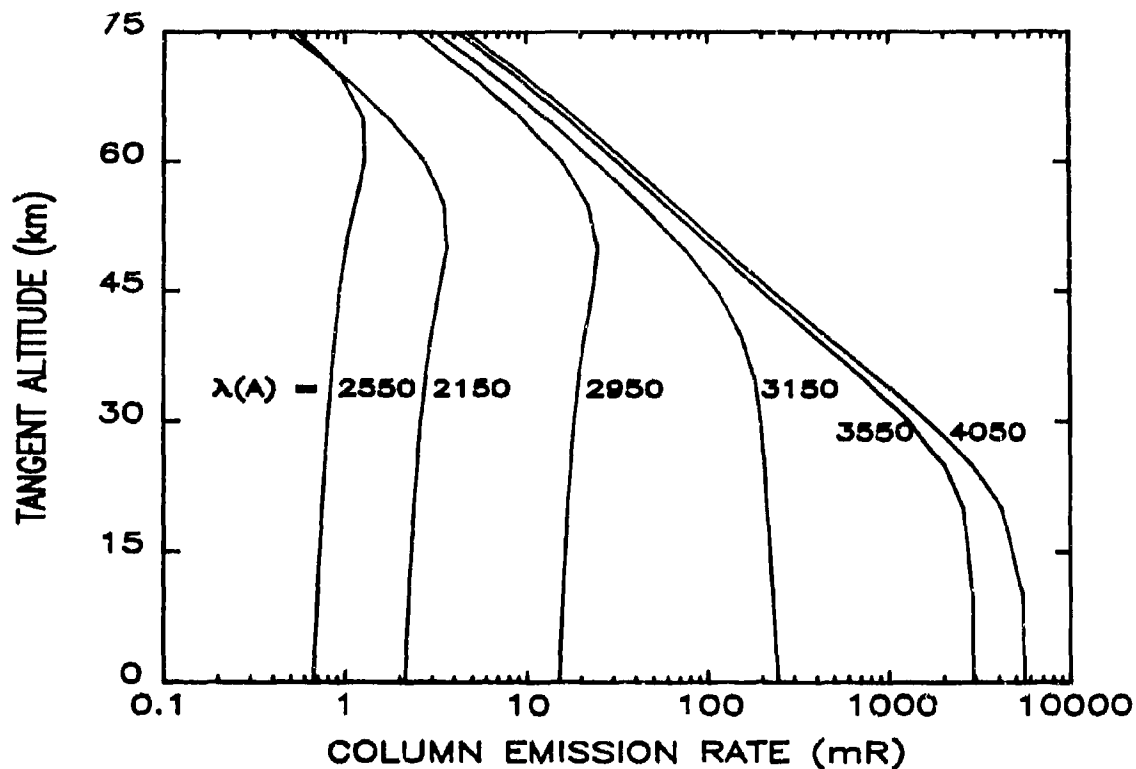


Figure 3. Limb profiles rate at $\theta_0 = 50^\circ$, where mR is 10^6 Rayleighs (see text). The wavelengths represent the center of a 100 Å interval over which the spectrum at each tangent altitude has been integrated.

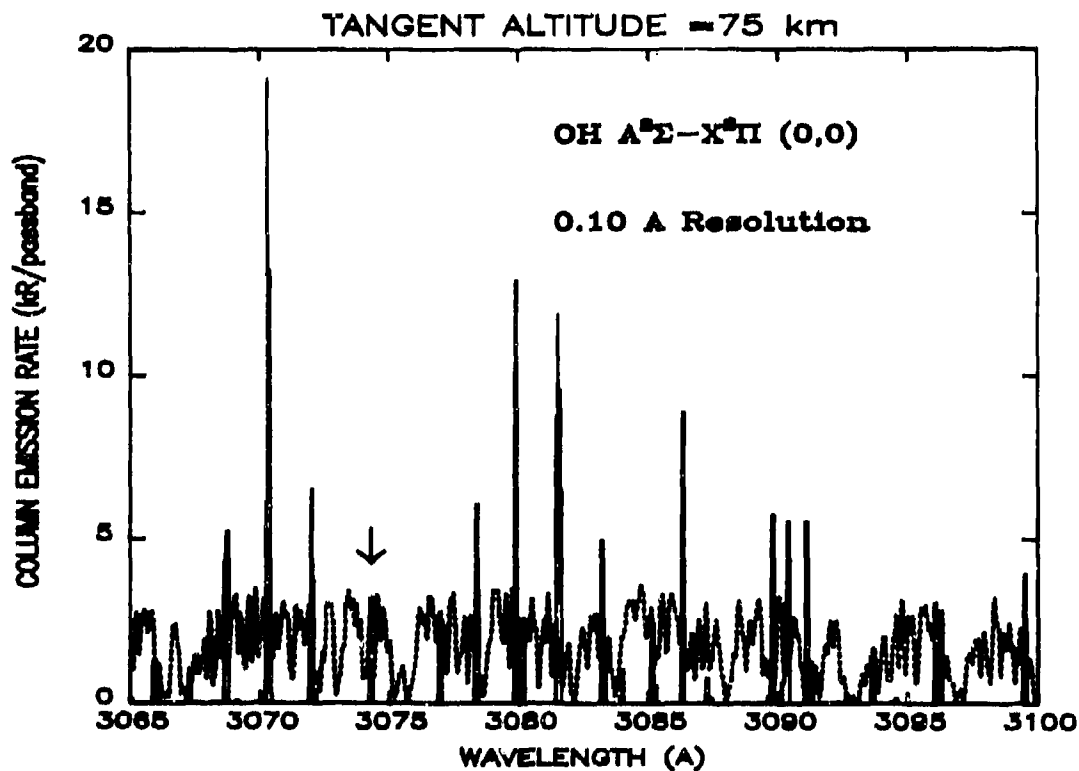


Figure 4. High resolution spectra of the solar flux (dotted curve) and the OH line emission (solid vertical lines) calculated for the MAHRS experiment passband of 0.1 Å for a tangent altitude of 75 km, $\theta_0 = 0$ and a Spring OH distribution (See Figure 3).

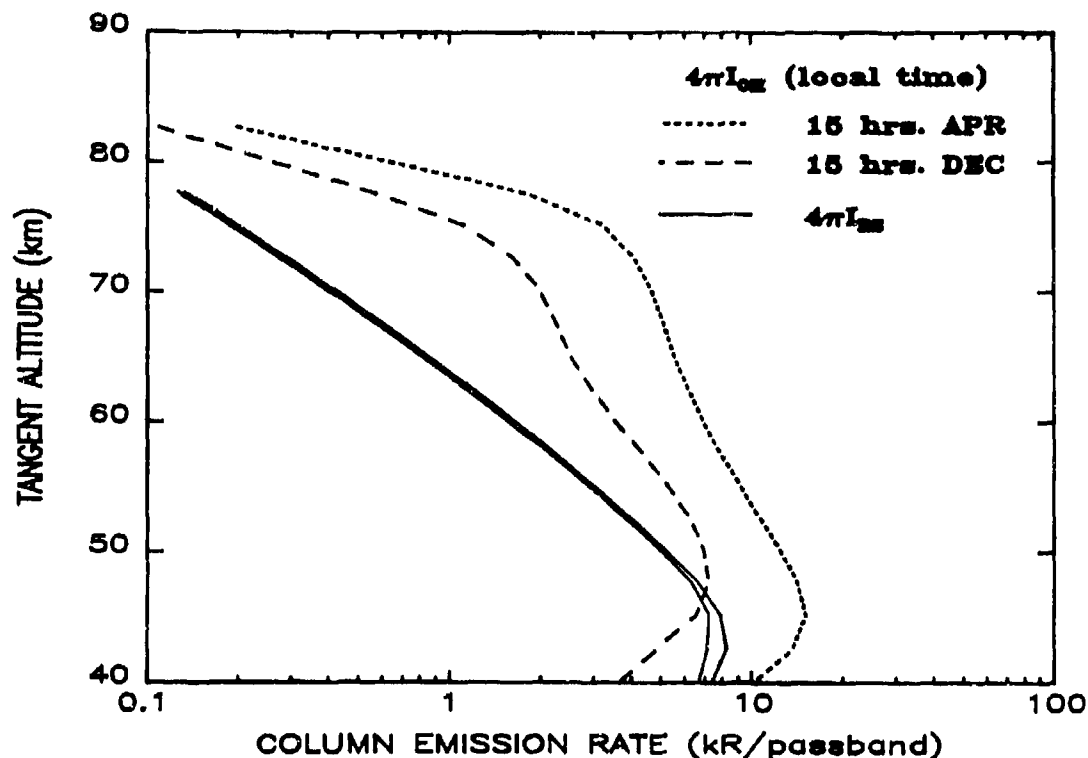


Figure 5. Limb profiles for the 3074.366 Å rotational line indicated by the arrow in Figure 4, where kR is 10^3 Rayleighs, the passband is 0.1 Å and $\theta_0 = 0^\circ$.

3. OPTICAL BACKGROUNDS FROM THE ATMOSPHERE ABOVE 90 KM

Nightglow, arising primarily from radiative recombination in the thermosphere will not be described here, but is included in the the radiance models described below. The radiance levels are quite low at night, typically less than 10 Rayleighs throughout the spectral region 1300-4000 Å. However, in the equatorial regions (± 20 degrees latitude) radiance levels at OI 1304 and 1356 Å can reach a few hundred Rayleighs and depend on ionospheric structure.

During the day, optical emissions from neutral and singly ionized atoms and molecules are observed throughout the atmosphere. The region above 100 km is dominated by emissions in the wavelength region 500-6000 Å which are produced by solar resonance excitation and photoelectron impact excitation.¹¹ Rayleigh scattering is negligible above 90 km, so that even at a spectral resolution of 25 Å information about thermosphere and ionosphere behavior can be deduced. We have developed a model which describes these emissions in detail and have validated it through analysis of rocket, ground-based and satellite data sets.¹² Through analysis of these data fundamental issues regarding emission sources and thermosphere characteristics have been addressed, and as a result the model is now accepted as a reliable diagnostic tool for analyzing optical backgrounds from the mesosphere, thermosphere and exosphere.

An example of dayglow emission between 1300 and 4000 Å calculated for an observation from above the thermosphere is shown in Figure 6 for tangent altitudes 130 and 200 km and a spectral resolution of 20 Å. The dominant features in the far UV (1000 to 2000 Å) are H I 1216 (not shown), O I 1304, O I 1356 and the N₂ LBH system of bands which start at 1273 Å and continue throughout the far UV. In the mid UV (2000 to 3000 Å) the prominent features are the NO γ bands, the N₂ VK and 2PG systems and the atomic lines O II 2471 and O I 2972. N₂ LBH also contributes at short wavelengths in this region. Finally, in the near UV (3000 to 4000 Å), the most intense emission features are the N₂ 2PG system of bands and the N₂ 1N bands. The brightest features are identified in Figure 6. The shape of the spectrum changes significantly with altitude because of the different altitude distributions of the emitting atoms and molecules, the different slant path absorption effects and the different excitation source distributions.¹¹ Altitude profiles for the spectral regions shown in Figure 3 are given in Figure 7 for the 75-250 km region. The limb emission profiles shown were calculated for a solar zenith angle of 50 degrees and an exospheric temperature of 1200K. Both the magnitude and shape of these curves change with solar zenith angle, solar activity, season and geographic location, but qualitatively the curves shown represent the range of expected variation in the magnitude of the emission. It should be noted that the range of variation in emission levels shown in Figures 3 and 7 is almost 10 orders of magnitude. Thus, for instruments designed to monitor this altitude-wavelength space, a large dynamic range in instrument response must be available. In addition, for tangent altitudes above 90 km, off axis scattering from below 90 km must be eliminated.

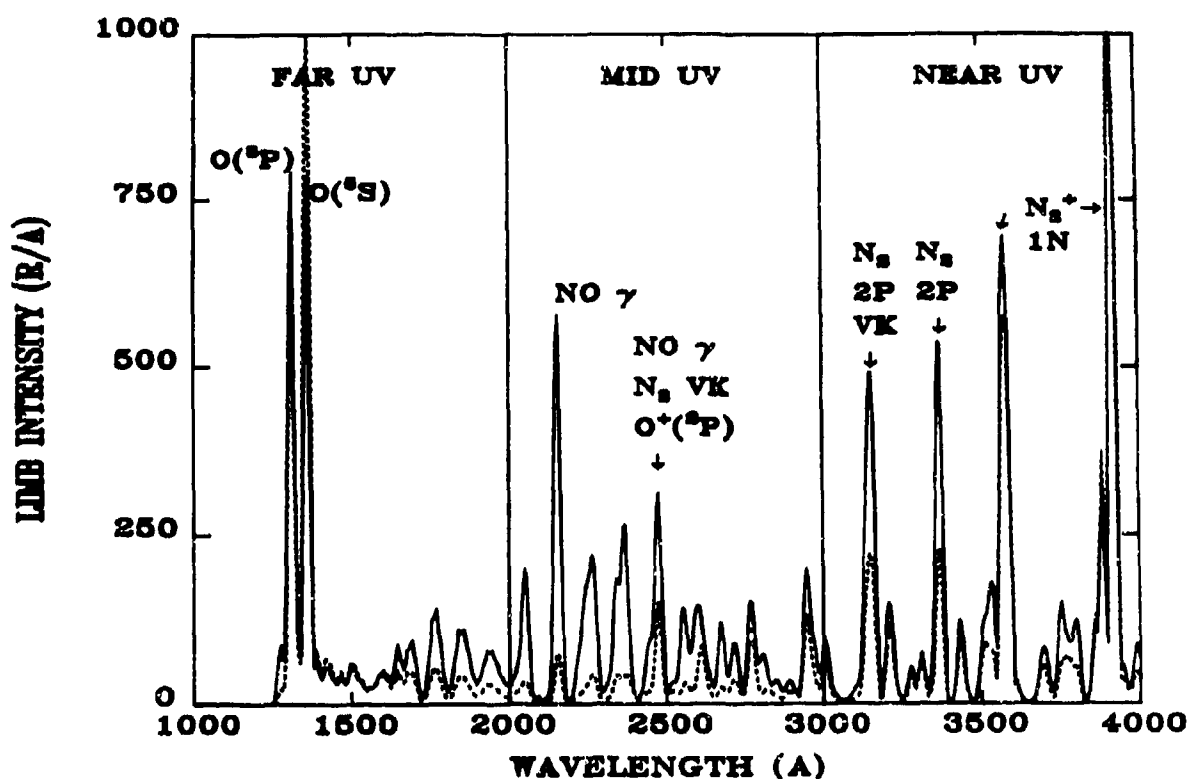


Figure 6. Dayglow emission excluding Rayleigh scattering. Spectra represent a 20 \AA spectral resolution and tangent altitudes 130 km and 200 km (dashed curve). Vertical axis is Rayleighs(R) per Angstrom(\AA).

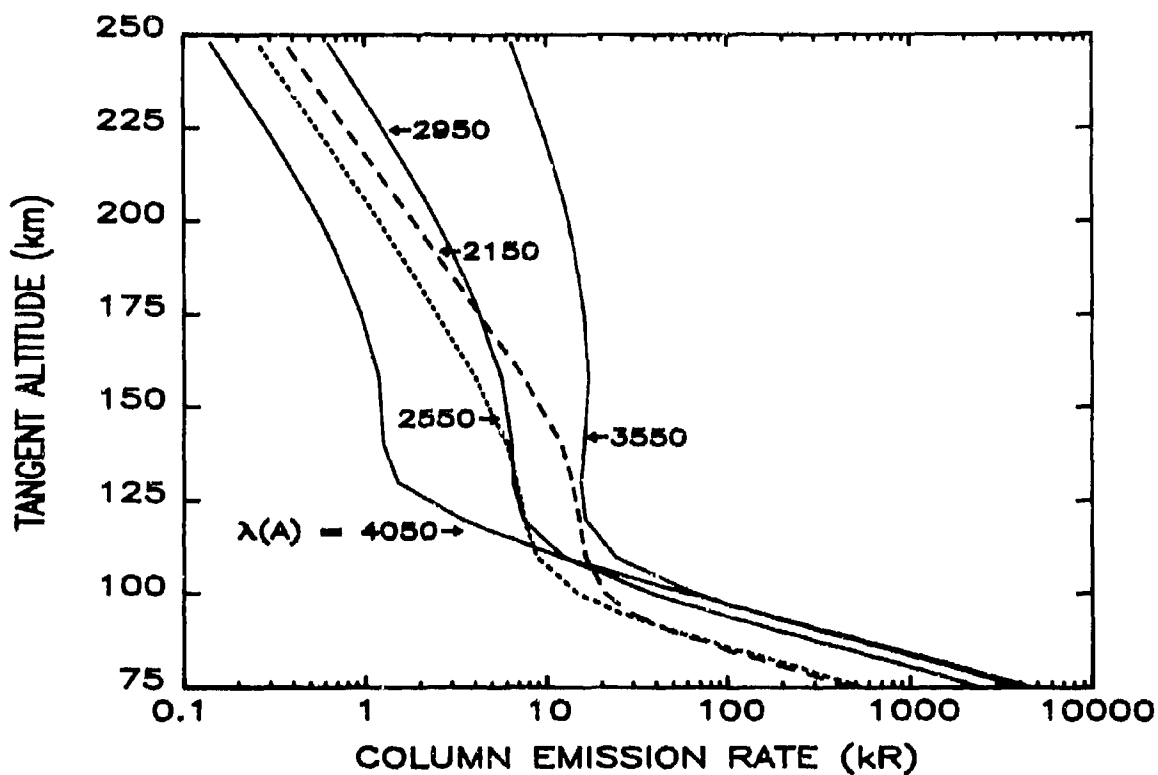


Figure 7. Limb profiles as in Figure 3, but for the mesosphere and thermosphere.

If the models described above are integrated into climatological models which are driven by solar activity indicators and include seasonal effects, then the capability exists to provide a prognostic model of optical background emission from the mesosphere, thermosphere and exosphere. In addition, analysis of emissions from singly ionized atomic oxygen, OH and nitric oxide provide the ability to monitor D, E and F region variations of the electron density.

In the auroral region, the systematic and, to some extent, predictable optical background variability present in the dayglow does not exist. The range of excitation energy variation encountered is large and any prognostic ability depends heavily on our understanding of magnetospheric response to changes in the solar wind and the interplanetary magnetic field as they sweep by the Earth. Part of this response is in the form of changes in energetic particle fluxes (mainly electrons and protons) entering the high latitude ionosphere (e.g., from the plasma sheet and from more local regions producing particle acceleration). To date, there is no reliable model of these effects, so that in the auroral regions, theoretical models are used primarily to investigate current or past observations. The results of these ongoing analysis efforts may ultimately lead to a prognostic model of auroral region optical emissions based on models that couple the chemistry and dynamics of the neutral atmosphere, ionosphere and magnetosphere.

Examples of typical incident electron spectra used in auroral modeling are shown in Figure 8. The upper panel shows four spectra characterized by Maxwellian distributions with the addition of low energy tails. The characteristic energies are .5, 1.0, 2.5 and 5.0 keV with mean energies of twice these values. Each spectrum contains an energy flux of $1 \text{ erg cm}^{-2} \text{ s}^{-1}$. Maxwellian-like distributions occur commonly in visible aurora, especially in what is termed the diffuse aurora whose energy source is precipitation from the plasma sheet. The lower panel in Figure 8 shows four spectra characterized by Gaussian distributions with the addition of high and low energy tails. Peak energies are 1, 2.5, 5.0 and 10 keV with energy fluxes of $1 \text{ erg cm}^{-2} \text{ s}^{-1}$ as in the upper panel. These type of spectra occur commonly in auroral arcs. The Gaussian-like portions are thought to arise from acceleration processes high in the ionosphere.

The volume emission rate for a given optical feature is determined by first performing an electron transport calculation whose boundary condition is given by the energy and angular dependence of the precipitating electrons.¹³ Figure 8 showed typical examples of the energy dependence. Isotropy over the downward hemisphere is usually chosen for the angular dependence at the upward boundary based on satellite particle observations. The transport calculation specifies the electron intensity versus altitude, energy and angle which is then integrated over 4π to give the spherical electron flux. The volume emission rate is then calculated by an integration over energy involving the product of this flux, an electron impact cross section for the emission feature of interest and the number density of the species being impacted. Figure 9 shows examples of the calculated quantity for a series of incident electron spectra given by Maxwellian distributions containing an energy flux of $1 \text{ erg cm}^{-2} \text{ s}^{-1}$.¹⁴ Shown is the total excitation rate of the B state of N_2^+ which produces the first negative (1N) system. The source of this emission is electron impact on N_2^+ . This system contains the bright bands at 3914 Å and 4278 Å which are two of the most commonly observed features in the aurora.

Over the past several decades of the study of auroral phenomena, almost all of the observed spectral features have been identified. The current model includes the prominent spectral features observable by typical satellite-borne spectrometric experiments. The magnitude of each feature is determined from the emission rate as described above. For molecules, the emission rate of an entire band is distributed among its rotational lines by utilization of spectral synthesis codes. The final result, radiance for a particular viewing geometry, is obtained by integration of these emission rates along the line of sight. In the case of optically thick emissions, multiple scattering within the atmosphere must be evaluated to determine the total emission rate. The radiance is then determined by integration along the line of sight, but with the inclusion of absorption effects. Figure 10 shows two examples of this radiance from 1000 to 4000 Å as observed by satellite for viewing in the nadir direction. At wavelengths longer than 3000 Å, Rayleigh scattering and ground albedo may serve to enhance the emission. The emission spectra correspond to incident electron spectra having the shapes shown in the lower panel of Figure 8 with peak energies of 1 and 10 keV, respectively. Radiance units are Rayleighs Å^{-1} with a chosen spectral resolution of 20 Å. The spectral brightness is linearly proportional to the energy flux of the incident electrons which is the same as for the above results ($1 \text{ erg cm}^{-2} \text{ s}^{-1}$). The features identified in Figure 6 are also present in Figure 10, with the exceptions that OI 1304 is not included nor are the NO γ bands, which are usually much less intense than other auroral features. The most notable differences between the two spectra in Figure 10 are the lower brightness of the "10 keV" spectrum at FUV wavelengths (1300 to 1700 Å) and over an extended region at Mid UV and Near UV wavelengths. The differences in the degree of pure absorption by O_2 for the two simulated auroras is the cause of the differences at FUV wavelengths.¹⁵ The differences at the longer wavelengths occur primarily in the N_2 VK bands which are weaker for the harder aurora ("10 keV"). This is caused by greater quenching of the excited state [$\text{N}_2(\text{A})$] at 10 keV, because this state is produced lower in the atmosphere.¹⁶

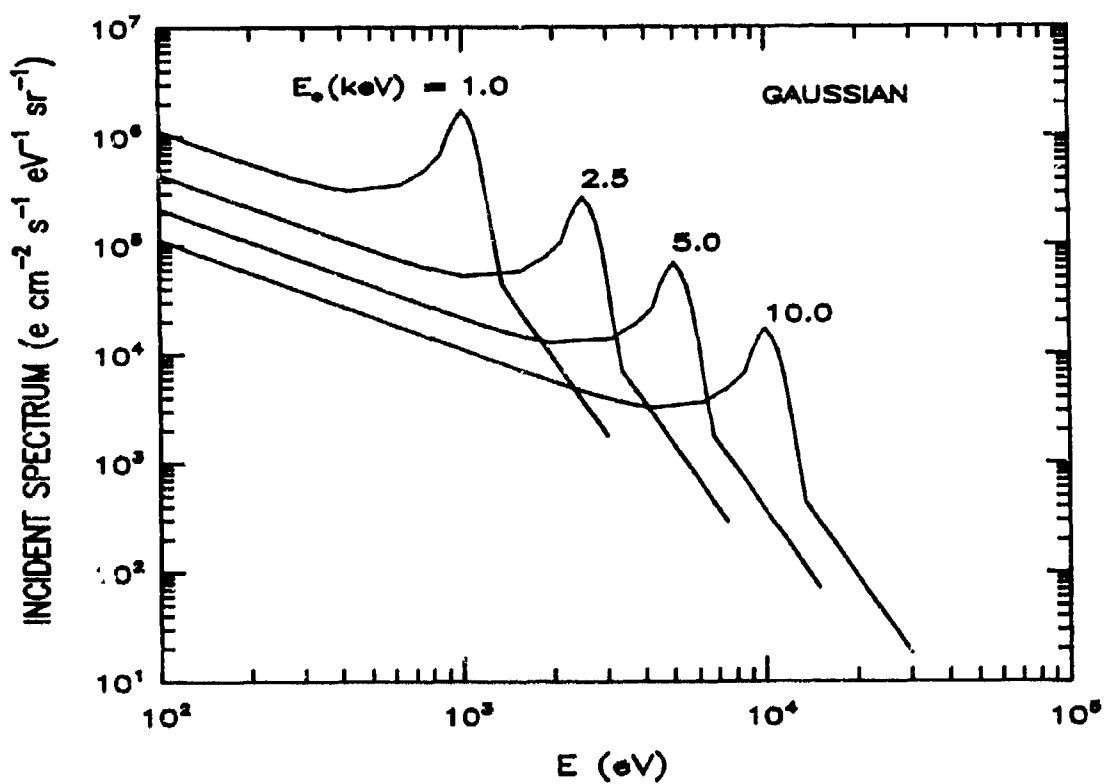
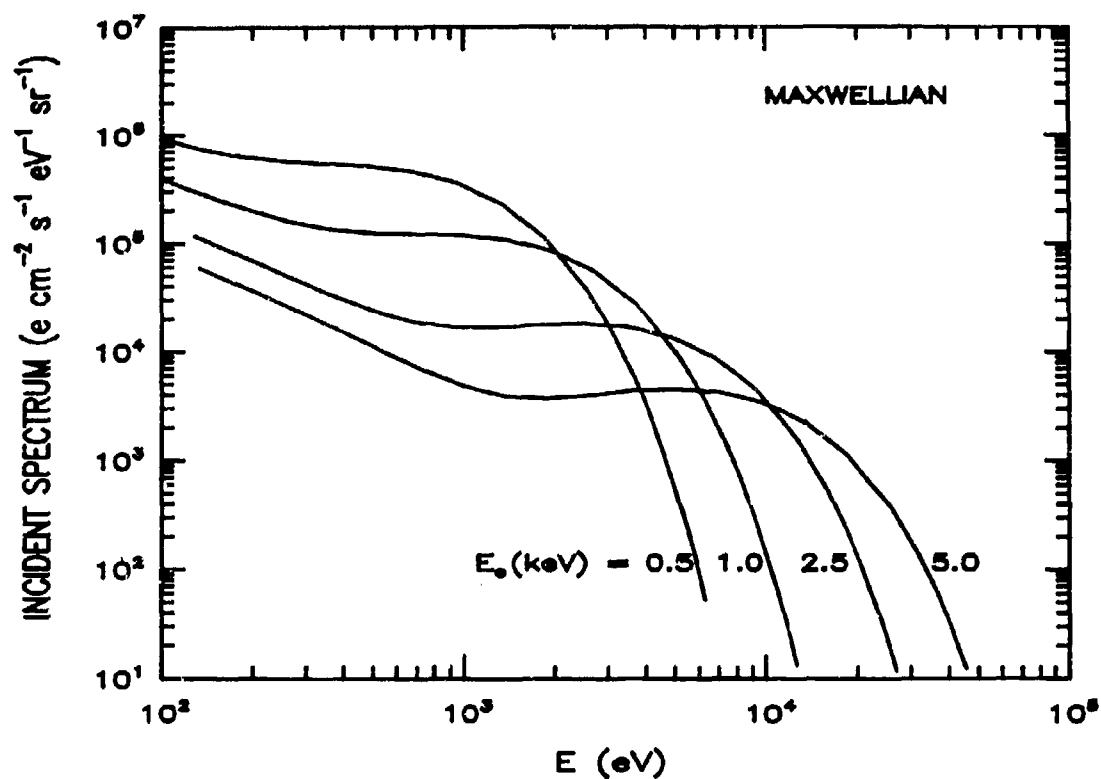


Figure 8. Incident auroral energy spectra, characterized by Maxwellian distributions with low energy tails (upper panel) and Gaussian distributions with high and low energy tails (lower panel), for a 1 erg aurora with energies indicated by E_0 , where keV is 10^3 electron volts.

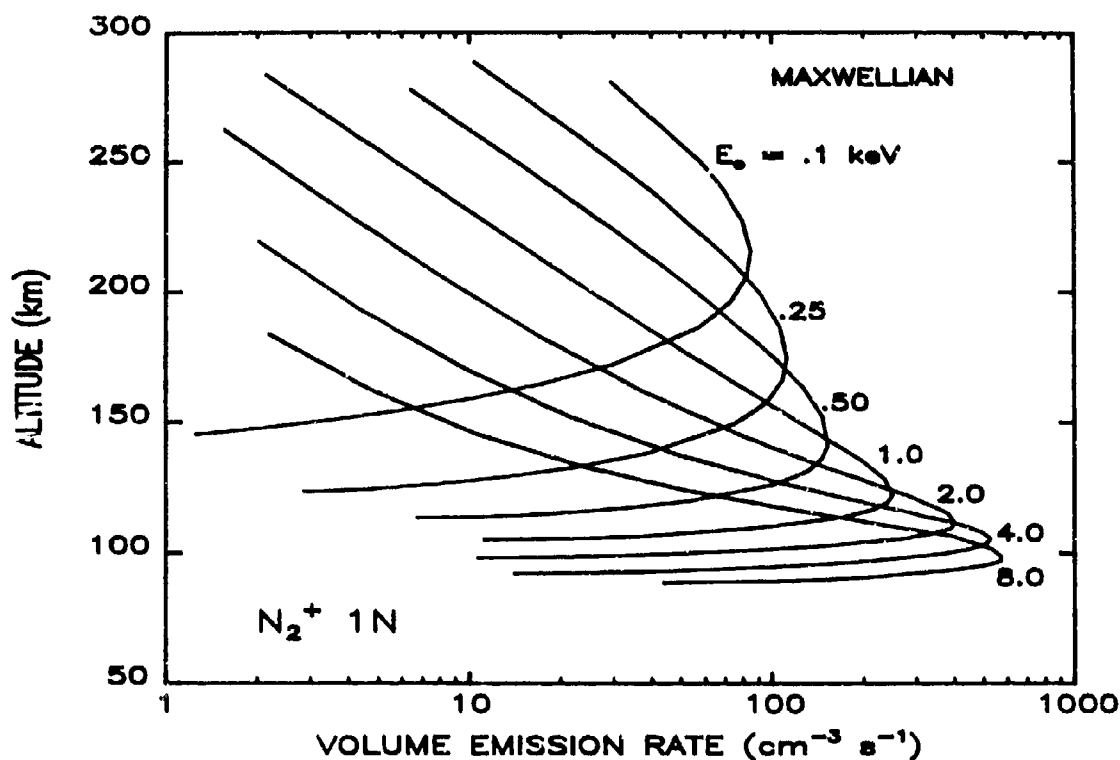


Figure 9. Volume emission rate for a 1 erg aurora with Maxwellian-like incident electron spectra with mean energies indicated by E_0 .

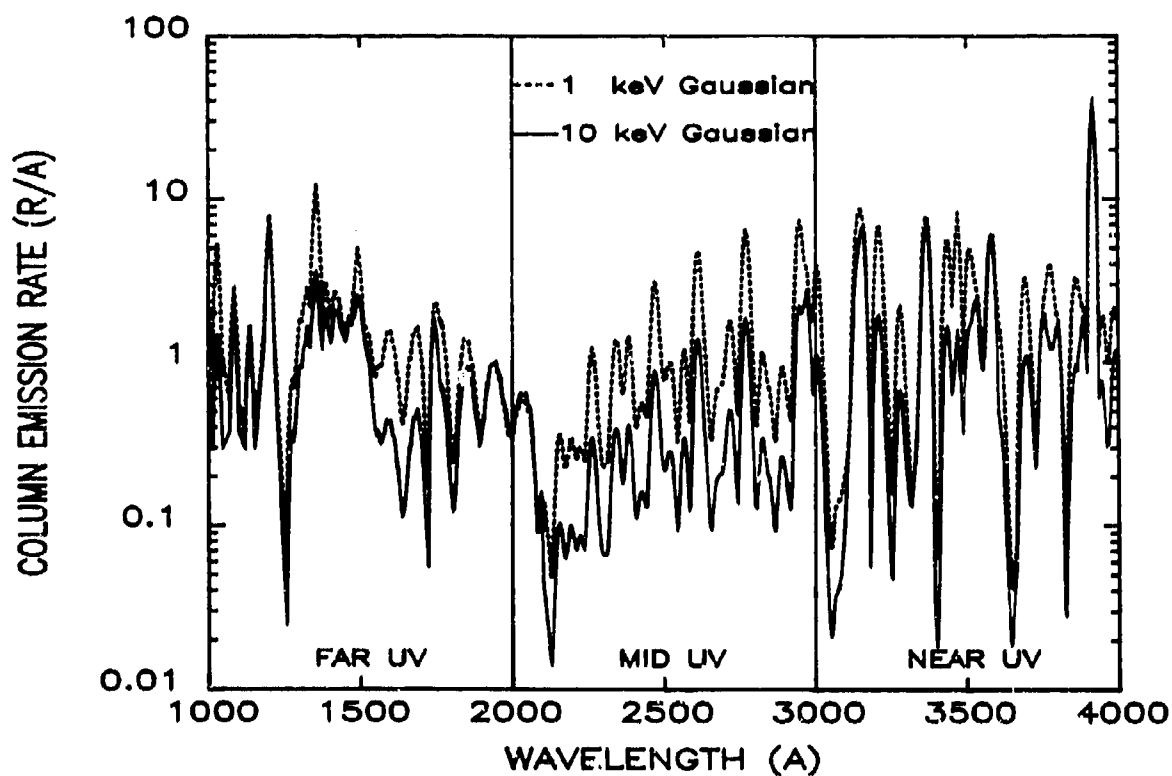


Figure 10. Nadir column emission rate for the auroral energy spectra shown in the lower panel of Figure 8 for 1 and 10 keV.

4. CONCLUSIONS

An understanding of the physical and chemical mechanisms leading to the UV-visible radiation field is a critical ingredient in the development of codes which predict UV-visible background scenes. In order to distinguish artificial sources from natural background variability, such an understanding must be present on a global scale. LOWTRAN7 will soon provide a global description of the atmosphere below 50 km, when minor constituent climatologies are incorporated. The main features of the UV-visible airglow and aurora are well understood in terms of radiation scattering theory and inversion of emission features to derive atmospheric parameters; and empirical models of the temperature and constituent distributions are being developed. However, no LOWTRAN-type model exists which could be assimilated easily into a global emission model for the atmosphere above 90 km.

Two investigations, RAIDS and the UV-visible portion of MSX, will provide data sets in the 1992-1995 time period which can be used to validate such a global emission model. In addition, the flight of MAHRS will provide a new and unique data set which should yield improved understanding of the chemistry and dynamics which drives global stratosphere and mesosphere variability. These investigations, when combined with collaborative modelling efforts, provide the potential to yield validated diagnostic and prognostic models of the coupled neutral atmosphere-ionosphere system.

5. REFERENCES

1. Kneizys, F.X., E.P. Shettle, L.W. Abreu, J.H. Chetwynd, G.P. Anderson, W.O. Gallery, J.E.A. Selby and S.A. Clough, 'Users Guide to LOWTRAN7', AFGL-TR-88-0177.
2. Anderson, Jr. D.E. and C.W. Hord, 'Multidimensional Radiative Transfer: Applications to Planetary Coronae', Planet. Space. Sci. 25, 563, 1977.
3. Anderson, Jr. D.E., 'The Troposphere-stratosphere radiation field at Twilight', Planet. Space Sci., 31, 1517, 1983.
4. Anderson, Jr., and S.A. Lloyd, 'Polar Twilight UV-Visible Radiation Perturbations due to Multiple Scattering, Ozone depletion, Stratosphere Clouds and Surface Albedo', submitted to J. Geophys. Res., 1989.
5. Maudet, J.P. and G.E. Thomas, 'Aerosol Optical Depth and Planetary Albedo in the Visible from the Solar Mesosphere Explorer', J. Geophys. Res. 92, 8773, 1987.
6. Clancy, R.T., 'El Chichon and "mystery cloud" aerosols between 30 and 55 km: Global Observations from the SME Visible Spectrometer', Geophys. Res. Lett. 13, 937, 1986.
7. Thomas, G.E., 'Solar Mesosphere Explorer Measurements of Polar Mesospheric Clouds (Noctilucent Clouds)', J. Atmos. and Terr. Phys. 46, 819, 1984.
8. Strickland, D.J., R.P. Barnes, R.J. Cox, D.E. Anderson, Jr., J.F. Carbary and C.-I. Meng, 'Analysis of UV Limb Data from Low Earth Orbit', in press, SPIE, August, 1989.
9. Conway, R.R., D.K. Prinz and G.H. Mount, 'Middle Atmosphere High Resolution Spectrograph', SPIE, 932-Ultraviolet Technology II, 30, 1988.
10. Strobel, D.F., M.E. Summers, R.M. Bevilacqua, M.T. DeLand and M. Allen, 'Vertical Constituent Transport in the Mesosphere', J. Geophys. Res. 92, 6691, 1987.
11. Anderson, Jr. and D.J. Strickland, 'Synthetic dayglow Spectra and the Rayleigh Scattering Background from the Far UV to the Visible', SPIE, 932-Ultraviolet Technology II, 170, 1988.
12. Meier, R.R., R.R. Conway, D.E. Anderson, Jr., P.D. Feldman, R.W. Eastes, E.P. Gentieu and A.B. Christensen, 'The Ultraviolet Dayglow at Solar Maximum 3. Photoelectron-excited emissions of N₂ and O', J. Geophys. Res. 90, 6608, 1985.
13. Strickland, D. J., D. L. Book, T. P. Coffey and J. A. Fadder, Transport Equation Techniques for the Deposition of Auroral Electrons, J. Geophys. Res., 81, 2755, 1976.
14. Strickland, D. J., R. R. Meier, J. H. Hecht and A. B. Christensen, Deducing Composition and Incident Electron Spectra from Ground-Based Auroral Optical Measurements: Theory and Model Results, in press, J. Geophys. Res., 1989.
15. Strickland, D. J., J. R. Jasperse and J. A. Whalen, Dependence of Auroral FUV Emissions on the Incident Electron Spectrum and Neutral Atmosphere, J. Geophys. Res., 88, 8051, 1983.
16. Daniell, R. E., Jr. and D. J. Strickland, "Dependence of Auroral Middle UV Emissions on the Incident Electron Spectrum and Neutral Atmosphere", J. Geophys. Res., 91, 321, 1986.

DISCUSSION

R. NICHOLLS

Do the O_2 (Meinel) vibration-rotation bands provide any contribution to the radiance?

AUTHOR'S REPLY

Yes they do. A very important source of nightglow.

CALCULATION OF IR PROPAGATION STATISTICS IN THE EASTERN ATLANTIC FOR SURVEILLANCE SYSTEM PERFORMANCE ASSESSMENT

by

J.M. Ridout

UK MOD ARE Portsdown
Cosham
Portsmouth, Hants PO6 4AA
United Kingdom

The assessment of Infra Red Search and Track systems requires a knowledge of the atmospheric propagation conditions in the geographic region of interest and how often these conditions arise. One area of interest to the UK Royal Navy is the Eastern Atlantic from the Iberian Basin in the South to the Greenland Sea in the North. A description of the meteorological conditions in this area in terms of air mass type has become available under NATO. The data have been used with the Lowtran 6 computer program to determine the atmospheric transmissions in the 3-5/ μ m and 8-12/ μ m bands and the associated occurrence values used to produce cumulative probabilities of occurrence of a given transmission. This data base gives the conditions in terms of air mass type which may distort the probability curves. A further meteorological data base is available which gives the atmospheric conditions over a period of several years for Weather Ship J in the West European Basin and a subset of this has been used to provide a check on the above calculations for this restricted region. It is shown that the degree of correlation between the two methods is reasonably good and that using the air mass type of approach is satisfactory. The effect of the calculated probability curves in sub regions of the Eastern Atlantic region on the selection of IR surveillance systems is indicated.

INTRODUCTION

The assessment of the performance of an IR surveillance system for use on Naval vessels is necessary before the decision to include the equipment within the sensor suite is made. In the case of the development of a new system this assessment must be made by modelling the expected performance against a number of targets in a specified scenario. One output required is the percentage of time the system will achieve a given detection range against a given target. In order to provide this information it is necessary to have an estimate of the atmospheric transmission as a function of occurrence. The transmission is normally calculated using the Lowtran computer program and hence this requirement is translated into a need for the weather statistics for the geographic region of interest. The transmission, and hence the performance can vary both with the spectral band used and the specific locality in a general geographic area. In one area of interest to the Royal Navy, the Eastern Atlantic, the conditions vary from the relatively warm Iberian Basin to the cold Greenland Sea. Thus a large number of different calculations are required to fully characterise the performance and any method of reducing the total amount of data which is considered is welcome.

TRANSMISSION CALCULATIONS

The largest amount of data needed is that to calculate the transmission statistics since small areas need to be considered and the probability of the occurrence of specific conditions is required. The direct way of obtaining the latter information is to perform a large number of transmission calculations using observed weather conditions and analysing the resultant transmissions. If a number of areas are required this may involve the calculation of many thousands of transmissions.

Canada has recently been involved in a task which allows another approach to the problem. The weather records of various areas have been examined and the conditions ascribed to a set of air mass types along with the frequency of occurrence of these types of air mass. The source air mass types considered in the North Atlantic are Maritime Tropical, Maritime Polar, Continental Arctic, Maritime Arctic and Cold Maritime Arctic. These air masses will be modified as they cross the region from their source and combinations of two or more different air masses are also considered. Also ascribed to these air masses in each region is a typical set of values for pressure, temperature, wind speeds etc. Care has to be taken in this process to make sure that the occurrence of precipitation in the ascribed data is consistent with the expected frequency. It is thus possible to use this set of weather parameters to calculate the atmospheric transmission and to use the frequencies of occurrence to provide the probabilities of certain transmissions occurring.

This type of calculation uses only a small number of different conditions and each condition is ascribed a particular set of values and the question arises as to whether the resultant occurrence statistics approximate to the real world. A check on this is possible, at least in one small area of interest. The Canadian data is available for Weather Ship J in the West European Basin and corresponding observed weather data is available covering a number of years observation at hourly intervals from the UK Meteorological Office. Two sets of calculations were performed, one based on the air mass type approach and the other for a subset of the direct data collected during 1973. The program used was Lowtran 6 in a horizontal path transmission mode with the Navy Maritime Aerosol model selected. A modification was made to the aerosol model as advised by the authors for high wind speed conditions. One problem with this aerosol model is the requirement for an air mass number (not to be confused with the air mass type referred to above) which is not directly contained in either weather data base. A precursor program was used to estimate the air mass number from a consideration of the available data by ensuring that the effects of visibility, wind speeds and precipitation

were consistent. Although the correct selection of this parameter is essential to obtain accurate transmission calculations, any error is present in both calculations and should not change the conclusions.

The result of this comparison is presented in Fig 1 which shows the cumulative probability of a given transmission being bettered versus the log of the transmission over 20 km for the average 3-5/ μ m and 8-12/ μ m bands.

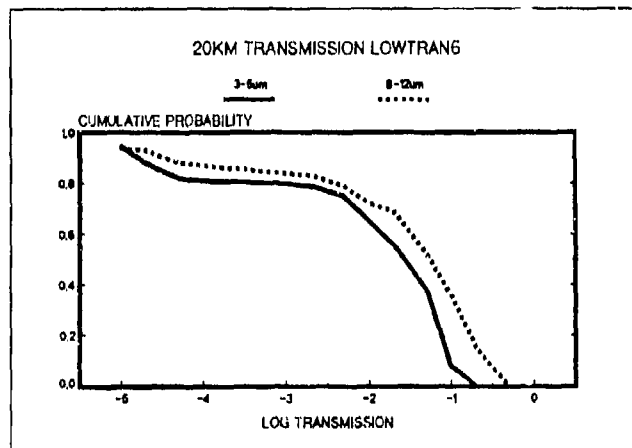


Fig 2. Average transmission in the Eastern Atlantic

It can be seen that although there are some discrepancies the overall agreement is satisfactory. Some of the fluctuations in the air mass type results may be due to the small number of weather scenarios considered, in this case 26, but for assessment purposes this type of calculation will provide adequate information.

EASTERN ATLANTIC TRANSMISSION

The air mass weather description for the Eastern Atlantic area covers six sub-regions from the Iberian Basin in the south to the Greenland Sea in the north. The atmospheric transmission has been calculated as described above for each of these regions. The average 20 km transmission over the complete region is shown in Fig 2.

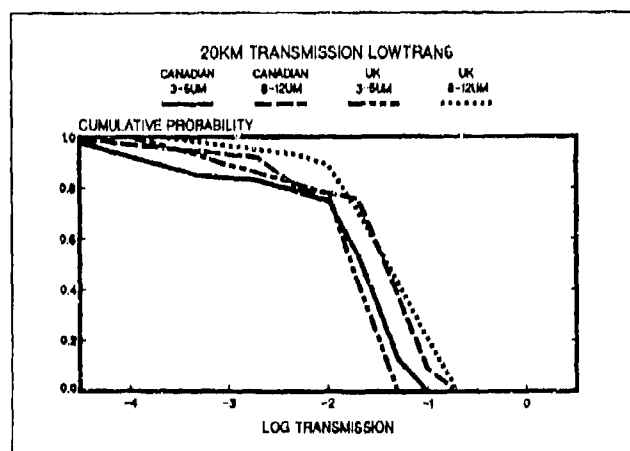


Fig 1. Weather ship J data comparison

The 8-12/ μ m transmission is better than the 3-5/ μ m transmission with transmissions better than 2.0×10^{-3} (equivalent to an extinction coefficient of 0.3/km) occurring for 80% of the time. A transmission of 10% occurs for 8% of the time in the 3-5/ μ m band and 36% in the 8-12/ μ m band. This result does not give the full picture however and the extreme sub-regions are given in Figs 3 and 4.

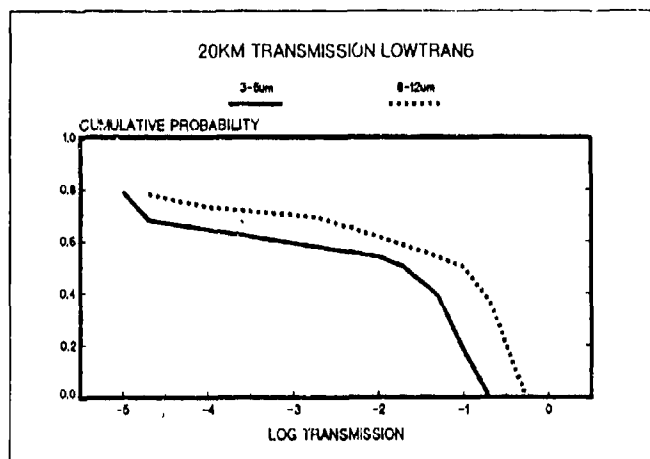


Fig 3. Transmission in the Greenland Sea

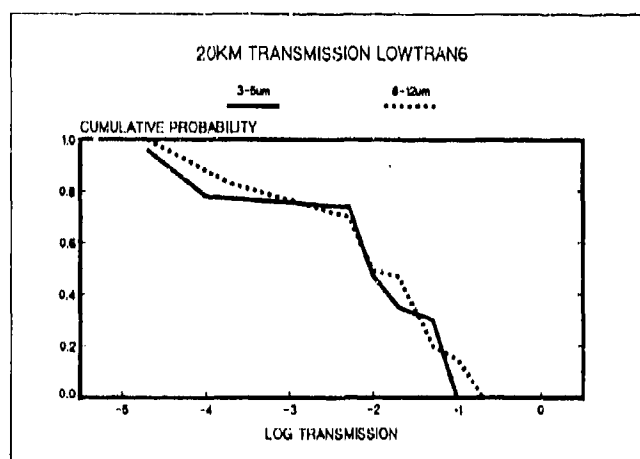


Fig 4. Transmission in the Iberian Basin

In the cold Greenland Sea the 8-12/ μ m band has better transmission than the 3-5/ μ m band but both bands have a lower transmission for a higher percentage of the time than the average region. This sub-region however has a good transmission in better weather conditions although these do not occur often. Transmissions of 10% occur for 18% of the time in the 3-5/ μ m band and 50% in the 8-12/ μ m band. The transmissions of each band in the warmer Iberian Basin sub-region are similar with the 3-5/ μ m band having a value close to the average but the 8-12/ μ m band transmissions being reduced. The derived curves cross each other in a time fashion and this probably due to the restricted number of cases considered in this region but some change is expected as each band is dependant upon different quantities in the calculation. This change of relative transmissions between the bands will affect the performance of systems based upon one or other of the bands according to the specific region of interest. It is therefore not sufficient just to consider a wide area such as the Eastern Atlantic when defining the weather conditions expected but also the variations within that region.

PERFORMANCE CALCULATIONS

The performance of Infra Red Search and Track (IRST) systems was calculated in a number of steps starting with an assumed source emission followed by transmission through the atmosphere and finally a conversion from irradiance correlated to probability of detection using data relevant to the particular IRST. Calculations for a supersonic target were performed in the Greenland Sea and Iberian Basin regions for a dual band

IRST. The data assumed for the IRST was purely generic and is not representative of any system or best achievable design. However the relative sensitivities in each band are correct to allow comparison of atmospheric transmission differences in the two bands. Fig 5 shows the cumulative probability of the 50% probability of detection at a given range against range. No modification has been made to the range for horizon cut-off, it being assumed that an infinite horizontal path length is available.

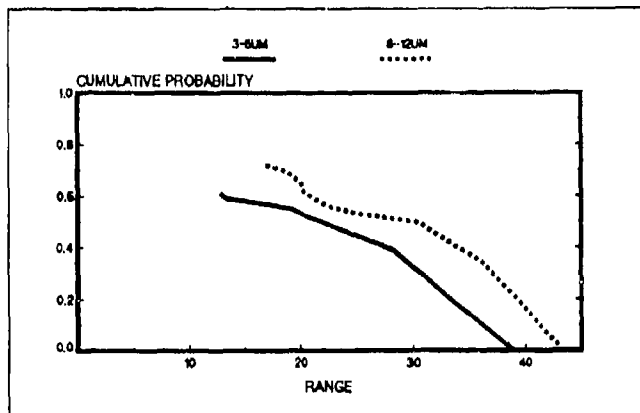


Fig 5. Performance against a supersonic target in the Greenland Sea

The 8-12/μm band has a superior capability in this geographic region even against a supersonic target which favours the 3-5/μm band. The equivalent performance in the Iberian Basin is given in Fig 6.

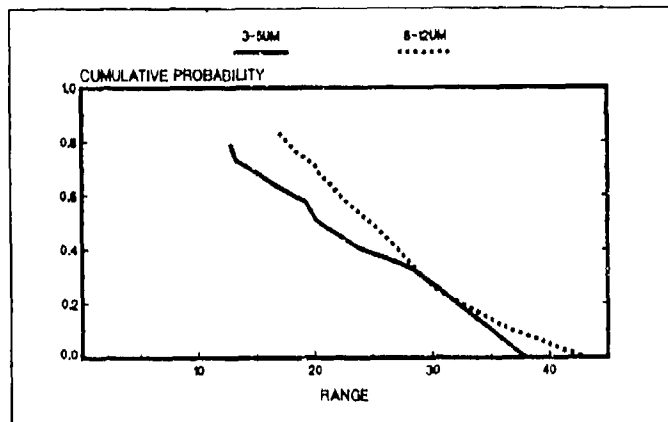


Fig 6. Performance against a supersonic target in the Iberian Basin

Here, at least during the better weather conditions, the performance is similar in both wavebands. If a warmer geographic area was considered it is probable that the 3-5/μm band could become better than the 8-12/μm band most of the time.

The detection range is a function of the source strength and size, the IRST spatial resolution and the atmospheric transmission. In this instance the transmission can cause a variation in the detection range of about a factor of four. In order to provide an accurate description of performance of the IRST it is not sufficient to use a worst case and a best case transmission scenario as these would produce similar results in both regions. A number of transmission values are needed to evaluate the percentage of time that detection range required for effective countermeasures can be achieved. Although not specifically addressed here, this information is required in a spectrally resolved form to allow for the correlation between the emission source and the absorbing species in the atmosphere and the spectral bandwidth of the IRST. The wide variation in the calculated detection range with different weather conditions means that a number of

calculations are required to provide an adequate indication of performance under all operating conditions. The use of air mass type descriptions of the weather occurring at each geographic location means that such performance curves for a particular location may be assessed from a few tens of transmission calculations rather than the few hundreds of individual calculations needed to provide adequate statistics from direct observations of conditions. The problem is further aggravated by the need to consider the actual band-pass of the IRST which may produce very different transmission characteristics than the full average 3-5/ μ m or 8-12/ μ m band. The use of the relatively small number of weather situations in the air mass type approach however does allow the possibility of a library of spectral transmissions reducing the calculations needed for parametric studies of IRST characteristics.

CONCLUSIONS

The need to consider small geographic regions when calculating the expected performance of IRST systems has been demonstrated. This need implies that many transmission calculations are required to describe the availabilities of the IRST in all these regions and that, to make the problem tractable, a reduction in the amount of data is required. The availability of an mass type description of the weather provides such an opportunity but the adequacy of these descriptions is open to question. Calculations have shown that in one geographic area the results of such a description are adequate and providing the partitioning is not coarse other regions should be the same.

Performance calculations for a generic IRST have demonstrated that choice of waveband or the need for a dual waveband can only be made if all operational areas are considered in a fine enough detail.

Copyright (C) Controller HMS LONDON 1989

4-1

**COMPUTATION OF BROAD SPECTRAL BAND ELECTRO-OPTICAL SYSTEM
TRANSMITTANCE RESPONSE CHARACTERISTICS TO MILITARY
SMOKES AND OBSCURANTS USING FIELD TEST DATA FROM
TRANSMISSOMETER SYSTEM MEASUREMENTS**

**W. Michael Farmer, and Roger Davis
Science and Technology Corporation
Las Cruces, New Mexico 88001 USA**

**Robert Laughman
US Army Project Manager for Smoke/Obscurant
Aberdeen Proving Ground, Maryland 21005**

**Wendall Watkins
US Army Atmospheric Sciences Laboratory
White Sands Missile Range, New Mexico 88002**

ABSTRACT

Electro-optical weapon system developers and users must know the smoke/obscurant countermeasure transmittance levels required to defeat their systems. This information is required in order to establish both operational smoke screen requirements and system scenario applicability. Transmittance data acquired in field tests such as the Smoke Work tests held by the Project Manager, Smoke/Obscurants have been developed for this purpose. Narrow-band transmittance data can be analyzed using the Beer-Douguer transmittance law to evaluate the performance of narrow-band electro-optical weapon systems such as laser rangefinders. However, broadband transmittance data for smokes such as phosphorus, fog oil, and dust in the visible, 3- to 5- μ m, or 8- to 12- μ m bands cannot be evaluated directly using the Beer-Douguer transmission law for broadband electro-optical systems such as FLIRs. A broadband transmittance measurement averages over the atmospheric spectrum, the source spectrum, the sensor detector/filter spectral response, and the mass extinction spectrum of the smoke/obscurant. The source spectrum and detector/filter response of a broadband electro-optical weapon system may be radically different from that of a transmissometer used to acquire field test data. Therefore, broadband transmittance that the electro-optical weapon sensor observes for a particular smoke type and concentration length can be radically different from that measured by a broadband transmissometer along the same line of sight. A method for transforming field-measured transmittance data into equivalent electro-optical system transmittance is required. The transmissometer system analysis developed in the Project Manager, Smoke/Obscurants TRANSMISSOMETER VALIDATION (TRANSVAL) program has provided the basis for developing such a method. This paper describes the method developed in the TRANSVAL program for computing equivalent broadband electro-optical sensor transmittance from field test data. It is shown that band averages of the mass extinction coefficient used with the Beer-Douguer transmission law do not yield correct estimates of equivalent electro-optical system transmittance. Examples are provided to illustrate the kinds of errors that can arise if sensor performance is incorrectly interpreted using field test data.

1. INTRODUCTION

The Project Manager, Smoke/Obscurants, aided by the U.S. Army Atmospheric Sciences Laboratory, has sponsored an ongoing TRANSMISSOMETER VALIDATION (TRANSVAL) program to identify, reduce, or eliminate transmissometer data inconsistencies. A primary objective of the TRANSVAL program has been to develop a methodology for expressing transmittance values measured by one system in terms of those measured by another. Since transmissometer systems are radiometers designed to measure signal attenuation, the method developed here for expressing transmittance response for different instruments applies in general to a number of electro-optical (EO) weapon systems, such as FLIRs, that depend on radiometric responses for system operation. Thus, for example, the transmittance of a smoke screen measured by a particular transmissometer system can be transformed into the transmittance observed by a FLIR operating in the same spectral band.

Our proposed method is structured 1) to provide information for electro-optical system developers who must estimate how well a system can perform against military smoke/obscurant countermeasures, and 2) to parallel the methods originally developed for evaluating EO system performance. To describe the proposed method, the original approach used for evaluating EO system performance against smokes/obscurants is first discussed, and the limitations in this approach are described. Next, characteristics of transmittance measurements in field tests for the measurement of smokes/obscurants are reviewed, and it is shown why these measurements cannot be used directly to evaluate EO system performance characteristics. The method for relating the field transmittance measurements to EO system performance is then described. An example is provided to illustrate the source and magnitude of potential differences in measured transmittance that make the proposed method necessary for the analysis of data.

2. ORIGINAL METHOD FOR SPECIFYING EO SYSTEM PERFORMANCE AGAINST SMOKES/OBSCURANTS

The original approach to specifying EO system performance against smokes/obscurants assumed that the Beer-Douguer transmission law directly applied to the transmittance data. The Beer-Douguer transmission law can be written as:

$$T(\lambda) = e^{-\alpha(\lambda)CL} \quad (1)$$

where $\alpha(\lambda)$ is the mass extinction coefficient (mean extinction cross section per mean particle mass), and CL is the concentration length product. Nearly all the original analyses assumed that the mass extinction coefficient was independent of time and that it could be used as a figure of merit for evaluating the relative attenuation capability of different smoke materials. During tests such as the Smoke Weeks provided by the Project Manager for Smoke/Obscurants, EO system developers could acquire system performance data relative to the obscuration capability of realistic concentrations of smokes/obscurants. System performance was determined by the times and time intervals during which the system could not adequately function. The EO system operator determined when the system did not function through design criteria developed specifically for the system. Attempts were made in these tests to assure alignment of the EO system with a transmissometer line of sight or with a linear array of mass sampling devices. The Beer-Bouguer law was assumed to apply to the measured transmittances. If the mass extinction coefficient for the smoke/obscurant used in a test was known, then the Beer-Bouguer law could be used to provide CL values as a function of time, t , through the following expression:

$$CL = \frac{-\ln(T(\lambda, t))}{\alpha(\lambda)} \quad (2)$$

If time-integrated CL (called dosage, D) was measured, then mass extinction coefficients could be determined as follows:

$$\alpha(\lambda) = \frac{-\int_0^{t'} \ln(T(\lambda, t)) dt}{\sum_{i=1}^N \Delta l(i) \int_0^{t'} C_i(t) dt} \quad (3)$$

Here, $\Delta l(i)$ is the path increment between dosimeters (typically 3 m). The EO system's performance relative to smoke/obscurant concentration length, determined using either linear arrays of concentration measuring devices or by transmittance measurements using Eq. (2), was then plotted as a function of time using bar charts of the type illustrated in Figure 1. Once CL thresholds for system performance were established, smoke screen transport and diffusion models could be used to estimate how the EO system would perform under conditions not encountered or produced in field tests. Smoke production analysts could then estimate the material and logistics requirements for producing an adequate smoke screen using the materials and EO systems evaluated in the tests. It was recognized early in the program that this system evaluation approach would be satisfactory for narrow-band systems such as laser rangefinders, but that the mass extinction coefficient for broadband EO systems must be interpreted as an average.

Since transmissometers were operated in bands similar to those of the EO systems and the transmissometers and linear mass measuring arrays were used to experimentally determine mass extinction coefficients, it was assumed that the approach would still apply to broadband systems if the appropriate experimentally measured mass extinction coefficient were used with the experimentally measured CL values. Unfortunately, the latter assumption has been found incorrect, and leads to erroneous system performance estimates and logistical supply requirements for EO system smoke/obscurant countermeasures. The Beer-Bouguer transmission law cannot be directly applied to the interpretation of broadband transmittance measurements; the Beer-Bouguer transmittance must be averaged over the spectral characteristics of the specific system making the measurement and the atmosphere in which the broadband transmittance was measured.

Broadband transmittance relative to that in clear air for normally operating transmissometers or EO systems attempting to operate through smokes/obscurants is given by:

$$T(t > t_0) = \frac{\int_0^\infty \exp\left[-\alpha(\lambda) \int_0^{t'} C(z, t > t_0) dz\right] P(\lambda) f(\lambda) F(\lambda) A(\lambda) O(\lambda) d\lambda}{\int_0^\infty P(\lambda) f(\lambda) F(\lambda) A(\lambda) O(\lambda) d\lambda} \quad (4)$$

where the functions of λ , $P()$, $f()$, $F()$, $A()$, and $O()$, are the source power, spectral transmission of the system filter, detector response, atmospheric transmittance, and optical system transmission respectively. Equation (4) shows that broadband transmittance is an average of the Beer-Bouguer transmittance over the spectral characteristics of the transmissometer system making the measurements or the EO system operating against the smoke screen. Unless $f(\lambda)$, $F(\lambda)$, $A(\lambda)$, and $O(\lambda)$ are the same for both the transmissometer and the EO system, the effective transmittance values through a smoke screen with a given CL value cannot be expected to be the same for both devices.

(5)

Since a multispectral transmissometer acquires data simultaneously in its various spectral bands, a regression analysis can be performed that eliminates the time dependence of the transmittance data and relates optical depth in one band to that in another. The optical depth regression yields relationships between optical depths in the various spectral bands in the form:

$$\tau(1) = b(\tau(2))^a \quad (6)$$

where $\tau(1)$ and $\tau(2)$ are the optical depths for spectral bands 1 and 2 respectively, and a and b are constants produced by the regression analysis. The optical depth for a narrow spectral band can be defined in terms of the Beer-Bouguer transmission law (Eq. (1)) parameters according to:

$$\tau(\Delta\lambda) = \alpha(\Delta\lambda) \int_0^{Z(SMK)} C(Z,t) dz \quad (7)$$

where $C(Z,t)$ is the mass concentration as a function of position Z in the smoke, t is time as defined previously, $Z(SMK)$ is the pathlength through the smoke/obscurant, and $\alpha(\Delta\lambda)$ is the mass extinction coefficient for the band, $\Delta\lambda$. All spectral responses involved in the measurement process are used to "average" the measured transmittances over the band. When the mass extinction spectrum is narrow relative to the spectral characteristics of the measurement system, virtually no spectral averaging occurs, and the transmittance is given by the Beer-Bouguer transmission law. When the optical depths in two narrow spectral bands are regressed, $a = 1$ in Eq. (6), and b is the ratio of the mass extinction coefficients for bands 1 and 2. When the mass extinction spectral band is wide relative to the spectral characteristics of the transmissometer system, the Beer-Bouguer transmittance is "averaged" over the spectral characteristics of the transmissometer using Eq. (4). Choosing spectral band 1 in Eq. (6) to be that for a narrow spectral band makes the mass extinction coefficient a constant, α_1 , and the optical depth for the broad spectral band, which will be called $\Delta\lambda$, is given by:

$$\tau(\Delta\lambda) = \left(\frac{\alpha_1 g}{b} \right)^{1/a} \quad (8)$$

In Eq. (8), g is the concentration length defined by the integral in Eq. (7).

Therefore the broadband transmittance can be written using Eq. (8) to express the optical depth in Eq. (5). Taking the antilog for the transmittance, we

$$T(\Delta\lambda) = \exp \left[- \left(\frac{\alpha_1 g}{b} \right)^{1/a} \right] \quad (9)$$

Equation (9) is the experimental expression for the band-averaged transmittance. Equation (4) provides a form of the theoretical expression for $T(\Delta\lambda)$. When the assumptions leading to Eq. (4) apply, then the right-hand side of Eq. (9) can be equated to the right-hand side of Eq. (4).

The concentration length, g , is independent of wavelength. Therefore, both Eq. (4) and Eq. (9) can be integrated from 0 to infinity with respect to g to eliminate the functional dependence on g . The result of the integration is:

$$\left| a \right| \left(\frac{b}{\alpha_1} \right) \Gamma(a) = \psi \quad (10)$$

where ψ is given by:

$$\psi = \frac{\int_0^\infty (\phi(CA,\lambda)/\alpha_2(\lambda)) d\lambda}{\int_0^\infty \phi(CA,\lambda) d\lambda} \quad (11)$$

and $\Gamma(a)$ is a gamma function of argument a . The function $\phi(CA,\lambda)$ is given by $P(\lambda) f(\lambda) F(\lambda) A(\lambda) O(\lambda)$. Equation (10) shows that the integral of the ratio of the clear-air spectral response of the system to the mass extinction coefficient spectrum is the primary mechanism that affects the a and b constants in the curve fit. Solution of Eq. (10) for a and b after computing Eq. (11) can be accomplished by iterative computations for the quantity a after calculating b . An expression for b can be found by solving Eq. (4) for $g = 1/\alpha_1$. (This value of g makes the narrow-band optical depth 1.)

The constants a and b are in general unique for a particular transmissometer system and atmospheric transmittance. Once computed for the transmissometer and for the test in which the transmissometer was used, they can be applied to the measured transmittance to obtain a value of the concentration length using Eq. (9) in the form:

$$g = \frac{(-\ln(T(\lambda)))^2}{a_1} b$$

(12)

This value of concentration length is independent of the transmissometer system that measured it. A detailed knowledge of the mass extinction spectrum over the band of interest is required in order to compute the constants. Ideally, the problem is simplified by using a narrow band to estimate the concentration length, in which case the Beer-Rouguer law can be applied. Unfortunately, the narrow-band wavelengths often have either too much or too little sensitivity for the smoke/obscurant concentration lengths measured in field trials, and broadband data must be used.

After the establishment of the experimental value of the concentration length, the equivalent transmittance for any system of interest can be computed by applying the spectral response of the system in the equations used to compute a and b . The constants a and b for the system and the mass extinction coefficient for the narrow band then fully specify how the system should perform for a given concentration length.

4. EXAMPLES OF BAND-AVERAGING EFFECTS ON MEASURED TRANSMITTANCE

Section 3 discussed a method for extracting concentration length data from band-averaged transmittance data. In addition to showing that optical depth regression plots for band-averaged transmittance data can be nonlinear, Eq. (4) has further implications. In this section, we provide examples to illustrate the care that must be exercised in interpreting band-averaged transmittance data. We also illustrate the application of such data in evaluating EO system performance against smokes once concentration lengths are determined. We consider the effects that differences in source spectra have on the relative transmittance through a smoke with spectral structure in its mass extinction coefficient. In order to develop an understanding of the physical principles that affect the transmittance in one example, approximations are made for the source spectra and for the mass extinction coefficient that allow the integrations required by Eq. (4) to be performed analytically in closed form. In the second example, we use measured mass extinction spectra for phosphorus-derived smoke with the same source spectra as in the first example.

Assume that two transmittance measurements are made under identical circumstances. Assume that the same filter, $f(\lambda)$, detector, $F(\lambda)$, and optical system transmittance spectral responses apply, and that these responses are independent of wavelength. Assume also that the atmospheric transmittance is independent of wavelength.

4.1 APPROXIMATIONS TO SOURCE SPECTRAL DISTRIBUTION

Let the first set of measurements employ a black-body source operating at 300 K (27 °C). This source temperature is approximately what might be encountered from a military target such as a tank at normal operating temperature. Let the second set of measurements employ a black body source operating at 1773 K. This source temperature is comparable to that commonly found in transmissometer systems used in smoke/obscurant field tests.

The radiant power produced by a black body is given by the Planck function as:

$$P(\lambda, T) = \frac{C_2}{\lambda^5 (\exp(C_1/\lambda T) - 1)} \quad (13)$$

where C_2 and C_1 are constants and T is the source temperature in Kelvin. In the case of the 300-K source temperature, and for wavelengths up to 12 μm , the Wein approximation to the Planck function applies and is given by:

$$P(\lambda, T) = \frac{C_2 \exp\left[-\frac{C_1}{\lambda T}\right]}{\lambda^5} \quad (14)$$

In the case of the 1773-K source temperatures, and for wavelengths down to 2 to 3 μm , the Rayleigh-Jeans approximation to the Planck function applies and is given by:

$$P(\lambda, T) = \frac{(C_2/C_1)T}{\lambda^4} \quad (15)$$

4.2 APPROXIMATION FOR THE MASS EXTINCTION COEFFICIENT

For the first example, and using a closed-form analytical solution for the band-averaged transmittance, assume that the particle size distribution of the smoke/obscurant is such that the extinction efficiency of the smoke/obscurant material can be approximated by a linear function given by:

$$Q_E = C_3 \frac{\pi D}{\lambda} \quad (16)$$

where C_3 is a constant specifying the slope of the extinction efficiency over the range of the approximation and D is the particle diameter.

This approximation, first used by Chylek for water fogs (Chylek, 1978), has been found to be reasonably accurate for middle and far infrared extinction. This approximation also applies, with less accuracy, to smokes such as fog oil or anthracene when absorption bands are ignored. The mean extinction cross section with this approximation can be shown to be:

$$\bar{\sigma} = \frac{C_3 \pi^2 \mu_3}{4\lambda} \quad (17)$$

where μ_3 is the third moment of the particle size distribution, and is proportional to the particle volume. The mean particle mass is given by:

$$\bar{m} = \frac{\pi}{6} \rho_p \mu_3 \quad (18)$$

where ρ_p is the particle material density. The mass extinction coefficient is defined as the ratio of mean extinction cross section to mean particle mass. Computing the mass extinction coefficient using Eqs. (17) and (18) yields:

$$\alpha(\lambda) = \frac{1.5\pi C_3}{\lambda \rho_p} \quad (19)$$

4.3 RELATIVE TRANSMITTANCE FOR 300-K SOURCE FOR THE MASS EXTINCTION COEFFICIENT INVERSELY DEPENDENT ON WAVELENGTH

The Wein approximation for the Planck function, Eq. (14), and the approximation for the mass extinction coefficient in Eq. (19) can be used in Eq. (4), along with the assumptions for system spectral response, to compute the relative transmittance for a 300-K source through a smoke screen over a spectral band from λ_1 to λ_2 . The result is:

$$T(\Delta\lambda, 300 \text{ K}) = \left(\frac{\gamma}{\beta}\right)^4 \frac{\left[f\left(\frac{\beta}{\lambda_2}\right) - f\left(\frac{\beta}{\lambda_1}\right)\right]}{\left[f\left(\frac{\gamma}{\lambda_2}\right) - f\left(\frac{\gamma}{\lambda_1}\right)\right]} \quad (20)$$

where

$$f(X) = \exp(-X)(X^3 + 3X^2 + 6X + 6) \quad (21)$$

$$\beta = \frac{1.5\pi C_3 g}{\rho_p} + \gamma \quad (22)$$

$$\gamma = \frac{C_1}{T} \quad (23)$$

4.4 RELATIVE TRANSMITTANCE FOR 1773-K SOURCE FOR THE MASS EXTINCTION COEFFICIENT INVERSELY DEPENDENT ON WAVELENGTH

The Rayleigh-Jeans approximation for the Planck function, Eq. (15), and the approximation for the mass extinction coefficient in Eq. (19) can be used in Eq. (4), along with the assumptions for system spectral response, to compute the relative transmittance for a 1773-K source through a smoke screen over a spectral band from λ_1 to λ_2 . The result is:

$$T(\Delta\lambda, 1773 \text{ K}) = \frac{3 \left[F\left(\frac{\beta-\gamma}{\lambda_2}\right) - F\left(\frac{\beta-\gamma}{\lambda_1}\right) \right]}{\left(\frac{\beta-\gamma}{\lambda_1}\right)^3 - \left(\frac{\beta-\gamma}{\lambda_2}\right)^3} \quad (24)$$

where

$$F(X) = \exp(-X)(X^2 + 2X + 2) \quad (25)$$

4.5 COMPARISON OF 300-K AND 1773-K SOURCE RELATIVE TRANSMITTANCES FOR THE MASS EXTINCTION COEFFICIENT INVERSELY DEPENDENT ON WAVELENGTH

Equations (20) and (24) have been used to compute relative transmittance for sources operating at 300 K and 1773 K over bands of 3 to 5 μm and 8 to 12 μm . It has been assumed that the specific gravity of the smoke/obscurant material is 1, and that the slope of the extinction efficiency is 1. The results are shown in Figures 2 and 3. Figure 2 shows the ratio of transmittances as a function of concentration length, g , for target source temperatures relative to a source temperature of 1773 K for the 3- to 5- μm band; Figure 3 shows a similar plot for the 8- to 12- μm band. The difference between the transmittances for the two source temperatures is striking. Note that the difference in the 3- to 5- μm band as a function of g is slightly greater than that for the 8- to 12- μm band. These figures show that the cooler source has a much higher relative transmittance than the hotter source as g increases. For this example, these results suggest that transmittance computed using measured g values inferred from transmittance data as suggested in Section 2 would not be closely comparable to the transmittance applicable to a typical EO weapon system target such as a tank. In fact, the relative transmittance to the tank would generally be much higher than that predicted by the transmissometer.

4.6 COMPARISON OF 300-K AND 1773-K SOURCE RELATIVE TRANSMITTANCES FOR THE MASS EXTINCTION COEFFICIENT OF PHOSPHORUS

Phosphorus is one of the most common sources of military smoke screens. An example of the spectral structure of the mass extinction coefficient for phosphorus is shown in Figure 4, for a relative humidity of 70%. Phosphorus-derived smoke is hygroscopic. The shape and magnitude of the mass extinction spectrum is dependent on relative humidity. Transmittance as a function of concentration length has been computed for phosphorus-derived smoke at 17%, 50%, and 90% relative humidity and spectral source temperatures of 300 K and 1773 K. The same atmospheric and radiometer response characteristics as used in the first example have been assumed. The Electro-Optical Systems Atmospheric Effects Library (EOSAEL) model, COMBIC, uses band-averaged mass extinction coefficients with the Beer-Bouguer transmission law to compute transmittance as a function of concentration length. This approach does not include the effects of source spectra or system response characteristics in the computation of transmittance, and is the method commonly used for estimating band-averaged transmittance through a smoke screen. The Beer-Bouguer transmittance as a function of concentration length using a band-averaged mass extinction coefficient was included in the computations as a point of reference. Figures 5 and 6 show the results of using equation 4 to compute the 3- to 5- μm band-averaged transmittance as function of concentration length through phosphorus-derived smoke for relative humidities of 17% and 90% and for source temperatures of 300 K and 1773 K. In this band, the band-averaged mass extinction coefficient transmittance estimate best approximates the band-averaged transmittance at 17% relative humidity, 1773 K source temperature, and for transmittance greater than 0.1. These effects are reversed for the 8- to 12- μm band computations shown in Figures 7 and 8. Here, agreement with the Beer-Bouguer transmittance estimate using a band-averaged mass extinction coefficient more nearly agrees with the band-averaged transmittance at 90% relative humidity. The differences in transmittance due to source spectra at relative humidities of 17% and 90% are shown for the 3- to 5- μm and 8- to 12- μm bands in Figures 9 and 10. In Figures 9 and 10, the ratio of band-averaged transmittances for 300-K relative to those for 1773-K source temperature spectra are plotted as a function of concentration length.

5. CONCLUSION

Physically, the results in both examples are not difficult to understand. The largest value of the mass extinction coefficient occurs at the shortest wavelength in the band. Most of the energy in the 1773-K source occurs at the shortest wavelength in the band, where the smoke/obscurant will be most effective in attenuating the source energy. Most of the energy in lower temperature sources occurs at the longest wavelength, where the mass extinction coefficient is the smallest in the band and therefore the smoke is least effective. Therefore, the relative transmittance of the cooler target is higher because of the mismatch between source and extinction coefficient spectra.

It should be clearly understood that calculations in the example where the mass extinction coefficient varies inversely with wavelength are not universally applicable. The calculations for this example apply only for the assumptions made for the analysis in order that a closed-form integration could be performed using the band averaging integrals in Eq. (4) for the relative transmittance. Nevertheless, the computation is reasonable for natural fogs, and the trend should also apply for any obscurant whose mass extinction coefficient varies approximately inversely with wavelength in the band of interest.

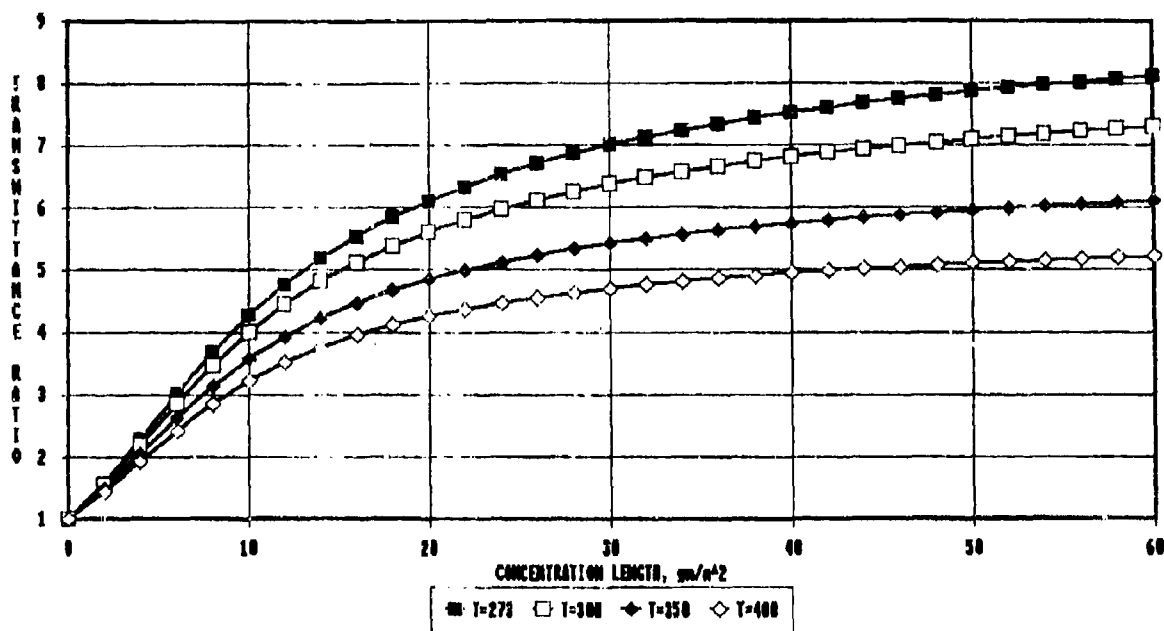


Figure 2. Smoke transmittance over the 3- to 5- μm band for black body source temperatures of 273 to 400 K relative to that for 1773 K.

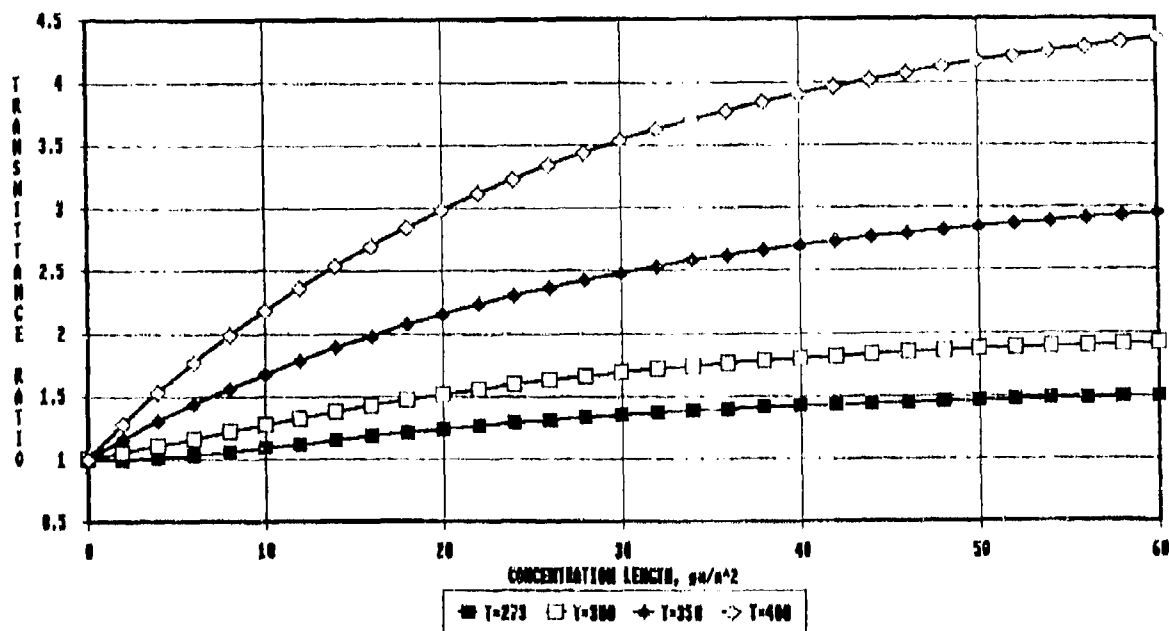


Figure 3. Smoke transmittance over the 8- to 12- μm band for black body source temperatures of 273 to 400 K relative to that for 1773 K.

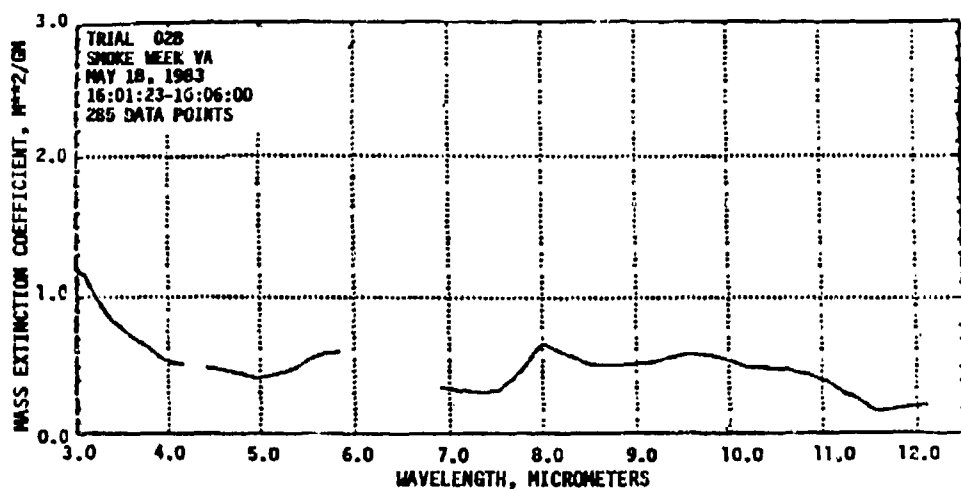


Figure 4. Mass extinction spectrum for phosphorus smoke at 70% as measured at Smoke Week VA.

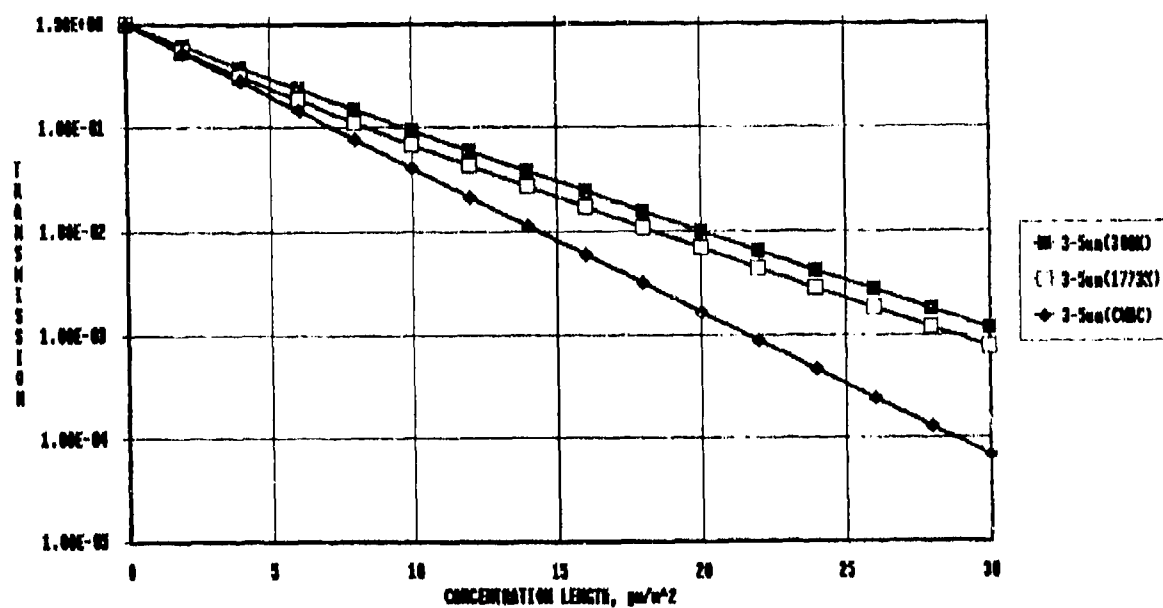


Figure 5. Comparison of 3- to 5- μm transmission for black body source temperatures of 300 K and 1773 K and 17% RH phosphorus smoke with COMBIC predictions using band-averaged mass extinction spectra.

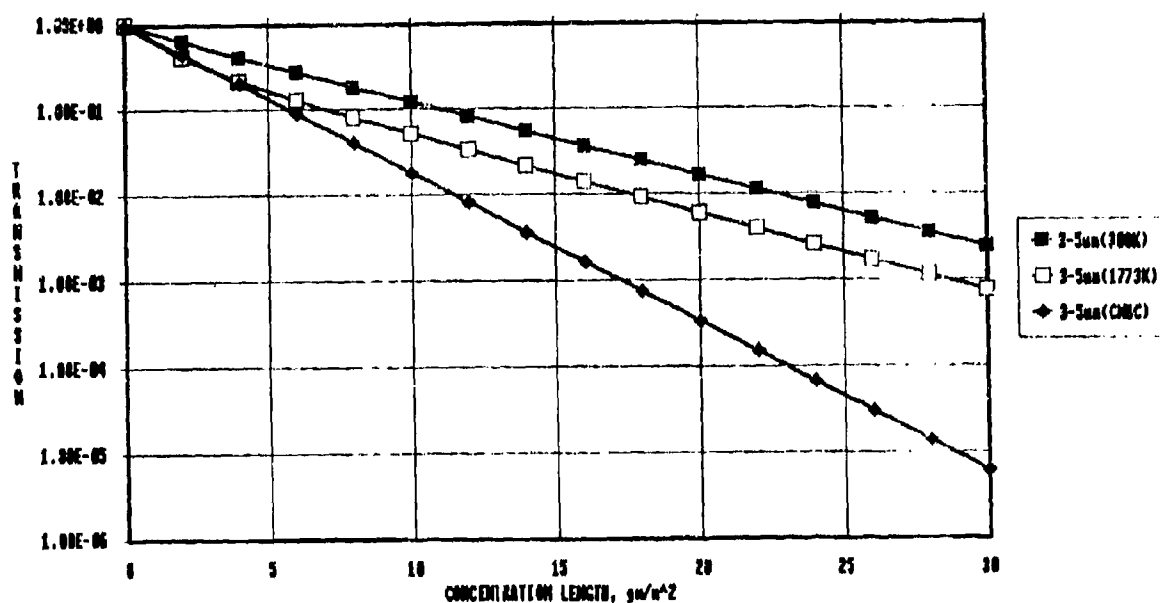


Figure 6. Comparison of 3- to 5- μ m transmission for black body source temperatures of 300 K and 1773 K and 90% RH phosphorus smoke with COMBIC prediction using band-averaged mass extinction spectra.

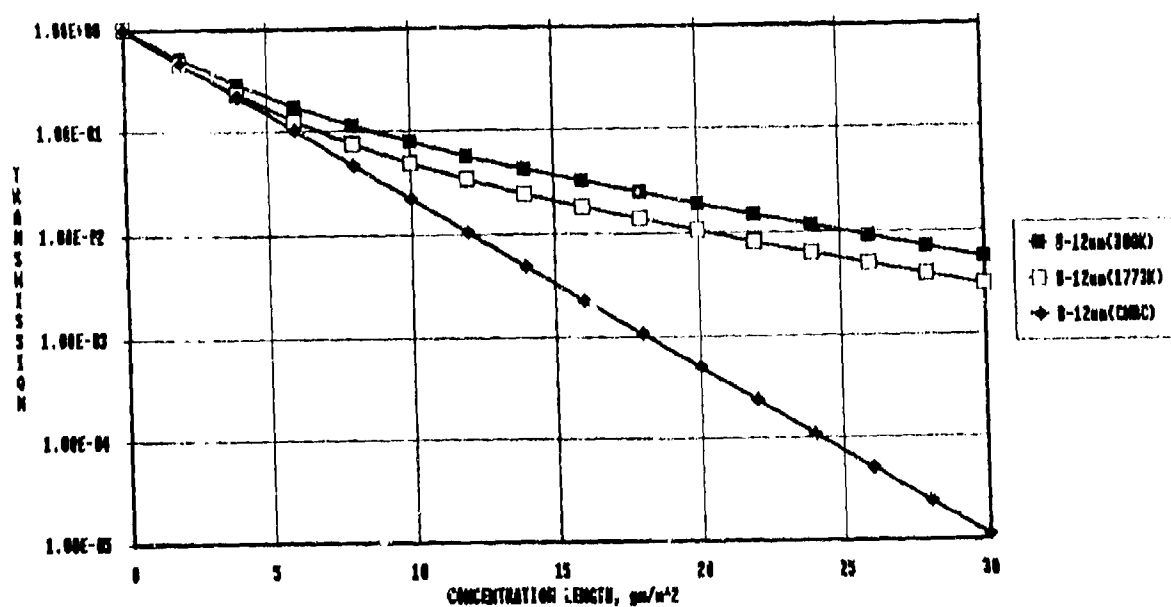


Figure 7. Comparison of 8- to 12- μ m transmission for black body source temperatures of 300 K and 1773 K and 17% RH phosphorus smoke with COMBIC predictions using band-averaged mass extinction spectra.

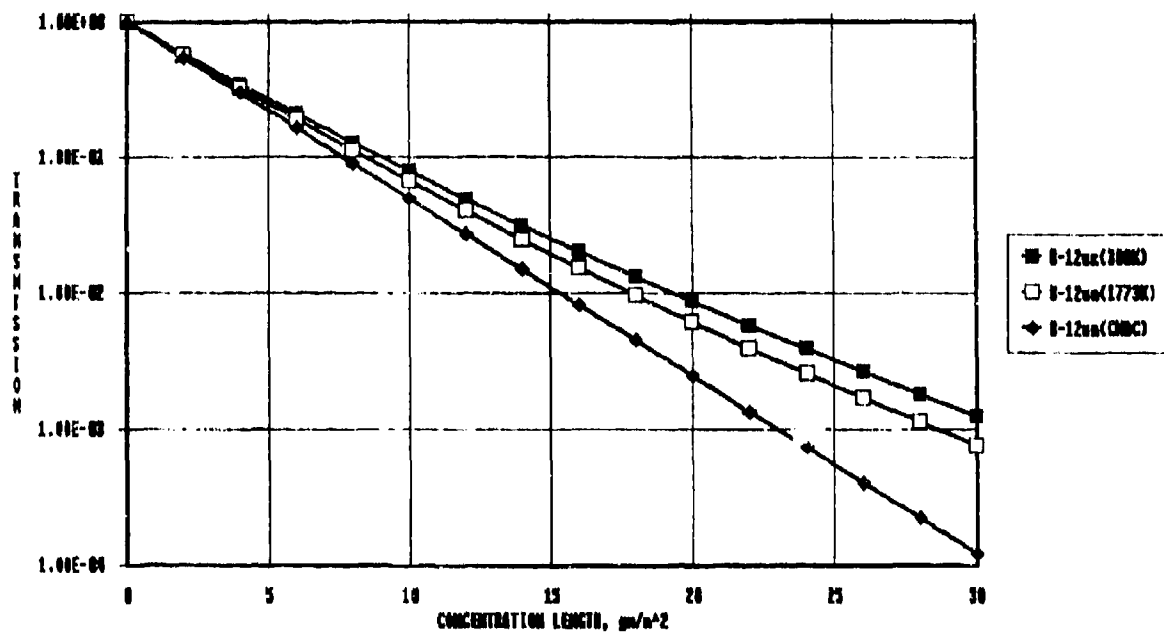


Figure 8. Comparison of 8- to 12- μ m transmission for black body source temperatures of 300 K and 1773 K and 90% RH phosphorus smoke with COMBIC using band-averaged mass extinction spectra.

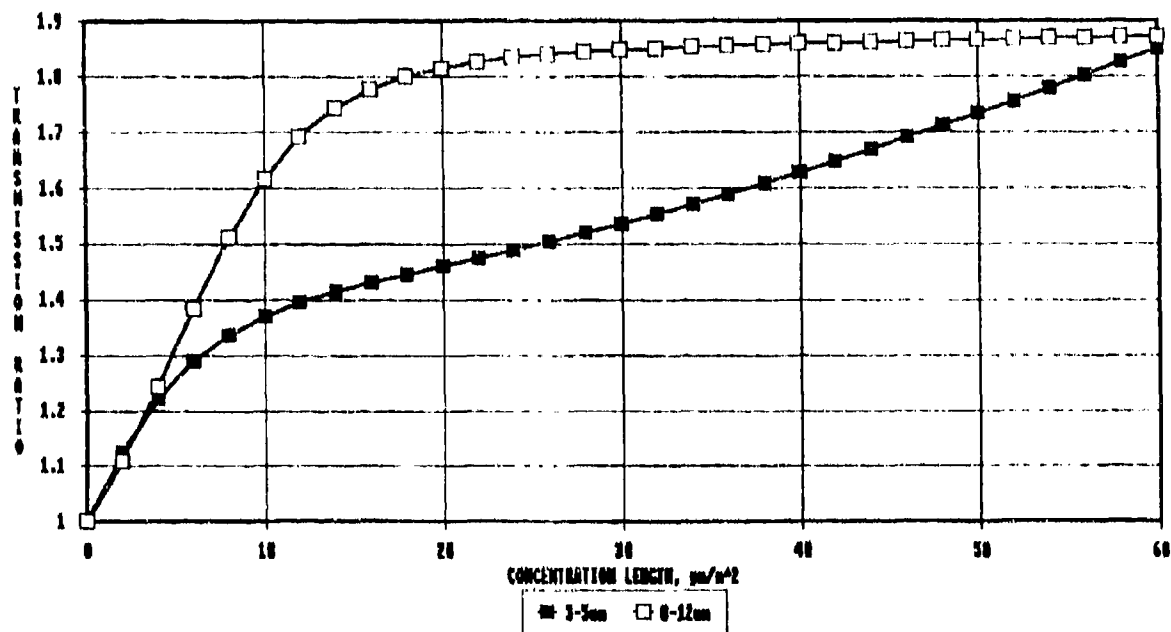


Figure 9. Smoke transmission ratio in 3- to 5- μ m and 8- to 12- μ m bands for black body source temperatures of 300 K and 1773 K for 17% RH laboratory phosphorus mass extinction spectrum.

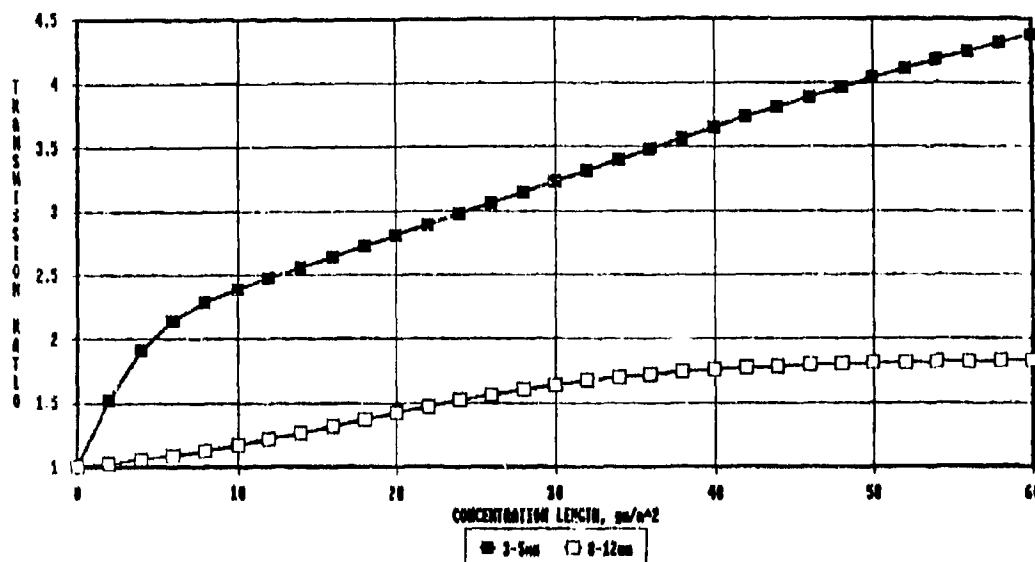


Figure 10. Smoke transmission ratio in 3- to 5- μ m and 8- to 12- μ m bands for black body source temperatures of 300 K and 1773 K for 90% RH laboratory phosphorus mass extinction spectrum.

Significant differences have been shown to arise between transmittance estimates made using approximations involving band-averaged mass extinction coefficients in the Beer-Bouguer transmission law and direct computations of band-averaged transmittance for phosphorus-derived smoke. This example showed that as the concentration length increases, variations in spectral structure in the source and mass extinction coefficient can cause the band-averaged mass extinction coefficient approximation to be significantly in error.

This analysis shows that field-measured transmittances through smokes/obscurants having spectral structure in the mass extinction coefficient cannot be compared directly between transmissometer systems having different spectral responses. Similarly, the transmittance data obtained with a transmissometer over the same spectral band as that used by a particular EO system cannot be applied directly to the evaluation of system performance relative to smoke/obscurant screening capability. The observed transmittance through a smoke/obscurant with a transmissometer or EO system is the result of averaging the spectral transmittance of the smoke/obscurant being observed over the spectral response of the transmissometer or EO system. If the spectral responses of any two systems are different, then the band-averaged transmittance through the smoke/obscurant can be expected to be different.

A method has been presented for computing constants that will allow band-averaged transmissometer system measurements to be related to narrow-band measurements through measurements of optical depths for each band. The method for computing the constants has general applicability to the estimation of band-averaged transmittances for virtually any EO system if the band response characteristics of the system are known. After the constants for a specific system are determined, then the band-averaged response of a system to a smoke screen can be specified with three parameters: 1) the mass extinction coefficient for the reference narrow band, 2) the concentration length, and 3) the two constants, a and b , which are system specific. The constants are used in a simple exponential function rather than in complicated integrals to express band-averaged transmittance. The exponential function has as an argument a constant multiplying the concentration length raised to the power of the second constant. The first constant multiplies the concentration length in the same way the band-averaged mass extinction coefficient multiplies the concentration length in the approximation using the Beer-Bouguer transmission law. This constant, however, is not a mass extinction coefficient. The second constant is the value of the band-averaged transmittance for a particular value of concentration length. However, when the spectral factors in the band-averaged transmittance are changed, these constants change. Therefore, it is important that standardized atmospheric, smoke extinction spectra, and electro-optical sensor conditions be chosen for computing these constants.

REFERENCES

- Chylek, P., 1978: Extinction and Liquid Water Content of Fogs and Clouds, *J. Atmos. Sci.*, **35**, 296-311.
- Farmer, W. Michael, Edward J. Buribaw, and Thelma A. Chenault, 1987: AAODL Transmission Statistics Data, STC Technical Report 2147, Science and Technology Corp., 101 Research Drive, Hampton, VA.
- Farmer, W. Michael, Brian Locke, and Roger E. Davis, 1989: U.S. Army Transmissometer Validation Program Summary Report, Volume I, Program Summary, STC Technical Report 3003, Project Manger Smoke/Obscurants, Aberdeen Proving Ground, MD.

Effect of Atmospheric Turbulence on Electro-Optical Systems

by

Walter B. Miller

Jennifer C. Ricklin

David H. Marlin

Atmospheric Sciences Laboratory

US Army Laboratory Command

White Sands Missile Range, New Mexico 88002-5501 USA

SUMMARY

The IMTURB model characterizes the effects of clear air optical turbulence on electro-optical (EO) imaging devices and laser transmitters operating in the atmospheric surface boundary layer and is valid for wavelengths from the visible through the far infrared. Similarity theory and the Kolmogorov principle of universal equilibrium are employed to characterize optical turbulence structure over regions typical of applications, based on simple environmental observables. A profile for the refractive index structure parameter is estimated, then used as input to a weak perturbation propagation model. Receiver coherence diameter, log-amplitude variance, scintillation averaging length, isoplanatism effective path length, and related subsidiary propagation statistics are then estimated for a selected propagation path. Outer and inner scale profiles are also estimated for advanced applications. Model results for two sample cases are discussed.

1. INTRODUCTION

It is well understood that irregularities in the atmospheric refractive index result in distortion of propagating electromagnetic waveforms. In a landmark analysis based on the work of Kolmogorov,^{1,2} it was postulated that a primary source of such irregularities is the turbulent motion of the atmosphere in the presence of temperature and moisture gradients. It was further postulated that these irregularities possess a quantifiable statistical structure.³ The validity of these postulates is generally accepted, and the term "optical turbulence" has come into general usage to denote random, turbulence-induced fluctuations in the atmospheric refractive index.

When an electromagnetic wave propagates through an atmosphere where optical turbulence is present, the wave front acquires a progressive degree of distortion. Departure of the phase front from its nominal shape results in a decrease in registered image quality for EO imaging systems. Images appear distorted and blurred. A laser beam exhibits an increase in beam diameter in excess of that predicted by diffraction theory. In addition, the entire beam is subject to optical turbulence-induced random translations of the beam centroid, a phenomenon called beam wander. The purpose of the IMTURB model is to quantify these and related effects.⁴

IMTURB differs from typical propagation models for optical turbulence in that a profile is calculated for the refractive index structure parameter (often referred to as a " C_n^2 profile") from simple meteorological and environmental information. Previous methods often relied on the use of one or more measured point values for the refractive index structure parameter. From these measurements, profiles were extrapolated by a scaling law.⁵ In the region of the atmosphere where terrain surface features play a significant role in determining optical turbulence structure, such an approach may impose severe limitations. This region of the atmosphere, called the surface boundary layer, ranges in height from tens to hundreds of meters depending on atmospheric conditions. Above the surface boundary layer, the degree of statistical consistency over regions commensurate with propagation path length may be such that point measurements of C_n^2 or even free atmosphere models may be adequate to specify global optical turbulence structure. This is the case with many astronomical applications. However, within the surface boundary layer, a propagation path may cross several differing optical turbulence regimes, each driven by slightly

different environmental factors. Point measurements, extended to a profile with a power law and extrapolated over the total propagation path, may give rise to misleading results. In response to the problems inherent in modeling this scenario, IMTURB employs environmental parameters exhibiting statistical consistency over regions consistent with most laser transmitter and imaging applications.

In the complex environment of the atmospheric surface boundary layer, a precise and comprehensive description of surface energy fluxes driving the optical turbulence mechanism is difficult. The number of observations necessary to quantify point-specific behavior of the surface fluxes is greater than available even in well-instrumented field experiments. In addition, spatial and temporal variations in environmental factors along the length of the propagation path challenge the validity of even the most carefully performed site characterizations. To combat these difficulties, the modeling basis for IMTURB combines the micrometeorology of the atmospheric surface boundary layer with the well-understood and documented weak fluctuation theory of electromagnetic propagation through optical turbulence.^{6,7,8,9} To characterize the micrometeorology, Obukhov similarity theory^{10,11,12} is used to determine basic flux profile relationships. The Kolmogorov principle of universal equilibrium¹³ employs these relationships to define profiles for the turbulent inner and outer scales and the refractive index structure parameter. Both Obukhov similarity theory and the Kolmogorov principle of universal equilibrium are concerned with modeling the behavior of surface energy fluxes in a statistically consistent environment. Therefore, the shape of the calculated C_n^2 profile reflects the total environmental state more completely than would a profile obtained from a scaling law. A profile for outer scale occurs naturally in the application of the universal equilibrium principle; inner scale is obtained using a method described by Ochs and Hill.¹⁴ Although the version of IMTURB currently available through the Electro-Optical Systems Atmospheric Effects Library (EOSAEL) uses the Kolmogorov spectrum to calculate propagation statistics, planned updates include extension to strong perturbation theory and use of the modified von Karman or Andrews spectrums.¹⁵ Profiles for inner and outer turbulence scales are included for advanced applications.

2. MODELING OPTICAL TURBULENCE STRUCTURE

Obukhov similarity theory is used to calculate surface energy fluxes and related quantities for a specified geographical location, date, and time of day. The meteorological observables required are percent cloud cover, and a value for temperature, pressure, and wind speed. The earth's aerodynamic features are summarized by specification of a roughness length¹⁶ or by calculation of a roughness length from an observed roughness element.¹⁷ The algorithms used by IMTURB to estimate flux profile relationships were first proposed by Stewart¹⁸ for use in determining turbulent velocity spectra over complex terrain. These algorithms were later refined and extended¹⁹ to calculate C_n^2 and outer scale profiles. The computational flow detailing calculation of these profiles is as follows.

From latitude, longitude and Greenwich mean time (GMT), solar zenith angle may be calculated. From solar zenith angle, the amount of solar irradiance on the earth's surface in the absence of cloud cover may be estimated for the specified location and time.²⁰ Knowledge of percent cloud cover allows determination of global irradiance and radiation class,²¹ and a first estimate of sensible heat flux.²² Mean horizontal wind speed, atmospheric pressure, and temperature, estimated for a specified height within the surface boundary layer, may be combined with radiation class to estimate the Pasquill fractional stability parameter. When combined with terrain roughness length, the Pasquill fractional stability parameter allows estimation of both the Obukhov length and scaling ratio.²³ The scaling ratio appears as the independent variable in the dimensionless wind shear and lapse rate, both basic quantities from similarity theory. Two forms for dimensionless wind shear and lapse rate are included, one proposed by Businger,²⁴ and the other by Hansen.^{25,26} From either of the two forms, the corresponding diabatic influence functions are calculated. An equation deriving from basic similarity relationships involving mean horizontal wind speed and the diabatic influence function for momentum allows calculation of friction velocity.²⁷

Knowledge of a value for temperature, used in the similarity equation defining characteristic temperature, allows an independent second estimate of sensible heat flux. To maintain consistency among the similarity parameters, an iterative scheme is employed to adjust friction velocity and Obukhov length so that values for sensible heat flux predicted by similarity theory and solar irradiance are in agreement.

From this adjusted set of parameters, profiles are obtained for both potential temperature and the potential temperature gradient.²⁸ Sufficient information now exists to estimate profiles for the potential temperature structure parameter and, ultimately, the refractive index structure parameter.

Rigorous development of the theoretical link between the gradient profile for potential temperature and the profile for the refractive index structure parameter may be found in Tatarski²⁹ and Ishimaru.³⁰ The refractive index of the atmosphere is a function of wavelength, temperature, pressure, and specific humidity. For optical and infrared wavelengths, humidity over land is negligible, and the refractive index may be expressed as³¹

$$n = 1 + \frac{77.6 P}{K} [1 + 7.52 \times 10^{-3} \lambda^{-2}] 10^{-6} \quad (1)$$

where P is pressure in millibars, K is temperature in °K and λ is wavelength in micrometers. This expression, when combined with the mean potential temperature gradient, results in the following approximation for the gradient of the mean refractive index³²

$$\frac{\partial n}{\partial z} = \frac{(-77.6 \times 10^{-6} P) [1 + 7.52 \times 10^{-3} \lambda^{-2}]}{k z (\theta - \alpha z)^2} T_* \Phi_h \left[\frac{z}{L} \right] \quad (2)$$

where n is mean refractive index, θ is mean potential temperature, z is height above ground in meters, α is the adiabatic lapse rate, k is von Karman's constant, T_* is characteristic temperature, and $\Phi_h \left[\frac{z}{L} \right]$ is dimensionless lapse rate. Used with results from the Kolmogorov principle of universal equilibrium, Equation (2) allows calculation of profiles for the refractive index structure parameter.³³

3. PROPAGATION STATISTICS DESCRIBING SYSTEM PERFORMANCE

For each propagation path through the atmosphere, a choice of statistics may be estimated describing loss in system performance due to optical turbulence. The statistics chosen for IMTURB derive from a comprehensive and flexible propagation model based on weak fluctuation theory³⁴ wherein all propagation statistics are weighted integrals of the refractive index structure parameter over the propagation path. The four basic propagation statistics are (1) receiver coherence diameter, (2) log-amplitude variance, (3) scintillation averaging length, and (4) isoplanatism effective path length. Subsidiary statistics include limiting resolution source length, isoplanatism source size and normalized intensity variance. Other options available to the IMTURB user include (1) choice of plane or spherical wave, (2) spatial power spectrum for log-amplitude and phase variations, (3) fast and slow modulation transfer functions, (4) imaging optics resolution/transmitter beam spread, (5) heterodyne receiver analysis, (5) predetection compensation analysis, and (6) normalized, aperture-averaged intensity receiver analysis. The four basic propagation statistics are described below.

The receiver coherence diameter is the most widely known of the basic propagation statistics. It is a fundamental measure of wave front distortion and is required for estimation of such fundamental forms as the mutual coherence function and modulation transfer function. In an atmosphere free of optical turbulence, an imaging system has the potential for virtually unlimited increase in resolution with corresponding increases in optics diameter. However, when the same system is operated in the presence of optical turbulence, there is a diameter beyond which further size increases produce no significant increase in resolution. This diameter is reflected in the receiver coherence diameter.³⁵ Reciprocally, the degree of optical turbulence-induced beam spread for focused or collimated laser transmitters may be approximated from the receiver coherence diameter for spherical or plane wave propagation, respectively.

The variance of the log-amplitude ratio is a point statistic relating to optical turbulence-induced random fluctuations in the amplitude of an electromagnetic wave. The log-amplitude ratio is the real part of a complex stochastic integral describing electromagnetic propagation through optical turbulence. Derivation and interpretation of this integral is a major concern of weak perturbation theory. This propagation statistic, commonly called the log-amplitude variance,³⁶ is useful in predicting the onset of saturation. Saturation occurs when multiple scattering among optical turbules becomes significant; weak fluctuation theory is then said to "saturate."

The last two basic propagation statistics are scintillation averaging length and isoplanatism effective path length. The scintillation averaging length³⁷ describes the phenomenon of aperture averaging. As "photon bucket" type photoreceivers increase in area, there is a corresponding decrease in the fluctuations of measured intensity. The scintillation is said to be "averaged" over the area. Apertures with diameters one tenth the scintillation averaging length exhibit variations in intensity similar to those predicted for a point, while apertures on the order of ten times the scintillation averaging length exhibit little variation in intensity. The isoplanatism effective path length, used with receiver coherence diameter, defines the isoplanatic angle and hence the isoplanatic patch.³⁸ Within a region the size of the isoplanatic patch, wave front distortion is nearly constant, and image quality may be improved by the removal of wave front tilt. Isoplanatic patch size is useful in the design of adaptive devices for partial correction of optical turbulence effects.

In addition to the interpretive value of basic and subsidiary propagation statistics, IMTURB provides path-specific fast and slow modulation transfer functions. These may be used in conjunction with an image processing system to allow simulation of specified EO systems behavior in a controlled, sterile environment.

4. SAMPLE MODEL RESULTS

Two sample scenarios are described here to illustrate typical model results. In the first scenario, Case A, an EO imaging sensor operating at 1.06 microns and located 2 meters above the ground observes a target 500 meters distant and 11 meters above the ground. Spherical wave propagation is appropriate with the source at the target. The site is White Sands Missile Range, New Mexico (USA), located at latitude 32° north, longitude 106° west. The date is 31 May, 1984; the time, 1300 hours Mountain Standard Time (MST), translating to a GMT of 2000 hours. The day is cloudless; the upwind terrain is a broad region of desert brush and scrub, having a tabulated roughness length of 16 cm. From a nearby observation tower with sensors located 10 meters above the ground, air temperature is 35° centigrade, pressure is 850 millibars (the altitude of the Tularosa Basin where the Missile Range is located is 4000 feet above sea level), and the average wind speed is 3 m/s. IMTURB characterizes the atmosphere as strongly unstable, with the height of the surface boundary layer estimated at 11 m. The set of basic and subsidiary propagation statistics for Case A is given in Table 1. Note that log-amplitude variance is 0.206, indicating that Case A is within the limits of weak fluctuation theory.

Table 1. Basic and subsidiary propagation statistics for Case A.

| Basic Propagation Statistics | | Subsidiary Propagation Statistics | |
|------------------------------------|----------------------|-----------------------------------|------------------|
| Receiver Coherence Diameter | 1.54 centimeters | Limiting Resolution Source Length | 3.89 centimeters |
| Log-Amplitude Variance | 0.206 nepers-squared | Isoplanatism Source Size | 3.26 centimeters |
| Scintillation Averaging Length | 2.78 centimeters | Normalized Intensity Variance | 1.28 |
| Isoplanatism Effective Path Length | 117.7 meters | | |

The conditions chosen for Case B illustrate the significant difference in optical turbulence structure arising from relatively minor changes in environmental conditions. The location, terrain, time of day, temperature, and pressure are identical to Case A. However, cloud cover has increased to 25% and wind speed to 5 m/s. IMTURB predicts a moderately unstable atmosphere with the height of the surface boundary layer near 43 m. The basic and subsidiary propagation statistics for Case B are listed in Table 2, from which we see that log-amplitude variance is reduced to 0.092, well within the bounds of weak fluctuation theory.

Table 2. Basic and subsidiary propagation statistics for Case B.

| Basic Propagation Statistics | | Subsidiary Propagation Statistics | |
|------------------------------------|----------------------|-----------------------------------|------------------|
| Receiver Coherence Diameter | 2.65 centimeters | Limiting Resolution Source Length | 2.26 centimeters |
| Log-Amplitude Variance | 0.092 nepers-squared | Isoplanatism Source Size | 5.25 centimeters |
| Scintillation Averaging Length | 2.93 centimeters | Normalized Intensity Variance | 0.44 |
| Isoplanatism Effective Path Length | 125.99 meters | | |

Due to space limitations, the variety of atmospheric stability and similarity parameters descriptive of the micrometeorology have been omitted. However, we have included profiles for the turbulent inner and outer scales, and the refractive index structure parameter. These profiles characterize the optical turbulence structure over the region encompassing the propagation path and are adequate even for advanced applications. The three profiles for Cases A and B are listed in Figures 1, 2, and 3. All profiles are terminated at the maximum extent of the surface boundary layer, by definition the absolute value of the Obukhov length. Note that outer scale follows the rule-of-thumb for unstable atmospheres, i.e., outer scale approximately equals height above ground. Inner scale exhibits the dependence on wind velocity observed by numerous investigators. The severity of optical turbulence can be determined from the C_n^2 profiles, as shown in Figure 3. Notice that optical turbulence strength decreases rapidly with height in both cases. For these examples, one would expect significant degradation in performance for EO systems operating in the visible to near IR, and in the far IR over longer ranges. Values for the receiver coherence diameter of 1.5 cm and 2.6 cm for Cases A and B, respectively, attest to this fact.

Related to the receiver coherence diameter is the subsidiary statistic limiting resolution source size. This is the maximum resolution possible for the propagation path and wavelength regardless of optics size. In terms of laser performance, the limiting resolution source size is the "spot" size of a laser focused to a point. In Case A, the value is 3.9 cm; for Case B, 2.3 cm. In the former case, a sensor would be able to resolve nothing smaller than 3.9 cm on the target at 500 meters. In Case B the same system can resolve details as small as 2.3 cm.

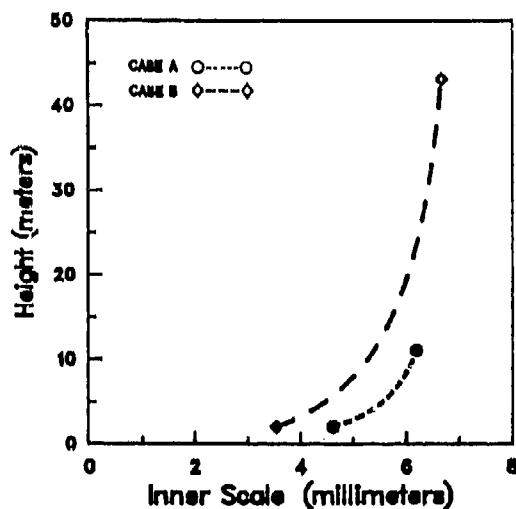


Figure 1. Plot of the turbulent inner scale with height for Cases A and B.

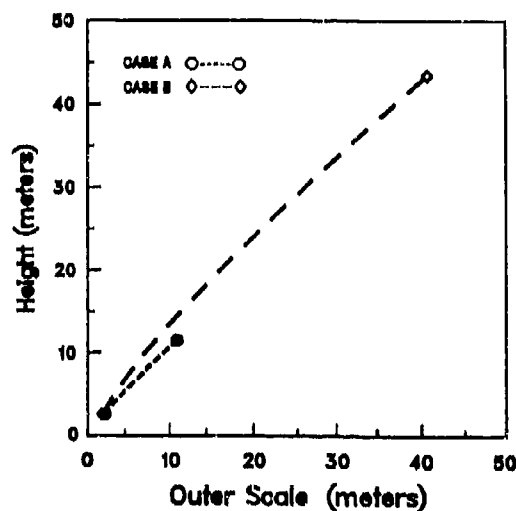


Figure 2. Plot of the turbulent outer scale with height for Cases A and B.

Figure 4 provides a comparative plot of log-amplitude variance with range for Cases A and B. The increase in range of validity for weak fluctuation theory in the latter case is noticeable. The relatively short distances to saturation in comparison with normal engagement ranges is a strong incentive to extend model results by use of strong perturbation theory. It is also instructive to plot receiver coherence diameter vs. range for Cases A and B. Referring to Figure 5, we see that as range increases, the integrated

effect of optical turbulence is evident, as is the consistently superior performance of the system operated under the environmental conditions of Case B.

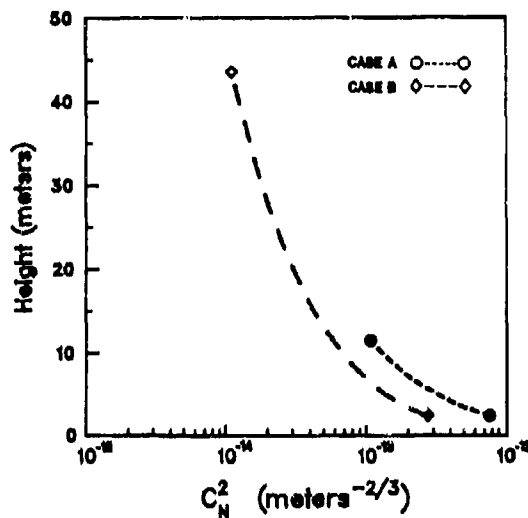


Figure 3. Plot of the refractive index structure parameter with height for Cases A and B.

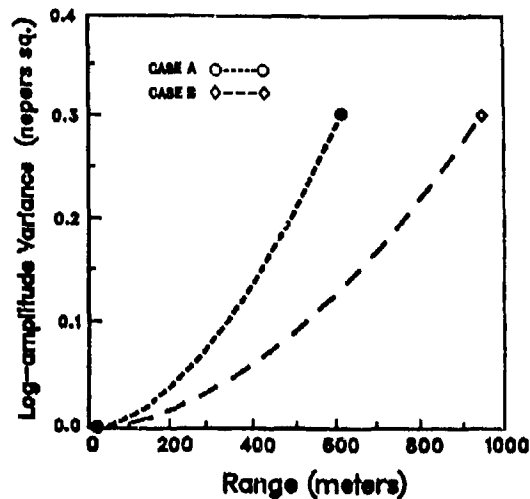


Figure 4. Plot of the log-amplitude variance with range, extended to saturation. The sensor is at 2 meters and target is at 11 meters (Cases A and B).

An interesting property of certain propagation statistics that occur as integrals over the propagation path is the phenomenon of path weighting. For spherical wave propagation, receiver coherence diameter exhibits this trait. Consider a scenario identical to Case A with the exception that the sensor and target positions are reversed. The receiver coherence diameter calculated for a sensor at 11 meters and target at 2 meters, with a path length of 500 meters, is 2.6 cm. This represents, coincidentally, the increase in system performance of Case B over Case A. A plot of receiver coherence diameter vs. range for the two sensor/target geometries is given in Figure 6.

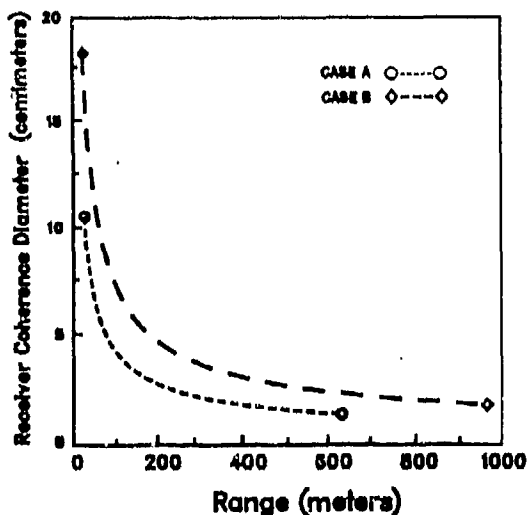


Figure 5. Plot of the receiver coherence diameter with range for a sensor at 2 meters and target at 11 meters (Cases A and B).

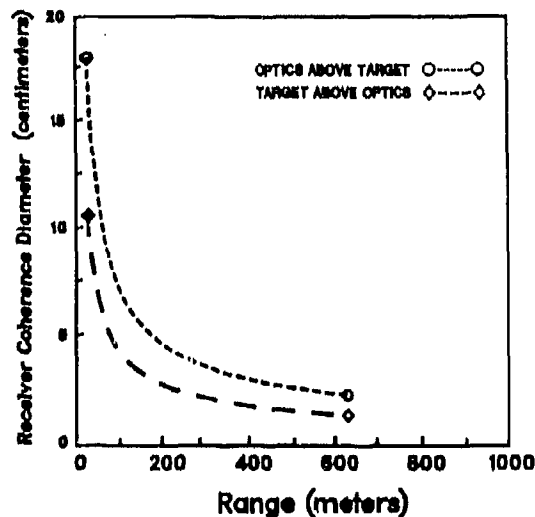


Figure 6. Plot of receiver coherence diameter vs. range for Case A, and with target and optics positions reversed.

Perhaps the most exciting application of the IMTURB model arises from its use in simulating degradation due to optical turbulence using digital image processing techniques.^{39,40} The Atmospheric Sciences Laboratory (ASL) has incorporated an IMTURB clone into ASL's library of models for simulation of atmospheric effects on system performance, called BATL. BATL is currently under development at the ASL Image Processing Laboratory and employs a Gould IP8500 with Real Time Digital Disk and VAX 11/780 host computer. Examples of image degradation due to optical turbulence performed in near real-time using a convolution technique are given below. Figure 7 shows an image of a tank taken at a far-IR wavelength over a 2330 m path. Figure 8 is the same image, viewed over a horizontal path through moderate optical turbulence. If the sensor is raised about 10 meters above the ground, we see that optical turbulence effects are reduced, as shown in Figure 9. Figure 10 demonstrates the blurring effect severe optical turbulence produces.

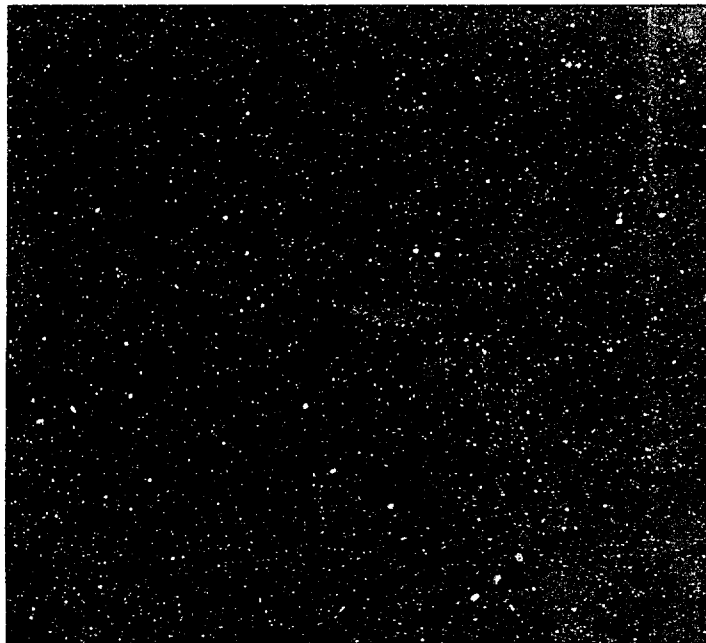


Figure 7. Image of a tank taken at a far-IR wavelength over a 2330 m path.

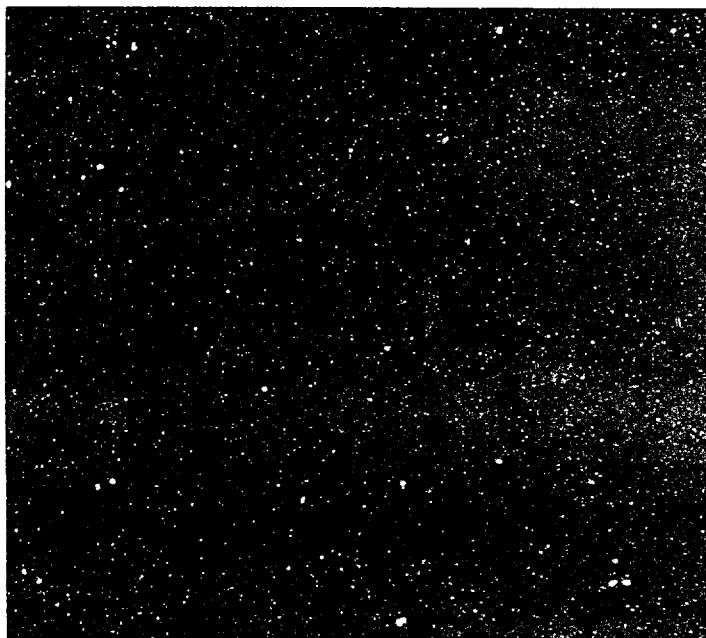


Figure 8. Same image as above but viewed over a horizontal path through moderate optical turbulence.

This Document
Reproduced From
Best Available Copy

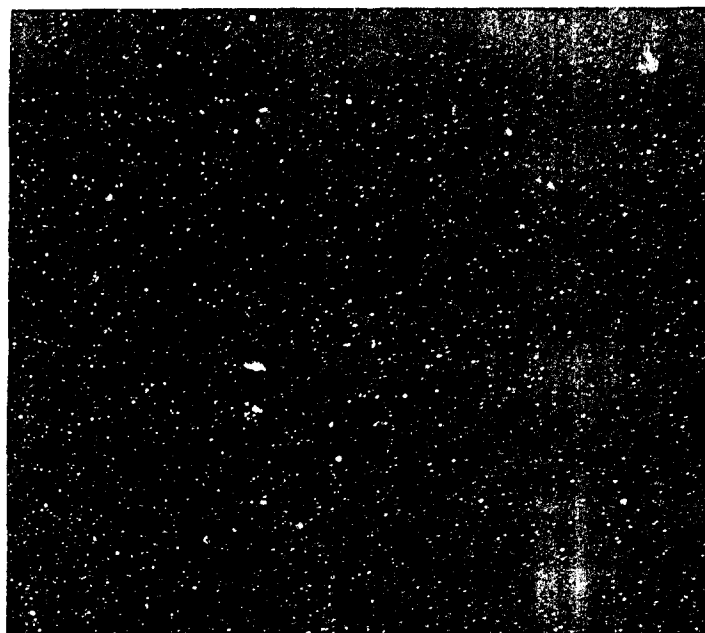


Figure 9. Optical turbulence effects are reduced when the sensor is raised about 10 meters above the ground.



Figure 10. The blurring effect severe optical turbulence produces.

**This Document
Reproduced From
Best Available Copy**

5. REFERENCES

- ¹A.N. Kolmogorov, C.R. Acad. Sci., U.S.S.R. 30 (1941) pp. 301-305
- ²C.K. Batchelor, "Kolmogoroff's Theory of Locally Isotropic Turbulence," Proc. Camb. Phil. Soc. 43 (1947) p. 533
- ³V.I. Tatarski, *Wave Propagation in a Turbulent Medium*, trans. R.A. Silverman (New York: McGraw-Hill Book Co., 1961)
- ⁴W.B. Miller and J.C. Ricklin, US Army Atmospheric Sciences Laboratory, WSMR, NM, *IMTURB: A Module for Imaging Through Optical Turbulence* (1989) ASL-TR-0221-27
- ⁵J.C. Ricklin, US Army Atmospheric Sciences Laboratory, WSMR, NM, *The Impact of Optical Turbulence on Target Acquisition* (1986) ASL-TR-0209
- ⁶Tatarski, op. cit.
- ⁷S.F. Clifford, "The Classical Theory of Wave Propagation in a Turbulent Medium," in *Laser Beam Propagation in a Turbulent Atmosphere*, ed. by J.W. Strohbehn (New York: Springer-Verlag, 1978) ch. 2
- ⁸A. Ishimaru, *Wave Propagation and Scattering in Pandom Media*, (New York: Academic Press, 1978) Vols. I and II
- ⁹J.W. Goodman, *Statistical Optics*, (New York: John Wiley & Sons, 1985) ch. 8
- ¹⁰N.E. Busch, "On the Mechanics of Atmospheric Turbulence," in *Workshop on Micrometeorology*, ed. by D.A. Haugen (American Meteorological Society, 1973) ch. 1
- ¹¹J.A. Businger, "Turbulent Transfer in the Atmospheric Surface Layer," in *Workshop on Micrometeorology*, ed. by D.A. Haugen (American Meteorology Society, 1973) ch. 2
- ¹²J.C. Wyngaard, "On Surface Layer Turbulence," in *Workshop on Micrometeorology*, ed. by D.A. Haugen (American Meteorological Society, 1973) ch. 3
- ¹³Ishimaru, op. cit., Vol. II, Appendix C
- ¹⁴G.R. Ochs and R.J. Hill, "Optical-Scintillation Method of Measuring Turbulence Inner Scale," Appl. Opt. 24, (1985) p. 2430
- ¹⁵L.C. Andrews and R.L. Phillips, "New Temperature Spectrum Model Based on Fluctuations in the Average Dissipation Rates," in *Propagation Engineering*, ed. by W.B. Miller and N.S. Kopeika (SPIE, 1989) Vol. 1115
- ¹⁶Miller and Ricklin, op. cit., Appendix B
- ¹⁷E.C. Kung, Dept. of Meteorology, Univ. of Wisconsin, "Climatology of Aerodynamic Roughness Parameter and Energy Dissipation in the Planetary Boundary Layer of the Northern Hemisphere," in *Annual Report Studies of the Effects of Variations in Boundary Conditions on the Atmospheric Boundary Layer* (1963) Contract DA-36-039-AMC-00878
- ¹⁸W.J. Stewart, US Army Atmospheric Sciences Laboratory, WSMR, NM, *An HP-9825 Computer Model for Turbulent Velocity Spectra* (1985) ASL-CR-85-0100-2
- ¹⁹W.B. Miller, J.C. Ricklin and W.J. Stewart, US Army Atmospheric Sciences Laboratory, WSMR, NM, *An Optical Turbulence Code for the Surface Boundary Layer* (1987) ASL-TR-0220
- ²⁰Miller and Ricklin, op. cit., Appendix C
- ²¹F.B. Smith, "The Relation Between Pasquill Stability P and Kazanski-Monin Stability (In Neutral and Unstable Conditions)," Atmospheric Environment 13 (United Kingdom: Pergamon Press Ltd., 1979) pp. 879-881
- ²²F.B. Smith, "Proceedings of the Third Meeting of the Expert Panel on Air Pollution Modeling," in *NATO Committee on the Challenges of Modern Society* (Paris, France, 1972) ch. XVII
- ²³M. Liu et al., National Technical Information Service, *The Chemistry, Dispersion and Transport of Air Pollutants Emitted From Fossil Fuel Power Plants in California: Data Analysis and Emission Impact Model* (1976) PB-264-822, p. 136
- ²⁴Businger, op. cit.
- ²⁵F.V. Hansen, US Army Atmospheric Sciences Laboratory, WSMR, NM, *Flux Profile Relationships for Development of Standards of Comparison* (1980) Internal Report
- ²⁶F.V. Hansen, US Army Atmospheric Sciences Laboratory, WSMR, NM, *The Critical Richardson Number* (1977) ECOM Technical Report 5829
- ²⁷C.A. Paulson, "The Mathematical Representation of Wind Speed and Temperature Profiles in an Unstable Atmospheric Surface Layer," Journal of Applied Meteorology 9, (1970) pp. 857-861
- ²⁸F.B. Smith and R.M. Blackhall, "The Application of Field Experiment Data to the Parameterization of Plumes from Ground Level and Elevated Sources," in *Mathematical Modeling of Turbulent Diffusion in the Environment*, ed. by C.J. Harris (New York: Academic Press, 1979)
- ²⁹Tatarski, op. cit.
- ³⁰Ishimaru, op. cit.
- ³¹S.F. Clifford, "The Classical Theory of Wave Propagation in a Turbulent Medium," in *Laser Beam Propagation in a Turbulent Medium*, ed. by J.W. Strohbehn (New York: Springer-Verlag, 1978)
- ³²Miller and Ricklin, "Description of Optical Turbulence Effects on Propagation in the Atmospheric Surface Boundary Layer," in *Optical, Infrared and Millimeter Wave Propagation Engineering*, ed. by W.B. Miller and N.S. Kopeika (SPIE, 1988) Vol. 926
- ³³Miller and Ricklin, op. cit.
- ³⁴D.L. Fried, Rome Air Development Center, Griffiss AFB, NY, *Theoretical Study of Non-Standard Imaging Concepts* (1976) RADCR-76-51 (AD A023627)

³⁵D.L. Fried, "Optical Resolution Through a Randomly Inhomogeneous Medium for Very Long and Very Short Exposures," J.Opt.Soc.Am. 56 (1966) 1372

³⁶D.L. Fried, "Aperture Averaging of Scintillation," J.Opt.Soc.Am. 57 (1967) 169

³⁷D.L. Fried, "Theoretical Analysis of Aperture Averaging," Optical Science Consultants Report No. DR-015, Final Report on NASA Contract NAS5-23272

³⁸D.L. Fried, "Theoretical Study of Non-Standard Imaging Concepts," Interim Tech. Report on RADC Contract No. F30602-74-C-0115, RADC Report No. TR-74-185 (1974) and RADC Report No. TR-74-276 (1974)

³⁹D.L. Durack, "Method to Compute Space-Variant Image Degradation by Atmospheric Turbulence," in *Optical, Infrared and Millimeter Wave Propagation Engineering*, ed. by W.B. Miller and N.S. Kopeika (SPIE, 1988) Vol. 926

⁴⁰M.K. Giles and D.L. Durack, "A Convolution Model of Long-Exposure Image Blur Due to Atmospheric Turbulence," in *Optical, Infrared and Millimeter Wave Propagation Engineering*, ed. by W.B. Miller and N.S. Kopeika (SPIE, 1988) Vol. 926

DISCUSSION

V. THIEMANN

Ground humidity turned out to be a very important input parameter in models for C_n^2 . Do you plan to include this in future version of your model in order to make it more applicable to mid-latitude conditions?

AUTHOR'S REPLY

We certainly do. I realize that similarity theory allows for prediction of dq/dz , but I am uncertain how to do this best from a readily obtainable source; that is, the readily obtainable meteorological parameters. I will contact you later to obtain your suggestions. They will no doubt be valuable.

**Atmospheric Modelling Studies:
A Modelling Comparison Between IR and Millimetric Atmospheric Propagation.**

A.R. Tooth,
Advanced Information Processing Dept.,
British Aerospace P.L.C.,
Sowerby Research Centre,
Filton,
Bristol BS12 7QW.
UK.

Summary.

When viewing through the atmosphere, whether by naked eye or with some electro-optic sensor, your viewing performance is largely dictated by the composition of the intervening atmosphere. The composition of this atmosphere is continually changing with the fluctuations of the prevailing meteorology and will also differ in different geographical locations.

Despite the fact that it is known that prevailing meteorology affects sensor and consequently overall system performance the phenomena is seldom explored and is often made excessively complicated. A technique developed at the Sowerby Research Centre, at British Aerospace, allows the meteorological effect to be rigorously, but simply, evaluated.

Using the technique we have developed, in conjunction with atmospheric propagation models, for example LOWTRAN, we are able to perform realistic comparisons between different waveband IR systems and different millimetric frequency systems.

1. Introduction.

It is commonly accepted that the performance of electro-optic systems in particular, and other systems in general, is affected by the prevailing meteorology (weather). For example, the shorter wavelength systems (infra-red) used for communication links propagating through the atmosphere are critically dependent upon the prevailing weather. The longer wavelength systems too are not immune to the effects of weather, albeit to a lesser extent. However, when such systems are mathematically modelled this major factor contributing to system performance is often only given a cursory acknowledgement. At the BAe. Sowerby Research Centre we have resolved this problem by trying to find straightforward relationships between meteorology, properties of the atmosphere, and system performance.

The vital link between meteorology and system performance is made through a series of models, the majority of which we have developed ourselves and include models for target and background radiance, turbulence and the probability of achieving a cloud free line of sight or field of view. The internationally accepted LOWTRAN models, Ref. 1-3, are often used to relate meteorological data to atmospheric properties such as scattering and absorption, etc which in turn give rise to atmospheric transmission for specified wavelengths. A modified version of EOSAEL, (Electro-Optic System Atmospheric Effects Library), Ref. 4, provides similar information for the millimetric frequencies. The transmission is then used in conjunction with the other atmospheric models, and system models which describe the physical properties of the transmitter/receiver/target signature of the system in order to predict total operational performance.

In this paper we describe the techniques that we are currently using and a recent study to compare IR and millimetric atmospheric transmission.

2. The Use of Meteorological Data.

In the past it has been common practice to use average or synoptic meteorological records for modelling purposes, but statistically derived data of this nature has lost the all important correlation between the individual meteorological parameters. That is to say, a predicted value or statistically derived value of any meteorological parameter need not necessarily occur at the same time as any other predicted value. For example the average value of temperature will seldom occur at the same time as the average value of humidity or at the same time as any other average value.

We have found that using non correlated meteorological data gives rise to results which can be very misleading; in practice you are evaluating a system for conditions that in real life do not occur. We have also found that it is dangerous to assess 'weather related' effects in isolation from the interactions between the various constituent parts of the system and the system as a whole because this too can lead to a distorted view of total system performance. We have now devised a technique to predict 'All Year All Weather' system performance which has the ability to maintain the vital correlation between meteorological parameters. The technique also preserves the gross, but never the less interesting, effects such as diurnal and seasonal performance variations. One must also appreciate that just as meteorology varies from geographical location to location (deployment area) system performance will also vary and this too must be taken into account if a full and representative evaluation of a system is to take place.

When using our technique, firstly, a data base has to be constructed which contains a year's period of meteorological data. The meteorological descriptions required for the data base are collected from the geographical area of interest via the UK Meteorological Office at Bracknell and have been collected at 3

hourly intervals. The parameters within the data base usually cover phenomena such as visibility, cloud details, precipitation, temperature and humidity, etc.

The performance of each constituent part of the system (usually electro-optic or millimetric) is evaluated at each of the 3-hourly resolution steps throughout the data base (i.e. 2920 individual evaluations take place) in conjunction with the results from the atmospheric models. The sub-system results so obtained are then combined and a measure of total system performance obtained. The performance measure obtained at each step, for example a probability of target acquisition, is averaged at the end of the year's assessment in order to achieve an 'All Year All Weather' system performance.

3. Choice of Meteorological Data.

In order to achieve a realistic performance assessment care must be taken to ensure that the year chosen for the meteorological data base is a 'normal' year, i.e. not a year containing abnormal variations of weather such as very high or very low temperatures, excessive precipitation, etc as these could lead to unrepresentative results. To alleviate the problem of choosing what year to use we often do not choose a single year but several consecutive years, normally a ten year period. The ten year period is then statistically sampled, Ref. 5, in order to produce a single year which is 'representative' of the ten years of data. This technique enables the important correlations between individual items of meteorology to be maintained. However the lesser important correlation between adjacent time intervals is lost.

A validation exercise has shown that there are only small differences between the cumulative probability of occurrence curves derived from the 'representative year' and the curves derived from the original ten years of data. Sample of the validation curves are shown in Figures 1 and 2.

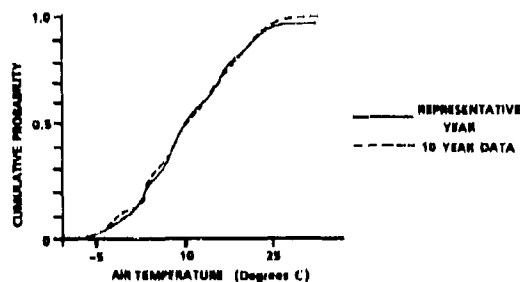


Figure 1. Validation of data base - Air Temperature.

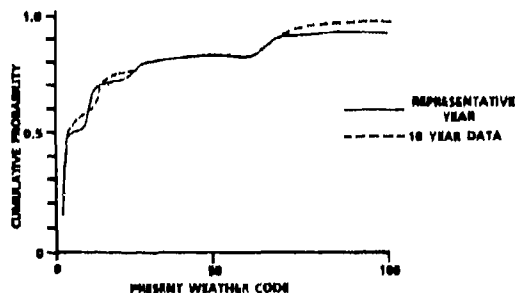


Figure 2. Validation of data base - Present Weather Code.

A further set of comparisons (using the 50% level) between the 'representative Year' and published Meteorological Office data has led us to accept the validity of our data reduction technique.

A development of the technique described above allows data from different but adjacent geographical locations to also be combined into a single representative year which can then be used for system assessments.

4. Infra-red vs. Millimetric Study.

In a current study, which uses the techniques described above, we are evaluating the all year variations between millimetric and infra-red atmospheric transmission. A small selection of the results which have been obtained are shown in Figures 3-6. These results are in the form of IR transmission vs. millimetric transmission for identical meteorological conditions. The IR wavelength transmissions have been predicted using LOWTRAN for both the 3-5 μm . and 8-12 μm . wavebands. The millimetric frequency transmissions have been predicted using our modified version of EOSAEL for 22, 35, and 94 GHz. Each of the following presented figures contain 2920 individual assessments of atmospheric transmission using meteorology from our meteorological data base for Northern Europe, a constant one way path of 5 km. has been used. Figure 3 compares the atmospheric transmissions of 22 GHz. and 35 GHz.

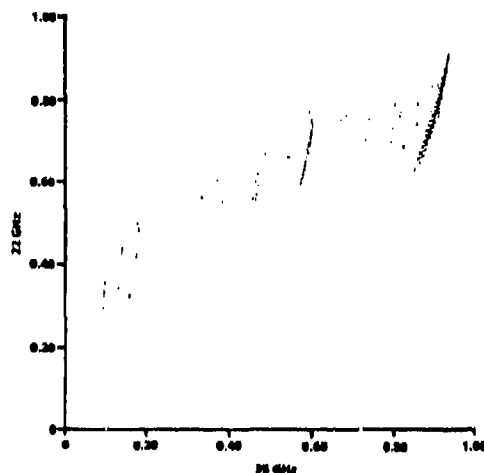


Figure 3. Comparison between transmission at 22 GHz and 35 GHz.

As expected the comparison shown in Figure 3 indicates that for the majority of occasions (85% of the time) the 35 GHz. frequency gives larger transmission values than the 22 GHz frequency. The occasions when 22 GHz. achieves higher transmission than 35 GHz. are attributable to rain events which affects the higher frequencies more than the lower frequencies.

If we consider IR transmission against that of millimetric, Figure 4 compares 3-5 μm . transmission against 94 GHz. We can see that on all occasions the millimetric transmission is higher than that of the IR waveband. However the transmission performance from the 8-13 μm . waveband, as shown in Figure 5, is greater than that of the 3-5 μm . band but still does not equal that of 94 GHz.

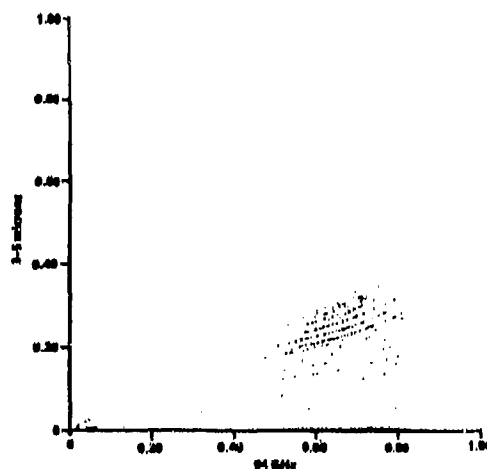


Figure 4. Comparison between transmission at 3 - 5 μm . and 94 GHz.

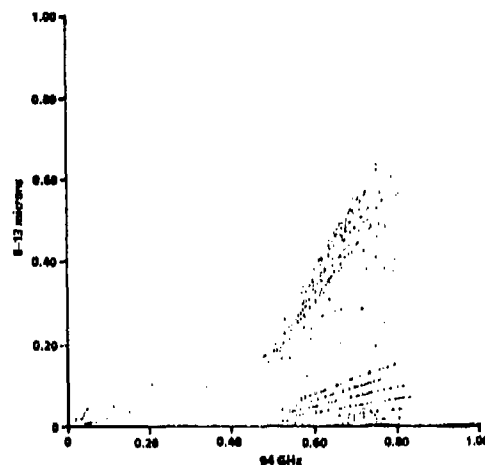


Figure 5. Comparison between transmission at 8 - 13 μ m. and 94 GHz.

Finally, Figure 6 compares 35 GHz. transmission against 94 GHz. It is interesting to note both the superiority of 35 GHz. and the overall trend of the data. These modelled results have been favourably compared with measured IR and millimetric transmission data obtained by the Radio Communications Research Unit at the Rutherford Appleton Laboratory, Ref. 6.

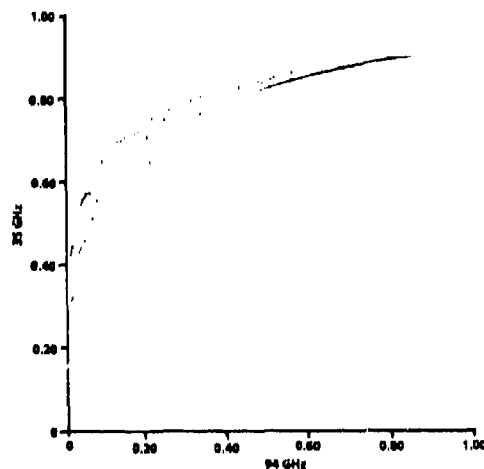


Figure 6. Comparison between transmission at 35 GHz and 94 GHz.

5. Conclusion.

We have developed a flexible but yet rigorous technique to help evaluate the effects of meteorology on system performance, and we have shown the relative magnitudes of IR and millimetric atmospheric transmissions. The philosophy of our technique is to use the atmospheric properties of the environment in order to predict the system performance that could be anticipated if that system was operating in a particular geographical area. Variations in performance may be produced on a yearly/seasonal/ diurnal basis for any geographical area where the meteorological records are available.

References.

1. McClatchey et al. Air Force Cambridge Research Laboratories. Atmospheric Transmittance from 0.25 - 28.5 μm . LOWTRAN 3, AFCL-TR-0255, 1975.
2. McClatchey et al. Air Force Geophysics Laboratory. Atmospheric Transmittance from 0.25 - 28.5 μm . Computer Code LOWTRAN 5, AFGL-TR-80-006, 1980.
3. Kneizys et al. Air Force Geophysics Laboratory. Atmospheric Transmittance/Radiance Computer Code LOWTRAN 6, AFGL-TR-83-0187, 1983.
4. D'Arcy, E. EOSAEL 84 (Vol. 23). Millimetre Wave System Performance Module, RADAR. TR-0160-23.
5. Tooth, A.R. Weather Related System Modelling. SPIE Vol. 492, 1984.
6. Gibbins, C.J. et al. Millimetre, Infra-red, and Optical Propagation Studies on a 500m. Range. Proc. V. Int. Conf. on Antennas and Propagation, ICAP 87. IEE Conf. Publ. 247, pp. 50-53.

FORMULES DE CALCUL RAPIDE DE LA TRANSMISSION INFRAROUGE EXEMPLES DE CALCUL

par A.M. Bouchardy
Office National d'Etudes et de Recherches Aérospatiales
BP 72, 92322 Châtillon Cedex, France

et A.P. Junchat
Centre Electronique de l'Armement
35998 Rennes Armées, France

RESUME

Une méthode de calcul rapide de la transmission infrarouge est décrite ; elle permet d'effectuer des calculs de transmission sur des trajets horizontaux avec une très bonne précision. Deux exemples d'application de cette méthode sont présentés ; le premier concerne la description d'une station météorologique permettant la détermination de la transmission infrarouge sur le terrain, le deuxième est la réalisation d'un atlas de la transmission infrarouge en France.

1. INTRODUCTION

Avec le développement des systèmes optroniques et l'utilisation accrue de matériels fonctionnant dans l'infrarouge, la connaissance des perturbations induites par l'atmosphère apparaît aujourd'hui comme une exigence fondamentale. Ce besoin s'exerce depuis la conception jusqu'à l'utilisation de ces matériels.

Au cours de la conception de ces instruments et de l'évaluation pratique ou théorique de leurs performances, il est en effet nécessaire de disposer de données statistiques sur la transmission atmosphérique sur les types de trajets envisagés et dans les lieux considérés.

Lors de leur utilisation opérationnelle, il est intéressant de disposer de moyens permettant d'optimiser le choix du domaine spectral du système d'arme à engager suivant les conditions d'environnement extérieures rencontrées. Pour ceci, il est donc nécessaire de disposer de modèles fiables, rapides en temps de calcul et fonctionnant sur de petits calculateurs. Les données d'entrée de ces modèles doivent être les plus simples possibles et facilement mesurables sur le terrain.

Après avoir passé rapidement en revue les phénomènes régissant la transmission infrarouge, une méthode de calcul rapide de la transmission infrarouge sera proposée et décrite. Deux exemples d'application seront ensuite présentés ; le premier concerne la description d'une station météorologique permettant la détermination de la transmission infrarouge sur le terrain, le deuxième est la réalisation d'un atlas de la transmission infrarouge en France.

2. PHENOMENES PHYSIQUES REGISSANT LA TRANSMISSION INFRAROUGE

Dans l'infrarouge, les phénomènes entrant en jeu pour atténuer le rayonnement transmis par l'atmosphère sont l'absorption et la diffusion par les constituants gazeux, d'une part, et l'absorption et la diffusion par les particules solides ou liquides en suspension : aérosols, brumes, brouillards, pluie, neige, nuages, aérosols produits artificiellement, d'autre part. Nous nous limiterons ici au cas de la transmission atmosphérique sur un trajet horizontal au voisinage du sol dans une atmosphère naturelle ; nous ne prendrons en compte ni la présence de nuages, ni les aérosols produits artificiellement, tels qu'on les trouve sur le champ de bataille [1, 2].

Les problèmes posés par le calcul sont différents suivant qu'il s'agit des gaz ou des particules ; nous allons les traiter successivement.

2.1. Diffusion moléculaire et absorption par les gaz

La diffusion par les gaz se traite par la diffusion Rayleigh. Le coefficient de diffusion est, dans ce cas, inversement proportionnel à la puissance quatrième de la longueur d'onde.

L'absorption par les gaz dans l'infrarouge est un phénomène extrêmement variable avec la longueur d'onde, car les gaz présentent un grand nombre de raies d'absorption dont la largeur typique est de $0,1 \text{ cm}^{-1}$, dans les conditions normales de température et de pression.

Cette absorption peut se calculer de manière exacte en utilisant des codes de calcul dits haute résolution ou raie par raie [3, 4, 5], qui prennent en compte toutes

les raies d'absorption caractéristiques des gaz actifs dans le domaine spectral considéré ; ces codes nécessitent des temps de calcul importants dans le cas d'intervalles spectraux larges. Leur utilisation est cependant indispensable pour le calcul de la transmission de faisceaux laser.

Nous nous limiterons ici au cas de la transmission dans une bande spectrale large (très supérieure à 20 cm^{-1}). Dans ce cas, des modèles de bande peuvent être utilisés. Leur principe consiste à supposer une distribution simple pour les intensités et les positions des raies de manière à pouvoir calculer aisément les coefficients d'absorption moyens sur une bande spectrale large par rapport à la largeur des raies.

Un des modèles de bande le plus connu dans les applications atmosphériques est le modèle LOWTRAN, développé par l'AFGL [6, 7]. Les absorbants gazeux pris en compte dans LOWTRAN sont : la vapeur d'eau, l'ozone, les gaz uniformément mélangés (CO_2 , N_2O , CH_4 , CO , O_3 et N_2).

Le calcul de l'absorption par les gaz sur un trajet donné peut se faire en utilisant LOWTRAN à condition de connaître la longueur du trajet, la pression, la température, la quantité de vapeur d'eau (la connaissance de la quantité d'ozone n'est pas nécessaire si on se limite à des altitudes inférieures à 10 km).

La précision des calculs est bonne et les résultats ont été validés tout au moins pour des distances inférieures à 10 km.

2.2. Absorption et diffusion par les particules

L'absorption et la diffusion par les particules varient nettement moins avec la longueur d'onde que dans le cas des gaz. Pour les calculer, il faut connaître le coefficient d'absorption ou de diffusion. Ceux-ci sont fonction de la distribution de taille des particules, de leur forme, de l'indice de réfraction complexe, de la longueur d'onde ; ils se calculent en utilisant la théorie de Mie dans le cas de particules sphériques [8]. Plus récemment, des codes ont été mis au point pour le cas de particules non-sphériques de formes particulières [9].

Cependant, la seule mesure météorologique systématique permettant d'appréhender le contenu en aérosols est la mesure de visibilité qui permet d'obtenir le coefficient d'extinction du milieu à $0,55 \mu\text{m}$ à l'aide de la formule :

$$\sigma(0,55) = 3,92/VIS. \quad (1)$$

Il n'existe toutefois pas de relation univoque entre le coefficient d'extinction à $0,55 \mu\text{m}$ et le coefficient d'extinction dans l'infrarouge.

Dans LOWTRAN, les aérosols de la basse atmosphère sont définis par leur type (rural, urbain, maritime) et par la visibilité. Pour chaque type d'aérosol, est fournie la correspondance entre la visibilité ou coefficient d'extinction dans le visible et les coefficients d'extinction aux différentes longueurs d'onde infrarouges. Le choix du type d'aérosol est l'une des principales difficultés rencontrées, le problème est un peu moins délicat dans le cas des brouillards et de la pluie.

Une méthode pour choisir le type d'aérosol sera proposée dans la suite. Elle est basée sur l'exploitation des résultats de mesures de transmission infrarouge effectuées au cours du programme OPAQUE [10, 11].

3. DESCRIPTION DE LA METHODE DE CALCUL RAPIDE

Compte tenu des problèmes différents posés par le calcul de la transmission par les molécules et par les particules, il est apparu important de pouvoir traiter séparément ces deux types de contribution.

La première hypothèse est que la transmission de l'atmosphère sur un trajet homogène de longueur D , intégrée sur une bande spectrale large (large par rapport à 20 cm^{-1}) peut s'écrire sous la forme d'un produit de deux termes :

$$T = T_m \times T_p \quad (2)$$

où T_m est la transmission moléculaire intégrée sur le même intervalle spectral et T_p la transmission due aux particules. Cette hypothèse est bien vérifiée, spécialement dans les fenêtres de transmission atmosphérique [12].

3.1. Calcul de T_m

La transmission moléculaire T_m peut s'écrire sous la forme :

$$T_m = \frac{\int_{V_1}^{V_2} S(V) \cdot R(V) \cdot \tau_m(V, D) dV}{\int_{V_1}^{V_2} S(V) \cdot R(V) dV} \quad (3)$$

où $S(V)$ est la luminance de la source au nombre d'onde V , $R(V)$ est la réponse spectrale de l'appareil de mesure et $\tau_m(V, D)$ est la transmission moléculaire sur le trajet D au nombre d'onde V .

Le principe de la méthode de calcul rapide consiste à faire des calculs dits exacts avec LONTRAM pour différentes conditions et représenter toutes les valeurs de T_m ainsi obtenues par un polynôme dont les coefficients sont obtenus par une méthode des moindres carrés. Pour limiter le nombre de paramètres à prendre en compte, on ne traitera que le cas d'un trajet horizontal de longueur variable au ras du sol, pour une fonction source et une réponse spectrale du récepteur connus. Dans ce cas, des calculs doivent être effectués pour différentes valeurs de la distance D , de la température de l'air t et de l'humidité relative RH ; les valeurs choisies pour ces trois variables doivent couvrir l'ensemble des conditions pour lesquelles on veut pouvoir utiliser les formules de calcul rapide.

La transmission moléculaire T_m peut se calculer à l'aide de la formule suivante :

$$T_m = \exp \left[a_1 + a_2 D + a_3 t' + a_4 \sqrt{WH \cdot D} + a_5 \sqrt{t' \cdot D} + a_6 \sqrt{t'} + a_7 \sqrt{D} + a_{10} \sqrt{WH} + a_{11} WH^2 + a_{12} D \sqrt{WH} + a_{13} D \cdot WH^2 \right] \quad (4)$$

où $a_1, a_2, a_3, a_4, a_5, a_6, a_7, a_{10}, a_{11}, a_{12}$ et a_{13} sont déterminés par une méthode des moindres carrés, WH est la quantité de vapeur en $g \cdot m^{-3}$, t' : température réduite ($t' = t/273,15$).

De telles formules ont été déterminées dans différents cas ; nous donnerons à titre d'exemple les cas suivants :

- S est un corps noir à une température supérieure de $5^\circ C$ à la température de l'air ambiant ;
- deux cas sont considérés pour R , correspondant à des réponses spectrales typiques de système dans la bande $3-5 \mu m$ et dans la bande $8-12 \mu m$ (Fig. 1a et 1b) ;

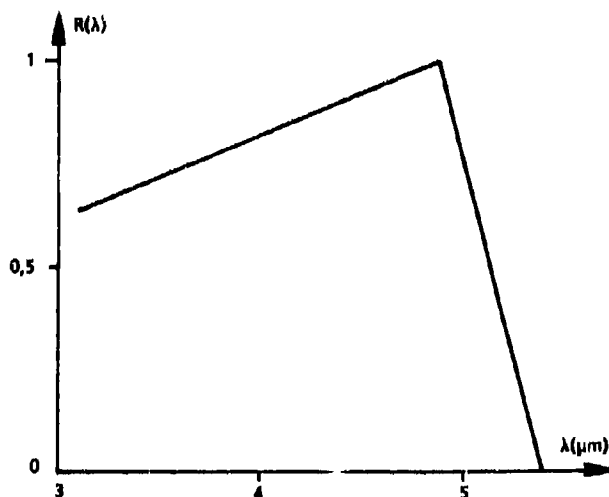


Fig. 1a - Réponse spectrale du filtre I.

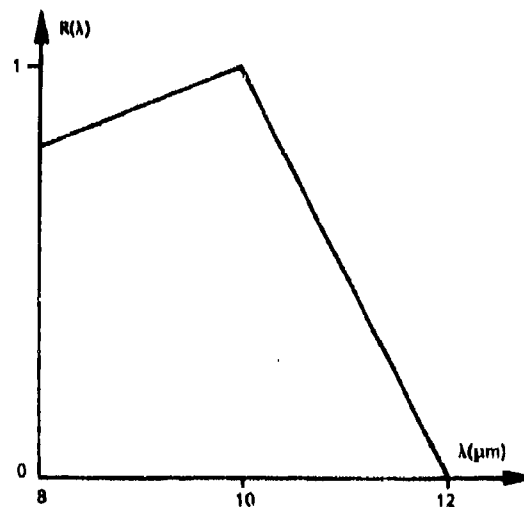


Fig. 1b - Réponse spectrale du filtre II.

- les valeurs de la distance D sont comprises entre 500 m et 5 km ;
- les valeurs de la température de l'air entre - 40° et + 40°C ;
- les valeurs de l'humidité relative sont comprises entre 20 et 99 %.

Les coefficients obtenus sont donnés dans les tableaux 1 et 2.

TABLEAU I
Coefficients des
polynômes donnant la
transmission moléculaire
pour le filtre I

-0,161332860.10²
0,149978170.10²
-0,479665207.10²
-0,158601651
0,120748378
0,533365884.10²
-0,255794485
0,106168701.10²
0,372892532.10²

TABLEAU II
Coefficients des
polynômes donnant la
transmission pour le
filtre II

-0,101290891.10³
-0,180136213.10⁻¹
-0,211764431.10³
-0,945825248.10⁻¹
0,793163546
0,276443669.10³
-0,691683000
0,365343221.10²
-0,564004194.10⁻²
0,489623633.10⁻¹
-0,866948422.10⁻⁴
0,132029218.10⁻¹
-0,4599119913.10⁻³

3.2. Calcul de T_p

On traite indépendamment le cas des aérosols, du brouillard et de la pluie ; la transmission T_p peut donc s'écrire sous la forme :

$$T_p = T_a \times T_{br} \times T_{pl} \quad (5)$$

où T_a est la transmission due aux aérosols, T_{br} celle due aux brouillards et T_{pl} celle due à la pluie.

Pour le calcul de la transmission due aux aérosols, on traite séparément le cas des trois modèles d'aérosols : ruraux, urbains ou maritimes. Pour chacun de ces modèles, la formule utilisée est la suivante :

$$T_a = \exp \left[a_1 + a_2 \cdot D \cdot RH^{-1} + a_3 \cdot D \cdot VIS^{-1} + a_4 \cdot D \cdot RH^{-2} + a_5 \cdot D \cdot RH^{-1} \cdot VIS^{-1} + a_6 \cdot D \cdot RH^{-1} + a_7 \cdot VIS^{-1} + a_8 \cdot D^2 \cdot VIS^{-2} + a_9 \cdot D \cdot RH^{-1/2} + a_{10} \cdot D \cdot VIS^{-1/2} + a_{11} \cdot D \cdot VIS^{-1} \cdot RH^{-1/2} + a_{12} \cdot D \cdot RH^{-1} \cdot VIS^{-1/2} \right] \quad (5)$$

où RH est l'humidité relative en % et VIS la visibilité en km. De telles formules ont été déterminées pour les conditions citées précédemment et pour des valeurs de la visibilité comprises entre 50 et 1 km. Les coefficients obtenus sont donnés dans les tableaux 3 et 4.

Pour la transmission due aux brouillards, la formule suivante est utilisée :

$$T_{br} = \exp [- 4,26 \cdot D \cdot VIS^{-1}] \quad (6)$$

Pour la transmission due à la pluie, la formule suivante a été retenue :

$$T_{pl} = \exp \left[- D \cdot (0,39 R^{1/2} + 0,03 R - 0,00016 R^2) \right] \quad (7)$$

Les résultats obtenus en utilisant ces formules sont en accord avec ceux obtenus avec LOWTRAN à mieux que 1 %. Le temps de calcul nécessaire est 100 fois plus faible que celui nécessaire avec LOWTRAN.

TABLEAU III
Coefficients des polynômes donnant la transmission
par les aérosols pour le filtre I.

| | AEROSOL RURAL | AEROSOL MARITIME | AEROSOL URBAIN |
|----------------------------------|---|--|--|
| Coefficients b_1 à b_{13} | 0,496722301.10 ⁻¹ 0,116204112 -0,284044408 0,677503697.10 ⁻¹ 0,209867002 -0,423463953.10 ⁻² -0,331392271.10 ⁻³ -0,109580400.10 ⁻³ 0,311730497.10 ⁻³ 0,552712152.10 ⁻¹ -0,597721695.10 ⁻³ -0,545826856 -0,269924422.10 ⁻² | -0,106744439.10 ⁻² 0,366393532 -0,300648638 -0,208031679 0,385606677.10 ¹ 0,106040874.10 ⁻¹ 0,581972509.10 ⁻³ 0,942989239.10 ⁻² 0,225600979.10 ⁻¹ -0,159206635 0,562181449.10 ⁻¹ -0,689055346.10 ¹ -0,494354053.10 ⁻¹ | 0,786115960.10 ⁻⁴ -0,192189662 -0,481693419 0,112570207 -0,810464800.10 ⁻¹ -0,707639773.10 ⁻² -0,515515089.10 ⁻³ -0,224527140.10 ⁻³ 0,511248823.10 ⁻³ 0,893889054.10 ⁻¹ -0,807267158.10 ⁻³ -0,378572360.10 ⁻² -0,344874076.10 ⁻² |

TABLEAU IV
Coefficients des polynômes donnant la transmission
par les aérosols pour le filtre II.

| | AEROSOL RURAL | AEROSOL MARITIME | AEROSOL URBAIN |
|----------------------------------|--|--|---|
| Coefficients b_1 à b_{13} | 0,300340000.10 ⁻¹ -0,152787278 -0,342753352 0,852706527.10 ⁻¹ -0,989051697.10 ⁻² -0,558614109.10 ⁻² -0,229704174.10 ⁻² -0,264696092.10 ⁻⁴ 0,353550645.01 ⁻² 0,722503789.10 ⁻¹ -0,309435019.10 ⁻² -0,130938827 -0,160877469.10 ⁻¹ | 0,357396137.10 ⁻² 0,763318749.10 ⁻¹ -0,163642339 -0,223094981.10 ⁻¹ 0,136502234.10 ¹ 0,819524609.10 ⁻³ 0,253127257.10 ⁻¹ -0,400847888.10 ⁻² 0,958051509.10 ⁻² -0,229633578.10 ⁻¹ 0,169260519.10 ⁻¹ -0,279731582.10 ¹ -0,168215905 | -0,812596623.10 ⁻⁴ -0,172369602 -0,410737778 0,994862786.10 ⁻¹ -0,157530637 -0,637544712.10 ⁻² 0,646295729.10 ⁻³ -0,910442908.10 ⁻⁴ 0,113152824.10 ⁻² 0,801364593.10 ⁻¹ -0,155434255.10 ⁻² 0,152983277 0,451058917.10 ⁻² |

4. EXEMPLES D'APPLICATIONS

4.1. Une station météorologique transportable dédiée aux mesures dans l'infrarouge [13]

La transmission des rayonnements infrarouges dans l'atmosphère est une donnée particulièrement importante, qui peut avoir une certaine influence sur la précision des mesures de signatures thermiques des cibles par exemple. C'est aussi une donnée permettant d'orienter le choix du système d'arme à engager.

Sur le terrain, on peut la mesurer avec un transmissionmètre ayant une réponse spectrale voisine de celle du capteur à utiliser ; mais les utilisateurs ne disposent pas toujours du matériel nécessaire. Aussi, une autre approche consiste à utiliser une station météorologique transportable et à calculer la transmission à partir des données mesurées et des formules simplifiées présentées précédemment.

Dans ce dernier contexte, une station météorologique transportable a été réalisée par le CELAR (Fig. 2). Elle comprend :

- un thermomètre,
- un hygromètre,
- un baromètre,

- une girouette,
- un anémomètre,
- un visibilimètre (VIDEOGRAPH fabriqué par la Société Impuls Physik, RFA).

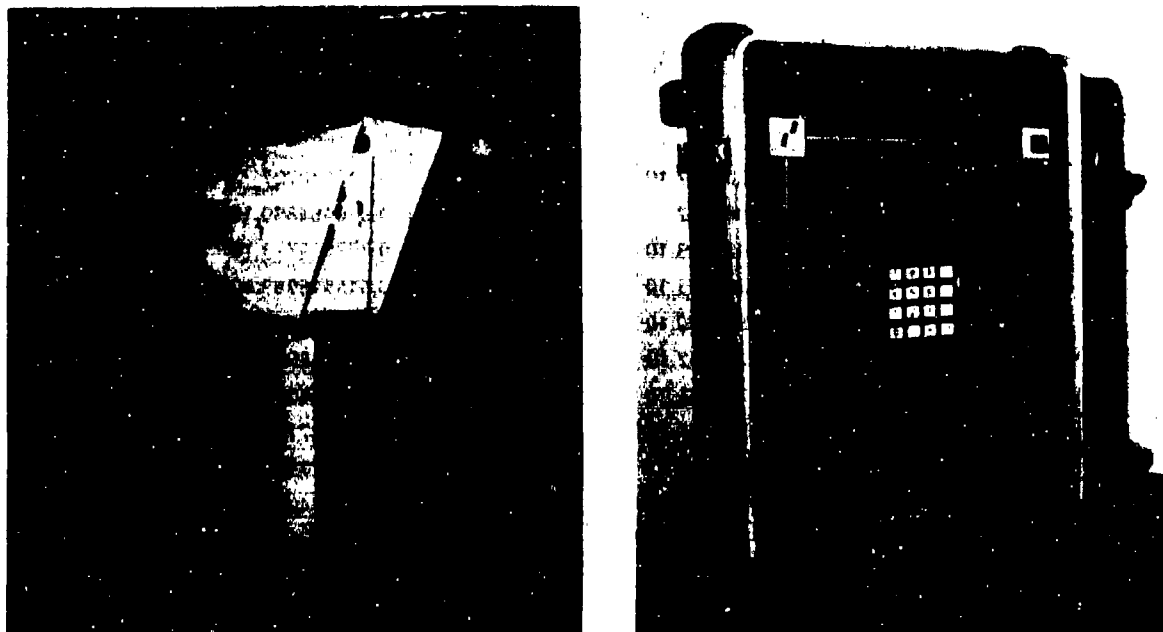


Fig. 2 - Photographies de la station.

La station est entièrement numérique et fonctionne avec un microprocesseur MSC 800.

Les formules de calcul rapide de la transmission infrarouge présentées ci-dessus ont été programmées ; il suffit donc d'introduire la distance pour obtenir les deux valeurs de la transmission.

4.2. Atlas de la transmission infrarouge en France [14]

Comme il a déjà été signalé dans l'introduction, il est important de pouvoir disposer de données statistiques de transmission dans la phase de conception d'un matériel fonctionnant dans l'infrarouge.

C'est pour répondre à ce besoin que le CELAR, avec l'aide du Service Central de la Météorologie Nationale, a calculé sur tout le territoire français des probabilités de transmission en bandes 3-5 et 8-12 μm , pour répondre à des applications terrestres (à noter qu'un atlas à peu près similaire a été réalisé pour la Marine Nationale).

Les transmissions ont été calculées en utilisant les formules simplifiées décrites précédemment et les triplets tri-horaires de température, humidité, visibilité mesurés par la Météorologie Nationale. Ces données proviennent des relevés synoptiques effectués entre 1949 et 1982 dans treize stations météorologiques françaises.

La figure 3 montre les emplacements géographiques des stations météorologiques choisies et les régions dont elles sont représentatives.

Les données d'entrée nécessaires au calcul des transmissions effectué à l'aide des formules simplifiées sont les suivantes :

- température : on utilise la valeur mesurée ;
- humidité relative et quantité de vapeur d'eau : on utilise la valeur mesurée de l'humidité relative et on calcule, à l'aide de la formule classique, la quantité de vapeur d'eau à partir des valeurs de l'humidité relative et de la température mesurées ;
- visibilité : on utilise la valeur mesurée ;
- type de particule : on n'a considéré ici que le cas des aérosols et des brouillards et on a éliminé les conditions "avec pluie" pour lesquelles on ne disposait pas de données suffisantes. Lorsque la visibilité est inférieure à 1 km, on utilise la formule correspondant au brouillard ; lorsque la visibilité est supérieure ou égale à 1 km, on choisit un type d'aérosol en utilisant la méthode ci-après.

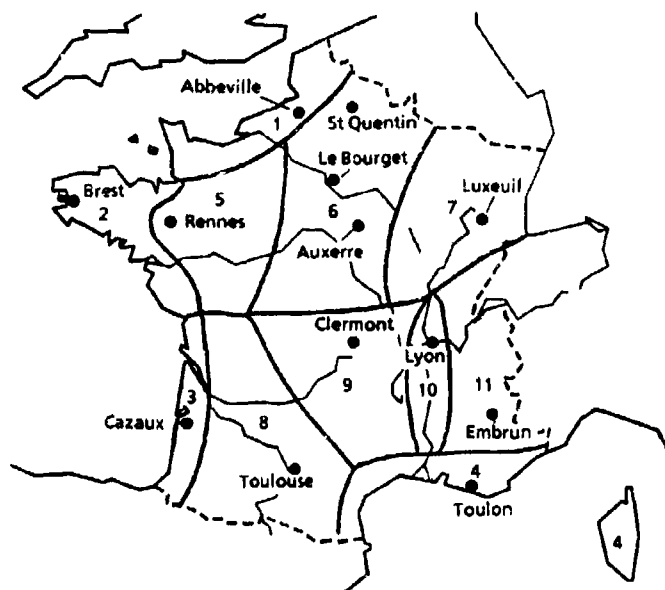


Fig.3 - Position géographique des stations.

Le coefficient d'extinction est calculé en utilisant la formule suivante :

$$\sigma_{e,t}(\lambda) = C_1 \sigma_{e,s}(\lambda) + C_2 \sigma_{e,u}(\lambda) + C_3 \sigma_{e,r}(\lambda) \quad (8)$$

avec :

$$\begin{aligned} 0 &\leq D_c < 10 \text{ km} & C_1 &= 0,5 \\ 20 &\leq D_c < 100 \text{ km} & C_1 &= 0,3 \\ C_1 + C_2 + C_3 &= 1 \end{aligned}$$

idem pour C_2

Les transmissions dans les deux bandes infrarouges choisies sont ensuite calculées pour chaque station, chaque triplet tri-horaire pour les 35 années de mesure et pour différentes valeurs de la distance : 500, 1000, 1420, 3000 et 5000 m. Un temps de calcul 100 fois plus faible que celui qu'aurait nécessité l'utilisation de LOWTRAN a été obtenu.

Les résultats ont été traités de manière à obtenir des probabilités d'avoir une transmission donnée en un lieu donné, sur une distance donnée, pour différentes saisons ou pour différentes heures de la journée ; des exemples de résultats sont montrés sur la figure 4.

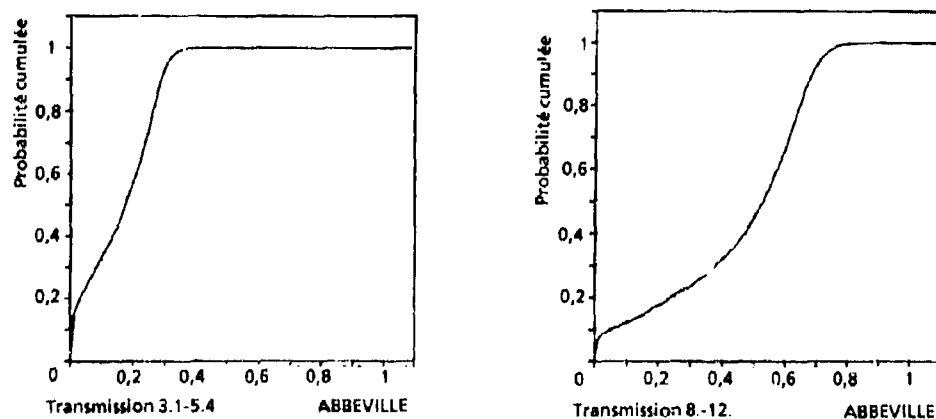


Fig. 4 - Statistiques des transmissions sur un trajet de 3000 m à Abbeville.
a) bande I; b) bande II.

Les résultats de cet atlas sont contenus dans cinq disquettes de 5 1/4 pouces MS DOS ; un menu permet de choisir :

- la station,
- le mois,
- la bande spectrale,
- la distance,
- la période de la journée : 0 à 6 h, 12 à 18 h et 0 à 24 h.

Le résultat obtenu est un histogramme cumulé.

5. CONCLUSION

Des formules permettant un calcul rapide de la transmission sur des trajets horizontaux ont été établis pour deux bandes spectrales typiques ; ces formules permettent de calculer les transmissions avec une précision identique à celle du code LOWTRAN, puisqu'il a été montré que l'écart entre les valeurs des transmissions calculées avec ces formules ou avec LOWTRAN ne dépasse jamais 1 %. Cette précision est nettement supérieure aux incertitudes introduites par le choix d'un modèle d'aérosol.

Concernant ce choix du modèle d'aérosol, une méthode qui donne de bons résultats d'un point de vue statistique a été proposée.

REFERENCES

- [1] R.C. Shirkey, *Determination of atmospheric effects through EOSAEL*, SPIE, 925, Optical, Infrared and Millimeter Wave Propagation Engineering, p. 205-212, 1988.
- [2] D.H. Höhn, *Introduction to optical problems of systems*, AGARD Lecture Series 93, p. 1.1-1.8, 1978.
- [3] S.A. Clough, F.X. Kneizys, E.P. Shettle, G.P. Anderson, *Atmospheric radiance and transmittance: FASCOD2*, 6th Conference on Atmospheric Radiation, Williamsburg, mai 1986.
- [4] W.L. Ridgway, R.A. Moose, A.C. Cogley, *Atmospheric transmittance/radiance computer code FASCOD2*, AFGL-TR-82-0392, octobre 1982.
- [5] L.S. Rothman, R.R. Gamache, L.R. Brown, R.A. Toth, H.M. Pickett, R.L. Foynter, J.P. Flaud, C. Camy-Peyret, A. Barbe, N. Husson, C.P. Rinsland, M.A.H. Smith, *The HITRAN database: 1986 Edition*, Applied Optics, 26, 4058, 1987.
- [6] F.X. Kneizys, E.P. Shettle, *Atmospheric transmittance, radiance: computer code LOWTRAN 5*, AFGL-TR-80-0067, 1980.
- [7] F.X. Kneizys, E.P. Shettle, *Atmospheric transmittance, radiance: computer code LOWTRAN 6*, AFGL-TR-83-0187, 1983.
- [8] E.J. McCartney, *Optics of the atmosphere scattering by molecules and aerosols*, John Wiley & Sons, 1976.
- [9] H. Takano, J. Hirose, S. Okuda, *Light scattering properties of non-spherical aerosol particles*, *Aerosols: Formation and Reactivity*, 1986.
- [10] T. Bakker, *The measurement program OPAQUE of AC/243 (Panel IV/RSG8) on sky and terrain radiation*, AGARD Conference Proceedings, 183, p. 14.1-14.10, 1975.
- [11] A. Junchat, *Technical information sheet on the OPAQUE programme*, Rapport CELAR, n° DT/50200, 1980.
- [12] A.M. Bouchardy, *Méthode de calcul rapide de la transmission infrarouge de l'atmosphère*, *La Recherche Aérospatiale*, 3, p. 193-201, 1984.
- [13] A.P. Junchat, *Station météorologique transportable dédié aux mesures infrarouges*, Rapport CELAR ASRE/042/ASRE 16424, 16/2, 1988.
- [14] A.P. Junchat, *Atlas de la transmission infrarouge dans l'atmosphère en France*, Rapport CELAR ASRE/152/ASRE 65403, 3/7, 1985.

REMERCIEMENTS

Les auteurs souhaitent adresser leurs remerciements au Service Central de la Météorologie Nationale et à G. Le Khun (CELAR) pour la réalisation de l'atlas infrarouge.

Leur gratitude s'adresse aussi au groupe de coordination optronique GC3 de la Direction de l'Electronique et de l'Informatique, grâce au financement duquel ces travaux ont pu être menés à bien.

| REPORT DOCUMENTATION PAGE | | | |
|---|--|--|--|
| 1. Recipient's Reference | 2. Originator's Reference AGARD-CP-454 | 3. Further Reference ISBN 92-835-0548-4 | 4. Security Classification of Document UNCLASSIFIED |
| 5. Originator | Advisory Group for Aerospace Research and Development North Atlantic Treaty Organization 7 rue Ancelle, 92200 Neuilly sur Seine, France | | |
| 6. Title | ATMOSPHERIC PROPAGATION IN THE UV, VISIBLE, IR AND MM-WAVE REGION AND RELATED SYSTEMS ASPECTS | | |
| 7. Presented at | the Electromagnetic Wave Propagation Panel Specialists' Meeting held in Copenhagen, Denmark, 9—13 October 1989. | | |
| 8. Author(s)/Editor(s) Various | 9. Date March 1990 | | |
| 10. Author's/Editor's Address Various | 11. Pages 378 | | |
| 12. Distribution Statement | This document is distributed in accordance with AGARD policies and regulations, which are outlined on the Outside Back Covers of all AGARD publications. | | |
| 13. Keywords/Descriptors | | | |
| <div style="display: flex; justify-content: space-between;"> <div> MM waves Propagation models Atmospheric absorption </div> <div> Laser radar, Sensing, Performance modelling. </div> </div> | | | |
| 14. Abstract | | | |
| <p>Atmospheric propagation of electromagnetic waves at frequencies above 30 GHz, i.e. millimetre (MM) waves and infra-red (IR), visible and to some extent also ultra-violet (UV) radiation, is of importance to many current and future military applications. Propagation phenomena affect and often limit navigation, communications, surveillance, search, target acquisition, fire control, autonomous weapons guidance, kill assessment, countermeasures and medium to high power laser applications.</p> <p>Recent advances in components and technology have prompted extensive studies and novel applications in the above wavelength region. Specifically, second generation infra-red detector technology, smart image processing, as well as active coherent detection systems, i.e. millimetre wave and laser radars, have required dedicated propagation studies, including much longer ranges over land and sea, multiple scattering effects and especially turbulence induced systems limitations.</p> <p>An exchange of information between scientists and engineers involved in research and development in this wavelength region is expected to benefit further development of systems and explore new areas of research as well as military and civilian applications. The following topics have been discussed during the 45th symposium of EPP.</p> <div style="display: flex; justify-content: space-between;"> <div> 1. Propagation measurements; 2. Propagation models; 3. Sensing of the propagation environment; </div> <div> 4. System aspects and performance modelling; 5. Countermeasures. <i>Keywords</i> </div> </div> | | | |